Award Number: W81XWH-15-1-0272

TITLE: Low-Cost, High-Throughput 3D Pulmonary Imager Using Hyperpolarized Contrast Agents and Low-Field MRI

PRINCIPAL INVESTIGATOR: Boyd M. Goodson, Ph.D.

CONTRACTING ORGANIZATION: Southern Illinois University
Carbondale, IL 62901

REPORT DATE: October 2016

TYPE OF REPORT: Annual

PREPARED FOR: U.S. Army Medical Research and Materiel Command
Fort Detrick, Maryland 21702-5012

DISTRIBUTION STATEMENT: Approved for Public Release;
Distribution Unlimited

The views, opinions and/or findings contained in this report are those of the author(s) and should not be construed as an official Department of the Army position, policy or decision unless so designated by other documentation

REPORT DOCUMENTATION PAGE

Form Approved
OMB No. 0704-0188

Public reporting burden for this collection of information is estimated to average 1 hour per response, including the time for reviewing instructions, searching existing data sources, gathering and maintaining the data needed, and completing and reviewing this collection of information. Send comments regarding this burden estimate or any other aspect of this collection of information, including suggestions for reducing this burden to Department of Defense, Washington Headquarters Services, Directorate for Information Operations and Reports (0704-0188), 1215 Jefferson Davis Highway, Suite 1204, Arlington, VA 22202-4302. Respondents should be aware that notwithstanding any other provision of law, no person shall be subject to any penalty for failing to comply with a collection of information if it does not display a currently valid OMB control number. **PLEASE DO NOT RETURN YOUR FORM TO THE ABOVE ADDRESS.**

1. REPORT DATE
October 2016

2. REPORT TYPE
Annual

3. DATES COVERED
30 Sep 2015 - 29 Sep 2016

4. TITLE AND SUBTITLE
Low-Cost, High-Throughput 3D Pulmonary Imager Using Hyperpolarized Contrast Agents and Low-Field MRI

5a. CONTRACT NUMBER

5b. GRANT NUMBER
W81XWH-15-1-0272

5c. PROGRAM ELEMENT NUMBER

6. AUTHOR(S)
Boyd M. Goodson, Ph.D.

E-Mail: bgoodson@chem.siu.edu

5d. PROJECT NUMBER

5e. TASK NUMBER

5f. WORK UNIT NUMBER

7. PERFORMING ORGANIZATION NAME(S) AND ADDRESS(ES)
Southern Illinois University,
Carbondale IL 62901

8. PERFORMING ORGANIZATION REPORT NUMBER

9. SPONSORING / MONITORING AGENCY NAME(S) AND ADDRESS(ES)
U.S. Army Medical Research and Materiel Command
Fort Detrick, Maryland 21702-5012

10. SPONSOR/MONITOR'S ACRONYM(S)

11. SPONSOR/MONITOR'S REPORT NUMBER(S)

12. DISTRIBUTION / AVAILABILITY STATEMENT
Approved for Public Release; Distribution Unlimited

13. SUPPLEMENTARY NOTES

14. ABSTRACT
According to the original statement of work we have focused our activities on three specific aims. With regards to Aim #1, we have completed the design & prototyping of ^{129}Xe automated hyperpolarizer & began polarizer prototype/final design construction and testing; With regards to Aim #2, we have focused a considerable amount of time on investigating the fundamental parameters of propane hyperpolarization and lifetimes in the gas and liquid phase. In particular, we have studied the pressure dependence of the propane lifetimes and high and low magnetic fields. We also discovered that propane lifetime can be significantly extended in the liquid state. Moreover, we also investigated both approaches: homogeneous and heterogeneous hydrogenation in the context of propane hyperpolarization and demonstrated that up to 9% polarization can be achieved (an order of magnitude improvement vs. preliminary results. These discoveries guided our efforts for the overall propane hyperpolarizer design. Regarding aim #3, we have worked with equipment vendors and finalized the design of the low-field MRI scanner. We also note that we are submitting a duplicating report for two partnering PI awards of the same project: W81XWH-15-1-0271 and W81XWH-15-1-0272.

15. SUBJECT TERMS
low-field MRI; pulmonary imaging, high-throughput; low cost

16. SECURITY CLASSIFICATION OF:			17. LIMITATION OF ABSTRACT	18. NUMBER OF PAGES	19a. NAME OF RESPONSIBLE PERSON
a. REPORT	b. ABSTRACT	c. THIS PAGE			USAMRMC
Unclassified	Unclassified	Unclassified	Unclassified	203	19b. TELEPHONE NUMBER *(include area code)*

Table of Contents

Page

1. INTRODUCTION 4

2. KEYWORDS 4

3. ACCOMPLISHMENTS 5

TASK 1.1. DESIGN OF AUTOMATED ^{129}XE HYPERPOLARIZER 5
TASK 1.2. PROTOTYPING OF AUTOMATED ^{129}XE HYPERPOLARIZER 5
TASK 1.3. PROTOTYPE CONSTRUCTION AND TESTING 5
TASK 1.4. FINAL DESIGN 5
TASK 1.5. FINAL CONSTRUCTION 6
TASK 2.1. CHEMISTRY OF LARGE SCALE PHIP OF PROPANE 6
TASK 2.2. INITIAL PHIP POLARIZER DESIGN 7
TASK 3.1. DESIGN LOW-FIELD MRI SYSTEM WITH COMMERCIAL VENDORS 7
TASK 3.2. LOW-FIELD MRI SYSTEM CONSTRUCTION BY VENDORS 7
WHAT OPPORTUNITIES FOR TRAINING AND PROFESSIONAL DEVELOPMENT HAS THE PROJECT PROVIDED? 7
HOW WERE THE RESULTS DISSEMINATED TO COMMUNITIES OF INTEREST? 8

4. IMPACT 8

WHAT WAS THE IMPACT ON THE DEVELOPMENT OF THE PRINCIPAL DISCIPLINE(S) OF THE PROJECT? 8
WHAT WAS THE IMPACT ON OTHER DISCIPLINES? 8
WHAT WAS THE IMPACT ON TECHNOLOGY TRANSFER? 8
WHAT WAS THE IMPACT ON SOCIETY BEYOND SCIENCE AND TECHNOLOGY? 8

5. CHANGES / PROBLEMS 8

6. PRODUCTS 8

ORAL PRESENTATIONS 8
CONFERENCE ABSTRACTS 9
PEER-REVIEWED MANUSCRIPTS, DISSERTATION & BOOK CHAPTERS 9
INVENTIONS, PATENT APPLICATIONS AND LICENSES 10

7. PARTICIPANTS & OTHER COLLABORATING ORGANIZATIONS 11

INDIVIDUALS WORKED ON THE PROJECT 11
HAS THERE BEEN A CHANGE IN THE ACTIVE OTHER SUPPORT OF THE PD/PI(S) OR SENIOR/KEY PERSONNEL SINCE THE LAST REPORTING PERIOD? 15
WHAT OTHER ORGANIZATIONS WERE INVOLVED AS PARTNERS? 15

8. SPECIAL REPORTING REQUIREMENTS 15

COLLABORATIVE AWARD 15

9. APPENDICES 16

APPENDIX 1: ORIGINAL STATEMENT OF WORK, YEARS 1-3 16
APPENDIX 2: ABSTRACTS PRESENTED AND MANUSCRIPTS PUBLISHED AND ACCEPTED 19

1. Introduction

We are developing clinical scale production of two gaseous hyperpolarized contrast agents and hyperpolarized MRI allowing for ultrafast (potentially sub-second) and high-throughput molecular imaging of lung function. The key additional focus of this project is on significantly lower cost of our imaging technology of low-field MRI compared to conventional high-field (1.5 T and beyond) MRI due to much higher patient throughput/much faster exams and the use of low field = low cost MRI. We focus our research effort on the high-risk and critical challenges that must be solved to enable clinical implementation of hyperpolarized gases for pulmonary imaging.

Specifically, the research efforts during Year 1 have focused on three specific aims as described in Statement of Work (Appendix 1):

Aim 1: Develop and construct a fully automated high-pressure low-cost stand-alone ^{129}Xe hyperpolarizer
Aim 2: Develop a large-scale hyperpolarization method for HP propane
Aim 3: Develop and construct a 0.05 T MRI scanner

It should also be noted that this report cites many recently published works, and the report is therefore significantly streamlined with references to relevant publications. All pertaining details can be found in the corresponding peer-reviewed publications and manuscripts, which are supplied in this progress report. We also note that 14 such publications, accepted manuscripts and 1 dissertation have been produced during Year 1 of the funding period, which represents our commitment to research and overall progress tempo with regards to this project, and also demonstrates the fact that the work conduced under this funding is novel. The copies of all publications, submitted manuscripts and conference abstract are provided in the Appendix 2. They contain a significant amount of technical and specialized information.

2. Keywords

Low-field MRI, lung imaging, molecular imaging, functional imaging; propane; xenon-129; NMR; MRI; hyperpolarization.

3. ACCOMPLISHMENTS

Please, refer to Appendix 1 for the statement of work of the entire project. The following sections describe the specific areas/tasks of the project conducted during Year 1 of this project.

Task 1.1. Design of automated ^{129}Xe hyperpolarizer

This project funded our activities for construction of the 3rd generation automated ^{129}Xe clinical-scale hyperpolarizer. Naturally, this project builds on the success of two previous generations of the ^{129}Xe clinical-scale hyperpolarizers. We have completed the design of the hyperpolarizer device in a timely manner and developed a few key components' prototypes. All key mechanical elements were designed in SolidWorks 3D CAD software. We have also decided on the vendors for all key components of this hyperpolarizer device. Despite the fact that most components were new, we ordered all parts during Year 1. This included a low-cost high-resolution IR-spectrometer, water chiller, and more critically, a new (more spectroscopically homogenous and more energy efficient) LDA laser. Moreover, we identified the vendor for custom-made software for automation and integration of the hyperpolarizer device and the low-field low-cost NMR spectrometer. We placed all orders for these custom components. Outsourcing these key components will significantly accelerate the overall tempo of this project Aim.

Task 1.2. Prototyping of automated ^{129}Xe hyperpolarizer

We have prototyped several components of the hyperpolarizer.

a) First, we explored the idea that full metal optical-pumping cell would allow for SEOP hyperpolarization of ^{129}Xe if it is coated with protecting layer of siliconizing agent. The prototype was made by the VU team and tested by the SIU team. While the first results are encouraging, we realize that it will require developing specialized coating agent and procedure for this method to work as good as the glass optical-pumping cell design. So, we did NOT proceed with this design for the final hyperpolarizer construction under this project (but this approach will still be a subject of future study).
b) In parallel, we have developed the prototype for the aluminum jacket for a glass optical-pumping cell to serve as a heating and cooling elements. After two rounds of manufacturing, we were able to successfully develop the prototypes, which passed our tests for cooling and heating the cell so far. This design was used in the final design of the hyperpolarizer;
c) We have also experimented with addition of He gas to a Xe/N_2 mix to increase gas thermal conductivity. The initial tests are very encouraging (and show no deterioration of the hyperpolarization SEOP process performance) and will likely be used in the final design.
d) Finally, we re-designed the optical pumping cell with improved stopcock valve operation.

Task 1.3. Prototype Construction and testing

As described above we developed and tested a few prototypes related to the very core of the SEOP polarization procedure. We have performed addition design work related to the RF coil design for operation at 40 kHz. After several prototypes, we developed an integrated RF coil solution that provides excellent RF shielding from the environment via 1-2 mm aluminum wall shielding. The integrated design also allowed us to incorporate a water phantom that will serve as an internal calibration standard for quality assurance of the produced ^{129}Xe hyperpolarized gas as well as would allow for the static magnetic field calibration (note the direction of the Earth's field may shift our resonance frequency by up to 2 kHz).

We have also developed and prototyped an 8" diameter compensated electromagnet using a home-built magnet winding setup. The initial tests with low-field NMR were very encouraging, and the prototype magnet will be used in the final construction of the hyperpolarizer. Remarkably, this design allows decreased power consumption by approximately 2 fold (to ~100 W) at <10% of the previous generation magnet weight. This achievement is the result of two advances: use of a solenoid geometry/design and reduction of the electromagnet diameter from 24" to 8". The latter improvement has also led to overall footprint reduction of the hyperpolarizer device.

Task 1.4. Final Design

Final Design of the ^{129}Xe hyperpolarizer has been completed and we have placed all purchase orders for key components. Some of the components arrived and allowed us to begin the final construction of the ^{129}Xe hyperpolarizer.

Task 1.5. Final Construction

Final construction of the ^{129}Xe hyperpolarizer has just begun. It will consume most of our activities during Year 2 of the project – in line with the proposed SOW.

Task 2.1. Chemistry of Large Scale PHIP of propane

The chemistry of the large-scale parahydrogen induced polarization (PHIP) of propane was investigated using two different approaches of homogeneous (in liquid medium) and heterogeneous (gas over solid-phase support) hydrogenation methods.

With regards to heterogeneous hydrogenation, we have developed a prototype setup for hyperpolarization and used it for mapping key relaxation parameters in the gaseous phase in high and low magnetic field regimes as a function of partial pressures of gases (parahydrogen and propane). This systematic approach confirmed our initial observation that low fields enable longer relaxation times for hyperpolarized propane gas. Moreover, we identified that the relaxation constant can be extended up to 10 s (vs. 5 s shown previously) under conditions of higher gas pressures. We have also demonstrated that the relaxation constant can be as long as 1 minute in the liquid phase (so the intermediate gas condensation can be a very good strategy to increase the production quantity without increasing the production flow-rate: e.g. instead of producing gas for 3 s, we can potentially produce for 30 s and store the polarization in the liquid state without significant polarization losses!). Overall, we strongly believe that the relaxation gains explored will make the low-field production and imaging a viable approach for production of clinical-scale quantities of hyperpolarized propane gas.

We have additionally experimented with more advanced heterogeneous catalysts: with reduced particle size – now down to 7 Å vs. the previously used ~13 Å particle size (~4X smaller in surface area). So far we have finished the tests with the liquid phase (liquid over solid-phase catalysts), but we will extend it to propane in our hyperpolarizer device. Working with our collaborators from ITC, Novosibirsk, Russia, we secured sufficient quantities of 1% loaded nanoparticles on TiO_2 catalyst for construction of a clinical scale device (~2 g vs. 0.01-0.05 g previously used in the feasibility studies). Note that this is a state-of-the-art nanomaterial not available commercially.

Figure 1. Clinical 15-ton 80-cm gap 0.05 T magnet during installation in Vanderbilt University Hospital building.

In the context of homogenous hydrogenation of propene to produce hyperpolarized propane via PHIP hyperpolarization process, we have demonstrated that although the continuous-flow operation provides very low polarization yields (~0.1%), the batch-mode hydrogenation can provide up to 9% proton polarization. While the initial prototype will be constructed based on heterogeneous hydrogenation, we will likely attempt to test automated homogenous production in the context of an automated device. Both technologies of propane production are scalable.

Despite the fact that the MRI scanner will be constructed later in the project, we utilized our recently installed MRI systems (operating at the same field, one of them is shown in Figure 1) for initial tests to study spin-lock induced crossing (SLIC) transformation of the long-lived pseudo-singlet states into observable magnetization – the key aspect of imaging technology making propane production feasible and useful at low-magnetic fields, because the use of low magnetic fields extends the lifetime of the hyperpolarized state. We studied this phenomenon in both the liquid state (using model systems and compounds) as well as in gaseous hyperpolarized propane. We found excellent quantitative agreement between theory and experiment. This is critical, because now when the theory is validated, it can serve as a detailed model for future simulations and optimizations. Practically speaking we demonstrated and studied a key parameter affecting the efficiency of SLIC transformation. Specifically, it was confirmed that the magnetic field (B_0) homogeneity of the main magnet is critical. Indeed, B_0 inhomogeneity must be smaller or on the order of the B_1 power used to drive these SLIC transitions. We also confirmed that the magnet constructed under the synergistic DOD award will be of sufficiently good quality for the studies proposed. This determination eliminates a lot of risks for this naturally high-risk/high-reward project.

Task 2.2. Initial PHIP Polarizer Design

Based on the advances described above we completed the overall polarizer design and the prototyping efforts. The polarizer will include the driver module and an NMR spectrometer. These already have been ordered from the commercial vendor, who will also design custom software for running the automated operation of the propane hyperpolarizer. The additional components will include a gas manifold, and potentially in situ detection capability – subject to future testing. The prototype system will take advantage of the high-resolution NMR spectrometer (purchased and already installed) providing 1.4 T field, sufficient for high-resolution NMR studies to optimize the prototype that will be developed during Year 2 of the project. We have also completed the overall prototype design, which will be constructed during Year 2 of the project.

Task 3.1. Design low-field MRI system with commercial vendors

The overall system design was developed through multiple and thorough contacts with vendors. The design is finalized using (in part) the resources of the synergistic DOD award. Specifically, we will employ the same 0.05 T magnet (shown in Figure 1), TecMag dual-channel MRI console, and the set of gradients and amplifiers made by Techron and integrated by TecMag in their system.

Task 3.2. Low-field MRI system construction by Vendors

This has been delayed: see the explanation below.

While RF coil design was not part of the proposed studies during Year 1 (instead it was designed for Year 2), our team has designed an RF coil prototype of ~0.5 L size to test key parameters related to RF coil performance at 2 MHz. We find that the prototype performed well (it was already used to generate publishable data for hyperpolarized propane) in addition to the good performance of the developed RF shield (to eliminate the background noise). In the next few months (of Year 2) our team is focusing on scaling up this prototype to a human-scale RF coil and shield and developing two RF coils for ^{129}Xe and ^{1}H imaging as proposed under this project.

Summary Statement: Overall, we believe the progress towards Aim 3 was slower than anticipated due to delays with equipment delivery for other projects that provide a significant degree of synergy: *i.e*. this synergistic project is paving the way to this project with respect to LF MRI system design, integration, etc. Since we experienced significant delays with equipment delivery for the other project, it impacted this project because we could not make a good judgment for making the purchasing decision. While we managed to come up with the overall design for the LF MRI system, and discussed the key components with the vendors, we did not place the orders yet. These orders will be placed during Year 2 of the project. As a result of the above delays, our team has focused more effort on Aim #1: indeed, we significantly outpaced our progress and completed not only the activities planned for Year 1, but also completed some of the activities initially planned for Year 2. During the next years of project performance, we expect that the progress will achieve overall balance. The activities towards Aim 2 of the project were on time with the approved schedule on original SOW (see Appendix 1).

What opportunities for training and professional development has the project provided?

This project provided numerous opportunities and enabled a great deal of career development.

1) Prof. Chekmenev received a very prestigious honor. He was named a Professor of the Russian Academy of Sciences for his efforts to develop imaging markers for cancer and lung disease using hyperpolarized magnetic resonance imaging (MRI) in February 2016. A copy of the Vanderbilt University press release is provided in Appendix 2.
2) Prof. Chekmenev was promoted to Associate Professor with tenure at the Department of Radiology and Radiological Sciences at Vanderbilt University Medical Center (VUMC) in February 2016 with effective date of Oct. 2015.
3) A participating post-doctoral fellow, Dr. Aaron Coffey, received a F32 career award from NIH NIBIB 1F32EB021840.
4) Dr. Roman V. Shchepin was promoted to a junior faculty position of Research Assistant Professor at the Department of Radiology and Radiological Sciences at Vanderbilt University Medical Center (VUMC).
5) One of the PIs of this partnering PI award received an unrestricted funding in the form of a gift from ExxonMobil Research and Engineering Company: $25,000.
6) This project enabled research activity for an 8-week rotation of PhD student Mr. Anthony Phipps.

7) SIUC undergraduate student Drake Anthony graduated and was admitted to the optics PhD program at the University of Rochester (the top program of its type in the US), where he now attends graduate school.
8) SIUC physics graduate student Kaili Ranta earned her PhD and now attends medical school at Ohio State University.
9) Trainees from each US site routinely visit the other site to perform experiments and work together in highly interdisciplinary environments; trainees also got the opportunity to work with (and learn from) visiting Russian collaborators.
10) Most trainees working on this project had an opportunity to attend at least one National or International Conference to publicize the work performed and also for their exposure to biomedical science.

How were the results disseminated to communities of interest?

Nothing to Report

4. IMPACT

What was the impact on the development of the principal discipline(s) of the project?

Nothing to Report.

What was the impact on other disciplines?

Nothing to Report.

What was the impact on technology transfer?

There were two key areas of impact on the technology transfer:

1) The Vanderbilt team has filed a provisional application for detecting sulfur containing compounds using NMR hyperpolarization; this technology may take advantage of non-hydrogenative HET-PHIP catalysis in the future.
2) More importantly, we provided the disclosure regarding the development of ^{129}Xe hyperpolarizers (for all three generations including the one funded by this award) to both SIUC and Vanderbilt University. Based on our preliminary discussions with the tech transfer office at Vanderbilt, VU (and most likely SIUC) will not file for patent protection for this technology. Instead, we expect to have the ownership to go back to the inventors (subject to the DOD regulations and approval). This tech transfer arrangement will eventually allow a trainee of this project Dr. Nikolaou to lead the commercialization effort for this technology in XeUS Technologies LTD in Europe. The appeal of the low-cost and high-throughput was a key element proposed for this project, which we believe will be of significant benefit to the patients suffering from the lung disease once the technology is commercialized and once it is eventually available to the end users.

What was the impact on society beyond science and technology?

Nothing to Report.

5. CHANGES / PROBLEMS

1) As described above we did not use the first prototype of full metal optical pumping cell for ^{129}Xe hyperpolarizer due to sub-par performance. Instead, we developed an alternative solution.

2) We have also experienced the delays with the delivery of our first 0.05 T magnet funded by the DOD on other project. As a result of that, this has delayed the overall work on the third aim of this project. We hope to accelerate towards this Aim during Year 2 of this project as we learn a lot more about NMR imaging and spectroscopy at such low magnetic fields.

6. PRODUCTS

Oral Presentations

1. Chekmenev EY. NMR Sensitivity Enhancement by Hyperpolarization and Molecular Imaging. 2015 November 16; Eastern Analytical Symposium (EAS), Somerset, NJ.
2. Chekmenev EY. Molecular Imaging and Hyperpolarized Contrast Agents. 2016 February 23; DOD CDMRP Leading Innovative Networking and Knowledge Sharing (LINKS) Meeting, Towson, MD.

3. Chekmenev EY. Molecular Imaging and Hyperpolarized Contrast Agents. 2016 February 24; DOD CDMRP Leading Innovative Networking and Knowledge Sharing (LINKS) Meeting, Towson, MD.
4. Chekmenev EY. New and Old Molecular Targets for Parahydrogen Induced Polarization. 2016 February 25; The Fourth International Workshop on Hyperpolarized Carbon-13 and Its Applications in Metabolic Imaging, University of Pennsylvania, Philadelphia, PA.
5. Chekmenev EY. Hyperpolarized NMR Contrast Agents for Molecular Imaging. 2015 September 25; Southern Illinois University Carbondale (SIUC), Department of Chemistry Seminar, Carbondale, IL, USA.
6. Chekmenev EY. New and Old Molecular Targets for Parahydrogen Induced Polarization & Beyond. 2015 November 3, University of Florida (UF), Department of Chemistry Physical Chemistry Seminar, Gainesville, FL, USA.
7. Chekmenev EY. NMR Hyperpolarized Contrast Agents for Molecular Imaging. 2015 December 10; University of Michigan, Center for Molecular Imaging Special Seminar, Ann Arbor, MI, USA.
8. Chekmenev EY. NMR Hyperpolarized Contrast Agents for Molecular Imaging. 2016 February 17; Huntington Medical Research Institutes (HMRI), Site visit Seminar, Pasadena, CA, USA.
9. Chekmenev, E. Y. In *Hyperpolarization Of Nuclear Spins and Its Application in Biomedicine*, Russian Acedemy of Sciences Lecture Series, March 22; RAS House of Scientists, Moscow, Russia, 2016.
10. Goodson BM "Novel Approaches for Enhancing NMR and MRI via SABRE Involving Heterogeneous Conditions, Aqueous Solutions, and Heteronuclei." Invited talk at: The Fourth International Workshop on Hyperpolarized Carbon-13 and Its Applications in Metabolic Imaging. University of Pennsylvania, February 25, 2016.
11. Ranta K, Murphy M, Porter J, Anthony D, Stephenson S, Rosen MS, Barlow MJ, & Goodson BM "Update on ^{131}Xe Polarization via SEOP." NOPTREX Collaboration Meeting, University of Kentucky, May 23, 2016; contributed talk.

Conference Abstracts

1. Barskiy, D. A.; Pravdivtsev, A. N.; Ivanov, K. L.; Salnikov, O. G.; Kovtunov, K. V.; Koptyug, I. V.; Shchepin, R. V.; Coffey, A. M.; Chekmenev, E. Y. Understanding the interplay between the chemical kinetics and the nuclear spin dynamics for the efficient hyperpolarization by PHIP and SABRE techniques. In *57th Experimental ENC Conference*, Pittsburgh, PA, April 10-15, 2016.
2. Gemeinhardt, M.; Alsuhaibani, B.; Anthony, D.; Heine, B.; Bales, L.; Gesiorski, J.; Totheroh, A.; Shi, F.; Coffey, A. M.; Shchepin, R. V.; Barskiy, D. A.; Chekmenev, E. Y.; Goodson, B. M. Exploring Rapid Bulk Heteronuclear Hyperpolarization "On the Cheap" Using PHIP/SABRE-Based Methods. In *57th Experimental ENC Conference*, Pittsburgh, PA, April 10-15, 2016.
3. Coffey, A. M.; Chekmenev, E. Y. In *Open-Source Automation of PHIP and SEOP Hyperpolarizers*, Vanderbilt University Institute of Imaging Science Annual Retreat, Nashville, TN, USA, June 22-25; Nashville, TN, USA, 2015.
4. Chekmenev, E. Y. Molecular Imaging and Hyperpolarized Contrast agents. In *DOD CDMRP Breast Cancer Program, LINKS Meeting*, Poster presentation: Pittsburgh, PA, February 23, 2016.
5. Ranta K, Murphy M, Porter J, Anthony D, Stephenson S, Rosen MS, and Goodson BM "In Situ NMR Investigation of Clinical-Scale Co-Production of Hyperpolarized 131Xe and 129Xe via Stopped-Flow Spin-Exchange Optical Pumping." 57th Experimental Nucl. Magn. Reson. Conference, Pittsburgh, PA, April 2016; poster.
6. Coffey AM, Nikolaou P, Ranta K, Muradyan I, Rosen MS, Patz S, Barlow MJ, Goodson BM, and Chekmenev EY. "Clinical-Scale, Stopped-flow 129Xe Hyperpolarizer Development." 24th Annual Meeting of the International Society for Magnetic Resonance in Medicine (ISMRM), Singapore, May 7-13, 2016 (poster).

Peer-Reviewed Manuscripts, Dissertation & Book Chapters

1. Goodson, B. M.; Whiting, N.; Coffey, A. M.; Nikolaou, P.; Shi, F.; Gust, B.; Gemeinhardt, M. E.; Shchepin, R. V.; Skinner, J. G.; Birchall, J. R., et al. Hyperpolarization Methods for MRS. In *Emagres: Handbook of in Vivo Magnetic Resonance Spectroscopy*, Griffiths, J.; Bottomley, P.; Wasylishen, R. E., Eds. John Wiley & Sons, Ltd: West Sussex, UK, 2015; Vol. 4, pp 797–810.
2. Goodson, B. M.; Ranta, K.; Skinner, J.; Coffey, A. M.; Nikolaou, P.; Gemeinhardt, M. E.; Anthony, D.; Stephenson, S.; Hardy, S.; Owers-Bradley, J.; Barlow, M. J.; Chekmenev, E. Y. The Physics of Hyperpolarized Gas MRI (Invited Chapter). In *Hyperpolarized and Inert Gas MRI in Research and Medicine*; Albert, M., Hane, F., Eds.; Elsevier Inc.: San Diego, CA, United States, 2017, pp. 23-46.

3. Salnikov, O. G.; Barskiy, D. A.; Coffey, A. M.; Kovtunov, K. V.; Koptyug, I. V.; Chekmenev, E. Y. Efficient Batch-Mode Parahydrogen-Induced Polarization of Propane. *ChemPhysChem* **2016**, DOI 10.1002/cphc.201600564.
4. Kovtunov, K. V.; Romanov, A. S.; Salnikov, O. G.; Barskiy, D. A.; Chekmenev, E. Y.; Koptyug, I. V. Gas Phase UTE MRI of Propane and Propene. *Tomography* **2016,** *2*, 49-55.
5. Shchepin, R. V.; Barskiy, D. A.; Coffey, A. M.; Manzanera Esteve, I. V.; Chekmenev , E. Y. Efficient Synthesis of Molecular Precursors for Para-Hydrogen-Induced Polarization of Ethyl Acetate-1-^{13}C and Beyond. *Angew. Chem. Int. Ed.* **2016,** *55*, 6071-6074.
6. Kovtunov, K. V.; Barskiy, D. A.; Shchepin, R. V.; Salnikov, O. G.; Prosvirin, I. P.; Bukhtiyarov, A. V.; Kovtunova, L. M.; Bukhtiyarov, V. I.; Koptyug, I. V.; Chekmenev, E. Y. Production of Pure Aqueous ^{13}C-Hyperpolarized Acetate by Heterogeneous Parahydrogen-Induced Polarization. *Chem. Eur. J.* **2016**, DOI 10.1002/chem.201603974.
7. Barskiy, D. A.; Coffey, A. M.; Nikolaou, P.; Mikhaylov, D. M.; Goodson, B. M.; Branca, R. T.; Lu, G. J.; Shapiro, M. G.; Telkki, V.-V.; Zhivonitko, V. V.; Koptyug, I. V.; Salnikov, O. G.; Kovtunov, K. V.; Bukhtiyarov, V. I.; Rosen, M. S.; Barlow, M. J.; Safavi, S.; Hall, I. P.; Schröder, L.; Chekmenev, E. Y. NMR Hyperpolarization Techniques of Gases. *Chem. Eur. J.* **2016**, DOI 10.1002/chem.201603884.
8. Shi, F.; He, P.; Best, Q. A.; Groome, K.; Truong, M. L.; Coffey, A. M.; Zimay, G.; Shchepin, R. V.; Waddell, K. W.; Chekmenev, E. Y.et al. Aqueous NMR Signal Enhancement by Reversible Exchange in a Single Step Using Water-Soluble Catalysts. *J. Phys. Chem. C* **2016**, *120*, 12149–12156.
9. Shchepin, R. V.; Barskiy, D. A.; Coffey, A. M.; Goodson, B. M.; Chekmenev, E. Y. NMR Signal Amplification by Reversible Exchange of Sulfur-Heterocyclic Compounds Found in Petroleum. *ChemistrySelect* **2016**, *1*, 2552-2555.
10. Shchepin, R. V.; Barskiy, D. A.; Coffey, A. M.; Theis, T.; Shi, F.; Warren, W. S.; Goodson, B. M.; Chekmenev, E. Y. ^{15}N Hyperpolarization of Imidazole-$^{15}N_2$ for Magnetic Resonance pH Sensing Via SABRE-SHEATH. *ACS Sensors* **2016**, *1*, 640–644.
11. Kovtunov, K. V.; Barskiy, D. A.; Salnikov, O. G.; Shchepin, R. V.; Coffey, A. M.; Kovtunova, L. M.; Bukhtiyarov, V. I.; Koptyug, I. V.; Chekmenev, E. Y. Toward Production of Pure ^{13}C Hyperpolarized Metabolites Using Heterogeneous Parahydrogen-Induced Polarization of Ethyl [1-^{13}C]-Acetate and Beyond. *RSC Adv.* **2016**, *6*, 69728-69732.
12. Coffey, A. M.; Shchepin, R. V.; Truong, M. L.; Wilkens, K.; Pham, W.; Chekmenev, E. Y. Open-Source Automated Parahydrogen Hyperpolarizer for Molecular Imaging Using ^{13}C Metabolic Contrast Agents. *Anal. Chem.* **2016**, *88*, 8279-8288.
13. Barskiy, D. A.; Shchepin, R. V.; Coffey, A. M.; Theis, T.; Warren, W. S.; Goodson, B. M.; Chekmenev, E. Y. Over 20% ^{15}N Hyperpolarization in Under One Minute for Metronidazole, an Antibiotic and Hypoxia Probe. *J. Am. Chem. Soc.* **2016**, *138*, 8080–8083.
14. Barskiy, D. A.; Salnikov, O. G.; Shchepin, R. V.; Feldman, M.; Coffey, A. M.; Kovtunov, K. V.; Koptyug, I. V.; Chekmenev, E. Y. NMR SLIC Sensing of Hydrogenation Reactions Using Parahydrogen in Low Magnetic Fields. *J. Phys. Chem. C* **2016**: DOI: 10.1021/acs.jpcc.6b07555.
15. "Clinical-Scale Hyperpolarization of ^{129}Xe and ^{131}Xe via Stopped-Flow Spin-Exchange Optical Pumping", Kaili Ranta. A Dissertation Submitted in Partial Fulfillment of the Requirements for the Doctor of Philosophy Degree in Applied Physics at Department of Physics, Southern Illinois University Carbondale, 139 pages, Defense date: July 25, 2016.

Inventions, patent applications and licenses

1 new provisional patent application has been filed. Copies of non-confidential summary statements are provided in Appendix 2.

1. Chekmenev, E. Y.; Shchepin, R.V. Vanderbilt University, assignee. Methods of Detecting Sulfur-Containing Compounds. December, 2015, Vanderbilt University Reference No. VU16062.

7. PARTICIPANTS & OTHER COLLABORATING ORGANIZATIONS

Individuals worked on the project

The following personnel worked on the project

Name:	Eduard Chekmenev
Project Role:	Initiating PI (Vanderbilt)
Researcher Identifier (ORCID ID):	orcid.org/0000-0002-8745-8801
Nearest person month worked:	3
Contribution to Project:	Dr. Chekmenev was responsible for the overall progress of the project, performing some experiments with hyperpolarized propane and hyperpolarized xenon-129, developing RF coils, analyzing some of the data for the above-mentioned experiments, preparing the manuscripts.
Funding Support:	DOD W81XWH-12-1-0159/BC112431; NSF CHE-1416268; NIH 1R21EB018014; NIH 1R21EB020323; ExxonMobil Knowledge Build Award; NIH 1U01CA202229

Name:	Matthew S. Rosen
Project Role:	Consultant
Researcher Identifier (e.g. ORCID ID):	
Nearest person month worked:	1
Contribution to Project:	Prof. Rosen served as a consultant for RF pulse sequence design for TecMag MRI platform and on instrumentation for hyperpolarized Xe-129 production. He also actively participated in preparation of peer-reviewed manuscript.
Funding Support:	NIH R01-EB018976 NIH R21NS087344

Name:	Aaron M. Coffey
Project Role:	Postdoctoral Fellow
Researcher Identifier (e.g. ORCID ID):	
Nearest person month worked:	3
Contribution to Project:	Dr. Coffey participated in the design of ^{129}Xe hyperpolarizer and assisted with hyperpolarized propane experiments. Developed full metal optical pumping prototype, and RF coil prototypes. He also designed compensated electromagnet.
Funding Support:	NIH 1F32EB021840

Name:	Panayiotis Nikolaou
Project Role:	Postdoctoral Fellow
Researcher Identifier (e.g. ORCID ID):	
Nearest person month worked:	6
Contribution to Project:	Dr. Nikolaou led the design of ^{129}Xe hyperpolarizer. Developed optical pumping aluminum jacket prototype, made most of 3D drawings in the CAD software, placed

	most orders, and built RF coil & electromagnet prototypes.
Funding Support:	DOD W81XWH-12-1-0159/BC112431

Name:	Roman V. Shchepin
Project Role:	Research Assistant Professor
Researcher Identifier (e.g. ORCID ID):	
Nearest person month worked:	1
Contribution to Project:	Dr. Shchepin helped with propane hyperpolarization experiments, equipment installation. He was also involved in some aspects of testing heterogeneous catalysts for PHIP hyperpolarization.
Funding Support:	DOD W81XWH-12-1-0159/BC112431; NIH 1R21EB018014; NIH 1R21EB020323; NIH 1U01CA202229

Name:	Danila A. Barskiy
Project Role:	Postdoctoral Fellow
Researcher Identifier (e.g. ORCID ID):	orcid.org/0000-0002-2819-7584
Nearest person month worked:	3
Contribution to Project:	Dr. Barskiy performed propane hyperpolarization experiments, built some RF coils. He was also tested heterogeneous catalysts for PHIP hyperpolarization.
Funding Support:	DOD W81XWH-12-1-0159/BC112431

Name:	Matthew Feldman
Project Role:	PhD Student
Researcher Identifier (e.g. ORCID ID):	
Nearest person month worked:	1
Contribution to Project:	Mr. Feldman designed RF isolation prototype equipment and worked with the vendors on integration of gradient amplifiers for other DOD project – during this work we developed the equipment design for the MRI system for this project.
Funding Support:	DOD W81XWH-12-1-0159/BC112431

Name:	Anthony Phipps
Project Role:	PhD Student
Researcher Identifier (e.g. ORCID ID):	
Nearest person month worked:	1
Contribution to Project:	Mr. Phipps assisted to Dr. Danila Barskiy with PHIP hyperpolarization experiments of propane.
Funding Support:	

Name:	Boyd M. Goodson
Project Role:	Partnering PI (SIUC)
Researcher Identifier (ORCID ID):	orcid.org/0000-0001-6079-5077
Nearest person month worked:	2
Contribution to Project:	Prof. Goodson was responsible for the overall progress of the project at the

	partnering site, performing some experiments with hyperpolarized xenon-129 and xenon-131, alternate cells designs, gas mixtures, etc., analyzing some of the data for the above-mentioned experiments, preparing manuscripts and presentations.
Funding Support:	SIUC DOD PRMRP W81XWH-15-1-0272 NSF-CHE-1416432 NSF-DMR-1461255 NIH-1R21EB018014 NIH-1R21EB020323

Name:	Kaili Ranta
Project Role:	PhD physics graduate student
Researcher Identifier (ORCID ID):	
Nearest person month worked:	6
Contribution to Project:	Dr. Ranta led many of the experiments concerning hyperpolarized xenon-129 and xenon-131, alternate cells designs, gas mixtures, etc., analyzing some of the data for the above-mentioned experiments, and helping to prepare manuscripts and presentations
Funding Support:	DOD PRMRP W81XWH-15-1-0272

Name:	Bryce Kidd
Project Role:	Postdoctoral fellow
Researcher Identifier (ORCID ID):	
Nearest person month worked:	1
Contribution to Project:	Dr. Kidd just joined the group, and has begun to lead experiments concerning hyperpolarized xenon-129, high-power lasers, MR detection, etc.
Funding Support:	NSF-CHE-1416432 DOD PRMRP W81XWH-15-1-0272 NIH-1R21EB018014

Name:	Drake Anthony
Project Role:	Undergraduate student researcher
Researcher Identifier (ORCID ID):	
Nearest person month worked:	
Contribution to Project:	Mr. Anthony participated in some of the experiments concerning hyperpolarized xenon-129 and xenon-131, alternate cells designs, gas mixtures, etc., analyzing some of the data for the above-mentioned experiments, and helping to prepare presentations. He also worked on design and testing of optical/laser components.
Funding Support:	2

Name:	Shawn Stephenson
Project Role:	Undergraduate student researcher
Researcher Identifier (ORCID ID):	

Nearest person month worked:	
Contribution to Project:	Mr. Stephenson participated in some of the experiments concerning hyperpolarized xenon-129 and xenon-131, alternate cells designs, gas mixtures, etc., analyzing some of the data for the above-mentioned experiments, and helping to prepare presentations. He also worked on RF, hardware, and software issues with experimental apparatus
Funding Support:	1

Name:	Megan Murphy
Project Role:	Undergraduate student researcher
Researcher Identifier (ORCID ID):	
Nearest person month worked:	6
Contribution to Project:	Ms. Murphy participated in most of (and now leads some of) the experiments concerning hyperpolarized xenon-129 and xenon-131, alternate cells designs, gas mixtures, etc., analyzing some of the data for the above-mentioned experiments, and helping to prepare manuscripts and presentations.
Funding Support:	DOD PRMRP W81XWH-15-1-0272

Name:	Justin Porter
Project Role:	Undergraduate student researcher
Researcher Identifier (ORCID ID):	
Nearest person month worked:	4
Contribution to Project:	Mr. Porter participated in some of the experiments concerning hyperpolarized xenon-129 and xenon-131, alternate cells designs, gas mixtures, etc., analyzing some of the data for the above-mentioned experiments, and helping to prepare manuscripts and presentations.
Funding Support:	DOD PRMRP W81XWH-15-1-0272

Name:	Dustin Basler
Project Role:	Undergraduate student researcher
Researcher Identifier (ORCID ID):	
Nearest person month worked:	0
Contribution to Project:	Mr. Basler is new to the group, and has begun to participate in some experiments involving hyperpolarized xenon-129.
Funding Support:	NIH/SIUC “Bridges to the Baccalaureate” Program; AF ROTC

Name:	Max Gemeinhardt
Project Role:	PhD chemistry graduate student
Researcher Identifier (ORCID ID):	
Nearest person month worked:	1
Contribution to Project:	Mr. Gemeinhardt assisted with some high-field NMR experiments involving the

	testing of alternate cell designs (e.g. metal cells).
Funding Support:	SIUC / NMR Facility

Name:	Hallie Johnson
Project Role:	Undergraduate student worker
Researcher Identifier (ORCID ID):	
Nearest person month worked:	1
Contribution to Project:	Ms. Johnson assisted with the acquisition of materials for experiments and group operations.
Funding Support:	DOD PRMRP W81XWH-15-1-0272 NSF-CHE-1416432 NSF-DMR-1461255 NIH-1R21EB018014 NIH-1R21EB020323

Name:	Brittney Hesser
Project Role:	Undergraduate student worker
Researcher Identifier (ORCID ID):	
Nearest person month worked:	1
Contribution to Project:	Ms. Hesser assisted with the acquisition of materials for experiments and group operations; she also assists with lab safety and maintaining chemical inventory.
Funding Support:	DOD PRMRP W81XWH-15-1-0272 NSF-CHE-1416432 NSF-DMR-1461255 NIH-1R21EB018014 NIH-1R21EB020323

Has there been a change in the active other support of the PD/PI(s) or senior/key personnel since the last reporting period?

Nothing to report

What other organizations were involved as partners?

In addition to the two performing sites (and consultant listed on the original application), we have a collaborating scientists engaged in this project for Aim 2.

Organization Name: International Tomography Center

Location of Organization: Novosibirsk, Russia

Partner's contribution to the project:

In-kind support: Our collaborators provided catalyst materials for propane hyperpolarizer development work as well as for the final polarizer design;

Collaboration: The Partners' staff work with project staff on the project, we had a two two-month (each) visits with two collaborators visiting us at Vanderbilt and SIUC performing sites. We performed collaborative experiments, analyzed the data, and prepared manuscripts for peer-reviewed publications.

Personnel exchanges: See above. During collaboration, the partnering visiting scientists gave two oral departmental presentations, and participated in mentoring PhD and undergraduate students.

8. SPECIAL REPORTING REQUIREMENTS

Collaborative Award

Since this is a collaborative award with two partnering PIs, we note that we are submitting a duplicating report for two partnering PI awards of the same project: W81XWH-15-1-0271 and W81XWH-15-1-0272. The responsibility of each PI is clearly marked in the Appendix 1.

9. APPENDICES

Appendix 1: Original Statement of work, Years 1-3

STATEMENT OF WORK – 10/10/2014
PROPOSED START DATE September 1, 2015

Site 1:	Vanderbilt University		Site 2:	Southern Illinois University
	1161 21st Ave South MCN AA-1105 Nashville, TN 37232-2310			900 SOUTH NORMAL AVENUE CARBONDALE, IL 62901
	PI: Chekmenev			Partnering PI: Goodson

Specific Aim 1	Timeline	Site 1 (Vanderbilt)	Site 2 (SIU)
Develop and construct a fully automated high-pressure low-cost stand-alone ^{129}Xe hyperpolarizer	Months		
1.1. Design	1-5	80%	20%
1.2. Prototyping	6-10	75%	25%
1.3. Prototype construction and testing	11-15	90%	10%
Milestone Achieved	Prototype ^{129}Xe polarizer constructed		
1.4. Final Design	16-20	80%	20%
1.5. Final Construction	21-24	90%	10%
1.6. Final Testing	25-30	75%	25%
1.7. Polarizer Integration with MRI scanner	31-34	90%	10%
Milestone Achieved	Final ^{129}Xe polarizer constructed		
1.8. Replica Polarizer Construction and Testing	31-36	50%	50%
Milestone Achieved	Replica ^{129}Xe polarizer constructed		

Specific Aim 2	Timeline	Site 1 (Vanderbilt)	Site 2 (SIU)
Develop a large-scale hyperpolarization method for HP propane			
2.1. Chemistry of Large Scale PHIP of propane	1-6	75%	25%
Milestone Achieved:	Clinical Scale Production of HP Propane is developed		
2.2. Initial Polarizer Design	7-12	100%	0%
2.3. Polarizer Prototyping	13-18	100%	0%
Milestone Achieved:	Prototype Polarizer Constructed		
2.4. Prototype Optimization	19-24	100%	0%
2.5. Final Polarizer Construction	25-30	100%	0%
2.6. Final Polarizer Testing and Integration with low-field MRI system	31-36	75%	25%
Milestone(s) Achieved:	Final Propane Polarizer Constructed		
Specific Aim 3	**Timeline**	**Site 1 (Vanderbilt)**	**Site 2 (SIU)**
Develop and construct a 0.05 T MRI scanner	Months		
3.1. Design low-field MRI system with commercial vendors	1-6	50%	50%
3.2. Low-field MRI system construction by Vendors	7-12	50%	50%
3.3. Low-field MRI system installation and fine-tuning at site 1 (Vanderbilt)	13-18	100%	0%
Milestone Achieved:	Clinical low-field MRI system for high-		

	throughout pulmonary imaging is installed		
3.4. RF coils (^{129}Xe and ^{1}H) construction for pulmonary imaging	19-24	100%	0%
3.5. Pulse-sequence development and installation	25-30	50%	50%
Milestone Achieved:	Low-field MRI system is ready for use with contrast agents		
3.6. MRI system integration with Propane Hyperpolarizer	31-36	100%	0%
3.7. MRI system integration with Propane Hyperpolarizer	31-34	90%	10%
3.8. Demonstration of high-speed MRI and high-speed contrast agent production/ imaging scan	35-36	90%	10%
Milestones Achieved:	Functional high-speed MRI of hyperpolarized propane and ^{129}Xe; System ready for clinical trial.		

Appendix 2: Abstracts Presented and Manuscripts Published and Accepted

14 manuscripts are reported: all are peer-reviewed manuscripts or peer-reviewed book chapters.
3 scientific conference/meeting presentations are reported.
1 provisional patent application has been filed. Their non-confidential summaries are provided.
PDF files of these materials are provided below in the Appendix 2.

Hyperpolarization Methods for MRS

Boyd M. Goodson[1], Nicholas Whiting[2], Aaron M. Coffey[3], Panayiotis Nikolaou[3], Fan Shi[1], Brogan M. Gust[1], Max E. Gemeinhardt[1], Roman V. Shchepin[3], Jason G. Skinner[4], Jonathan R. Birchall[4], Michael J. Barlow[4] & Eduard Y. Chekmenev[3]

[1] *Southern Illinois University, Carbondale, IL, USA*
[2] *The University of Texas MD Anderson Cancer Center, Houston, TX, USA*
[3] *Vanderbilt University, Nashville, TN, USA*
[4] *University of Nottingham, Nottingham, UK*

This article covers the fundamental principles and practice of NMR hyperpolarization techniques, which are proving useful for in vivo magnetic resonance spectroscopy (MRS) studies of metabolism in animal models, and clinical trials with hyper-enhanced sensitivity. Fundamentally, hyperpolarization methods enhance nuclear spin polarization by orders-of-magnitude, resulting in concomitant improvement in NMR detection sensitivity. The hyperpolarization methods described here – dynamic nuclear polarization (DNP), *para*-hydrogen induced polarization (PHIP), signal amplification by reversible exchange (SABRE), and spin-exchange optical pumping (SEOP) – are capable of achieving nuclear spin polarization approaching the theoretical maximum of unity on nuclear spin sites of molecular or atomic agents suitable for in vivo administration. Importantly, hyperpolarization is inherently nonequilibrium in nature: the duration of the hyperpolarization is frequently short-lived, often being limited by the in vivo spin–lattice relaxation times (T_1) that are on the order of seconds to a minute. Nevertheless, sufficient amounts of nuclear spin polarization can survive the process of preparation, administration, and in vivo circulation to provide extraordinary enhancement of the hyperpolarized agent. The chemical shift dispersion of these agents at the molecular location of interest reports on functional, metabolic, and other processes at the molecular level, enabling true molecular MRS imaging.

Keywords: hyperpolarization, DNP, PHIP, *para*-hydrogen, xenon, SABRE, carbon-13, SEOP

How to cite this article:
eMagRes, 2015, Vol 4: 797–810. DOI 10.1002/9780470034590.emrstm1457

Introduction

The sensitivity and signal-to-noise ratio (SNR) of the NMR experiment is directly proportional to the nuclear spin polarization factor P, which represents the fraction of the alignment of the nuclear spin ensemble with an applied magnetic field $\boldsymbol{B}_0$. In conventional NMR, $P \approx \gamma \hbar \boldsymbol{B}_0 / 2kT$ under thermal-equilibrium conditions governed by the Boltzmann distribution (with $\gamma =$ the gyro magnetic ratio, $\hbar =$ Planck's constant/2π, $k =$ Boltzmann's constant, and $T =$ absolute temperature). In vivo conditions imply temperatures in excess of 300 K. As a result, even if a high-field magnet – e.g., a 3-T clinical magnetic resonance (MR) imaging (MRI) scanner – is employed for MR spectroscopy (MRS), the value of P of proton (^{1}H) and carbon-13 (^{13}C) nuclear spins is only 1×10^{-5} and 2.5×10^{-6}, respectively. Therefore, the vast majority of the nuclear spin ensemble does not in fact contribute to the NMR signal. For this reason, NMR in general and MRS, in particular, are frequently considered insensitive probes.

However, P can be artificially increased significantly relative to the thermal-equilibrium level, via a process called NMR *hyperpolarization*. Several hyperpolarization techniques realize enhancements of P by several orders-of-magnitude over the Boltzmann level and allow P to approach the theoretical maximum of unity. The corresponding enhancement factor, ε, is field dependent and defined as a ratio of P in the hyperpolarized (HP) state to that in the thermal-equilibrium state (e.g., $\varepsilon = 10^4$ to 10^5 for ^{13}C at 3 T).[1]

The fundamental concept of NMR hyperpolarization and its use in MRS is attractive because it offers extraordinary advantages over conventional MRS.[2] First, the SNR can be significantly improved even using much lower concentrations of detected compounds than are present endogenously. Second, the data acquisition time can be dramatically decreased from tens of minutes down to subsecond scans. Third, a HP contrast agent (HCA) entering the biological system (i.e., excised organ, living organism) and reporting on metabolic functional events can provide insightful dynamic information on in vivo metabolism in real time as compared to the static picture typically obtained with conventional single or multi-voxel MRS. Not surprisingly, biomedical applications represent the major driving force behind the fields of NMR hyperpolarization and HCA development, owing to their potential for revolutionizing medical diagnostics, drug therapy development, and probing physiological mechanisms.

However, HP NMR techniques are no panacea, as they have inherent disadvantages and shortcomings that must frequently

 © 2015 John Wiley & Sons, Ltd.

be confronted during HCA production. First, HCAs are nearly always prepared exogenously in a hyperpolarization apparatus, frequently requiring sophisticated and expensive hardware. Second, HCAs must retain a HP state sufficiently long for quality assurance, transport, administration, in vivo delivery, and NMR/MRS measurements. These requirements limit the number of molecular sites (i.e., moieties of ^{13}C, ^{15}N, ^{129}Xe) suitable for HP MRS, to those whose spin–lattice relaxation times (T_1) are long enough to accomplish all this. Finally, the decay of the HP state to thermal equilibrium is irrecoverable. Therefore, signal acquisition must be fast and efficient to account for polarization losses via T_1 relaxation, RF pulsing (for detection), and the effects of in vivo metabolism and dilution.[3]

This article describes four hyperpolarization techniques: (1) dynamic nuclear polarization (DNP), (2) *para*-hydrogen induced polarization (PHIP), (3) signal amplification by reversible exchange (SABRE), and (4) spin-exchange optical pumping (SEOP) of ^{129}Xe. These techniques have already proven effective for preparing HCAs that can be used for tracking metabolic and functional processes in vivo (see ***Hyperpolarized Carbon-13 MRI and MRS Studies***[3]), because they are capable of achieving P values approaching the theoretical maximum of unity on nuclear spin sites of molecular or atomic HCAs. Moreover, the HCAs for MRS fundamentally offer a wide dynamic range of chemical shift dispersions either through metabolism (e.g., ^{13}C metabolites) or by their sensitivity to the local environment (e.g., ^{129}Xe). Many HCAs have been validated in animal models,[2] while some HCAs (e.g., HP ^{13}C-pyruvate and ^{129}Xe) are being tested in clinical trials.[4]

The primary focus in this article is on the fundamentals of these hyperpolarization techniques (i.e., how they are generated and their physical and chemical properties), their existing or emerging MRS relevance, and a description of the hyperpolarization equipment (frequently referred to as *hyperpolarizers*) required to perform these techniques. Accordingly, the article describes and cites only selected works in these areas, and the reader may additionally benefit from some recent comprehensive reviews.[2,5–9]

Dynamic Nuclear Polarization (DNP)

Fundamentals

Despite the demonstration by Overhauser in the early 1950s of the underlying basis of DNP – that P could be enhanced by cross-relaxation with nearby electrons owing to differences in their gyromagnetic ratios ($\gamma_e/\gamma_I \sim 660$) – only recently has interest in its potential applications for biomedical MRI and MRS emerged.[10] While various methods fall under the DNP umbrella, the 'dissolution DNP' (d-DNP) method is the most commonly used method for in vivo applications.[1,9] In biological d-DNP MRS experiments, the general preparation procedure involves (i) mixing the MR-active species of interest with a paramagnetic source of free electrons; (ii) placing the mixture in a high magnetic field at low cryogenic temperatures; (iii) subsequent irradiation with a microwave source resonant on the electron spin resonance (ESR) frequency to mediate the transfer of electron polarization to nearby nuclei[11] followed by (iv) rapid sample thawing using a hot solvent to warm the frozen polarized sample and transferring it to the MR scanner for in vivo injection as a liquid. These conditions generate electron spin polarizations that can approach unity as shown in Figure 1, with a significant fraction of the prepared P largely surviving the rapid dissolution in step (iv).

Dissolution DNP (d-DNP) Instrumentation

Both commercial and home-built d-DNP devices have been extensively used for in vivo MRS. While each polarizer design may have unique characteristics, they are all comprised of the same basic components: a superconducting magnet that provides a $\boldsymbol{B}_0$ of 3–7 T, a liquid helium cryostat for sample cooling to 1–4 K, a microwave source to transfer polarization from the electrons to nuclei (~100 mW), and a mechanism that rapidly dissolves the frozen sample pellet and delivers the solution for collection.[9]

Step (i) of the typical d-DNP experiment proceeds as follows: the species of interest is mixed with a radical source and a glassing agent in a typically flat sample container (up to a few hundred μL) and lowered into the cryostat, as depicted in Figure 2. There in step (ii), the sample is frozen into an amorphous solid at low temperatures either by submersion into a liquid helium bath (where vacuum-pumping reduces the vapor pressure, and hence bath temperature) or by exposure to a stream of continuously flowing liquid helium. The microwave source, whose frequency is set to the ESR line of the chosen radical species at the $\boldsymbol{B}_0$ of the polarizer (typically within ~80–140 GHz, with a ~0.5 GHz sweep range), irradiates the sample for ~1 h in step (iii), using an antenna that takes advantage of the large flat surface area of the sample container. An on-board NMR system can check the HP signal while sweeping the microwave source to allow for optimization of the microwave frequency and excitation power (Figure 1c) and for monitoring the buildup of hyperpolarization over time (Figure 1d).

Step (iv) of the procedure requires a superheated solvent with high heat capacity, which is typically satisfied by pH-buffered saline. This is injected into the sample cup inside the cryostat. The lifetime of the HP signal is determined by the T_1 of the HCA, so to mitigate P losses, the rapid dissolution is performed at high $\boldsymbol{B}_0$ to minimize the sudden depolarizing effects of the paramagnetic centers as the temperature rises above ~4 K. Dissolution also reduces the relative concentration of radicals and lowers their contribution to the nuclear spin-relaxation rate[9] as the sample volume expands by an order of magnitude (this process also dilutes the HP agent). The room-temperature (RT) T_1 values of most HCAs used for biomedical MRS are ≤1 min but $\boldsymbol{B}_0$ changes between the polarizer and MR scanner may further reduce T_1. Rapid shuttling of the sample from the polarizer to the scanner is key and is typically performed pneumatically using helium gas through small diameter tubing. There, the polarized solution is quickly filtered to remove persistent radicals using anion-exchange or polyethylene filters[9] and injected into the subject (Figure 2).

A commercially available d-DNP device for clinical use has recently been developed (SPINlab; GE Healthcare) that operates at 5 T and 1.1 K.[12] The system uses an on-board helium recycling system that dramatically lowers the consumption of liquid helium, which is expensive. While many other features

© 2015 John Wiley & Sons, Ltd.

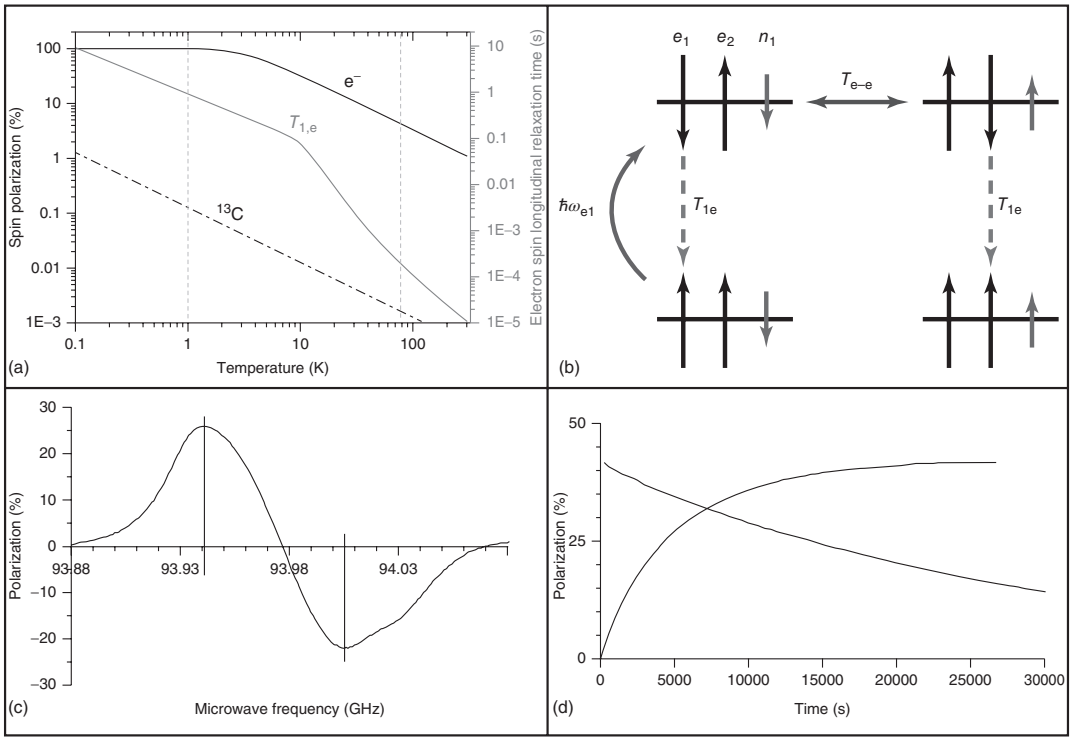

Figure 1. Effects of DNP conditions on electronic and nuclear spins. (a) Effects of temperature on ^{13}C (dashed black curve) and electron (e^-, solid black curve) spin polarizations at 5 T, along with electronic T_1 relaxation time ($T_{1,e}$, gray solid curve) at 0.35 T. (Reprinted with permission from A. Comment and M. E. Merritt, Biochemistry, 2014, **53**, 7333.[9] Copyright 2014 American Chemical Society.) (b) The energy response of a two-electron nuclear spin system during the DNP process: microwave irradiation (with energy $\hbar\omega_{e1}$) induces spin flips of coupled electrons (left), which then cross-relax with nearby nuclei (top right), driving the nuclear spins into the same HP spin state (bottom right). (c) Example of a microwave sweep used to calibrate the optimal excitation frequency for ^{13}C DNP. (Reproduced with permission from Ref. 1. © National Academy of Sciences, 2003) (d) Exemplary buildup and decay of ^{13}C polarization over time with the DNP microwave source engaged (increasing curve) and turned off (decreasing curve). (Reproduced with permission from Ref. 1. © National Academy of Sciences, 2003)

of its design and operation are similar to that described above, additional quality-control steps are incorporated to ensure that the injectable solution meets clinical criteria for pH, temperature, P value, sterility, purity, and residual radical species concentration. In general, the larger sample volumes required for human use necessitate longer dissolution, transport, quality control, and injection periods, such that significant time (e.g., >65 s) may elapse between the initial dissolution and final injection. Nevertheless typical ^{13}C P values are ~15–20% after quality control, which is certainly sufficient to perform HP MRI/MRS in human patients with great advantage vs conventional MRS with $P \sim 10^{-3}$%.[4]

Common HP Agents Produced with d-DNP

^{13}C-labeled Small Biomolecules. The overall P, T_1, and biological relevance of the agent are the main criteria for choosing a HP species for MRS applications. Further considerations include the ability to form a glassy matrix in a sufficiently high concentration to mitigate dilution effects from the dissolution step, sufficient chemical shift range to differentiate the primary polarized species from any downstream products, the cost of isotopic enrichment, the ability to lessen the depolarization effects of nearby protons via deuteration,[13] and toxicity. While a number of MR-active nuclei are eligible for DNP, the most commonly pursued are ^{13}C-labeled carboxyl sites of metabolites. Of the latter, ^{13}C-pyruvate has garnered the most attention because of its relatively high P values (>50 %), long T_1 (~60 s), and ability to probe the tricarboxylic acid (TCA) cycle and glycolysis within a T_1-relevant timescale.[14] Additional notable ^{13}C-labeled small molecules pursued for DNP studies include urea,[1] fumarate, glutamine, fructose, lactate, glucose, diethyl succinate, and acetate.[2,13]

Extension to Other Nuclei. Beyond ^{13}C, the most commonly pursued d-DNP species for MRS studies are biologically relevant ^{15}N-labeled compounds, such as urea and choline. However, despite some benefits (the T_1 of ^{15}N-choline ~4 min),[13] the lower gyromagnetic ratio makes ^{15}N MRS more challenging for achieving useful signal intensities and

© 2015 John Wiley & Sons, Ltd.

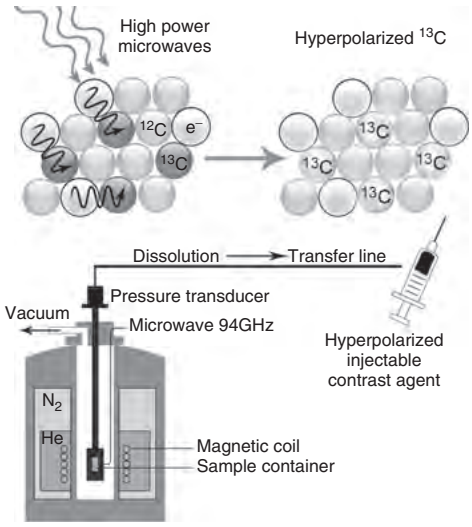

Figure 2. Overview of the d-DNP process. Within the high magnetic field of the DNP polarizer, high-power microwaves excite free electrons in free radical species mixed with the HP substrate and frozen into an amorphous solid. The electrons undergo spin-exchange with nearby ^{13}C nuclei and over time, the entire sample becomes polarized via direct dipole–dipole interactions as well as nuclear spin diffusion involving the ^{1}H nuclei present in the HP substrate or glassing agent. After polarization, the HCA sample is rapidly dissolved in hot solvent and shuttled into the MR scanner room for injection into the animal or human subject

gradient strengths for spatial localization with typical scanner hardware. Other species that can be HP by DNP and may have potential for future in vivo applications include ^{1}H, ^{6}Li, ^{29}Si, ^{31}P, ^{89}Y, ^{107}Ag, and ^{129}Xe.

Secondary and Co-polarization. The enhanced signal from isotopically labeled HP small molecules may be translated into their chemical reaction products. This process, referred to as secondary polarization, allows the study of biologically relevant molecules that may not polarize well on their own, but have metabolic predecessors that do. This process can either be enzymatically regulated, such as with [1,1-$^{13}C_2$]acetic anhydride breaking into different [1-^{13}C]N-acetylated amino acids,[13] or nonenzymatically regulated – for instance, the reaction of 1,2-^{13}C-pyruvate with H_2O_2 to form $^{13}CO_2$, ^{13}C-acetate, and ^{13}C-bicarbonate.[15] Co-polarization of a single 'batch' of different small molecules using d-DNP during agent production allows the simultaneous study of different biophysical parameters and processes such as pH, metabolism, necrosis, and perfusion.[13] While the commingled molecules' solid-state polarization P and T_1 values are often similar to their individual values, drawbacks include lower concentrations of, and potential interactions among, the small molecules involved.

Radicals and Glassing Agents

Choice of Radical Species. The buildup time and hyperpolarization level for all species are highly dependent on the choice of radical used to mediate the DNP. Typical radical concentrations range from 15 to 60 mM and may persist post-thawing, requiring filtering before administration. The most widely used sources of free electrons for ^{13}C DNP have been the trityl and 1,3-bisdiphenylene-2-phenylallyl (BDPA) radicals. Because their ESR lines are narrower than the ^{1}H resonance frequency dispersion, the probability of cross-polarization with ^{1}H is lowered, which increases the chances of polarizing nearby ^{13}C nuclei.

Further improvements in the P level and reductions in buildup time can be gained by the addition of a Gd^{3+} complex to the trityl radical solutions. The highly efficient electron-^{1}H cross-polarization of nitroxyl radicals (e.g., TEMPO; 2,2,6,6-tetramethylpiperidine-1-oxyl) can also be used in conjunction with a ^{1}H–^{13}C cross-polarization scheme to decrease ^{13}C polarization time, albeit with lower overall ^{13}C polarization compared to trityl or BDPA radicals. Liquid-state P can be further increased using a deuterated solvent for the nitroxyl radicals.[9] Additional gains have been reported using biradicals comprised of two TEMPO radicals tethered by a polyethylene chain.[16]

Choice of Glassing Agent. The DNP process is most efficient when the HP molecule is homogenously mixed with the radical species and formed into a glass, as already noted. This amorphous state allows the paramagnetic centers to achieve close contact with nearby nuclei, which is not the case in a crystalline lattice. Typical glassing agents include glycerol and dimethyl sulfoxide (DMSO), which act to prevent crystallization. Some HP molecules such as neat ^{13}C-pyruvate are capable of self-glassing,[17] which allows for a higher concentration of ^{13}C nuclei that speeds ^{13}C spin diffusion resulting in a more homogenously polarized sample.[18]

DNP Advantages, Limitations, and Future Prospects

As a hyperpolarization method, DNP's versatility lies in its ability to hyperpolarize a variety of biologically relevant molecules not easily polarized by other methods. Target molecules can achieve high P with sufficiently long T_1 values for probing metabolic pathways, and clinical trials are already underway for HP ^{13}C-pyruvate. The main limitations thus far are the high cost of purchase, maintenance, and infrastructure required for the polarizers. Improvements in cryogen recovery and solid-state cooling can lower operational costs, and further optimization of the physical and chemical environment of the HP species should improve P and T_1 values, as would the ability to store the enhanced polarization in a singlet state until it is ready for MRS applications. Finally, the demonstration of a clinically important application of HP MRI – such as using ^{13}C-pyruvate to study prostate cancer or heart dysfunction – will greatly hasten the development of all d-DNP aspects.[9]

para-Hydrogen (*para*-H_2) Production

In addition to its more recent applications in HP MRS, the properties of *para*-hydrogen (*para*-H_2) have proved important for hydrogen's use as a rocket fuel by minimizing boil-off due to state conversion, and even earlier, *para*-H_2 served as a prototypical system during the development of quantum theory.

© 2015 John Wiley & Sons, Ltd.

The dihydrogen molecule possesses two nuclear spin isomers, denoted as '*ortho*-' and '*para*-' states, comprised of a nuclear triplet state and a singlet state, respectively. Importantly, while representing the simplest nuclear singlet state, *para*-H_2, per se, has net spin $I = 0$ and is therefore NMR invisible. As will be seen in the following sections, its use in NMR/MRS is as an extremely powerful vector for transferring HP to HCAs of interest. For further discussion of the physics of *para*-hydrogen, we direct the interested reader to the books by Farkas on hydrogen[19] and Linus Pauling on quantum mechanics,[20] and the review by Green *et al.*[5]

Inter-conversion of *ortho*-hydrogen (*ortho*-H_2) to *para*-H_2 (with a heat of conversion of 670 J g^{-1}) is forbidden according to the selection rules of quantum mechanics. It thus occurs very slowly. Spontaneous emission of radiation was calculated by Wigner to result in a conversion rate of $\sim 10^{-10}$ s^{-1}, or approximately one transition per 1 gram every 300 years.[19] In 1930, Hall and Oppenheimer calculated that molecular collisions at atmospheric pressure result in a rate of one per $\sim 10^8$ s/1 g for the *ortho*-*para* transition half lifetime, or about 3 years.[19] While such a slow inter-conversion rate is nominally unfavorable to *para*-H_2 production, Bonhoeffer and Harteck discovered in 1929 that paramagnetic catalysts, including, for example, activated charcoal, nickel, and hydrated iron-III oxide, greatly accelerate the establishment of thermodynamic equilibrium for the ratio of *ortho*-H_2/*para*-H_2.

The instrumentation used to generate high-purity *para*-state dihydrogen is commonly called a '*para*-hydrogen generator', shown in Figure 3. The essential purpose of the generator is to pass bulk H_2 at RT (i.e., $\sim$293 K) over a paramagnetic catalyst at a cryogenic temperature of $\sim$20 K to rapidly equilibrate the 75% *ortho*-H_2 fraction to the lower-temperature Boltzmann thermal equilibrium, thereby creating *para*-H_2 with nearly 100% *para*-fraction. Typically, the gas flows through a catalyst chamber attached to a two-stage, Joule–Thomson effect, helium cryocooler cold-head. The flow is regulated with either (i) flow restrictors such as mass flow controllers, snubbers, or needle valves[21,22] or (ii) by releasing small batches of compressed H_2 between automatically sequenced solenoid valves.[23] After separation of the *para*-H_2 from the catalyst and subsequent storage at RT, quantum-mechanical symmetry selection rules forbid reestablishment of the RT equilibrium. Provided the *para*-H_2 storage vessel contains no paramagnetic impurities (as is the case for those glass-lined or of aluminum, although the absence of O_2 is also important), the relaxation rate of the *para*-hydrogen back to the RT equilibrium can be on the order of months.[21–23] Thus, *para*-H_2 experiments are possible long after production.

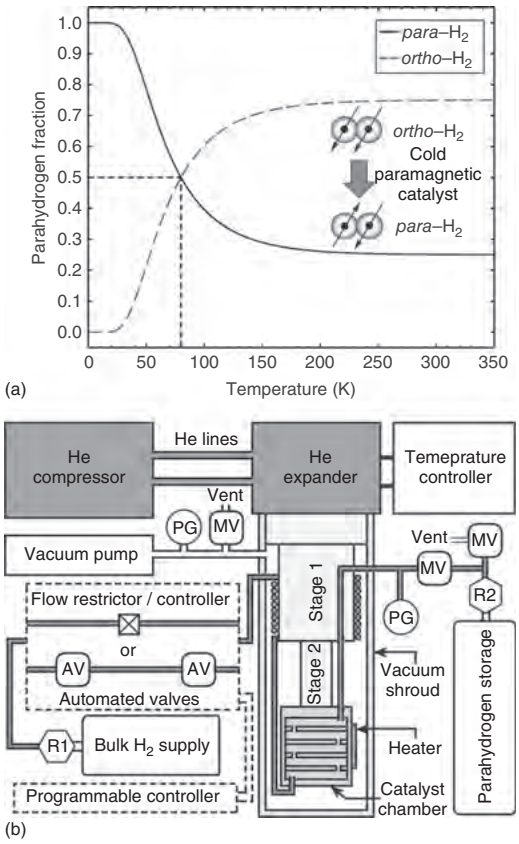

Figure 3. Production of *para*-hydrogen (*para*-H_2). (a) H_2 passes over a paramagnetic catalyst that rapidly increases the *para*-H_2 fraction to the thermodynamic equilibrium at the given cryogenic temperature. (b) Production typically involves a '*para*-hydrogen generator' built around a two-stage He cryocooled cold-head involving pressure gauges (PG), manual valves (MV), gas pressure regulators (R), and automated valves (AV)

para-Hydrogen-Induced Polarization (PHIP)

Fundamentals

While the *para*-H_2 molecule is itself NMR invisible, Bowers and Weitekamp[24] have demonstrated that the *para*-H_2 singlet can be unlocked via the chemical reaction of hydrogenation provided that the *para*-H_2 is added in a pairwise manner (best exemplified in the molecular mechanism of H_2 addition) and that the nascent protons in the resulting hydrogenation product are no longer magnetically equivalent. This phenomenon of symmetry breaking the *para*-H_2 nuclear singlet state via hydrogenative processes is termed PHIP.[25]

While the *para*-H_2 singlet can be preserved for weeks and months, once the symmetry is broken and the *para*-H_2 pair is incorporated into the molecular framework of a product molecule (Figure 4), the relaxation decay processes (via T_1 and the spin–spin-relaxation time, T_2) are significantly more efficient (on a timescale of seconds) – leading to rapid depolarization. For the majority of metabolically relevant injectable contrast agents that can be envisioned, fast T_1 relaxation limits any meaningful preparation of HCA for biomedical use.

This initial fundamental PHIP challenge was overcome in the early 2000s, when an adjacent ^{13}C carboxyl (and potentially ^{15}N or others) with significantly longer T_1 was introduced by Golman *et al.*[26] and Goldman and Johannesson.[27] In addition, deuteration of the PHIP molecular precursor can extend the

© 2015 John Wiley & Sons, Ltd.

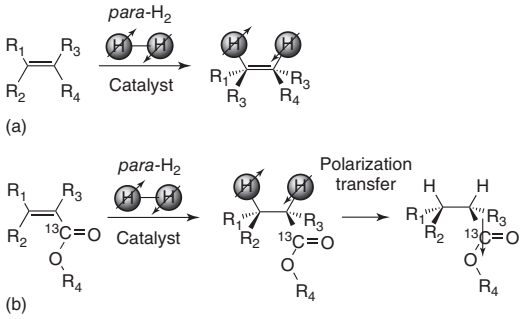

Figure 4. Schematics of *para*-H_2 pairwise addition in PHIP. (a) Symmetry breaking of nascent *para*-hydrogen's nuclear spin state via chemical reaction creates a nonsymmetric product. (b) *para*-H_2 state symmetry breaking through chemical reaction with pairwise addition followed by polarization transfer to ^{13}C produces a HP contrast agent comprised of a ^{13}C HP carboxyl moiety with a long T_1 lifetime

T_1 lifetime of the nascent protons, which has proven especially useful in PHIP of gases.[28] In the PHIP process, polarization from nascent *para*-H_2 protons is efficiently transferred to the ^{13}C nucleus via the network of J-couplings using either magnetic field cycling or RF pulse-based methods. Regardless of the approach used, the chemical reaction between *para*-H_2 and the unsaturated substrate molecule must be performed on a relatively fast timescale (seconds), i.e., significantly shorter than the effective relaxation times of the nascent *para*-H_2 protons, in order to minimize polarization losses during the reaction. Post-reaction, the polarization is typically transferred to the ^{13}C nucleus within a second. Moreover, even in the case of RF-based polarization transfer, which has proven to be more efficient as gauged by the %*P* delivered to ^{13}C, to date, the PHIP method is relatively low cost because the PHIP process can be performed at very low magnetic fields (a few mT) using relatively simple NMR hardware.

Molecular Precursors and Contrast Agents

The design of PHIP precursor molecules for biomedical applications and MRS is a challenging process that must meet critical requirements. In particular, the molecule must possess an unsaturated (typically C=C) bond adjacent to ^{13}C to provide a J-coupling contact between the nascent *para*-H_2 protons and the ^{13}C to enable efficient polarization transfer. Furthermore, the efficiency of this polarization transfer in RF pulse-based polarization transfer methods can greatly benefit from deuteration of the precursor molecule[29] as a means to keep the nuclear spin system effectively constrained to just the three involved spins: the two nascent para-hydrogens and the ^{13}C nucleus.[27] Lastly, because the hydrogenation reaction may be incomplete, both the precursor and product molecules should have relatively low in vivo toxicity. Meeting all these requirements represents the main disadvantage of PHIP, and only a limited number of potentially amenable precursor molecules and HCAs have qualified for in vivo use, so far.

Those that have been successfully HP and used for in vivo MRS include HP ^{13}C-succinate, which highlights metabolites of the TCA cycle[30]; ^{13}C-tetrafluoropropyl propionate, for sensing lipids in atherosclerotic plaques;[31] and ^{13}C-phospholactate,[29] for preparation of HP ^{13}C-lactate, which has been shown to be useful for in vivo metabolic imaging of elevated glycolysis in tumors.

Homo- and Heterogeneous PHIP Catalysis

Homogeneous Catalysis in Organic Solvents. PHIP[24,25] has attracted the attention of those working in catalysis owing to its promise to increase the NMR sensitivity of key low-concentration species. The PHIP process of pairwise *para*-H_2 addition requires an efficient catalyst to complete the process within seconds (i.e., on the timescale of relaxation processes). Initially, PHIP catalytic systems were based on Wilkinson's catalyst $RhCl(PPh_3)_3$,[24] Vaska's complex $Ir(CO)Cl(PPh_3)_2$, and Crabtree's catalyst $[(COD)Ir(PCy_3)(Py)]^+PF_6^-$, (COD = 1,4-cyclooctadiene, PCy_3 = tricyclohexylphosphine, Py = pyridine). These transition metal-based systems catalyze the molecular hydrogenation reaction, where *para*-H_2 is added to an unsaturated precursor via a molecular mechanism. Undergoing a molecular rather than a radical mechanism is essential for preserving the *para*-H_2 spin order, which allows the observation of a PHIP effect.[5,24] A number of other transition metals and chelating ligands have been evaluated.[5] In particular, implementation of bidentate ligands such as $Ph_2P(CH_2)_4PPh_2$ using Rh(I) as a catalyst has proven to be particularly effective for the ultrafast molecular addition of *para*-H_2 to double and triple bonds, resulting in polarization enhancements of $\sim 10^4$ upon transfer to adjacent ^{13}C nuclei.[26] Despite the apparent synthetic success of this methodology, the approach has been limited to organic solvents, thus limiting biological applications where aqueous catalysts and substrates are desired.

Homogeneous Aqueous Catalysis. Chemical modification of phosphine-based ligands has permitted preparation of efficient water-soluble Rh(I)-based catalytic systems. By far, the most common variation utilizes 4-bis[(phenyl-3-propanesulfonate) phosphine] butane di-sodium or its close variant,[22] where Rh(I) is chelated by norbornadiene and two phosphines connected by a four- or three-carbon bridge.[5] While aqueous homogeneous catalysts have opened the door to the first generation of mammalian in vivo imaging aided by PHIP,[30,31] the presence of Rh(I) catalysts in the HCA solution is presently an obstacle to clinical applications. Replacement of homogeneous PHIP by heterogeneous PHIP (HET-PHIP) processes will likely be the key to PHIP clinical applications. HET-PHIP catalysis was extensively reviewed a few years ago,[32] and is briefly discussed here in the context of recent advances and applications for aqueous media.

Heterogeneous (Solid/Liquid) Catalysis. A number of immobilized Rh complexes, based on either Wilkinson's catalyst or closely related systems based on Rh(I) derived from $[Rh(COD)_2]^+[BF_4]^-$, have been evaluated for PHIP, typically using diphenylphosphinoethyl-modified silica as a stationary phase. While some PHIP signal was often observed, the enhancement values were generally low due to slow

© 2015 John Wiley & Sons, Ltd.

hydrogenation rates, loss of *para*-H_2 polarization on the stationary phase surfaces, and chemical degradation of the catalyst. Alternatively, the application of transition metal nanoparticles is well established for gas–solid PHIP (see below) and has been demonstrated for capped platinum nanoparticles[33] in liquid–solid PHIP, where HP liquids are generated over solid-phase catalysts. Finally, Rh/TiO_2 nanoparticles have also been used for PHIP processes, and PHIP hyperpolarization of acrylamide and allyl methyl in D_2O solutions was demonstrated using these Rh/TiO_2 nanoparticles. This approach is promising for in vivo applications in spite of the low *P* levels demonstrated to date.

Heterogeneous (Solid/Gas) Catalysis. A silica-embedded Wilkinson's catalyst was also the first catalytic system enabling PHIP of gases at polarization levels sufficient for in vitro imaging.[34] Further progress in this area has been driven by the development of more robust nanoparticle catalysts such as Pt, Pd, or Rh on TiO_2, SiO_2, Al_2O_3, or ZrO_2 solid substrates. In general, better polarization transfer results were obtained with smaller nanoparticles: Rh and Pt provide superior results to Pd, while Al_2O_3 and especially TiO_2 were superior performing substrates.[32]

Hyperpolarization Instrumentation

The controlled reaction of *para*-H_2 with an unsaturated chemical precursor to produce a HCA takes place within an instrument referred to as a 'PHIP hyperpolarizer'. The features and underlying polarization transfer technique differentiate the hyperpolarizers constructed to date.[26,35,36] In general, inert gases such as N_2 shuttle the precursor through a manifold during injection into a heated reactor wherein it is rapidly and thoroughly mixed with a *para*-H_2 atmosphere, as shown in Figure 5. Before injection, the precursor is typically preheated to further speed the chemical reaction of pairwise addition. Two approaches to precursor/*para*-H_2 mixing have involved: (i) jet entrainment mixing[22] and, more commonly, (ii) spray mixing (Figure 5).[26,35,36] Other differences in hyperpolarizer designs concern the method used to transfer the spin order of *para*-H_2 after chemical synthesis to the heteronucleus, which include (i) field cycling[26] or (ii) more efficiently,[26,35,36] the application of RF pulses.[27] In the latter method, RF pulses may be synchronized with the operation of the manifold by a LabView interface to a National Instruments data acquisition card[26,35,36] or by a low-field NMR spectrometer.[36] In order to facilitate calibration of the RF pulse sequence parameters, in situ NMR detection capability for the hyperpolarizer is desirable.[36] The latter can result in a stand-alone PHIP hyperpolarizer with built-in quality assurance for the *P* produced.

Signal Amplification by Reversible Exchange (SABRE)

Another route to achieve hyperpolarization in solution is SABRE, introduced by Duckett and coworkers in 2009.[37] Similar to traditional PHIP, SABRE also takes advantage of the transfer of the spin order of *para*-H_2 to a target substrate

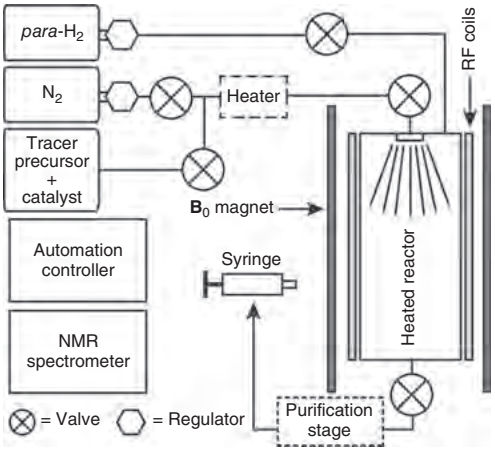

Figure 5. Generic PHIP hyperpolarizer schematic. Optional elements are boxes with dotted lines. In the PHIP hyperpolarization cycle: (i) *para*-H_2 is filled in the previously deoxygenated (via extensive N_2 gas venting) heated reactor, (ii) 'tracer PHIP precursor and catalyst' solution is loaded into an optional 'Heater' element followed by (iii) rapid solution spraying in the *para*-H_2-filled reactor under conditions of ^1H decoupling; (iv) when the spraying is finished (a few seconds), the polarization transfer sequence immediately transforms (<1 s) hyperpolarization from nascent *para*-hydrogen protons (Figure 4b) to hyperpolarization on the ^{13}C nucleus; (v) the solution containing the ^{13}C HP compound is ejected from the reactor through an optional purification stage for in vivo administration. The system can be purged with N_2 gas (typically ~1 min) to remove any residual solution from the PTFE lines to prepare for the next PHIP hyperpolarization production cycle

brought together by an organometallic catalyst. The key difference is that with SABRE, the transfer of spin order is not dependent on the hydrogenation of an unsaturated bond of the substrate. This difference brings about two advantages (i) the expansion of the range of applications of PHIP[24,25] with respect to the types of molecules that can serve as substrates and (ii) that destruction or alteration of the original structure of those substrates is not required – one does not need to develop a precursor structure that will yield a desired agent upon hydrogenation. SABRE is the newest of the hyperpolarization techniques described in this article, and consequently, its development for MRS/MRI is less advanced. It has some intrinsic advantages including simplicity, low cost, scalability, and the potential for continuous agent production, which are promising for biomedical applications. Indeed, it has already achieved substantial polarization enhancements in solution, with polarizations reaching ~10%.[38–40]

In order for SABRE to work, the catalyst must transiently bind both the target substrate and the atoms of *para*-H_2 with residence times that are long enough to allow the transfer of spin order or polarization to occur, but short enough to allow rapid turnover and subsequent accumulation of HP substrate in the solution. The process is illustrated in Figure 6. Although multiple organometallic complexes have been tested for SABRE, all to date use an iridium atom at the center – including the most successful SABRE catalyst, IrCl(COD)(IMes), where

© 2015 John Wiley & Sons, Ltd.

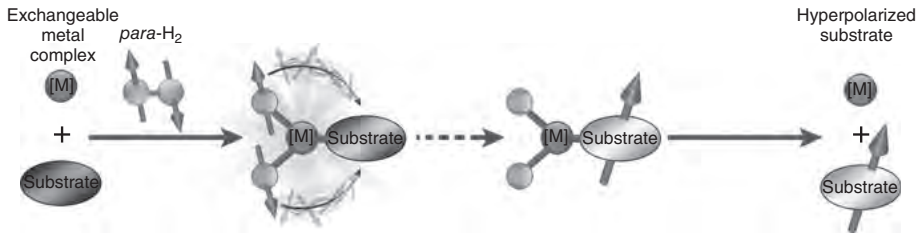

Figure 6. Schematic of the SABRE process. Reversible exchange of *para*-H_2 and the substrate on a metal catalyst ([M]) leads to a HP substrate. (Reproduced with permission from Ref. 6. © John Wiley & Sons, Ltd., 2015)

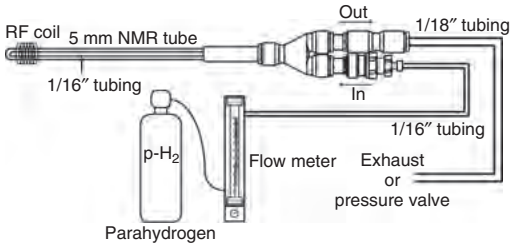

Figure 7. Experimental setup for SABRE. *Para*-H_2 bubbles through a catalytic solution in a conventional 5-mm NMR tube. The solution sits in a medium-wall-thickness NMR tube where *para*-H_2 is delivered via Teflon® tubing, and the expended gas leaves via an exhaust line that can be capped with a pressure-calibrated safety valve to allow SABRE at elevated *para*-H_2 pressure. (Reprinted with permission from M. L. Truong, *et al.*, *J. Phys. Chem. B*, 2014, **18**, 13882.[42] Copyright 2014 American Chemical Society)

IMes = 1,3-bis(2,4,6-trimethyl-phenyl)imidazol-2-ylidene and COD = cyclooctadiene. While the latter is not commercially available, its preparation is straightforward for those experienced with synthesis in inert-atmosphere environments.[41]

As with many catalysts used in traditional PHIP, the basic iridium-based SABRE catalyst must first be activated before use. This typically involves dissolving the catalyst in an organic solvent along with excess substrate such as pyridine or a structural derivative: attempting to activate the catalyst without excess substrate can lead to irreversible deactivation of the catalyst.[42] The solution is charged with *para*-H_2, either by loading a few atm of *para*-H_2 over the sample within a pressure-resistant vessel or by continuously bubbling the *para*-H_2 within a specially designed apparatus/tube, such as that depicted in Figure 7. Stepwise hydrogenation of the molecular COD-ring and binding of the H_2 to the Ir leads to loss of the eight-carbon ring, and the formation of a hexacoordinate site complex, with ligands comprising the IMes group, two hydrides, and three substrates, two of which are exchangeable. The progress of activation may be followed by observing changes in the characteristics of hydride resonances of transient species and the final activated structure.[42]

SABRE experiments can be divided into two types: ex situ and in situ, depending on the location of the sample vessel during polarization transfer with respect to the MR magnet. The vast majority of SABRE experiments are performed ex situ: spin order is transferred via scalar couplings between the involved nuclear spins during the lifetime of the catalyst complex. The spin flips must be nearly energy conserving: thus, the magnetic field must be sufficiently low to make the frequency difference between the hydride spins and the substrate spins similar to the scalar coupling between them. This corresponds to ~6 mT for ^{1}H and ~1 μT for ^{15}N.[40] Thus, the sample must be outside the MR magnet or within a fringe field for polarization transfer, and the sample rapidly moved to the magnet for detection. However, SABRE enhancements can also be observed in situ at high field.[41] In this case, the mechanism appears to be mediated by dipolar cross-relaxation between the HP hydride spins and the substrate spins.[41,42] While much less efficient, in situ SABRE does not require sample shuttling. In addition, the application of RF pulse sequences, for example, to allow mixing of spin states by driving the spins into level anti-crossing regimes,[43] may dramatically improve the efficiency of SABRE in situ.

To date, only a limited number of HCAs have been HP via SABRE. Besides pyridine (with ^{1}H and ^{15}N polarizations approaching ~10%[38,40]), SABRE enhancements of amino acids and small peptides have been reported at low field.[44] Most attention has been directed at biologically relevant pyridine derivatives. For example, ^{1}H enhancements of ~230 and ~1400 vs conventional MRS were reported for the tuberculosis drugs isoniazid and pyrazinamide in deuterated methanol at 700 MHz, respectively, corresponding to ^{1}H P values (P_H) of nearly ~1.3 and ~8%.[39] Nicotinamide was used to demonstrate SABRE in pure water, albeit with a more modest enhancement of ~33-fold at 9.4 T,[42] by first activating the catalyst in ethanol, drying it, and reconstituting it in an aqueous solution.

Finally, in addition to the limitations imposed by the catalysts and substrates that are presently available and the need to perform SABRE in biologically compatible media, the catalysts themselves present an obstacle to the application of SABRE in the clinic. The catalysts are expensive and potentially toxic, making their recovery desirable after agent hyperpolarization. In this regard, following efforts of heterogeneous PHIP (HET-PHIP) by Koptyug and coworkers,[32] 'HET-SABRE' enhancement of pyridine using SABRE catalysts that were covalently immobilized onto solid substrates of microscale polymer beads has been achieved.[45] Although the enhancements were small (approximately fivefold), the feasibility of creating separable catalysts for the creation of pure SABRE HP agents was demonstrated.

© 2015 John Wiley & Sons, Ltd.

Spin-exchange Optical Pumping (SEOP)

Hyperpolarization of noble gases via SEOP was first demonstrated by Bouchiat *et al.* in 1960, following earlier pioneering work involving OP of alkali metal vapors by Kastler and others.[46] Over time, the technique has been refined with an aim to increase efficiencies of the OP and SE steps, as well as to reduce spin-relaxation or 'spin-destruction' rates, to enable the production of HP gases with sufficiently high P in large enough quantities for NMR/MRI applications. Major technical advances in these areas came with the implementation of high-power laser diode arrays (LDAs)[47] and the introduction of buffer gases and cell coatings.[46] These improvements have contributed to increases in noble gas polarization, including values as high as ~90% for ^{129}Xe (e.g., Ref. 48), upon which our discussion will focus.

Although the complexity of SEOP setups may vary, one minimally needs (i) an OP 'cell' that contains the noble gas of interest (^{129}Xe) and a small amount of alkali metal (Rb in the following discussion); (ii) a source of circularly polarized light resonant with the Rb electronic transition; (iii) a heater for the cell (to vaporize the Rb); and (iv) a magnetic field source. Circularly polarized laser light is used to optically pump Rb electrons into a selected spin state, as shown in Figure 8. A usually weak (~30 Gauss) magnetic field provides hyperfine Zeeman splitting of the Rb electronic energy states. Angular momentum is then transferred from the Rb electrons to the ^{129}Xe nuclear spins (Figure 8b) via gas-phase collisions.[46] Provided the OP/SE rates, respectively, exceed the electron and nuclear spin-relaxation rates, ^{129}Xe polarization can be increased far above thermal equilibrium according to[49]

$$P_{\mathrm{Xe}}(t_{\mathrm{p}}) = \frac{\gamma_{\mathrm{se}}}{\gamma_{\mathrm{se}} + \gamma_{\mathrm{w}}} \langle P_{\mathrm{Rb}} \rangle \left(1 - \mathrm{e}^{-(\gamma_{\mathrm{se}} - \gamma_{\mathrm{w}}) t_{\mathrm{p}}}\right) \qquad (1)$$

where P_{Xe} and P_{Rb} represent the polarizations of xenon nuclei and rubidium electrons, respectively, γ_{se} is the SE rate, γ_{w} the rate of ^{129}Xe spin destruction, and t_{p} the polarization time. Also present is N_2 as a buffer gas, which at a pressure of ~100–200 Torr is sufficient to collisionally quench alkali metal fluorescence, thus avoiding re-emission of photons with random polarization that would otherwise decrease P_{Rb}.[46,50] One challenge for hyperpolarizing ^{129}Xe is that most Rb/Xe collisions tend to depolarize Rb atoms *without* conserving spin angular momentum, making the Rb spin-destruction rate effectively proportional to the xenon nuclear density [Xe] – an issue that can be mitigated through the use of higher resonant laser fluxes (albeit with greater demands on thermal regulation[50]) and/or lower Xe partial pressures. Conducting SEOP for ^{129}Xe at lower total cell pressures also enables more efficient spin-exchange through three-body van der Waals collisions, in addition to the binary spin-exchange that is dominant at higher gas pressures.[51] On the other hand, higher cell pressures can broaden the Rb spectral lines resulting in more efficient absorption of the light.[49] Finally, silicon coatings are often used to reduce Xe nuclear spin destruction, and all the components of the SEOP setup must be chosen to minimize exposure of the HP gas to paramagnetic centers, strong field gradients, and zero crossings of the magnetic field.

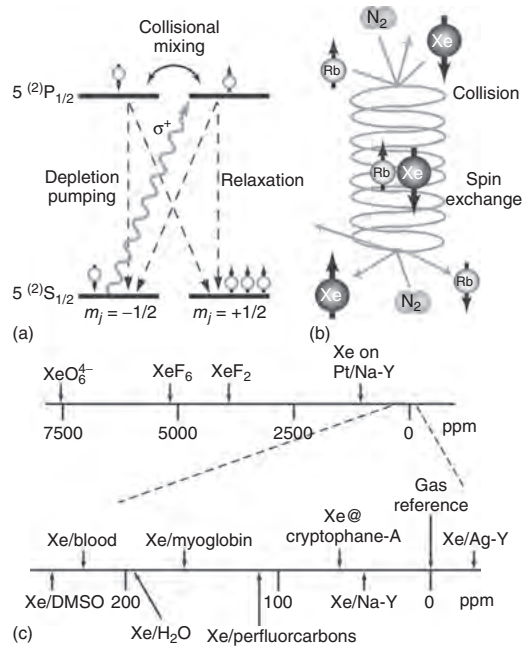

Figure 8. SEOP hyperpolarization and chemical shift sensitivity of ^{129}Xe. (a) Application of circularly polarized laser light and subsequent nonradiative relaxation results in depletion of one Rb electron (m_j) level and accrual of population in the other, rendering the Rb electronically spin polarized (Rb nuclear spin levels not shown). (b) Gas-phase collisions allow spin-exchange between Rb electrons and ^{129}Xe nuclei, resulting in HP ^{129}Xe with time. A three-body collision is shown in this example, with N_2 molecules facilitating formation and break-up of the complex. (c) Chemical shifts for ^{129}Xe in different environments. (Reproduced with permission from Ref. 7. © Elsevier, 2002)

Many different polarizers have been developed to maximize the achievable polarization, P_{Xe}, and/or the rate of production of HP Xe. Their designs are typically grouped into two categories. First, in the continuous-flow (CF) method illustrated in Figure 9,[49,51] a xenon gas mixture is polarized as it passes continuously through the OP cell and is subsequently collected using a cryogenic 'cold finger',[49] where it is stored at high field (>500 G) before it is carefully warmed[52] to allow transfer to a secondary vessel with minimal losses of P_{Xe}. For example, Ruset *et al.*[51] (Figure 9a) employed a number of features – including a Rb presaturator upstream of a ~1.8 m optical cell, a high laser power (~90 W), a carefully designed optical path, and a relatively low Xe density and total pressure (allowing it to exploit the more efficient three-body van der Waals SE interaction) – to attain a peak ^{129}Xe polarization of ~67% and a high output rate of 6 L Xe/h at $\%P_{\mathrm{Xe}} = 22\%$.

Second, the stopped-flow (SF) method (Figure 9b[48,53]) takes place in a closed system where gas delivery, SEOP, and collection are performed sequentially. The cell is loaded with the desired gas mixture, and the gas is illuminated by the laser

 © 2015 John Wiley & Sons, Ltd.

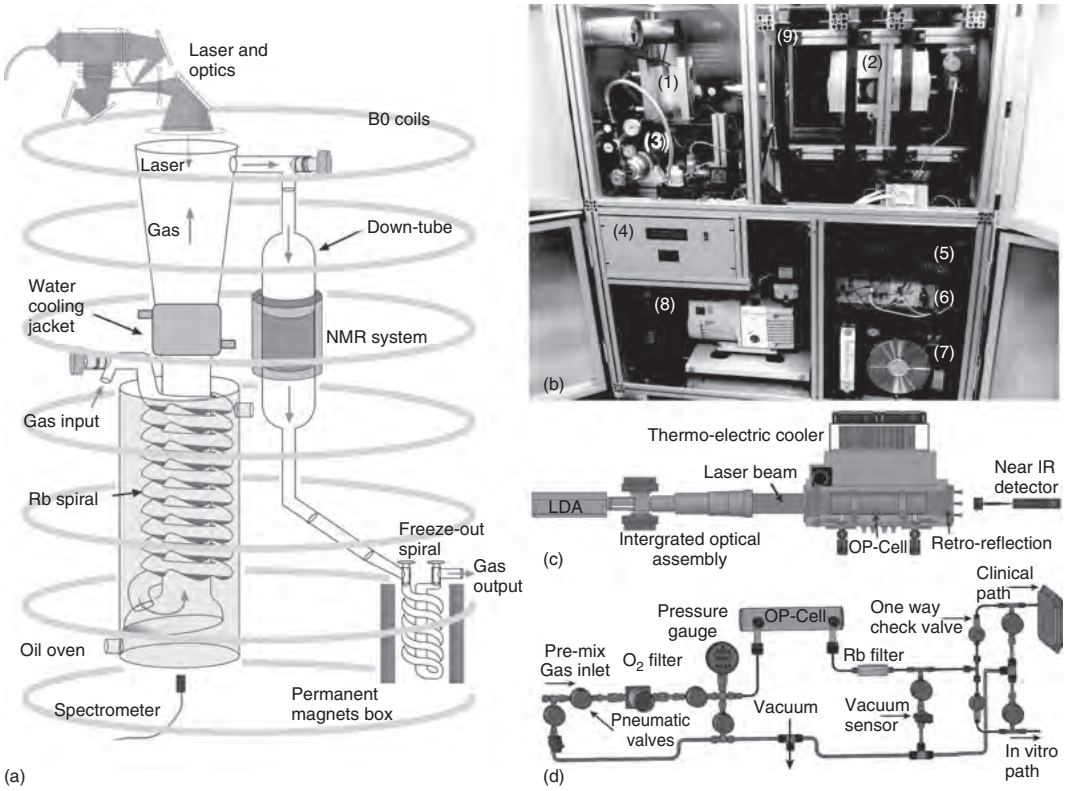

Figure 9. Examples of ^{129}Xe hyperpolarizers. (a) Diagram showing the CF design of Ruset *et al.*[51] (Reproduced with permission from Ref. 51. © American Physical Society, 2006) (b–d) Our Consortium's second-generation SF Xe hyperpolarizer. The photo in (b) shows the principal components of the device [(1) laser; (2) 3-D printed oven; (3) Xe gas supply; (4) microcontroller box; (5) power supplies; (6) low-frequency NMR spectrometer; (7) water chiller; (8) vacuum pumps; (9) electromagnetic coils]. Diagrams showing the oven/optical path and gas manifold are shown, respectively, in (c) and (d). (Reprinted with permission from P. Nikolaou, *et al.*, *Anal. Chem.*, 2014, **86**, 8206.[54] Copyright 2014 American Chemical Society)

for ~10–30 min until P_{Xe} nears a steady state. Before collection, the SEOP cell is cooled to condense the alkali metal vapor. The HP Xe can then be cryo-collected or simply expanded into another container (e.g., a Tedlar® bag).

The second approach is simpler and easier to automate, and the reduction in magnetization density that results from HP gas dilution with buffer gas can be mitigated using high [Xe] mixes.[48] Nikolaou *et al.* recently presented an 'open-source' SF polarizer design (Figure 9b–d[54]) utilizing a 200-W narrowed (~0.27 nm FWHM) LDA capable of attaining polarizations of ~90%, ~57%, ~50%, ~30%, for Xe partial pressures of ~300, ~500, ~760, and ~1570 Torr backfilled with N_2 to 2000 Torr, with a throughput of ~1 L h^{-1}.[48]

Standard diagnostic techniques used in SEOP experiments include in situ low-field NMR spectroscopy to determine and control for P_{Xe}, and near-infrared optical absorption spectroscopy to monitor pump laser wavelength, absorption profile, and inferred electronic P_{Rb}. While not strictly necessary for HP Xe preparation, additional diagnostic techniques such as Faraday rotation,[55] ESR[46] to measure alkali metal density and spin polarization, and Raman spectroscopy to map elevated gas temperatures within the OP cell have also been implemented to better understand the complex processes underlying mass, energy, and polarization transport within the SEOP apparatus.

MRS applications of HP Xe typically exploit the extraordinary sensitivity of xenon's chemical shift to its local molecular environment (Figure 8c).[7] Of the two NMR-active xenon isotopes – ^{129}Xe ($I = 1/2$) and ^{131}Xe ($I = 3/2$) – only ^{129}Xe has sufficiently long relaxation times in condensed phases to allow MRS. Xenon's highly polarizable electron cloud also allows it to participate in relatively substantial van der Waals interactions with proteins, lipid membranes, and living tissues. Xenon is not naturally found in the body in appreciable concentrations, which is both an advantage and a limitation: HP ^{129}Xe spectra will be background-free, but achieving efficient HP Xe delivery to the body is key. Delivery options are respiration and dissolution into the blood from the lungs; direct or intravenous injection of Xe-saturated solutions[7]; or ex vivo gas dissolution into the blood or other solutions using off-the-shelf gas-exchange modules.[56]

© 2015 John Wiley & Sons, Ltd.

When Xe is dissolved in bodily tissues, a number of resonances corresponding to different cellular and tissue compartments may be observed generally within a range ~185–215 ppm downfield from the gas reference at ~0 ppm.[7] For example, the shift of ^{129}Xe is so sensitive that its resonance in red blood cells responds to changes in blood oxygenation.[57] Functional studies of the brain are thus possible. The large ^{129}Xe shift between xenon in the lung space and that dissolved in tissues may be exploited for a variety of pulmonary functional MRS/MRI studies, including studies of gas-exchange efficiency in healthy versus pathological tissues. Nevertheless, without further intervention xenon's concentration in the body is generally too low – and its interactions too weak and nonspecific – for ^{129}Xe MRS to provide much more in the way of specific biomolecular information.

To overcome this low sensitivity and improve its specificity, HP ^{129}Xe can be augmented with a host molecule, which can be functionalized to act as a *biosensor* as exemplified in Figure 10.[58] The approach exploits the strong interaction between xenon and cryptophanes, which are molecules that can bind Xe atoms within their internal hydrophobic cavities. Indeed, cryptophanes are an excellent choice for the superstructure of xenon biosensors, not only because of their relatively high xenon affinity (association constant, $K_a \sim 10^3 - 10^4\ M^{-1}$) but also because the exchange and relaxation timescales are compatible with MRS. Moreover, they can be chemically functionalized to facilitate both aqueous solubility and covalent linkage to a chosen functional group to target specific bioanalytes. In principle, almost any ligand or antibody can be used as a functional group for the purposes of biosensing,[8] and multiple cages/biosensors could be simultaneously employed to allow multiplexed bioanalyte detection. The key feature empowering the biosensor approach is that the chemical shift of Xe within a biosensor cage that has bound a bioanalyte is measurably different from that of Xe residing within an unbound cage – thereby allowing the binding event to be detected via HP ^{129}Xe MRS. It is expected that for in vivo applications, rather than delivering Xe-loaded biosensors to the body in a single bolus, one would first administer the biosensors to the subject and allow them time to bind to their biomolecular targets. Then later, HP Xe may be delivered (using an above method) so that it would have the opportunity to locate the biosensor cages immediately before MRS.

This type of direct-detection experiment would yield three types of ^{129}Xe peaks: one for unbound Xe in the bulk environment, one for Xe trapped in an unbound host biosensor molecule, and one for Xe residing in biosensor molecules bound to targeted analytes. However, if the targeted bioanalyte is in low concentration, the bound Xe signal can be buried in noise. One way around this problem is to employ HP chemical exchange saturation transfer, or Hyper-CEST.[59] Hyper-CEST requires that the exchange of HP nuclei between sites is slow enough to give rise to unique, addressable resonances – yet fast enough to allow significant fractions of the populations to undergo exchange during the experiment.[8] Thus, if a saturating RF pulse is applied at the frequency for a bound Xe resonance, it will reduce the magnetization not only for the bound Xe pool but also for the (typically much larger) *bulk* Xe pool: off-resonance saturation provides a control/reference signal. The greater sensitivity afforded by indirectly measuring the presence of activated biosensors via the more sensitive bulk Xe signal allows detection of concentrations as low as ~100 nM, with further optimization not inconceivably improving the detection limit to the ~700 fM range.[8]

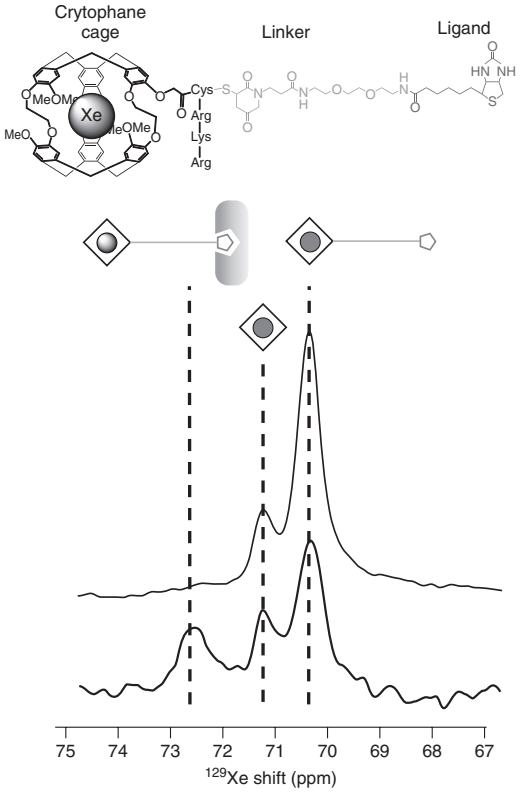

Figure 10. Structure and MR of a xenon biosensor. The chemical structure of a xenon biosensor molecule comprises a cryptophane cage, a linker group, and a molecule (e.g., biotin) to bind to a targeted bioanalyte (e.g., avidin) with high affinity and specificity.[58] Below the structure are ^{129}Xe spectra monitoring the binding of biotin-functionalized xenon to the prototypical bioanalyte avidin. The spectra show only the cryptophane-bound peaks; the (much larger) peak corresponding to free xenon in water is at 193 ppm. The spectra differ by the absence (top) and presence (bottom) of 80 nmol avidin in solution, manifesting in the bottom spectrum by the appearance of a new peak at ~72.5 ppm. Adapted from figures courtesy of Prof. Alex Pines

Conclusions

In summary, four hyperpolarization techniques have been described here in detail that either successfully enable in vivo MRS studies (d-DNP, PHIP, and SEOP/Xe) or have a strong potential for in vivo MRS in the near future (SABRE). Key features of these hyperpolarization methods from the perspective of their biomedical use are compared in Table 1.

© 2015 John Wiley & Sons, Ltd.

Table 1. Comparison of four hyperpolarization methods

Parameter	d-DNP	PHIP	SABRE	SEOP/Xe
Wide range of agents	Yes	No	No	No
Straightforward scalability	No	Yes	Yes	Yes
High (>50%/order-unity) polarization	Yes	Yes	No	Yes
Moderately high (>1%) polarization	Yes	Yes	Yes	Yes
Continuous generation	No	Yes	Yes	Yes
Different modes of production, i.e., continuous (C) vs batch (B)/stopped-flow (SF)	B/SF	C and B/SF	C and B/SF	C and B/SF
Preparation of 'pure' agents	Yes	Under development	Under development	Yes
Preparation of concentrated agent suitable for in vivo MRS use	Yes	Yes	No	Yes
Long-lived in vitro agent (relaxation time > 1 min)	Yes	Yes	Yes	Yes
Long-lived in vivo agent (relaxation time > 0.5 min)	Yes	Yes	No	No
Technology cost	High	Low	Low	Medium
Operational cost	High	Low	Low	Medium
Commercially available device	Yes/multiple	No (but yes for *para*-H_2 generator)	Yes	Yes
Phase of agent	Gas/liquid/solid	Liquid/gas	Liquid	Gas
Environment sensing (ES) and penetration of biochemical pathways (BP)	BP and ES	BP and ES	ES	ES

Some of these techniques have evolved rapidly from proof-of-principle studies using custom-built instrumentation to robust commercial equipment. This in turn has fueled reliable in vivo experimentation – including the first clinical trials in human volunteers. The ongoing innovations in instrumentation and the fundamental technology of hyperpolarization will likely continue to significantly and positively impact access and applications for the broader biomedical community, expanding the utility of HP methods as a new tool for probing fundamental biomedical questions.

Acknowledgments

The authors thank funding support by NSF under grants CHE-1416268, CHE-1416432, NIH 1R21EB018014, 1R21EB020323, by the DOD CDMRP breast cancer award W81XWH-12-1-0159/BC112431, and by CDMRP PRMRP awards W81XWH-15-1-0271 and W81XWH-15-1-0272. M.J.B. acknowledges the support of the School of Medicine, University of Nottingham and ESPRC grant EP/G003076/1. N.W. acknowledges the support of the MDACC Odyssey Program, NCI R25T CA057730, and DoD PC131680.

Biographical Sketches

Boyd Goodson graduated from Princeton University in 1995 and earned his PhD in chemistry in 1999 with Alexander Pines at U.C. Berkeley. Following postdoctoral work with Ahmed Zewail at Caltech, in 2002, Goodson joined the faculty at Southern Illinois University Carbondale and was promoted to full professor in 2014. Goodson's research interests concern NMR/MRI sensitivity enhancement and hyperpolarization.

Nicholas Whiting, b 1983. PhD (supervisor Prof. Boyd Goodson) 2010, Southern Illinois University, Carbondale, IL, USA. NSF International Research Fellow at the University of Nottingham, UK (with Dr. Michael Barlow and Prof. Peter Morris). Odyssey and NCI Cancer Prevention Fellow (with Prof. Pratip Bhattacharya) at UT MD Anderson Cancer Center.

Aaron M. Coffey, PhD 2014, Vanderbilt University, Nashville, TN, USA. Postdoctoral Fellow at Vanderbilt University Institute of Imaging Science (with Prof. Eduard Y. Chekmenev). Co-authored >30 peer-reviewed articles covering advanced MR detection hardware and utilizing hyperpolarization techniques to enable MR contrast agents for in vivo molecular imaging for improved human health.

Panayiotis Nikolaou, b 1978, PhD (supervisor Prof. Boyd Goodson) 2010, Southern Illinois University, Carbondale, IL, USA. Currently, Postdoctoral Fellow, Vanderbilt University, Nashville, TN, USA (with Prof. Eduard Y. Chekmenev) at the Vanderbilt University Institute of Imaging Science.

Fan Shi. After graduating with BS/MS degrees from Zhengzhou University (China), he joined the Goodson Lab at SIUC (USA) in 2011. His research has concerned the development and application of SABRE catalysts – particularly under heterogeneous conditions (HET-SABRE). Fan graduated with a PhD in 2015 and is now an intern with Cabot Labs in Chicago, IL.

Brogan Gust graduated with a BS degree in chemistry from Southern Illinois University Carbondale in 2013. While at SIUC, he was under the guidance of Boyd Goodson researching NMR enhancement using Xenon-129 hyperpolarization.

Max Gemeinhardt joined the Goodson Lab at SIUC in 2011 as undergraduate working on pH-sensing SPIONs. He graduated in 2012 with a BS degree and is currently pursuing a MS degree at SIUC in the Goodson Lab, where his current research interests include cryptophane host–guest inclusion complexes and SABRE NMR enhancement.

Roman V. Shchepin, b 1978, PhD (Prof. Patrick Dussault) 2006 in University of Nebraska-Lincoln (Lincoln, NE). Postdoctoral Fellow at Vanderbilt University Department of Chemistry (2007–2009) with Prof. Ned A. Porter and VUIIS (2010–2013) with Prof. Eduard Y. Chekmenev. He is currently a Research Instructor at VUIIS with main focus on the chemistry of hyperpolarized NMR/MRI. Coauthored >30 peer-reviewed original research publications.

Jason G. Skinner. b 1989. M.Phys., 2012. PhD research student (supervisors: Prof. I. Hall, Prof. P. Morris, Dr. M. Barlow), University of Nottingham, UK. Research interests include spin-exchange optical pumping, hyperpolarized noble gas lung MRI, and disease detection via exhaled volatile organic compounds.

 © 2015 John Wiley & Sons, Ltd.

Jonathan R. Birchall, b 1991, M.Phys., 2013, PhD research student (supervisors: Prof. I. Hall, Dr. M. Barlow, Prof. J. Owers-Bradley), University of Nottingham, UK. Research interests include development and analysis of spin-exchange optical pumping techniques for functional human lung imaging.

Michael J. Barlow, b 1958, PhD (Supervisor Prof. Brian Ridley FRS) 1988 University of Essex, UK. Postdoctoral Fellow at MOD Malvern, Durham University, Surrey University, Imperial College London and Rutherford Appleton Lab, Oxford. Instrument Manager – MAG team NASA Cassini Mission. Faculty Fellow University of Nottingham. Co-authored >20 peer-reviewed publications in the areas of semiconductor physics, space physics, solid-state NMR, laser physics, and hyperpolarized MRI.

Eduard Y. Chekmenev, b 1977, PhD (supervisor Prof. Richard J. Wittebort) 2003, University of Louisville, KY, USA. Postdoctoral Fellow at NHMFL, Tallahassee, FL, USA (with Prof. Timothy Cross) and at Caltech (with Prof. Daniel P. Weitekamp) and HMRI (with Dr. Brian D. Ross). Co-authored >70 peer-reviewed original research publications in the areas of solid-state NMR of proteins and hyperpolarized NMR/MRI. Research interests include development of methods of hyperpolarization for Biomedical applications.

References

1. J. H. Ardenkjaer-Larsen, B. Fridlund, A. Gram, G. Hansson, L. Hansson, M. H. Lerche, R. Servin, M. Thaning, and K. Golman, *Proc. Natl. Acad. Sci. U. S. A.*, 2003, **100**, 10158.
2. J. Kurhanewicz, D. B. Vigneron, K. Brindle, E. Y. Chekmenev, A. Comment, C. H. Cunningham, R. J. DeBerardinis, G. G. Green, M. O. Leach, S. S. Rajan, R. R. Rizi, B. D. Ross, W. S. Warren, and C. R. Malloy, *Neoplasia*, 2011, **13**, 81.
3. R. Sriram, J. Kurhanewicz, and D. B. Vigneron, in eMagRes, John Wiley & Sons, Ltd: Chichester, 2014, Chap. Hyperpolarized carbon-13 MRI and MRS studies, 311.
4. S. J. Nelson, J. Kurhanewicz, D. B. Vigneron, P. E. Z. Larson, A. L. Harzstark, M. Ferrone, M.van Criekinge, J. W. Chang, R. Bok, I. Park, G. Reed, L. Carvajal, E. J. Small, P. Munster, V. K. Weinberg, J. H. Ardenkjaer-Larsen, A. P. Chen, R. E. Hurd, L. I. Odegardstuen, F. J. Robb, J. Tropp, and J. A. Murray, *Sci. Transl. Med.*, 2013, 5.
5. R. A. Green, R. W. Adams, S. B. Duckett, R. E. Mewis, D. C. Williamson, and G. G. R. Green, *Prog. Nucl. Mag. Res. Sp.*, 2012, **67**, 1.
6. P. Nikolaou, B. M. Goodson, and E. Y. Chekmenev, *Chem. Eur. J.*, 2015, **21**, 3156.
7. B. M. Goodson, *J. Magn. Reson.*, 2002, **155**, 157.
8. L. Schroder, *Phys. Medica*, 2013, **29**, 3.
9. A. Comment and M. E. Merritt, *Biochemistry*, 2014, **53**, 7333.
10. R. G. Griffin and T. F. Prisner, *Phys. Chem. Chem. Phys.*, 2010, **12**, 5737.
11. T. Maly, G. T. Debelouchina, V. S. Baja, K.-N. Hu, C.-G. Joo, M. L. Mak-Jurkauskas, J. R. Sirigiri, P. C. A.van der Wel, J. Herzfeld, R. J. Temkin, and R. G. Griffin, *J. Chem. Phys.*, 2008, **128**, 052211.
12. J. H. Ardenkjaer-Larsen, A. M. Leach, N. Clarke, J. Urbahn, D. Anderson, and T. W. Skloss, *NMR Biomed.*, 2011, **24**, 927.
13. P. Dutta, G. Martinez, and R. Gillies, *Biophys. Rev.*, 2013, **5**, 271.
14. H. Johannesson, S. Macholl, and J. H. Ardenkjaer-Larsen, *J. Magn. Reson.*, 2009, **197**, 167.
15. Y. Lee, N. M. Zacharias, D. Piwnica-Worms, and P. K. Bhattacharya, *Chem. Comm.*, 2014, **50**, 13030.
16. K.-N. Hu, H.-H. Yu, T. M. Swager, and R. G. Griffin, *J. Am. Chem. Soc.*, 2004, **126**, 10844.
17. T. R. Eichhorn, Y. Takado, N. Salameh, A. Capozzi, T. Cheng, J.-N. Hyacinthe, M. Mishkovsky, C. Roussel, and A. Comment, *Proc. Natl. Acad. Sci. U. S. A.*, 2013, **110**, 18064.
18. L. Lumata, Z. Kovacs, C. Malloy, A. D. Sherry, and M. Merritt, *Phys. Med. Biol.*, 2011, **56**, N85.
19. A. Farkas, Ortho-Hydrogen, Para-Hydrogen, and Heavy Hydrogen, Cambridge University Press: Cambridge, UK, 1935.
20. L. Pauling and E. B.Wilson Jr, Introduction to Quantum Mechanics, with Applications to Chemistry, New edn, Dover: Mineola, New York, United States, 1935.
21. J. B. Hövener, S. Bar, J. Leupold, K. Jenne, D. Leibfritz, J. Hennig, S. B. Duckett, and D.von Elverfeldt, *NMR Biomed.*, 2013, **26**, 124.
22. S. Kadlecek, V. Vahdat, T. Nakayama, D. Ng, K. Emami, and R. Rizi, *NMR Biomed.*, 2011, **24**, 933.
23. B. Feng, A. M. Coffey, R. D. Colon, E. Y. Chekmenev, and K. W. Waddell, *J. Magn. Reson.*, 2012, **214**, 258.
24. C. R. Bowers and D. P. Weitekamp, *Phys. Rev. Lett.*, 1986, **57**, 2645.
25. T. C. Eisenschmid, R. U. Kirss, P. P. Deutsch, S. I. Hommeltoft, R. Eisenberg, J. Bargon, R. G. Lawler, and A. L. Balch, *J. Am. Chem. Soc.*, 1987, **109**, 8089.
26. K. Golman, O. Axelsson, H. Johannesson, S. Mansson, C. Olofsson, and J. S. Petersson, *Magn. Reson. Med.*, 2001, **46**, 1.
27. M. Goldman and H. Johannesson, *C. R. Physique*, 2005, **6**, 575.
28. K. V. Kovtunov, M. L. Truong, D. L. Barskiy, O. G. Salnikov, V. I. Bukhtiyarov, A. M. Coffey, K. W. Waddell, I. V. Koptyug, and E. Y. Chekmenev, *J. Phys. Chem. C*, 2014, **118**, 28234.
29. R. V. Shchepin, A. M. Coffey, K. W. Waddell, and E. Y. Chekmenev, *Anal. Chem.*, 2014, **86**, 5601.
30. N. M. Zacharias, H. R. Chan, N. Sailasuta, B. D. Ross, and P. Bhattacharya, *J. Am. Chem. Soc.*, 2012, **134**, 934.
31. P. Bhattacharya, E. Y. Chekmenev, W. F. Reynolds, S. Wagner, N. Zacharias, H. R. Chan, R. Bünger, and B. D. Ross, *NMR Biomed.*, 2011, **24**, 1023.
32. K. V. Kovtunov, V. V. Zhivonitko, I. V. Skovpin, D. A. Barskiy, and I. V. Koptyug, *Top. Curr. Chem.*, 2013, **338**, 123.
33. M. Irfan, N. Eshuis, P. Spannring, M. Tessari, M. C. Feiters, and F. P. J. T. Rutjes, *J. Phys. Chem. C*, 2014, **118**, 13313.
34. L. S. Bouchard, S. R. Burt, M. S. Anwar, K. V. Kovtunov, I. V. Koptyug, and A. Pines, *Science*, 2008, **319**, 442.
35. J.-B. Hövener, E. Chekmenev, K. Harris, W. Perman, L. Robertson, B. Ross, and P. Bhattacharya, *Magn. Reson. Mater. Phy.*, 2009, **22**, 111.
36. K. W. Waddell, A. M. Coffey, and E. Y. Chekmenev, *J. Am. Chem. Soc.*, 2011, **133**, 97.
37. R. W. Adams, J. A. Aguilar, K. D. Atkinson, M. J. Cowley, P. I. P. Elliott, S. B. Duckett, G. G. R. Green, I. G. Khazal, J. Lopez-Serrano, and D. C. Williamson, *Science*, 2009, **323**, 1708.
38. M. J. Cowley, R. W. Adams, K. D. Atkinson, M. C. R. Cockett, S. B. Duckett, G. G. R. Green, J. A. B. Lohman, R. Kerssebaum, D. Kilgour, and R. E. Mewis, *J. Am. Chem. Soc.*, 2011, **133**, 6134.
39. H. Zeng, J. Xu, J. Gillen, M. T. McMahon, D. Artemov, J.-M. Tyburn, J. A. B. Lohman, R. E. Mewis, K. D. Atkinson, G. G. R. Green, S. B. Duckett, and P. C. M.van Zijl, *J. Magn. Reson.*, 2013, **237**, 73.
40. T. Theis, M. L. Truong, A. M. Coffey, R. V. Shchepin, K. W. Waddell, F. Shi, B. M. Goodson, W. S. Warren, and E. Y. Chekmenev, *J. Am. Chem. Soc.*, 2015, **137**, 1404.
41. D. A. Barskiy, K. V. Kovtunov, I. V. Koptyug, P. He, K. A. Groome, Q. A. Best, F. Shi, B. M. Goodson, R. V. Shchepin, A. M. Coffey, K. W. Waddell, and E. Y. Chekmenev, *J. Am. Chem. Soc.*, 2014, **136**, 3322.

 © 2015 John Wiley & Sons, Ltd.

42. M. L. Truong, F. Shi, P. He, B. Yuan, K. N. Plunkett, A. M. Coffey, R. V. Shchepin, D. A. Barskiy, K. V. Kovtunov, I. V. Koptyug, K. W. Waddell, B. M. Goodson, and E. Y. Chekmenev, *J. Phys. Chem. B*, 2014, **18**, 13882.
43. A. N. Pravdivtsev, A. V. Yurkovskaya, H.-M. Vieth, and K. L. Ivanov, *Phys. Chem. Chem. Phys.*, 2014, **16**, 24672.
44. S. Gloggler, R. Muller, J. Colell, M. Emondts, M. Dabrowski, B. Blumich, and S. Appelt, *Phys. Chem. Chem. Phys.*, 2011, **13**, 13759.
45. F. Shi, A. M. Coffey, K. W. Waddell, E. Y. Chekmenev, and B. M. Goodson, *Angew. Chem. Int. Ed.*, 2014, **53**, 7495.
46. T. G. Walker and W. Happer, *Rev. Mod. Phys.*, 1997, **69**, 629.
47. M. E. Wagshul and T. E. Chupp, *Phys. Rev. A*, 1989, **40**, 4447.
48. P. Nikolaou, A. M. Coffey, L. L. Walkup, B. M. Gust, N. Whiting, H. Newton, S. Barcus, I. Muradyan, M. Dabaghyan, G. D. Moroz, M. Rosen, S. Patz, M. J. Barlow, E. Y. Chekmenev, and B. M. Goodson, *Proc. Natl. Acad. Sci. U. S. A.*, 2013, **110**, 14150.
49. B. Driehuys, G. D. Cates, E. Miron, K. Sauer, D. K. Walter, and W. Happer, *Appl. Phys. Lett.*, 1996, **69**, 1668.
50. A. L. Zook, B. B. Adhyaru, and C. R. Bowers, *J. Magn. Reson.*, 2002, **159**, 175.
51. I. C. Ruset, S. Ketel, and F. W. Hersman, *Phys. Rev. Lett.*, 2006, **96**, 053002.
52. N. N. Kuzma, B. Patton, K. Raman, and W. Happer, *Phys. Rev. Lett.*, 2002, **88**, 147602.
53. M. S. Rosen, T. E. Chupp, K. P. Coulter, R. C. Welsh, and S. D. Swanson, *Rev. Sci. Instrum.*, 1999, **70**, 1546.
54. P. Nikolaou, A. M. Coffey, M. J. Barlow, M. Rosen, B. M. Goodson, and E. Y. Chekmenev, *Anal. Chem.*, 2014, **86**, 8206.
55. E. Babcock, I. Nelson, S. Kadlecek, B. Driehuys, L. W. Anderson, F. W. Hersman, and T. G. Walker, *Phys. Rev. Lett.*, 2003, **91**, 4.
56. Z. I. Cleveland, H. E. Moller, L. W. Hedlund, and B. Driehuys, *J. Phys. Chem. B*, 2009, **113**, 12489.
57. J. Wolber, A. Cherubini, M. O. Leach, and A. Bifone, *Magn. Reson. Med.*, 2000, **43**, 491.
58. M. M. Spence, S. M. Rubin, I. E. Dimitrov, E. J. Ruiz, D. E. Wemmer, A. Pines, S. Q. Yao, F. Tian, and P. G. Schultz, *Proc. Natl. Acad. Sci. U. S. A.*, 2001, **98**, 10654.
59. L. Schroder, T. J. Lowery, C. Hilty, D. E. Wemmer, and A. Pines, *Science*, 2006, **314**, 446.

 © 2015 John Wiley & Sons, Ltd.

CHAPTER

2

The Physics of Hyperpolarized Gas MRI

B.M. Goodson, K. Ranta, J.G. Skinner, A.M. Coffey, P. Nikolaou, M. Gemeinhardt, D. Anthony, S. Stephenson, S. Hardy, J. Owers-Bradley, M.J. Barlow and E.Y. Chekmenev

INTRODUCTION

Hyperpolarized (HP) gases have helped realize a growing list of potential applications—particularly within the biomedical and clinical realms. Integral to their use are the properties of such gaseous agents, as well as how they are prepared, stored, and delivered to the sample or subject. For example, arguably the most important property of a HP gas—besides its biological compatibility—is the lifetime of its highly nonequilibrium nuclear spin polarization ("hyperpolarization"). Such lifetimes must be sufficiently long to allow hyperpolarization to accumulate so that it lasts long enough for the agent to be delivered to the sample or target organ for imaging or spectroscopy. In turn, this crucial lifetime requirement dramatically limits the types of gases that can serve effectively as HP gas agents, and places practical constraints on how the gases are handled to best preserve and utilize the hyperpolarization. On the other hand, once delivered the polarization lifetime provides a powerful means of contrast—along with other key properties like density, position, motion, spectral frequency, and signal dynamics from chemical exchange.

The available methods of hyperpolarization are also vitally important. Although such methods were originally created and developed as part of fundamental physics or chemistry research with generally quite different—if any—uses in mind, biomedical applications have now grown to comprise a strong force driving the development of hyperpolarization technology. Additionally, such methods not only determine the amounts of HP gases produced and polarization levels that can be attained, but also further limit the viable choices of HP gas agents for potential biomedical applications. To date, virtually all biomedical HP gas studies have involved noble gases, with small hydrocarbons and other small-molecule gases showing promise. Such HP gases may be generated via either spin-exchange optical pumping (SEOP), metastability exchange optical pumping (MEOP), "brute-force" polarization (BFP), dynamic nuclear polarization (DNP), and/or parahydrogen-induced polarization (PHIP). Each of these approaches has advantages and limitations, and understanding how they work to produce and deliver a given HP gas is thus necessary for integration with a desired biomedical application.

This chapter is organized as follows. First, we describe the properties and behavior of HP gases. Following an introduction of the general properties of these substances, particular attention is given to modes of relaxation, general rules for care and handling of these gases, and some considerations on how best to utilize them in magnetic resonance (MR) studies (e.g., with respect to pulse sequences). Then we discuss the aforementioned methods of generating HP gases, with particular focus on SEOP, MEOP, DNP, and PHIP. The principles of each method are introduced, along with key design features and production performance of select gas "hyperpolarizers." Finally, we provide a summary and conclude with an outlook for HP gas approaches and technological development.

© 2017 Elsevier Inc. All rights reserved.

TABLE 2.1 MR Properties of Selected Gases of Interest for Hyperpolarized MRI

HP gas	Isotopes of interest	Nuclear spin (I)	Isoptope natural abundance	Gyromagnetic ratio (relative to ^{1}H)	Most effective HP methods
Xenon	^{129}Xe ^{131}Xe	1/2 3/2	26.44%, 21.18%	(−)0.27856 0.08257	SEOP & DNP
Helium	^{3}He	1/2	0.00014%	(−)0.76181	MEOP & SEOP
Krypton	^{83}Kr	9/2	11.55%	(−)0.03862	SEOP
Propane, d_6-propane	^{1}H ^{13}C	1/2 1/2	99.985%, 1.11%	(1) 0.25145	PHIP
Nitrous oxide	^{15}N	1/2	0.37%	(−)0.10137	DNP

HP GASES: PROPERTIES AND CONSIDERATIONS

General Properties

The physical properties that define the gas phase have significant implications for how HP gases are prepared and administered. For example, the weak intermolecular forces between gas particles give rise to characteristically low densities under ambient conditions—roughly three orders of magnitude lower than for condensed phases. In comparison to standard magnetic resonance imaging (MRI), such low densities represent a major limitation for MR detection and imaging, but this limitation is more than compensated by hyperpolarization. The low viscosity and high compressibility of gases facilitate rapid transport, storage, and delivery of HP gases to the subject via the lungs, and the miscibility of gases enables rapid and facile preparation of arbitrary admixtures. In terms of biological interactions the gases investigated for use in HP MRI are considered "simple" asphyxiants, although many possess varying degrees of anesthetic properties. Dilution and/or mixing with O_2 for respiration may be required for some applications, which may in turn impact signal strength and the lifetime of the HP state. On the other hand, the same solubility of some gases (e.g., xenon) in tissues that gives rise in part to anesthetic effects also can enable MR applications beyond gas-space imaging (particularly those that exploit chemical exchange between different environments), as discussed elsewhere in this book.

How gases move and interact with each other (and their surroundings) on the atomic level has significant implications for nuclear spin relaxation, as discussed in the next subsection. The restriction of free diffusive motion, often quantified by the apparent diffusion coefficient, can reflect microscale changes in lung structure. On the macroscopic level, because gases expand to adopt the shape of their containers, HP gas imaging allows investigation of lung void-space dynamics and the absence of signal can map pathological obstruction of gas flow. Moreover, agent dose is readily calculated using the ideal gas law (with quantities often measured in L · atm, referring to the volume and pressure of the gas). Nevertheless, HP gases must ultimately be delivered to subjects under ambient conditions (∼1 atm)—often requiring that the gas be expanded, compressed, condensed, and/or sublimated prior to agent administration. Finally, MR detection of HP gases obviously requires the presence of HP-storing nuclear spins, and thus the ready availability of clinical-scale quantities of a given gas with sufficient (naturally abundant or enriched) spins can influence the viability of an approach under consideration. Some key MR properties of selected gases discussed in this chapter are provided in Table 2.1.

Spin Relaxation Mechanisms of HP Gases

Gas-phase nuclear spin relaxation is one of the primary determinants of a prospective HP gaseous agent's viability. It not only determines the lifetime of the HP state, but also limits the level of polarization that can be achieved. Contributions to the nuclear spin relaxation rate of a gas can be categorized into intrinsic (i) and extrinsic (e) processes (e.g., Ref. [1]):

$$T_1^{-1} = \Gamma_i + \Gamma_e.$$

For example, the ^{129}Xe T_1 is commonly disassembled into five dominating contributions [2]:

$$T_1^{-1} = \Gamma_{it} + \Gamma_{ip} + \Gamma_{eo} + \Gamma_{eg} + \Gamma_{ew},$$

where contributions to the intrinsic rate are from (t)ransient Xe_2 dimers and (p)ersistent Xe_2 dimers, and extrinsic processes comprise paramagnetic (o)xygen interactions, diffusion through magnetic field (g)radients, and (w)all collisions. The first three terms can be quantified by [1,3]

$$\frac{1}{T_1} = \frac{[\mathrm{Xe}]}{56.1\ \mathrm{h}} + \frac{1 + (3.65 \times 10^{-3})}{4.59\ \mathrm{h}\left(1 + r_{\mathrm{B}}\frac{[B]}{[\mathrm{Xe}]}\right)} + 0.4\ \mathrm{s}^{-1}\ \mathrm{amg}^{-1} \times n_{\mathrm{O}_2},$$

where r_B is the persistent dimer breakup efficiency of a secondary gas B in the mixture relative to that of xenon, and n_{O2} is the oxygen concentration in amagats. In the absence of O_2 contamination, typical ^{129}Xe T_1 values are limited to a few hours and are dominated by spin rotation suffered during persistent dimer relaxation and paramagnetic relaxation from wall collisions. Variations in glass, coatings, and container geometry have made wall relaxation contributions notoriously difficult to quantitatively predict, but with careful preparation and protection, they can be as long as tens of hours [1,4]. Wall relaxation is commonly mitigated with siloxane glass coatings such as SurfaSil, and is also reduced at fields near a few Tesla [1].

In general, intrinsic relaxation for molecular gases is typically dominated by spin-rotation interactions. For example, for partially deuterated propane a T_1 of $\sim$6 s has been measured at low field [5], necessitating rapid transfer to samples when using HP propane. The T_1 for (*ortho*-)hydrogen is even shorter, on the millisecond timescale (although HP *ortho*-H_2 has been created in solution [6]). However, loss of the pure spin order of the singlet state of *para*-hydrogen requires interconversion with *ortho*-hydrogen, which can take weeks if proper precautions are taken with the storage vessel. Intrinsic relaxation of ^3He is known to be slow as well ($T_1 \sim$ days) so that hyperpolarization lifetime is typically limited by the presence of paramagnetic centers such as oxygen contamination or wall impurities. Indeed, ^3He relaxation times of hundreds of hours have been reported [7].

Intrinsic relaxation of quadrupolar noble gas nuclei (e.g., ^{131}Xe, ^{83}Kr) is much faster and is usually dominated by quadrupolar contributions suffered during Xe−Xe or Kr−Kr binary exchange [8]:

$$1/T_1^{131\mathrm{Xe}} = 0.0395\ \mathrm{s}^{-1}\ \mathrm{amg}^{-1} \times n_{\mathrm{Xe}},$$

$$1/T_1^{83\mathrm{Kr}} = 0.0016\ \mathrm{s}^{-1}\ \mathrm{amg}^{-1} \times n_{\mathrm{Kr}},$$

where the n values are in density units of amagat (1 amg is the number of gas particles per unit volume at 1 atm and 0 °C). These lifetimes can be orders of magnitude faster than the corresponding intrinsic effects measured in spin 1/2 nuclei—therefore limiting the densities that can be effectively polarized or stored [9]. In fact, quadrupolar contributions from van der Waals complexes and wall collisions make actual relaxation rates even higher. On the other hand, the low gyromagnetic ratio for ^{83}Kr makes it less susceptible to dipolar relaxation from the presence of oxygen in biological environments. While fast depolarization limits the achievable hyperpolarization magnitude and storage times for quadrupolar noble gases, it has also been shown to be useful as a form of contrast to probe surfaces, and fast relaxation may allow sufficiently rapid signal averaging to potentially support the utility of thermal polarizations in some circumstances [10].

Finally, extrinsic relaxation of each of these species can also be brought about by diffusion through magnetic field gradients, and thus care should be taken to ensure that fields used to produce or store HP gases are kept homogeneous [2]—particularly important for ^3He, because of its high gyromagnetic ratio ($\Gamma_{eg} \propto \gamma^2$) and otherwise ultralong relaxation times—with no zero-field crossings [11].

Storage and Delivery Considerations for HP Gases

Besides ensuring its biological compatibility and safe administration, the most important considerations for using any HP gas involve experimental design to maximize nuclear spin polarization and agent throughput, achieve efficient HP agent delivery, and maintain polarization levels as much as possible throughout the study.

First, any contributors to hyperpolarization destruction need to be addressed within and "downstream" of the polarization chamber. Although the lifetime of a given gas's polarization is physically capped by its intrinsic T_1 relaxation rate, this source of spin destruction is often small compared to extrinsic sources of polarization loss while transporting and delivering HP gas for imaging experiments. Indeed, gas polarizations can be unintentionally destroyed via a number of ways in an experimental setup, including paramagnetic relaxation, diffusion through magnetic field gradients, and movement of the gas through magnetic "zero-field" crossings. Paramagnetic relaxation can be mitigated first by ensuring that all polarizer materials that can come in contact with the HP gas have minimal magnetic impurities (e.g., PFA/PTFE vs stainless steel), and that gas lines are well

evacuated and/or purged with ultrapure gases to minimize O_2 exposure. When it comes to HP gas MRI on aerobic organisms, oxygen exposure will be unavoidable, but addition of O_2 to create breathable admixtures with HP gas should be performed only at the last possible step prior to agent administration. For HP ^{129}Xe, borosilicate glass components are often coated with silicon-based polymers (SurfraSil, etc.) [12,13], thereby limiting paramagnetic wall relaxation and increasing hyperpolarization lifetimes. However, for the smaller ^{3}He atoms, such coatings may hurt more than they help—and thus it can be important to choose glass with minimal paramagnetic impurities (e.g., GE180) [7]. For quadrupolar nuclei, hydrophobic coatings can accelerate relaxation [14] by enhancing physisorption, and thus uncoated (naturally hydrophilic) clean glass surfaces are desired.

Permanent magnets or smaller auxiliary fields are sometimes used to accumulate or transport gases to avoid field relaxation. Particularly for ^{3}He, minimizing field gradients using homogeneous fields (e.g., Helmholtz coils or other arrangements) [15] can be important for minimizing polarization losses. During the transfer of a prepared HP gas sample to a subject, special attention needs to be placed toward keeping the applied magnetic field as uniform as possible, and avoiding areas of zero-field crossings. For ^{3}He cells, degaussing may need to be performed [16] on occasion to remove weak permanent fields that have developed owing to impurities embedded in the glass. Automation of gas hyperpolarizers is highly desirable for maximizing throughput, maintaining reproducibility, and minimizing errors during HP gas preparation and delivery, but fields produced by some solenoid valve designs can be problematic [17]. Transit through a given gas's phase diagram can also be a source of relaxation. For example, the T_1 of solid ^{129}Xe at liquid-N_2 temperature (77K) can be several hours [18,19] (facilitating purification and storage [20]), but only if kept from warming too close to the Xe melting point (where the T_1 can drop to seconds). Polarized solid xenon needs to be maintained in a strong field ($>$500 G) in order to suppress (1) dipolar relaxation from lattice vacancy hopping [21] and (2) thermal mixing with fast-relaxing ^{131}Xe present in the lattice [19]. Freezing or dissolving quadrupolar gases results in immediate loss of hyperpolarization because of subsecond T_1s in condensed phases unless at cryogenic temperatures. Thus, in addition to the fact that hyperpolarization processes themselves need to be monitored for consistent production of HP substances, the seemingly endless ways to destroy hard-won polarization necessitates that polarizers are designed to include in situ polarimetry for quality assurance of the HP agent.

Finally, although the physical mechanisms themselves underlying the hyperpolarization processes in SEOP, MEOP, DNP, and PHIP are sufficiently different that few generalizations about polarizer design are discussed here (the reader is instead directed to subsections below), the use of *gases* does provide some advantages regardless of hyperpolarization mechanism. Importantly, HP gases are relatively easy to physically separate from auxiliary substances (e.g., alkali metals (AMs), radicals, or catalysts) found in polarizers that may be toxic or otherwise undesirable if administered in significant dosage to a patient. Additionally, HP gases are relatively easy to administer to a living subject via inhalation—although alternative approaches wherein the agent is dissolved in a biocompatible liquid prior to administration (e.g., Ref. [22]) would ultimately be subject to similar sterile-path considerations needed for condensed-phase HP agents [23].

Pulse Sequence Considerations

HP gas delivered by inhalation enters the lungs as a bolus, whereas in chemical exchange saturation transfer using hyperpolarized nuclei (Hyper-CEST) applications (see chapter: Xenon Biosensor HyperCEST MRI) a steady-state supply of HP ^{129}Xe is desired/maintained in other organs and tissues for CEST-based sensing. In both cases, the ultimate goal is to maximize the SNR through optimization of MRI pulse sequences used in conventional MRI. Unlike in conventional MRI, where the consumed (through the RF excitation) magnetization recovers via thermal equilibration with the external magnetic field, a HP magnetization pool can only decay after in vivo administration—i.e., the hyperpolarization can only be refreshed by using a new bolus. As a result, pulse sequences used in HP gas MRI eliminate the "recovery" steps typically found in conventional MRI, and primarily focus on signal "encoding" and "detection" steps, which typically results in RF sequences with very short repetition time (TR) [24]. The latter is highly desirable, because HP gaseous agents have an in vivo T_1 on the order of seconds to tens of seconds resulting in a relatively narrow imaging time window. On the other hand, the greatly increased signal strength provided by hyperpolarization also obviates the need for signal averaging. As a result, multislice 2D and 3D images of HP gases in the lungs can be recorded in seconds and on a single breath-hold [25]. In addition to TR reduction, compressed sensing, where only a small fraction of *k*-space is sampled during imaging acquisition, can be employed—thereby significantly reducing the total scan time even further. This practice is especially advantageous for 3D sequences [26].

An additional complication of the "nonrenewable" nature of the HP magnetization is that each RF pulse consumes a nonlinear fraction of the remaining HP magnetization. One approach is to use small-angle excitation RF pulses for each line of *k*-space [27]. The resulting MRI signal is significantly lower than that recorded using a maximum RF pulse angle (i.e., 90°) with the benefit that the bulk of magnetization is preserved for further RF excitations. Nevertheless, the accumulating loss of magnetization from the application of many constant—even if small—flip-angle pulses over the course of image acquisition can lead to image blurring or other artifacts. Therefore, versions of this approach often use variable-tipping-angle pulses calculated to compensate for signal loss and thereby provide approximately the same amount of signal for each scan [27].

An alternative strategy is to use fast imaging with steady precession (FISP) [28] sequences [29], where near-90° RF pulses can be used for excitation, and nearly the entire magnetization pool contributes to the signal formation for each line of *k*-space [30]. Once the signal is recorded during the "detection" step, the magnetization is quickly "rewound" back to the *z*-axis for use in the next *k*-space step. The advantage of this second approach is the significantly greater SNR. However, these sequences require that the T_2 value of the HP gas be significantly larger than the "detection" time period (i.e., in order to take full advantage of the long T_2 of the HP contrast media). Furthermore, FISP sequences are more susceptible to B_1 and B_0 inhomogeneities [31], potentially resulting in imaging artifacts.

For further special pulse sequence considerations related to Hyper-CEST, please refer to Chapter 17, Xenon Biosensor HyperCEST MRI.

METHODS FOR GENERATING HP GASES

Dynamic Nuclear Polarization

For nuclear spin $I = ½$ nuclei such as ^{129}Xe (or ^{1}H, ^{13}C, ^{15}N, etc.), nuclear spin polarization P in the high-temperature limit is approximately given by the following equation: $|P| \approx \gamma\hbar B_0/2kT$, where $\hbar$ is the reduced Planck's constant, k is Boltzmann's constant, T is temperature in Kelvin, and γ is the gyromagnetic ratio of the nucleus in question. From this equation it follows that a change in temperature from 310K (body temperature) to liquid helium at 4.2K can enhance ^{129}Xe P (e.g.) by $\sim$75-fold. Fig. 2.1 also reveals that sufficiently low temperatures in static magnetic fields of several Tesla lead to electronic spin polarization reaching order of unity. For example, for $B_0 = 3.35T$ and $T = 1$K, electronic polarization is $\sim$98% as electrons possess a very high gyromagnetic ratio compared to protons, or $|\gamma_e/\gamma_{1H}| \sim 658$, $|\gamma_e/\gamma_{129Xe}| \sim 2380$. Conversely, ^{129}Xe nuclear polarization is only 0.0947% for these conditions! In order for nuclear spin polarization to reach $\geq$10% under thermal equilibrium conditions, a sample at high field (several Tesla) would generally need to be stored at milliKelvin temperatures (e.g., using a ^{3}He/^{4}He dilution refrigerator). Indeed, such time-consuming BFP approaches have been used to achieve high nuclear spin polarizations in different systems, including noble gases [32–35].

In a seminal theoretical paper published in 1953 Albert Overhauser proposed to use electron spins to enhance nuclear spin polarization, which was shortly thereafter confirmed experimentally by Carver and Slichter [36].

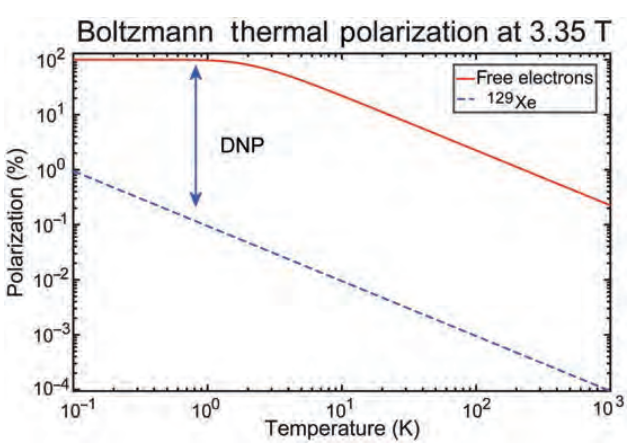

FIGURE 2.1 Boltzmann thermal polarization of electrons and ^{129}Xe nuclear spins for $B_0 = 3.35T$ as a function of temperature. RF fields facilitate transfer of polarization from electron spins to surrounding nuclear spins (e.g., ^{129}Xe).

The process of DNP utilizes the very high Boltzmann polarization of unpaired electrons attained at very low temperatures and magnetic field strengths of several Tesla described above, and transfers this polarization via dipolar or scalar couplings to nuclear spins (e.g., ^{1}H, ^{13}C, ^{15}N, ^{129}Xe, etc.), thereby dramatically enhancing the nuclear spin polarization of the target substances. The requisite unpaired electrons are typically introduced into a sample by adding persistent radicals [37].

Dissolution DNP (d-DNP) is the DNP approach typically employed for small molecules that may be used in biomedical applications. d-DNP is often explained in terms of the cross effect, a three-spin (two-electron, one-nucleus) process in which the electron spin transitions are driven by resonant microwaves and the difference in energy of the electron spin flips roughly matches the energy needed to flip the nuclear spin [38,39]. In the cross effect, the electron linewidth generally exceeds the nuclear spin Larmor frequency. The d-DNP hyperpolarizer instrumentation was first introduced in 2003 [37], primarily for production of liquid ^{13}C-HP contrast agents. The device consists of three major components: (1) a superconducting magnet establishing the B_0 field strength; (2) a helium cryostat connected to vacuum pumps to cool the sample to $\sim$1K; and (3) a microwave source enabling polarization transfer from unpaired electron spins to nuclear spins. Such hyperpolarizers include the commercial platforms of the HyperSense [37] by Oxford Instruments operating at 3.35T and 1.2−1.6K, the SPINlab [23] for clinical use developed by GE Healthcare operating at 5T and 1.1K, as well as numerous home-built solutions.

In addition to substances that comprise liquid solutions at room temperatures, DNP has also garnered recent attention as a means to hyperpolarize gases. For example, DNP devices have recently been shown to be effective for hyperpolarization of ^{129}Xe, reaching $P_{\mathrm{Xe}} \sim 30\%$ in about 90 min at $\sim$1K [40] despite a previously identified spin-diffusion (e$\rightarrow^{129}$Xe) bottleneck [41]. Other experiments have investigated the potential of hyperpolarizing ^{15}N-labeled N_2O, with the idea being to exploit the long-lived singlet-state lifetime at low field, quantified by an exponential time constant T_S, of 26 min [42,43]. However, to date the production has been modest—achieving polarizations of $P_{15\mathrm{N}} \sim 10\%$ over 37 h in $\sim$25 cc volumes [42].

The DNP technique is capable of efficient ^{129}Xe hyperpolarization using homogeneous mixing of ^{129}Xe and radical agents when a cosolvent (e.g., ethanol or propanol) is employed [40]. Once ^{129}Xe is HP in the solid state, it is sublimated to leave the hyperpolarizer as a pure gas, and the process is therefore termed sublimation DNP [40]. A key strength of this approach is a relatively widespread network of DNP hyperpolarizers. Limitations of using DNP for hyperpolarizing gases include (1) the relatively high costs associated with device purchase, operation, and maintenance and (2) relatively low throughput ($\ll$100 scc/h) and scalability (e.g., the ease by which production could be scaled by an order of magnitude). For ^{129}Xe, polarization levels are also generally lower than what can be achieved with available SEOP polarizers, although the aforementioned improvements in the technology for producing HP ^{129}Xe via DNP [40] may ultimately allow ^{129}Xe polarizations to approach unity using this technique.

Spin-Exchange Optical Pumping

SEOP History and Theoretical Background

SEOP is a method of generating high polarizations in noble gas nuclei. Spin order is derived from circularly polarized laser light used to selectively deplete one of the electronic ground states of an alkali metal (AM), typically Rb, Cs, or K. Gas-phase collisions then transfer polarization from the AM electrons to the noble gas nuclei via Fermi-contact interactions.

It was in Kastler's pioneering work [44] where the ability to use light to polarize electron spins was first demonstrated. Polarization of the nuclei of noble gases via spin exchange with optically pumped AM vapors was later demonstrated by Bouchiat et al. [45] and Grover [46], leading to detailed study and advancement of the SEOP approach by Happer, Cates, Walker, and many others (e.g., Refs. [47−51]).

SEOP is most commonly used to polarize nuclear spin ½ ^{129}Xe and ^{3}He, though it is also possible to polarize the quadrupolar species ^{21}Ne [52,53], ^{83}Kr [14], and ^{131}Xe [9] (where $I = 3/2$, 9/2, 3/2, respectively). Rb is often the AM of choice due to its low melting point [54] facilitating vaporization, and the availability of high-powered, frequency-narrowed lasers tunable to the D_1 transition [55,56].

The polarization of the AM electrons (Fig. 2.2A), P_{AM}, is determined by the optical pumping rate γ_{OP} and the rate of spin-destruction lost to nonangular-momentum-conserving interactions, Γ_{SD} [52]:

$$P_{\mathrm{AM}}(z,r) = \frac{\gamma_{\mathrm{OP}}(z,r)}{\gamma_{\mathrm{OP}}(z,r) + \Gamma_{\mathrm{SD}}},$$

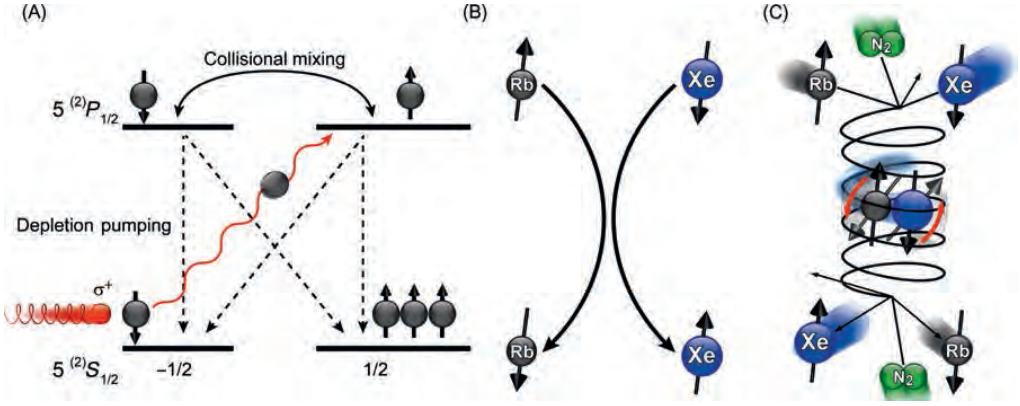

FIGURE 2.2 The two-step process of SEOP. (A) First step: Optical pumping of the electronic spins of an AM vapor (Rb); hyperfine splittings caused by the presence of the Rb nuclear spins are omitted for clarity. (B,C) Second step: Spin exchange between the Rb electron and noble gas (here, Xe) nuclear spin during binary (B) and/or three-body (C) gas-phase collisions.

where both P_{AM} and γ_{OP} are a function of position within the OP cell. γ_{OP} is determined by the frequency overlap between the laser's spectral profile and the pressure-broadened AM D_1 transition line, and Γ_{SD} is the electronic spin-destruction rate [52]:

$$\Gamma_{SD} = \sum_i k_{SD}^i \cdot [M_i],$$

where k_{SD}^i quantifies the rate of spin-destroying collisions with each of the ith gas species present in the cell and $[M_i]$ is the number density of that species. At any significant distance from the cell walls, collisions with Xe typically dominate the AM electronic spin destruction; k_{SD}^{Xe} has been measured to be orders of magnitude greater than $k_{SD}^{N_2}$ and k_{SD}^{He} [57,58]—a fact that makes it more difficult to hyperpolarize ^{129}Xe at higher xenon densities (alkali–alkali collisions may also be relevant during ^{3}He pumping).

Once the AM vapor is polarized, angular momentum may be transferred from the AM electron spins to the nuclei of the noble gas (NG) through gas-phase collisions. This spin-exchange process may be mediated by two distinct mechanisms: "two-body" transient dimers (brief AM–NG interactions—simple collisions, Fig. 2.2B) or "three-body" persistent dimers (longer interactions between an AM atom and a heavy NG atom, where a third species facilitates the formation and destruction of van der Waals complexes; Fig. 2.2C). For example, for ^{3}He only two-body collisions contribute to spin exchange, but for ^{129}Xe, more complex collision mechanisms can contribute significantly—with the more-efficient three-body term dominating under conditions of low gas density (particularly Xe density) [48]. Since AM/Xe interactions are often not spin-conserving, the probability of the AM electron spin order being transferred to the noble gas nuclei in any one collision is low. However, AM polarization lost to collisions is quickly recovered by photon reabsorption, so that order lost to spin-rotation interactions is quickly regained—provided the resonant photon flux is sufficiently high.

The AM electron spin polarization reaches steady state on a timescale much faster than the spin-exchange rate (γ_{SE}), and thus the nuclear spin polarization of the NG accumulates over time according to simple exponential behavior. For example, for ^{129}Xe the time-dependent polarization is governed by [52]

$$P_{Xe} = \langle P_{AM}(z,r)\rangle \cdot \left(\frac{\gamma_{SE}}{\gamma_{SE} + \Gamma_{Xe}}\right) \cdot \left\{1 - \exp\left[-(\gamma_{SE} + \Gamma_{Xe})t\right]\right\},$$

where $\langle P_{AM}(z,r)\rangle$ is the spatially averaged AM polarization, $\Gamma_{Xe} = (T_1^{Xe})^{-1}$, and γ_{SE} is given by [52]

$$\gamma_{SE} = [AM] \cdot \left\{\frac{\gamma_{AMXe}}{[Xe]}\left(\frac{1}{1+br}\right) + \langle \sigma v\rangle\right\},$$

where [AM], [Xe] are number densities, γ_{AMXe} is the three-body interaction rate, $\langle \sigma v\rangle$ is the velocity-averaged binary SE cross-section, and the factor $1/(1+br)$ accounts for the ratio of nitrogen to xenon in the cell and their

relative efficiencies in facilitating formation/breakup of persistent dimers (br = 0.275 · (N_2 pressure)/(Xe pressure)). Thus, the SE rate γ_{SE} is proportional to the AM density. Moreover, as discussed above the relaxation rates of ^{129}Xe and ^{3}He are typically much slower than the SE rates during SEOP, allowing the NG polarization to ultimately approach $\langle P_{AM}(z,r)\rangle$ in some circumstances. These long relaxation times also facilitate HP gas storage and transport.

SEOP Instrumentation

A number of essential experimental components are required to conduct an SEOP experiment (illustrated in Fig. 2.1): (1) an optical pumping cell made typically of borosilicate (Pyrex) glass, containing a small quantity of AM and the noble gas to be polarized; (2) an oven to vaporize the AM and control the temperature during (and between) SEOP runs; (3) a magnetic field of tens of Gauss; and (4) a source of circularly polarized laser light tuned to the optical D_1 transition of the AM [49].

Polarizers harness the SEOP process to produce large quantities of HP gas for use in further applications. In these applications it is often high magnetization—the product of the HP noble gas (HPNG) polarization and concentration—that is desired. Polarizers are therefore often designed to optimize these parameters. Broadly, these SEOP devices are typically divided into two categories based on their modes of operation and design features—stopped-flow polarizers and continuous-flow polarizers—as described below.

STOPPED-FLOW POLARIZERS

In stopped-flow polarizers [11,25,59–66] (Fig. 2.3A–C) the optical cell is sealed during SEOP and holds a static quantity of gas mixture that is heated using an oven and optically pumped with a high-powered laser source. Steady-state nuclear polarization is typically achieved within minutes or tens of minutes for ^{129}Xe [25], ^{83}Kr [10], ^{131}Xe [9,69], and ^{21}Ne [70], and hours for ^{3}He [71], at which point the cell can be cooled within the oven—thereby condensing the AM vapor on the inner surface of the optical cell, and allowing for the extraction of the HP gas mixture for use in experiments [25,65].

CONTINUOUS-FLOW POLARIZERS

In continuous-flow polarizers [20,68,72–78] the gas mixture flows through a heated optical pumping cell where it undergoes SEOP with AM vapors during transit through the cell. The now-polarized gas can then be flowed continuously into an experiment, recirculated through the polarizer [75,78], or—in the case of xenon—cryogenically collected using a cold finger submerged in liquid nitrogen at high field [21]. At 77K ^{129}Xe solidifies while largely maintaining its polarization. The accumulation time is constrained however by the T_1 of xenon in the solid phase ($\sim$3 h at 77K) [19–21]. Cryogenic collection is not practical for the quadrupolar HP nuclei, as the T_1 values are far too short in the solid state. A diagram of one continuous-flow design is provided in Fig. 2.3D [68]. This variant employs a "counterflow" design wherein the premixed gas (containing ^{129}Xe to be HP) flows toward the incident laser light, such that the gas mixes with the most highly polarized Rb vapor before leaving the OP cell. To mitigate deleterious Rb-induced thermal runaway [73,79,80]—and possibly the formation of Rb clusters [81]—the majority of the Rb within the system resides outside of the pump beam within a Rb presaturator located upstream of the OP cell, saturating the gas mixture as it flows through—even at high flow rates.

SEOP Gas Mixes and Operating Regimes

There are substantial differences in the gas mixes and operating regimes employed in stopped-flow and continuous-flow polarizers. The first continuous-flow polarizer was operated at high pressure ($\sim$10 atm) to optimally couple the Rb D_1 line to the broadband pump laser via collisional broadening [20]; note that broadband LDAs have spectral linewidths of $\sim$2–3 nm (FWHM). However, in order to maximize P_{Xe} the xenon fraction was kept low (typically 1%) to minimize Rb-Xe spin destruction, thus, helium became a major constituent of the mixture due to its low Rb spin-destruction cross-section. In order to suppress radiation trapping [82] (i.e., to suppress radiative decay of the excited Rb), a small fraction of nitrogen was added to the mix. High concentrations and substantial volumes of HP xenon could then be obtained by cryo-accumulation of the xenon gas, a process which separates it from the rest of the gas mix [20]. The continuous-flow pressure polarizer in Fig. 2.3D [68] operates within an atypical, lower pressure—so called "long-lived" or van der Waals—regime in order to exploit the faster SE rates that prevail there. This shift in approach was made possible in part by the high-power pump laser (90 W, with moderate linewidth of $\sim$1.5 nm FWHM) it employed.

Likewise, stopped-flow polarizers have progressed significantly with the advent of frequency-narrowed high-power lasers (with spectral typical widths of $\sim$0.2–0.4 nm) [56,62,64]. Most notably, these lasers have enabled

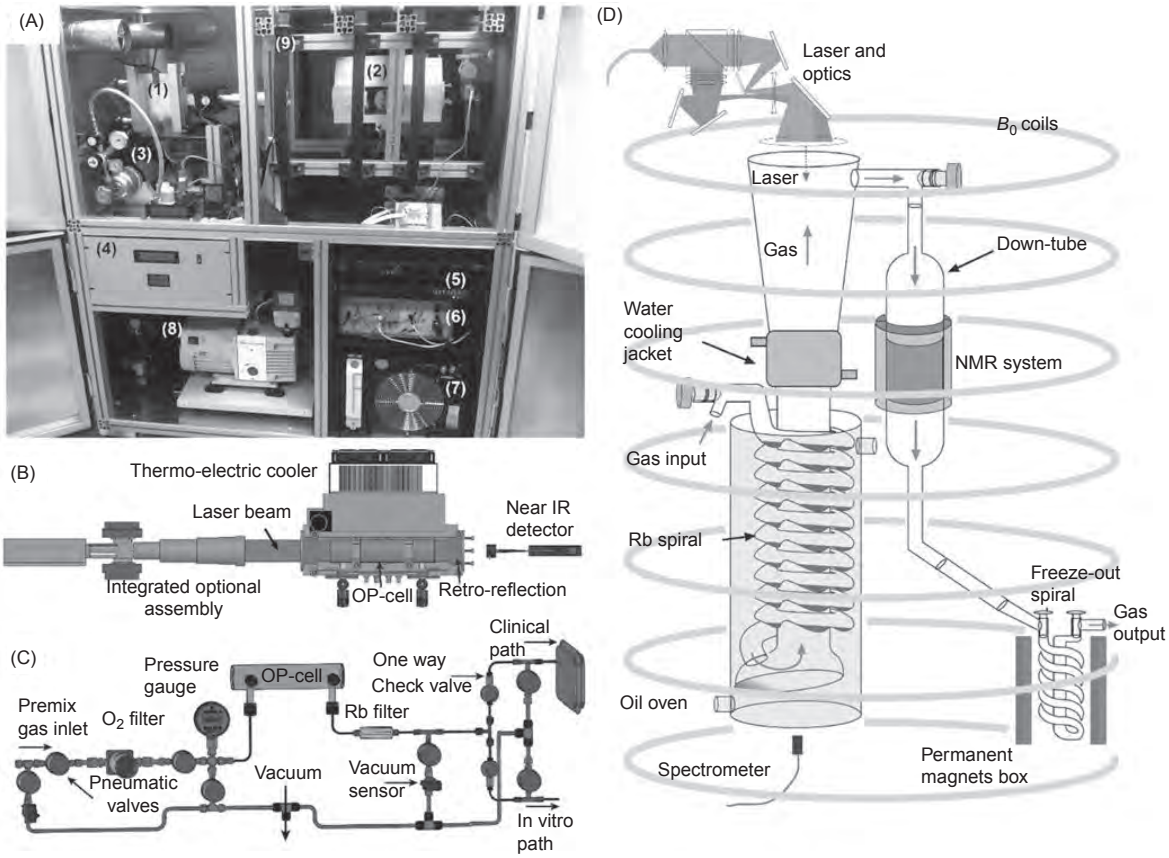

FIGURE 2.3 Examples of ^{129}Xe hyperpolarizers. (A–C) Our Consortium's second-generation stopped-flow (SF) Xe hyperpolarizer. The photo in (A) shows the principal components of the device ((1) laser; (2) 3D-printed oven; (3) Xe gas supply; (4) microcontroller box; (5) power supplies; (6) low-frequency NMR spectrometer; (7) water chiller; (8) vacuum pumps; (9) electromagnetic coils). Diagrams showing the oven/optical path and gas manifold are shown respectively in (B) and (C). (D) Diagram showing the continuous-flow (CF) design of Ruset and colleagues [68]. *Source: For (C) from Nikolaou P, Coffey AM, Barlow MJ, Rosen MS, Goodson BM, Chekmenev EY. Temperature-ramped 129Xe spin exchange optical pumping. Anal Chem 2014;19:8206–12 [67]. For (D) figure courtesy of W. Hersman.*

operational regimes to be found where high polarizations can be achieved with relatively high xenon densities in cells that no longer required helium for pressure broadening [17,25,80,83]. Indeed, where higher xenon densities are used this approach can obviate the need for cryo-collection while still obtaining high concentrations of highly polarized xenon in sufficient quantities for clinical lung imaging [25].

SEOP Characterization

A number of diagnostic techniques have been applied to SEOP over the years, driven by a desire to deconvolute the complex interplay among the relevant experimental parameters—thereby aiding both the understanding of fundamental SEOP phenomena and the optimization of polarizer performance. Of these, the most easily employed are in situ (low-field) NMR and IR spectroscopies. Based on NMR and IR data alone, one can detect and quantify the HPNG magnetization (via NMR), obtain spin-exchange and spin-destruction rates (using fits to build up T_1 decay curves from the HPNG NMR), observe spatial variations in the noble gas nuclear spin polarization, monitor optical absorption by the AM (via IR [25]), and estimate the globally averaged AM polarization using a simple field cycling method, now described [25,83]. In this approach, the simplest and most readily implemented for obtaining a measure of P_{AM}, one compares absorption spectra of the pump laser transmitted through the cell when the magnetic field is cycled [25,62]. The technique utilizes a simplistic Beer's law approach

and the "bleaching" of the IR absorption spectrum resulting from the depletion pumping of the ground-state magnetic sublevels. The first step of the OP process—whereby the Rb electrons become spin-polarized—leaves a smaller concentration of Rb atoms in the laser-absorbing m_J state. In turn, this population reduction allows more laser light to be transmitted through the cell, allowing P_{AM} to be estimated from the difference [62].

To monitor the buildup of P_{Xe} via in situ NMR, single-shot "pulse-acquire" experiments suffice, and the ability to signal average is only needed if a calibration of the signal against water is required. Thus, a number of groups have constructed low-field spectrometers [84–87], though commercial systems (such as Magritek's Kea and Aurora spectrometers) exist. Requirements for the IR spectrometer are governed by the line width and tunability of the laser source, and are met by devices that are commercially available (e.g., Ocean Optics HR4000).

Nevertheless, these probes provide only part of the picture of what occurs within an SEOP cell during optical pumping. For example, it is often desired to have a direct measure of the AM electronic polarization. Such measurements can be made using optically detected electron spin resonance (ODESR) [88], measurement of collisional frequency shifts [89], and Faraday rotations [70,90,91]. Such measurements can provide insight into limitations of the nuclear spin polarization (since it is ultimately bound by P_{AM}).

An ODESR experimental setup is illustrated in Fig. 2.4A and B [88]. This method probes the AM electronic sublevels using (1) a transverse RF field tuned to the Rb EPR resonance frequency; (2) a low-power circularly polarized D_1 (or D_2) probe laser (usually) orthogonal to the pump beam; and (3) a photodetector coupled to a lock-in amplifier which detects the modulation of the probe laser transmission caused by the precessing Rb magnetization. By sweeping B_0 across the Zeeman sublevels one can obtain a spectrum in which the relative intensity of the peaks provides a direct measure of the relative populations of the sublevels [76,88,92–94]. When combined with gradients the peaks can be spatially encoded and high-resolution AM polarization images of less than 1 mm can be obtained [88,93,94].

Another approach for probing spin polarization within SEOP cells involves precise measurement of polarization-dependent shifts of the Larmor frequency of the NG—and vice versa: collisional frequency shifts in He and Xe NMR spectra (Fig. 2.4C–E) have been shown to be a function of Rb magnetization, thereby providing a simultaneous measure of HPNG and AM polarization [89]. The effect arises directly from the Fermi-contact interaction and its magnitude is characterized by the dimensionless enhancement factor κ_0, measured as $(\kappa_0)_{RbHe} = 4.52 + 0.00934T$ (with T in °C) [95,96] and, more recently, $(\kappa_0)_{RbXe} = 493 \pm 31$ [89]. These values, when combined with a measurement of the frequency shift of the NG in question (and an estimate of the AM density, discussed below), can be used to obtain a volume-averaged expectation value for the z-component of the AM electron spin $\langle S_z \rangle$ (where Rb magnetization is proportional to $[\mathrm{Rb}]\langle S_z \rangle$) according to the relation given in Ref. [89].

Faraday rotation—the rotation of the plane of polarization of nearly resonant light as it traverses the SEOP cell—provides another method for the determination of AM polarization. This approach exploits the fact that the B_0-induced Zeeman splitting of the AM metal vapor induces a phase shift between the circular components of the linearly plane-polarized light, resulting in a rotation in the plane of polarization [70,90,91,97,98].

In an alternative configuration, Faraday rotation can also be used to measure the AM vapor density—another key parameter governing SEOP [98]. The spin-exchange rate increases as a function of the AM density, and knowledge of the AM density is thus necessary in order to extract (per-atom) spin-exchange cross-sections. A simpler (and older) route for measuring the AM density utilizes the empirical thermionic emission data published by Killian [99]. The AM density can be roughly predicted from the cell temperature using AM density curves (see, e.g., Ref. [54]); other such formulae can be used (e.g., Ref. [100]) and may achieve better quantitative agreement when compared to results from other methods [101]. Alternatively, relatively simple optical absorption methods can be used for the direct measurement of AM density during SEOP by monitoring absorption of light from (for instance) a 421.5 nm source by the $5S_{1/2}$–$6P_{1/2}$ Rb transition [102], though other transitions may be used [103].

Finally, temperature is another important parameter governing SEOP. In addition to determining the AM density, temperature can affect the values of many parameters mentioned above. Exterior cell wall temperatures and oven air temperatures can be measured trivially via thermocouples; however, measurement of the internal gas temperature can be challenging. As mentioned previously, nitrogen buffer gas is often present in the HPNG mix, making it possible to monitor the in-cell temperature of the gas mixture by Raman spectroscopy [104,105]. Nitrogen collisionally deexcites the excited Rb atoms via radiationless, two-body quenching collisions and concomitantly accumulates energy in its rovibrational manifolds. Irradiating the gas with a probe laser causes Raman scattering. The relative peak intensities of the resulting Raman spectra reveal the distribution of energy across the rotational states and is a function of temperature [106]. To date, the method has shown that temperatures within the OP cell can be elevated by hundreds of degrees above ambient [104], particularly when Xe

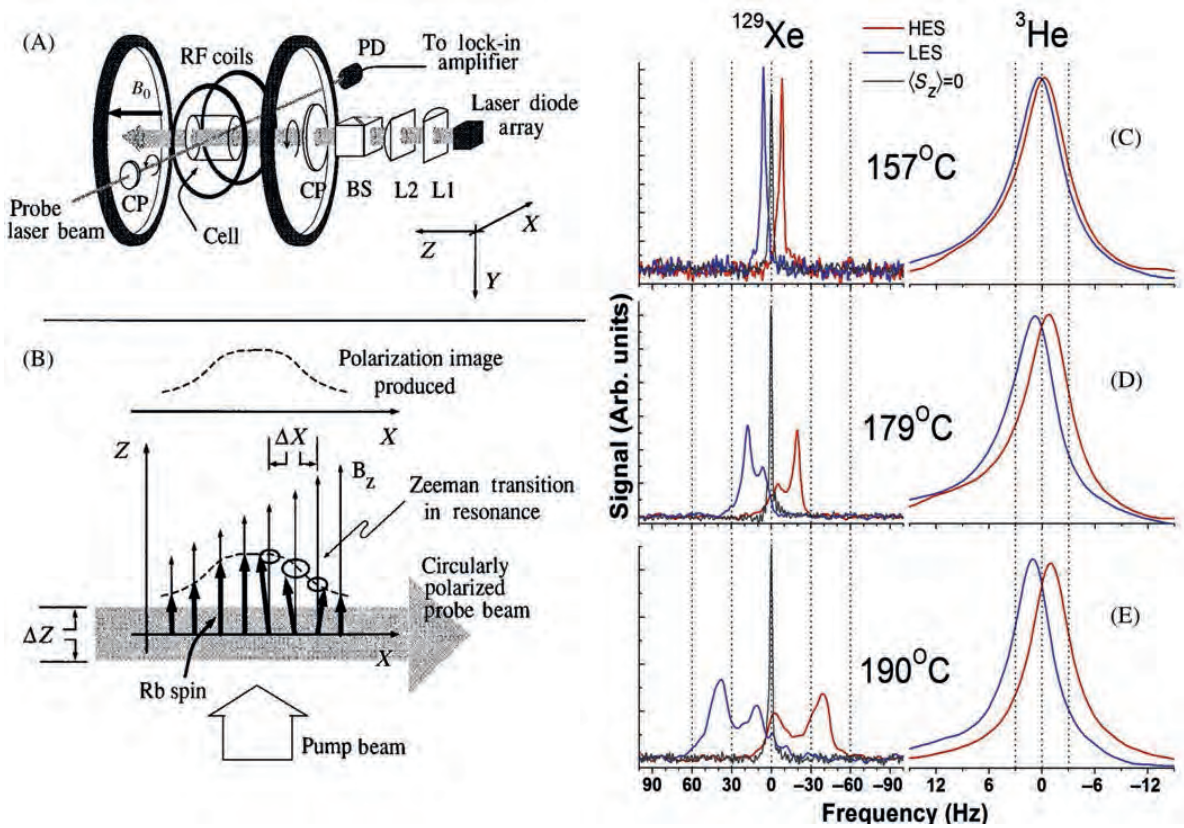

FIGURE 2.4 ODESR and collisional frequency shifts. (A) ODESR experimental apparatus, described in text and in full in Ref. [88]. The total magnetic field B is the resultant of a uniform field B_0 and a linear gradient field ($r\nabla B$), both along the z axis. Not depicted are the coils used to generate the gradient fields and the oven. (B) Schematic sketch of imaging with a linear gradient. The signal arises solely from the Rb spins in resonance. As B_0 is swept linearly in time, the volume element in resonance is swept along the x axis. (C), (D), and (E) Typical ^{3}He and ^{129}Xe collisional shift spectra from cell 155B acquired one-after-the-other under steady-state SEOP conditions. The narrow ^{129}Xe peak at 0 Hz was acquired with the laser blocked (such that the ^{129}Xe was still HP whereas the Rb was not); it has been amplitude normalized to appear on the same graph. The double peak, in the ^{129}Xe spectra at all but the lowest temperatures, represents regions of highly polarized and nearly unpolarized Rb vapor; the lines are broadened and begin to coalesce due to diffusion of ^{129}Xe between these two regions. For ^{3}He, the much smaller frequency-shift dispersion and more rapid diffusion yield a single narrow peak in all cases. The respective shifts in the spectral "center of mass" upon reversal of the Rb magnetization were used to extract $(\kappa_0)_{RbXe}$. LES and HES (low and high Zeeman polarization energy state) respectively appear on the left and right in each of the plots in (C), (D), and (E). Alternation between LES and HES was achieved by inverting the quarter wave plate of the pump laser.

density is high [107]; convection plays a key role in the heat transport within the cell [104]; and there is impact of narrowed versus broadband sources on the thermal dynamics within the OP cell [105]. Raman spectroscopy is well-placed to provide further insight into the deleterious "rubidium runaway" [73,79,80] and Rb cluster formation [81] phenomena, which may become critical issues as ever more powerful pump lasers are used.

Applications of SEOP-Prepared HP Gases

HPNGs continue to be utilized in an ever-growing number of fields. For example, ^{3}He has been widely adopted for applications varying from biomedical imaging [108−111] and apparent diffusion coefficient (ADC) measurements of the lungs [112,113]; studies of fundamental symmetries [114,115]; and in polarized neutron spin filters and targets for electron scattering experiments [116−120]. However, the main supply of ^{3}He is through tritium decay in nuclear warheads, and with diminishing stockpiles the price of ^{3}He is becoming prohibitively expensive [121], likely limiting its future use.

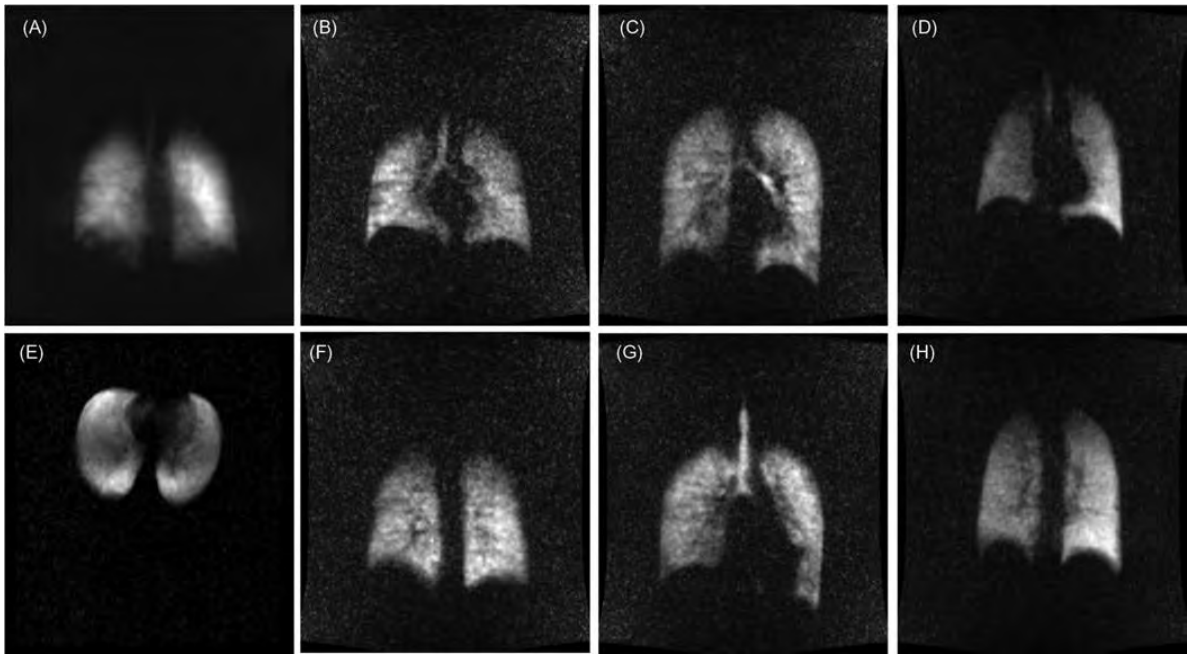

FIGURE 2.5 Examples of xenon MR images of heathy human lungs taken during a breath-hold. (A) Infinite coronal slice in a 26-year-old male. (E) Infinite axial slice in a 23-year-old female. (B,F), (C,G), and (D,H) pairs of coronal images from three healthy volunteers: a 26-year-old male, a 22-year-old male, and a 29-year-old male, respectively. HP Xe gas was produced on a GE2000 Polarizer using a 2% Xe natural-abundance mix. ^{129}Xe polarization was typically $\sim 9\% \pm 0.5\%$. FGRE sequence used for all images, FOV = 48 cm × 48 cm, TE = 4.2 ms, TR = 9 ms, FA = $\sim 5.5^{\circ}$, Res = 128 × 128, Slice thickness = Inf. for (A,E); 25 mm for (B,C,D,F,G,H). *Source: University of Nottingham.*

Unlike ^{3}He, xenon is naturally abundant and is a by-product of oxygen production. ^{129}Xe is mildly soluble in blood and organic solvents and has a broad chemical-shift range that makes it attractive for a number of applications. To date, these features have been exploited in studies of porous materials (e.g., Ref. [122]) and surface interactions (e.g., Ref. [59]); and extensively in a variety of chemical, biophysical, and biomedical applications, including those involving cryptophane-based host systems and void-space imaging (reviewed in Refs. [123–128]); extensively in studies of the lungs (e.g., Refs. [111,129–140] and Fig. 2.5); the brain (e.g., Refs. [24,141–151]); and other bodily tissues [152] including the blood [153–156]. Indeed, the biomedical applications of HP ^{129}Xe and ^{3}He will dominate most of the remaining book chapters.

Contrary to ^{129}Xe and ^{3}He, the quadrupolar species ^{21}Ne, ^{83}Kr, and ^{131}Xe undergo rapid spin relaxation, as mentioned above. This rapid relaxation makes many applications challenging, but also provides—particularly in the cases of ^{83}Kr and ^{131}Xe—a unique and complementary sensitivity to the chemical composition of surfaces in porous media and the shape, size, and symmetry of void spaces [69,157–160], including (in the case of ^{83}Kr) the lungs [14,161]. ^{21}Ne, the least studied of the HPNGs, has potential for use as a navigational gyroscope [70], and in precision tests of Lorentz and CTP symmetries as a comagnetometer [162].

Metastability Exchange Optical Pumping

MEOP History and Theoretical Background

An alternative to SEOP is MEOP, an approach that relies on optical pumping of an atom's metastable state possessing nonzero spin angular momentum. Optical pumping had already been successfully applied to vapors of AMs and mercury to polarize the electronic and nuclear magnetic moments of such atoms [163], but it was not until 1960 that the technique was applied to the electronic ^{4}He $2^{3}S_{1}$ metastable state [164], and then to ^{3}He in 1962 [165]. The technique has also been successfully applied to polarize the electronic and nuclear states of ^{21}Ne [166], ^{83}Kr [167], and ^{131}Xe [168], the latter using an electron beam for pumping instead of an optical source.

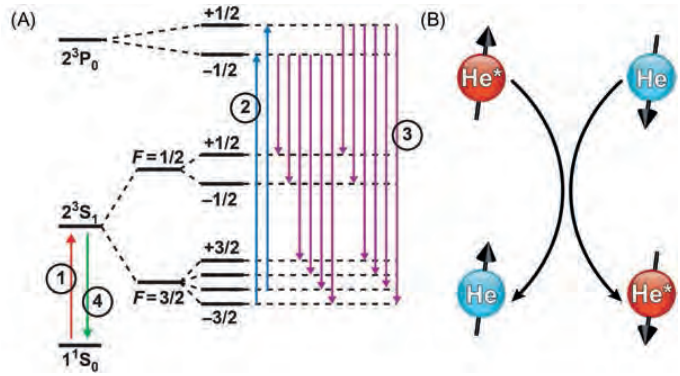

FIGURE 2.6 (A) Energy transitions involved in metastable optical pumping of helium. (1) Excitation due to RF discharge. (2) Excitation due to pumping light. (3) Decay back to all metastable states. (4) Decay due to metastability exchange collision. (B) Metastability exchange Collision. Nuclear orientation is represented by an arrow, and polarized metastable electronic states by an asterisk (*).

MEOP has also been used to polarize the electronic states of ^{129}Xe [169], but nuclear polarization was not seen, likely due to strong nuclear relaxation mechanisms.

Fig. 2.6A shows the energy levels involved in the optical pumping of the helium metastable states. An RF discharge placed across a low-pressure sample (e.g., within a glass cell) excites a small fraction of the He atoms from the 1^1S_0 ground state to the long-lived 2^3S_1 metastable state (label 1). Resonant circularly polarized light then excites population from the 2^3S_1 to the 2^3P_0 state, according to the selection rule $\Delta m = +1$ (label 2). This selectivity means that the pumping light only excites atoms from the metastable $m = -{}^1/_2$ and $m = -{}^3/_2$ sublevels to the $m = +{}^1/_2$ and $m = -{}^1/_2$ sublevels, respectively. The population then decays back to all 2^3S_1 sublevels with roughly equal probability (label 3). The net result is the transfer of atoms from the lower magnetic quantum numbers ($m = -{}^1/_2, -{}^3/_2$) to the higher magnetic quantum numbers ($m = +{}^1/_2, +{}^3/_2$). Unlike He^4, He^3 has a nonzero nuclear spin, and there is efficient coupling between the nucleus and the electrons (the hyperfine interaction)—resulting in an entanglement of electronic and nuclear spin states. Because of this interaction, optical pumping of the electronic angular momentum simultaneously induces nuclear orientation as well [170]. Finally the metastable and ground-state sublevels are coupled via metastability exchange collisions (label 4). Fig. 2.6B shows a representation of the metastability exchange interaction between metastable atoms (denoted He*) and ground state atoms, with the arrows representing their nuclear spin states.

It was realized that as a consequence of hyperfine interaction and the metastability exchange collisions in ^{3}He atoms, the emerging ground-state atom has a polarized nucleus. It was found that the metastability exchange collision dominates the ground-state ^{3}He nuclear magnetic relaxation rate (T_1), leading to a polarization of the ground-state ^{3}He nuclei—matching the degree of polarization of the electronic spins of the metastable atoms [165]. Typical polarization rates have been reported as 10^{18} atoms/s (e.g., Refs. [171,172]); in those examples, steady-state polarization was achieved in $\sim$0.5–3 min for low-pressure (<10 Torr), small cells (<300 cm^3).

Initially, there were two limitations of the MEOP technique. The first was the type of polarizing light source that was available. Early experiments were performed using helium discharge lamps, leading to low polarizations. To get higher levels of metastable (and hence nuclear) pumping, a more powerful source is required. The second limitation was the low pressure, around 1 mbar required by the RF discharge. For any experiment or application requiring HP ^{3}He at greater than 1 mbar pressures, a polarization-preserving compressor is needed. New techniques developed in 2002 [173] using high magnetic fields have allowed polarization at higher pressures. However, even then a compressor is required before the polarized gas can be used experimentally. These issues are discussed in greater detail below.

MEOP Laser Technology

Helium discharge lamps are inefficient sources for the 1083 nm circularly polarized light required for the 2^3S_1 to 2^3P_0 excitation; e.g., a 10 W helium discharge lamp generates less than 1 mW of useful pumping light at 1083 nm. Nevertheless, these early studies reported polarizations from $\sim$20% to $\sim$40%, typically using 5 cm diameter spherical cells of ^{3}He at $\sim$10 Torr [165].

It was not until the advent of tunable laser sources at 1083 nm that ^{3}He and ^{4}He MEOP became more viable. In the late 1980s a laser with a medium comprised of a crystal of $La_{1-x}Nd_xMgAl_{11}O_{19}$ (known as LNA) became readily available [174], allowing for higher polarizations of $\sim$60% (110 cm^3 cell at 0.3 Torr) [175] and even $\sim$85% (70–300 cm^3 cells at 0.1–1.0 Torr) [171] for HP ^{3}He. However the LNA lasers still had notable limitations,

including significant variations in the quality of the LNA crystals, thermal conductivity and gradient issues within the LNA, as well as nontrivial space, cooling, and power requirements.

The mid-1990s saw the advent of low-power laser diodes capable of operating at the required 1083 nm. It was found that polarizations approaching the theoretical limit of 100% could be routinely achieved using such lasers, albeit within low-volume collimated beams [176]. However, the output power is low compared to the LNA lasers (only $\sim$50 mW) and as such these sources have generally been unable to polarize clinically relevant quantities of ^{3}He in a sufficiently short period of time. MEOP of ^{3}He using a newer compact, high-efficiency tunable 1083 nm source based on a ytterbium (Yb) fiber laser was first reported in 1997 [177]. These air-cooled table-top lasers can have electrical input/optical output efficiencies of $>$25% [177]. Yb fiber laser powers of 1.5 W have been used to achieve polarizations of up to 82% (260 cm^3 at 0.3 Torr) [172], matching that of equivalent LNA lasers. Since then, the optical power of commercial Yb fiber lasers has greatly increased, enabling higher polarization values while also allowing for more HP ^{3}He to be prepared in a given time [178].

MEOP Compressor Technology

There are several fields of research that utilize dense samples of HP He^3 gas, such as a target in nuclear physics [179], medical imaging [129], and neutron scattering [180]. Such applications have thus required a method of compressing the low-pressure HP ^{3}He polarized via MEOP with minimal polarization loss in order to achieve gas densities required for these uses.

The earliest solution reported was by Daniels and Timsit [181] who used a Toepler pump to compress the polarized ^{3}He. A Toepler pump is comprised entirely of glass, and uses a reservoir of mercury that when raised and lowered acts as a piston to compress the ^{3}He gas. The main issue with the Toepler pump is that its valves suffer from sticking and/or leaking problems, and its slow pumping speed (15–30 s per "stroke") [182]—much slower than a conventional piston pump.

The 1990s saw developments in new compression methods with the advent of titanium-based piston pumps [183]. It was found that the ^{3}He T_1 relaxation time for contact with certain materials (Pyrex, titanium, copper, brass, aluminum, glass, etc.) was long enough ($\sim$60 min) that their use would not lead to large ^{3}He depolarization losses. Since then other groups have built upon this work, creating optimized pumping systems to increase the speed of compression and the maximum pressure attainable, while also lessening the impact of the pump on the polarization losses of the gas [178,184]. Simpler and more compact compression solutions include modified diaphragm pumps [185] and peristaltic pumps, with which continuous flow polarization has been reported [186].

MRI Applications of MEOP-Polarized Gases

Following the first reported use of HP ^{129}Xe MRI on ex vivo air spaces in 1994 [129], HP ^{3}He was tested as a potential alternative [187]. ^{3}He has several advantages over ^{129}Xe, namely that it has a higher gyromagnetic ratio and can be inhaled in larger quantities without substantial risk, as it is not absorbed by the tissue of the lungs—as is known from deep sea diving and special lung function tests [188]. Until recently, it was also easier to achieve higher polarizations in ^{3}He than ^{129}Xe. Initial images obtained with HP ^{3}He prepared were taken on excised guinea pigs [187]. MEOP-prepared HP ^{3}He has since been successfully used to take images of human lungs [108], with considerable research into finer more detailed images, and the differences in the ventilation of the lungs afflicted by various illnesses.

HP ^{3}He has also been used to assess the lung's microstructure by making use of diffusion weighting gradients to measure the ADC of the smaller airways [189]. This technique has been used to explore the progression and effect of thoracic diseases such as COPD [190], asthma [191], emphysema [113], and pulmonary fibrosis [189] at the alveolar level (Fig. 2.7). However, owing to the ever-increasing expense of ^{3}He because of the worldwide shortage of this isotope [192], future research into lung MRI is likely to concentrate on naturally abundant alternatives, such as ^{129}Xe and quadrupolar species such as ^{83}Kr and ^{131}Xe [193].

Parahydrogen-Induced Polarization

Principles

The production of macroscopic quantities of gases with high spin order—a key topic of this entire book—arguably owes its origin to the studies of the spin isomers of molecular hydrogen (H_2) gas by Bonhoeffer and Harteck [194]. Because ^{1}H nuclei are fermions, the overall wave function for H_2 must be antisymmetric with respect to exchange. All H_2 molecules in the (symmetric) ground rotational state ($J = 0$) must be in the (antisymmetric)

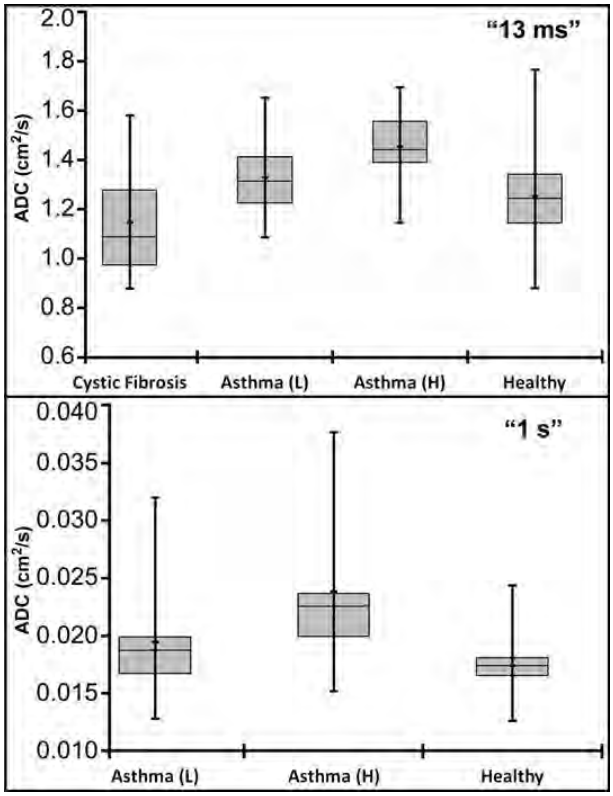

FIGURE 2.7 Apparent diffusion coefficients measurements using HP ^{3}He. Top Graph: Short timescale ADC results (13 ms). Bottom Graph: Long timescale ADC results (1 s). *Source: The University of Nottingham. Data was acquired using relatively small quantities of HP ^{3}He (0.5 L of 1:18 ^{3}He:^{4}He mix) prepared via MEOP, at two different diffusion timescales, on a total of 317 volunteers (18 with CF, 33 with Asthma (Low S_{acin}), 15 with Asthma (High S_{acin}), and 251 healthy).*

singlet spin state $[\propto(|\uparrow\downarrow\rangle\text{-}|\downarrow\uparrow\rangle)]$ (a.k.a. "para-hydrogen," *para*-H_2), and all H_2 molecules in the antisymmetric $J=1$ state must be in the (symmetric) triplet nuclear spin state $[\propto(|\uparrow\downarrow\rangle+|\downarrow\uparrow\rangle,|\uparrow\uparrow\rangle,|\downarrow\downarrow\rangle)]$ (a.k.a. "ortho-hydrogen"). Thus, the significant energy difference between the ground and excited rotational states provides the means to prepare and separate *para*-H_2: although the ratio of *para*-H_2:*ortho*-H_2 is about 25%:75% at room temperature, reduction to liquid-N_2 temperature (77K) with concomitant exposure to a paramagnetic catalyst that accelerates the ortho-para conversion (like iron oxide) enriches *para*-H_2 to 50% of the mixture, and reduction to 20K can enrich the *para*-H_2 fraction to well over 90%. Importantly, in the absence of exposure to paramagnetic centers (e.g., from O_2 gas or those within container walls) the exchange between *para*-H_2 and *ortho*-H_2 is extremely inefficient—allowing *para*-H_2 to be stored effectively for weeks [195].

However, the pure spin order of the singlet state of *para*-H_2 is actually NMR-invisible. Instead, HP gases may be produced using PHIP, where PHIP-prepared HP gases have been demonstrated initially in the context of void-space imaging [196]. This process still fundamentally relies on the singlet of *para*-H_2 molecule to be the source of spin order, which can be transformed into observable nuclear spin polarization by the process of symmetry breaking typically conduced via a process of pairwise chemical addition of *para*-H_2 to an unsaturated precursor molecule [197]—as shown schematically in Fig. 2.8; a key requirement is that the unsaturated bond must be structurally asymmetric, such that the nascent ^{1}H positions following hydrogenation are magnetically inequivalent. While the process underlying PHIP has been known for many decades, it was not until the advent of efficient heterogeneous catalysts promoting significant fractional pairwise addition of *para*-H_2 (vs radical addition [196]) that efficient (high P), relatively large-scale production of PHIP HP gases became possible. Notably, the *radical* addition of *para*-H_2 does not lead to PHIP, because *para*-H_2 singlet order is scrambled. $P_H \sim 1\%$ has been recently demonstrated in HP propane, enabling submillimeter 3D MRI of the flowing propane gas [198]. The propane molecule represents the shortest hydrocarbon framework for breaking *para*-H_2 symmetry without deuterium or ^{13}C enrichment. Furthermore, propane is an otherwise nontoxic "simple" asphyxiant with anesthetic properties qualitatively similar to those of xenon. Despite achieving $P_H \sim 1\%$ in seconds, HP propane gas cannot be easily used for biomedical applications, because its T_1 is on the order of 1 s at high magnetic fields. However,

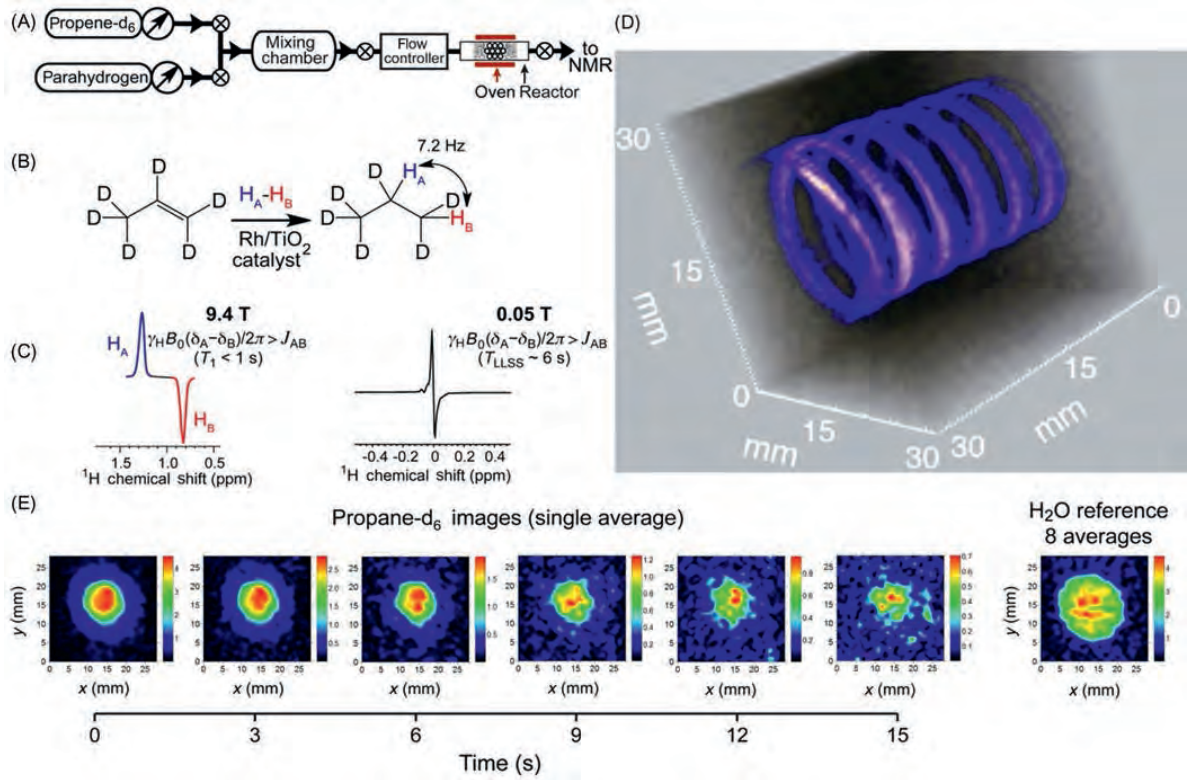

FIGURE 2.8 (A) The schematic representation of PHIP hyperpolarization hardware required for preparation of HP propane gas. (B) The schematics of pairwise addition of parahydrogen gas to an unsaturated precursor molecule resulting in hyperpolarization of propane-d_6 gas via the PHIP approach. (C) Spectroscopic appearance of HP propane-d_6 gas under conditions of high and low magnetic fields corresponding to the two regimes of chemical-shift dominance and *J*-coupling dominance, respectively. (D) 3D 4.7*T* MRI of "flowing" (where a constantly renewing bolus of polarization is delivered) propane-d_6 gas with $0.5 \times 0.5 \times 0.5$ mm^3 spatial resolution. (E) 2D subsecond molecular imaging of "stopped" (i.e., gas is no longer flowing to renew the hyperpolarization pool for signal encoding and readout) HP propane-d_6 gas at 0.05*T* (pixel size 0.88×0.88 mm^2). All images are recorded using the same batch of HP propane-d_6 with apparent $P_H \sim 0.1\%$ [5].

the use of low magnetic fields has been shown to be efficient for extending the lifetime of HP propane through the use of long-lived spin states (LLSS) [199,200] in HP propane [201] and propane-d_6 [5]. The latter exhibits the longest $T_{LLSS} \sim 6$ s [5], which is sufficiently long for imaging of "stopped" gas (i.e., gas that is not flowing and without freshly delivered boluses of hyperpolarization), Fig. 2.8 [5].

PHIP Instrumentation

Besides the hardware needed to create the supply of *para*-H_2 (discussed briefly above), the hardware prerequisites are relatively simple for PHIP hyperpolarization of propane and other hydrocarbons. The setup shown in Fig. 2.8 requires mixing two gases: *para*-H_2 and propene precursor stored in separate containers. The prepared mix passes through a high-temperature reactor containing the heterogeneous catalyst bed, where the hydrogenation reaction takes place to enable pairwise addition of *para*-H_2 to unsaturated precursor. Once prepared in this fashion, the HP propane is ready for use. The setup does not require the use of any alternating or static fields, representing one of the key advantages of this technology: simplicity, scalability, and relatively low-cost production of an HP gaseous agent.

Potential for Biomedical Applications of HP Propane

While efficient production of HP gases by PHIP has been demonstrated only on a relatively small scale of ~ 10 scc/s this approach can be potentially scaled to meet preclinical and clinical requirements. Potential

applications include high-resolution lung imaging given propane's status as a nontoxic gas [202]. Indeed, while propane is flammable, it has lower flammability level and upper flammability level values of ~2.4% and ~9.6%, respectively, and a relatively high ignition temperature of >920°F. Thus, in addition to other favorable properties (see Ref. [203] for details), the range of conditions required to ignite propane are relatively narrow compared to many other species, making propane more difficult to accidentally ignite—and as a consequence help make propane relatively safe. As a result, flammability is not anticipated here to be an unsurmountable translational challenge. Indeed cyclopropane, which has similar properties to propane, has been used previously as an anesthetic (e.g., Ref. [204], which also discusses accidental but preventable ignitions); and unlike the case with anesthetic use, any propane used for MRI applications could be administered in a variable concentration range and with appropriate mixtures (e.g., coadministered with N_2 gas) to ensure safety. Furthermore, the P_H can also be potentially improved to further enhance the detection sensitivity of HP propane. HP propane offers two other key advantages over HP ^{129}Xe and other noble gases. First, the gyromagnetic ratio of ^{1}H is ~3.6 times greater than that of ^{129}Xe, and each propane molecule can carry at least two HP protons, making HP propane nearly an order of magnitude more sensitive than HP ^{129}Xe at the same level of polarization. Second, clinical translation of HP propane will likely be significantly faster, because proton detection capability is universally available on all MRI scanners, unlike the requirement for heteronuclear MRI scanner capability for HP ^{129}Xe and other noble gas isotopes. Furthermore, conventional MRI sequences and MRI coils could be employed for HP propane readout, taking advantage of already available infrastructure. The key disadvantage of HP propane is the requirement of using a low-field MRI scanner rather than a high-field MRI device (in order to exploit the significantly longer hyperpolarization lifetime at low field). However, next-generation low-field MRI instruments are currently under development; moreover, low-field MRI can offer more SNR for imaging HP contrast agents than high-field MRI [205], thereby potentially providing further sensitivity benefits for HP propane technology.

HP GASES: SUMMARY AND OUTLOOK

Examples of nominal polarization values and production rates for several of the HP gases discussed in this chapter are summarized and compared in Table 2.2. A number of HP gases can be prepared with a significant degree of polarization P at quantities (approaching ~1 L dose) sufficient for lung imaging and other in vivo imaging applications—including ^{3}He, ^{129}Xe, propane, and ^{83}Kr. Multiple factors determine the practicality of their in vivo and clinical effectiveness as HP contrast agents: (1) the availability and cost of the involved substances; (2) the cost and production throughput of hyperpolarization equipment; (3) the lifetime of the HP gas state; and (4) the availability of suitable MRI imaging hardware (e.g., heteronuclear MRI scanner capability is required for most HP gases). Moreover, some hyperpolarization techniques for gases (e.g., SEOP) have been

TABLE 2.2 Summary of Hyperpolarization Methods, Polarization Results, and Production Rates for Various Gases

Agent	Hyperpolarization method	Nominal/peak polarization values (%)	Estimated production rates (L · atm/h)	Selected references
Xenon-129	SEOP, CF[a]	P_{Xe} ~ 30–60	~1–5	[206–208]
	SEOP, SF[a]	P_{Xe} ~ 30–90	~0.1–1.2[b]	[25,67,80]
	d-DNP	P_{Xe} ~ 30	<0.1	[40]
Xenon-131	SEOP, SF[a]	$P_{Xe} \leq 2.2$	~0.04[b,c]	[9]
Helium-3	SEOP, SF[a]	P_{He} ~ 60–85	~0.1	[7,180,209]
	MEOP	P_{He} ~65–80	~1–3	[120]
Krypton-83	SEOP, SF[a]	P_{Kr} ~4–27	~0.015–0.4[b,c]	[65]
N_2O	d-DNP	P_N ~10	~0.001	[42]
d_6-propane	PHIP	P_H~1	~27[b,c]	[198]

[a] *CF, continuous flow; SF, stopped flow.*
[b] *Estimated production rate of the gaseous agent in question at STP, not counting the additional presence of diluting gases (N_2, He, and/or H_2), varying from 25% to 95% of the mixture.*
[c] *Extrapolated from small amounts quoted with short production times.*

available for >30 years (and therefore are more robust), whereas others (DNP and PHIP) are newcomers to the field of gas hyperpolarization, providing opportunities for improvement.

Historically, human lung MRI with ^{3}He has been demonstrated first, which was relatively quickly followed by lung MRI demonstration with ^{129}Xe. Other agents with sufficient hyperpolarization lifetime will likely follow this trend—i.e., demonstration of in vivo and human MRI feasibility despite the aforementioned challenges—because these new agents may provide additional (and frequently complementary) biomedical information to what is already feasible with the established HP gases, clinically available imaging modalities, and other tests. For example, while ^{3}He drove the initial feasibility demonstrations of ventilation and diffusion imaging, the advent of clinical-scale production of HP ^{129}Xe enabled the expansion of biomedical HP gas applications to include gas-perfusion imaging, brown fat imaging [210], and brain imaging. Thus, it is not unreasonable to expect that HP propane, ^{83}Kr, and others may provide other benefits to the research community as they are developed, embodying new tools in biomedical research. Indeed, the HP gas research field will likely enjoy substantial growth benefiting from the advent of new HP agents, more advanced instrumentation, and corresponding applications.

However, despite the breakthroughs in science and technology, the in vivo and human demonstrations, and the number of successfully completed clinical trials with HP ^{129}Xe and ^{3}He, HP gases are not yet being used for clinical diagnosis, primarily due to the combinations of the factors outlined above. Therefore, the widespread clinical use of HP agents relies on addressing these translational challenges. While it is not yet clear which of the agents and type(s) of hyperpolarization technique will enjoy clinical adaptation, fundamental changes in MR hardware may be required to achieve clinical use. For example, multinuclear upgrade of 1.5*T* or 3*T* clinical scanners is costly (>$0.5 M) and cumbersome (i.e., most hardware vendors are not providing the required software) for HP ^{129}Xe, ^{3}He, ^{83}Kr, or other heteronuclei. As an alternative approach, a dedicated low-field (LF) MRI scanner may have unique advantages as a platform for the clinical adaptation of HP gases. LF-MRI scanners are fundamentally less expensive than high-field superconductive MRI scanners; yet, LF-MRI can yield more SNR for HP applications [205]; furthermore, LF-MRI can provide enhanced patient safety due to significantly lower specific absorption rate at low RF frequencies [211], and significantly higher patient throughput—because patient-tailored magnet shimming and RF coil calibration steps can be obviated. Moreover, LF-MRI is also ideally suited for HP propane imaging, because of the longer-lived HP state.

To conclude, while HP gas MRI is an established field, new advances in preparation and imaging of HP gases continue to emerge and may significantly and positively impact this field. While there are no *fundamental* barriers for clinical translation and adaptation of HP gas MRI, which can be useful for a number of functional MRI applications, significant clinical translation challenges remain and must be addressed before one can expect to see this promising family of approaches become routinely available in the clinic.

References

[1] Anger BC, Schrank G, Schoeck A, Butler KA, Solum MS, Pugmire RJ, et al. Gas-phase spin relaxation of Xe129. Phys Rev A 2008;78.

[2] Saam B. T1 relaxation of 129Xe and how to keep it long. In: Meersmann T, Brunner E, editors. Hyperpolarized xenon-129 magnetic resonance: concepts, production, techniques and applications. London: Royal Soc Chem; 2015. p. 122–41.

[3] Jameson CJ, Jameson AK, Hwang JK. Nuclear spin relaxation by intermolecular dipole coupling in the gas phase. 129Xe in oxygen. J Chem Phys 1988;89:4074–81.

[4] Repetto M, Babcock E, Blümler P, Heil W, Karpuk S, Tullney K. Systematic T1 improvement for hyperpolarized 129xenon. J Magn Reson 2015;252:163.

[5] Kovtunov KV, Truong ML, Barskiy DA, Salnikov OG, Bukhtiyarov VI, Coffey AM, et al. Propane-d_6 heterogeneously hyperpolarized by parahydrogen. J Phys Chem C 2014;118:28234–43.

[6] Barskiy DA, Kovtunov KV, Koptyug IV, He P, Groome KA, Best QA, et al. The feasibility of formation and kinetics of NMR signal amplification by reversible exchange (SABRE) at high magnetic field (9.4 T). J Am Chem Soc 2014;136:3322–5.

[7] Chen WC, Gentile TR, Ye Q, Walker TG, Babcock E. On the limits of spin-exchange optical pumping of 3He. J Appl Phys 2014;116:014903.

[8] Meersmann T, Pavlovskaya GE. Beyond spin $I = 1/2$; hyperpolarized 131Xe and 83Kr magnetic resonance. Hyperpolarized xenon-129 magnetic resonance. Hyperpolarized xenon-129 magnetic resonance : concepts, production, techniques and applications. London: R Soc Chem; 2015.

[9] Stupic KF, Cleveland ZI, Pavlovskaya GE, Meersmann T. Hyperpolarized 131Xe NMR spectroscopy. J Magn Reson 2011;208:58–69.

[10] Stupic KF, Cleveland ZI, Pavlovskaya GE, Meersmann T. Quadrupolar relaxation of hyperpolarized krypton-83 as a probe for surfaces. Solid State Nucl Magn Reson 2006;29:79–84.

[11] Ruth U, Hof T, Schmidt J, Fick D, Jänsch HJ. Production of nitrogen-free, hyperpolarized 129Xe gas. Appl Phys B 1999;68:93–7.

[12] Breeze SR, Lang S, Moudrakovski I, Ratcliffe CI, Ripmeester JA, Simard B, et al. Coatings for optical pumping cells and extending the lifetime of hyperpolarized xenon. J Appl Phys 1999;86:4040–2.

[13] Breeze SR, Lang S, Moudrakovski I, Ratcliffe CI, Ripmeester JA, Santyr G, et al. Coatings for optical pumping cells and short-term storage of hyperpolarized xenon. J Appl Phys 2000;87:8013–17.
[14] Pavlovskaya GE, Cleveland ZI, Stupic KF, Basaraba RJ, Meersmann T. Hyperpolarized krypton-83 as a contrast agent for magnetic resonance imaging. Proc Natl Acad Sci USA 2005;102:18275–9.
[15] Barker JR. New coil systems for the production of uniform magnetic fields. J Sci Instrum 1949;26:273–5.
[16] Jacob RE, Morgan SW, Saam B, Leawoods JC. Wall relaxation of He3 in spin-exchange cells. Phys Rev Lett 2001;87:143004.
[17] Nikolaou P, Coffey AM, Walkup LL, Gust BM, Whiting N, Newton H, et al. XeNA: An automated 'open-source' 129Xe hyperpolarizer for clinical use. Magn Reson Imag 2014;32:541–50.
[18] Cates GD, Benton DR, Gatzke M, Happer W, Hasson KC, Newbury NR. Laser production of large nuclear-spin polarization in frozen xenon. Phys Rev Lett 1990;65:2591–4.
[19] Gatzke M, Cates GD, Driehuys B, Fox D, Happer W, Saam B. Extraordinarily slow nuclear spin relaxation in frozen laser-polarized 129Xe. Phys Rev Lett 1993;70:690–3.
[20] Driehuys B, Cates G, Miron E, Sauer K, Walter D, Happer W. High-volume production of laser-polarized 129Xe. Appl Phys Lett 1996;69:1668–70.
[21] Kuzma N, Patton B, Raman K, Happer W. Fast nuclear spin relaxation in hyperpolarized solid 129 Xe. Phys Rev Lett 2002;88:147602.
[22] Goodson BM. Using injectable carriers of laser-polarized noble gases for enhancing NMR and MRI. Concepts Magn Reson 1999;11:203–23.
[23] Ardenkjaer-Larsen JH, Leach AM, Clarke N, Urbahn J, Anderson D, Skloss TW. Dynamic nuclear polarization polarizer for sterile use intent. NMR Biomed 2011;24:927–32.
[24] Nikolaou P, Goodson BM, Chekmenev EY. NMR hyperpolarization techniques for biomedicine. Chemistry 2015;21:3156–66.
[25] Nikolaou P, Coffey AM, Walkup LL, Gust BM, Whiting N, Newton H, et al. Near-unity nuclear polarization with an open-source 129Xe hyperpolarizer for NMR and MRI. Proc Natl Acad Sci USA 2013;110:14150–5.
[26] Sarracanie M, Armstrong BD, Stockmann J, Rosen MS. High speed 3D Overhauser-enhanced MRI using combined b-SSFP and compressed sensing. Magn Reson Med 2014;71:735–45.
[27] Zhao L, Mulkern R, Tseng CH, Williamson D, Patz S, Kraft R, et al. Gradient-Echo imaging considerations for hyperpolarized 129Xe MR. J Magn Reson B 1996;113:179–83.
[28] Oppelt A, Graumann R, Barfuss H, Fischer H, Hartl W, Schajor W. Fast imaging with steady precession a new fast magnetic resonance imaging sequence. Electromedica (English edition) 1986;54:15–18.
[29] Wild JM, Teh K, Woodhouse N, Paley MNJ, Fichele S, De Zanche N, et al. Steady-state free precession with hyperpolarized He-3: Experiments and theory. J Magn Reson 2006;183:13–24.
[30] Svensson J, Månsson S, Johansson E, Petersson JS, Olsson LE. Hyperpolarized 13C MR angiography using trueFISP. Magn Reson Med 2003;50:256–62.
[31] Haacke EM, Tkach JA. Fast MR imaging: techniques and clinical applications. Am J Roentgenol 1990;155:951–96.
[32] Frossati G. Polarization of He-3, D-2 and (eventually) Xe-129 using low temperatures and high magnetic fields. J Low Temp Phys 1998;111:521–32.
[33] Tanaka M, Kunimatsu T, Fujiwara M, Kohri H, Ohta T, Utsuro M, et al. Nuclear spin imaging with hyperpolarized nuclei created by brute force method. J Phys: Conf Ser 2011;295:012167.
[34] O'Neill JD, Krjukov EV, Owers-Bradley JR, Xia Y. NMR spectroscopy of adsorbed Xe-129 at low temperatures and high magnetic fields. J Low Temp Phys 2007;146:563–79.
[35] Krjukov EV, O'Neill JD, Owers-Bradley JR. Brute force polarization of Xe-129. J Low Temp Phys 2005;140:397–408.
[36] Carver TR, Slichter CP. Polarization of Nuclear Spins in Metals. Phys Rev 1953;92:212–13.
[37] Ardenkjær-Larsen JH, Fridlund B, Gram A, Hansson G, Hansson L, Lerche MH, et al. Increase in signal-to-noise ratio of >10,000 times in liquid-state NMR. Proc Natl Acad Sci USA 2003;100:10158–63.
[38] Hu K-N, Bajaj VS, Rosay M, Griffin RG. High-frequency dynamic nuclear polarization using mixtures of TEMPO and trityl radicals. J Chem Phys 2007;126:044512.
[39] Thurber KR, Tycko R. Theory for cross effect dynamic nuclear polarization under magic-angle spinning in solid state nuclear magnetic resonance: the importance of level crossings. J Chem Phys 2012;137:084508.
[40] Capozzi A, Roussel C, Comment A, Hyacinthe JN. Optimal glass-forming solvent brings sublimation dynamic nuclear polarization to Xe-129 hyperpolarization biomedical imaging standards. J Phys Chem C 2015;119:5020–5.
[41] Pourfathi M, Kuzma NN, Kara H, Ghosh RK, Shaghaghi H, Kadlecek SJ, et al. Propagation of dynamic nuclear polarization across the xenon cluster boundaries: elucidation of the spin-diffusion bottleneck. J Magn Reson 2013;253:71–6.
[42] Kuzma NN, Håkansson P, Pourfathi M, Ghosh RK, Kara H, Kadlecek SJ, et al. Lineshape-based polarimetry of dynamically-polarized (N2O)-*N*-15 in solid-state mixtures. J Magn Reson 2013;234:90–4.
[43] Levitt MH. Singlet nuclear magnetic resonance. Annu Rev Phys Chem 2012;63:89–105.
[44] Brossel J, Kastler A. La detection de la resonance magnetique des niveaux excites – l'effet de depolarization des radiations de resonance optique et de fluorescence. C R Acad Sci 1949;229:1213–15.
[45] Bouchiat MR, Carver TR, Varnum CM. Nuclear polarization in He3 gas induced by optical pumping and dipolar exchange. Phys Rev Lett 1960;5:373–5.
[46] Grover BC. Noble-gas NMR detection through noble-gas-rubidium hyperfine contact interaction. Phys Rev Lett 1978;40:391.
[47] Happer W, Miron E, Schaefer S, Schreiber D, Wijngaarden WAV, Zeng X. Polarization of the nuclear spins of noble-gas atoms by spin exchange with optically pumped alkali-metal atoms. Phys Rev A 1984;29:3092–110.
[48] Cates GD, Fitzgerald RJ, Barton AS, Bogorad P, Gatzke M, Newbury NR, et al. Rb-129Xe spin-exchange rates due to binary and three-body collisions at high Xe pressures. Phys Rev A 1992;45:4631–9.
[49] Walker TG, Happer W. Spin-exchange optical pumping of noble-gas nuclei. Rev Mod Phys 1997;69:629.
[50] Walker TG. Fundamentals of Spin-Exchange Optical Pumping. J Phys: Conf Ser 2011;294:012001.

[51] Chupp TE, Wagshul ME, Coulter KP, Mcdonald AB, Happer W. Polarized, high-density, gaseous He 3 targets. Phys Rev C 1987;36:2244–51.
[52] Chupp T, Coulter K. Polarization of 21Ne by spin exchange with optically pumped Rb vapor. Phys Rev Lett 1985;55:1074.
[53] Stoner R, Walsworth R. Measurement of the 21Ne Zeeman frequency shift due to Rb – 21Ne collisions. Phys Rev A 2002;66:032704.
[54] D. Steck. Rubidium 85 D line data, Rubidium 87 D line data. (2008), http://steck.us/alkalidata/rubidium87numbers.pdf.
[55] Babcock E, Chann B, Nelson IA, Walker TG. Frequency-narrowed diode array bar. Appl Opt 2005;44:3098–104.
[56] Whiting N, Nikolaou P, Eschmann N, Barlow M, Lammert R, Ungar J, et al. Using frequency-narrowed, tunable laser diode arrays with integrated volume holographic gratings for spin-exchange optical pumping at high resonant fluxes and xenon densities. Appl Phys B 2012;106:775–88.
[57] Nelson IA, Walker TG. Rb-Xe spin relaxation in dilute Xe mixtures. Phys Rev A 2001;65:012712.
[58] Bouchiat MA, Brossel J, Pottier LC. Experimental methods for the study of relaxation in an optically oriented alkali metal vapour. J Chem Phys 1972;56:3703–14.
[59] Raftery D, Long H, Meersmann T, Grandinetti PJ, Reven L, Pines A. High-field NMR of adsorbed xenon polarized by laser pumping. Phys Rev Lett 1991;66:584.
[60] Rosen MS, Chupp TE, Coulter KP, Welsh RC, Swanson SD. Polarized 129Xe optical pumping/spin exchange and delivery system for magnetic resonance spectroscopy and imaging studies. Rev Sci Instrum 1999;70:1546.
[61] Desvaux H, Gautier T, Le Goff G, Pétro M, Berthault P. Direct evidence of a magnetization transfer between laser-polarized xenon and protons of a cage-molecule in water. Eur Phys J B 2000;12:289–96.
[62] Nikolaou P, Whiting N, Eschmann NA, Chaffee KE, Goodson BM. Generation of laser-polarized xenon using fiber-coupled laser-diode arrays narrowed with integrated volume holographic gratings. J Magn Reson 2009;197:249–54.
[63] Parnell SR, Deppe MH, Parra-Robles J, Wild JM. Enhancement of 129Xe polarization by off-resonant spin exchange optical pumping. J Appl Phys 2010;108:064908.
[64] Whiting N, Nikolaou P, Eschmann NA, Goodson BM, Barlow MJ. Interdependence of in-cell xenon density and temperature during Rb/129Xe spin-exchange optical pumping using VHG-narrowed laser diode arrays. J Magn Reson 2011;208:298–304.
[65] Six JS, Hughes-Riley T, Stupic KF, Pavlovskaya GE, Meersmann T. Pathway to cryogen free production of hyperpolarized krypton-83 and xenon-129. PloS ONE 2012;7:49927.
[66] Hughes-Riley T, Six JS, Lilburn DM, Stupic KF, Dorkes AC, Shaw DE, et al. Cryogenics free production of hyperpolarized 129Xe and 83Kr for biomedical MRI applications. J Magn Reson 2013;237:23–33.
[67] Nikolaou P, Coffey AM, Barlow MJ, Rosen MS, Goodson BM, Chekmenev EY. Temperature-ramped 129Xe spin exchange optical pumping. Anal Chem 2014;19:8206–12.
[68] Ruset IC, Ketel S, Hersman FW. Optical pumping system design for large production of hyperpolarized Xe-129. Phys Rev Lett 2006;96:053002.
[69] Wu Z, Happer W, Kitano M, Daniels J. Experimental studies of wall interactions of adsorbed spin-polarized Xe131 nuclei. Phys Rev A 1990;42:2774.
[70] Ghosh RK. Spin exchange optical pumping of neon and its applications. Princeton, NJ: Department of Physics, Princeton University; 2009.
[71] Fain S, Schiebler ML, McCormack DG, Parraga G. Imaging of lung function using hyperpolarized helium-3 magnetic resonance imaging: review of current and emerging translational methods and applications. J Magn Reson Imaging 2010;32:1398–408.
[72] Haake M, Pines A, Reimer JA, Seydoux R. Surface-enhanced NMR using continuous-flow laser-polarized xenon. J Am Chem Soc 1997;119:11711–12.
[73] Zook AL, Adhyaru BB, Bowers CR. High capacity production of >65% spin polarized xenon-129 for NMR spectroscopy and imaging. J Magn Reson 2002;159:175–82.
[74] Mortuza MG, Anala S, Pavlovskaya GE, Dieken TJ, Meersmann T. Spin-exchange optical pumping of high-density xenon-129. J Chem Phys 2003;181:1581.
[75] Knagge K, Prange J, Raftery D. A continuously recirculating optical pumping apparatus for high xenon polarization and surface NMR studies. Chem Phys Lett 2004;397:11–16.
[76] Schrank G, Ma Z, Schoeck A, Saam B. Characterization of a low-pressure high-capacity 129Xe flow-through polarizer. Phys Rev A 2009;80:063424.
[77] Norquay G, Parnell SR, Xu X, Parra-Robles J, Wild JM. Optimized production of hyperpolarized 129Xe at 2 bars for in vivo lung magnetic resonance imaging. J Appl Phys 2013;113:044908.
[78] Nossov A, Haddad E, Guenneaua F, Gédéon A. Application of continuously circulating flow of hyperpolarized (HP) 129Xe-NMR on mesoporous materials. Phys Chem Chem Phys 2003;5:4473–8.
[79] Witte C, Kunth M, Rossella F, Schröder L. Observing and preventing rubidium runaway in a direct-infusion xenon-spin hyperpolarizer optimized for high-resolution hyper-CEST (chemical exchange saturation transfer using hyperpolarized nuclei) NMR. J Chem Phys 2014;140:084203.
[80] Nikolaou P, Coffey AM, Ranta K, Walkup LL, Gust BM, Barlow MJ, et al. Multidimensional mapping of spin-exchange optical pumping in clinical-scale batch-mode 129Xe hyperpolarizers. J Phys Chem B 2014;118:4809–16.
[81] Freeman MS, Emami K, Driehuys B. Characterizing and modeling the efficiency limits in large-scale production of hyperpolarized 129Xe. Phys Rev A 2014;90:023406.
[82] Saha I, Nikolaou P, Whiting N, Goodson BM. Characterization of violet emission from Rb optical pumping cells used in laser-polarized xenon NMR experiments. Chem Phys Lett 2006;428:268–76.
[83] Nikolaou P, Coffey AM, Walkup LL, Gust BM, LaPierre CD, Koehnemann E, et al. A 3D-printed high power nuclear spin polarizer. J Am Chem Soc 2014;136:1636–42.
[84] Parnell SR, Woolley EB, Boag S, Frost CD. Digital pulsed NMR spectrometer for nuclear spin-polarized 3He and other hyperpolarized gases. Meas Sci Technol 2008;19:045601.

[85] Korchak SE, Kilian W, Mitschang L. Configuration and performance of a mobile 129Xe polarizer. Appl Magn Reson 2013;44:65–80.
[86] Saam BT, Conradi MS. Low frequency NMR polarimeter for hyperpolarized gases. J Magn Reson 1998;134:67–71.
[87] Borowiak R, Schwaderlapp N, Huethe F, Lickert T, Fischer E, Bär S, et al. A battery-driven, low-field NMR unit for thermally and hyperpolarized samples. Magn Reson Matter Phy 2013;26:491–9.
[88] Young AR, Appelt S, Ben-Amar Baranga A, Erickson C, Happer W. Three-dimensional imaging of spin polarization of alkali-metal vapor in optical pumping cells. Appl Phys Lett 1997;70:3081–3.
[89] Ma Z, Sorte E, Saam B. Collisional 3He and 129Xe Frequency Shifts in Rb–Noble-Gas Mixtures. Phys Rev Lett 2011;106:193005.
[90] Mort J, Lüty F, Brown FC. Faraday rotation and spin-orbit splitting of the F center in alkali halides. Phys Rev 1965;137:A566–73.
[91] Erickson CJ, Levron D, Happer W, Kadlecek S, Chann B, Anderson LW, et al. Spin relaxation resonances due to the spin-axis interaction in dense rubidium and cesium vapor. Phys Rev Lett 2000;85:4237.
[92] Babcock E, Nelson I, Kadlecek S, Driehuys B, Anderson LW, Hersman FW, et al. Hybrid spin-exchange optical pumping of 3He. Phys Rev Lett 2003;91:123003.
[93] Baranga AB-A, Appelt S, Erickson CJ, Young AR, Happer W. Alkali-metal-atom polarization imaging in high-pressure optical-pumping cells. Phys Rev A 1998;58:2282.
[94] Shah NJ, Unlü T, Wegener HP, Halling H, Zilles K, Appelt S. Measurement of rubidium and xenon absolute polarization at high temperatures as a means of improved production of hyperpolarized 129Xe. NMR Biomed 2000;13:214–19.
[95] Romalis M, Cates G. Accurate 3He polarimetry using the Rb Zeeman frequency shift due to the Rb − 3He spin-exchange collisions. Phys Rev A 1998;58:3004.
[96] Babcock E, Nelson IA, Kadlecek S, Walker TG. He3 polarization-dependent EPR frequency shifts of alkali-metal–He3 pairs. Phys Rev A 2005;71:013414.
[97] Babcock ED. Spin-exchange optical pumping with alkali-metal vapors. Madison, MI: University of Wisconsin-Madison: Physics; 2005.
[98] Stenger J, Beckmann M, Nagengast W, Rith K. A compact Faraday rotation monitor for density and polarization of optically pumped alkali atoms. Nucl Instrum Meth A 1997;384:333–6.
[99] Killian TJ. Thermionic phenomena caused by vapors of rubidium and potassium. Phys Rev 1926;27:578.
[100] Lide D. Handbook of chemistry and physics. 85th ed. Boca Raton, FL: CRC Press; 2004.
[101] Shao W, Wang G, Hughes EW. Measurement of spin-exchange rate constants between Xe 129 and alkali metals. Phys Rev A 2005;72:022713.
[102] Dregely IM, Ruset IC, Kotkowski EJ, Hersman FW. Scaling up 129Xe Hyperpolarization—a diagnostic tools system *International Society for Magnetic Resonance in Medicine*. Proc Intl Soc Mag Reson Med, Vol. 15. Berlin: ICC; 2007. p. 1265.
[103] Gallagher A, Lewis E. Determination of the vapor pressure of rubidium by optical absorption. J Opt Soc Am 1973;63:864–9.
[104] Walter D, Griffith W, Happer W. Energy transport in high-density spin-exchange optical pumping cells. Phys Rev Lett 2001;86:3264–7.
[105] Newton H, Walkup LL, Whiting N, West L, Carriere J, Havermeyer F, et al. Comparative study of in situ N2 rotational Raman spectroscopy methods for probing energy thermalisation processes during spin-exchange optical pumping. Appl Phys B 2014;115:167–72.
[106] Hickman R, Liang L. Rotational temperature measurement in nitrogen using Raman spectroscopy. Rev Sci Instrum 1972;43:796–9.
[107] Whiting N, Newton H, Morris P, Barlow MJ, Goodson BM. Observation of energy thermalization and ~1000 K gas temperatures during spin-exchange optical pumping at high xenon densities. Phys Rev A 2014;118(18):4809–16.
[108] Ebert M, Grossmann T, Heil W, Otten WE, Surkau R, Leduc M, et al. Nuclear magnetic resonance imaging with hyperpolarised helium-3. Lanclet 1996;11:9011.
[109] Leawoods JC, Yablonskiy DA, Saam B, Gierada DS, Conradi MS. Hyperpolarized 3He gas production and MR imaging of the lung. Concepts Magn Reson 2001;13:277–93.
[110] Möller HE, Chen XJ, Saam B, Hagspiel KD, Johnson GA, Altes TA, et al. MRI of the lungs using hyperpolarized noble gases. Magn Reson Med 2002;47:1029–51.
[111] Wild JM, Marshall H, Xu X, Norquay G, Parnell SR, Clemence M, et al. Simultaneous imaging of lung structure and function with triple-nuclear hybrid MR imaging. Radiology 2013;267:251–5.
[112] Saam BT, Yablonskiy DA, Kodibagkar VD, Leawoods JC, Gierada DS, Cooper JD, et al. MR imaging of diffusion of 3He gas in healthy and diseased lungs. Magn Reson Med 2000;44:174–9.
[113] Salerno M, de Lange EE, Altes TA, Truwit JD, Brookeman JR, Mugler III JP. Emphysema: hyperpolarized helium 3 diffusion MR imaging of the lungs compared with spirometric indexes—initial experience 1. Radiology 2002;222:252–60.
[114] Chupp TE, Hoare RJ, Walsworth RL, Wu B. Spin-exchange-pumped 3He and 129Xe Zeeman masers. Phys Rev Lett 1994;72:2363.
[115] Newbury NR, Barton AS, Bogorad P, Cates GD, Gatzke M, Saam B, et al. Laser polarized muonic helium. Phys Rev Lett 1991;67:3219.
[116] Thompson AK, Bernstein AM, Chupp TE, DeAngelis DJ, Dodge GE, Dodson G, et al. Quasielastic scattering of polarized electrons from polarized 3he and measurement of the neutron's form factors. Phys Rev Lett 1992;68:2901.
[117] Singh JT, Dolph PAM, Tobias WA, Averett TD, Kelleher A, Mooney KE, et al. Development of high performance alkali-hybrid polarized 3He targets for electron scattering. Phys Rev C 2015;91:055205.
[118] Lelievre-Berna E. Mid-term report of the NMI3 neutron spin filter project. Physica B Cond Mat 2007;397:162–7.
[119] Gentile TR, Chen WC. Polarized 3He spin filters for neutron science. Proc Sci (PSTP) 2013;022:1–11.
[120] Karpuk S, Allmendinger F, Burghoff M, Gemmel C, Güldner M, Heil W, et al. Spin polarized 3He: from basic research to medical applications. Phys Partic Nucl 2013;44:904–8.
[121] J.C. Woods, Subcommittee on Investigations and Oversight Committee of Science and Technology United States House of Representatives. Congressional hearing: "caught by surprise: causes and consequences of the helium-3 supply crisis"; 2010.
[122] Terskikh VV, Moudrakovski IL, Breeze SR, Lang S, Ratcliffe CI, Ripmeester JA, et al. A general correlation for the 129Xe NMR chemical shift-pore size relationship in porous silica-based materials. Langmuir 2002;18:5653–6.
[123] Goodson BM. Nuclear magnetic resonance of laser-polarized noble gases in molecules, materials, and organisms. J Magn Reson 2002;155:157–216.
[124] Cherubini A, Bifone A. Hyperpolarised xenon in biology. Prog Nucl Magn Reson Spectrosc 2003;42:1–30.

[125] Lilburn DML, Pavlovskaya GE, Meersmann T. Perspectives of hyperpolarized noble gas MRI beyond 3He. J Magn Reson 2013;229:173–86.
[126] Taratula O, Dmochowski IJ. Functionalized 129Xe contrast agents for magnetic resonance imaging. Curr Opin Chem Biol 2010;14:97–104.
[127] Berthault P, Huber G, Desvaux H. Biosensing using laser-polarized xenon NMR/MRI. Prog Nucl Magn Reson Spectrosc 2009;55:35–60.
[128] Schroder L. Xenon for NMR biosensing—inert but alert. Phys Med 2013;29:3–16.
[129] Albert MS, Cates GD, Driehuys B, Happer W, Saam B, Springer CS, et al. Biological magnetic resonance imaging using laser-polarized 129Xe. Nature 1994;370:199–201.
[130] Patz S, Muradyan I, Hrovat MI, Dabaghyan M, Washko GR, Hatabu H, et al. Diffusion of hyperpolarized 129Xe in the lung: a simplified model of 129Xe septal uptake and experimental results. New J Phys 2011;13:015009.
[131] Mugler III JP, Altes TA. Hyperpolarized 129Xe MRI of the human lung. J Magn Reson Imaging 2013;37:313–31.
[132] Mugler III JP, Driehuys B, Brookeman JR, Cates GD, Berr SS, Bryant RG, et al. MR imaging and spectroscopy using hyperpolarized 129Xe gas: preliminary human results. Magn Reson Med 1997;37:809–15.
[133] Patz S, Hersman FW, Muradian I, Hrovat MI, Ruset IC, Ketel S, et al. Hyperpolarized 129Xe MRI: a viable functional lung imaging modality? Eur J Radiol 2007;64:335–44.
[134] Dregely I, Mugler JP, Ruset IC, Altes TA, Mata JF, Miller GW, et al. Hyperpolarized Xenon-129 gas-exchange imaging of lung microstructure: first case studies in subjects with obstructive lung disease. J Magn Reson Imaging 2011;33:1052–62.
[135] Kaushik SS, Cleveland ZI, Cofer GP, Metz G, Beaver D, Nouls J, et al. Diffusion-weighted hyperpolarized 129Xe MRI in healthy volunteers and subjects with chronic obstructive pulmonary disease. Magn Reson Med 2011;65:1154–65.
[136] Matsuoka S, Patz S, Albert MS, Sun Y, Rizi RR, Gefter WB, et al. Hyperpolarized gas MR imaging of the lung: current status as a research tool. J Thorac Imaging 2009;24:181–8.
[137] Lilburn DML, Hughes-Riley T, Six JS, Stupic KF, Shaw DE, Pavlovskaya GE, et al. Validating excised rodent lungs for functional hyperpolarized xenon-129 MRI. PloS ONE 2013;8:e73468.
[138] Kadlecek S, Mongkolwisetwara P, Xin Y, Ishii M, Profka H, Emami K, et al. Regional determination of oxygen uptake in rodent lungs using hyperpolarized gas and an analytical treatment of intrapulmonary gas redistribution. NMR Biomed 2011;24:1253–63.
[139] Mugler III JP, Altes TA, Ruset IC, Dregely IM, Mata JF, Miller GW, et al. Simultaneous magnetic resonance imaging of ventilation distribution and gas uptake in the human lung using hyperpolarized xenon-129. Proc Nat Acad Sci USA 2010;107:21707–12.
[140] Walkup LL, Woods JC. Translational applications of hyperpolarized He-3 and Xe-129. NMR Biomed 2014;27:1429–38.
[141] Duhamel G, Choquet P, Grillon E, Lamalle L, Leviel JL, Ziegler A, et al. MR imaging and spectroscopy of rat brain using arterial delivery of hyperpolarized xenon in a lipid emulsion. Magn Reson Med 2001;46:208–12.
[142] Swanson SD, Rosen MS, Agranoff BW, Coulter KP, Welsh RC, Chup TE. Brain MRI with laser-polarized 129Xe. Magnetic resonance in medicine. Magn Reson Med 1997;38:695–8.
[143] Mazzanti ML, Walvick RP, Zhou X, Sun Y, Shah N, Mansour J, et al. Distribution of hyperpolarized xenon in the brain following sensory stimulation: preliminary MRI findings. PloS ONE 2011;6:e21607.
[144] Imai H, Kimura A, Akiyama K, Ota C, Okimoto K, Fujiwara H. Development of a fast method for quantitative measurement of hyperpolarized 129Xe dynamics in mouse brain. NMR Biomed 2012;25:210–17.
[145] Kershaw J, Nakamura K, Kondoh Y, Wakai A, Suzuki N, Kanno I. Confirming the existence of five peaks in 129Xe rat head spectra. Magn Reson Med 2007;57:791–7.
[146] Kimura A, Imai H, Wakayama T, Fujiwara H. A simple method for quantitative measurement and analysis of hyperpolarized 129Xe uptake dynamics in mouse brain under controlled flow. Magn Reson Med 2008;7:179–85.
[147] Nakamura K, Kondoh Y, Wakai A, Kershaw J, Wright D, Kanno I. 129Xe spectra from the heads of rats with and without ligation of the external carotid and pterygopalatine arteries. Magn Reson Med 2005;53:528–34.
[148] Wakai A, Nakamura K, Kershaw J, Kondoh Y, Wright D, Kanno I. A method for measuring the decay time of hyperpolarized 129Xe magnetization in rat brain without estimation of RF flip angles. Magn Reson Med Sci 2005;4:19–25.
[149] Wakai A, Nakamura K, Kershaw J, Kanno I. In vivo MR spectroscopy of hyperpolarized 129Xe in rat brain. International Congress Series 2004;1265:139–43.
[150] M. Rao, N. Stewart, G. Norquay, Wild J. Proc Intl Soc Mag Reson Med Milan, Italy; 2014. p. 3532.
[151] M. Rao, N. Stewart, G. Norquay, Wild J. COST Hyperpol. Vol 4. Zurich, Switzerland; 2014.
[152] Swanson SD, Rosen MS, Coulter KP, Welsh RC, Chupp TE. Distribution and dynamics of laser-polarized 129Xe magnetization in vivo. Magn Reson Med 1999;24:1137–45.
[153] Norquay G, Leung G, Stewart NJ, Tozer GM, Wolber J, Wild JM. Relaxation and exchange dynamics of hyperpolarized 129Xe in human blood. Magn Reson Med 2014;74:303–11.
[154] Chen RY, Fan FC, Kim S, Jan KM, Usami S, Chien S. Tissue-blood partition coefficient for xenon: temperature and hematocrit dependence. J Appl Physiol 1980;49:178–83.
[155] Bifone A, Song Y-Q, Seydoux R, Taylor RE, Goodson BM, Pietrass T, et al. NMR of laser-polarized xenon in human blood. Proc Nat Acad Sci USA 1996;93:1232–12936.
[156] Albert MS, Schepkin VD, Budinger TF. Measurement of 129Xe T1 in blood to explore the feasibility of hyperpolarized 129Xe MRI. J Comput Assist Tomogr 1995;19:975–8.
[157] Moudrakovski IL, Ratcliffe CI, Ripmeester JA. 131Xe, a new NMR probe of void space in solids. J Am Chem Soc 2001;123:2066–7.
[158] Meersmann T, Smith SA, Bodenhausen G. Multiple-quantum filtered xenon-131 NMR as a surface probe. Phys Rev Lett 1998;80:1398.
[159] Millot Y, Man PP, Springuel-Huet M-A, Fraissard J. Quantification of electric-field gradient in the supercage of Y zeolites with 131Xe (I = 3/2) NMR. C R Acad Sci Ser II C 2001;4:815–18.
[160] Horton-Garcia CF, Pavlovskaya GE, Meersmann T. Introducing krypton NMR spectroscopy as a probe of void space in solids. J Am Chem Soc 2005;127:1958–62.

[161] Six JS, Hughes-Riley T, Lilburn DM, Dorkes AC, Stupic KF, Shaw DE, et al. Pulmonary MRI contrast using Surface Quadrupolar Relaxation (SQUARE) of hyperpolarized (83)Kr. Magn Reson Imag 2014;32:48–53.
[162] R. Stoner Testing Local Lorentz Invariance with Zeeman Masers. *1st Meeting on CPT and Lorentz Symmetry (CPT 98)*. Bloomington, IN: CPT and Lorentz Symmetry: Proceedings; 1991.
[163] Kastler A. Optical methods of atomic orientation and of magnetic resonance. J Opt Soc Am 1957;47:460–5.
[164] Colegrove FD, Franken PA. Optical pumping of helium in the 3S1 metastable state. Phys Rev 1960;119:680–90.
[165] Colegrove FD, Scheare LD, Walters GK. Polarization of He3 gas by optical pumping. Phys Rev 1963;132:2561–72.
[166] Schearer LD. Optical pumping of neon P 2 3 metastable atoms. Phys Rev 1969;180:83–90.
[167] Young L, Yang D, Dunford RW. Optical production of metastable krypton. J Phys B 2002;35:2985–92.
[168] Hadeishi T, Chung-Heng L. Nuclear alignment of the 1S0 ground state of 131Xe by electron pumping and metastability-exchange collisions. Phys Rev Lett 1967;19:211.
[169] Lefevre-Seguin V, Leduc M. Metastability-exchange and depolarising collisions in xenon and krypton. J Phys B 1977;10:2157.
[170] Batz M, Nacher PJ, Tastevin G. Fundamentals of metastability exchange optical pumping in helium. J Phys Conf Series 2011;294.
[171] Gentile TR, McKeown RD. Spin-polarizing He nuclei with an arc-lamp-pumped neodymium-doped lanthanum magnesium hexaluminate laser. Phys Rev 1993;47:456.
[172] Gentile TR, Hayden ME, Barlow MJ. Comparison of metastability-exchange optical pumping sources. J Opt Soc Am 2003;33:265–6.
[173] Courtade E, Marion F, Nacher PJ, Tastevin G, Kiersnowski K, Dohnalik T. Magnetic field effects on the 1083 nm atomic line of helium. J Eur Phys D 2002;21:25–55.
[174] Schearer LD, Padetha T. Tunable lasers at 1080 nm for helium optical pumping. J Appl Phys 1990;68:943–9.
[175] Daniels JM, Schearer LD, Leduc M, Nacher PJ. Polarizing 3He nuclei with neodymium La 1-xNdxMgAl 11 O 19 lasers. J Opt Soc Am B 1987;4:1133–5.
[176] Wallace CD, Bixler DL, Monroe TJ, Dunning FB, Walters GK. Optical pumping of a He(23S) metastable atom beam using a diode laser. Rev Sci Instrum 1995;66:265–6.
[177] Chernikov SV, Taylor JR, Platonov NS, Gapontsev VP, Nacher PJ, Tastevin G, et al. 1083 nm ytterbium doped fibre amplifier for optical pumping of helium. Electronic Lett 1997;33:787–9.
[178] Batz M, Baeßler S, Heil W, Otten EW, Rudersdorf D, Schmiedeskamp J, et al. 3He spin filter for neutrons. J Res Natl Inst Stand Technol 2005;110:293–8.
[179] Phillips GC, Perry RR, Windham PM, Walters GK, Schearer LD, Colegrove FD. Demonstration of a polarized He3 target for nuclear reactions. Phys Rev lett 1962;9:502–4.
[180] Chen WC, Gentile TR, Fu CB, Watson S, Jones GL, McIver JW, et al. Polarized 3He cell development and application at NIST. J Phys Conf Series 2011;294:012003.
[181] Timsit RS, Daniels JM, Dennig EI, Kiang AKC, May AD. An experiment to compress polarized 3He gas. J Cand Phys 1971;49:508–16.
[182] Timsit RS, Hilger W, Daniels JM. A gas circulation system, using a Toepler pump, for the construction of a polarized 3He target. Rev Sci Instrum 1973;44:508–16.
[183] Becker J, Heil W, Krug B, Leduc M, Meyerhoff M, Nacher PJ, et al. Study of mechanical compression of spin-polarized 3He gas. Nucl Instrum Meth A 1994;346:45–51.
[184] Hussey DS, Rich DR, Belov AS, Tong X, Yang H, Bailey C, et al. Polarized 3He gas compression system using metastability-exchange optical pumping. Rev Sci Instrum 2005;76:053503.
[185] Gentile TR, Rich DR, Thompson AK, Snow WM, Jones GL. Compressing spin-polarized 3He with a modified diaphragm pump. J Res Natl Inst Stand Technol 2001;106:709–29.
[186] Nacher PJ, Tastevin G, Maitre X, Dollat X, Lemaire B, Olejnik J. A peristaltic compressor for hyperpolarized helium. Eur J Radiol 1999; 9:b18.
[187] Middleton H, Black RD, Saam B, Cates GD, Cofer GP, Guenther R, et al. MR Imaging with Hyperpolarized 3He Gas. Magn Reson Med 1995;33:271–5.
[188] Kauczor HU, Hofmann D, Kreitner KF, Nilgens H, Surkau R, Heil W, et al. Normal and abnormal pulmonary ventilation: visualization at hyperpolarized He-3 MR imaging. Radiology 1996;2:564–8.
[189] Yablonskiy DA, Sukstanskii AL, Leawoods JC, Gierada DS, Bretthorst GL, Lefrak SS, et al. Quantitative in vivo assessment of lung microstructure at the alveolar level with hyperpolarized 3He diffusion MRI. Proc Nat Acad Sci USA 2002;99:3111–16.
[190] Swift AJ, Wild JM, Fichele S, Woodhouse N, Fleming S, Waterhouse J, et al. Emphysematous changes and normal variation in smokers and COPD patients using diffusion 3 He MRI. Eur J Radiol 2005;54:352–8.
[191] Wang C, Altes TA, Mugler III JP, Miller GW, Ruppert K, Mata JF, et al. Assessment of the lung microstructure in patients with asthma using hyperpolarized 3He diffusion MRI at two time scales: comparison with healthy subjects and patients with COPD. J Magn Reson Imaging 2008;28:80–8.
[192] D.A. Shea, D. Morgan The helium-3 shortage: supply, demand, and options for Congress. In: Service Cr, ed. CRS; 2010.
[193] Cleveland ZI, Pavlovskaya GE, Elkins ND, Stupic KF, Repine JE, Meersmann T. Hyperpolarized 83 Kr MRI of lungs. J Magn Reson 2008;195:232–7.
[194] Farkas A. Orthohydrogen, parahydrogen, and heavy hydrogen. Cambridge: Cambridge University Press; 1935.
[195] Feng B, Coffey AM, Colona RD, Chekmenev EY, Waddell KW. A pulsed injection parahydrogen generator and techniques for quantifying enrichment. J Magn Reson 2012;214:258–62.
[196] Bouchard LS, Burt SR, Anwar MS, Kovtunov KV, Koptyug IV, Pines A. NMR imaging of catalytic hydrogenation in microreactors with the use of para-hydrogen. Science 2008;319:442–5.
[197] Bowers CR, Weitekamp DP. Para-hydrogen and synthesis allow dramatically enhanced nuclear alignment. J Am Chem Soc 1987;109:5541–2.
[198] Kovtunov KV, Barskiy DA, Coffey AM, Truong ML, Salnikov OG, Khudorozhkov AK, et al. High-resolution 3D proton hyperpolarized gas MRI enabled by parahydrogen and Rh/TiO2 heterogeneous catalyst. Chem Eur J 2014;20:11636–9.

[199] Carravetta M, Levitt MH. Long-lived nuclear spin states in high-field solution NMR. J Am Chem Soc 2004;126:1711–14.
[200] Warren WS, Jenista E, Branca RT, Chen X. Increasing hyperpolarized spin lifetimes through true singlet eigenstates. Science 2009;323:1711–14.
[201] Kovtunov KV, Truong ML, Barskiy DA, Koptyug IV, Coffey AM, Waddell KW, et al. Long-lived spin states for low-field hyperpolarized gas MRI. Chem Eur J 2014;20:14629–32.
[202] McKee RH, Herron D, Saperstein M, Podhasky P, Hoffman GM, Roberts L. The toxicological properties of petroleum gases. Int J Toxicol 2014;33:28S–51S.
[203] All Gas Inc. Propane Gas Properties. 2015. http://www.allgasinc.com/propane-gas-properties.php.
[204] Greene BA. The hazards of fire and explosion in anesthesia: Report of a clinical investigation in 230 cases. Anesthesiology 1941;2:144–60.
[205] Coffey AM, Truong ML, Chekmenev EY. Low-field MRI can be more sensitive than high-field MRI. J Magn Reson 2013;237:169–74.
[206] Polarian Inc. (2015) www.polarean.com.
[207] Xemed LLC. (2015) https://www.xemed.com/.
[208] Rao M, Wild JM. RF instrumentation for same-breath triple nuclear lung MR imaging of 1H and hyperpolarized 3He and 129Xe at 1.5T. Magn Reson Med 2015;75(4):1841–8.
[209] Chen WC, Gentile TR, Walker TG, Babcock E. Spin-exchange optical pumping of 3He with Rb-K mixtures and pure K. Phys Rev A 2007;75:013416.
[210] Branca RT, He T, Zhang L, Floyd CS, Freeman M, White C, et al. Detection of brown adipose tissue and thermogenic activity in mice by hyperpolarized xenon MRI. Proc Natl Acad Sci USA 2014;111:18001–6.
[211] Hayden ME, Bidinosti CP, Chapple EM. Specific absorption rates and signal-to-noise ratio limitations for MRI in very-low magnetic fields. Concepts Magn Reson 2012;40A:281–94.

ChemPubSoc Europe
DOI: 10.1002/cphc.201600564
CHEMPHYSCHEM Communications

Efficient Batch-Mode Parahydrogen-Induced Polarization of Propane

Oleg G. Salnikov,[a, b] Danila A. Barskiy,[c] Aaron M. Coffey,[c] Kirill V. Kovtunov,[a, b] Igor V. Koptyug,[a, b] and Eduard Y. Chekmenev*[c, d]

We report on a simple approach for efficient NMR proton hyperpolarization of propane using the parahydrogen-induced polarization (PHIP) technique, which yielded ≈6.2% proton polarization using ≈80% parahydrogen, a record level achieved with any hyperpolarization technique for propane. Unlike in previously developed approaches designed for continuous-flow operation, where reactants (propene and parahydrogen) are simultaneously loaded for homogeneous or heterogeneous pairwise addition of parahydrogen, here a batch-mode method is applied: propene is first loaded into the catalyst-containing solution, which is followed by homogeneous hydrogenation via parahydrogen bubbling delivered at ≈7.1 atm. The achieved nuclear spin polarization of this contrast agent potentially useful for pulmonary imaging is approximately two orders of magnitude greater than that achieved in the continuous-flow homogeneous catalytic hydrogenation, and a factor of 3–10 more efficient compared to the typical results of heterogeneous continuous-flow hydrogenations.

Hyperpolarization of nuclear spins enables enhancement of nuclear magnetic resonance (NMR) signal by several orders of magnitude.[1] Therefore, NMR hyperpolarization is an efficient approach for overcoming the sensitivity challenges of NMR spectroscopy and magnetic resonance imaging (MRI). Production of hyperpolarized (HP) contrast agents for clinical and industrial applications is a rapidly developing field. The most widespread hyperpolarization techniques in the context of biomedical applications are dissolution dynamic nuclear polarization (d-DNP),[1b,2] spin-exchange optical pumping (SEOP)[3] and parahydrogen-induced polarization (PHIP).[4] D-DNP is well established for production of HP solutions of metabolites (e.g. pyruvate), which can be used as contrast agents for molecular imaging of cancer[5] and other pathologies.[6] HP noble gases (e.g. ^{129}Xe or ^{3}He) obtained by SEOP can be employed for functional MRI of lungs[7] and other applications.[8] However, both the DNP and SEOP techniques have significant drawbacks: ≈1 h long polarization cycles, expensive and sophisticated hardware. Moreover, MRI detection of heteronuclei (i.e., other than proton) is not common for standard clinical MRI facilities. On the other hand, PHIP technique for production of proton-hyperpolarized gases obviates all of the above shortcomings, because it is very simple and instrumentationally non-demanding. In PHIP, singlet spin order of parahydrogen (p-H_2) is used to create non-equilibrium spin states[4a] via pairwise addition of two atoms from the same p-H_2 molecule to some asymmetric unsaturated substrate (Figure 1 a). Once the symmetry of p-H_2 molecule is broken as the nascent parahydrogen protons become magnetically non-equivalent in the reaction product, a non-equilibrium nuclear spin polarization is produced, which can be conveniently detected using conventional proton detection universally available on nearly all NMR spectrometers and MRI scanners.

Despite the initial PHIP phenomenon discovery in the 1980s,[4a] it was deemed to be relatively impractical to design molecular contrast agents with hyperpolarization pool stored on protons, because of their relatively short T_1 resulting in rapid (few seconds or less) depolarization. Indeed, much of the later biomedical efforts were focused on polarization transfer from nascent parahydrogen protons to significantly slower relaxing (a minute or more) ^{13}C sites for in vivo angiography[9] and molecular imaging[10] applications. However, the discovery of the long-lived spin states[11] (LLSS) provided a glimpse of hope that the lifetime of proton HP for contrast agents produced by PHIP could be extended. Indeed, LLSS of HP protons in gaseous propane were recently demonstrated with T_{LLSS} reaching 5–6 s,[12] which is sufficiently long for potential biomedical use as inhalable contrast agents for functional pulmonary imaging.

HP propane is a non-toxic gas[13] and is a promising alternative to HP ^{129}Xe, because its PHIP production is relatively inexpensive, its NMR/MRI detection does not require specialized ^{129}Xe radiofrequency hardware and software, and it can enable 3D MRI with superb spatial (≈0.5×0.5×0.5 mm^3 voxel size) resolution even at nuclear spin polarization (%P_H) of ≈1%.[12] Increasing the %P_H of propane and other HP gases is certainly required, and it is an area of extensive experimental efforts.[14]

[a] O. G. Salnikov, Dr. K. V. Kovtunov, Prof. I. V. Koptyug
International Tomography Center, SB RAS
Insitutskaya Street 3A, 630090 Novosibirsk (Russia)

[b] O. G. Salnikov, Dr. K. V. Kovtunov, Prof. I. V. Koptyug
Novosibirsk State University
Pirogova Street 2, 630090 Novosibirsk (Russia)

[c] Dr. D. A. Barskiy, Dr. A. M. Coffey, Prof. E. Y. Chekmenev
Institute of Imaging Science (VUIIS)
Department of Radiology, Department of Biomedical Engineering
Vanderbilt-Ingram Cancer Center (VICC)
Vanderbilt University, Nashville, Tennessee, 37232-2310 (USA)
E-mail: eduard.chekmenev@vanderbilt.edu

[d] Prof. E. Y. Chekmenev
Russian Academy of Sciences
Leninskiy Prospect 14, 119991 Moscow (Russia)

Supporting Information and the ORCID identification number(s) for the author(s) of this article can be found under http://dx.doi.org/10.1002/cphc.201600564.

© 2016 Wiley-VCH Verlag GmbH & Co. KGaA, Weinheim

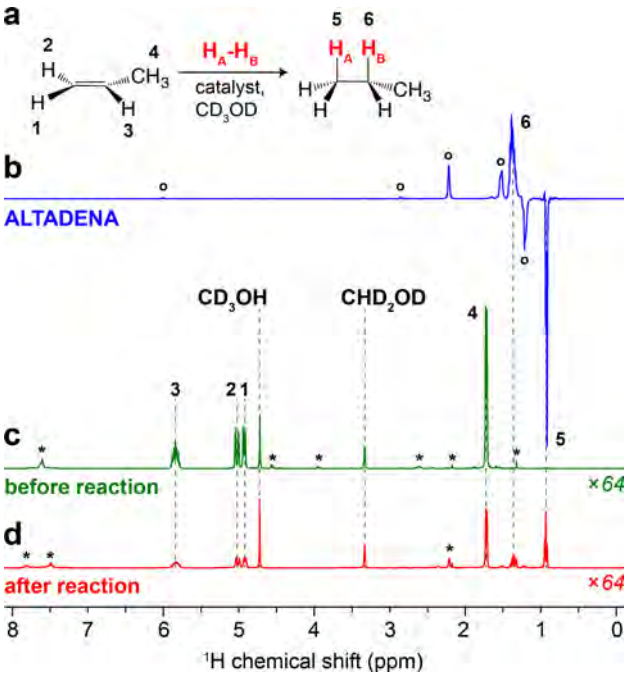

Figure 1. a) Scheme of p-H_2 pairwise addition to propene. b) ALTADENA[19] ^{1}H NMR spectrum acquired after PHIP of propene with p-H_2 with separate loading of reactants into the catalyst solution in CD_3OD (duration of p-H_2 bubbling is 8 s) corresponding to the batch-mode condition (corresponding PASADENA spectrum obtained using 50% p-H_2 is provided in Figure S4). c) ^{1}H NMR spectrum of thermally-polarized solution with loaded propene before p-H_2 bubbling. d) ^{1}H NMR spectrum of fully relaxed (i.e. thermally-polarized condition) reaction mixture obtained after the experiment (b). Note that spectra (c) and (d) are scaled by a factor of 64. SE = 1910 for CH_2 group of propane, corresponding to $\%P_H = 6.2\%$ (80% p-H_2). Resonances labeled with * correspond to the initial $[Rh(NBD)(dppb)]BF_4$ complex and its reduced form. Note the additional HP resonances labeled with ° correspond to HP norbornene and norbornane due to PHIP process of these catalyst-derived compounds.[20]

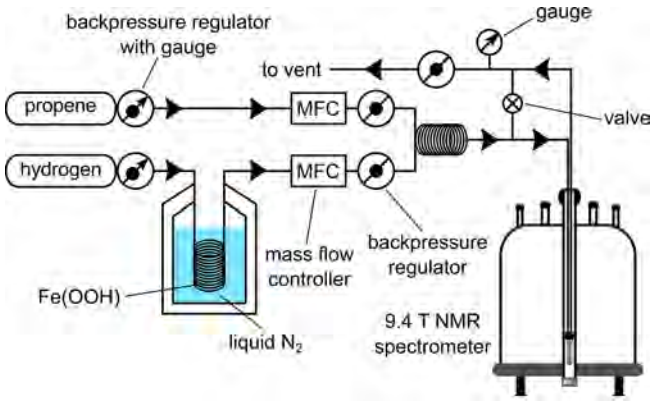

Figure 2. The diagram of the experimental setup. In the continuous-flow experiment, both gas flows are operating simultaneously and enable continuous simultaneous loading of propene and p-H_2 through the catalyst solution placed in the NMR tube. Normal ultra-high purity (>99.999%) hydrogen gas passes through Fe(OOH) catalyst at liquid N_2 temperature (≈77 K) or utilizes a p-H_2 generator using cryo-cooling (and producing ≈80% p-H_2). Both gas flows are controlled by the mass flow controllers (MFC), and the system pressure is regulated by the safety valve (labeled as ø set to ≈7.1 atm) immediately before the vent. Manual valve (⊗) enables fast (in less than 1 s) cessation of gas flow through solution placed in the NMR tube. In batch-mode production method, propene gas is loaded in the solution first, and it is followed by hydrogen gas flow only. Hydrogenation is performed inside 9.4 T spectrometer under PASADENA condition[19] and in the Earth's magnetic field under ALTADENA[4b] condition, respectively.

Pairwise p-H_2 addition can be achieved by either homogeneous[9] or heterogeneous (HET)[15] catalysis. The important advantage of HET-PHIP is the ability to produce pure HP gases, for example, propane.[12a,14a,c] However, the level of proton polarization of HP propane produced by HET-PHIP is relatively low at $\%P_H \approx 1\%$.[14a] An alternative approach is the biphasic gas–liquid hydrogenation of propene by bubbling its mixture with p-H_2 through a catalyst solution.[16] This approach also allows producing HP propane in the gas phase in a continuous-flow regime, however $\%P_H$ achieved to date were relatively low, that is, <1%. In principle, near 100% pairwise addition of p-H_2 is theoretically possible,[4a,b] and because of our long-term goal of using HP propane as HP inhalable contrast agent, the motivation for this work is to improve $\%P_H$ of HP propane via PHIP. Herein, we explore PHIP of propane using a previously established batch-mode approach for production of injectable contrast agents,[9,17] where catalyst and to-be-hyperpolarized substrate are loaded in the liquid phase first, which is followed by pairwise addition of p-H_2 gas and produces a batch of HP contrast agent.

In this study, we utilized the $[Rh(L)(dppb)]BF_4$ complex most widely used in PHIP experiments as a catalyst for p-H_2 pairwise addition [L = NBD (norbornadiene) or = COD (cyclooctadiene), dppb = 1,4-bis(diphenylphosphino)butane]. First, the simultaneous loading of propene and p-H_2 into the catalyst solution in a continuous-flow regime was tested, similarly to the experimental protocol used previously.[16] However, here an elevated p-H_2 pressure (≈7 atm vs. 1 atm) was employed (Figure 2), because it increases p-H_2 concentration in the liquid phase[18] and consequently increases the rate of hydrogenation.[17b] NMR detection of HP propane was performed in the liquid phase of CD_3OD. HP NMR resonances of propane were observed under both ALTADENA[19] and PASADENA[4b] conditions with good reproducibility (>10 experiments were repeated on the same catalyst solution portion, Figures S2 and S3). However, the NMR signal enhancements (SE) of HP propane's methyl and methylene resonances were low (only ca. 3–10-fold, corresponding to $\%P_H$ of 0.01–0.03% using ≈50% p-H_2).

In the batch-mode approach, propene is loaded first (by saturating the catalyst solution by propene bubbling at 1 atm pressure) followed by pressurizing the sample and bubbling with p-H_2 through the solution at ≈7.1 atm. This experimental protocol is ≈100 times more efficient than the continuous-flow method described above, and yielded signal enhancements and polarizations as high as SE ≈1910 and $\%P_H \approx 6.2\%$ under ALTADENA conditions (Figure 1) using ≈80% p-H_2 without taking into account possible polarization losses due to relaxation processes. Correspondingly, when ≈50% p-H_2 was used (Figure S8), SE and $\%P_H$ were decreased to 840 and 2.7% respectively.

© 2016 Wiley-VCH Verlag GmbH & Co. KGaA, Weinheim

The comparison of two catalysts at several concentrations shown in Figure 3a clearly indicates that the catalyst performance with NBD ligand is significantly better than that with COD ligand. Additionally, in both cases, catalyst concentration also impacts the apparent $\%P_H$. Moreover, Figure 3b shows a definite advantage of using high p-H_2 pressure for improving apparent $\%P_H$ for HP propane in liquid phase hydrogenation. Furthermore, additional experiments performed at various hydrogenation temperatures exhibit a temperature dependence of $\%P_H$ as well (Figure 3c).

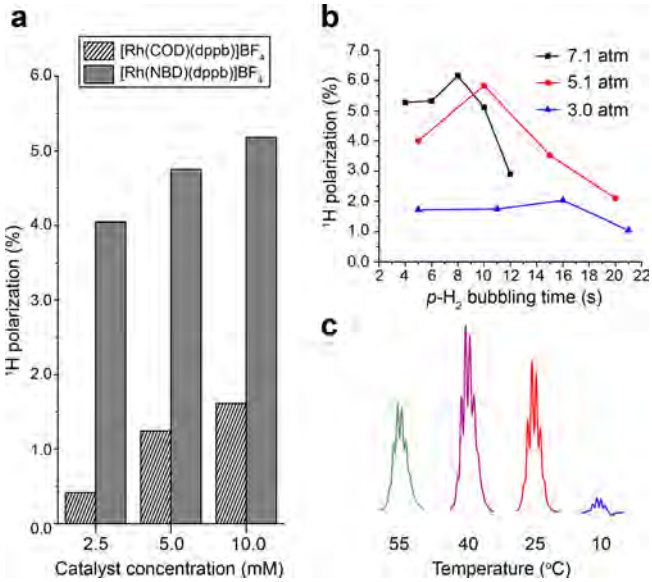

Figure 3. a) Proton polarization of HP propane as a function of catalyst concentration for two representative Rh-based catalysts; duration of p-H_2 bubbling is 10 s. b) Proton polarization of HP propane as a function of p-H_2 bubbling time in three different pressure regimes. c) Optimization of propane hyperpolarization by monitoring hyperpolarized ^1H signal (of -CH_2- group) by varying the temperature (estimated values) of the sample (p-H_2 bubbling duration is 8 s). Experimental data shown in (b) and (c) is collected for the [Rh(NBD)dppb]BF_4 catalyst.

The potential possible explanation of such a dramatic difference in catalyst's performance between continuous-flow and batch-mode hyperpolarization procedures is partially based on the differences in concentrations of reactants in the solution, which is in line with previously published studies. These studies reported high level of hyperpolarization achieved via batch-mode loading of substrate following by reaction with p-H_2: that is, utilizing 2-hydroxyethyl acrylate,[9] fumarate,[21] phosphoenolpyruvate,[22] and more recently vinyl acetate[17b,23] with similar or identical catalyst, where high levels of hyperpolarization were detected for ^1H[17b] or ^{13}C[23b] nuclei (the latter is an indirect confirmation that proton polarization was high prior to polarization transfer from nascent parahydrogen protons[17b] to ^{13}C[17b,23b]) In case of separate loading of reactants using batch-mode production, the initial concentration of loaded propene is 330 ± 45 mM (according to reference signals of catalyst's thermally polarized protons). On the other hand, H_2 solubility in methanol is only ≈28 mM at 7.1 atm.[24] Moreover, simultaneous loading of propene and excess p-H_2 in the continuous-flow mode also likely results in the irreversible catalyst degradation of some fraction of Rh catalyst. This is indirectly confirmed by the fact that once the propene substrate is depleted in the batch-mode procedure, and the catalyst solution is further bubbled with p-H_2, the subsequent attempts to reload the propene substrate to repeat the hyperpolarization cycle were unsuccessful (i.e. >1 order of magnitude lower polarization signals). Furthermore, continuous-flow mode experiments utilized somewhat lower p-H_2 partial pressure, likely resulting in a slower production of hyperpolarized product.

The reported here $\%P_H$ value of $\approx6.2\%$ was obtained with $\approx80\%$ p-H_2, so that utilization of 100% p-H_2 would increase proton polarization to $\approx9\%$ for hyperpolarized propane.[25] This value is substantially greater than typical values reported for propane or any other hydrocarbon gas hyperpolarized by PHIP so far. For PHIP, the highest reported $\%P_H$ value was $\approx1\%$ for HP propane.[14a,15b] To date, no other HP techniques have reported hyperpolarization on hydrocarbon gases. We note that although the nascent proton polarization in PHIP can exceed 50% for some injectable contrast agents,[17a,26] 1) the direct proton detection is usually not performed in situ of production inside a hyperpolarizer, and 2) proton polarization is too short-lived to be useful for injectable contrast agents. While d-DNP can hyperpolarize proton sites in principle,[27] no reports have been shown that d-DNP can efficiently hyperpolarize any gas besides ^{129}Xe[28] and $^{15}N_2O$.[29]

The presented polarization values are likely somewhat underestimated due to residual hydrogenation of the substrate during the delay between the acquisitions of the ALTADENA spectrum and the spectrum of fully relaxed solution. This delay (of >2 min) is mandatory, because HP must return back to the equilibrium state for probing propane concentration in the solution; also note that the alternative efforts of using normal H_2 at room temperature yielded small (yet detectable) HP signatures of propane, and therefore are unsuitable for quantification. The T_1 relaxation time constants of propane HP states induced via ALTADENA condition in solution are 22.4 ± 0.5 s for CH_2 group and 16.1 ± 0.3 s for CH_3 group, respectively, which is in qualitative agreement with T_1 measurements of dissolved thermally polarized propane using inversion recovery technique (23.3 ± 0.3 s and 19.6 ± 0.3 s, respectively). These values are significantly greater than the corresponding relaxation decay constants of HP propane in the gas phase.[12a,30] Moreover, the decay constants could be even greater at low magnetic fields due to LLSS presence.[12a] Therefore, the production of HP propane in the liquid (vs. gas) phase using the presented batch-mode approach may be advantageous, because the decay of the HP state can potentially minimize polarization losses, and hydrogenation process can continue significantly longer without significant polarization decay losses.

Future studies are certainly warranted to optimize the HP propane production by the batch-mode approach, including catalyst improvement to yield greater degree of the p-H_2 pairwise addition and greater % conversion (up to $\approx100\%$ from the 40–80% conversion levels achieved here, Figure S6), further optimization of p-H_2 pressure and reaction temperature,

© 2016 Wiley-VCH Verlag GmbH & Co. KGaA, Weinheim

and others. Moreover, HP propane separation from the liquid phase and filtration from residual propene, H_2 and norbornene/norbornane certainly have to be addressed in the context of potential biomedical use of HP propane gas, which was not pursued in the feasibility study described here.

Acknowledgements

OGS, KVK and IVK acknowledge the grant from the Russian Science Foundation (14-35-00020) for the support of homogeneous hydrogenation experiments, and FASO Russia project # 0333-2014-0001 for basic funding. DAB, AMC and EYC thank NIH 1R21EB018014, T32 EB001628, 1R21EB020323, U01 CA202229 and 1F32EB021840, NSF CHE-1416268 and CHE-1416432, DOD CDMRP W81XWH-12-1-0159/BC112431, W81XWH-15-1-0271 and W81XWH-15-1-0272, and ExxonMobil Research and Engineering Company Knowledge Build.

Keywords: hydrogenation · hyperpolarization · nmr spectroscopy · parahydrogen-induced polarization · propane

[1] a) P. Nikolaou, B. M. Goodson, E. Y. Chekmenev, *Chem. Eur. J.* **2015**, *21*, 3156 – 3166; b) J. H. Ardenkjaer-Larsen, B. Fridlund, A. Gram, G. Hansson, L. Hansson, M. H. Lerche, R. Servin, M. Thaning, K. Golman, *Proc. Natl. Acad. Sci. USA* **2003**, *100*, 10158 – 10163.
[2] a) J. H. Ardenkjaer-Larsen, *J. Magn. Reson.* **2016**, *264*, 3 – 12; b) A. Comment, *J. Magn. Reson.* **2016**, *264*, 39 – 48.
[3] M. A. Bouchiat, T. R. Carver, C. M. Varnum, *Phys. Rev. Lett.* **1960**, *5*, 373 – 375.
[4] a) C. R. Bowers, D. P. Weitekamp, *Phys. Rev. Lett.* **1986**, *57*, 2645 – 2648; b) C. R. Bowers, D. P. Weitekamp, *J. Am. Chem. Soc.* **1987**, *109*, 5541 – 5542; c) T. C. Eisenschmid, R. U. Kirss, P. P. Deutsch, S. I. Hommeltoft, R. Eisenberg, J. Bargon, R. G. Lawler, A. L. Balch, *J. Am. Chem. Soc.* **1987**, *109*, 8089 – 8091.
[5] a) J. Kurhanewicz, D. B. Vigneron, K. Brindle, E. Y. Chekmenev, A. Comment, C. H. Cunningham, R. J. DeBerardinis, G. G. Green, M. O. Leach, S. S. Rajan, R. R. Rizi, B. D. Ross, W. S. Warren, C. R. Malloy, *Neoplasia* **2011**, *13*, 81 – 97; b) S. J. Nelson, J. Kurhanewicz, D. B. Vigneron, P. E. Z. Larson, A. L. Harzstark, M. Ferrone, M. van Criekinge, J. W. Chang, R. Bok, I. Park, G. Reed, L. Carvajal, E. J. Small, P. Munster, V. K. Weinberg, J. H. Ardenkjaer-Larsen, A. P. Chen, R. E. Hurd, L. I. Odegardstuen, F. J. Robb, J. Tropp, J. A. Murray, *Sci. Transl. Med.* **2013**, *5*, 198ra108.
[6] a) K. M. Brindle, *J. Am. Chem. Soc.* **2015**, *137*, 6418 – 6427; b) A. Comment, M. E. Merritt, *Biochemistry* **2014**, *53*, 7333 – 7357; c) I. V. Koptyug, *Mendeleev Commun.* **2013**, *23*, 299 – 312.
[7] J. P. Mugler, T. A. Altes, *J. Magn. Reson. Imaging* **2013**, *37*, 313 – 331.
[8] B. M. Goodson, *J. Magn. Reson.* **2002**, *155*, 157 – 216.
[9] K. Golman, O. Axelsson, H. Johannesson, S. Mansson, C. Olofsson, J. S. Petersson, *Magn. Reson. Med.* **2001**, *46*, 1 – 5.
[10] P. Bhattacharya, E. Y. Chekmenev, W. F. Reynolds, S. Wagner, N. Zacharias, H. R. Chan, R. Bünger, B. D. Ross, *NMR Biomed.* **2011**, *24*, 1023 – 1028.
[11] a) M. Carravetta, M. H. Levitt, *J. Am. Chem. Soc.* **2004**, *126*, 6228 – 6229; b) W. S. Warren, E. Jenista, R. T. Branca, X. Chen, *Science* **2009**, *323*, 1711 – 1714.
[12] a) K. V. Kovtunov, M. L. Truong, D. A. Barskiy, I. V. Koptyug, K. W. Waddell, E. Y. Chekmenev, *Chem. Eur. J.* **2014**, *20*, 14629 – 14632; b) K. V. Kovtunov, M. L. Truong, D. A. Barskiy, O. G. Salnikov, V. I. Bukhtiyarov, A. M. Coffey, K. W. Waddell, I. V. Koptyug, E. Y. Chekmenev, *J. Phys. Chem. C* **2014**, *118*, 28234 – 28243.
[13] R. D. Stewart, P. E. Newton, E. D. Baretta, A. A. Herrmann, H. V. Forster, R. J. Soto, *Environ. Health Perspect.* **1978**, *26*, 275 – 285.
[14] a) K. V. Kovtunov, D. A. Barskiy, A. M. Coffey, M. L. Truong, O. G. Salnikov, A. K. Khudorozhkov, E. A. Inozemceva, I. P. Prosvirin, V. I. Bukhtiyarov, K. W. Waddell, E. Y. Chekmenev, I. V. Koptyug, *Chem. Eur. J.* **2014**, *20*, 11636 – 11639; b) R. Sharma, L. S. Bouchard, *Sci. Rep.* **2012**, *2*, 5; c) R. Zhou, E. W. Zhao, W. Cheng, L. M. Neal, H. Zheng, R. E. Quiñones, H. E. Hagelin-Weaver, C. R. Bowers, *J. Am. Chem. Soc.* **2015**, *137*, 1938 – 1946; d) E. W. Zhao, H. Zheng, K. Ludden, Y. Xin, H. E. Hagelin-Weaver, C. R. Bowers, *ACS Catal.* **2016**, *6*, 974 – 978.
[15] a) K. V. Kovtunov, V. V. Zhivonitko, I. V. Skovpin, D. A. Barskiy, I. V. Koptyug, *Top. Curr. Chem.* **2012**, *338*, 123 – 180; b) K. V. Kovtunov, I. E. Beck, V. I. Bukhtiyarov, I. V. Koptyug, *Angew. Chem. Int. Ed.* **2008**, *47*, 1492 – 1495; *Angew. Chem.* **2008**, *120*, 1514 – 1517; c) I. V. Koptyug, K. V. Kovtunov, S. R. Burt, M. S. Anwar, C. Hilty, S. I. Han, A. Pines, R. Z. Sagdeev, *J. Am. Chem. Soc.* **2007**, *129*, 5580 – 5586.
[16] K. V. Kovtunov, V. V. Zhivonitko, I. V. Skovpin, D. A. Barskiy, O. G. Salnikov, I. V. Koptyug, *J. Phys. Chem. C* **2013**, *117*, 22887 – 22893.
[17] a) M. Goldman, H. Johannesson, O. Axelsson, M. Karlsson, *C. R. Chim.* **2006**, *9*, 357 – 363; b) R. V. Shchepin, D. A. Barskiy, A. M. Coffey, I. V. Manzanera Esteve, E. Y. Chekmenev, *Angew. Chem. Int. Ed.* **2016**, *55*, 6071 – 6074; *Angew. Chem.* **2016**, *128*, 6175 – 6178.
[18] M. L. Truong, F. Shi, P. He, B. Yuan, K. N. Plunkett, A. M. Coffey, R. V. Shchepin, D. A. Barskiy, K. V. Kovtunov, I. V. Koptyug, K. W. Waddell, B. M. Goodson, E. Y. Chekmenev, *J. Phys. Chem. B* **2014**, *118*, 13882 – 13889.
[19] M. G. Pravica, D. P. Weitekamp, *Chem. Phys. Lett.* **1988**, *145*, 255 – 258.
[20] K. V. Kovtunov, D. Barskiy, R. V. Shchepin, A. M. Coffey, K. W. Waddell, I. V. Koptyug, E. Y. Chekmenev, *Anal. Chem.* **2014**, *86*, 6192 – 6196.
[21] P. Bhattacharya, E. Y. Chekmenev, W. H. Perman, K. C. Harris, A. P. Lin, V. A. Norton, C. T. Tan, B. D. Ross, D. P. Weitekamp, *J. Magn. Reson.* **2007**, *186*, 150 – 155.
[22] R. V. Shchepin, A. M. Coffey, K. W. Waddell, E. Y. Chekmenev, *J. Am. Chem. Soc.* **2012**, *134*, 3957 – 3960.
[23] a) E. Cavallari, C. Carrera, T. Boi, S. Aime, F. Reineri, *J. Phys. Chem. B* **2015**, *119*, 10035 – 10041; b) F. Reineri, T. Boi, S. Aime, *Nat. Commun.* **2015**, *6*, 5858.
[24] Q. S. Liu, F. Takemura, A. Yabe, *J. Chem. Eng. Data* **1996**, *41*, 1141 – 1143.
[25] C. R. Bowers, in *Encycl. Magn. Reson.* (Eds.: D. M. Grant, R. K. Harris), Wile, Chichester, **2002**, pp. 750 – 770.
[26] a) M. Goldman, H. Johannesson, *C. R. Phys.* **2005**, *6*, 575 – 581; b) E. Y. Chekmenev, J. Hovener, V. A. Norton, K. Harris, L. S. Batchelder, P. Bhattacharya, B. D. Ross, D. P. Weitekamp, *J. Am. Chem. Soc.* **2008**, *130*, 4212 – 4213.
[27] A. Bornet, R. Melzi, A. J. Perez Linde, P. Hautle, B. van den Brandt, S. Jannin, G. Bodenhausen, *J. Phys. Chem. Lett.* **2013**, *4*, 111 – 114.
[28] M. Pourfathi, N. N. Kuzma, H. Kara, R. K. Ghosh, H. Shaghaghi, S. J. Kadlecek, R. R. Rizi, *J. Magn. Reson.* **2013**, *235*, 71 – 76.
[29] N. N. Kuzma, P. Hakansson, M. Pourfathi, R. K. Ghosh, H. Kara, S. J. Kadlecek, G. Pileio, M. H. Levitt, R. R. Rizi, *J. Magn. Reson.* **2013**, *234*, 90 – 94.
[30] D. A. Barskiy, O. G. Salnikov, K. V. Kovtunov, I. V. Koptyug, *J. Phys. Chem. A* **2015**, *119*, 996 – 1006.

Manuscript received: May 26, 2016
Accepted Article published: July 26, 2016
Final Article published: ■■ ▮▮, 2016

© 2016 Wiley-VCH Verlag GmbH & Co. KGaA, Weinheim

More contrast: A simple approach for efficient NMR proton hyperpolarization of propane using parahydrogen-induced polarization technique is presented. This technique yields ≈6.2% proton polarization with ≈80% parahydrogen. Hyperpolarized propane is a potential gaseous MRI contrast agent for molecular imaging.

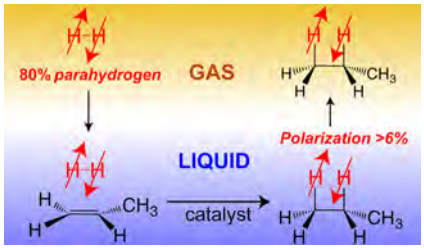

*O. G. Salnikov, D. A. Barskiy, A. M. Coffey, K. V. Kovtunov, I. V. Koptyug, E. Y. Chekmenev**

■■ – ■■

Efficient Batch-Mode Parahydrogen-Induced Polarization of Propane

© 2016 Wiley-VCH Verlag GmbH & Co. KGaA, Weinheim

Gas Phase UTE MRI of Propane and Propene

Kirill V. Kovtunov[1,2], Alexey S. Romanov[1,2], Oleg G. Salnikov[1,2], Danila A. Barskiy[3], Eduard Y. Chekmenev[3], and Igor V. Koptyug[1,2]

[1]International Tomography Center, Siberian Branch of the Russian Academy of Sciences, Novosibirsk, Russia; [2]Novosibirsk State University, Novosibirsk, Russia; and [3]Department of Radiology, Vanderbilt University Institute of Imaging Science (VUIIS), and Department of Biomedical Engineering, Vanderbilt-Ingram Cancer Center (VICC), Nashville, Tennessee

Corresponding Author:
Kirill V. Kovtunov, PhD
International Tomography Center, SB RAS, 3A Institutskaya St., 630090, Novosibirsk, Russia;
E-mail: kovtunov@tomo.nsc.ru

Key Words: gas MRI, propane, UTE, parahydrogen, polarization

Abbreviations: Proton magnetic resonance imaging (^{1}H MRI), hyperpolarized (HP), ultrashort echo time (UTE), magnetic resonance imaging (MRI), magnetic resonance (MR), signal-to-noise ratio (SNR), nuclear magnetic resonance (NMR), radiofrequency (RF), parahydrogen-induced polarization (PHIP), echo times (TE), field of view (FOV)

ABSTRACT

Proton magnetic resonance imaging (^{1}H MRI) of gases can potentially enable functional lung imaging to probe gas ventilation and other functions. Here, ^{1}H MR images of hyperpolarized (HP) and thermally polarized propane gas were obtained using ultrashort echo time (UTE) pulse sequence. A 2-dimensional (2D) image of thermally polarized propane gas with $\sim 0.9 \times 0.9$ mm^2 spatial resolution was obtained in <2 seconds, showing that even non-HP hydrocarbon gases can be successfully used for conventional proton magnetic resonance imaging. The experiments were also performed with HP propane gas, and high-resolution multislice FLASH 2D images in ~510 seconds and non-slice-selective 2D UTE MRI images were acquired in ~2 seconds. The UTE approach adopted in this study can be potentially used for medical lung imaging. Furthermore, the possibility of combining UTE with selective suppression of ^{1}H signals from 1 of the 2 gases in a mixture is shown in this MRI study. The latter can be useful for visualizing industrially important processes where several gases may be present, eg, gas–solid catalytic reactions.

INTRODUCTION

Magnetic resonance imaging (MRI) is an established tomographic modality for morphological and functional medical imaging to detect abnormalities in the structure and function of human tissues and organs. However, morphological imaging of the lungs is dominated by such established methods as chest radiography and computed tomography, whereas functional ventilation imaging is conventionally accomplished with the scintigraphy technique (1). In contrast, clinical MRI of human lungs is challenging, because of their low overall density (about one-third of that of muscle tissue) (2) and, consequently, low proton density. Therefore, the signal-to-noise ratio (SNR) that can be achieved in the MRI of the lungs is relatively low. Moreover, the presence of numerous air–tissue interfaces in the lungs leads to significant susceptibility-induced magnetic field gradients, resulting in very short T2* times of the human lung protons [~1 millisecond in a 1.5 T nuclear magnetic resonance (NMR) scanner (3)]. This further degrades the SNR in the MR images of the lungs. Therefore, the lungs typically appear as dark areas in the conventional proton magnetic resonance (^{1}H MRI) images. The challenge of direct imaging of lung airspace is the main disadvantage for pulmonary applications of MRI.

MRI application for pulmonary imaging is a relatively recent but a rapidly developing field (4). In recent years, significant efforts were made to overcome the limitations of MRI of the lungs (5, 6). In this context, numerous applications have been developed to solve the problem with image artifacts caused by motion. The image acquisition technique during breath-hold or using respiratory gating was developed (7). The problem of susceptibility-induced gradients can be solved by using spin echo radiofrequency (RF) pulse sequences with an extremely short echo time (TE) (8, 9, 10). One of the developed approaches is based on the inhalation of a paramagnetic contrast agent such as gadolinium aerosol (11) or molecular oxygen gas (12, 13) to increase the relaxation rates of tissue protons (14). Nevertheless, a very weak ^{1}H NMR signal from the lung tissue remains the main problem for ^{1}H MRI of the lung. Therefore, the development and utilization of new contrast agents is a very important and promising direction for lung MRI research.

An entirely different approach to the MRI of void spaces in a broad range of materials and structures in general, and lung MRI in particular, is the direct imaging of a suitable gas filling those voids. In particular, perfluorinated gases such as SF_6 and C_nF_{2n+2} (n = 1–3) (15) are a potentially good alternative for pulmonary MRI (16), because the ^{19}F isotope has a high gyromagnetic ratio and 100% natural abundance. Utilization of perfluorinated gases allows for a high contrast with the surrounding tissue because of the lack of a background signal. However, the gas-phase MRI of the lung faces the same motion and susceptibility problems as the ^{1}H MRI of the lung, whereas the spin density problem for gases is the severest, which results in a relatively low spatial and temporal resolution (17, 18). For

© 2016 The Authors. Published by Grapho Publications, LLC This is an open access article under the CC BY-NC-ND license (http://creativecommons.org/licenses/by-nc-nd/4.0/).
ISSN 2379-1381 http://dx.doi.org/10.18383/j.tom.2016.00112

^{19}F MRI of gases, a low SNR can be partially compensated by the use of short repetition time (TR), as the gases' T1 is in the millisecond range. The problem of low sensitivity is also addressed by using hyperpolarized (HP) nonproton contrast gas agents such as ^{3}He or ^{129}Xe (19, 20, 21). However, in the case of He, Xe, or fluorinated gases, multinuclear RF coil and transmitter/receiver are required, whereas standard clinical MRI scanners lack these capabilities. In addition, production of HP noble gases is relatively expensive and requires sophisticated *hyperpolarizer* instrumentation (22-25). Nevertheless, the potential advantages of gas MRI for pulmonary imaging, such as lack of ionizing radiation, and the potential applicability for diagnostics and monitoring response to therapy of various diseases, for example, chronic obstructive pulmonary disease, emphysema, asthma, and cystic fibrosis, make further efforts in this field worthwhile.

^{1}H MRI of hydrocarbon gases may be of interest for a range of applications, including imaging of materials, chemical reactors, and lung MRI. One of the promising candidate gases is propane, which is widely used in the food industry and in cosmetics. It is a nontoxic asphyxiant gas, and it was reported that brief inhalation exposures to 10 000 ppm of propane causes no toxicity in humans (26). Moreover, propane in concentrations of 250, 500, or 1000 ppm for periods of 1 minute to 8 hours did not produce any unfavorable physiological effects in humans. Repetitive exposures to propane also did not cause any measurable physiological effects (27). The major advantage of using hydrocarbon gases in MRI is that the ^{1}H transmit/receive capability can be implemented on any MRI system.

However, ^{1}H MRI of gases is an underdeveloped research area, largely because of the challenges of gas imaging discussed above. Nevertheless, the feasibility of ^{1}H MRI of hydrocarbon gases such as acetylene, propane, and butane at atmospheric pressures was shown about 15 years ago, with 2-dimensional (2D) images of flowing and static gas and flow velocity maps in pipes and multichannel monolith structures detected using a spin-echo pulse sequence (28, 29). In addition to the low spin density of gases, the rapid diffusion of gases in applied magnetic field gradients further reduces the detected signal for pulse sequences with relatively long TE. Therefore, image acquisition times were fairly long (20–40 minutes for the each 2D image), which may significantly limit gas MRI applications (30). Thus, imaging of gases may considerably benefit from the development of pulse sequences with ultrashort TE, as shown recently in the spectroscopic imaging study of ethylene to ethane conversion in a model catalytic reactor (31).

Another strategy for improving sensitivity in gas MRI is the use of HP gases, as mentioned above, for ^{3}He and ^{129}Xe. Hyperpolarization techniques are also available for producing hydrocarbon gases. Parahydrogen-induced polarization (PHIP) (32-34) is a unique technique for producing gases with HP ^{1}H nuclei by heterogeneous (35) or biphasic (36) pairwise addition of parahydrogen to a suitable unsaturated gaseous substrate (eg, hydrogenation of propene to propane). Heterogeneous hydrogenation is the most robust approach, because the catalyst can be recycled many times and the produced HP gas is free from the catalyst. In addition, the HP gas can be continuously produced, and thus, can be continuously renewed in the voids of an object under study to maintain high signal intensity for the duration of image acquisition, as demonstrated in 2D (37, 38) and 3-dimensional (3D) imaging of various model objects with submillimeter spatial resolution (39). Moreover, the use of remote detection allows to image micro-channels with appropriate resolution by using the HP gas (40, 41). However, despite favorable properties of HP propane, such as high polarization levels and continuous production, a significant fundamental challenge for the use of HP propane is its relatively short T1 in high magnetic fields (<1 second at standard temperature and pressure) (42). This becomes a major problem in the studies where continuous HP gas replenishment is not feasible, for instance, in lung imaging. One promising option is the use of long-lived spin states that can be used to store polarization for time periods significantly exceeding T1 (43, 44). Recently, a relatively long hyperpolarization lifetime T_{LLSS} was achieved for HP propane-d_6 ($\sim$6.0 seconds) (45) and for HP propane (4.7 $\pm$ 0.5 s) (46) in low magnetic fields. Thus, to make HP propane that is produced via propene hydrogenation with parahydrogen over different supported metals (47, 48) a promising candidate for lung imaging and other applications, implementation of rapid image acquisition schemes with imaging times of the order of 1–2 seconds or less is required.

Motivated by the aforementioned technical and biomedical challenges, the present work focused on the development of strategies for ^{1}H MRI visualization of both HP and thermally polarized propane gas for high-resolution MRI applications.

METHODOLOGY

NMR and MRI experiments were performed on an Avance™ III 400 MHz NMR spectrometer (Bruker) equipped with microimaging accessories. The experiments were conducted with a commercial 15-mm ID RF coil (Bruker) using ^{1}H channel. In all MRI experiments, shim values optimized on a sample comprising propane gas in a standard 10-mm NMR tube (Wilmad) were used, resulting in line width at half maximum of $\sim$5 Hz. MR images were obtained using ParaVision (Bruker) software. Ultrashort echo time (UTE) pulse sequence was used with a total acquisition time of 2 seconds for MRI imaging of propane and total acquisition time of 8 seconds, and a spectral width of 100 kHz for propane and propene. TR was 20 milliseconds and TE was 0.226 milliseconds. The k-space in the UTE sequence is scanned along radial trajectories, and the number of projections was equal to 100 and 400 for 32 $\times$ 32 and 128 $\times$ 128 image matrix sizes, respectively. The image resolution of 0.94 $\times$ 0.94 mm^2 (32 $\times$ 32 matrix) was used for experiments with HP propane and 0.39 $\times$ 0.39 mm^2 (matrix 128 $\times$ 128) for experiments with selective NMR signal suppression. The pulse angle was equal to 25° for a FLASH sequence and 15° for all experiments with the UTE sequence. All MRI experiments with thermally polarized propane were conducted using a single 15-mm NMR tube. For MRI experiments with selective signal suppression, a 10-mm NMR tube filled with propene was placed inside a 15-mm tube containing propane. For HP propane production, a mixture containing 50% parahydrogen and 50% orthohydrogen (referred to as pH_2 below) was first produced by passing normal hydrogen through the ortho-para conversion catalyst (FeO(OH)) kept at 77 K. The propane:pH_2 (1:4) gas mixture was

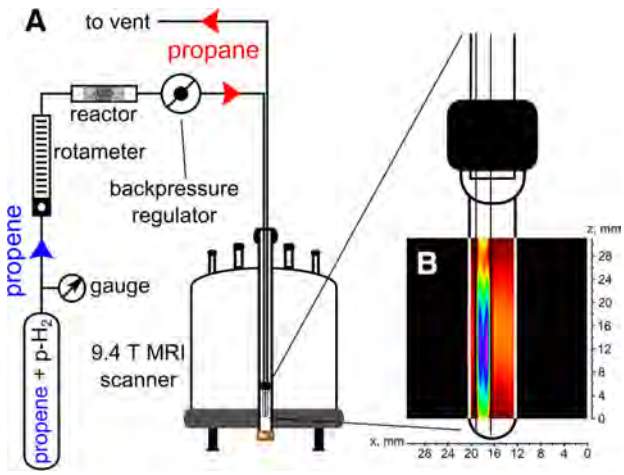

Figure 1. The schematic representation of the experimental setup for producing parahydrogen-induced polarization (PHIP) hyperpolarized (HP) propane via heterogeneous pairwise hydrogenation of propene with parahydrogen (A). An overlay of hydrogen 1 (^{1}H) magnetic resonance imaging (^{1}H MRI) FLASH image of hyperpolarized (HP) propane flowing into the 10-mm nuclear magnetic resonance (NMR) tube via 1/16″ OD Teflon capillary (B). The field of view (FOV) was 3.1 × 3.1 cm with 256 × 32 matrix size, and the total acquisition time was ~510 seconds. Note that the NMR tube is schematically shown, and its length does not correlate with the actual scale of the 2-dimensional (2D) magnetic resonance (MR) image.

passed through Rh/TiO_2 heterogeneous catalyst held at 250°C [ALTADENA experimental conditions (49)]. The flow rate of HP propane/pH_2 mixture was maintained at ~20 mL/s for the duration of imaging acquisition. HP propane was flowing through the 1/16″ OD Teflon capillary extended to the bottom of a standard 10-mm NMR tube. The modified FLASH pulse sequence (50) was also used for image acquisition. The modification by using the selective saturation of the unwanted resonance of CH_2 propane group immediately before application of a FLASH sequence was applied. Thus, the problem of cancellation of the opposite CH_3 ALTADENA NMR signal of propane with negative CH_2 ALTADENA propane signal was solved. The total imaging time to acquire 4 slices with 256 × 32 matrix size was ~8.5 minutes. The schematic representation of the experimental setup and the corresponding overlay of FLASH MRI image are shown in Figure 1.

RESULTS AND DISCUSSION

FLASH MRI

HP propane was produced via heterogeneous hydrogenation of propene with pH_2 over Rh/TiO_2 catalyst (31). The reaction scheme for HP propane formation is shown in Figure 2A. The initial experiments on propane ^{1}H MRI (41) were performed using the same type of setup and a relatively time-consuming 2D image FLASH acquisition of ~510 seconds. Here, we used conventional FLASH pulse sequence to acquire four 2D slices with the spatial resolution of 0.1 × 0.8 mm^2 with the same total acquisition time. Therefore, using FLASH may be preferable for multislice 2D gas MRI. Note that significant signal enhancement obtained via PHIP is crucial for ^{1}H FLASH MRI of the gaseous phase. Signal enhancement of up to 30 times for HP propane versus thermally polarized propane (Figure 2B) allows one to detect images with spatial resolution that is sufficient to detect flowing HP gas in a 1/16″ OD Teflon capillary (Figure 2C). The 2 bright spots in the capillary are the artifacts of the FLASH pulse sequence and show the position of the main flow inside the capillary. Note that the same experiment with thermally polarized propane did not produce any meaningful image because of the insufficient SNR (data not shown). However, as discussed above, the visualization of HP gas with short T1 faces additional difficulties for applications where the imaged volume cannot be continuously replenished with the HP gas, considerably limiting the possibilities for widespread biomedical utilization of the gas-phase lung MRI. Therefore, despite the obvious success of obtaining high-resolution FLASH images above, this approach will face considerable challenges for clinical translation. Therefore, the development of ultrafast imaging approaches for imaging of nonflowing gas (ie, simulating the conditions of inhaled gas in the in vivo studies) is much desired for potential MRI of the lungs.

Recently, ultrafast MRI pulse sequences based on radial acquisition of k-space data were used for lung MRI owing to the fact that they can reduce TE down to 100 μs. Such short TE allows one to minimize the signal decay caused by the short transverse relaxation time (T2*) of the lung tissue (8, 51). Moreover, it was shown that the short TE makes it possible to quantitatively verify regional T2* values and morphological changes in mice by comparing normal lungs and lungs with pulmonary emphysema (52, 53). Furthermore, such ultrashort TE sequences could arguably be beneficial for contrast agents with short T2 and T1 as well, which was the next step in our investigation.

UTE Studies

First, conventional UTE pulse sequence (as implemented in Bruker ParaVision) was used for ^{1}H MR imaging of static propane gas at thermal polarization levels. It was shown that UTE can indeed visualize a hydrocarbon gas with good spatial resolution (Figure 3A). UTE allowed for a very short TE of 200 μs in our gas experiments, which is approximately one order of magnitude improvement compared with the previous studies of continuously flowing gas at high magnetic fields (38) and ~35-fold improvement compared with the low-field MRI studies of stopped propane gas (35). Therefore, the negative impact of fast diffusion on the signal loss during gradient switching is considerably reduced. By decreasing the matrix size, we were able to reduce the image acquisition time to 2 seconds.

In the next experiment, HP propane gas produced by heterogeneous hydrogenation of propene over Rh/TiO_2 catalyst with pH_2 was imaged in a similar way to the thermally polarized gas above, except that HP propane was flowing during imaging. The signal intensity of HP propane is only 2 times higher than

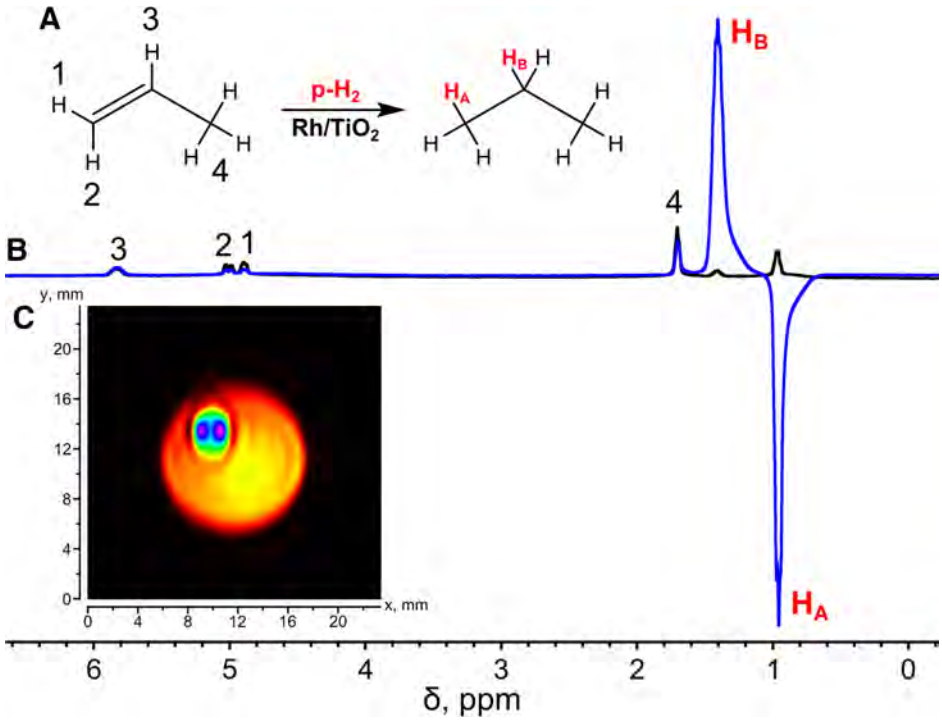

Figure 2. Heterogeneous hydrogenation of propene to propane with pH_2 over Rh/TiO_2 catalyst with partial preservation of spin order of parahydrogen in the final HP product (A). ^{1}H NMR spectra of HP propane (blue) and thermally polarized propane (black) obtained in heterogeneous hydrogenation of propene with parahydrogen; the signal enhancement was ~30-fold (B). ^{1}H MRI of HP propane flowing through a 1/16″ OD Teflon capillary inside a 10-mm NMR tube obtained with a FLASH pulse sequence (C). The FOV was 3.1 × 2.5 cm with 256 × 32 matrix size, and the total acquisition time was ~510 seconds with slice thickness of ~0.7 cm. The signal intensity color scale ranges from black (zero) to blue (maximum).

that of thermally polarized propane (Figure 3, A and B). Simultaneously, comparison of the corresponding ^{1}H NMR spectra acquired under the same conditions gave the signal enhancement factor of ~10. This apparent discrepancy in signal enhancements between ^{1}H MR images and ^{1}H NMR spectra can be explained as an intrinsic feature of the UTE pulse sequence and, to a greater extent, by the nature of acquisition under stopped and flowing gas conditions. More importantly, we believe that this is the first report of the feasibility to acquire gas-phase ^{1}H MR image of a hydrocarbon gas in time suitable for image acquisition of nonflowing gas on a single patient breath-hold (~2 seconds). Although some additional parameters can be optimized in the future and the imaging can be extended to either 3D or a multislice 2D version, the use of short TE and UTE sequences paves the way for future biomedical and other uses of thermally polarized gases, as well as HP gases. Arguably, the acquisition time needs to be further shortened for HP imaging application for contrast agents with T1 <1 second. Alternatively, the advances in development and design of long-lived spin states can be potentially used to increase the relaxation time of HP hydrocarbons at high magnetic fields (36, 44, 54).

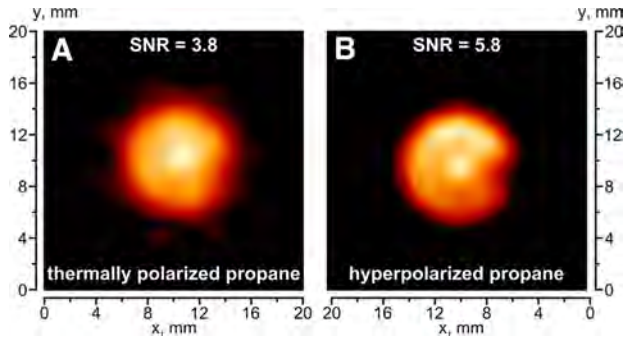

Figure 3. MR images of 15-mm NMR tube filled with thermally polarized propane (A) and PHIP HP propane (the same experimental setup as for Figure 1) (B). The FOV was 3 × 3 cm with 32 × 32 matrix size, the total acquisition time was ~2 seconds, and the slice thickness in the z direction was 10 mm.

MRI of Gases with Chemical Selectivity

In some applications, it would be desirable to combine rapid gas imaging with chemical (spectroscopic) selectivity. For instance, binary gas mixtures can be imaged using selective signal suppression of one of the gases, which could be potentially useful for chemical selectivity for future *operando* imaging studies of catalytic reactors. Nowadays, MRI of the lung with HP noble

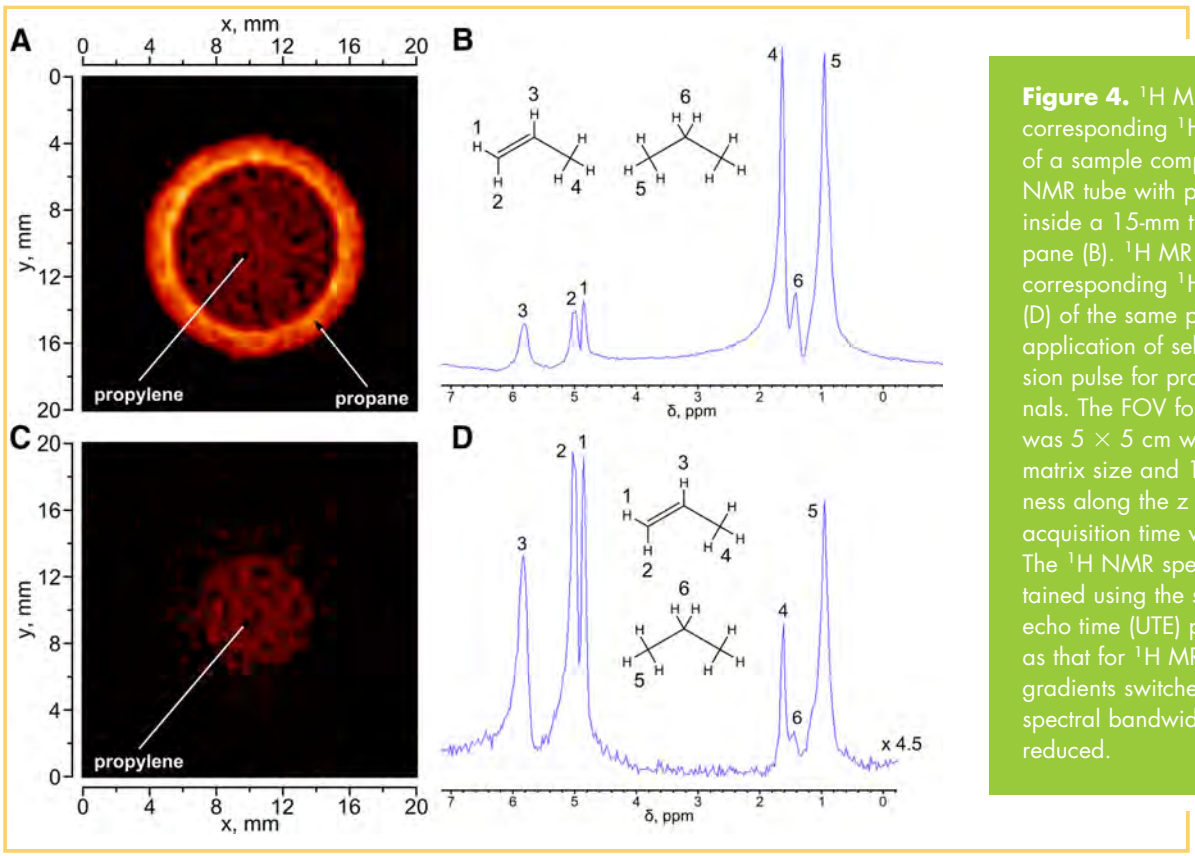

Figure 4. ^{1}H MR image (A) and corresponding ^{1}H NMR spectrum of a sample comprising a 10-mm NMR tube with propylene placed inside a 15-mm tube with propane (B). ^{1}H MR image (C) and corresponding ^{1}H NMR spectrum (D) of the same phantom with application of selective suppression pulse for propane NMR signals. The FOV for both images was 5 × 5 cm with 128 × 128 matrix size and 10-mm slice thickness along the z axis; the total acquisition time was ~8 seconds. The ^{1}H NMR spectrum was obtained using the same ultrashort echo time (UTE) pulse sequence as that for ^{1}H MRI but with the gradients switched off and the spectral bandwidth appropriately reduced.

gases and conventional ^{1}H MRI can be simultaneously performed within the same inhalation (55). Such an approach has many potential applications, allowing side-by-side quantitative analysis of early signs of impaired lung function from HP gases and anatomic signs of disease from the ^{1}H MR images (56).

Therefore, we used the approach presented above to demonstrate the feasibility of selective suppression of NMR signals in a specific region of an NMR spectrum during the gas-phase MRI. To this end, we used a model sample comprising a 10-mm NMR tube with 1 atm of propylene placed inside a 15-mm NMR tube with 1 atm of propane (Figure 4A).

The results show that the conventional UTE pulse sequence allows one to simultaneously visualize propane and propylene (Figure 4A) without significant image artifacts. This is possible owing to a very large spectral width used during signal acquisition (100 kHz), corresponding to the image encoding with ~3.125 kHz/pixel, which exceeds the chemical shift dispersion of ~2.2 kHz at 9.4 T (Figure 4). However, the ^{1}H MRI signal of propylene is somewhat less intense, and this fact may be explained by different relaxation times of propane and propylene and fewer protons in the propylene molecule. The acquired ^{1}H NMR spectrum (Figure 4B) shows the presence of propane and propylene in the same phantom and their relative quantities. For the next set of experiments, selective suppression pulse for CH_3 and CH_2 groups of propane was added to the UTE sequence before image detection. This significantly changes the ^{1}H NMR spectrum (Figure 4D), and the NMR line intensities of the CH_3 and CH_2 groups of propane show an ~10-fold decrease. This also reduces the signal of the CH_3 group of propylene, so that the major signals remaining in the ^{1}H NMR spectrum are those of the CH and CH_2 groups of propylene. Their ^{1}H signal is sufficient to visualize propylene by ^{1}H MRI (Figure 4C). Such observations have not been previously reported.

CONCLUSIONS

^{1}H MRI of continuously flowing HP propane gas produced by heterogeneous hydrogenation of propylene with parahydrogen (ALTADENA regime) was performed using 2 different MRI pulse sequences. Compared with the FLASH sequence, the use of UTE MRI significantly decreases the total imaging time down to the regime sufficient for MRI of a patient within a single breath-hold in future clinical translation. Further reduction in the acquisition time via compressed sensing and further reduction in TR may render 3D UTE gas-phase imaging possible on a single breath-hold.

It was found that a conventional UTE pulse sequence allows one to obtain a 2D image of thermally polarized gas with ~0.9 × 0.9 mm^2 spatial resolution in ~2 seconds, which is much faster compared with the FLASH acquisition even if the latter is optimized to reduce the imaging time. Importantly, it was shown for the first time that the UTE pulse sequence is very efficient for ^{1}H MRI of a thermally polarized gas. The imaging of HP gas with UTE provided additional signal enhancement gains - a major advantage in the context of biomedical and industrial applications. Note that in the case of the HP gas, a single image can be acquired if the gas is not flowing, whereas for repetitive imaging, the HP gas should be imaged under flow conditions. In contrast, thermally polarized gas and UTE pulse sequence allow one to detect multiple images even at 1 inhalation. Moreover, the ability of selective suppression of proton signals enables MRI

imaging with chemical selectivity in the gas phase without significant sacrifice in the total imaging speed. The obtained results are transitional steps for converting the described approach to medical lung imaging, and the UTE pulse sequence appears to be the main candidate for in vivo imaging of lung with a nontoxic hydrocarbon gas.

ACKNOWLEDGMENTS

KVK, IVK, OGS and ASR thank RFBR grants (16-03-00407-a, 14-03-93183-MCX-a, and 14-03-00374-a), KVK thanks the Council on Grants of the President of the Russian Federation (MK-4498.2016.3), and the joint SB RAS–MoST grant. The basic funding for researchers from ITC SB RAS was provided by FASO. EYC thanks NSF (CHE-1416432 and CHE-1416268), NIH 1R21EB018014 and 1R21EB020323, DOD CDMRP W81XWH-15-1-0271, W81XWH-12-1-0159/BC112431, and Exxon Mobil Knowledge Build for financial support.

Conflicts of Interest: None reported.

Disclosure: No disclosures to report.

REFERENCES

1. Bajc M, Neilly JB, Miniati M, Schuemichen C, Meignan M, Jonson B, EANM Committee. EANM guidelines for ventilation/perfusion scintigraphy: Part 1. Pulmonary imaging with ventilation/perfusion single photon emission tomography. Eur J Nucl Med Mol Imaging. 2009;36(8):1356–1370.
2. Hatabu H, Alsop DC, Listerud J, Bonnet M, Gefter WB. T2* and proton density measurement of normal human lung parenchyma using submillisecond echo time gradient echo magnetic resonance imaging. Eur J Radiol. 1999; 29(3):245–248.
3. Stock KW, Chen Q, Hatabu H, Edelman RR. Magnetic resonance T2* measurements of the normal human lung in vivo with ultra-short echo times. Magn Reson Imaging. 1999;17(7):997–1000.
4. Conradi MS, Saam BT, Yablonskiy DA, Woods JC. Hyperpolarized He-3 and perfluorocarbon gas diffusion MRI of lungs. Prog Nucl Mag Res Sp. 2006;48(1): 63–83.
5. Ohno Y, Oshio K, Uematsu H, Nakatsu M, Gefter WB, Hatabu H. Single-shot half-Fourier RARE sequence with ultra-short inter-echo spacing for lung imaging. J Magn Reson Imaging. 2004;20(2):336–339.
6. Eibel R, Herzog P, Dietrich O, Rieger CT, Ostermann H, Reiser MF, Schoenberg SO. Pulmonary abnormalities in immunocompromised patients: comparative detection with parallel acquisition MR imaging and thin-section helical CT. Radiology. 2006;241(3):880–891.
7. Larson AC, Kellman P, Arai A, Hirsch GA, McVeigh E, Li D, Simonetti OP. Preliminary investigation of respiratory self-gating for free-breathing segmented cine MRI. Magn Reson Med. 2005;53(1):159–168.
8. Johnson KM, Fain SB, Schiebler ML, Nagle S. Optimized 3D ultrashort echo time pulmonary MRI. Magn Reson Med. 2013;70(5):1241–1250.
9. Togao O, Ohno Y, Dimitrov I, Hsia CC, Takahashi M. Ventilation/perfusion imaging of the lung using ultra-short echo time (UTE) MRI in an animal model of pulmonary embolism. J Magn Reson Imaging. 2011;34(3):539–546.
10. Ohno Y, Koyama H, Yoshikawa T, Matsumoto K, Takahashi M, Van Cauteren M, Sugimura K. T2* measurements of 3-T MRI with ultrashort TEs: capabilities of pulmonary function assessment and clinical stage classification in smokers. AJR Am J Roentgenol. 2011;197(2):W279–W285.
11. Sood BG, Shen Y, Latif Z, Chen X, Sharp J, Neelavalli J, Joshi A, Slovis TL, Haacke EM. Aerosol delivery in ventilated newborn pigs: an MRI evaluation. Pediatr Res. 2008;64(2):159–164.
12. Bauman G, Eichinger M. Ventilation and perfusion magnetic resonance imaging of the lung. Pol J Radiol. 2012;77(1):37–46.
13. Ohno Y, Hatabu H, Takenaka D, Van Cauteren M, Fujii M, Sugimura K. Dynamic oxygen-enhanced MRI reflects diffusing capacity of the lung. Magn Reson Med. 2002;47(6):1139–1144.
14. Mosbah K, Ruiz-Cabello J, Berthezène Y, Crémillieux Y. Aerosols and gaseous contrast agents for magnetic resonance imaging of the lung. Contrast Media Mol Imaging. 2008;3(5):173–190.
15. Ruiz-Cabello J, Barnett BP, Bottomley PA, Bulte JWM. Fluorine (19F) MRS and MRI in biomedicine. NMR Biomed. 2011;24(2):114–129.
16. Jacob RE, Chang YV, Choong CK, Bierhals A, Hu DZ, Zheng J, Yablonskiy DA, Woods JC, Gierada DS, Conradi MS. 19F MR imaging of ventilation and diffusion in excised lungs. Magn Reson Med. 2005;54(3):577–585.
17. Kuethe DO, Caprihan A, Gach HM, Lowe IJ, Fukushima E. Imaging obstructed ventilation with NMR using inert fluorinated gases. J Appl Physiol (1985). 2000; 88(6):2279–2286.
18. Kuethe DO, Caprihan A, Fukushima E, Waggoner RA. Imaging lungs using inert fluorinated gases. Magn Reson Med. 1998;39(1):85–88.
19. Lilburn DM, Pavlovskaya GE, Meersmann T. Perspectives of hyperpolarized noble gas MRI beyond ^{3}He. J Magn Reson. 2013;229:173–186.
20. Nikolaou P, Goodson BM, Chekmenev EY. NMR hyperpolarization techniques for biomedicine. Chem Eur J. 2015;21:3156–3166.
21. Kirby M, Ouriadov A, Svenningsen S, Owrangi A, Wheatley A, Etemad-Rezai R, Santyr GE, McCormack DG, Parraga G. Hyperpolarized ^{3}He and ^{129}Xe magnetic resonance imaging apparent diffusion coefficients: physiological relevance in older never- and ex-smokers. Physiol Rep. 2014;2(3). pii: e12068.
22. Goodson BM. Nuclear magnetic resonance of laser-polarized noble gases in molecules, materials, and organisms. J Magn Reson. 2002;155(2):157–216.
23. Capozzi A, Roussel C, Comment A, Hyacinthe JN. Optimal glass-forming solvent brings sublimation dynamic nuclear polarization to ^{129}Xe hyperpolarization biomedical imaging standards. J Phys Chem C. 2015;119(9):5020–5025.
24. Nikolaou P, Coffey AM, Walkup LL, Gust BM, Whiting N, Newton H, Barcus S, Muradyan I, Dabaghyan M, Moroz GD, Rosen M, Patz S, Barlow MJ, Chekmenev EY, Goodson BM. Near-unity nuclear polarization with an open-source 129Xe hyperpolarizer for NMR and MRI. Proc Natl Acad Sci U S A. 2013; 110(35):14150–14155.
25. Mugler JP, Altes TA. Hyperpolarized ^{129}Xe MRI of the human lung. J Magn Reson Imaging. 2013;37(2):313–331.
26. Braker W, Mossman AL. Matheson Gas Data Book. 6th ed. Secaucus, NJ: Matheson Gas Products-USA; 2010.
27. Stewart RD, Newton PE, Baretta ED, Herrmann AA, Forster HV, Soto RJ. Physiological response to aerosol propellants. Environ Health Perspect. 1978;26: 275–285.
28. Koptyug IV, Altobelli SA, Fukushima E, Matveev AV, Sagdeev RZ. Thermally polarized (1)H NMR microimaging studies of liquid and gas flow in monolithic catalysts. J Magn Reson. 2000;147(1):36–42.
29. Koptyug IV, Matveev AV, Altobelli SA. NMR studies of hydrocarbon gas flow and dispersion. Appl Magn Reson. 2002;22:187–200.
30. Newling B. Gas flow measurements by NMR. Prog Nucl Magn Reson Spectrosc. 2008;52:31–48.
31. Ulpts J, Dreher W, Klink M, Thoming J. NMR imaging of gas phase hydrogenation in a packed bed flow reactor. Applied Catalysis A: General. 2015;502: 340–349.
32. Bowers CR, Weitekamp DP. Transformation of symmetrization order to nuclear-spin magnetization by chemical reaction and nuclear magnetic resonance. Phys Rev Lett. 1986; 57(21):2645–2648;
33. Natterer J, Bargon J. Parahydrogen induced polarization. Prog Nucl Magn Reson Spectrosc. 1997;31(4):293–315.
34. Bowers CR, Weitekamp DP. Parahydrogen and synthesis allow dramatically enhanced nuclear alignment. J Am Chem Soc. 1987;109(18):5541–5542.
35. Kovtunov KV, Beck IE, Bukhtiyarov VI, Koptyug IV. Observation of parahydrogen-induced polarization in heterogeneous hydrogenation on supported metal catalysts. Angew Chem Int Ed Engl. 2008;47(8):1492–1495.
36. Kovtunov KV, Zhivonitko VV, Skovpin IV, Barskiy DA, Salnikov OG, Koptyug IV. Toward continuous production of catalyst-free hyperpolarized fluids based on biphasic and heterogeneous hydrogenations with parahydrogen. J Phys Chem C. 2013;117(44):22887–22893.
37. Bouchard LS, Kovtunov KV, Burt SR, Anwar MS, Koptyug IV, Sagdeev RZ, Pines A. Parahydrogen-enhanced hyperpolarized gas-phase magnetic resonance imaging. Angew Chem Int Ed Engl. 2007;46(22):4064–4068.
38. Bouchard LS, Burt SR, Anwar MS, Kovtunov KV, Koptyug IV, Pines A. NMR imaging of catalytic hydrogenation in microreactors with the use of para-hydrogen. Science. 2008;319(5862):442–445.
39. Kovtunov KV, Barskiy DA, Coffey AM, Truong ML, Salnikov OG, Khudorozhkov AK, Inozemtseva EA, Prosvirin IP, Bukhtiyarov VI, Waddell KW, Chekmenev EY, Koptyug IV. High-resolution 3D proton MRI of hyperpolarized gas enabled by parahydrogen and Rh/TiO2 heterogeneous catalyst. Chemistry - A European Journal. 2014;20:11636–11639.

40. Zhivonitko VV, Telkki VV, Koptyug IV. Characterization of microfluidic gas reactors using remote-detection MRI and parahydrogen-induced polarization. Angew Chem Int Ed Engl. 2012;51(32):8054–8058.
41. Telkki VV, Zhivonitko VV, Ahola S, Kovtunov KV, Jokisaari J, Koptyug IV. Microfluidic gas-flow imaging utilizing parahydrogen-induced polarization and remote-detection NMR. Angew Chem Int Ed. 2010;49(45):8363–8366.
42. Barskiy DA, Salnikov OG, Kovtunov KV, Koptyug IV. NMR signal enhancement for hyperpolarized fluids continuously generated in hydrogenation reactions with parahydrogen. J Phys Chem A. 2015;119(6):996–1006.
43. Warren WS, Jenista E, Branca RT, Chen X. Increasing hyperpolarized spin lifetimes through true singlet eigenstates. Science. 2009;323(5922):1711–1714.
44. Carravetta M, Levitt MH. Long-lived nuclear spin states in high-field solution NMR. J Am Chem Soc. 2004;126(20):6228–6229.
45. Kovtunov KV, Truong ML, Barskiy DA, Salnikov OG, Bukhtiyarov VI, Coffey AM, Waddell KW, Koptyug IV, Chekmenev EY. Propane-d6 heterogeneously hyperpolarized by parahydrogen. J Phys Chem C. 2014;118(48):28234–28243.
46. Kovtunov KV, Truong ML, Barskiy DA, Koptyug IV, Waddell KW, Chekmenev EY. Long-lived spin states for low-field hyperpolarized gas MRI. Chemistry - A European Journal. 2014;20(45):14629–14632.
47. Zhao EW, Zheng H, Ludden K, Xin Y, Hagelin-Weaver HE, Bowers CR. Strong metal–support interactions enhance the pairwise selectivity of parahydrogen addition over Ir/TiO2. ACS Catal. 2016;6(2):974–978.
48. Salnikov OG, Kovtunov KV, Barskiy DA, Bukhtiyarov VI, Kaptein R, Koptyug IV. Kinetic study of propylene hydrogenation over Pt/Al2O3 by parahydrogen-induced polarization. Appl Magn Reson. 2013;44(1):279–288.
49. Pravica MG, Weitekamp DP. Net NMR alignment by adiabatic transport of parahydrogen addition products to high magnetic field. Chem Phys Lett. 1988; 145(4):255–258.
50. Haase A, Frahm J, Matthaei D, Hanicke W, Merboldt KD. FLASH imaging: rapid NMR imaging using low flip angle pulses. J Magn Reson. 2011;213(2):533–541.
51. Gewalt SL, Glover GH, Hedlund LW, Cofer GP, MacFall JR, Johnson GA. MR microscopy of the rat lung using projection reconstruction. Magn Reson Med. 1993;29:99–108.
52. Togao O, Tsuji R, Ohno Y, Dimitrov I, Takahashi M. Ultrashort echo time (UTE) MRI of the lung: assessment of tissue density in the lung parenchyma. Magn Reson Med. 2010;64(5):1491–1498.
53. Takahashi M, Togao O, Obara M, Cauteren M, Ohno Y, Doi S, Kuro-o M, Malloy C, Hsia CC, Dimitrov I. Ultrashort echo time (UTE) MR imaging of the lung: comparison between normal and emphysematous lungs in mutant mice. J Magn Reson Imaging. 2010;32(2):326–333.
54. Pileio G, Carravetta M, Hughes E, Levitt MH. The long-lived nuclear singlet state of 15N-nitrous oxide in solution. J Am Chem Soc. 2008;130(38):12582–12583.
55. Horn FC, Tahir BA, Stewart NJ, Collier GJ, Norquay G, Leung G, Ireland RH, Parra-Robles J, Marshall H, Wild JM. Lung ventilation volumetry with same-breath acquisition of hyperpolarized gas and proton MRI. NMR Biomed. 2014;27(12): 1461–1467.
56. Wild JM, Marshall H, Xu X, Norquay G, Parnell SR, Clemence M, Griffiths PD, Parra-Robles J. Simultaneous imaging of lung structure and function with triple-nuclear hybrid MR imaging. Radiology. 2013;267(1):251–255.

Isotopic Labeling

International Edition: DOI: 10.1002/anie.201600521
German Edition: DOI: 10.1002/ange.201600521

Efficient Synthesis of Molecular Precursors for Para-Hydrogen-Induced Polarization of Ethyl Acetate-1-^{13}C and Beyond

*Roman V. Shchepin, Danila A. Barskiy, Aaron M. Coffey, Isaac V. Manzanera Esteve, and Eduard Y. Chekmenev**

Abstract: *A scalable and versatile methodology for production of vinylated carboxylic compounds with ^{13}C isotopic label in C1 position is described. It allowed synthesis of vinyl acetate-1-^{13}C, which is a precursor for preparation of ^{13}C hyperpolarized ethyl acetate-1-^{13}C, which provides a convenient vehicle for potential in vivo delivery of hyperpolarized acetate to probe metabolism in living organisms. Kinetics of vinyl acetate molecular hydrogenation and polarization transfer from para-hydrogen to ^{13}C via magnetic field cycling were investigated. Nascent proton nuclear spin polarization (%P_H) of ca. 3.3% and carbon-13 polarization (%P_{13C}) of ca. 1.8% were achieved in ethyl acetate utilizing 50% para-hydrogen corresponding to ca. 50% polarization transfer efficiency. The use of nearly 100% para-hydrogen and the improvements of %P_H of para-hydrogen-nascent protons may enable production of ^{13}C hyperpolarized contrast agents with %P_{13C} of 20–50% in seconds using this chemistry.*

Hyperpolarized (HP) magnetic resonance[1] is a rapidly growing field, which enables real-time metabolic imaging.[2] This is possible because nuclear spin polarization (P) of long-lived (on the order of a minute or more) ^{13}C sites in biologically relevant molecules can be enhanced transiently by 4–8 orders of magnitude[3] to the order of unity or 100%. Dissolution dynamic nuclear polarization (d-DNP)[3a] is one of the leading hyperpolarization technologies, which has advanced into clinical trials,[4] and its success has been largely driven by a wide range of biomolecules amenable for efficient hyperpolarization. The alternative hyperpolarization technique of para-hydrogen induced polarization (PHIP)[5] has two advantages over d-DNP: 1) fast production speed of under 1 min versus tens of minutes[6] to several hours, and 2) it is significantly less instrumentation demanding.[7] Therefore, PHIP may potentially become an ultra-fast and low-cost hyperpolarization technique for affordable production of multiple doses of HP contrast agents within minutes.[8] However, unlike d-DNP, the PHIP technique relies on the pairwise addition of para-hydrogen (para-H_2) to an unsaturated precursor usually followed by polarization transfer from nascent protons to ^{13}C centers, with substantially longer P decay times (T_1) required for in vivo applications.[9] While a number of metabolic ^{13}C HP contrast agents have been developed for in vivo applications with $\%P_{13C} \geq 10\%$ in aqueous medium (e.g. succinate[2e,10] and phospholactate[3b,11]), PHIP remained a relatively restricted technology because of the chemical challenge of inserting para-H_2 adjacently to ^{13}C in molecular frameworks to yield metabolically relevant contrast agents: for example, acetate, pyruvate.[11a]

Recently PHIP using side arm hydrogenation (SAH) was demonstrated,[12] in which para-H_2 is added into vinyl moiety, and para-H_2-derived polarization is transferred to carboxylic ^{13}C atom. This is fundamentally possible, because in PHIP-SAH the ^{13}C atom is hyperpolarized by nascent protons three and four chemical bonds away using $^3J_{H-13C}$ and $^4J_{H-13C}$[12,13] rather than the $^2J_{H-13C}$ and $^3J_{H-13C}$ in the conventional PHIP approach.[9,14] As a result, PHIP-SAH significantly expands the reach of amenable-to-hyperpolarization biomolecules, including ethyl acetate-1-^{13}C, ethyl pyruvate-1-^{13}C, and potentially many others. Ethylation is not necessarily a drawback, because the produced HP contrast agent can be de-protected,[12] or used directly, because ethylation of carboxylic acids leads to better cellular[10b] and brain uptake.[15] The uptake in the brain is especially relevant to ethyl acetate, because acetate is one of a few metabolites directly utilized by the brain as a fuel source.[16]

Despite the potential of PHIP-SAH to revolutionize molecular imaging, it is faced with two fundamental challenges. First, an efficient synthesis of vinylated 1-^{13}C-carboxylates must be developed. Second, $\%P_{13C}$ of only 2.3% (using on 92% of para-H_2) was achieved by Cavallari et al.,[13] and a further significant $\%P_{13C}$ boost is required for in vivo applications. Hence, this work is focused on 1) developing an efficient synthetic procedure for production of vinyl acetate-1-^{13}C, and 2) investigating the field cycling polarization transfer process used in PHIP-SAH to improve $\%P_{13C}$.

A number of methodologies for the preparation of vinyl acetate with various isotopic labeling patterns have been described. Roberts et al.[17] developed a procedure based on the mercury-catalyzed reaction of ^{14}C-labeled acetylene and acetic acid. Similar methodology, based on stoichiometric amount of mercury ethoxide and acetyl chloride-D_3, was

[*] Prof. R. V. Shchepin, Dr. D. A. Barskiy, Dr. A. M. D. Coffey, Dr. I. V. Manzanera Esteve, Prof. E. Y. Chekmenev
Department of Radiology
Vanderbilt University Institute of Imaging Science (VUIIS)
Department of Biomedical Engineering
Vanderbilt-Ingram Cancer Center (VICC)
Vanderbilt University
Nashville, TN 37232 (USA)
Prof. E. Y. Chekmenev
Russian Academy of Sciences
119991 Moscow (Russia)
E-mail: eduard.chekmenev@vanderbilt.edu

Supporting information (all experimental procedures, additional NMR spectra as well as the schematic description of the hyperpolarization setup) for this article can be found under http://dx.doi.org/10.1002/anie.201600521.

 © 2016 Wiley-VCH Verlag GmbH & Co. KGaA, Weinheim

applied to the preparation of vinyl acetate-D_3 by Kim and Caserio.[18] Alternatively, Livshits and Isagulyants[19] showed an efficient reaction between the ^{14}C-labeled acetic acid and acetylene catalyzed by zinc acetate in the gas-phase. While vinyl acetate is industrially produced by vapor-phase acetoxylation of ethylene over Pd-based catalysts,[20] such large-scale gas-phase processes are poorly suited for significantly smaller-scale production of isotopically enriched vinyl acetate-1-^{13}C. Earlier variants of synthetic procedures with interexchange of vinyl groups were based on mercury catalysis,[21] which had some obvious disadvantages of toxicity and laborious workup. Another potential alternative is based on the recent advances in ruthenium-based catalysis.[22] However, the equilibrium between vinyl acetate-1-^{13}C and its unlabeled counterpart was not directly amenable to the preparation of vinyl acetate-1-^{13}C.

Replacement of natural abundance vinyl acetate (VA) by vinyl laurate and the application of distillation column allowed for convenient removal of vinyl acetate-1-^{13}C (VA-1-^{13}C) from the reaction mixture (Scheme 1 a). Owing to the

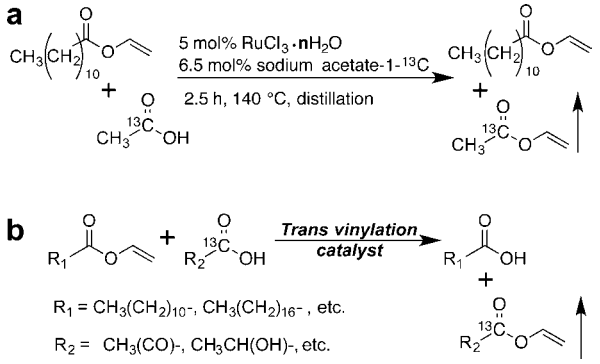

Scheme 1. a) Reaction scheme for the preparation of vinyl acetate-1-^{13}C (VA-1-^{13}C). b) Generalized scheme for preparation of potential targets with vinylated ^{13}C carboxyl groups. The vertical arrows indicate that the product leaves the mixture as a gas.

flexible nature of the substrates participating in the vinyl exchange, this method of ^{13}C enrichment can be applied to a variety of potential PHIP targets, such as pyruvate and lactate derivatives (Scheme 1 b).

We utilized the Rh catalyst [Rh(NBD)(dppb)]BF_4 ([(bicyclo[2.2.1]hepta-2,5-diene)[1,4-bis(diphenylphosphino)butane]rhodium(I) tetrafluoroborate) for molecular addition of para-H_2 to VA, analogous to that used in the recent PHIP-SAH studies (Figure 1 a).[12,13] A previously developed setup for high-pressure experiments with para-H_2 was utilized (Supporting Information),[23] demonstrating that higher para-H_2 pressure significantly accelerates VA hydrogenation to EA (Figure 1 b). Therefore, the highest pressure achievable in this setup (ca. 7.2 bar) was used in further PHIP-SAH experiments. Pairwise addition of 50 % para-H_2 was performed in the Earth magnetic field (ca. 50 μT) and then the sample was quickly (ca. 2 s) adiabatically transferred to 9.4 T for HP ^1H NMR detection of nascent protons (corresponding to ALTADENA[24] conditions). The

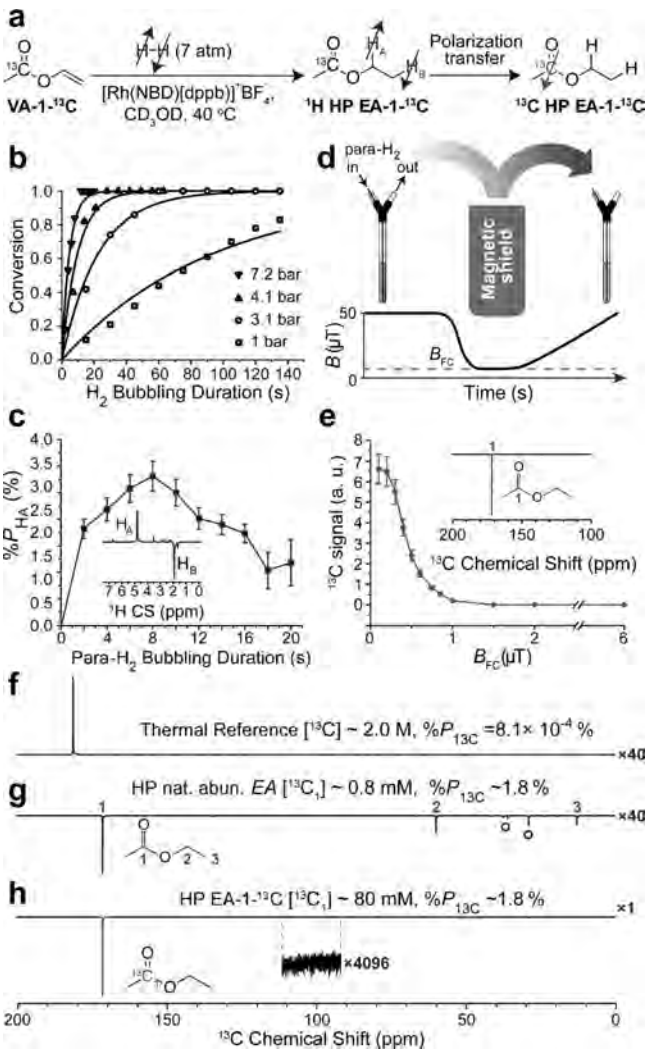

Figure 1. a) Molecular addition of para-H_2 to vinyl acetate-1-^{13}C (VA-1-^{13}C) followed by polarization transfer resulting in ^{13}C hyperpolarized ethyl acetate-1-^{13}C (^{13}C HP EA-1-^{13}C); b) Conversion profile for vinyl acetate (VA, 80 mM, in [D_4]MeOH, at ca. 40 °C maintained by the 9.4 T NMR spectrometer) hydrogenation reaction in four pressure regimes; c) Dependence of "H_A" signal of hyperpolarized ethyl acetate (^1H HP EA) on the para-H_2 bubbling duration at the Earth's magnetic field (resulting in ALTADENA[24]-type spectrum shown in inset); d) Top: schematic representation of the experimental setup for magnetic field cycling: hydrogenation is carried out at the Earth's magnetic field, the sample then is quickly moved inside a μ-metal shield (with magnetic field B_{FC}) and slowly transferred from the shield for subsequent NMR detection; bottom: schematic magnetic field profile during the field cycling; e) Dependence of HP 1–^{13}C NMR signal (shown in the insert) of ethyl acetate (^{13}C HP EA) on the B_{FC}; f) Thermal spectrum of ^{13}C signal reference sodium acetate-1-^{13}C (ca. 2.0 M); g) ^{13}C HP spectrum of natural abundance 80 mM ethyl acetate (^{13}C HP EA). Note the resonances labeled with ° correspond to HP ^{13}C resonances originating from the hydrogenation catalyst (Figure S7); h) HP ^{13}C spectrum of 80 mM ethyl acetate-1-^{13}C (^{13}C HP EA-1-^{13}C).

detected HP ^1H NMR signal initially rises (during fast product build-up) and then decreases (when the contribution of HP product relaxation overweighs formation of new HP

 © 2016 Wiley-VCH Verlag GmbH & Co. KGaA, Weinheim

species) with the duration of para-H_2 bubbling (Figure 1 c). The conditions corresponding to bubbling duration of about 8–10 s yielded maximum observed $\%P_H$ of 3.3 % (equivalent to ^{1}H signal enhancement $\varepsilon_{1H} > 1000$ fold) and thus, were used to transfer polarization from HP nascent protons to 1-^{13}C using magnetic field cycling[9,12] (Figure 1 d). In this approach, the pairwise para-H_2 addition is performed in the Earth's field, the sample is then quickly moved in a magnetic field < 1 μT (B_{FC}) and hyperpolarization is transferred to ^{13}C during slow (adiabatic) sample transfer back to the Earth's field (Figures 1 c,d). B_{FC} adjustment of polarization transfer was carried out by measuring ^{13}C HP NMR signal of natural abundance EA (ca. 1.1 % ^{13}C in each carbon site) produced by hydrogenation of 80 mM VA with para-H_2 (Figure 1 e). In-shield field (B_{FC}) of 0.1–0.2 μT provided the maximal HP transfer efficiency, and therefore it was used in all subsequent polarization transfer experiments.

The maximum detected ε_{13C} in HP EA was over 2200 fold for the 1-^{13}C site corresponding to $\%P_{13C}$ of around 1.8 % using 50 % para-H_2 (Figure 1 g). A similar $\%P_{13C}$ was also achieved for HP ^{13}C EA-1-^{13}C (Figure 1 h). When compared to natural abundance HP EA, HP ^{13}C EA-1-^{13}C carries around a 90-times greater polarization payload owing to the 98 % ^{13}C isotopic enrichment of the ^{13}C site. The enriched site was employed for ^{13}C 3D ultra-fast magnetic resonance imaging (MRI; Figure 2) showing the feasibility of high-resolution (pixel size of $0.5 \times 0.5 \times 4$ mm^3 and ca. 2.5 s duration) molecular imaging with this contrast agent using 15.2 T Bruker MRI scanner.

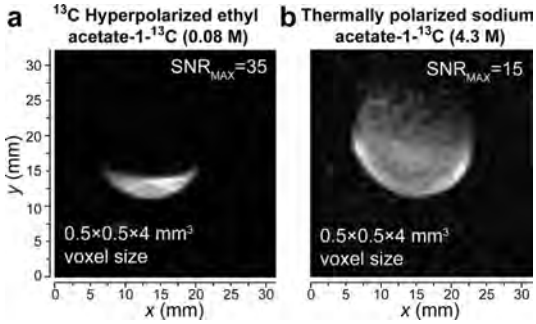

Figure 2. ^{13}C 3D MRI of a) a hollow spherical plastic ball partially filled with 80 mM HP EA-1-^{13}C and b) a plastic sphere (ca. 2.8 mL) filled with thermally polarized 4.3 M sodium acetate-1-^{13}C reference phantom. Both 3D true-FISP images were acquired using 15 mm outside-diameter (OD) round radio-frequency (RF) surface coil tuned to 163.4 MHz in 15.2 T small-animal Bruker MRI scanner (see Supporting Information for additional details). One representative slice is shown for each 3D image. SNR = signal to noise ratio.

If around 100 % para-H_2[25] were to be employed, the effective $\%P_H$ and $\%P_{13C}$ would be tripled to yield 10 % and 5.5 % respectively. These values would more than double the reported pioneering results.[13] Moreover, the efficiency of polarization transfer from nascent para-H_2 protons to 1-^{13}C was approximately 50 %, which is in quantitative agreement with previous theoretical simulation for similar spin system of 2-hydroxyethyl propionate-1-^{13}C.[14] The expected $\%P_{13C}$ of approximately 5.5 % is clearly largely limited by the HP source of $\%P_H$ of around 10 % in this study and most likely in recent work by Reineri and co-workers.[13] Therefore, future studies must focus on the $\%P_H$ increase and understanding factors leading to the polarization losses. There are three possible major $\%P_H$-reducing barriers: 1) the degree of pair-wise addition of para-H_2 to the vinyl moiety,[5a,26] 2) nascent protons' P relaxation, and 3) singlet–triplet mixing of nascent protons.[14] The first challenge is not a fundamental barrier, because similar catalysts yielded $\%P_{13C}$ of around 30–50 % on similar molecules[14,27] indicating that $\%P_H$ was 50–100 %. On the other hand, the other two barriers have always been addressed via the use of high-pressure automated spray-injection PHIP polarizers[8,28] operating at elevated temperatures, and enabling ultra-fast substrate conversion (1–3 s and thereby minimizing the effects of spin-lattice relaxation) and ^{1}H decoupling that allows all molecules to retain the singlet states during the course of hydrogenation reaction.[14] While additional future studies investigating the reasons behind low $\%P_H$ in this and previous PHIP-SAH studies are certainly warranted, the use of such PHIP polarizers[8,28] will likely provide the remedy and can potentially yield $\%P_{13C}$ of up to 50 % based on the efficiency of H→^{13}C polarization transfer demonstrated herein. The generality and flexibility of our *trans* vinylation approach will benefit future efficient preparation of other vinylated analogues of metabolically relevant compounds, such as lactate and pyruvate for PHIP-SAH.[2a,b] This would pave the way for the future in vivo imaging of metabolically impaired conditions such as cancer[2a,b] and brain[16] damage. In particular, future in vivo studies in animal models can be carried out with[8a] or without Rh-based PHIP catalysts removal (which are generally well tolerated by animals and cause no clinical toxicity[29]) in a manner similar to the previous use of HP succinate-1-^{13}C[2e,8b,10b] and HP 2-hydroxyethyl propionate.[9,27] The ultimate clinical translation will require employing Rh-based PHIP catalyst filtration/removal[8a] and improving of the filtration/removal step or the alternative use of improved heterogeneous PHIP catalysis.[26] Moreover, future in vivo translation of this work would require the use of water-soluble catalysts, which have been successfully employed in combination with high-pressure PHIP polarizers[8,28] to produce aqueous solution of HP succinate-^{13}C,[10a] phospholactate-1-^{13}C[3b] and others with $\%P_{13C}$ exceeding 15 % and T_1 in excess of 40 s.

Acknowledgements

This work was supported by NIH 1R21EB018014 and 1R21EB020323, NSF CHE-1416268, DOD CDMRP W81XWH-12-1-0159/BC112431, and W81XWH-15-1-0271. We are grateful to Oleg Salnikov for preparing the schematic description of the hyperpolarization setup in the Supporting Information.

Keywords: contrast agents · ethyl acetate · hyperpolarization · MRI · para-hydrogen induced polarization (PHIP)

 © 2016 Wiley-VCH Verlag GmbH & Co. KGaA, Weinheim

How to cite: *Angew. Chem. Int. Ed.* **2016**, *55*, 6071 – 6074
Angew. Chem. **2016**, *128*, 6175 – 6178

[1] a) A. Abragam, M. Goldman, *Rep. Prog. Phys.* **1978**, *41*, 395 – 467; b) B. M. Goodson, *J. Magn. Reson.* **2002**, *155*, 157 – 216; c) P. Nikolaou, B. M. Goodson, E. Y. Chekmenev, *Chem. Eur. J.* **2015**, *21*, 3156 – 3166.

[2] a) J. Kurhanewicz, D. B. Vigneron, K. Brindle, E. Y. Chekmenev, A. Comment, C. H. Cunningham, R. J. DeBerardinis, G. G. Green, M. O. Leach, S. S. Rajan, R. R. Rizi, B. D. Ross, W. S. Warren, C. R. Malloy, *Neoplasia* **2011**, *13*, 81 – 97; b) K. M. Brindle, *J. Am. Chem. Soc.* **2015**, *137*, 6418 – 6427; c) A. Comment, M. E. Merritt, *Biochemistry* **2014**, *53*, 7333 – 7357; d) K. Golman, R. in't Zandt, M. Thaning, *Proc. Natl. Acad. Sci. USA* **2006**, *103*, 11270 – 11275; e) P. Bhattacharya, E. Y. Chekmenev, W. H. Perman, K. C. Harris, A. P. Lin, V. A. Norton, C. T. Tan, B. D. Ross, D. P. Weitekamp, *J. Magn. Reson.* **2007**, *186*, 150 – 155.

[3] a) J. H. Ardenkjaer-Larsen, B. Fridlund, A. Gram, G. Hansson, L. Hansson, M. H. Lerche, R. Servin, M. Thaning, K. Golman, *Proc. Natl. Acad. Sci. USA* **2003**, *100*, 10158 – 10163; b) R. V. Shchepin, A. M. Coffey, K. W. Waddell, E. Y. Chekmenev, *Anal. Chem.* **2014**, *86*, 5601 – 5605.

[4] S. J. Nelson, J. Kurhanewicz, D. B. Vigneron, P. E. Z. Larson, A. L. Harzstark, M. Ferrone, M. van Criekinge, J. W. Chang, R. Bok, I. Park, G. Reed, L. Carvajal, E. J. Small, P. Munster, V. K. Weinberg, J. H. Ardenkjaer-Larsen, A. P. Chen, R. E. Hurd, L. I. Odegardstuen, F. J. Robb, J. Tropp, J. A. Murray, *Sci. Transl. Med.* **2013**, *5*, 198ra108.

[5] a) C. R. Bowers, D. P. Weitekamp, *Phys. Rev. Lett.* **1986**, *57*, 2645 – 2648; b) T. C. Eisenschmid, R. U. Kirss, P. P. Deutsch, S. I. Hommeltoft, R. Eisenberg, J. Bargon, R. G. Lawler, A. L. Balch, *J. Am. Chem. Soc.* **1987**, *109*, 8089 – 8091; c) C. R. Bowers, D. P. Weitekamp, *J. Am. Chem. Soc.* **1987**, *109*, 5541 – 5542.

[6] A. Bornet, R. Melzi, A. J. Perez Linde, P. Hautle, B. van den Brandt, S. Jannin, G. Bodenhausen, *J. Phys. Chem. Lett.* **2013**, *4*, 111 – 114.

[7] W. Jiang, L. Lumata, W. Chen, S. Zhang, Z. Kovacs, A. D. Sherry, C. Khemtong, *Sci. Rep.* **2015**, *5*, 9104.

[8] a) J.-B. Hövener, E. Chekmenev, K. Harris, W. Perman, L. Robertson, B. Ross, P. Bhattacharya, *Magn. Reson. Mater. Phys.* **2009**, *22*, 111 – 121; b) J.-B. Hövener, E. Chekmenev, K. Harris, W. Perman, T. Tran, B. Ross, P. Bhattacharya, *Magn. Reson. Mater. Phys.* **2009**, *22*, 123 – 134.

[9] K. Golman, O. Axelsson, H. Johannesson, S. Mansson, C. Olofsson, J. S. Petersson, *Magn. Reson. Med.* **2001**, *46*, 1 – 5.

[10] a) E. Y. Chekmenev, J. Hovener, V. A. Norton, K. Harris, L. S. Batchelder, P. Bhattacharya, B. D. Ross, D. P. Weitekamp, *J. Am. Chem. Soc.* **2008**, *130*, 4212 – 4213; b) N. M. Zacharias, H. R. Chan, N. Sailasuta, B. D. Ross, P. Bhattacharya, *J. Am. Chem. Soc.* **2012**, *134*, 934 – 943.

[11] a) R. V. Shchepin, A. M. Coffey, K. W. Waddell, E. Y. Chekmenev, *J. Am. Chem. Soc.* **2012**, *134*, 3957 – 3960; b) R. V. Shchepin, W. Pham, E. Y. Chekmenev, *J. Labelled Compd. Radiopharm.* **2014**, *57*, 517 – 524.

[12] F. Reineri, T. Boi, S. Aime, *Nat. Commun.* **2015**, *6*, 5858.

[13] E. Cavallari, C. Carrera, T. Boi, S. Aime, F. Reineri, *J. Phys. Chem. B* **2015**, *119*, 10035 – 10041.

[14] M. Goldman, H. Johannesson, *C. R. Phys.* **2005**, *6*, 575 – 581.

[15] R. E. Hurd, Y.-F. Yen, D. Mayer, A. Chen, D. Wilson, S. Kohler, R. Bok, D. Vigneron, J. Kurhanewicz, J. Tropp, D. Spielman, A. Pfefferbaum, *Magn. Reson. Med.* **2010**, *63*, 1137 – 1143.

[16] S. Blüml, A. Moreno-Torres, F. Shic, C. H. Nguy, B. D. Ross, *NMR Biomed.* **2002**, *15*, 1 – 5.

[17] J. D. Roberts, C. C. Lee, W. H. Saunders, *J. Am. Chem. Soc.* **1954**, *76*, 4501 – 4510.

[18] J. K. Kim, M. C. Caserio, *J. Am. Chem. Soc.* **1982**, *104*, 4624 – 4629.

[19] V. S. Livshits, G. V. Isagulyants, *Russ. Chem. Bull.* **1966**, *15*, 1801 – 1802.

[20] a) M. Kuhn, J. Jeschke, S. Schulze, M. Hietschold, H. Lang, T. Schwarz, *Catal. Commun.* **2014**, *57*, 78 – 82; b) S. Nakamura, T. Yasui, *J. Catal.* **1970**, *17*, 366 – 374.

[21] R. L. Adelman, *J. Org. Chem.* **1949**, *14*, 1057 – 1077.

[22] J. Ziriakus, T. K. Zimmermann, A. Pothig, M. Drees, S. Haslinger, D. Jantke, F. E. Kuhn, *Adv. Synth. Catal.* **2013**, *355*, 2845 – 2859.

[23] M. L. Truong, T. Theis, A. M. Coffey, R. V. Shchepin, K. W. Waddell, F. Shi, B. M. Goodson, W. S. Warren, E. Y. Chekmenev, *J. Phys. Chem. C* **2015**, *119*, 8786 – 8797.

[24] M. G. Pravica, D. P. Weitekamp, *Chem. Phys. Lett.* **1988**, *145*, 255 – 258.

[25] B. Feng, A. M. Coffey, R. D. Colon, E. Y. Chekmenev, K. W. Waddell, *J. Magn. Reson.* **2012**, *214*, 258 – 262.

[26] a) K. V. Kovtunov, V. V. Zhivonitko, I. V. Skovpin, D. A. Barskiy, I. V. Koptyug, *Top. Curr. Chem.* **2013**, *338*, 123 – 180; b) O. G. Salnikov, K. V. Kovtunov, I. V. Koptyug, *Sci. Rep.* **2015**, *5*, 13930.

[27] L. E. Olsson, C.-M. Chai, O. Axelsson, M. Karlsson, K. Golman, J. S. Petersson, *Magn. Reson. Med.* **2006**, *55*, 731 – 737.

[28] a) K. W. Waddell, A. M. Coffey, E. Y. Chekmenev, *J. Am. Chem. Soc.* **2011**, *133*, 97 – 101; b) S. Kadlecek, V. Vahdat, T. Nakayama, D. Ng, K. Emami, R. Rizi, *NMR Biomed.* **2011**, *24*, 933 – 942.

[29] H. R. Chan, P. Bhattacharya, A. Imam, A. Freundlich, T. T. Tran, W. H. Perman, A. P. Lin, K. Harris, E. Y. Chekmenev, M.-L. Ingram, B. D. Ross in *17th ISMRM Conference*, *April 18 – 24*, *Vol. 17*, Honolulu, Hawaii, **2009**, p. 2448.

Received: January 18, 2016
Revised: February 18, 2016
Published online: April 8, 2016

 © 2016 Wiley-VCH Verlag GmbH & Co. KGaA, Weinheim

NMR Spectroscopy

Production of Pure Aqueous ^{13}C-Hyperpolarized Acetate by Heterogeneous Parahydrogen-Induced Polarization

Kirill V. Kovtunov,*[a, b] Danila A. Barskiy,[c] Roman V. Shchepin,[c] Oleg G. Salnikov,[a, b] Igor P. Prosvirin,[b, d] Andrey V. Bukhtiyarov,[b, d] Larisa M. Kovtunova,[b, d] Valerii I. Bukhtiyarov,[b, d] Igor V. Koptyug,*[a, b] and Eduard Y. Chekmenev*[c, e]

Abstract: A supported metal catalyst was designed, characterized, and tested for aqueous phase heterogeneous hydrogenation of vinyl acetate with parahydrogen to produce ^{13}C-hyperpolarized ethyl acetate for potential biomedical applications. The Rh/TiO_2 catalyst with a metal loading of 23.2 wt% produced strongly hyperpolarized ^{13}C-enriched ethyl acetate-1-^{13}C detected at 9.4 T. An approximately 14-fold ^{13}C signal enhancement was detected using circa 50% parahydrogen gas without taking into account relaxation losses before and after polarization transfer by magnetic field cycling from nascent parahydrogen-derived protons to ^{13}C nuclei. This first observation of ^{13}C PHIP-hyperpolarized products over a supported metal catalyst in an aqueous medium opens up new possibilities for production of catalyst-free aqueous solutions of non-toxic hyperpolarized contrast agents for a wide range of biomolecules amenable to the parahydrogen induced polarization by side arm hydrogenation (PHIP-SAH) approach.

The methods based on magnetic resonance (NMR, MRI) are routinely used as sensitive analytical tools in chemistry and medicine. However, despite their impressive achievements, a potentially wider reach of these techniques is limited by their inherently limited sensitivity associated with the low nuclear spin polarization at thermal equilibrium. The advent of hyperpolarization NMR techniques significantly expands the range of potentially feasible MR applications.[1–9] One of these hyperpolarization techniques is dynamic nuclear polarization (DNP), which allows the hyperpolarization of a wide range of ^{13}C-labeled compounds[10,11] and their use for metabolic NMR/MRI.[12–14] However, the main limitations of the DNP technique are: 1) a long hyperpolarization time and 2) the high cost of the hyperpolarizer. Parahydrogen-induced polarization (PHIP) is an alternative hyperpolarization technique using singlet spin order of parahydrogen.[15–17] Pairwise addition of parahydrogen (p-H_2), that is, addition of the two H atoms from one p-H_2 molecule to magnetically nonequivalent positions of a substrate molecule, creates hyperpolarization on the nascent protons in the product molecule. Importantly, the polarization transfer from nascent parahydrogen atoms through spin–spin couplings to heteronuclei (for example, to ^{13}C) results in hyperpolarized (HP) contrast agents with sufficiently long lifetimes for biomedical applications.[18–20]

PHIP allows the production of HP liquids that can be directly used for signal enhancement in various NMR/MRI applications.[18,20] Despite the relative complexity of the synthesis of ^{13}C-labeled PHIP precursor compounds, many successful examples with high polarization levels on ^{13}C nuclei ($P_{13C} > 10\%$) in biomolecules have been reported: ^{13}C-succinate,[21] ^{13}C-tetrafluoropropionate,[22] and more recently ^{13}C-phospholactate.[23] While the corresponding pioneering in vivo studies are encouraging,[22,24,25] they were performed using injections of a liquid HP contrast agent containing a homogeneous Rh-based catalyst,[26] which is potentially toxic and thus a definite roadblock for eventual application in humans. Two alternative approaches can potentially address this obstacle: 1) catalyst removal by filtration/extraction or 2) utilization of a heterogeneous catalyst for pairwise p-H_2 addition (HET-PHIP).[9,27–29] The second approach is more advantageous because it additionally allows catalyst recycling.

Importantly, the PHIP medium must be biocompatible, that is, aqueous. The first observation of heterogeneous PHIP effects in an aqueous medium was reported in 2010,[30] utilizing

[a] Dr. K. V. Kovtunov, O. G. Salnikov, Prof. I. V. Koptyug
Laboratory of Magnetic Resonance Microimaging
International Tomography Center, SB RAS
3A Institutskaya St., Novosibirsk 630090 (Russia)
E-mail: kovtunov@tomo.nsc.ru
koptyug@tomo.nsc.ru

[b] Dr. K. V. Kovtunov, O. G. Salnikov, Dr. I. P. Prosvirin, Dr. A. V. Bukhtiyarov, Dr. L. M. Kovtunova, Prof. V. I. Bukhtiyarov, Prof. I. V. Koptyug
Novosibirsk State University
2 Pirogova St., Novosibirsk 630090 (Russia)

[c] Dr. D. A. Barskiy, Dr. R. V. Shchepin, Prof. E. Y. Chekmenev
Department of Radiology, Department of Biomedical Engineering
Department of Physics and Astronomy
Vanderbilt University Institute of Imaging Science (VUIIS)
Nashville, Tennessee, 37232-2310 (USA)
E-mail: eduard.chekmenev@vanderbilt.edu

[d] Dr. I. P. Prosvirin, Dr. A. V. Bukhtiyarov, Dr. L. M. Kovtunova, Prof. V. I. Bukhtiyarov
Boreskov Institute of Catalysis SB RAS
5 Acad. Lavrentiev Pr., Novosibirsk 630090 (Russia)

[e] Prof. E. Y. Chekmenev
Russian Academy of Sciences
Leninskiy Prospekt 14, 119991 Moscow (Russia)

Supporting information for this article and ORCIDs for the author(s) are available on the WWW under: http://dx.doi.org/10.1002/chem.201603974.

© 2016 Wiley-VCH Verlag GmbH & Co. KGaA, Weinheim

supported metal catalysts. Recently, a similar observation (indicating the possibility of heterogeneous PHIP formation in water) was made using ligand-capped platinum nanoparticles.[31,32] Although the transfer of polarization from nascent parahydrogen protons to ^{13}C nuclei was accomplished at $P_{13C}=0.013\,\%$,[31] subsequent applications of this system face serious challenges, because 1) separation of HP solution from 2-nm-sized nanoparticles is required, 2) very low conversion levels were achieved (ca. 0.03% after 15 s of reaction),[31] and 3) the reaction product 2-hydroxyethyl propionate (HEP) has no biomedical relevance beyond angiographic applications.[18]

Recently, an efficient procedure of polarization transfer from nascent parahydrogen protons to ^{13}C using the side arm hydrogenation (SAH) approach in combination with adiabatic magnetic field cycling was introduced. It was exemplified with a range of esters bearing an unsaturated alcoholic or carboxylic moiety, including vinyl acetate, which yielded HP ethyl acetate-1-^{13}C upon hydrogenation and magnetic field cycling.[33,34] However, these previous studies employed a homogeneous catalyst in an organic medium, which is incompatible with the long-term goal of in-human application of PHIP-SAH, which otherwise paves a straightforward and scalable route to efficient ^{13}C hyperpolarization of many biomolecules including ^{13}C-pyruvate.[33–35] Moreover, recent results based on the vinyl acetate heterogeneous hydrogenation in the gas phase with subsequent dissolution in aqueous phases and hydrolysis resulting in the production of a mixture of hyperpolarized ethane and thermally polarized acetic acid allow the generation of pure, biocompatible, and catalyst-free hyperpolarized fluid.[36]

In this work, we demonstrate that both previous shortcomings of PHIP-SAH can be resolved. Specifically, 2–3 mm beads of TiO_2 with supported rhodium nanoparticles were utilized for the aqueous phase heterogeneous hydrogenation of vinyl acetate-1-^{13}C with p-H_2, followed by polarization transfer to ^{13}C nuclei by means of magnetic field cycling.[33–35]

Recently, it was shown that decreasing the size of metal nanoparticles leads to an increase in the pairwise p-H_2 addition level;[9,37] therefore, the catalyst under investigation should have the smallest metal nanoparticles possible. However, large amounts of metal introduced upon impregnation of a porous support often lead to larger particle sizes, which are disadvantageous in terms of PHIP efficiency. Therefore, in the preparation of the 23.2 wt% Rh/TiO_2 catalyst, an aqueous rhodium nitrate solution was used to obtain relatively small metal particles even at the high rhodium loading. Rh was chosen as an active component because it usually provides the highest PHIP signal enhancements compared with other metals.[38] The catalyst was characterized in detail by transmission electron microscopy (TEM) and X-ray photoelectron spectroscopy (XPS) (Figure 1 and the Supporting Information, Figure S2). The average particle size of the 23.2 wt% Rh/TiO_2 catalyst was estimated from TEM data as circa 3 nm, which is favorable for the observation of PHIP effects.[39] Therefore, this catalyst was used for heterogeneous hydrogenation of vinyl acetate in an aqueous medium with subsequent polarization transfer from parahydrogen-derived protons to ^{13}C nuclei and detection by ^{13}C NMR spectroscopy (Figure 2,3).

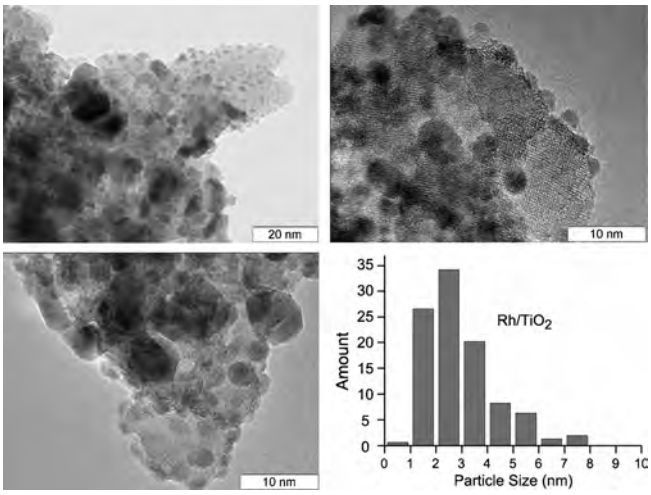

Figure 1. TEM images and metal particle size distribution for the 23.2 wt% Rh/TiO_2 catalyst obtained by wet impregnation from an aqueous rhodium nitrate solution. The average size of metal particles is ca. 3 nm.

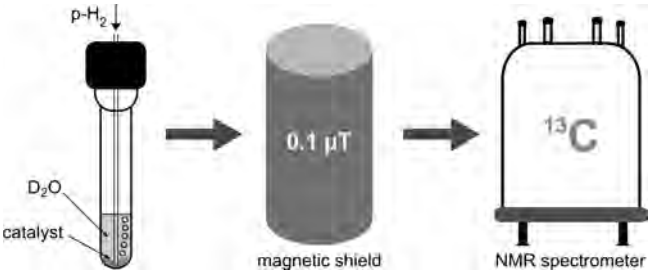

Figure 2. Experimental procedure for ^{13}C hyperpolarization and detection by NMR spectroscopy through PHIP-SAH and magnetic field cycling.

The catalyst's activity for vinyl acetate hydrogenation is expected to be lower in the aqueous medium (compared with that previously shown in organic solvents[40]), and the increase in the total available metal active centers by using 23.2 wt% Rh/TiO_2 catalyst was intended to compensate for this activity loss. Indeed, 20 s of hydrogen bubbling in our setup (ca. 0.5 mL of 0.08 M vinyl acetate-1-^{13}C solution, ca. 7.1 atm p-H_2 pressure at 150 standard cubic centimeters per minute (sccm) flow rate) was sufficient to reach a greater than 90% conversion of vinyl acetate to the reaction products (Figure 3 and the Supporting Information, Figure S3). An approximately 14-fold ^{13}C signal enhancement was observed under these conditions (see Figure 3).

Importantly, the hyperpolarized ^{13}C NMR signal was detected both when hydrogenation was carried out directly inside the magnetic shield and when the NMR tube with the hydrogenation products was briefly placed in the shield after the termination of the hydrogen bubbling. The latter approach generally resulted in greater ^{13}C polarization values. The size of the catalyst beads and the Rh loading can be potentially further optimized to maximize chemical conversion efficiency and the

© 2016 Wiley-VCH Verlag GmbH & Co. KGaA, Weinheim

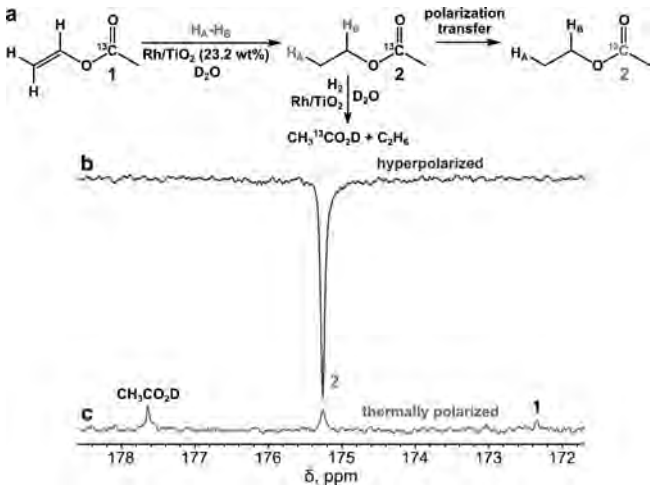

Figure 3. a) Scheme of vinyl acetate-1-^{13}C heterogeneous hydrogenation with parahydrogen (p-H_2) over 23.2 wt% Rh/TiO_2 catalyst in a D_2O solution with subsequent polarization transfer from protons to ^{13}C nuclei, b) ^{13}C NMR spectrum of HP ethyl acetate-1-^{13}C, and c) corresponding ^{13}C spectrum of thermally polarized sample after waiting for a time period longer than $5\times T_1$. All spectra were acquired with one signal scan. NMR tube with the hydrogenation products was placed in a magnetic shield after termination of hydrogen bubbling. The ^{13}C signal enhancement (ε_{13C}) is ca. 14-fold and $\%P_{13C}$ is ca. 0.011 %.

degree of pairwise addition, that is, to maximize the overall yield of ^{13}C hyperpolarization.

Figure 3 also shows that for the polarization transfer only the ^{13}C NMR signal from hyperpolarized ethyl acetate can be detected. However, in the ^{13}C NMR spectrum of the thermally polarized reaction products (Figure 3 c), the equilibrium signals of ^{13}C-labeled unreacted vinyl acetate, ethyl acetate, and acetic acid can be seen. Therefore, the formation of acetic acid by hydrogenolysis of ethyl acetate or by direct hydrogenation of vinyl acetate can be easily verified by ^{13}C NMR spectroscopy. Along with the acetic acid, ethane formed as a byproduct of the vinyl acetate heterogeneous hydrogenation with an estimated concentration of approximately 4 mM over the supported rhodium catalyst, and the corresponding ^{1}H NMR spectra before and after reaction are shown in the Supporting Information Figure S3.

It should also be emphasized that the circa 14-fold enhancement of the HET-PHIP ^{13}C signal (ε_{13C}) achieved here is a factor of circa 130 lower than that obtained under similar conditions using a homogeneous Rh catalyst in [D_4]MeOH.[35] However, the hydrogenation duration was 20 s in this study compared with 10 s in the previous report,[35] and additional T_1 relaxation losses have contributed to the lower ε_{13C} observed here (^{13}C T_1 of carboxyl ^{13}C sites is generally on the order of 30–60 s in vitro[21,22,33–35] and in vivo,[10,41] and T_1 of protons at low magnetic fields is generally on the order of 5–10 s[42,43]). It is likely that optimization of the catalyst structure and reaction conditions could lead to major improvements for the presented approach.

The stability of the catalyst under reactive conditions is also important, and XPS investigations of the catalyst before and after the reaction were carried out (see the Supporting Information for details). It was successfully confirmed that the catalyst did not undergo any changes after the reaction and Rh nanoparticles are present at the surface of titania only in the metallic state (Supporting Information, Figure S2).

Glöggler et al.[31] utilized circa 2 nm beads that will likely be challenging to separate rapidly. In contrast, the 2–3 mm catalytically active beads used here can be easily separated, for example, by simple decantation of the hyperpolarized aqueous solution from the catalyst. For instance, the Supporting Information Figure S4 b shows that even during hydrogenation, the beads reside at the bottom of the NMR tube. Alternatively, if the average diameter of the beads is decreased to 0.1 mm, the catalyst suspension (Supporting Information, Figure S4 a) can be potentially filtered.

The ability to produce hyperpolarized compounds in water using solid catalysts opens up new possibilities for the production of catalyst-free aqueous solutions of nontoxic hyperpolarized contrast agents. Furthermore, polarization transfer from parahydrogen-derived protons to heteronuclei by magnetic field cycling increases the lifetime of hyperpolarization of the produced compounds and minimizes the signal background. All these factors are of paramount importance for in vivo applications.[18] Therefore, the first observation of ^{13}C hyperpolarized molecules formed by heterogeneous hydrogenation of vinyl acetate with p-H_2 over supported rhodium nanoparticles is a major step forward to biomedical applications of the HET-PHIP approach, and HET-PHIP-SAH in particular, because the latter can be used to hyperpolarize a wide range of biomolecules.[33–35]

In conclusion, we have presented a new approach to produce catalyst-free aqueous solutions of a biomolecule carrying ^{13}C hyperpolarization. The approach is based on the heterogeneous side arm hydrogenation (SAH) of a suitable precursor molecule with p-H_2 over supported metal catalysts with subsequent or simultaneous polarization transfer from parahydrogen-derived protons to ^{13}C nuclei by magnetic field cycling. The achieved circa 90% conversion in the heterogeneous hydrogenation reaction in water, which is comparable to the conversion achieved by homogenous PHIP hyperpolarization[23] for in vivo ^{13}C imaging,[24] can be further increased by increasing p-H_2 pressure and flow rate and the amount of catalytically active sites on the catalyst surface. We believe that combination of aqueous phase heterogeneous catalysis by supported metals with HET-PHIP-SAH and the polarization transfer approach offers a powerful tool for the production of hyperpolarized biocompatible contrast agents for MRI because the demonstrated method is scalable and does not require complex instrumentation.

Experimental Section

For the liquid phase heterogeneous hydrogenation 23.2 wt% Rh/TiO_2 solid catalyst was placed at the bottom of a 5 mm high-pressure medium-wall NMR tube, which was then filled with the solution of ^{13}C-labeled vinyl acetate in D_2O. Subsequently, the NMR tube was pressurized to ca. 7.1 atm of p-H_2 and heated to 90 °C, and then p-H_2 was bubbled through the solution for 20 s at 150

© 2016 Wiley-VCH Verlag GmbH & Co. KGaA, Weinheim

sccm. The samples were not degassed before reaction and hyperpolarization process. As soon as bubbling was stopped, the NMR tube was transferred from the Earth's magnetic field to the very low magnetic field (ca. 0.1 μT) inside the magnetic shield and then adiabatically transferred to the 9.4 T high field of the NMR spectrometer, where ^{13}C NMR spectra were acquired (Figures 2,3). The detailed experimental setup is presented in the Supporting Information, Figure S1. The procedures for catalyst preparation, hydrogenation, and XPS experiments, and additional NMR spectra are given in the Supporting Information.

Acknowledgements

O.G.S. and I.V.K. acknowledge the grant from the Russian Science Foundation (14-13-00445) for the support of the heterogeneous hydrogenation experiments. K.V.K. thanks the president's grant MK-4498.2016.3 and RFBR grant 14-03-93183 MCX a for the high field NMR experiments; the I.T.C. team thanks FASO Russia (0333-2014-0001) for basic funding. The B.I.C. team thank RSF grant (14-23-00146) for the support of catalyst characterization by XPS and TEM, L.M.K. thanks FASO (0303-2015-0010) for the support of the catalyst preparation. The U.S. team thanks NIH 1R21EB018014 and 1R21EB020323, NSF CHE-1416268 and CHE-1416432, DOD CDMRP W81XWH-12-1-0159/BC112431 and W81XWH-15-1-0271, and ExxonMobil Research and Engineering Company Knowledge Build.

Keywords: ^{13}C NMR · hyperpolarization · parahydrogen · PHIP · polarization transfer

[1] P. Nikolaou, B. M. Goodson, E. Y. Chekmenev, *Chem. Eur. J.* **2015**, *21*, 3156 – 3166.
[2] J.-H. Ardenkjaer-Larsen, G. S. Boebinger, A. Comment, S. Duckett, A. S. Edison, F. Engelke, C. Griesinger, R. G. Griffin, C. Hilty, H. Maeda, *Angew. Chem. Int. Ed.* **2015**, *54*, 9162 – 9185; *Angew. Chem.* **2015**, *127*, 9292 – 9317.
[3] J. H. Ardenkjaer-Larsen, *J. Magn. Reson.* **2016**, *264*, 3 – 12.
[4] A. Comment, *J. Magn. Reson.* **2016**, *264*, 39 – 48.
[5] A. Comment, M. E. Merritt, *Biochemistry* **2014**, *53*, 7333 – 7357.
[6] K. M. Brindle, *J. Am. Chem. Soc.* **2015**, *137*, 6418 – 6427.
[7] B. M. Goodson, *J. Magn. Reson.* **2002**, *155*, 157 – 216.
[8] R. A. Green, R. W. Adams, S. B. Duckett, R. E. Mewis, D. C. Williamson, G. G. R. Green, *Prog. Nucl. Magn. Reson. Spectrosc.* **2012**, *67*, 1 – 48.
[9] K. V. Kovtunov, V. V. Zhivonitko, I. V. Skovpin, D. A. Barskiy, I. V. Koptyug, *Top. Curr. Chem.* **2012**, *338*, 123 – 180.
[10] J. H. Ardenkjaer-Larsen, B. Fridlund, A. Gram, G. Hansson, L. Hansson, M. H. Lerche, R. Servin, M. Thaning, K. Golman, *Proc. Natl. Acad. Sci. USA* **2003**, *100*, 10158 – 10163.
[11] J. Kurhanewicz, D. B. Vigneron, K. Brindle, E. Y. Chekmenev, A. Comment, C. H. Cunningham, R. J. DeBerardinis, G. G. Green, M. O. Leach, S. S. Rajan, R. R. Rizi, B. D. Ross, W. S. Warren, C. R. Malloy, *Neoplasia* **2011**, *13*, 81 – 97.
[12] K. M. Brindle, S. E. Bohndiek, F. A. Gallagher, M. I. Kettunen, *Magn. Reson. Med.* **2011**, *66*, 505 – 519.
[13] K. Brindle, *Nat. Rev. Cancer* **2008**, *8*, 94 – 107.
[14] K. Golman, R. in't Zandt, M. Thaning, *Proc. Natl. Acad. Sci. USA* **2006**, *103*, 11270 – 11275.
[15] C. R. Bowers, D. P. Weitekamp, *J. Am. Chem. Soc.* **1987**, *109*, 5541 – 5542.
[16] T. C. Eisenschmid, R. U. Kirss, P. P. Deutsch, S. I. Hommeltoft, R. Eisenberg, J. Bargon, R. G. Lawler, A. L. Balch, *J. Am. Chem. Soc.* **1987**, *109*, 8089 – 8091.
[17] M. G. Pravica, D. P. Weitekamp, *Chem. Phys. Lett.* **1988**, *145*, 255 – 258.
[18] K. Golman, O. Axelsson, H. Jóhannesson, S. Månsson, C. Olofsson, J. S. Petersson, *Magn. Reson. Med.* **2001**, *46*, 1 – 5.
[19] J.-B. Hövener, E. Y. Chekmenev, K. C. Harris, W. H. Perman, T. T. Tran, B. D. Ross, P. Bhattacharya, *Magn. Reson. Mater. Phys. Biol. Med.* **2009**, *22*, 123 – 134.
[20] M. Goldman, H. Jóhannesson, O. Axelsson, M. Karlsson, *C. R. Chim.* **2006**, *9*, 357 – 363.
[21] E. Y. Chekmenev, J. Hövener, V. A. Norton, K. Harris, L. S. Batchelder, P. Bhattacharya, B. D. Ross, D. P. Weitekamp, *J. Am. Chem. Soc.* **2008**, *130*, 4212 – 4213.
[22] P. Bhattacharya, E. Y. Chekmenev, W. F. Reynolds, S. Wagner, N. Zacharias, H. R. Chan, R. Bünger, B. D. Ross, *NMR Biomed.* **2011**, *24*, 1023 – 1028.
[23] R. V. Shchepin, A. M. Coffey, K. W. Waddell, E. Y. Chekmenev, *Anal. Chem.* **2014**, *86*, 5601 – 5605.
[24] A. M. Coffey, R. V. Shchepin, M. L. Truong, K. Wilkens, W. Pham, E. Y. Chekmenev, *Anal. Chem.* **2016**, *88*, 8279 – 8288.
[25] N. M. Zacharias, H. R. Chan, N. Sailasuta, B. D. Ross, P. Bhattacharya, *J. Am. Chem. Soc.* **2012**, *134*, 934 – 943.
[26] P. Bhattacharya, K. Harris, A. P. Lin, M. Mansson, V. A. Norton, W. H. Perman, D. P. Weitekamp, B. D. Ross, *Magn. Reson. Mater. Phys. Biol. Med.* **2005**, *18*, 245 – 256.
[27] K. V. Kovtunov, I. E. Beck, V. I. Bukhtiyarov, I. V. Koptyug, *Angew. Chem. Int. Ed.* **2008**, *47*, 1492 – 1495; *Angew. Chem.* **2008**, *120*, 1514 – 1517.
[28] A. M. Balu, S. B. Duckett, R. Luque, *Dalton Trans.* **2009**, 5074 – 5076.
[29] M. Irfan, N. Eshuis, P. Spannring, M. Tessari, M. C. Feiters, F. P. J. T. Rutjes, *J. Phys. Chem. C* **2014**, *118*, 13313 – 13319.
[30] I. V. Koptyug, V. V. Zhivonitko, K. V. Kovtunov, *ChemPhysChem* **2010**, *11*, 3086 – 3088.
[31] S. Glöggler, A. M. Grunfeld, Y. N. Ertas, J. Mccormick, S. Wagner, P. P. M. Schleker, L.-S. Bouchard, *Angew. Chem. Int. Ed.* **2015**, *54*, 2452 – 2456; *Angew. Chem.* **2015**, *127*, 2482 – 2486.
[32] S. Glöggler, A. M. Grunfeld, Y. N. Ertas, J. McCormick, S. Wagner, L.-S. Bouchard, *Chem. Commun.* **2016**, *52*, 605 – 608.
[33] F. Reineri, T. Boi, S. Aime, *Nat. Commun.* **2015**, *6*, 5858.
[34] E. Cavallari, C. Carrera, T. Boi, S. Aime, F. Reineri, *J. Phys. Chem. B* **2015**, *119*, 10035 – 10041.
[35] R. V. Shchepin, D. A. Barskiy, A. M. Coffey, I. V. Manzanera Esteve, E. Y. Chekmenev, *Angew. Chem. Int. Ed.* **2016**, *55*, 6071 – 6074; *Angew. Chem.* **2016**, *128*, 6175 – 6178.
[36] O. G. Salnikov, K. V. Kovtunov, I. V. Koptyug, *Sci. Rep.* **2015**, *5*, 13930.
[37] A. Corma, O. G. Salnikov, D. A. Barskiy, K. V. Kovtunov, I. V. Koptyug, *Chem. Eur. J.* **2015**, *21*, 7012 – 7015.
[38] K. V. Kovtunov, D. A. Barskiy, A. M. Coffey, M. L. Truong, O. G. Salnikov, A. K. Khudorozhkov, E. A. Inozemtseva, I. P. Prosvirin, V. I. Bukhtiyarov, K. W. Waddell, *Chem. Eur. J.* **2014**, *20*, 11636 – 11639.
[39] V. P. Ananikov, L. L. Khemchyan, Y. V. Ivanova, V. I. Bukhtiyarov, A. M. Sorokin, I. P. Prosvirin, S. Z. Vatsadze, A. V. Medved'ko, V. N. Nuriev, A. D. Dilman, *Russ. Chem. Rev.* **2014**, *83*, 885 – 985.
[40] K. V. Kovtunov, D. A. Barskiy, O. G. Salnikov, R. V. Shchepin, A. M. Coffey, L. M. Kovtunova, V. I. Bukhtiyarov, I. V. Koptyug, E. Y. Chekmenev, *RSC Adv.* **2016**, *6*, 69728 – 69732.
[41] R. E. Hurd, Y.-F. Yen, D. Mayer, A. Chen, D. Wilson, S. Kohler, R. Bok, D. Vigneron, J. Kurhanewicz, J. Tropp, D. Spielman, A. Pfefferbaum, *Magn. Reson. Med.* **2010**, *63*, 1137 – 1143.
[42] R. V. Shchepin, A. M. Coffey, K. W. Waddell, E. Y. Chekmenev, *J. Phys. Chem. Lett.* **2012**, *3*, 3281 – 3285.
[43] D. A. Barskiy, K. V. Kovtunov, I. V. Koptyug, P. He, K. A. Groome, Q. A. Best, F. Shi, B. M. Goodson, R. V. Shchepin, M. L. Truong, A. M. Coffey, K. W. Waddell, E. Y. Chekmenev, *ChemPhysChem* **2014**, *15*, 4100 – 4107.

Received: August 21, 2016
Published online on ■■ ■■, 0000

© 2016 Wiley-VCH Verlag GmbH & Co. KGaA, Weinheim

COMMUNICATION

A supported metal catalyst was designed, characterized, and tested for aqueous phase heterogeneous hydrogenation of vinyl acetate with parahydrogen to produce ^{13}C-hyperpolarized ethyl acetate for potential biomedical applications. An approximately 14-fold ^{13}C signal enhancement was detected using ca. 50% parahydrogen gas at 9.4 T.

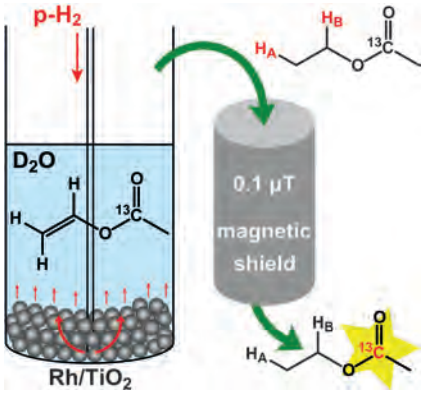

NMR Spectroscopy

K. V. Kovtunov, D. A. Barskiy, R. V. Shchepin, O. G. Salnikov, I. P. Prosvirin, A. V. Bukhtiyarov, L. M. Kovtunova, V. I. Bukhtiyarov, I. V. Koptyug,* E. Y. Chekmenev**

■■ – ■■

Production of Pure Aqueous ^{13}C-Hyperpolarized Acetate by Heterogeneous Parahydrogen-Induced Polarization

© 2016 Wiley-VCH Verlag GmbH & Co. KGaA, Weinheim

CHEMISTRY
A European Journal

A Journal of
ChemPubSoc Europe

Accepted Article

Title: NMR Hyperpolarization Techniques of Gases

Authors: Danila A Barskiy, Aaron M Coffey, Panayiotis Nikolaou, Dmitry M. Mikhaylov, Boyd M. Goodson, Rosa T Branca, George J. Lu, Mikhail G. Shapiro, Ville-Veikko Telkki, Vladimir V. Zhivonitko, Igor V. Koptyug, Oleg G. Salnikov, Kirill V. Kovtunov, Valerii I Bukhtiyarov, Matthew S. Rosen, Michael J. Barlow, Shahideh Safavi, Ian P. Hall, Leif Schröder, and Eduard Y. Chekmenev

This manuscript has been accepted after peer review and appears as an Accepted Article online prior to editing, proofing, and formal publication of the final Version of Record (VoR). This work is currently citable by using the Digital Object Identifier (DOI) given below. The VoR will be published online in Early View as soon as possible and may be different to this Accepted Article as a result of editing. Readers should obtain the VoR from the journal website shown below when it is published to ensure accuracy of information. The authors are responsible for the content of this Accepted Article.

To be cited as: *Chem. Eur. J.* 10.1002/chem.201603884

Link to VoR: http://dx.doi.org/10.1002/chem.201603884

Supported by ACES

WILEY-VCH

10.1002/chem.201603884

WILEY-VCH

NMR Hyperpolarization Techniques of Gases

Danila A. Barskiy,[a] Aaron M. Coffey,[a] Panayiotis Nikolaou,[a] Dmitry M. Mikhaylov,[b] Boyd M. Goodson,[c] Rosa T. Branca,[d] George J. Lu,[e] Mikhail G. Shapiro,[e] Ville-Veikko Telkki,[f] Vladimir V. Zhivonitko,[g,h] Igor V. Koptyug,[g,h] Oleg G. Salnikov,[g,h] Kirill V. Kovtunov,[g,h] Valerii I. Bukhtiyarov,[i] Matthew S. Rosen,[j] Michael J. Barlow,[k] Shahideh Safavi,[k] Ian P. Hall,[k] Leif Schröder[l] and Eduard Y. Chekmenev*[a,m]

Dedication ((optional))

Abstract: Nuclear spin polarization can be significantly increased through the process of hyperpolarization, leading to an increase in the sensitivity of nuclear magnetic resonance (NMR) experiments by 4–8 orders of magnitude. Hyperpolarized gases, unlike liquids and solids, can be more readily separated and purified from the compounds used to mediate the hyperpolarization processes. These pure hyperpolarized gases enabled many novel MRI applications including the visualization of void spaces, imaging of lung function, and remote detection. Additionally, hyperpolarized gases can be dissolved in liquids and can be used as sensitive molecular probes and reporters. This mini-review covers the fundamentals of the preparation of hyperpolarized gases and focuses on selected applications of interest to biomedicine and materials science.

[a] Dr. D. A. Barskiy, Dr. A. M. Coffey, Dr. P. Nikolaou, Prof. E. Y. Chekmenev
Department of Radiology
Vanderbilt University Institute of Imaging Science (VUIIS)
Department of Biomedical Engineering
Department of Physics
Vanderbilt-Ingram Cancer Center (VICC)
Vanderbilt University
Nashville, TN 37232, USA
E-mail: eduard.chekmenev@vanderbilt.edu
[b] Prof. Dmitry M. Mikhaylov
Huazhong University of Science and Technology
Wuhan, 100044, China
[c] Prof. B. M. Goodson
Southern Illinois University
Department of Chemistry and Biochemistry
Materials Technology Center
Carbondale, IL 62901, USA
[d] Prof. R. T. Branca
Department of Physics and Astronomy
Biomedical Research Imaging Center
University of North Carolina at Chapel Hill
Chapel Hill, NC 27599, USA
[e] Dr. G. J. Lu, Prof. M. G. Shapiro
Division of Chemistry and Chemical Engineering
California Institute of Technology
Pasadena, CA 91125, USA
[f] Dr. V.-V. Telkki
NMR Research Unit,
University of Oulu
90014 Oulu, Finland
[g] Dr. V. V. Zhivonitko, O. G. Salnikov, Dr. K. V. Kovtunov, Prof. I. V. Koptyug
International Tomography Center SB RAS,
630090 Novosibirsk, Russia
[h] Dr. V. V. Zhivonitko, O. G. Salnikov, Dr. K. V. Kovtunov, Prof. I. V. Koptyug
Department of Natural Sciences
Novosibirsk State University
Pirogova St. 2, 630090 Novosibirsk, Russia
[i] Prof. V. I. Bukhtiyarov
Boreskov Institute of Catalysis SB RAS
5 Acad. Lavrentiev Pr., 630090 Novosibirsk, Russia
[j] Prof. M. S. Rosen
MGH/A.A. Martinos Center for Biomedical Imaging
Boston, MA 02129, USA
[k] Dr. M. J. Barlow, Dr. S. Safavi, Prof. I. P. Hall
Respiratory Medicine Department
University of Nottingham Medical School
Queen's Medical Centre, Nottingham NG7 2UH, UK
[l] Dr. L. Schröder
Molecular Imaging, Department of Structural Biology, Leibniz-Institut für Molekulare Pharmakologie (FMP), 13125 Berlin, Germany
[m] Prof. E. Y. Chekmenev
Russian Academy of Sciences
119991 Moscow Russia

1. Introduction

The use of techniques to enhance nuclear spin polarization (*P*) to order unity (*i.e*. nearly 100%) results in corresponding gains in NMR sensitivity by 4-8 orders of magnitude.[1] This process of significant polarization enhancement—well above that achieved at thermal equilibrium—is termed *hyperpolarization*. Hyperpolarization of solids, liquids, and gases[2] has been demonstrated via a number of techniques including Brute Force Polarization (BFP),[3] Spin Exchange Optical Pumping (SEOP),[4] Dynamic Nuclear Polarization (DNP),[1c] Chemically-Induced Dynamic Nuclear Polarization (CIDNP)[5] photo-CIDNP,[6] Parahydrogen Induced Polarization (PHIP),[7] and Signal Amplification By Reversible Exchange (SABRE).[8]. A wide range of nuclei can be directly hyperpolarized, including ^{1}H,[9] ^{3}He,[10] ^{7}Li[11], ^{13}C,[1c, 12] ^{15}N,[13] ^{19}F,[14] ^{31}P,[15] ^{83}Kr,[16] and ^{129}Xe,[4, 17] among others.[18] Hyperpolarized (HP) substances are revolutionizing the fields of NMR spectroscopy and magnetic resonance imaging (MRI), because many applications that were previously impractical because of weak NMR signals (*e.g*. metabolites at sub-mM) are now becoming possible. Moreover, the enormous gain in attainable SNR allows spectroscopic detection and imaging of HP compounds to be performed in seconds, obviating the need for time-consuming signal averaging and thermal recovery of the spin magnetization. The ability to rapidly acquire signals with very high SNR from HP systems is the inherent feature that is greatly desirable for *in vivo* gas imaging applications: *i.e.* images can be acquired during a single breath hold; sufficient signal can be attained despite low density of gas compared to liquid. While liquid HP contrast agents are injected *in vivo* to probe metabolism[19] (extensively discussed in many recent reviews)[20] or used otherwise,[21] they typically cannot be used to probe gas-phase processes *in vitro* or *in vivo*. This mini-review focuses on the techniques allowing the production of HP gases with particular application to their use in biomedical applications, and explores some examples from materials science.

We begin with the fundamentals of SEOP in the context of NMR hyperpolarization of ^{129}Xe gas. Although other noble gases have been hyperpolarized, none are as widely used for magnetic resonance as HP ^{129}Xe, which has a relatively large natural abundance (ca. 26%) and is relatively cheap (ca. $20/L). The selected applications described here include functional lung imaging,[22] metabolic brown fat imaging,[23] and biosensors[24] (including those enabled by genetic encoding[25]). A recent demonstration of the DNP process to hyperpolarize ^{129}Xe[26] and hydrocarbon gases[27] is also described.

HP gases can also be efficiently produced via PHIP, when parahydrogen gas is added in a pairwise manner to a multiple chemical bond (C=C or C≡C) in an unsaturated molecule—resulting in a gaseous HP product. This process can be performed in heterogeneous fashion,[9a, 28] and despite low T_1 of the HP states, this powerful scalable technique allows for cheap

preparation of HP hydrocarbons on demand. Moreover, because protons are being directly hyperpolarized and detected, it is inexpensive and straightforward to perform (since expensive isotopic enrichment and heteroatoms-specific instrumentation can be obviated) and thus is readily applied with conventional clinical MRI scanners. This mini-review describes the fundamentals of PHIP for production of HP gases,[29] selected recent developments to extend the lifetime of the HP state through the use of the long-lived spin states (LLSS),[30] and HP gas application for void space imaging, remote sensing, time of flight imaging, and micro-fluidic imaging.

In all cases, the separation from other compounds required for hyperpolarization process (*e.g.* Rb in case of SEOP of HP ^{129}Xe, un-paired radicals in the case of DNP, and homogeneous or heterogeneous catalysts in the case of PHIP) is well known, and experiments can be performed with HP gases in a chemically pure form.

2. Fundamentals of Noble Gas Hyperpolarization

2.1. SEOP

The most commonly employed method for generating HP noble gases is spin-exchange optical pumping (SEOP). The development of SEOP is rooted in the pioneering work of Kastler,[31] who was recognized with the Nobel Prize in physics for demonstrating that electronic spin order can be created in alkali metal vapors using circularly polarized laser light. Later Bouchiat, Carver, and Varnum[32] showed that the addition of ^{3}He to the gas mixture permitted helium nuclear spins to be polarized by spin-exchange collisions with the optically pumped alkali vapor atoms—work that was extended to ^{129}Xe by Grover.[33] The rich physics of SEOP has been extensively explored by Happer, Cates, Chupp, Walker, and many others (*e.g.* Refs. [4, 17b, 34]), ultimately leading to the ability to produce large quantities of HP noble gases with nuclear spin polarization levels approaching unity for use in a variety of applications—including those described throughout this Mini-Review.

The underlying phenomenon of SEOP has been reviewed extensively elsewhere,[4, 35] but can be briefly described as follows (Figure 1): First, a heated alkali metal vapor is irradiated with resonant circularly polarized light. Angular momentum conservation results in population being driven from appropriate spin-state ground states (e.g. m_J=-1/2 with σ+ light, neglecting nuclear spin degrees of freedom). The ground state levels are repopulated at roughly the same rates, resulting in depletion of one spin state and population accumulation in the other—rendering the alkali metal vapor electronically spin polarized. Gas-phase collisions then transfer polarization from the electrons of the alkali metal to the spins of the noble gas nuclei via Fermi-contact interactions. This process is allowed to continue so that the nuclear spin polarization can accumulate over time, ultimately yielding a steady-state nuclear spin polarization given by:

$$P_{\mathrm{N}} = \langle P_{\mathrm{AM}} \rangle \cdot \left(\frac{\gamma_{\mathrm{SE}}}{\gamma_{\mathrm{SE}} + \Gamma_N} \right)$$

where $\langle P_{\mathrm{AM}} \rangle$ is the spatially averaged polarization of the alkali metal vapor, Γ_N is the noble gas nuclear longitudinal relaxation rate ($1/T_1$) in the optical pumping cell, and γ_{SE} is the spin-exchange rate (*i.e.*, the rate at which polarization can be transferred from alkali metal to the noble gas).

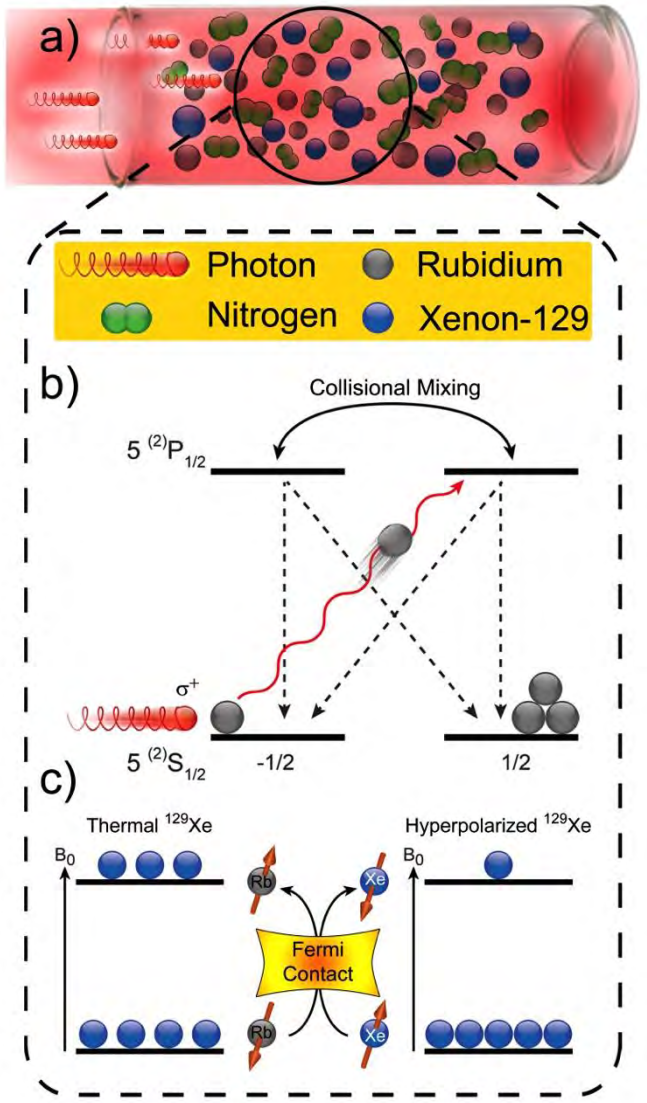

Figure 1. Schematic representations of SEOP.[2b, 4] (a) SEOP cell containing a noble gas (here, Xe), buffer gases (e.g. N_2), and a small quantity of vaporized alkali metal (here, Rb); the cell is irradiated by circularly polarized laser light that can be absorbed by the alkali metal atoms. (b) The first step of SEOP: in order to conserve angular momentum, photon absorption results in selective population depletion from one Rb ground electronic state (neglecting Rb nuclear spin for simplicity). Although gas-phase collisions work to equalize the excited-state populations (and hence, the ground-state repopulation rates), continuous depletion of one state by the laser leaves the AM vapor electronically spin-polarized. (c) The second step of SEOP: Gas-phase collisions occasionally allow spin order to be transferred from the AM atom electrons to the noble gas nuclei via Fermi contact hyperfine interactions, thereby hyperpolarizing the noble gas over time. Reproduced with permission from Ref. [2b] © John Wiley & Sons, Ltd., 2015.

Although the vast majority of SEOP experiments have employed the spin *I*=1/2 noble gas isotopes ^{129}Xe and ^{3}He, the quadrupolar species ^{21}Ne (*I*=3/2),[36] ^{83}Kr (*I*=9/2),[37] and ^{131}Xe[38] (*I*=3/2) can also be polarized via this method. For the alkali metal vapor, Rb is most-commonly employed for practical reasons—including its low melting point[39] (facilitating vaporization) and the availability of high-powered lasers resonant with its D_1 transition[40]; however, K and Cs are also utilized (particularly for ^{3}He[41] and ^{129}Xe,[42] respectively).

Technological developments for SEOP have been extensively reviewed elsewhere,[35] and only a brief description is given here. Devices for preparing HP noble gases may be grouped into two types: "stopped-flow" and "continuous-flow". In a stopped-flow device,[43] a batch of a desired gas mixture is loaded into an OP cell (which contains a quantity of AM) and is heated and optically pumped with a laser; once the gas is hyperpolarized, OP is stopped and the gas is transferred to the sample (usually after the cell has cooled to condense the AM); alternatively, multiple batches may be systematically polarized and collected to accumulate the HP gas prior to transfer. In a continuous-flow device,[44] a desired gas mixture is allowed to flow from its source continuously through a heated cell while it is irradiated by the laser; the flow rate is chosen to allow sufficient average residency of noble gas atoms in the cell to enable the gas to be hyperpolarized "on the fly". The HP gas mixture can then either be directed into the sample or a cryo-condenser (to collect the otherwise-dilute HP noble gas and deliver it purely and with high density, following sublimation[44a]).

All of the noble gas isotopes are amenable to the stopped-flow design[38, 43h, i, 45], whereas the relatively high spin-exchange rates and facile cryo-storage of ^{129}Xe's polarization[46] make it the best choice for use in a continuous-flow device. Both device designs have evolved considerably over the years, achieving ever-greater gas polarizations and production amounts/throughputs—benefiting in particular from the advent of compact, high-power, relatively low-cost light sources embodied by spectrally-narrowed laser diode arrays.[40, 43e, g, 44f, 47]

2.2. Other Methods for Hyperpolarizing Noble gases: MEOP, "Brute Force", and DNP

In addition to SEOP, HP noble gases can be prepared by metastability exchange optical pumping (MEOP), "brute force", and dynamic nuclear polarization (DNP), and we briefly describe these approaches here.

In MEOP,[48] an electrical discharge is used to create metastable (electronically excited) atoms in a dilute gas. The unpaired electrons of these metastable atoms can be spin-polarized via optical pumping with a laser. The angular momentum of the electron spin may then be transferred to the nuclear spin of another gas atom in the cell during a metastability-exchange collision. The process is allowed to continue until a bulk nuclear spin polarization develops across the cell. Finally, a pump is used to compress the HP gas to a sufficient density prior to use.[49] MEOP works well for ^{3}He[48] and has been highly effective at producing clinical-scale amounts for biomedical imaging experiments (e.g. [50]); MEOP is generally less effective for the heavier noble gas isotopes because of stronger relaxation mechanisms.[51]

Next, to understand the so-called brute-force (BF) approach, one should first consider the relation determining the equilibrium ("thermal") nuclear spin polarization (for *I*=1/2 nuclei):

$$P_{\mathrm{N}}^{\mathrm{eq}} \doteq \tanh\left(\frac{\gamma\hbar B_0}{2\mathrm{kT}}\right),$$

where γ is the nuclear gyromagnetic ratio, B_0 quantifies the strength of the magnetic field, T is the absolute temperature, $\hbar$ is Planck's constant divided by 2π, and k is Boltzmann's constant. At room temperature and in a typical superconducting magnet, P_N^{eq} will be ~10^{-5}-10^{-6}. Thus, if the sample temperature were lowered to milli-Kelvin temperatures (and enough time were allowed for the nuclear spins to relax to their new equilibrium conditions), the nuclear spin polarization would exceed 10%. Although the approach can be time consuming, such BF approaches have used ^{3}He/^{4}He dilution refrigerators to polarize the nuclear spins in different substances, including noble gases.[52]

Finally, noble gases can also be hyperpolarized via DNP.[53] Here, the approach is essentially the same as that of dissolution DNP (d-DNP), introduced by Golman and co-workers in 2003.[1c] Briefly, the approach requires the substance to be hyperpolarized (here, ^{129}Xe) to be mixed in a glassy frozen matrix containing molecules with unpaired electron spins (e.g., a stable radical or a photoinduced, non-persistent radical[53c]). With the matrix placed at very low temperatures (~1 K) and at high magnetic field (several T), the unpaired electrons obtain a near-unity spin polarization. The matrix is then irradiated with microwaves in order to drive the high spin polarization to surrounding nuclei in the matrix, allowing a high bulk nuclear spin polarization to accumulate over time. The matrix is then rapidly warmed, sublimating the HP xenon as a pure gas—hence the name "sublimation DNP" given for this approach.[53b] Using DNP, polarization values of ~30% have been achieved in ~1.5 hr,[53b] despite identified issues with a spin-diffusion bottleneck between electron and ^{129}Xe spins.[53a] Although the amounts and polarization values achieved thus far with DNP are not as high as corresponding values achieved with SEOP, the advantages are the increasing availability and general applicability of dissolution DNP polarizers in biomedical facilities—including Oxford's HyperSense[1c] and more recently, GE Healthcare's SPINlab.[54]

2.3. The Rise of Magnetic Resonance Applications of Hyperpolarized Noble Gases

Prior to finding their way into magnetic resonance, HP gases found their first applications in fundamental physics experiments (work that of course continues, see for example, Refs. [55],[56]). And although the portions of this Mini-Review that are dedicated to HP noble gases are largely concerned with biomedical applications of ^{129}Xe, the first MR applications actually involved studies of materials (as well as investigations of the use of HP ^{129}Xe as a *source* of hyperpolarization for other spins).

Soon after the demonstration of ultra-long ^{129}Xe relaxation times for frozen solid xenon,[46] Pines and co-workers used HP ^{129}Xe

NMR to probe the surfaces of powdered substances[43a] (and high-field gas-phase spectroscopy was also demonstrated by performing SEOP within an NMR magnet[42a]). Soon afterwards, the exquisite sensitivity of the ^{129}Xe chemical shift was investigated for probing surfaces of a number of porous materials and particles[57]—as was the ability to transfer the ^{129}Xe hyperpolarization to the nuclear spins of other substances.[58] The advent of continuous-flow production of HP ^{129}Xe[44a] was soon applied to greatly facilitate studies of materials surfaces,[59] including under conditions of magic angle spinning.[60] Since that work, HP xenon has been used to study diffusion in confined spaces or porous media[61],[62],[63]; image such systems as a function of gas flow[64] or ^{129}Xe chemical shift[65]; or spectroscopically probe single-crystal surfaces[66], liquid crystals,[67] or combustion processes.[68] However, the greatest body of materials-related work has concerned the effort to probe void spaces and surfaces in microporous or nanoporous materials with HP ^{129}Xe, thereby providing information about pore size, pore shape, and gas dynamics in: nanochanneled organic, organometallic, and peptide-based molecular materials[69] (including in macroscopically oriented single crystals[70]); multi-walled carbon nanotubes[71]; gas hydrate clathrates[72]; porous polymeric materials and aerogels[73]; metal-organic frameworks[74]; calixarene-based materials and nanoparticles[75]; organo-clays[76]; mesoporous silicas[77]; and zeolites and related materials[78] — efforts that have been aided by computational studies of xenon in confined spaces (e.g., Refs. [79]). For a more in-depth review of HP ^{129}Xe in microporous and nanoporous materials, see Ref. [80].

Indeed, ^{129}Xe has found the widest NMR/MRI application of the HP noble gases—a fact that is at least partially due to its significant natural abundance (26.44%) and ready recoverability from air during oxygen production. While ^{3}He does have the advantage of a roughly three-fold greater gyromagnetic ratio, its weak chemical shift dependence and lack of significant interaction with other substances make it a poor probe of other substances. More importantly, the lack of natural abundance (most ^{3}He comes from tritium decay) will limit the future use of this isotope for wide-scale magnetic resonance applications.[81] The rapid relaxation suffered by the quadrupolar isotopes (^{21}Ne, ^{83}Kr, and ^{131}Xe) presents a challenge for most HP NMR applications, although as pointed out by Meersmann and co-workers, the quadrupolar interaction also endows a unique sensitivity of HP ^{83}Kr to surface chemistry and local geometry that can be complementary to the information provided by ^{129}Xe chemical shift – a feature that can prove useful for probing porous materials, lung tissues, and other systems.[37, 68b, 82]

3. Clinical Application of Hyperpolarized Xenon-129 MRI

HP xenon-129 MRI (^{129}Xe-MRI) is an MRI modality first developed in 1990s for enhanced lung imaging of ventilation and perfusion and regional information on gas exchange. It has been used to image patients with a number of respiratory diseases, including asthma, COPD, and pulmonary fibrosis. In addition to its use in disease assessment and long-term management, *in vivo* gas-phase ^{129}Xe-MRI has the potential to provide imaging biomarkers of drug efficacy, which could be used to stratify treatment, improve patients' quality of life, and cut down healthcare costs. It can also be potentially employed by pharmaceutical companies to speed up decision-making in proof-of-concept studies in drug development.

3.1. From Mice to Men

Identified by British chemists William Ramsay and Morris Travers in 1898[83] (following their discovery of neon and krypton a few months beforehand), xenon is a colorless and odorless noble gas. Xenon initially captured the attention of clinicians as a general anesthetic agent when Albert Behnke, a US Navy physician, investigated the cause for 'drunkenness' observed in deep-sea divers.[84] Interestingly, Behnke also happened to be the clinician who had studied the anesthetic effects of nitrogen and helium in humans.[85] It was Lawrence *et al.*,[85] who first published experimental data on the general anesthetic effects of xenon with mice as their test subjects. It took clinicians 5 years to put xenon to use in clinical settings,[86] and xenon has continued to be used as a general anesthetic since.

3.2. The Motivation for Hyperpolarized Xenon-129 MRI

The next major clinical application of xenon-129 came in 1994 in the form of its use as an inhalational contrast agent for magnetic resonance imaging (MRI).[87]

Plain radiograph and computed tomography (CT) are currently the main modalities used to image the lungs in clinical settings. Despite their ability to provide detailed anatomical data, in particular with high resolution CT, their main drawbacks are the risks involved with repeated radiation exposure and the inability to provide physiological information on regional lung function. Although conventional MRI has been a game-changer in both neuro and hepatic imaging, its dependence on the protons of water molecules in tissue to provide nuclear magnetic resonance (NMR) signal[87] has meant that it is of little value in imaging the lungs due to poor image quality because of three factors: 1- low proton abundance within the lung parenchyma, 2- air-tissue interface causing magnetic field heterogeneity, and 3- image degradation secondary to cardiac and respiratory motion.[88]

The NMR signal strength of a given species depends on its nuclear spin, *i.e.* polarization, and the volume of the element. Except for those in water and fat, the concentrations of all other protons and nuclear species are too low to be of use in conventional MRI. However, hyperpolarization can be used to overcome the otherwise low detection sensitivity for low-concentration spins. For example, by delivering HP ^{129}Xe to excised mouse lungs, Albert and colleagues were able to obtain improved MR lung images compared to those obtained with conventional MRI.[87]

3.3. Hyperpolarized Xenon-129 MRI — There and Back Again

HP xenon-129 MRI of human lungs, which are obviously much larger than those of mice, proved challenging; it took physicists three years following Albert's paper in 1994 to be able to publish data on human studies.[89] The challenge was due to the need to produce much larger quantities of HP ^{129}Xe and to achieve adequate levels of polarization. Furthermore, conventional MR imaging sequences had to be modified as the polarization of the noble gas is non-renewable, and some polarization is lost every time an MR excitation pulse is applied.[90] These issues led to a shift in interest from ^{129}Xe to helium-3 (^{3}He), a fellow noble gas, whose larger gyromagnetic ratio and larger achievable polarization compared to ^{129}Xe at the time allowed for better signal intensity and image resolution for a given amount of HP gas.[91]

Interest in ^{129}Xe was reignited in the early 2010s; this resurgence was due to the fact that contrary to ^{129}Xe, which is naturally occurring, ^{3}He is a byproduct of tritium decay. ^{3}He had become scarce as the US sequestered ^{3}He for ^{3}He-based neutron detectors for national security, leading to extremely low availability of ^{3}He for scientific research and an exponential rise in its price.[91b] As a result, it was unlikely that ^{3}He-MRI would become a routine imaging modality in clinical settings, and so interest in ^{129}Xe-MRI was rekindled.

3.4. Safety & Tolerability Profile in Patient Groups

Over the past two decades, ^{129}Xe-MRI has been improved and utilized in imaging a wide range of respiratory diseases, including asthma,[92] chronic obstructive pulmonary disease (COPD),[92b, 93] cystic fibrosis (CF),[92a] and pulmonary fibrosis.[94] Studies specifically designed to investigate the safety and tolerability of ^{129}Xe-MRI have not shown major common side effects in various patient groups, including those with asthma,[92a] and mild-moderate COPD,[92a, 95] with light-headedness of very short duration as the main reported minor side effect.

3.5. Ventilation Imaging

Ventilation imaging provides valuable clinically relevant information relevant to regional lung function. Regions with normal ventilation typically appear bright and homogenous on ^{129}Xe-MRI, and in a healthy subject with normal lung function, both lungs show relatively homogenous ventilation except for two regions (as seen in Figure 2 and discussed in Figure 2 caption). In those with diseased lungs where regional ventilation is impaired, the abnormal regions will appear darker; these regions are called 'ventilation defects'.

Compared to healthy volunteers, ^{129}Xe distribution has been shown to be regionally heterogeneous with ventilation defects in a number of different patient groups, including those with asthma, COPD, and CF.[92a, 93c, d] Ventilation imaging has also been shown to correlate with spirometry [93c] and CT findings [96] in patients with COPD.

Additionally, ventilation imaging has been used to try and assess the efficacy of drug therapy. Studying the impact of salbutamol in patients with asthma, Parragra's group [92b] has reported a significant reduction in ventilation defects after salbutamol administration.

Hence ^{129}Xe-MR ventilation imaging, although appearing simple, can be used to not only assess disease, but to also assess drug efficacy and monitor disease progression.

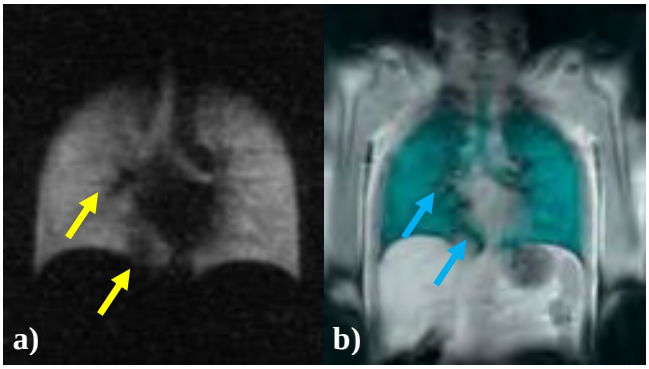

Figure 2. ^{129}Xe-MRI of a healthy volunteer. a) Coronal plane 25 mm slice ^{129}Xe-MR ventilation image of a healthy adult male, with ^{129}Xe appearing bright. The upper airways are delineated. b) Coronal plane 25 mm slice fused ^{129}Xe-MR ventilation and proton co-registration image, with ^{129}Xe appearing green. The two black regions pointed out in the fused image (yellow arrows) are due to a diaphragmatic eventration and pulmonary vasculature, clearly defined on the fused image (blue arrows). J. Thorpe, B. Haywood, M. Barlow, S. Safavi & I. Hall - University of Nottingham (Unpublished work).

3.6. Diffusion Imaging

The apparent diffusion coefficient (ADC) of gas within lung is a function of alveolar size and geometry. This can be assessed using ^{129}Xe-MRI to characterize pulmonary microstructure at the alveolar level, as seen in Figure 3.

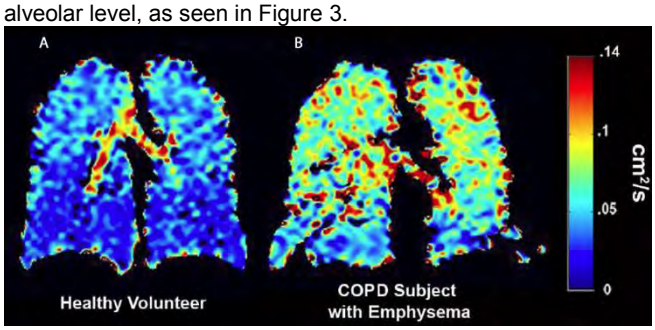

Figure 3. ADC map of a healthy volunteer and a patient with COPD. a) Healthy volunteer with a low mean ADC of 0.037±0.021 cm^{2}/s, indicating normal alveolar microstructure. b) Patient with COPD with high ADC values (0.068±0.028 cm^{2}/s) in the parenchyma, indicating alveolar destruction. Reproduced with permission from Ref. [95] © John Wiley & Sons, Ltd., 2011.

^{129}Xe-MRI derived ADC mapping has been shown to correlate well with pulmonary function tests,[93d, 95] including total diffusing capacity for the lung (TLco). This is of important clinical significance, as it clearly illustrates the ability of ^{129}Xe-MRI to provide regional quantitative lung function data. In addition to its potential use in disease diagnosis, monitoring and assessing therapeutic drug efficacy, diffusion imaging can also be used to

plan surgery, including tumor resection and lung volume reduction surgery for emphysema, as it can aid prediction of post-surgery lung function. The predicted post-surgery lung function is currently calculated using ventilation or perfusion scintigraphy and quantitative CT; however, there is a risk that scintigraphy, the most commonly used imaging modality, may underestimate post-operative lung function,[97] thereby, preventing the patient from undergoing potentially curative surgery.

3.7. Dissolved Phase Imaging

^{129}Xe (in contrast to ^{3}He) is highly lipophilic and soluble in biological tissues and thus is able to provide information on gas exchange and pulmonary perfusion particularly interesting in the context of functional lung imaging.[98] It is the associated persistent exchange of ^{129}Xe between the gas and dissolved compartments, each with its own different resonance frequencies, that is central to assessing gas exchange using ^{129}Xe-MRI.[99] Therefore, combined imaging of the gas phase ^{129}Xe and the dissolved phase ^{129}Xe would permit ventilation/perfusion (V/Q) imaging—and consequently a more direct mapping of lung function.[87] Hence, although ^{129}Xe-MRI initially lagged behind ^{3}He-MRI, developmentally, ^{129}Xe-MRI is likely to be the pragmatic HP noble gas MRI modality of choice.

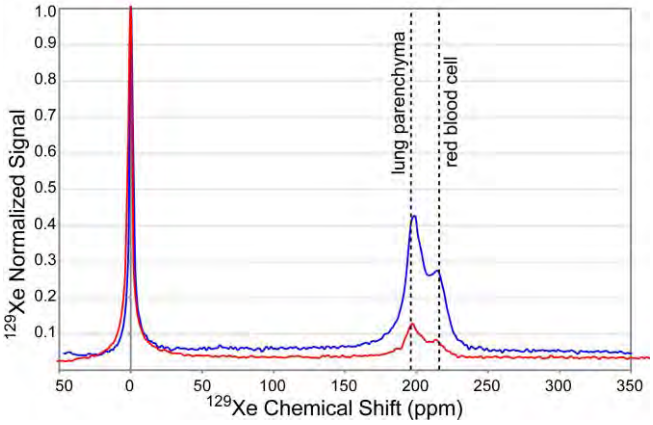

Figure 4. ^{129}Xe NMR spectra recorded from two healthy volunteers. Two dotted lines have been placed to represent the expected dissolved state peaks, the left most line representing the expected ~196 ppm lung parenchyma peak, and the right most line representing the expected 216 ppm red blood cell peak. S. Hardy, B. Haywood, M. Barlow, S. Safavi & I. Hall - University of Nottingham (Unpublished work).

Although the majority of the inhaled ^{129}Xe remains in the airspaces, where it exhibits its primary gas-phase resonance, a portion dissolves in alveolar septa and crosses the alveolar-capillary barrier to dissolve in the blood. The resulting shift in the resonance frequency leads to the appearance of two additional distinct resonances: 1- the barrier resonance, and 2- the hemoglobin-associated ^{129}Xe resonance, as seen in Figure 4 (We note the intensity differences between the two spectra are due primarily to the variation in the amount and speed at which hyperpolarised xenon gas was inhaled by the two volunteers. As volunteers became more familiar with the breathing protocol, the improvements in both ventilatory image quality and dissolved phase signal/noise were noted). This transfer pathway is identical to that followed by oxygen; therefore, in addition to being a ventilation probe, ^{129}Xe is also a gas diffusion transfer probe.[94a]

The signal intensity of the dissolved phase ^{129}Xe is approximately 2% of that remaining in the alveolar spaces, which presents a challenge to obtaining good quality images.[94a] However, as the alveolar space, alveolar septa, and capillary blood are in dynamic exchange, it is possible to use nearly all of the inhaled gas to generate 3D images of dissolved ^{129}Xe in a single breath-hold, as demonstrated in a number of studies.[94a, 100]

Another challenge is to distinguish between xenon dissolved in the alveolar septa and that dissolved in the blood. Various teams have used the chemical shift and the change in resonance frequency to distinguish xenon in these two compartments[98a, 101] as the dissolved-phase ^{129}Xe signal splits into two distinct peaks in alveolar septa and blood. These methods, known as the Xenon Polarization Transfer Contrast (XTC)[98a, 101b, c] and the Model of Xenon Exchange (MOXE),[101a, d, e] have been assessed in healthy volunteers[102] and patients with obstructive lung disease,[102a] with promising results.

Further testing these methods, Kaushik *et al.*[94a] hypothesized that there will be a reduction in ^{129}Xe signal intensity in the hemoglobin: alveolar septum ratio in patients with idiopathic pulmonary fibrosis (IPF), due to the thickening of the alveolar septa in this condition. MR spectroscopy was used to demonstrate the change in signal intensity in patients with IPF compared to healthy volunteers. The ratio was significantly lower in the IPF group compared to the healthy volunteer group, due to a 52% reduction in the hemoglobin signal and a 58% increase in the alveolar septa signal. There was a strong correlation between the hemoglobin: alveolar septum ratio and TLco. Therefore, this technique appears to provide a non-invasive measure of diffusion limitation and gas transfer impairment.

These findings suggest that ^{129}Xe-MRI has the potential to detect subtle lung function deterioration before irreversible structural changes become apparent, providing clinicians with the chance to offer therapy (when available), at an earlier stage in order to reverse, halt, or delay disease progression.

3.8. Neuroimaging

^{129}Xe-MR brain imaging is emerging as a distinct possibility. Just as xenon can be used as a gas exchange probe due to its ability to dissolve across the alveolar-capillary barrier, it can also be used as a cerebral blood flow (CBF) probe, as it can cross the blood-brain barrier and accumulate in the brain.[103] First used in its non-polarized form for CBF measurement using CT in 1982,[104] Swanson *et al.*[105] were the first group to publish data on brain MR imaging using HP ^{129}Xe as an inhaled neuroimaging contrast agent, albeit in rats. Animal studies have continued over the past two decades, using HP ^{129}Xe as both an inhalational[106] and injectable contrast agent.[107]

Diseased states have also been imaged in the rat model. Xenon signal in the brain is proportional to CBF, hence a decrease in the signal is expected to occur in areas of decreased CBF, such as those expected in ischemic stroke. Working on this principle, Zhou *et al.*[108] created a rat model of cerebral ischemia by using an intraluminal suture to occlude the middle cerebral artery, and demonstrated ^{129}Xe-MRI is able to detect the hypo-perfused area of focal cerebral ischemia, which was also confirmed on biopsy. Mazzanti *et al.*[109] further demonstrated the capacity of ^{129}Xe-MRI for functional neuroimaging by inducing pain in the rat's forepaw, and obtaining ^{129}Xe-MR images, which showed 13-28% increase in signal compared to the pre-stimulus images; these regions of increased signal corresponded to areas previously demonstrated by conventional functional MRI (f-MRI) as being activated by a forepaw pain stimulus.

It remains to be seen whether ^{129}Xe-MR neuro-imaging is feasible in humans and of value but developmental work is on-going.

3.9. Conclusion

Biomarkers of disease can be classified into diagnostic, prognostic, and theranostic. The ideal biomarker encompasses all groups, and ^{129}Xe-MRI has the potential to provide diagnostic, prognostic and theranostic biomarkers.

4. Brown-Fat MRI using Dissolved Hyperpolarized ^{129}Xe

For biological MR applications, one of the most interesting properties of HP xenon is its high tissue solubility and its chemical shift sensitivity to its molecular environment. However, MR imaging and spectroscopy applications of dissolved-phase HP xenon have been limited to brain and lung tissues (as described in the sections above), as the concentration of dissolved-phase xenon in other tissues is rarely high enough to yield good signal after the typical single breath-hold protocol used for human studies. Neglecting nuclear spin relaxation and magnetization loss due to NMR pulsing, the time dependence of xenon concentration in tissues $C_i(t)$ is well described by the Kety-Schmidt equation:[110]

$$C_i(t) = \lambda_i C_a \left(1 - e^{-\frac{F_i}{\lambda_i}t}\right),$$

where λ_i, is the xenon partition coefficient between tissue and blood, C_a is the arterial concentration of the inert gas, and F_i. is the blood flow to the tissue of interest. For most tissues, λ_i, which determines both the maximum concentration achievable in a given tissue and the time it takes to achieve maximum concentration, is close to unity.[111] However, F_i, which also determines wash-in rate, varies widely. For example, blood flow to the brain is very high (~0.5 L/min/kg) and the maximum xenon concentration in this tissue can be reached after a few seconds from the beginning of gas inhalation. On the other hand, while the solubility of xenon in fatty tissues is almost 20 times higher than in blood, because of the low tissue-perfusion (~0.01 L/min/kg), saturation can only be reached after several minutes. For HP ^{129}Xe gas, this is a clear limitation, as gas depolarization would limit the amount of detectable signal even under continuous HP xenon inhalation.

It was recently shown that the intensity of the xenon dissolved-phase signal could reach much higher levels than in the brain in a tissue called Brown Adipose Tissue (BAT).[112] Brown adipose tissue is a fatty tissue found in most mammals, including humans, and its primary function is to generate heat through a process called non-shivering thermogenesis.[113] During stimulation of non-shivering thermogenesis in this tissue, intracellular triglyceride oxidation is decoupled from ATP production so that triglycerides are mainly burned to produce heat. To support this metabolic activity, BAT is richly vascularized. During non–shivering thermogenesis, tissue perfusion increases by several fold as blood flow is needed to support the tissue's oxygen demand and to quickly dissipate the heat produced.

Aside from its thermoregulatory function, BAT has recently gained a great deal of interest because of its presumed role in the regulation of body weight and blood glucose level. For example, a series of studies in rodents have clearly shown that BAT function can directly regulate body weight and improve insulin sensitivity.[114] However, the detection of this tissue still remains a challenge, especially in humans,[115] where it is sparsely distributed and not easy to detect by standard MR techniques. In the paper by Branca *et al.*,[23] a strong enhancement of the intensity of the xenon-dissolved phase signal was reported in mice inhaling HP ^{129}Xe right after stimulation of non-shivering thermogenic activity in BAT, an effect which was ascribed to the strong enhancement in blood flow to BAT.[116] Blood flow to this tissue during stimulation can reach values as high as 5 L/min/kg,[116] considerably reducing xenon wash-in rate and allowing it to reach an in-tissue concentration of 10s of mM. Since the increase in blood flow is specific to brown fat cells, background free maps of this tissue could be generated.

More interestingly, it was also shown that xenon chemical shift information can provide a measure of the relative tissue hydration and tissue temperature. Specifically, two major peaks were observed in these studies. One signal, at ~197 ppm, corresponding to xenon dissolved in cell cytoplasm/blood, and one signal corresponding to xenon dissolved in the lipid droplets of the tissue (~190 ppm), and these signals are challenging to separate in mice). The lipid-dissolved peak was shown to have a temperature-sensitive chemical shift (-0.2 ppm/°C), which enabled direct measurement of the increase in tissue temperature (Figure 5) during non-shivering thermogenesis.[23] In addition, during non-shivering thermogenesis, a relative decrease of the lipid-dissolved phase peak was observed with respect to the cytoplasm/blood peak, yielding direct evidence of this tissue's oxidative metabolism of internal triglycerides.

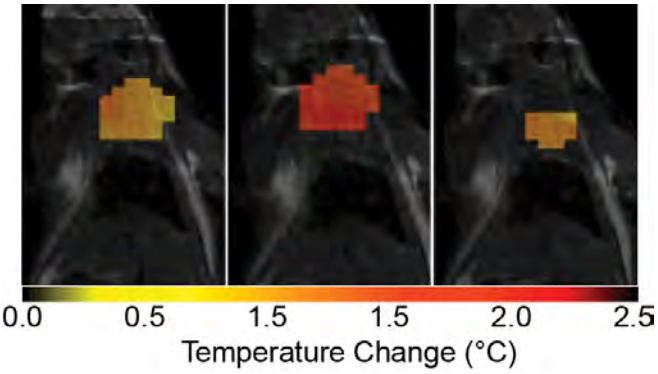

Figure 5. ^{129}Xe brown adipose tissue (BAT) temperature map overlaid on a sagittal ^{1}H image. These temperature maps were obtained by using the lipid-dissolved xenon signal as a temperature probe. The temperature coefficient of the lipid-dissolved xenon chemical shift was measured to be -0.2 ppm/°C.

More recently, the feasibility of BAT detection in humans during a single breath hold of HP xenon was demonstrated, with validation by FDG-PET.[117] As in mice, a strong increase in the lipid dissolved xenon signal was seen in the same glucose-avid area of the supraclavicular fat depot. More interestingly, xenon spectra showed, in addition to the lipid-dissolved phase peak, a nearby peak around 200 ppm that was attributed to xenon dissolved in red blood cells (RBCs), a signal that provided direct evidence of the strong increase in tissue blood flow as the main drive for the increase in xenon tissue uptake.
By being a highly vascularized fatty tissue, BAT is clearly an easy target for the lipophilic xenon. In this case, HP ^{129}Xe gas MRI is a “one-stop shop” for human BAT studies as it is capable of providing both morphological and functional information.

5. ^{129}Xe Cages and Hyper-CEST MRI

5.1. Bound xenon and molecular hosts

In addition to the NMR study of HP Xe in the gas phase and the studies of tissue-dissolved Xe as described above, the affinity of xenon to reside in hydrophobic pockets enables additional insights, This phenomenon made xenon a tool for exploring binding sites on protein surfaces[2c] with some effort being put on spin polarization transfer to nuclei in nearby residues that form the catalytic site of enzymes. Hence, detection of proton signals with and without adding HP nuclei could identify the pocket-related residues.[111] Xe NMR spectra themselves can also show signals indicative of bound atoms. Such a population could either cause a shift of the dissolution peak or a distinct signal given the exchange rate would fall into the right regime.[112] An example are red blood cells[113] where the signal of “bound” Xe is ascribed to the interaction with hemoglobin.[118] Several experiments first used lyophilized protein powder samples, *e.g.* of lipoxygenases.[119] NMR of dissolved Xe has been applied to identify binding pockets of lipid transfer protein,[120] and for observation of conformational changes in maltose binding protein,[121] and chemotaxis Y protein.[122] Besides specific site affinity for native structures, protein engineering also allowed for the design of conformation-sensitive binding pockets as demonstrated with the ribose binding protein.[123]
The binding of Xe to synthetic hosts where the cavity has a simpler design than in proteins can be even more pronounced. α-cyclodextrin[124] still comes with fast exchange but cucurbit[n]-urils[125] (CBn, n = 5,6) show distinct peaks for bound Xe as well as cryptophanes, a family of molecular cages with some members that show rather high Xe affinity (K > 10^3 M^{-1}).[126] It has been shown that different members of this group show distinct signals of bound xenon (Figure 6a). In particular cryptophane-A, CrA, is often used for conferring a distinct chemical shift to bound Xe *ca*. 130 ppm upfield from the signal of free Xe in aqueous solution.

5.2. Xenon biosensor concept

These molecular cages triggered the field of Xe biosensors where CrA is used as the NMR-active reporter being tethered to a binding unit to reveal the presence of a certain analyte (Figure 6b). The first implementation was shown with the biotin-avidin system.[127] This original publication also introduced the multi-plexing option that this concept offers. This feature is inherent to the different cage types (like in Figure 6a), but also small chemical modifications on the cage, *e.g.* deuteration,[127b] already provide a host-guest system with a different resonance frequency. Thus the combination of different hosts with different targeting units would allow for detecting multiple analytes simultaneously.

The sensing capability initially relied on a change in chemical shift and direct detection of the bound Xe signal–a concept that was later partially revised due to anticipated loss of spectral resolution in cells and live animals. Optimization for this concept included first and foremost increasing the Xe affinity and maximizing the detected chemical shifts. It is obvious that the cage size impacts the binding constant as illustrated in a comparative review,[128] but substitutions on CrA and cryptophane-111 can also increase the affinity.[129] Understanding the details behind the complexation of Xe revealed induced fit properties[130] and displacement of water[131] as contributing forces. The linker length between cage and targeting unit is a critical parameter for enabling the right balance between sufficient mobility required for narrow resonances and desired surface contact with the target to shift the signal.[132] Another relevant aspect of cryptophane-based sensors is the poor water solubility of the host. While many cages were first characterized in organic solvents, various synthesis studies succeeded to improve solubility.[129c, 131, 133]

5.3. Hyper-CEST signal amplification

The focus on the binding properties somewhat shifted with the advent of MR imaging protocols for such sensors. The low concentration of caged atoms (typically < 10^{-5} M) requires extensive signal averaging for conventional detection. Initial imaging applications were slow and limited to selected spatial dimensions.[134] To improve this situation, the chemical exchange

of Xe became an important parameter. One method for enhanced sensitivity in spectroscopy applications uses selective read-out of the caged Xe signal while the pool of dissolved Xe serves as a polarization reservoir.[135] This principle was also used in imaging[136] but has its limitations due to the timing that comes with frequency selective excitation pulses with defined flip angles.

However, inverting the roles of the participating pools, *i.e.* manipulating the dilute pool and detecting the abundant solution pool, enables significant signal enhancements. The method with selectively saturating the magnetization from the dilute pool (either through cw irradiation, or by using a train of shaped excitation pulses) and observing the signal decrease of the other pool (Figure 6c) is called chemical exchange saturation transfer (CEST), first introduced by Balaban and co-workers.[137] Combining CEST with HP nuclei was first demonstrated by the Pines lab for an imaging application and coined Hyper-CEST.[138] With Hyper-CEST, host concentrations as low as ~10^{-8} M become accessible—even for imaging.[139] The effect strongly depends on the exchange rate and therefore it can also sense system parameters like ambient temperature.[140] The spectral dimension can be recovered by performing a series of experiments in which the saturation pulse is swept over a certain frequency range (Figure 6d), thus providing another method to sense parameters that influence the chemical shift.[141] It also preserves the multiplexing option mentioned early on.

5.4. Xe Biosensor Applications in Cell Biology

The improved detection limits for imaging made it possible to address problems under more biologically realistic conditions. To date, cryptophane-based sensors that use specific binding to the target have been implemented for sensing the enzyme MMP7,[142] nucleotides,[143] human carbonic anhydrase,[144] MHC class II,[145] zinc ions,[146] the glycoprotein CD14[147] and the receptors for integrin,[148] transferrin,[149] EGF,[150] and folate.[151] An indirect binding approach was pursued through *in situ* click chemistry with metabolically labeled cell surface glycans.[152] Conformational changes of the sensor induced by changes in pH represent an approach for stimulus-induced binding.[153]

As part of these studies, cell uptake and toxicity evaluations set the bar for target concentrations of functionalized hosts.[148, 154] Xe itself passes the cell membrane[149] and does not require further attention to reach intracellular targets. Cell-penetrating peptides proved to be a valuable measure for achieving micromolar intracellular concentrations. However, they are not an absolute requirement since the hydrophobic character of CrA can mediate membrane-association and therefore enables certain types of cellular labeling.[155] Sensors with highly specific binding motifs (*e.g.*, antibodies[147, 150] or bioorthogonal reaction partners[152]) only require sample-averaged concentrations of 10^{-8} M for MRI.

Critically, the membrane affinity of CrA can be clearly identified by a *ca.* 10 ppm downfield shift for Xe in membrane-associated CrA.[156] This property proved primarily useful to identify cell-associated cages in the first live-cell experiments.[149, 155a] A closer look in combination with FRET data revealed partitioning coefficients on the order 10^2-10^3 for different membrane compositions.[157] This work also initiated a new class of Hyper-CEST experiments for investigating membrane fluidity and integrity: Due to the accelerated exchange, Xe signals from membrane-embedded cages do only differ marginally in chemical shift. However, build-up of the CEST effect can be very different depending on membrane fluidity. Comparative studies are possible when irradiating a pool of caged Xe at fixed saturation power and frequency but increasing saturation time. Evaluating the (multi-)exponential depolarization with an inverse Laplace transformation yields characteristic time constants for different environments.[158] The method called DeLTA (depolarization Laplace transform analysis) can also be used to discriminate cholesterol content and the onset of lipid domain fluctuations.[159]

5.5. Host Optimization

In order to explore a large chemical shift range of different sensors, the impact of metal ion chelation in close proximity to the cage provides a means to diversify signals.[160] Along this line, attached Gd-chelates can serve as relaxation switches for ^{129}Xe which are detachable through chemical reactions.[161] Regarding Hyper-CEST detection, improved efficiency depends on the exchange properties, which are sub-optimal for CrA. Faster exchanging hosts such as CB6[162] and CB7[163] are currently under investigation. Their binding properties for competitive guests must be taken into account but this versatile binding phenomenon on the other hand enables the option to implement detection of other guests via displacements approaches. An example is the mapping of lysine decarboxylase LDC activity where the enzymatic product cadaverine quenches the Hyper-CEST effect.[163] Related to this is an implementation of a sensor relay in which the cavity becomes accessible for Xe as soon as another host recruits the original guest from the CB6 cavity.[164] The macrocyclic host also allows construction of rotaxanes that keep the cavity blocked. Cleaving one of the rotaxane stoppers releases the thread and makes CB6 available for Hyper-CEST detection.[165] This recent design could serve as a development platform for various sensors based on cleavage reactions.

Many dilute targets will only be accessible with an increased number of CEST sites per targeting unit. For this purpose, multivalent carriers with 10^2 – 10^3 Xe hosts will be the right tool. They have been implemented with scaffolds such as bacterial phages,[150, 166] viral capsids,[167] and liposomes.[168] Alternatively, nano-compartments absorbing small amounts of Xe gas can be used, one example being PFOB nanodroplets.[169] The first imaging experiments with the latter substance also included the first multi-channel read-out of different host classes.[155b] Similar host compartments such as gas vesicles[170] and bacterial spores[171] will be discussed separately in the following section.

5.6. Hyper CEST analysis and data encoding

Stable and reproducible HP Xe delivery with shot-to-shot noise < 1% achieved through temperature stabilization of the pumping cell[172] allows one to further investigate the predicted line-shape

for Hyper-CEST spectra, i.e. an exponential Lorentzian.[173] Linked to this theoretical description is an approximation for the Bloch-McConnell equations that allows prediction of the build-up of the Hyper-CEST effect and quantification of the exchange parameters.[174] Comparison of hosts can then be done by using the gas turnover rate.[162b] The exchange dynamics also set the boundary conditions for maximum signal contrast and an orientation for optimum saturation parameters.[175] It is important to achieve the saturation transfer before the intrinsic T_1 relaxation dominates with its signal loss.

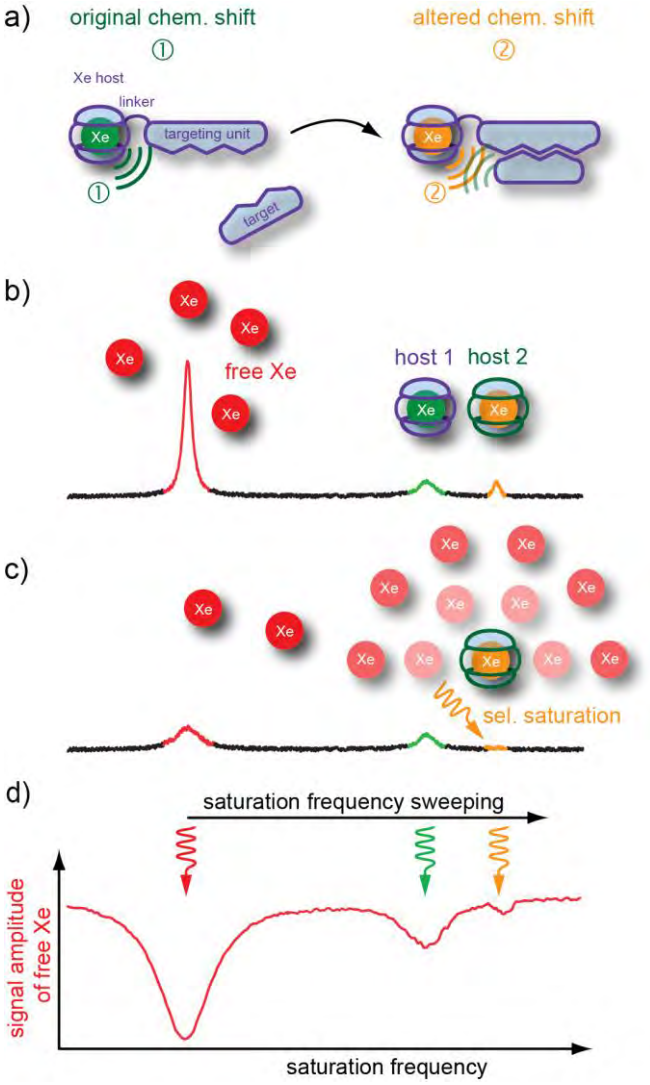

Figure 6. Caged Xe biosensor concept, and Hyper-CEST detection. a) Different Xe hosts confer different chemical shifts to the bound atoms that enable readout at distinct resonance frequencies. b) Xe inside a molecular host changes its resonance frequency upon binding to a target structure. c) Selective Hyper-CEST saturation at one of these frequencies causes a cloud of depolarized Xe around the respective host. The reduced signal from free Xe represents an amplified information from the small amount of cages. d) Sweeping the saturation pulse over a certain frequency range and subsequent observation of the magnetization from free Xe yields a Hyper-CEST spectrum for comparing the performance of different hosts.

For imaging, the CEST information needs to be encoded as fast as possible. Fast imaging sequences can replace the original point-wise encoding[138] given sufficient magnetization. Echo planar imaging (EPI) allows sub-second imaging,[139] with particular application to hyperpolarized imaging using variable flip-angle excitation in an approach called smashCEST. These rapid imaging approaches enable time-resolved studies, including the monitoring of diffusion.[139] Image quality can be improved by exploiting redundancies in the spectral domain[176] during encoding and post-processing. Spin-echo encoding is an alternative for cases where T_2* relaxation makes EPI encoding impractical.[155a]

Interest in Hyper-CEST agents has led to the development of fast strategies for gradient-encoded CEST spectra at up to 40-fold reduced scan times.[177]

6. Genetically Encodable Hyperpolarized ^{129}Xe MRI Contrast Agents

Genetically encoded MRI reporters are contrast agents that can be produced by genetically transfected cells to enable the tracking of cells, imaging of gene expression, or sensing of specific aspects of cellular function. Among the advantages of these reporters over synthetic agents are that they can be introduced into cells using established gene-delivery techniques, avoid dilution with cell division, and that a large genetic engineering toolbox can be used to modify and optimize protein-based reporter performance. Furthermore, these agents leverage the recent boom in molecular biology methods to manipulate and deliver genetic materials to animals, such as transgenic mouse lines, viral therapy, RNA interference, and genome editing.

Most existing genetic reporters have been designed for ^{1}H MRI. Examples include enzymes or transporters that can act on synthetic contrast agents,[178] proteins that naturally contain paramagnetic metals, including ferritin,[179] MagA,[180] MntR,[181] tyrosinase,[182] and cytochrome P450,[183] and diamagnetic CEST agents such as lysine rich-protein,[184] human protamine sulfate[185] and proteins that alter water diffusivity in tissue.[186] Comparatively fewer contrast agents have been designed for heteronuclear MRI, all of them based on enzymatic or transporter interactions with ^{19}F compounds,[187] HP ^{13}C compounds,[187c, 188] or ^{31}P substrates.[189] A major challenge of all of these agents is their relatively low molecular sensitivity, typically of the micromolar or higher order, which limits their range of *in vivo* applications. Several excellent reviews have been written on these classes of MRI reporters.[190]

Given the sensitivity gains of HP ^{129}Xe MRI and in particular HyperCEST, there is a strong incentive to develop genetically encoded MRI reporters acting on xenon. However, this prospect is challenging due to the weak interaction of xenon with most proteins. Xenon-binding proteins have been identified through X-ray crystallography, wherein xenon is used as a heavy atom marker to aide in structure elucidation,[191] and NMR, wherein the ^{129}Xe chemical shift can probe proteins' confirmation and ligand binding.[192] Examples of proteins shown to interact with xenon

include myoglobin[193] and hemoglobin, maltose binding protein[112] and lysozyme[119]. These interactions are attributed primarily to enthalpic Debye and London interactions, with a smaller entropic contribution from xenon dehydration as it enters a hydrophobic cavity.[192b] Unfortunately, although protein binding was shown to shift the resonance frequency of xenon by several ppm/mM, these proteins are not suitable as ^{129}Xe-MRI contrast agents because their xenon affinities (~10 mM) would require unrealistic quantities of protein to be present to achieve significant direct contrast, while their xenon exchange rates (dissociation constant ~ 10^5 s^{-1})[193] are too fast compared to the induced xenon chemical shift ($\Delta\omega$ ~ 10^3 - 10^4 s^{-1}) to enable efficient HyperCEST contrast.

A major advance in the development of genetically encoded reporters for Xe-MRI was made in 2014, when Shapiro et al. reported that an unusual class of gas-filled protein nanostructures called gas vesicles (GVs) could produce efficient HyperCEST contrast at picomolar concentrations.[25] GVs, which evolved in photosynthetic microbes as a means to regulate buoyancy, comprise hollow gas compartments at hundreds of nm in size and possess a 2 nm protein shell that is permeable to gas but excludes liquid water[194] (Figure 7a,b). Shapiro et al. showed that GVs can interact with xenon to produce HyperCEST contrast with peak saturation approximately 175 ppm upfield from dissolved ^{129}Xe (Figure 7c,d). The large chemical shift separation enables the contrast to be extremely efficient, with a GV detection limit in the picomolar range (Figure 7e), orders of magnitude lower than comparable proton contrast agents. Furthermore, GVs formed by different species of bacteria and archaea, in which these nanostructrues differ in size and shape, produce HyeprCEST saturation at different chemical shifts, thereby enabling multiplexed imaging. In their initial study, Shapiro et al. provided proofs of concept for GVs as antibody-functionalized markers of cancer cells and as reporters of gene expression in *E. coli*. In addition to GVs, other biological structures may be able to serve as HyperCEST agents. For example, bacterial spores, a dormant cellular state comprising a multi-layered structure of ~ 1.5 μm size, were recently demonstrated for HyperCEST at a chemical shift 4.5 ppm downfield from aqueous xenon.[171]

The discovery of GVs as highly efficient biomolecular reporters for HyperCEST leads to several interesting questions and possibilities that merit further investigation. If we assume that an optimal CEST saturation can always be achieved with sufficient RF power and that the relaxation of ^{129}Xe is minimal during CEST experiment, then HyperCEST sensitivity is determined by (a) the chemical shift difference and (b) the exchange rate between the contrast-agent-bound and the dissolved ^{129}Xe spins.[195] Regarding the chemical shift, each GV has a several-attoliter gas chamber containing thousands of gas atoms or molecules, where ^{129}Xe atoms presumably experience an environment similar to gas phase, and consequently compared to the synthetic contrast agents, GV-associated ^{129}Xe chemical shift is usually closer to that of the gas phase. Intriguingly, the specific value of chemical shift appears to be genetically determined.[25] It will be interesting to study how this chemical shift relates to other genetically encoded GV properties, including their size, shape and aggregation state, and the extent to which these properties can be tuned at the genetic level. In terms of the exchange rate, when the Z spectra (*i.e.* the frequency-dependent saturation effects are visualized similar to conventional magnetization transfer spectra by plotting the water saturation (S_{sat}) normalized by the signal without saturation (S_0) as a function of saturation frequency) acquired with intact and collapsed GV are compared with those acquired with synthetic agents, both the GV-bound and the dissolved ^{129}Xe peaks appear to be broader, suggesting the exchange rate is in the intermediate regime. It will be interesting to define quantitatively the optimal RF saturation parameters for the specific exchange rate of GVs. On the molecular level, though the atomic-level structure of the GV wall has not been solved, some hypotheses have been proposed regarding the channels on the protein shell that allow gas exchange in and out of the nanostructure[194b]; it is possible that variation (natural or engineered) in the amino acid sequence of GV proteins could alter the permeability of these putative pores. Taken together, GVs present a wide dynamic range for ^{129}Xe chemical shifts and exchange rates, and these two properties are likely amenable to protein engineering for new and optimized forms of ^{129}Xe HyperCEST.

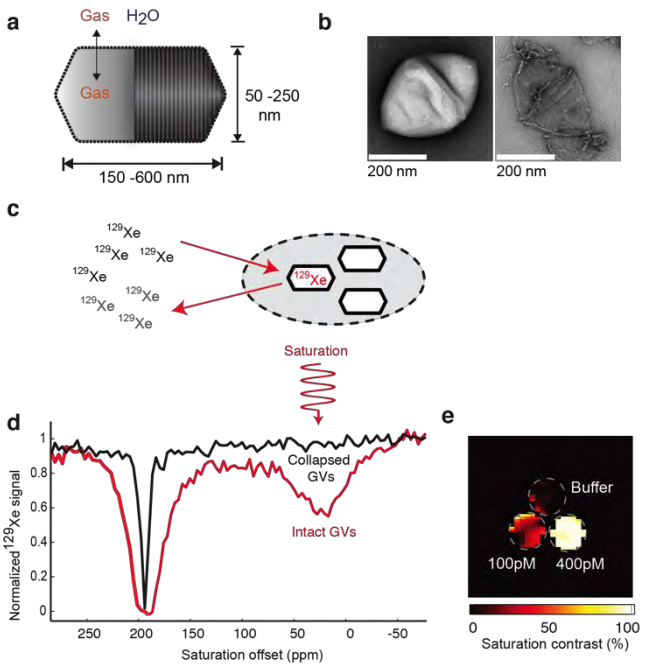

Figure 7. Gas vesicles as genetically encodable HyperCEST reporters detectable at pM concentrations. (**a**) Diagram of a gas vesicle: a hollow gas nano-compartment (solid shading) surrounded by a gas-permeable protein shell (ribbed shading). (**b**) Transmission electron micrographs of individual GVs purified from *Halobacterium* NRC-1 in their intact (left) and collapsed (right) state. (**c**) Diagram of ^{129}Xe CEST between bulk aqueous solvent (left) and GVs (hexagons) either in isolation or inside a cell (gray). (**d**) Frequency-dependent saturation spectra for intact (red) and collapsed (black) GVs. (**e**) Saturation contrast image of a three-compartment phantom containing 400 pM GVs, 100 pM GVs and buffer. Reprinted by permission from Macmillan Publishers Ltd: Nature Chemistry,[170] copyright 2014.

It is also worth noting that in addition to serving as HyperCEST reporters, GVs produce contrast in at least two complementary imaging modalities. First, they are the first genetically encodable imaging agents for ultrasound,[196] where their low density and high elasticity relative to surrounding media allows them to scatter sound waves. Secondly, their gas-filled interior, which has a different magnetic susceptibility from surrounding solution, allows GVs to produce ^{1}H MRI contrast in susceptibility-weighted imaging.[197]

The list of genetically encoded ^{129}Xe-based HyperCEST reporters has been recently expanded to include β-Lactamase by Dmochowski and co-workers.[198] As a small protein encoded by a single gene, this reporter may be easier to use in some settings than GVs, albeit with somewhat lower molecular sensitivity.

7. Parahydrogen

Hydrogen exists in two nuclear spin isomers denoted as *ortho*- and *para*- corresponding to the nuclear triplet and singlet states, respectively, where parahydrogen corresponds to the states with an even rotational quantum number *J* whereas orthohydrogen corresponds to odd values of *J*. The ratio of the two isomers is determined by the Boltzmann thermal equilibrium for the given rotational state *J*, Figure 8.[199] For a more detailed discussion of the physics and applications of parahydrogen beyond the scope of this mini-review, we refer the interested reader to the 1935 book by Farkas on hydrogen[199] or various excellent discussions.[200]

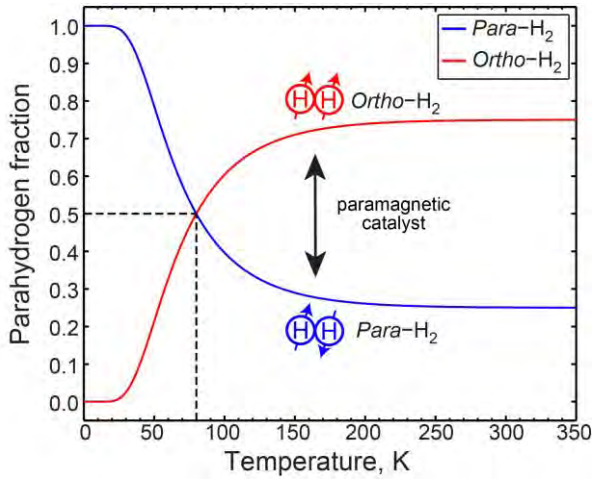

Figure 8. Parahydrogen conversion. Passage of H_2 gas over a paramagnetic catalyst, given sufficient contact time, converts the *ortho*-H_2 fraction to *para*-H_2 fraction as a function of temperature.

Importantly, conversion between the two states occurs extremely slowly due to the transition being forbidden by the selection rules of quantum mechanics, leaving only statistically unlikely naturally occurring processes of sufficient energy (radiation, molecular collisions, etc.) to foment interconversion. Therefore, after its production (and provided lack of exposure to sources of paramagnetic impurities in the storage vessel), parahydrogen may be stored for long periods before use, as the relaxation rate of the parahydrogen back to room-temperature equilibrium can be on the order of months.[201] Production rates are significantly faster, however, since as discovered in 1929 by Bonhoeffer and Harteck, the use of paramagnetic catalysts (*i.e.* activated charcoal, nickel, hydrated iron (III) oxide) promotes establishment of Boltzmann thermodynamic equilibrium between *ortho*-H_2/*para*-H_2 states for a given temperature at greatly accelerated rates. In practice, normal hydrogen gas (*i.e.* equilibrium ratio at room temperature) consisting of 75% *ortho*- and 25% *para*- isomers is passed through a paramagnetic catalyst filled chamber at cryogenic temperatures, where the equilibration to the isomer ratio governed by the Boltzmann distribution occurs. For example, a parahydrogen generator based on 77 K (obtained conveniently by a liquid-N_2 bath) yields ~50% parahydrogen mixture, whereas the designs based on cryo-chillers (*e.g.* T≤20 K) yield ≥99% parahydrogen (Figure 8).

8. Fundamentals of Parahydrogen-Induced Polarization (PHIP)

In 1986 Russ Bowers and Daniel Weitekamp proposed a method for achieving very high nuclear polarizations using parahydrogen.[7a] Dubbed PASADENA (Parahydrogen And Synthesis Allow Dramatically Enhanced Nuclear Alignment), the effect predicted strongly enhanced ^{1}H NMR signals for hydrogenation reaction products when unsaturated molecular precursors are hydrogenated with parahydrogen. Later they demonstrated the effect experimentally by hydrogenating acrylonitrile with parahydrogen using Wilkinson's catalyst.[7b] Anti-phase ^{1}H NMR multiplets were demonstrated for the reaction product, propionitrile, and for dihydride rhodium complex – the reaction intermediate. It was later realized that experimental demonstrations of the PASADENA effect had already been published,[202] but had been misinterpreted as chemically-induced dynamic nuclear polarization.[7c] PASADENA and (the later discovered) ALTADENA[203] are collectively dubbed as the process denoted as parahydrogen-induced polarization (PHIP).[11c] This seminal discovery of Bowers and Weitekamp opened up a new strategy for hyperpolarization of various compounds, and currently PHIP and its recent modification, SABRE (Signal Amplification By Reversible Exchange),[8] are used to obtain HP molecules with ^{1}H,[11c, 200b] ^{13}C,[12] ^{15}N,[13d] ^{19}F,[14] and ^{31}P[15] nuclei in a hyperpolarized state. Detailed explanation of the spin dynamics and chemical kinetics behind PHIP can be found in several comprehensive reviews.[11c, 200, 204] Here we briefly discuss the main principles of PHIP to qualitatively describe the phenomena discussed below. As an example, we take the simplest two-spin system. The two-spin system of the hydrogen molecule gives rise to four nuclear spin energy levels. As described above, three of these energy levels correspond to orthohydrogen, the state with total nuclear spin 1 (triplet state), whereas the remaining fourth energy level corresponds to parahydrogen (singlet state), the state with zero total nuclear spin. Transitions between singlet and triplet spin

states are forbidden by symmetry;[7a] and the spin 0 parahydrogen is NMR-silent.

Bowers and Weitekamp's idea was to break the magnetic equivalence of two hydrogen nuclei by using parahydrogen in a hydrogenation reaction (Figure 9a), thus, making prohibited transitions allowed. Indeed, upon incorporation of a parahydrogen molecule into an asymmetric molecular precursor, the symmetry of the *para*-H_2 molecule becomes broken. This situation strongly depends on the magnetic field at which the hydrogenation reaction takes place. If hydrogenation is performed at high magnetic field B_0 (*i.e.*, wherein the chemical shift difference between the two *para*-H_2-nascent protons, $\Delta\delta$, is much greater than the spin-spin coupling J between them ($\gamma\,\Delta\,\delta B_0 > 2\pi J$)), then the population of the singlet spin state ($\alpha\beta - \beta\alpha$) of *para*-$H_2$ is transferred to the population of spin states $\alpha\beta$ and $\beta\alpha$ of the formed weakly coupled AX spin system (PASADENA effect, Figure 9b).[7b] The NMR spectrum of the AX system populated in this way will contain four peaks grouped in two antiphase multiplets (Figure 9b). Two lines (positive-negative or negative-positive, depending on the sign of spin-spin coupling constant J) in each multiplet are separated by J Hz in the case of isotropic liquids and/or gases.[205] PASADENA-hyperpolarized organic molecules are typically manifested in ^{1}H NMR spectra as positive-negative multiplets, whereas multiplets for hydride intermediates are negative-positive, since through-electron mediated J couplings are negative for metal hydrides.[206] Interestingly, signal intensity of PASADENA spectrum is maximized when 45° (instead of 90°) pulse is applied for signal acquisition, which may be shown using density operator description of the PHIP process.[204]

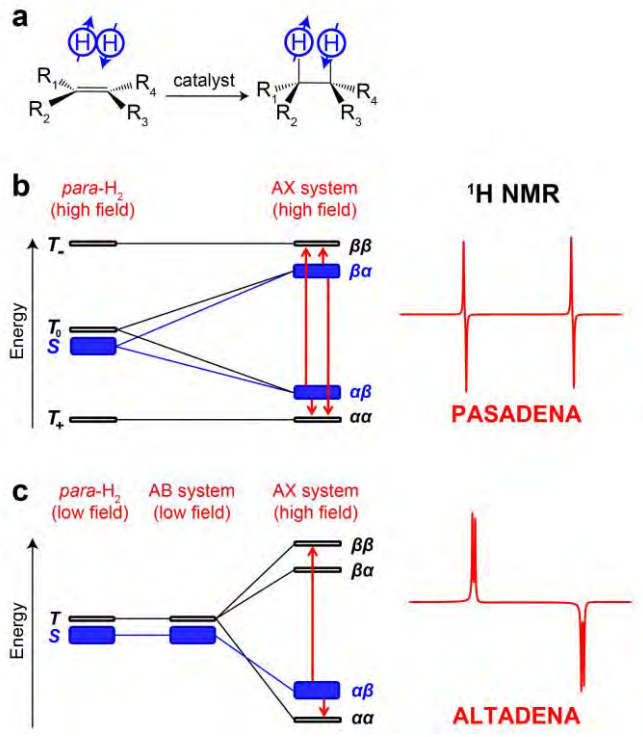

Figure 9. a) Molecular diagram of parahydrogen (*para*-H_2) addition to the substrate performed with a homogeneous or heterogeneous catalyst. b) PASADENA effect: nuclear spin energy level diagram of *para*-H_2 at high magnetic field (left), An AX spin system is formed upon pairwise addition of *para*-H_2 to the unsaturated substrate at high magnetic field and corresponding ^{1}H NMR spectrum (right). c) ALTADENA effect: nuclear spin energy level diagram of *para*-H_2 at low magnetic field (left), An AB spin system is formed upon pairwise addition of *para*-H_2 to the unsaturated substrate at low magnetic field, An AX spin system is obtained after adiabatic transfer of the reaction product from low to high magnetic field. The corresponding ^{1}H NMR spectrum is shown at right.

On the other hand, if the hydrogenation reaction takes place at low magnetic field (such that $\gamma\Delta\delta B_0 \leq 2\pi J$; *e.g.*, at the Earth's magnetic field), and afterwards the hydrogenation product is adiabatically transferred to a high magnetic field, then there is a single state that is overpopulated, *i.e.* $\alpha\beta$ *or* $\beta\alpha$—depending on the sign of the J-coupling constant between the nuclei (ALTADENA effect, Figure 9c).[203] In this case spectral pattern will consist of four lines grouped in two "integral multiplets" simply corresponding to one spin "up" and second spin "down" state (Figure 9c).

In order to be able to observe PHIP for the molecule of interest several key conditions must be fulfilled:[11c]

1. The addition of parahydrogen to the unsaturated precursor should occur in a pairwise manner. Pairwise addition implies that two hydrogen atoms from the same H_2 molecule are included in the product molecule together as a pair, thus preserving spin correlation between the two proton spins.
2. The characteristic nuclear spin relaxation time for *para*-H_2-nascent protons should be longer than the time needed to complete the pairwise hydrogenation process.
3. The magnetic equivalence of the two correlated nuclear spins should be broken during the hydrogenation[207] or in the product of the hydrogenation reaction.[7b]

If all of the above-mentioned conditions are fulfilled, the product of the hydrogenation reaction will possess a non-equilibrium population distribution of its nuclear spin energy levels owing to either the PASADENA or ALTADENA process.

One should note that the final polarization of the hydrogenation reaction product does not depend on the magnetic field strength, and the polarization obtained by PHIP in principle can reach 100% (neglecting spin relaxation and/or decoherence).[7a, 204] In principle, enhancement of the NMR signal can be as high as several thousand-fold above ordinary thermal signals from high-field NMR spectrometers and even a million-fold at low magnetic fields.

Since the hydrogenation reaction does not proceed spontaneously, the key component of the system is a catalyst (Figure 9a), which (i) enables hydrogenation reaction, and (ii) provides efficient pairwise addition of molecular hydrogen to the substrate. All hydrogenation catalysts can be classified as homogeneous or heterogeneous depending on their phase relative to the substrate. Homogeneous catalysts are present in the same phase as the to-be-hydrogenated substrate (typically, liquid phase), whereas heterogeneous catalysts are present in a phase different from the phase of the substrate (usually, a solid catalyst and a gaseous or liquid substrate). Since the first

demonstration by Bowers and Weitekamp,[7b] homogeneous catalysts have become widely used to produce PHIP, which is reasonable: it is known that hydrogenation mechanisms using metal complexes can usually provide an efficient route for pairwise hydrogen addition. For a long time, the feasibility of using *hetero*geneous catalysts for production of PHIP was rejected based on the known mechanism of heterogeneous hydrogenation, *i.e.* the Horiuti-Polanyi mechanism. According to Horiuti and Polanyi,[208] hydrogen molecules dissociate on metals (typically used as heterogeneous hydrogenation catalysts) and form a pool of randomly moving free hydrogen atoms, thus not fulfilling condition 1 (pairwise addition) above.[209] Nevertheless, it was shown that various classes of heterogeneous catalysts, *i.e.* immobilized metal complexes,[9a] supported metal nanoparticles,[28b] etc., can enable the PHIP effect. In the current mini-review both classes of catalysts are considered.

9. Gases hyperpolarized via PHIP

As mentioned in the introduction, MRI of gases suffers from poor sensitivity due to their low molecular density compounded with the low thermal polarization of their nuclear spins. These problems can make it challenging to image gas-filled void spaces due to the very low signal-to-noise ratio (SNR) and the usually long signal-averaging times, which can be prohibitive for many clinical applications. HP noble gases[210] can be used to address these issues. However, the production of HP noble gases is relatively expensive, necessitating costly hyperpolarizer equipment. Moreover, imaging of HP noble gases requires a dedicated X-band channel (for the heteronucleus of interest) and radio-frequency probe, which are not standard features of clinical MRI scanners (although they are becoming increasingly prevalent). Therefore, production of non-toxic HP proton-containing gases via PHIP could be a promising alternative that avoids the above technical requirements of HP noble gases.

9.1. Production of hyperpolarized gases using PHIP

Historically, experiments with parahydrogen were predominantly conducted in the liquid phase, wherein fluids hyperpolarized by PHIP reside in a solution along with a homogeneous hydrogenation catalyst.[200b] Heterogeneous catalysts can be used to separate the HP product from the catalyst.[29, 211] At the same time, it is also possible to produce catalyst-free HP gases by combining the main advantage of homogeneous (high selectivity) and heterogeneous catalysis (easiest catalyst separation) by using gas-liquid biphasic hydrogenation. Utilization of a homogeneous catalyst dissolved in the liquid phase for biphasic hydrogenation of unsaturated gases with *para*-H_2 allows one to produce HP gas that is free from contamination by the catalyst. In the demonstration of this approach it was shown that the reaction product can return to the gas phase while retaining a significant degree of hyperpolarization.[212] This feature significantly extends the range of gases that can be hyperpolarized. It was shown that utilization of a simple experimental procedure allows one to achieve signal enhancements of 300 for propyne hydrogenation to propylene using the bidentate cationic complex $[Rh(PPh_2\text{-}(CH_2)_4\text{-}PPh_2)(COD)]BF_4$.[212] Another approach for HP gas production is the use of homogeneous catalysts based on a judicious choice of the metal complex (homogeneous hydrogenation catalyst) in which the desired unsaturated substrate is coordinated to the metal center.[213] In that case hydrogenation with parahydrogen allows the substrate to leave the metal center and to migrate to a different phase with preservation of the spin order of the two nascent protons derived from the *para*-H_2 molecule. Indeed, it was shown that PHIP-hyperpolarized gas can be obtained in a catalysis-free regime using a chemical reaction with molecular addition of parahydrogen to a water-soluble Rh(I) complex carrying a payload of a compound with double (C=C) bonds.[213] Hydrogenation of the norbornadiene ligand leads to the formation of norbornene, which is expelled from the Rh(I) complex to the aqueous phase, but due to its insolubility in water HP norbornene quantitatively leaves the solution to the gas phase (Figure 10).[213]

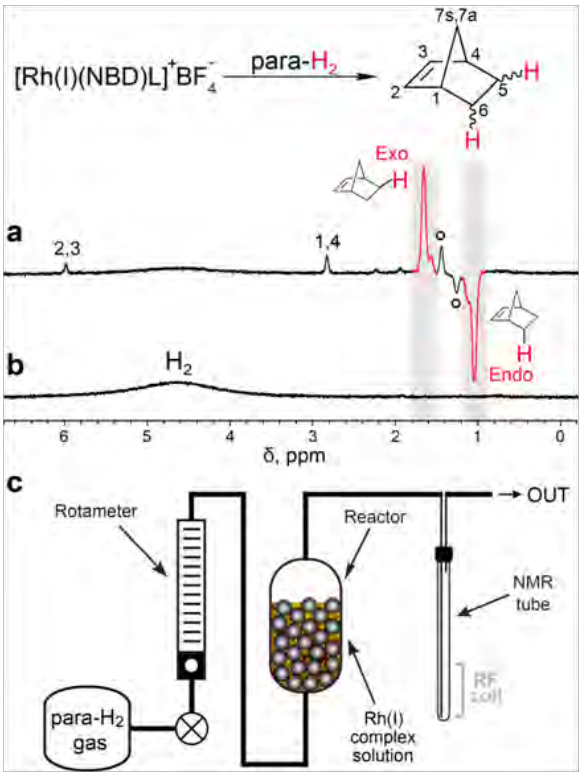

Figure 10. ALTADENA ^1H NMR spectra of a gaseous stream during bubbling of parahydrogen **(a)** and normal H_2 **(b)** through the solution of $[Rh(I)(NBD)L]^+BF_4^-$ in D_2O at 70-80 °C. The broad signal labeled "H_2" belongs to *ortho*-H_2 gas: the resonances labeled with open circles correspond to norbornane. **c)** Diagram of the experimental setup with the NMR detection performed in the high field. Reprinted with permission from Kovtunov, K. V.; et al. *Anal. Chem.* **2014**, *86*, 6192.[213]

As soon as PHIP was successfully demonstrated in heterogeneous hydrogenations over immobilized[9a] and

supported metal catalysts,[28b] the production of HP gases over these catalysts became an important area of PHIP-related investigations. Many different heterogeneous catalysts were used for the production of HP gases in the past eight years, with the aim to find the catalyst with the highest level of pairwise hydrogen addition for a given substrate.[29, 214] Without doubt the utilization of a solid catalyst allows one to produce HP gases in the continuous-flow regime by passing a mixture of an unsaturated substrate with *para*-H_2 through the catalyst layer. In this approach, hydrogenation occurs at the Earth's magnetic field and corresponds to the ALTADENA[203] type of PHIP experiment. Note that the nature of the heterogeneous solid catalyst can have a significant impact on the polarization level, and titania-supported metal catalysts were shown to exhibit larger PHIP effects compared to metals on other supports.[215] The polarization level for HP gases produced over supported metal catalysts can be several percent,[28b, 216] and it increases with the decrease in the size of the supported metal nanoparticles.[217]

9.2. MRI of hyperpolarized hydrocarbon gases

Continuous production of HP gases via heterogeneous hydrogenation paves the way to the potential practical applications for imaging of void spaces by MRI. The first experiments were related to MRI visualization of HP propane in a NMR tube with a cross-shaped partition or with a series of capillaries.[9b] For that work, a mixture of *para*-H_2 and propene gas was flowed through a reactor cell with the heterogeneous catalyst (*e.g.* Rh immobilized on titania). After that the product (HP propane gas, Figure 11) was transferred to the NMR magnet and the ALTADENA enhancement was evident in the MR images, Figure 12a.

For both model samples, detection of the NMR signal of a thermally polarized gas did not produced observable images, whereas the use of PHIP-polarized propane gas allowed one to visualize the corresponding structures of the objects used in the experiments.[9b] Importantly, the demonstrated 300-fold signal enhancement in the gas-phase MRI is sufficient to image gases with a similar spatial resolution as that in corresponding liquid-phase MRI experiments. The subsequent development of the strategies for ^{1}H MRI visualization of both hyperpolarized and thermally polarized propane gas for high-resolution MRI applications allowed one to significantly decrease the imaging time. Compared to FLASH MRI[218] (Figure 12), the use of UTE MRI[219] decreases the total imaging time significantly, down to the regime sufficient for MRI of a patient within a single breath-hold in a future clinical translation. It was shown that utilization of UTE MRI makes it possible to obtain 2D images of thermally polarized with ca. 0.9 × 0.9 mm^2 spatial resolution in *ca.* 2 s (and potentially with better resolution for HP gases).[220]

Recently, HP propane gas produced by heterogeneous hydrogenation of propene over supported metal catalysts was utilized for 3D ^{1}H MRI with micro-scale spatial resolution (625×625×625 μm^3), large imaging matrix size (128x128x32) and short (17.4 s) image acquisition time.[215a]

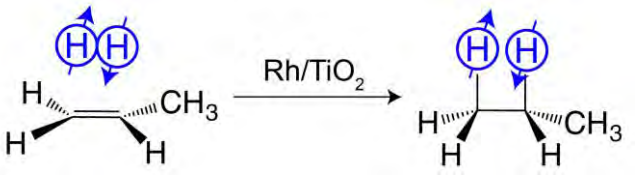

Figure 11. Heterogeneous pairwise hydrogenation of propene to propane with *para*-H_2 over Rh/TiO_2 catalyst with preservation of spin order of parahydrogen in the final HP product.

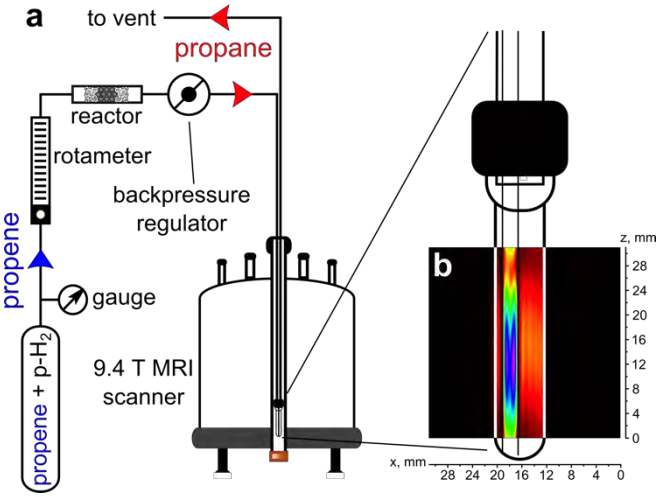

Figure 12. (a) Schematic representation of the experimental setup for using PHIP to produce HP propane via heterogeneous hydrogenation of propene with parahydrogen. (b) ^{1}H MRI FLASH image of HP propane flowing into a 10 mm NMR tube via 1/16 in. OD Teflon capillary. Note that the NMR tube is shown schematically and its length does not match the actual scale of the 2D MR image. Reprinted with permission from Kovtunov, K. V.; et al. *Tomography* **2016**, *2*, 49.[220]

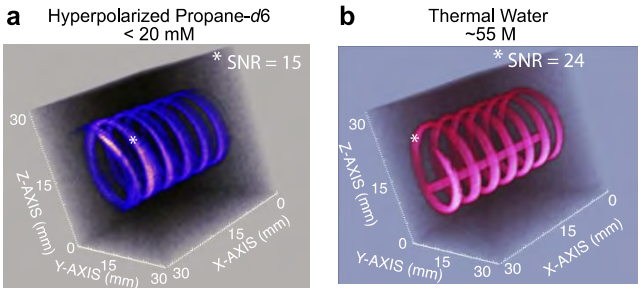

Figure 13. High-resolution 3D gradient echo (GRE) MRI at 4.7 T. a) 3D MRI of flowing HP propane gas (~20 mM concentration) with 0.5×0.5×0.5 mm^3 spatial and 17.7 s temporal resolution and 32×32×32 mm^3 field of view. b) The corresponding image of (stationary) thermally polarized tap water (55 M). Reprinted with permission from Kovtunov, K. V.; et al. *J. Phys. Chem. C* **2014**, *118*, 28234.[221]

Utilization of a fully deuterated substrate (propene-d_6) in the heterogeneous hydrogenation with *para*-H_2 permitted acquisition of a high-resolution 3D MRI image of flowing HP propane-d_6 gas with 0.5 × 0.5 × 0.5 mm^3 spatial and ~18 s temporal resolution

(Figure 13a).[221] It was shown that the signal-to-noise ratio in the 3D images of HP propane-d_6 gas (Figure 13a) and water (Figure 13b) are similar. This observation confirms that the utilization of a gas hyperpolarized by PHIP allows one to obtain MR images with quality similar to that obtained with water as the signal source.

Utilization of HP gases produced by PHIP is not limited only to void space imaging. Indeed, it was shown that a catalytic reactor positioned inside an NMR magnet can be imaged *in situ* during heterogeneous hydrogenation of propene to propane with parahydrogen.[28a] *In situ* MRI of a catalytic reaction allows one to visualize the regions in the catalyst layer where the hydrogenation reaction occurs. Importantly, based on the significant signal enhancement the velocity map for HP gas forming in and flowing through the catalyst bed was obtained.[28a]

Given the above results, PHIP is clearly becoming an important technique for signal enhancement in both fundamental, basic science and biomedical MRI investigations. Moreover, the use of PHIP to produce HP gases can be useful for their potential utilization in medical MRI applications.

10. Remote-detection MRI of Hyperpolarized Gases

MRI of gases in small voids, such as in porous media, microreactors, and microfluidic devices, suffers from particularly low sensitivity due to an additional exacerbating factor: low filling factor in the NMR coil, which may be less than 10^{-5} in some cases. While HP methods partially compensate for the low sensitivity, an additional sensitivity boost provided by alternative detection methods may be required. These methods include, for example, surface RF microcoils, RF microslots, and remote detection (RD), to name a few.[222]

In RD MRI,[223] encoding of spatial information and signal detection are performed with different coils (see Figure 14a). The encoding RF coil is a large coil around the whole sample, so that all spins can be excited. Signal detection is performed outside the sample with a much smaller and more sensitive RF coil, with an optimized filling factor.[224] The technique requires that the encoded spins are transported to the detector before the magnetization is fully relaxed, and it inflicts one additional dimension as compared to conventional MRI, because it is based on phase encoding only. Nevertheless, it provides a substantial sensitivity boost as an ultrasensitive detection solenoid may be hundreds of times more sensitive than the encoding coil.[225] Furthermore, the flow delivers spins from the different parts of the sample to the detector at different times, and this inherent time dimension can be utilized to produce time-of-flight (TOF) flow images.[226]

10.1. Time-of-flight flow imaging with HP gases

HP Xe is an ideal probe fluid in RD MRI experiments, because the T_1 relaxation time of ^{129}Xe can be extremely long, allowing correspondingly long transport times from the sample to the detector. HP Xe RD MRI has been used for imaging flow through porous materials,[223, 227] rocks,[226] microfluidic devices,[225] and wood,[228] as well as for quantifying diffusion through membranes.[229] Figure 14b shows a remarkable example of 3D TOF images of HP Xe flowing through a rock sample. The shortest TOF image (TOF = 0.27 s) shows spins that were at the top of the encoding region, because they arrived first to the detector, and the longest TOF image (TOF = 0.98 s) shows the spins at the sample bottom.

Gaseous HP hydrocarbons produced by PHIP have been used in RD MRI experiments as well.[230] T_1 values for spins of hydrocarbons are typically much shorter (~ 1 s) than that of ^{129}Xe, limiting the transport time of fluid from the sample to the detector; however, if the sample coil and the detection coil are close enough and the flow rate is sufficiently high, the experiments are feasible. Because the gyromagnetic ratio and the natural abundance of ^{1}H is much higher than for ^{129}Xe, the sensitivity in PHIP experiments may be significantly higher.

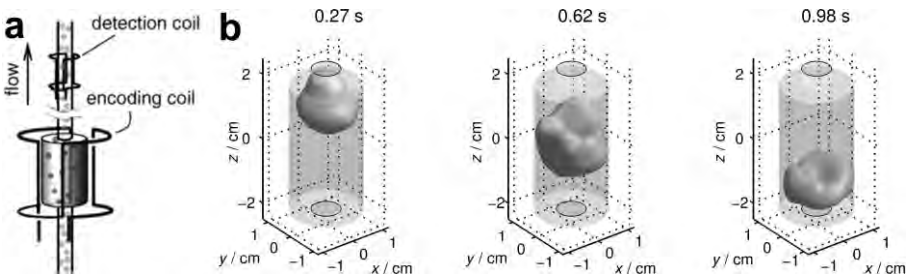

Figure 14. RD MRI of flow of HP ^{129}Xe through a rock sample. (a) The rock sample is inside a large RF coil used to encode spatial information into spin coherences, and the signal is read out by a smaller and more sensitive coil around the outlet tubing, with optimized filling factor. (b) 3D TOF images. The silhouettes represent the rock sample. TOF, *i.e.*, the time instant the signal is detected after the encoding, is shown above the images. Reprinted with permission from Granwehr, J.; Harel, E.; Han, S.; Garcia, S.; Pines, A.; Sen, P. N.; Song, Y. Q. *Phys. Rev. Lett.* **95**, 075503 (2005). Copyright (2005) by the American Physical Society.

As an example, Figure 15b shows 2D RD MR images of HP propane, which was produced by propene hydrogenation with para-H_2 over an Rh catalyst, flowing in a microfluidic capillary.[230a] Overall, the combined sensitivity gain provided by the RD scheme and PHIP was 48,000-fold, and the experiments turned out to be one to two orders of magnitude more sensitive than the corresponding RD experiments with HP Xe. Comparison of the TOF images of a gas and a liquid (Figures 15b and 15c) nicely depicts different flow behavior of these phases; laminar flow of a liquid translates the encoded liquid molecules over a large distance (Figure 15c), whereas for a gas the three orders of magnitude faster diffusion causes efficient mixing of the flow lamellas, leading to a significantly less dispersed, plug-like flow behavior (Figure 15b).[230a, b]

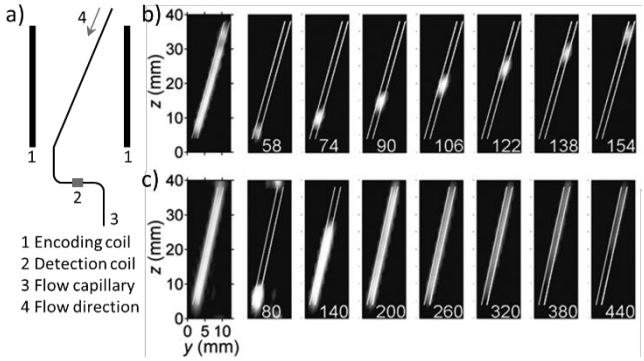

Figure 15. (a) RD MRI setup of a simplified microfluidic system consisting of a capillary leading through the encoding and detection coils. TOF RD MRI visualization of (a) HP propane and (b) water flow in the capillary (outlined in white), revealing much more extensive dispersion of liquid than that of gas molecules. TOF (ms) is shown at the bottom of the panels. The panels on the left are sums of the other panels.[230a]

Experiments with model microfluidic chips have supported the viability of the RD-PHIP approach for visualization of complex microfluidic geometries and flow quantification, Figure 16.[230a] Moreover, these experiments exposed the manufacturing imperfections of the chips. The gas flow in different channels varied in an irregular manner, and the signal amplitude profiles revealed an inhomogeneous distribution of the gas, implying that the channel depth varied from one channel to another.

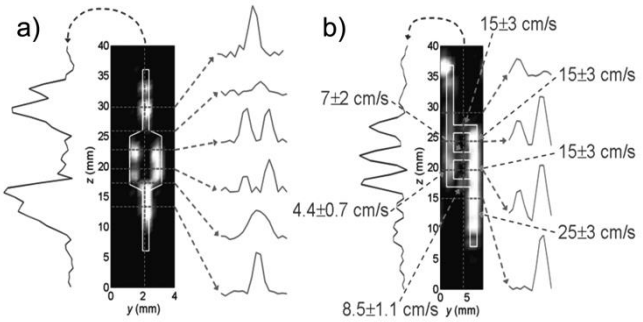

Figure 16. RD MRI of HP propane in microfluidic chips with (a) a widened channel in the middle part and (b) ladder-like channels (outlined in white). These images are the sum of the panels measured at different TOF instances, and they expose, *e.g.*, manufacturing imperfections. Flow velocities extracted from TOF data are shown in (b). Reproduced with permission from Ref. [230a] © John Wiley & Sons, Ltd., 2010.

10.2. Microfluidic reactor imaging

The natural ability of *para*-H_2 to participate in many important chemical reactions, including those performed with the use of microfluidic devices, opens an avenue for scientifically and technologically fascinating studies using HP gases. Combined RD MRI and PHIP methodologies in such studies was exemplified by the demonstration of catalytic reaction imaging of microscale catalyst layers.[230c] Tiny layers of heterogeneous Rh catalyst packed in thin capillaries (150-800 μm in diameter) served as model microfluidic reactors. It was shown that the RD-PHIP methodology can be used for visualization of mass transport and progress of gas-phase propene hydrogenation reaction inside the reactors.

The white dashed rectangles in Figure 17 highlight the locations of the catalyst layers. The accumulation of produced HP propane with the distance that gas mixture travels inside the catalyst layer is visualized by the increased signal amplitude in the lower part of the reactor. It was shown that under the given conditions (relatively short travel times), the signal decay due to nuclear spin relaxation was quite insignificant, and the amplitude of the HP propane signal was directly proportional to reaction yield, allowing the determination of the rate of propene hydrogenation.

In addition, the experiments enabled the observation of gas adsorption effects in the microfluidic reactors during their *in situ* operation, and an elegant approach for quantifying the amount of absorbed gas using RD NMR was proposed. The authors also introduced the concept of a microfluidic nuclear polarizer based on their findings about PHIP produced in the microscale heterogeneous catalytic hydrogenation.

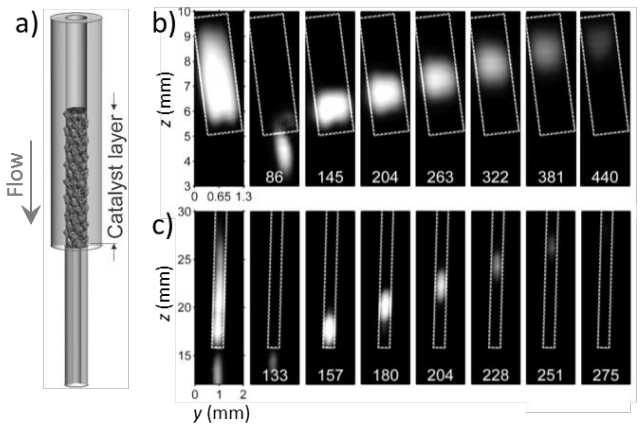

Figure 17. RD MRI visualization of reaction progress inside a catalyst layer packed in a thin capillary. (a) Sample setup. 2D TOF images of HP propane resulting from the hydrogenation reaction in the reactors of (a) 800 and (b) 150

μm in diameter. The reactors are outlined by a white dashed line in the figures. TOF (ms) is shown at the bottom of the panels. The panels on the left are the sums of all other panels in each series.[230c]

Further efforts were directed to the development of the concept by employing micro-engineering technologies to produce micro-structured lab-on-a-chip reactors with the catalyst (sputtered Pt) deposited on the inner surface of the channels.[231] It was found that these reactors did not provide PHIP. However, these studies provided a platform for further development of RD NMR for future HP applications, *e.g.*, by using Hadamard encoding to achieve a better chemical resolution.[231b]

10.3. Outcome and perspectives

The current advances in RD MRI with HP gases already offer many interesting applications as highlighted above. The major issues concerning the methodology are related to the availability of HP gases and the lifetime of hyperpolarization. HP ^{129}Xe is typically more expensive than the ^{1}H HP hydrocarbon gases produced using PHIP. On the other hand, the nuclear spin relaxation causes more severe problems in the case of HP hydrocarbons. Recent developments in the field of long-lived nuclear spin states,[232] however, may alleviate the latter problem. For instance, it has been shown that a long-lived HP state in ethylene gas can survive for *ca*. 15 min.[233] The further RD NMR development could concern utilization of such extremely long-lived HP. In addition, the progress achieved in the field of single-scan ultra-fast NMR techniques[234] also offers new capabilities, which earlier were considered incompatible with NMR hyperpolarization. For example, recent work demonstrates the feasibility of single-scan 2D Laplace NMR experiments of dissolved HP propene,[235] and the method should be applicable, *e.g.*, for the investigation of dynamics and physical environments of HP gases in porous media, both with high-field and low-field (mobile) NMR instruments.[235-236]

11. Conclusion

The development and applications of HP gases continue to advance, and show no sign of slowing down. In addition to SEOP hyperpolarization for production of HP ^{3}He and ^{129}Xe, (i) the SEOP HP technique has been expanded to several other noble gases, (ii) the heterogeneous PHIP[28a] technique has enabled production of HP hydrocarbons in pure form (free from contamination by the catalyst), and (iii) the dissolution DNP technique was demonstrated for production of HP ^{129}Xe[26, 53a] and $^{15}N_2O$ gases.[237] Thus, many other gases could be potentially amenable to DNP hyperpolarization.

As a result of these fundamental advances in the physics, chemistry and engineering of hyperpolarization processes, which enabled more efficient production of established HP gases (*e.g*. higher throughput and greater polarization in ^{129}Xe hyperpolarizers[43i, 238]) and other advances that enabled the production of *new* HP gases, it was possible to significantly expand the reach of applications of HP gases in biomedicine and other fields. For example, as described in this mini-review, HP ^{129}Xe is now being employed for *in vivo* thermometry, brown fat imaging, targeted biosensors, and many other exciting applications, whereas HP hydrocarbons are already used for high-resolution 3D imaging, remote detection, and microfluidic imaging. Many other new applications will likely emerge given that HP gases are becoming more available to researchers, because hyperpolarization equipment is becoming more readily available through commercial sources (as opposed to custom made in the research labs of specialists, as was generally the case only one decade ago). So far, physicists have been the main driving force behind the development of MRI of hyperpolarized gases. However, before their entry into routine clinical practice, further research is needed to improve image quality and validate its use, qualitatively and quantitatively, in respiratory disease. This will undoubtedly require collaboration between physicists and clinicians. Moreover, the better-established applications (*e.g*. lung imaging using HP ^{129}Xe) will likely continue to be more fully developed, to the point when studies will be driven by medical doctors (the ultimate users of this technology) rather than by the physicists and chemists who pioneered the technology and helped bring it from the proof-of-principle stage to the clinical scale. We look forward to all of these developments with great excitement.

Boyd M. Goodson graduated from Princeton University in 1995 (thesis research with Warren Warren and Herschel Rabitz) and earned his PhD in chemistry in 1999 with Alexander Pines at the University of California, Berkeley / LBNL. Following postdoctoral work with Ahmed Zewail at Caltech, in 2002 Goodson joined the faculty at Southern Illinois University Carbondale and was promoted to full professor in 2014. His research and teaching have been recognized by an NSF CAREER award, Research Innovation and Cottrell Scholar Awards from the Research Corporation for Science Advancement, the ORAU Powe Junior Faculty Award, and the Kaplan Award for Research, Sigma Xi Society (SIUC Chapter). Goodson's research interests concern magnetic resonance and optical spectroscopies, NMR/MRI sensitivity enhancement, and hyperpolarization.

Matthew S. Rosen received his PhD in Physics at the University of Michigan in 2001, where he developed the first ^{129}Xe high-volume hyperpolarizer for *in vivo* use, and with it demonstrated the first use of ^{129}Xe as a MRI tracer *in vivo*. His career bridges the spectrum from fundamental physics to applied bioimaging work. He an Assistant Professor of Radiology at Harvard Medical School and the Director of the Low-Field MRI and Hyperpolarized Media Laboratory at the MGH/Martinos Center for Biomedical Imaging. He currently leads an effort to develop tools and techniques for

robust ultra-low-magnetic-field implementations of MRI.

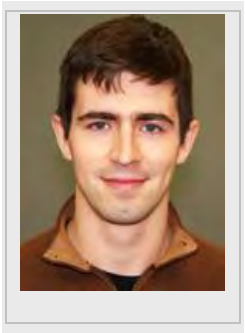

Dr. Danila A. Barskiy studied Chemistry in Novosibirsk State University where he obtained PhD in 2015. He is currently pursuing his research interests as a Postdoctoral Fellow at the Vanderbilt University Institute of Imaging Science in the laboratory of Prof. Eduard Chekmenev. His research interests include spin dynamics and chemical kinetics of parahydrogen-based nuclear spin hyperpolarization techniques (SABRE and PHIP) and applications of these techniques for NMR spectroscopy and imaging of biomedical and industrial processes.

Prof. Dmitry Mikhaylov studied applied physics at the National Research Nuclear University MEPHI (NRNU MEPHI). He got his PhD in 2011 under the guidance of Prof. M. Ivanov. In 2012 he became the head of Engineering Science Center of NRNU MEPHI, one of the biggest R&D centers in Russia. In 2012 he received one of the biggest Russian State research grants for research in the area of endoscopy. In 2013, he started collaboration with Vanderbilt University for research in field of endoscopy and nanomaterials. In 2015, he received an award from Russian Airspace Agency to conduct research in gravity free biological processes. In 2016, he moved to China to continue research.

Panayiotis Nikolaou studied Chemistry with a primary focus on (i) developing and applying new technologies to understand and improve hyperpolarized ^{129}Xe production and (ii) studying the host-guest dynamics of ^{29}Xe–cryptophane inclusion complexes at Southern Illinois University Carbondale (under the guidance of Prof. Boyd M. Goodson), where he earned his PhD in 2010. He is currently a Post-Doctoral fellow with Prof. Eduard Chekmenev at Vanderbilt, where he has designed and built two automated clinical-scale xenon polarizers. Current Research interests include the development of fully-automated xenon hyperpolarizer technology, hyperpolarized contrast agents, and their biomedical application in MR.

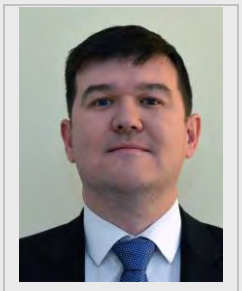

Eduard Y. Chekmenev, b 1977, PhD in Physical Chemistry (supervisor Prof. Richard J. Wittebort) 2003, University of Louisville, KY, USA. Postdoctoral Fellow at NHMFL to work on structural biology of membrane proteins in Tallahassee, FL, USA (with Prof. Timothy Cross) and in NMR hyperpolarization at Caltech (with Prof. Daniel P. Weitekamp) and hyperpolarized in vivo imaging at HMRI (with Dr. Brian D. Ross). In 2009, Dr. Chekmenev started his hyperpolarization program at Vanderbilt University Institute of Imaging Science (VUIIS), and he was tenured in 2015. In 2016, he was elected as a Professor of the Russian Academy of Sciences. Research interests include development of methods of hyperpolarization and their Biomedical and industrial applications.

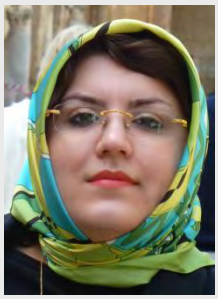

Shahideh Safavi studied Medicine at St George's University of London, graduating in 2008. She undertook her general medicine training in London, followed by specialist training in respiratory medicine in London and Nottingham. She is currently pursuing her research interests at University of Nottingham, as a clinical research fellow, under the supervision of Prof. Ian Hall and Dr. Michael Barlow. Her research is focused on development and use of novel functional MRI techniques in respiratory medicine.

Michael Barlow studied Physics at Essex University where he obtained his Ph.D in the study of hot electron transport in semiconductor quantum wells. His interest in optical pumping arose from work on helium magnetometers when he was instrument manager for the NASA Cassini MAG team. This work continues to the present day with optical pumping and Raman techniques to explore spin exchange optical pumping for the production of hyperpolarized xenon. He is currently lead physicist for the Nottingham xenon Lung imaging team.

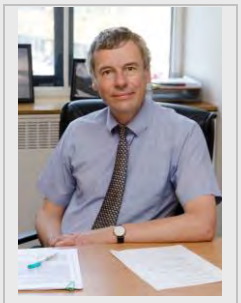

Professor Ian Hall is currently the Boots' Professor of Therapeutics and Director of the Centre for Biomolecular Sciences at the University of Nottingham. His main clinical interest is in respiratory medicine. He completed his clinical studies at the University of Oxford before moving to Nottingham for specialist and research training. Subsequently he was an MRC travelling fellow at the University of Pennsylvania and National Asthma Campaign Senior Research Fellow back in Nottingham. Current research interests include the genetic basis of lung disease and novel imaging approaches.

Rosa Tamara Branca studied Physics at the University of Rome La Sapienza, where she obtained her Bachelors of Science and Masters degree in 2002. In 2006 she obtained her PhD in Biophysics under the guidance of Dr. B. Maraviglia and Dr. W. Warren while studying non-linear MR effects due to dipolar-dipolar interactions and radiation damping. In 2006 she moved to Duke University, first as a Post-Doctoral Fellow and then as an Assistant Research Professor (2009). She began working with hyperpolarized gases in 2009, while working on a project to detect targeted lung metastases with HP Helium. In 2012 she moved to the University of North Carolina at Chapel Hill, where she holds a faculty appointment in the Department of Physics and Astronomy and in the Biomedical Research Imaging Center. Her current research interests include applications of hyperpolarized gases in lung and brown fat imaging.

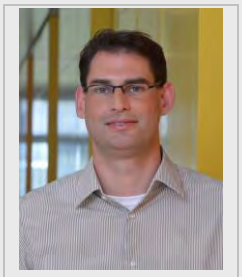

Leif Schröder studied Physics in Göttingen and Heidelberg where he obtained a PhD in Physics while being affiliated with the German Cancer Research Center to investigate the quantum mechanical fine structure of in vivo NMR spectra. His subsequent stay at the University of California at Berkeley and Lawrence Berkeley National Laboratory was supported by an Emmy Noether fellowship from the German Research Foundation to work hyperpolarized xenon biosensors. He is a co-developer of the Hyper-CEST technique for which he received national and international prizes, including the IUPAP Young Scientist Award in Medical Physics. He further received an Emmy Noether fellowship to start his own group at the FMP, Berlin, where he also managed the ERC Project BiosensorImaging and is currently heading the Molecular Imaging Group.

Mikhail G. Shapiro is an Assistant Professor of Chemical Engineering and a Heritage Principal Investigator at the California Institute of Technology. His laboratory works on biomolecular technologies for non-invasive imaging and control of biological function. He received his PhD in Biological Engineering from MIT and held post-doctoral fellowships at the University of Chicago and the University of California, Berkeley. He has pioneered protein-based MRI sensors of neurotransmission, reporter genes for several forms of MRI, including xenon and diffusion, and genetically encoded reporters for ultrasound. His awards include the Burroughs Wellcome Career Award, the DARPA Young Faculty Award, the Pew Biomedical Scholarship and the Technology Review's TR35 list of the top innovators under age 35.

Dr. George J. Lu obtained his B.S. degree at University of Alberta, Canada, where he worked with Prof. Brian Sykes and Prof. Michael James on protein NMR and X-ray crystallography. He received his Ph.D. at the University of California, San Diego (UCSD), where he studied solid-state NMR methodology and membrane protein structural biology with Prof. Stanley Opella. He is currently a postdoctoral fellow at Caltech with Prof. Mikhail Shapiro, and his research applies the technique of protein engineering to the development of MRI contrast agents and new imaging and therapeutic methods.

Dr. Aaron M. Coffey conducted undergraduate studies in Electrical Engineering at the University of Arizona, Tucson. He completed a PhD in Biomedical Engineering in 2014 at Vanderbilt University under the guidance of Prof. Eduard Chekmenev in the area of hyperpolarized and low-field NMR and MRI, where he continued as a postdoctoral fellow. He recently received the Ruth L. Kirschstein postdoctoral fellowship 1F32EB021840-01 for 'Ultra-fast molecular MRI of human adipose tissue with hyperpolarized xenon-129 contrast agent.' His research interests include advancing MR detection hardware and utilizing hyperpolarization techniques to enable MR contrast agents for molecular imaging and high sensitivity spectroscopic NMR studies.

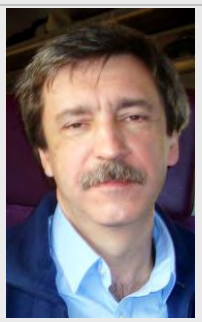

Prof. Igor V. Koptyug received his PhD degree in 1991; in 1992–1995 he was a postdoctoral researcher in the photochemistry group of Professor N. J. Turro (Columbia University, New York). He earned his Dr. Sci. (Habilitation) degree in catalysis in 2003 and a title of Professor in 2006; currently, he is the head of the Laboratory of Magnetic Resonance Microimaging at the International Tomography Center, Siberian Branch of the Russian Academy of Sciences, Novosibirsk. His research interests include signal enhancement in NMR and applications of NMR and MRI in catalysis and biological studies *in vivo* and *in vitro*.

Dr. Kirill V. Kovtunov studied chemistry at the Novosibirsk State University, Russia. He completed a PhD in Physical Chemistry in 2008 at the International Tomography Center under the supervision of Prof. Igor Koptyug in the area of utilization of parahydrogen in heterogeneous processes, where he obtained heterogeneous PHIP effects for the first time. His research interests include heterogeneous catalysis and utilization of parahydrogen-

10.1002/chem.201603884
WILEY-VCH

induced polarization techniques to produce highly polarized contrast agents for NMR/MRI and mechanistic studies of heterogeneous reactions involving hydrogen. Currently, he is a senior scientific researcher in the group of Prof. Igor Koptyug.

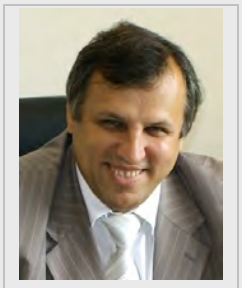

Valerii I. Bukhtiyarov received his PhD degree in 1989. In 1993, Valeriy I. Bukhtiyarov held a post-doc position at University of Wales College of Cardiff (UK) supervised by Professor M. Wyn Roberts. He earned his Dr. Sci. (Habilitation) degree in catalysis in 1998 and a title of Professor in 2003. Since 2000, he is a head of the Surface Science Laboratory in the Boreskov Institute of Catalysis (BIC) of the Siberian Branch of the Russian Academy of Sciences, Novosibirsk; since July 2015, he is the director of BIC. The scientific interests of Valerii I. Bukhtiyarov include bridging between surface science and heterogeneous catalysis; application of physical methods to study adsorption and surface chemical reactions, including *in-situ* measurements; and application of nanoscience approaches for modeling and study of heterogeneous catalysts.

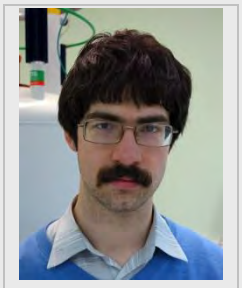

Oleg G. Salnikov completed his undergraduate studies in chemistry at Novosibirsk State University in 2014 and continued there as a PhD student. In 2012, he started working on the HET-PHIP project in the group of Prof. Igor Koptyug at the International Tomography Center SB RAS under the supervision of Dr. Kirill Kovtunov. His research interests include application of PHIP for mechanistic studies of heterogeneous catalytic reactions and development of MR contrast agents using HET-PHIP.

Ville-Veikko Telkki studied physics at the University of Oulu, Finland. He completed his PhD studies in 2006 under the guidance of Prof. Jukka Jokisaari. In 2005, before the final dissertation, he joined the research group of Prof. Alex Pines in UC Berkeley, concentrating on remote detection MRI. In 2007, he returned back to University of Oulu. Currently, he is a Research Fellow of Academy of Finland, and he is leading the Experimental NMR Research Group, focusing on the development and application of advanced NMR methods for materials research.

Dr. Vladimir V. Zhivonitko graduated from Novosibirsk State University, Russia, in 2005, where he studied chemistry. In the same year he started his PhD studies under supervision of Prof. Igor V. Koptyug at the International Tomography Center SB RAS. In 2008 he defended his PhD thesis concerning MRI of nonlinear chemical processes in model catalytic reactors. Thereafter, he joined the HET-PHIP project conducted in Prof. Koptyug's lab as a postdoctoral researcher. His interests include basic NMR research with hyperpolarized substances, development of catalytic systems for PHIP and NMR micro-imaging of catalytic reactors. Currently, he works as a senior scientific researcher at the same location.

Acknowledgements

The Hyperpolarised Lung Function Imaging Facility (HILF), within the Sir Peter Mansfield Magnetic Imaging Centre (SPMIC) at University of Nottingham, where the M.J.B, SS and IPH undertake research into novel functional MRI techniques, is the beneficiary of grants provided by UK's Medical Research Council (MRC) and Engineering and Physical Sciences Research Council (EPSRC). MGS thanks Burroughs Wellcome Fund Career Award at the Scientific Interface, Human Frontiers Science Program # RGP0050, and Heritage Medical Research Institute for funding. AMC thanks NIH 1F32EB021840 career award. We thank the following award for funding support: NSF CHE-1416268 and CHE-1416432 (EYC, BMG, IVK, KVK), NIH 1R21EB018014 and 1R21EB020323 (EYC and BMG), DOD CDMRP BRP W81XWH-12-1-0159/BC112431 (EYC), PRMRP W81XWH-15-1-0271 and W81XWH-15-1-0272 (EYC, MSR, BMG), ExxonMobil Research and Engineering Company Knowledge Build (EYC). KVK, VVZ and IVK thank the Russian Science Foundation (grant 14–35–00020) for support of the MRI experiments. V.-V.T. acknowledges the Academy of Finland (grant numbers 289649 and 294027) for the financial support. Part of this work has been supported by the European Research Council under the European Community's Seventh Framework Programme (FP7/2007-2013)/ERC grant agreement no. 242710 to L.S.) and the Leibniz Association (WGL; grant SAW-2011-FMP-2 to L.S.).

Keywords: xenon-129 • propane • NMR • gas • hyperpolarization • MRI

[1] a) P. Nikolaou, A. Coffey, M. Barlow, M. Rosen, B. Goodson and E. Chekmenev, *Anal. Chem.* **2014**, *86*, 8206-8212; b) C. Witte and L. Schröder, *NMR Biomed.* **2013**, *26*, 788-802; c) J. Ardenkjaer-Larsen, B. Fridlund, A. Gram, G. Hansson, L. Hansson, M. Lerche, R. Servin, M. Thaning and K. Golman, *Proc. Natl. Acad. Sci. USA* **2003**, *100*, 10158-10163.

[2] a) B. M. Goodson, N. Whiting, A. M. Coffey, P. Nikolaou, F. Shi, B. Gust, M. E. Gemeinhardt, R. V. Shchepin, J. G. Skinner, J. R. Birchall, M. J. Barlow and E. Y. Chekmenev in *Hyperpolarization Methods for MRS*, *Vol. 4* Eds.: J. Griffiths, P. Bottomley and R. E. Wasylishen), John Wiley & Sons, Ltd, West Sussex, UK, **2015**, pp. 797–810; b) P. Nikolaou, B. Goodson and E. Chekmenev, *Chem. Eur. J.* **2015**, *21*, 3156-3166; c) B. Goodson, *J. Magn. Reson.* **2002**, *155*, 157-216.

[3] M. L. Hirsch, N. Kalechofsky, A. Belzer, M. Rosay and J. G. Kempf, *J. Am. Chem. Soc.* **2015**, *137*, 8428-8434.

[4] T. Walker and W. Happer, *Rev. Mod. Phys.* **1997**, *69*, 629.

[5] H. R. Ward, *Acc. Chem. Res.* **1972**, *5*, 18-24.

[6] K. H. Mok and P. J. Hore, *Methods* **2004**, *34*, 75-87.

[7] a) C. Bowers and D. Weitekamp, *Phys. Rev. Lett.* **1986**, *57*, 2645-2648; b) C. Bowers and D. Weitekamp, *J. Am. Chem. Soc.* **1987**, *109*, 5541-5542; c) T. Eisenschmid, R. Kirss, P. Deutsch, S. Hommeltoft, R. Eisenberg, J. Bargon, R. Lawler and A. Balch, *J. Am. Chem. Soc.* **1987**, *109*, 8089-8091.

[8] R. Adams, J. Aguilar, K. Atkinson, M. Cowley, P. Elliott, S. Duckett, G. Green, I. Khazal, J. Lopez-Serrano and D. Williamson, *Science* **2009**, *323*, 1708-1711.

[9] a) I. V. Koptyug, K. V. Kovtunov, S. R. Burt, M. S. Anwar, C. Hilty, S.-I. Han, A. Pines and R. Z. Sagdeev, *J. Am. Chem. Soc.* **2007**, *129*, 5580-5586; b) L. S. Bouchard, K. V. Kovtunov, S. R. Burt, M. S. Anwar, I. V. Koptyug, R. Z. Sagdeev and A. Pines, *Angew. Chem. Int. Ed.* **2007**, *46*, 4064-4068.

[10] B. M. Goodson, *J. Magn. Reson.* **2002**, *155*, 157-216.

[11] a) T. R. Carver and C. P. Slichter, *Phys. Rev.* **1953**, *92*, 212-213; b) A. Overhauser, *Phys. Rev.* **1953**, *92*, 411-415; c) J. Natterer and J. Bargon, *Prog. Nucl. Magn. Reson. Spectrosc.* **1997**, *31*, 293-315.

[12] K. Golman, O. Axelsson, H. Johannesson, S. Mansson, C. Olofsson and J. Petersson, *Magn. Reson. Med.* **2001**, *46*, 1-5.

[13] a) C. Gabellieri, S. Reynolds, A. Lavie, G. S. Payne, M. O. Leach and T. R. Eykyn, *J. Am. Chem. Soc.* **2008**, *130*, 4598-4599; b) F. Reineri, A. Viale, S. Ellena, D. Alberti, T. Boi, G. Giovenzana, R. Gobetto, S. Premkumar and S. Aime, *J. Am. Chem. Soc.* **2012**, *134*, 11146-11152; c) T. Theis, M. Truong, A. Coffey, E. Chekmenev and W. Warren, *J. Magn. Reson.* **2014**, *248*, 23-26; d) T. Theis, M. Truong, A. Coffey, R. Shchepin, K. Waddell, F. Shi, B. Goodson, W. Warren and E. Chekmenev, *J. Am. Chem. Soc.* **2015**, *137*, 1404-1407.

[14] M. Plaumann, U. Bommerich, T. Trantzschel, D. Lego, S. Dillenberger, G. Sauer, J. Bargon, G. Buntkowsky and J. Bernarding, *Chem. Eur. J.* **2013**, *19*, 6334-6339.

[15] V. V. Zhivonitko, I. V. Skovpin and I. V. Koptyug, *Chem. Commun.* **2015**, *51*, 2506-2509.

[16] G. E. Pavlovskaya, Z. I. Cleveland, K. F. Stupic, R. J. Basaraba and T. Meersmann, *Proc. Natl. Acad. Sci. USA* **2005**, *102*, 18275-18279.

[17] a) B. Goodson, *Concepts Magn. Reson.* **1999**, *11*, 203-223; b) T. Walker, *J. Phys. Conf. Ser.* **2011**, p. 012001.

[18] D. Lilburn, G. E. Pavlovskaya and T. Meersmann, *J. Magn. Reson.* **2012**, *229*, 173–186.

[19] K. Golman, R. in't Zandt and M. Thaning, *Proc. Natl. Acad. Sci. U. S. A.* **2006**, *103*, 11270-11275.

[20] a) J. Kurhanewicz, D. Vigneron, K. Brindle, E. Chekmenev, A. Comment, C. Cunningham, R. DeBerardinis, G. Green, M. Leach, S. Rajan, R. Rizi, B. Ross, W. Warren and C. Malloy, *Neoplasia* **2011**, *13*, 81-97; b) K. M. Brindle, *J. Am. Chem. Soc.* **2015**, *137*, 6418-6427; c) A. Comment and M. E. Merritt, *Biochemistry* **2014**, *53*, 7333-7357; d) A. Comment, *J. Magn. Reson.* **2016**, *264*, 39-48; e) K. R. Keshari and D. M. Wilson, *Chem. Soc. Rev.* **2014**, *43*, 1627-1659; f) I. V. Koptyug, *Mendeleev Commun.* **2013**, *23*, 299-312; g) S. Meier, P. R. Jensen, M. Karlsson and M. H. Lerche, *Sensors* **2014**, *14*, 1576-1597; h) M. H. Lerche, P. R. Jensen, M. Karlsson and S. Meier, *Anal. Chem* **2015**, *87*, 119-132.

[21] a) N. Eshuis, B. van Weerdenburg, M. Feiters, F. Rutjes, S. Wijmenga and M. Tessari, *Angew. Chem. Int. Ed.* **2015**, *54*, 1481-1484; b) C. Hilty and M. Ragavan, *Anal. Chem.* **2014**, *87*, 1004-1008.

[22] J. Mugler and T. Altes, *J. Magn. Reson. Imaging* **2013**, *37*, 313-331.

[23] R. Branca, T. He, L. Zhang, C. Floyd, M. Freeman, C. White and A. Burant, *Proc. Natl. Acad. Sci. USA* **2014**, *111*, 18001-18006.

[24] L. Schroder, *Phys. Medica* **2013**, *29*, 3-16.

[25] M. G. Shapiro, R. M. Ramirez, L. J. Sperling, G. Sun, J. Sun, A. Pines, D. V. Schaffer and V. S. Bajaj, *Nat. Chem.* **2014**, *6*, 629-634.

[26] a) A. Comment, S. Jannin, J.-N. Hyacinthe, P. Miéville, R. Sarkar, P. Ahuja, P. R. Vasos, X. Montet, F. Lazeyras and J.-P. Vallée, *Phys. Rev. Lett.* **2010**, *105*, 018104; b) N. Kuzma, M. Pourfathi, H. Kara, P. Manasseh, R. Ghosh, J. Ardenkjaer-Larsen, S. Kadlecek and R. Rizi, *J. Chem. Phys.* **2012**, *137*.

[27] B. Vuichoud, E. Canet, J. Milani, A. Bornet, D. Baudouin, L. Veyre, D. Gajan, L. Emsley, A. Lesage, C. Copéret, C. Thieuleux, G. Bodenhausen, I. Koptyug and S. Jannin, *J. Phys. Chem. Lett.* **2016**, *7*, 3235-3239.

[28] a) L.-S. Bouchard, S. R. Burt, M. S. Anwar, K. V. Kovtunov, I. V. Koptyug and A. Pines, *Science* **2008**, *319*, 442-445; b) K. V. Kovtunov, I. E. Beck, V. I. Bukhtiyarov and I. V. Koptyug, *Angew. Chem. Int. Ed.* **2008**, *47*, 1492-1495.

[29] K. Kovtunov, V. Zhivonitko, I. Skovpin, D. Barskiy and I. Koptyug, *Top. Curr. Chem.* **2013**, *338*, 123-180.

[30] M. Carravetta, O. G. Johannessen and M. H. Levitt, *Phys. Rev. Lett.* **2004**, *92*, 153003.

[31] J. Brossel and A. Kastler, *C. R. Acad. Sci.* **1949**, *229*, 1213-1215.

[32] M. R. Bouchiat, T. R. Carver and C. M. Varnum, *Phys. Rev. Lett.* **1960**, *5*, 373-375.

[33] B. C. Grover, *Phys. Rev. Lett.* **1978**, *40*, 391.

[34] a) W. Happer, E. Miron, S. Schaefer, D. Schreiber, W. V. Wijngaarden and X. Zeng, *Phys. Rev. A* **1984**, *29*, 3092-3110; b) G. D. Cates, R. J. Fitzgerald, A. S. Barton, P. Bogorad, M. Gatzke, N. R. Newbury and B. Saam, *Phys. Rev. A* **1992**, *45*, 4631-4639; c) T. E. Chupp, M. E. Wagshul, K. P. Coulter, A. B. Mcdonald and W. Happer, *Phys. Rev. C* **1987**, *36*, 2244-2251.

[35] T. Meersmann and E. Brunner in *Hyperpolarized Xenon-129 Magnetic Resonance: Concepts, Production, Techniques and Applications*, *Vol.* RSC Publishing, Cambridge, UK, **2015**.

[36] a) T. E. Chupp and K. P. Coulter, *Phys. Rev. Lett.* **1985**, *55*, 1074; b) R. Stoner and R. Walsworth, *Phys. Rev. A.* **2002**, *66*, 032704.

[37] G. E. Pavlovskaya, Z. I. Cleveland, K. F. Stupic, R. J. Basaraba and T. Meersmann, *Proc. Natl. Acad. Sci. USA* **2005**, *102*, 18275-18279.

[38] K. F. Stupic, Z. I. Cleveland, G. E. Pavlovskaya and T. Meersmann, *J. Magn. Reson.* **2011**, *208*, 58-69.

[39] D. Steck in *Rubidium 85 D line data, Rubidium 87 D line data (revision 2.1.5, 13 January 2015)*, *Vol.*

[40] a) E. Babcock, B. Chann, I. A. Nelson and T. G. Walker, *Appl. Opt.* **2005**, *44*, 3098-3104; b) N. Whiting, P. Nikolaou, N. Eschmann, M. Barlow, R. Lammert, J. Ungar, W. Hu, L. Vaissie and B. Goodson, *Appl. Phys. B* **2012**, *106*, 775-788.

[41] E. Babcock, I. Nelson, S. Kadlecek, B. Driehuys, L. W. Anderson, F. W. Hersman and T. G. Walker, *Phys. Rev. Lett.* **2003**, *91*, 123003.

[42] a) X. Z. Zeng, C. J. Wu, M. X. Zhao, S. L. Li, L. Y. Li, X. T. Zhang, Z. D. Liu and W. Y. Liu, *Chem. Phys. Lett.* **1991**, *182*, 538–540; b) N. Whiting, N. A. Eschmann, B. M. Goodson and M. J. Barlow, *Phys. Rev. A* **2011**, *83*, 053428.

[43] a) D. Raftery, H. Long, T. Meersmann, P. J. Grandinetti, L. Reven and A. Pines, *Phys. Rev. Lett.* **1991**, *66*, 584-587; b) M. S. Rosen, T. E. Chupp, K. P. Coulter, R. C. Welsh and S. D. Swanson, *Rev. Sci. Instrum.* **1999**, *70*, 1546; c) U. Ruth, T. Hof, J. Schmidt, D. Fick and H. J. Jänsch, *Appl. Phys. B* **1999**, *68*, 93-97; d) H. Desvaux, T. Gautier, G. Le Goff, M. Pétro and P. Berthault, *Eur. Phys. J. B* **2000**, *12*, 289-296; e) P. Nikolaou, N. Whiting, N. A. Eschmann, K. E. Chaffee and B. M. Goodson., *J. Magn. Reson.* **2009**, *197*, 249-254; f) S. R. Parnell, M. H. Deppe, J. Parra-Robles and J. M. Wild, *J. Appl. Phys.* **2010**, *108*, 064908; g) N. Whiting, P. Nikolaou, N. A. Eschmann, B. M. Goodson and M. J. Barlow, *J. Magn. Reson.* **2011**, *208*, 298-304; h) J. S. Six, T. Hughes-Riley, K. F. Stupic, G. E. Pavlovskaya and T. Meersmann, *PloS One* **2012**, *7*, 49927; i) P. Nikolaou, A. Coffey, L. Walkup, B. Gust, N. Whiting, H. Newton, S. Barcus, I. Muradyan, M. Dabaghyan, G. Moroz, M. Rosen, S. Patz, M. Barlow, E. Chekmenev and B. Goodson, *Proc. Natl. Acad. Sci. USA* **2013**, *110*, 14150-14155; j) T. Hughes-Riley, J. S. Six, D. M. Lilburn, K. F. Stupic, A. C. Dorkes, D. E. Shaw, G. E. Pavlovskaya and T. Meersmann, *J. Magn. Reson.* **2013**, *237*, 23-33.

[44] a) B. Driehuys, G. Cates, E. Miron, K. Sauer, D. Walter and W. Happer, *Appl. Phys. Lett.* **1996**, *69*, 1668-1670; b) M. Haake, A. Pines, J. A. Reimer and R. Seydoux, *J. Am. Chem. Soc.* **1997**, *119*, 11711-11712; c) A. L. Zook, B. B. Adhyaru and C. R. Bowers, *J. Magn. Reson.* **2002**, *159*, 175-182; d) M. G. Mortuza, S. Anala, G. E. Pavlovskaya, T. J. Dieken and T. Meersmann, *J. Chem. Phys.* **2003**, *181*, 1581; e) K. Knagge, J. Prange and D. Raftery, *Chem. Phys. Lett.* **2004**, *397*, 11-16; f) I. C .Ruset, S. Ketel and F. W. Hersman, *Phys. Rev. Lett.* **2006**, *96*, 053002; g) G. Schrank, Z. Ma, A. Schoeck and B. Saam, *Phys. Rev. A* **2009**, *80*, 063424; h) G. Norquay, S. R. Parnell, X. Xu, J. Parra-Robles and J. M. Wild, *J. Appl. Phys.* **2013**, *113*, 044908; i) A. Nossov, E. Haddad, F. Guenneaua and A. Gédéon, *Phys. Chem. Chem. Phys.* **2003**, *5*, 4473-4478.

[45] a) K. F. Stupic, Z. I. Cleveland, G. E. Pavlovskaya and T. Meersmann, *Solid State Nucl. Magn. Reson.* **2006**, *29*, 79-84; b) Z. Wu, W. Happer, M. Kitano and J. Daniels, *Phys. Rev. A.* **1990**, *42*, 2774; c) R. K. Ghosh in *Spin Exchange Optical Pumping of Neon and its Applications*, *Vol.* Princeton University, **2009**; d) S. Fain, M. L. Schiebler, D. G. McCormack and G. Parraga, *J. Magn. Reson. Imaging.* **2010**, *32*, 1398-1408.

[46] G. D. Cates, D. R. Benton, M. Gatzke, W. Happer, K. C. Hasson and N. R. Newbury, *Phys. Rev. Lett.* **1990**, *65*, 2591-2594.

[47] a) B. Chann, I. Nelson and T. G. Walker, *Opt. Lett.* **2000**, *25*, 1352-1354; b) J. N. Zerger, M. J. Lim, K. P. Coulter and T. E. Chupp, *Appl. Phys. Lett.* **2000**, *76*, 1798-1800.

[48] F. D. Colegrove, L. D. Scheare and G. K. Walters, *Phys. Rev.* **1963**, *132*, 2561-2572.

[49] a) T. R. Gentile, D. R. Rich, A. K. Thompson, W. M. Snow and G. L. Jones, *J. Res. Natl. Inst. Stand. Technol.* **2001**, *106*, 709-729; b) P.J. Nacher, G. Tastevin, X. Maitre, X. Dollat, B. Lemaire and J. Olejnik, *Eur. J. Radiol.* **1999**, *9*, b18.

[50] M. Ebert, T. Grossmann, W. Heil, W. E. Otten, R. Surkau, M. Leduc, P. Bachert, M. V. Knopp, L. R. Schad and M. Thelen, *Lancet* **1996**, *11*, 9011.

[51] a) L. D. Schearer, *Phys. Rev.* **1969**, *180*, 83-90; b) L. Young, D. Yang and R. W. Dunford, *J. Phys. B* **2002**, *35*, 2985-2992; c) T. Hadeishi and L. Chung-Heng, *Phys. Rev. Lett.* **1967**, *19*, 211; d) V. Lefevre-Seguin and M. Leduc, *J. Phys. B* **1977**, *10*, 2157.

[52] a) G. Frossati, *J. Low Temp. Phys.* **1998**, *111*, 521-532; b) M. Tanaka, T. Kunimatsu, M. Fujiwara, H. Kohri, T. Ohta, M. Utsuro, M. Yosoi, S. Ono, K. Fukuda, K. Takamatsu, K. Ueda, J.-P. Didelez, G. Frossati and A. d. Waard, *J. Phys.: Conf. Ser.* **2011**, *295*, 012167; c) J. D. O'Neill, E. V. Krjukov, J. R. Owers-Bradley and Y. Xia, *J. Low Temp. Phys.* **2007**, *146*, 563-579; d) E. V. Krjukov, J. D. O'Neill and J. R. Owers-Bradley, *J. Low Temp. Phys.* **2005**, *140*, 397-408.

[53] a) M. Pourfathi, N. N. Kuzma, H. Kara, R. K. Ghosh, H. Shaghaghi, S. J. Kadlecek and R. R. Rizi, *J. Magn. Reson.* **2013**, *253*, 71-76; b) A. Capozzi, C. Roussel, A. Comment and J. N. Hyacinthe, *J. Phys. Chem. C.* **2015**, *119*, 5020-5025; c) A. Capozzi, J. N. Hyacinthe, T. Cheng, T. R. Eichhorn, G. Boero, C. Roussel, J. J. van der Klink and A. Comment, *J. Phys. Chem. C* **2015**, *119*, 22632-22639.

[54] J. H. Ardenkjaer-Larsen, A. M. Leach, N. Clarke, J. Urbahn, D. Anderson and T. W. Skloss, *NMR Biomed.* **2011**, *24*, 927-932.

[55] a) T. E. Chupp, R. J. Hoare, R. L. Walsworth and B. Wu, *Phys. Rev. Lett.* **1994**, *72*, 2363; b) N. R. Newbury, A. S. Barton, P. Bogorad, G. D. Cates, M. Gatzke, B. Saam, L. Han, R. Holmes, P. A. Souder, J. Xu and D. Benton, *Phys. Rev. Lett.* **1991**, *67*, 3219.

[56] a) A. K. Thompson, A. M. Bernstein, T. E. Chupp, D. J. DeAngelis, G. E. Dodge, G. Dodson, K. A. Dow, M. Farkhondeh, W. Fong, J. Y. Kim, R. A. Loveman, J. M. Richardson, H. Schmieden, D. R. Tieger, T. C. Yates, M. E. Wagshul and J. D. Zumbro, *Phys. Rev. Lett.* **1992**, *68*, 2901; b) J. T. Singh, P. A. M. Dolph, W. A. Tobias, T. D. Averett, A. Kelleher, K. E. Mooney, V. V. Nelyubin, Y. Wang, Y. Zheng and G. D. Cates, *Phys. Rev. C* **2015**, *91*, 055205; c) E. Lelievre-Berna, *Physica B Cond. Mat.* **2007**, *397*, 162-167; d) T. R. Gentile and W. C. Chen, *Proc. Sci. (PSTP)* **2013**, *022*, 1-11; e) S. Karpuk, F. Allmendinger, M. Burghoff, C. Gemmel, M. Güldner, W. Heil, W. Kilian, S. Knappe-Grüneberg, C. Mrozik, W. Müller, E. W. Otten, M. Repetto, Z. Salhi, U. Schmidt, A. Schnabel, F. Seifert, Y. Sobolev, L. Trahms and K. Tullney, *Phys. Part. Nucl.* **2013**, *44*, 904–908.

[57] a) D. Raftery, L. Reven, H. Long, A. Pines, P. Tang and J. A. Reimer, *J. Phys. Chem.* **1993**, *97*, 1649-1655; b) C. R. Bowers, T. Pietrass, E. Barash, A. Pines, R. K. Grubbs and A. P. Alivisatos, *J. Phys. Chem.* **1994**, *98*, 9400-9404; c) T. Pietrass, A. Bifone and A. Pines, *Surf. Sci.* **1995**, *334*, L730-L734.

[58] a) C. R. Bowers, H. W. Long, T. Pietrass, H. C. Gaede and A. Pines, *Chem. Phys. Lett.* **1993**, *205*, 168-170; b) B. Driehuys, G. D. Cates, W. Happer, H. Mabuchi, B. Saam, M. S. Albert and A. Wishnia, *Phys. Lett. A* **1993**, *184*, 88-92; c) H. W. Long, H. C. Gaede, J. Shore, L. Reven, C. R. Bowers, J. Kritzenberger, T. Pietrass, A. Pines, P. Tang and J. A. Reimer, *J. Am. Chem. Soc.* **1993**, *115*, 8491-8492; d) B. Driehuys, G. D. Cates and W. Happer, *Phys. Rev. Lett.* **1995**, *74*, 4943-4946; e) H. C. Gaede, Y. Q. Song, R. E. Taylor, E. J. Munson, J. A. Reimer and A. Pines, *Appl. Magn. Reson.* **1995**, *8*, 373-384; f) T. Room, S. Appelt, R. Seydoux, E. L. Hahn and A. Pines, *Phys. Rev. B* **1997**, *55*, 11604-11610; g) G. Navon, Y. Q. Song, T. Room, S. Appelt, R. E. Taylor and A. Pines, *Science* **1996**, *271*, 1848-1851; h) R. J. Fitzgerald, K. L. Sauer and W. Happer, *Chem. Phys. Lett.* **1998**, *284*, 87-92; i) T. Pietrass, R. Seydoux and A. Pines, *J. Magn. Reson.* **1998**, *133*, 299-303; j) S. Appelt, F. Haesing, S. Baer-Lang, N. Shah and B. Blumich, *Chem. Phys. Lett.* **2001**, *348*, 263-269.

[59] a) M. Haake, A. Pines, J. A. Reimer and R. Seydoux, *J. Am. Chem. Soc.* **1997**, *119*, 11711-11712; b) R. Seydoux, A. Pines, M. Haake and J. A. Reimer, *J. Phys. Chem. B* **1999**, *103*, 4629-4637; c) I. L. Moudrakovski, A. Nossov, S. Lang, S. R. Breeze, C. I. Ratcliffe, B. Simard, G. Santyr and J. A. Ripmeester, *Chem. Mater.* **2000**, *12*, 1181-1183.

[60] a) D. Raftery, E. MacNamara, G. Fisher, C. V. Rice and J. Smith, *J. Am. Chem. Soc.* **1997**, *119*, 8746-8747; b) E. Brunner, M. Haake, A. Pines, J. A. Reimer and R. Seydoux, *Chem. Phys. Lett.* **1998**, *290*, 112-116; c) E. Brunner, R. Seydoux, M. Haake, A. Pines and J. A. Reimer, *J. Magn. Reson.* **1998**, *130*, 145-148; d) E. MacNamara, G. Fisher, J. Smith, C. V. Rice, S. J. Hwang and D. Raftery, *J. Phys. Chem. B* **1999**, *103*, 1158-1160.

[61] a) B. Saam, N. Drukker and W. Happer, *Chem. Phys. Lett.* **1996**, *263*, 481-487; b) D. M. Schmidt, J. S. George, S. I. Penttila, A. Caprihan and E. Fukushima, *J. Magn. Reson.* **1997**, *129*, 184-187; c) Y. Song, B. Goodson, B. Sheridan, T. de Swiet and A. Pines, *J. Chem. Phys.* **1998**, *108*, 6233-6239.

[62] a) R. W. Mair, D. G. Cory, S. Peled, C. H. Tseng, S. Patz and R. L. Walsworth, *J. Magn. Reson.* **1998**, *135*, 478-486; b) R. W. Mair, G. P. Wong, D. Hoffmann, M. D. Hurlimann, S. Patz, L. M. Schwartz and R. L. Walsworth, *Phys. Rev. Lett.* **1999**, *83*, 3324-3327; c) S. Peled, C. H. Tseng, A. A. Sodickson, R. W. Mair, R. L. Walsworth and D. G. Cory, *J. Magn. Reson.* **1999**, *140*, 320-324.

[63] a) I. L. Moudrakovski, A. Sanchez, C. I. Ratcliffe and J. A. Ripmeester, *J. Phys. Chem. B* **2000**, *104*, 7306-7310; b) G. P. Wong, R. W. Mair, R. L. Walsworth and D. G. Cory, *Phys. Rev. Lett.* **2001**, *86*, 4156-4159.

[64] a) E. Brunner, M. Haake, L. Kaiser, A. Pines and J. A. Reimer, *J. Magn. Reson.* **1999**, *138*, 155-159; b) L. G. Kaiser, T. Meersmann, J. W. Logan and A. Pines, *Proc. Natl. Acad. Sci. USA* **2000**, *97*, 2414-2418.

[65] a) I. L. Moudrakovski, S. Lang, C. I. Ratcliffe, B. Simard, G. Santyr and J. A. Ripmeester, *J. Magn. Reson.* **2000**, *144*, 372-377; b) G. Pavlovskaya, J. Six, M. T., N. Gopinathan and S. P. Rigby, *AIChE J.* **2015**, *61*, 4013-4019.

[66] a) H. J. Jansch, T. Hof, U. Ruth, J. Schmidt, D. Stahl and D. Fick, *Chem. Phys. Lett.* **1998**, *296*, 146-150; b) H. J. Jansch, P. Gerhard and M. Koch, *Proc. Natl. Acad. Sci. USA* **2004**, *101*, 13715-13719.

[67] a) X. X. Li, C. Newberry, I. Saha, P. Nikolaou, N. Whiting and B. M. Goodson, *Chem. Phys. Lett.* **2006**, *419*, 233-239; b) A. E. Truxal, C. C. Slack, M. D. Gomes, C. C. Vassiliou, D. E. Wemmer and A. Pines, *Angew. Chem. Int. Ed.* **2016**, *55*, 4666.

[68] a) S. Anala, G. E. Pavlovskaya, P. Pichumani, T. J. Dieken, M. D. Olsen and T. Meersmann, *J. Am. Chem. Soc.* **2003**, *125*, 13298-13302; b) N. J. Rogers, F. Hill-Casey, K. F. Stupic and e. al., *Proc. Natl. Acad. Sci. USA* **2016**, *113*, 3164-3168

[69] a) T. Meersmann, J. W. Logan, R. Simonutti, S. Caldarelli, A. Comotti, P. Sozzani, L. G. Kaiser and A. Pines, *J. Phys. Chem. A* **2000**, *104*, 11665-11670; b) P. Sozzani, A. Comotti, R. Simonutti, T. Meersmann, J. W. Logan and A. Pines, *Angew. Chem. Int. Ed.* **2000**, *39*, 2695-2698; c) I. Moudrakovski, D. V. Soldatov, J. A. Ripmeester, D. N. Sears and C. J. Jameson, *Proc. Natl. Acad. Sci. USA* **2004**, *101*, 17924-17929; d) D. V. Soldatov, I. L. Moudrakovski, E. V. Grachev and J. A. Ripmeester, *J. Am. Chem. Soc.* **2006**, *128*, 6737-6744; e) C. Y. Cheng and C. R. Bowers, *J. Am. Chem. Soc.* **2007**, *129*, 13997-14002; f) C. Y. Cheng and C. R. Bowers, *ChemPhysChem* **2007**, *8*, 2077-2081; g) C. Y. Cheng, T. C. Stamatatos, G. Christou and C. R. Bowers, *J. Am. Chem. Soc.* **2010**, *132*, 5387-5393; h) C. R. Bowers, M. Dvoyashkin, S. R. Salpage, C. Akel, H. Bhase, M. F. Geer and L. S. Shimizu, *ACS Nano* **2015**, *9*, 6343-6353; i) R. Anedda, D. V. Soldatov, I. L. Moudrakovski, M. Casu and J. A. Ripmeester, *Chem. Mater.* **2008**, *20*, 2908-2920.

[70] A. Comotti, S. Bracco, L. Ferretti, M. Mauri, R. Simonutti and P. Sozzani, *Chem. Commun.* **2007**, 350-352.

[71] J. M. Kneller, R. J. Soto, S. E. Surber, J. F. Colomer, A. Fonseca, J. B. Nagy, G. Van Tendeloo and T. Pietrass, *J. Am. Chem. Soc.* **2000**, *122*, 10591-10597.

[72] I. L. Moudrakovski, A. A. Sanchez, C. I. Ratcliffe and J. A. Ripmeester, *J. Phys. Chem. B* **2001**, *105*, 12338-12347.

[73] a) A. V. Nossov, D. V. Soldatov and J. A. Ripmeester, *J. Am. Chem. Soc.* **2001**, *123*, 3563-3568; b) J. P. Butler, R. W. Mair, D. Hoffmann, M. I. Hrovat, R. A. Rogers, G. P. Topulos, R. L. Walsworth and S. Patz, *J. Phys. Condens. Matter* **2002**, *14*, L297-L304; c) I. L. Moudrakovski, L. Q. Wang, T. Baumann, J. H. Satcher, G. J. Exarhos, C. I. Ratcliffe and J. A. Ripmeester, *J. Am. Chem. Soc.* **2004**, *126*, 5052-5053; d) I. L. Moudrakovski, C. I. Ratcliffe, J. A. Ripmeester, L. Q. Wang, G. J. Exarhos, T. F. Baumann and J. H. Satcher, *J. Phys. Chem. B* **2005**, *109*, 11215-11222; e) R. Simonutti, S. Bracco, A. Comotti, M. Mauri and P. Sozzani, *Chem. Mater.* **2006**, *18*, 4651-4657; f) A. Comotti, S. Bracco, P. Sozzani, S. Horike, R. Matsuda, J. Chen, M. Takata, Y. Kubota and S. Kitagawa, *J. Am. Chem. Soc.* **2008**, *130*, 13664-13672.

[74] a) K. Campbell, K. J. Ooms, R. E. Wasylishen and R. R. Tykwinski, *Org. Lett.* **2005**, *7*, 3397-3400; b) K. J. Ooms and R. E. Wasylishen, *Microporous Mesoporous Mater.* **2007**, *103*, 341-351; c) S. Pawsey, I. Moudrakovski, J. Ripmeester, L. Q. Wang, G. J. Exarhos, J. L. C. Rowsell and O. M. Yaghi, *J. Phys. Chem. C* **2007**, *111*, 6060-6067.

[75] a) A. Dubes, I. L. Moudrakovski, P. Shahgaldian, A. W. Coleman, C. I. Ratcliffe and J. A. Ripmeester, *J. Am. Chem. Soc.* **2004**, *126*, 6236-6237; b) G. S. Ananchenko, I. L. Moudrakovski, A. W. Coleman and J. A. Ripmeester, *Angew. Chem. Int. Ed.* **2008**, *47*, 5616-5618.

[76] P. Sozzani, S. Bracco, A. Comotti, M. Mauri, R. Simonutti and P. Valsesia, *Chem. Commun.* **2006**, 1921-1923.

[77] a) A. Nossov, E. Haddad, F. Guenneau, C. Mignon, A. Gedeon, D. Grosso, F. Babonneau, C. Bonhomme and C. Sanchez, *Chem. Commun.* **2002**, 2476-2477; b) V. V. Terskikh, I. L. Moudrakovski, S. R. Breeze, S. Lang, C. I. Ratcliffe, J. A. Ripmeester and A. Sayari, *Langmuir* **2002**, *18*, 5653-5656; c) A. Nossov, E. Haddad, F. Guenneau, A. Galarneau, F. Di Renzo, F. Fajula and A. Gedeon, *J. Phys. Chem. B* **2003**, *107*, 12456-12460; d) A. Comotti, S. Bracco, P. Valsesia, L. Ferretti and P. Sozzani, *J. Am. Chem. Soc.* **2007**, *129*, 8566-8576; e) A. Galarneau, M. Nader, F. Guenneau, F. Di Renzo and A. Gedeon, *J. Phys. Chem. C* **2007**, *111*, 8268-8277.

[78] a) A. Nossov, F. Guenneau, M. A. Springuel-Huet, E. Haddad, V. Montouillout, B. Knott, F. Engelke, C. Fernandez and A. Gedeon, *Phys. Chem. Chem. Phys.* **2003**, *5*, 4479-4483; b) A. Sakthivel, S. J. Huang, W. H. Chen, Z. H. Lan, K. H. Chen, T. W. Kim, R. Ryoo, A. S. T. Chiang and S. B. Liu, *Chem. Mater.* **2004**, *16*, 3168-3175; c) A. Sakthivel, S. J. Huang, W. H. Chen, Z. H. Lan, K. H. Chen, H. P. Lin, C. Y. Mou and S. B. Liu, *Adv. Funct. Mater.* **2005**, *15*, 253-258; d) Y. Liu, W. P. Zhang, Z. C. Liu, S. T. Xu, Y. D. Wang, Z. K. Xie, X. W. Han and X. H. Bao, *J. Phys. Chem. C* **2008**, *112*, 15375-15381; e) Y. Liu, W. P. Zhang, S. J. Xie, L. Xu, X. W. Han and X. H. Bao, *J. Phys. Chem. B* **2008**, *112*, 1226-1231; f) L. Itani, Y. Liu, W. P. Zhang, K. N. Bozhilov, L. Delmotte and V. Valtchev, *J. Am. Chem. Soc.* **2009**, *131*, 10127-10139; g) H. C. Xin, J. Zhao, S. T. Xu, J. P. Li, W. P. Zhang, X. W. Guo, E. J. M. Hensen, Q. H. Yang and C. Li, *J. Phys. Chem. C* **2010**, *114*, 6553-6559; h) K. K. Zhu, J. M. Sun, J. Liu, L. Q. Wang, H. Y. Wan, J. Z. Hu, Y. Wang, C. H. F. Peden and Z.

M. Nie, *ACS Catal.* **2011**, *1*, 682-690; i) C. Z. Jin, G. Li, X. S. Wang, L. X. Zhao, L. P. Liu, H. O. Liu, Y. Liu, W. P. Zhang, X. W. Han and X. H. Bao, *Chem. Mater.* **2007**, *19*, 1664-1670; j) X. J. Li, W. P. Zhang, S. L. Liu, L. Y. Xu, X. W. Han and X. H. Bao, *J. Catal.* **2007**, *250*, 55-66.

[79] a) C. J. Jameson, *J. Chem. Phys.* **2002**, *116*, 8912-8929; b) C. J. Jameson and A. C. de Dios, *J. Chem. Phys.* **2002**, *116*, 3805-3821.

[80] E. Weiland, M. A. Springuel-Huet, A. Nossov and A. Gédéon, *Microporous Mesoporous Mater.* **2016**, *225*, 41-65.

[81] J. C. Woods in *Congressional Hearing: "Caught by Surprise: Causes and Consequences of the Helium-3 Supply Crisis"*, *Vol.* **2010**.

[82] a) J. S. Six, T. Hughes-Riley, D. M. Lilburn, A. C. Dorkes, K. F. Stupic, D. E. Shaw, P. G. Morris, I. P. Hall, G. E. Pavlovskaya and T. Meersmann, *Magn. Reson. Imag.* **2014**, *32*, 48-53; b) Z. I. Cleveland, K. F. Stupic, G. E. Pavlovskaya, J. E. Repine, J. B. Wooten and T. Meersmann, *J. Am. Chem. Soc.* **2007**, *129*, 1784-1792.

[83] W. Ramsay, *Nobel lecture, Dec* **1904**, *12*, 1901-1921.

[84] T. Marx, M. Schmidt, U. Schirmer and H. Reinelt, *J. R. Soc. Med.* **2000**, *93*, 513-517.

[85] J. Lawrence, W. Loomis, C. Tobias and F. Turpin, *J. Physiol.* **1946**, *105*, 197.

[86] S. C. Cullen and E. G. Gross, *Science* **1951**, *113*, 580-582.

[87] M. Albert, G. Cates, B. Driehuys, W. Happer, B. Saam, C. Springer and A. Wishnia, *Nature* **1994**, *370*, 199-201.

[88] a) R. Edelman, H. Hatabu, E. Tadamura, W. Li and P. Prasad, *Nat. Med.* **1996**, *2*, 1236-1239; b) H. Kauczor and K. Kreitner, *Eur. Radiol.* **1999**, *9*, 1755-1764.

[89] J. Mugler, B. Driehuys, J. Brookeman, G. Cates, S. Berr, R. Bryant, T. Daniel, E. deLange, J. Downs, C. Erickson, W. Happer, D. Hinton, N. Kassel, T. Maier, C. Phillips, B. Saam, K. Sauer and M. Wagshul, *Magn. Reson. Med.* **1997**, *37*, 809-815.

[90] L. Zhao and M. Albert, *Nucl. Instrum. Meth. A* **1998**, *402*, 454-460.

[91] a) H. Middleton, R. Black, B. Saam, G. Cates, G. Cofer, R. Guenther, W. Happer, L. Hedlund, G. Johnson, K. Juvan and J. Swartz, *Magn. Reson. Med.* **1995**, *33*, 271-275; b) L. Walkup and J. Woods, *NMR Biomed.* **2014**, *27*, 1429-1438.

[92] a) Y. Shukla, A. Wheatley, M. Kirby, S. Svenningsen, A. Farag, G. Santyr, N. Paterson, D. McCormack and G. Parraga, *Acad. Radiol.* **2012**, *19*, 941-951; b) S. Svenningsen, M. Kirby, D. Starr, D. Leary, A. Wheatley, G. N. Maksym, D. G. McCormack and G. Parraga, *J. Magn. Reson. Imaging* **2013**, *38*, 1521-1530.

[93] a) S. S. Kaushik, Z. I. Cleveland, G. P. Cofer, G. Metz, D. Beaver, J. Nouls, M. Kraft, W. Auffermann, J. Wolber and H. P. McAdams, *Magn. Reson. Med.* **2011**, *65*, 1154-1165; b) B. Driehuys, S. Martinez-Jimenez, Z. Cleveland, G. Metz, D. Beaver, J. Nouls, S. Kaushik, R. Firszt, C. Willis, K. Kelly, J. Wolber, M. Kraft and H. McAdams, *Radiology* **2012**, *262*, 279-289; c) M. Kirby, S. Svenningsen, A. Owrangi, A. Wheatley, A. Farag, A. Ouriadov, G. Santyr, R. Etemad-Rezai, H. Coxson, D. McCormack and G. Parraga, *Radiology* **2012**, *265*, 600-610; d) M. Kirby, S. Svenningsen, N. Kanhere, A. Owrangi, A. Wheatley, H. Coxson, G. Santyr, N. Paterson, D. McCormack and G. Parraga, *J. Appl. Physiol.* **2013**, *114*, 707-715.

[94] a) S. Kaushik, M. Freeman, S. Yoon, M. Liljeroth, J. Stiles, J. Roos, W. Foster, C. Rackley, H. McAdams and B. Driehuys, *J. Appl. Physiol.* **2014**, *117*, 577-585; b) N. J. Stewart, G. Leung, G. Norquay, H. Marshall, J. Parra - Robles, P. S. Murphy, R. F. Schulte, C. Elliot, R. Condliffe and P. D. Griffiths, *Magn. Reson. Med.* **2015**, *74*, 196-207.

[95] S. Kaushik, Z. Cleveland, G. Cofer, G. Metz, D. Beaver, J. Nouls, M. Kraft, W. Auffermann, J. Wolber, H. McAdams and B. Driehuys, *Magn. Reson. Med.* **2011**, *65*, 1155-1165.

[96] M. Kirby and G. Parraga, *Acad. Radiol.* **2013**, *20*, 1344-1356.

[97] B. G. Zeiher, T. J. Gross, J. A. Kern, L. A. Lanza and M. W. Peterson, *Chest* **1995**, *108*, 68-72.

[98] a) K. Ruppert, J. Brookeman, K. Hagspiel and J. Mugler, *Magn. Reson. Med.* **2000**, *44*, 349-357; b) J. Butler, R. Mair, D. Hoffmann, M. Hrovat, R. Rogers, G. Topulos, R. Walsworth and S. Patz, *J. Phys. Condens. Matter* **2002**, *14*, L297; c) H. E. Möller, X. J. Chen, B. Saam, K. D. Hagspiel, G. A. Johnson, T. A. Altes, E. E. De Lange and H. U. Kauczor, *Magn. Reson. Med.* **2002**, *47*, 1029-1051.

[99] K. Qing, K. Ruppert, Y. Jiang, J. Mata, W. Miller, Y. Shim, C. Wang, I. Ruset, F. Hersman, T. Altes and J. Mugler, *J. Magn. Reson. Imaging* **2014**, *39*, 346-359.

[100] Z. Cleveland, G. Cofer, G. Metz, D. Beaver, J. Nouls, S. Kaushik, M. Kraft, J. Wolber, K. Kelly, H. McAdams and B. Driehuys, *Plos One* **2010**, *5*, e12192.

[101] a) J. Mugler, T. Altes, I. Ruset, I. Dregely, J. Mata, G. Miller, S. Ketel, J. Ketel, F. Hersman and K. Ruppert, *Proc. Natl. Acad. Sci. USA* **2010**, *107*, 21707-21712; b) Y. V. Chang, J. D. Quirk, I. C. Ruset, J. J. Atkinson, F. W. Hersman and J. C. Woods, *Magn. Reson. Med.* **2014**, *71*, 339-344; c) K. Ruppert, J. Mata, J. Brookeman, K. Hagspiel and J. Mugler, *Magn. Reson. Med.* **2004**, *51*, 676-687; d) K. Ruppert, J. Mata, H. Wang, W. Tobias, G. Cates, J. Brookeman, K. Hagspiel and J. Mugler, *Magn. Reson. Med.* **2007**, *57*, 1099-1109; e) Y. Chang, J. Mata, T. Altes, J. Mugler III and K. Ruppert, *Proceedings of the Joint Annual Meeting of ISMRM-ESMRMB, Stockholm, Sweden* **2010**, p. 4602.

[102] a) Y. V. Chang, *Magn. Reson. Med.* **2013**, *69*, 884-890; b) I. Dregely, I. Ruset, J. Mata, J. Ketel, S. Ketel, J. Distelbrink, T. Altes, J. Mugler, G. Miller, F. Hersman and K. Ruppert, *Magn. Reson. Med.* **2012**, *67*, 943-953; c) I. Dregely, J. Mugler, I. Ruset, T. Altes, J. Mata, G. Miller, J. Ketel, S. Ketel, J. Distelbrink, F. Hersman and K. Ruppert, *J. Magn. Reson. Imaging* **2011**, *33*, 1052-1062.

[103] R. Chen, F.-C. Fan, S. Kim, K. Jan, S. Usami and S. Chien, *J. Appl. Physiol.* **1980**, *49*, 178-183.

[104] D. Gur, W. F. Good, S. K. Wolfson, H. Yonas and L. Shabason, *Science* **1982**, *215*, 1267-1268.

[105] S. D. Swanson, M. S. Rosen, B. W. Agranoff, K. P. Coulter, R. C. Welsh and T. E. Chupp, *Magn. Reson. Med.* **1997**, *38*, 695-698.

[106] a) A. Wakai, K. Nakamura, J. Kershaw, Y. Kondoh, D. Wright and I. Kanno, *Magn. Reson. Med. Sci.* **2005**, *4*, 19-25; b) X. Zhou, M. Mazzanti, J. Chen, Y. S. Tzeng, J. Mansour, J. Gereige, A. Venkatesh, Y. Sun, R. Mulkern and M. Albert, *NMR Biomed.* **2008**, *21*, 217-225.

[107] G. Duhamel, P. Choquet, J.-L. Leviel, J. Steibel, L. Lamalle, C. Julien, F. Kober, E. Grillon, J. Derouard and M. Décorps, *C. R. Acad. Sci.* **2000**, *323*, 529-536.

[108] X. Zhou, Y. Sun, M. Mazzanti, N. Henninger, J. Mansour, M. Fisher and M. Albert, *NMR Biomed.* **2011**, *24*, 170-175.

[109] M. Mazzanti, R. Walvick, X. Zhou, Y. Sun, N. Shah, J. Mansour, J. Gereige and M. Albert, *Plos One* **2011**, *6*, e21607.

[110] S. S. Kety, *Pharmacol. Rev.* **1951**, *3*, 1-41.

[111] C. Landon, P. Berthault, F. Vovelle and H. Desvaux, *Prot. Sci.* **2001**, *10*, 762-770.
[112] S. M. Rubin, S.-Y. Lee, E. J. Ruiz, A. Pines and D. E. Wemmer, *J. Mol. Biol.* **2002**, *322*, 425-440.
[113] A. Bifone, Y. Song, R. Seydoux, R. Taylor, B. Goodson, T. Pietrass, T. Budinger, G. Navon and A. Pines, *Proc. Natl. Acad. Sci. USA* **1996**, *93*, 12932-12936.
[114] a) S. C. Gunawardana and D. W. Piston, *Diabetes* **2012**, *61*, 674-682; b) X. Liu, S. Wang, Y. You, M. Meng, Z. Zheng, M. Dong, J. Lin, Q. Zhao, C. Zhang and X. Yuan, *Endocrinology* **2015**, *156*, 2461-2469.
[115] A. M. Cypess, C. R. Haft, M. R. Laughlin and H. H. Hu, *Cell Metab.* **2014**, *20*, 408-415.
[116] P. Thurlby and P. Trayhurn, *Pflügers Archiv* **1980**, *385*, 193-201.
[117] R. Branca, L. Zhang, A. Burant, L. Katz and A. McCallister, *Proceedings of the 24th Annual Meeting ISMRM* (Singapore) **2016**, p. 1054.
[118] B. P. Schoenborn, H. C. Watson and J. C. Kendrew, *Nature* **1965**, *207*, 28-30.
[119] C. Bowers, V. Storhaug, C. E. Webster, J. Bharatam, A. Cottone, R. Gianna, K. Betsey and B. Gaffney, *J. Am. Chem. Soc.* **1999**, *121*, 9370-9377.
[120] L. Dubois, P. Da Silva, C. Landon, J. G. Huber, M. Ponchet, F. Vovelle, P. Berthault and H. Desvaux, *J. Am. Chem. Soc.* **2004**, *126*, 15738-15746.
[121] S. M. Rubin, M. M. Spence, I. E. Dimitrov, E. J. Ruiz, A. Pines and D. E. Wemmer, *J. Am. Chem. Soc.* **2001**, *123*, 8616-8617.
[122] T. J. Lowery, M. Doucleff, E. J. Ruiz, S. M. Rubin, A. Pines and D. E. Wemmer, *Prot. Sci.* **2005**, *14*, 848-855.
[123] T. J. Lowery, S. M. Rubin, E. J. Ruiz, A. Pines and D. E. Wemmer, *Angew. Chem. Int. Ed.* **2004**, *43*, 6320-6322.
[124] Y. Song, B. Goodson, R. Taylor, D. Laws, G. Navon and A. Pines, *Angew. Chem. Int. Ed.* **1997**, *36*, 2368-2370.
[125] a) M. El Haouaj, M. Luhmer, Y. H. Ko, K. Kim and K. Bartik, *J. Chem. Soc., Perkin Trans. 2* **2001**, 804-807; b) G. Huber, F. X. Legrand, V. Lewin, D. Baumann, M. P. Heck and P. Berthault, *ChemPhysChem* **2011**, *12*, 1053-1055.
[126] a) K. Bartik, M. Luhmer, J.-P. Dutasta, A. Collet and J. Reisse, *J. Am. Chem. Soc.* **1998**, *120*, 784-791; b) M. Luhmer, B. Goodson, Y. Song, D. Laws, L. Kaiser, M. Cyrier and A. Pines, *J. Am. Chem. Soc.* **1999**, *121*, 3502-3512.
[127] a) M. M. Spence, S. M. Rubin, I. E. Dimitrov, E. J. Ruiz, D. E. Wemmer, A. Pines, S. Q. Yao, F. Tian and P. G. Schultz, *Proc. Natl. Acad. Sci. USA* **2001**, *98*, 10654-10657; b) T. Brotin, A. Lesage, L. Emsley and A. Collet, *J. Am. Chem. Soc.* **2000**, *122*, 1171-1174.
[128] T. Brotin and J.-P. Dutasta, *Chem. Rev.* **2008**, *109*, 88-130.
[129] a) P. A. Hill, Q. Wei, R. G. Eckenhoff and I. J. Dmochowski, *J. Am. Chem. Soc.* **2007**, *129*, 9262-9263; b) P. A. Hill, Q. Wei, T. Troxler and I. J. Dmochowski, *J. Am. Chem. Soc.* **2009**, *131*, 3069-3077; c) G. Huber, T. Brotin, L. Dubois, H. Desvaux, J.-P. Dutasta and P. Berthault, *J. Am. Chem. Soc.* **2006**, *128*, 6239-6246.
[130] a) D. R. Jacobson, N. S. Khan, R. Collé, R. Fitzgerald, L. Laureano-Pérez, Y. Bai and I. J. Dmochowski, *Proc. Natl. Acad. Sci. USA* **2011**, *108*, 10969-10973; b) O. Taratula, P. A. Hill, N. S. Khan, P. J. Carroll and I. J. Dmochowski, *Nat. Commun.* **2010**, *1*, 148.
[131] L. Gao, W. Liu, O.-S. Lee, I. J. Dmochowski and J. G. Saven, *Chem. Sci.* **2015**, *6*, 7238-7248.
[132] T. J. Lowery, S. Garcia, L. Chavez, E. J. Ruiz, T. Wu, T. Brotin, J. P. Dutasta, D. S. King, P. G. Schultz and A. Pines, *ChemBioChem* **2006**, *7*, 65-73.
[133] a) J. Canceill, L. Lacombe and A. Collet, *J. Chem. Soc., Chem. Commun.* **1987**, 219-221; b) R. M. Fairchild, A. I. Joseph, K. T. Holman, H. A. Fogarty, T. Brotin, J.-P. Dutasta, C. I. Boutin, G. Huber and P. Berthault, *J. Am. Chem. Soc.* **2010**, *132*, 15505-15507; c) T. Traoré, G. Clavé, L. Delacour, N. Kotera, P.-Y. Renard, A. Romieu, P. Berthault, C. Boutin, N. Tassali and B. Rousseau, *Chem. Commun.* **2011**, *47*, 9702-9704; d) Y. Bai, P. A. Hill and I. J. Dmochowski, *Anal. Chem.* **2012**, *84*, 9935-9941; e) E. Dubost, N. Kotera, S. Garcia-Argote, Y. Boulard, E. Léonce, C. Boutin, P. Berthault, C. Dugave and B. Rousseau, *Org. Lett.* **2013**, *15*, 2866-2868; f) R. Tyagi, C. Witte, R. Haag and L. Schröder, *Org. Lett.* **2014**, *16*, 4436-4439.
[134] C. Hilty, T. J. Lowery, D. E. Wemmer and A. Pines, *Angew. Chem. Int. Ed.* **2006**, *118*, 76-79.
[135] S. Garcia, L. Chavez, T. J. Lowery, S.-I. Han, D. E. Wemmer and A. Pines, *J. Magn. Reson.* **2007**, *184*, 72-77.
[136] N. Kotera, N. Tassali, E. Léonce, C. Boutin, P. Berthault, T. Brotin, J. P. Dutasta, L. Delacour, T. Traoré and D. A. Buisson, *Angew. Chem. Int. Ed.* **2012**, *51*, 4100-4103.
[137] K. Ward, A. Aletras and R. Balaban, *J. Magn. Reson.* **2000**, *143*, 79-87.
[138] L. Schröder, T. J. Lowery, C. Hilty, D. E. Wemmer and A. Pines, *Science* **2006**, *314*, 446-449.
[139] M. Kunth, J. Dopfert, C. Witte, F. Rossella and L. Schroder, *Angew. Chem. Int. Ed.* **2012**, *51*, 8217-8220.
[140] a) L. Schröder, T. Meldrum, M. Smith, T. J. Lowery, D. E. Wemmer and A. Pines, *Phys. Rev. Lett.* **2008**, *100*, 257603; b) L. Schröder, L. Chavez, T. Meldrum, M. Smith, T. J. Lowery, D. E. Wemmer and A. Pines, *Angew. Chem. Int. Ed.* **2008**, *47*, 4316-4320.
[141] F. Schilling, L. Schroder, K. Palaniappan, S. Zapf, D. Wemmer and A. Pines, *ChemPhysChem* **2010**, *11*, 3529-3533.
[142] Q. Wei, G. K. Seward, P. A. Hill, B. Patton, I. E. Dimitrov, N. N. Kuzma and I. J. Dmochowski, *J. Am. Chem. Soc.* **2006**, *128*, 13274-13283.
[143] V. Roy, T. Brotin, J. P. Dutasta, M. H. Charles, T. Delair, F. Mallet, G. Huber, H. Desvaux, Y. Boulard and P. Berthault, *ChemPhysChem* **2007**, *8*, 2082-2085.
[144] J. M. Chambers, P. A. Hill, J. A. Aaron, Z. Han, D. W. Christianson, N. N. Kuzma and I. J. Dmochowski, *J. Am. Chem. Soc.* **2008**, *131*, 563-569.
[145] A. Schlundt, W. Kilian, M. Beyermann, J. Sticht, S. Günther, S. Höpner, K. Falk, O. Roetzschke, L. Mitschang and C. Freund, *Angew. Chem. Int. Ed.* **2009**, *121*, 4206-4209.
[146] N. Kotera, N. Tassali, E. Leonce, C. Boutin, P. Berthault, T. Brotin, J. Dutasta, L. Delacour, T. Traore, D. Buisson, F. Taran, S. Coudert and B. Rousseau, *Angew. Chem. Int. Ed.* **2012**, *51*, 4100-4103.
[147] H. M. Rose, C. Witte, F. Rossella, S. Klippel, C. Freund and L. Schröder, *Proc. Natl. Acad. Sci. USA* **2014**, *111*, 11697-11702.
[148] G. K. Seward, Y. Bai, N. S. Khan and I. J. Dmochowski, *Chem. Sci.* **2011**, *2*, 1103-1110.
[149] C. Boutin, A. Stopin, F. Lenda, T. Brotin, J.-P. Dutasta, N. Jamin, A. Sanson, Y. Boulard, F. Leteurtre and G. Huber, *Bioorg. Med. Chem.* **2011**, *19*, 4135-4143.
[150] K. K. Palaniappan, R. M. Ramirez, V. S. Bajaj, D. E. Wemmer, A. Pines and M. B. Francis, *Angew. Chem. Int. Ed.* **2013**, *125*, 4949-4953.
[151] N. S. Khan, B. A. Riggle, G. K. Seward, Y. Bai and I. J. Dmochowski, *Bioconjugate Chem.* **2014**, *26*, 101-109.
[152] C. Witte, V. Martos, H. Rose, S. Reinke, S. Klippel, L. Schroder and C. Hackenberger, *Angew. Chem. Int. Ed.* **2015**, *54*, 2806-2810.

[153] B. A. Riggle, Y. Wang and I. J. Dmochowski, *J. Am. Chem. Soc.* **2015**, *137*, 5542-5548.

[154] G. K. Seward, Q. Wei and I. J. Dmochowski, *Bioconjugate Chem.* **2008**, *19*, 2129-2135.

[155] a) S. Klippel, J. Dopfert, J. Jayapaul, M. Kunth, F. Rossella, M. Schnurr, C. Witte, C. Freund and L. Schroder, *Angew. Chem. Int. Ed.* **2014**, *53*, 493-496; b) S. Klippel, C. Freund and L. Schroder, *Nano Letters* **2014**, *14*, 5721-5726; c) F. Rossella, H. Rose, C. Witte, J. Jayapaul and L. Schroder, *ChemPlusChem* **2014**, *79*, 1463-1471.

[156] T. Meldrum, L. Schroder, P. Denger, D. Wemmer and A. Pines, *J. Magn. Reson.* **2010**, *205*, 242-246.

[157] J. Sloniec, M. Schnurr, C. Witte, U. Resch‐Genger, L. Schröder and A. Hennig, *Chem. Eur. J.* **2013**, *19*, 3110-3118.

[158] M. Schnurr, C. Witte and L. Schröder, *Phys. Chem. Chem. Phys.* **2013**, *15*, 14178-14181.

[159] a) M. Schnurr, C. Witte and L. Schröder, *Biophys. J.* **2014**, *106*, 1301-1308; b) M. Schnurr, C. Witte and L. Schröder in *Chapter 16: Caged Xenon in Phospholipid Membrane Environments*, Eds.: T. Meersmann and E. Brunner), **2015**, pp. 288-300.

[160] K. Jeong, C. C. Slack, C. C. Vassiliou, P. Dao, M. D. Gomes, D. J. Kennedy, A. E. Truxal, L. J. Sperling, M. B. Francis and D. E. Wemmer, *ChemPhysChem* **2015**, *16*, 3573-3577.

[161] F. Zamberlan, C. Lesbats, N. J. Rogers, J. L. Krupa, G. E. Pavlovskaya, N. R. Thomas, H. M. Faas and T. Meersmann, *ChemPhysChem* **2015**, *16*, 2294-2298.

[162] a) Y. Wang and I. J. Dmochowski, *Chem. Commun.* **2015**, *51*, 8982-8985; b) M. Kunth, C. Witte, A. Hennig and L. Schroder, *Chem. Sci.* **2015**, *6*, 6069-6075.

[163] M. Schnurr, J. Sloniec‐Myszk, J. Döpfert, L. Schröder and A. Hennig, *Angew. Chem. Int. Ed.* **2015**, *54*, 13444-13447.

[164] Y. Wang, B. W. Roose, E. J. Palovcak, V. Carnevale and I. J. Dmochowski, *Angew. Chem. Int. Ed.* **2016**, *55*, 8984-8987.

[165] J. A. Finbloom, C. C. Slack, C. J. Bruns, K. Jeong, D. E. Wemmer, A. Pines and M. B. Francis, *Chem. Commun.* **2016**, *52*, 3119-3122.

[166] T. K. Stevens, K. K. Palaniappan, R. M. Ramirez, M. B. Francis, D. E. Wemmer and A. Pines, *Magn. Reson. Med.* **2013**, *69*, 1245-1252.

[167] T. Meldrum, K. L. Seim, V. S. Bajaj, K. K. Palaniappan, W. Wu, M. B. Francis, D. E. Wemmer and A. Pines, *J. Am. Chem. Soc.* **2010**, *132*, 5936-5937.

[168] M. Schnurr, K. Sydow, H. Rose, M. Dathe and L. Schroder, *Adv. Healthc. Mater.* **2015**, *4*, 40-45.

[169] T. K. Stevens, R. M. Ramirez and A. Pines, *J. Am. Chem. Soc.* **2013**, *135*, 9576-9579.

[170] M. Shapiro, R. Ramirez, L. Sperling, G. Sun, J. Sun, A. Pines, D. Schaffer and V. Bajaj, *Nat. Chem.* **2014**, *6*, 630-635.

[171] Y. Bai, Y. Wang, M. Goulian, A. Driks and I. J. Dmochowski, *Chem. Sci.* **2014**, *5*, 3197-3203.

[172] C. Witte, M. Kunth, F. Rossella and L. Schroder, *J. Chem. Phys.* **2014**, *140*.

[173] M. Zaiss, M. Schnurr and P. Bachert, *J. Chem. Phys.* **2012**, *136*, 144106.

[174] M. Kunth, C. Witte and L. Schroder, *J. Chem. Phys.* **2014**, *141*, 194202.

[175] M. Kunth, C. Witte and L. Schroder, *NMR Biomed.* **2015**, *28*, 601-606.

[176] J. Dopfert, C. Witte, M. Kunth and L. Schroder, *Contrast Media Mol. Imaging* **2014**, *9*, 100-107.

[177] a) J. Dopfert, C. Witte and L. Schroder, *ChemPhysChem* **2014**, *15*, 261-264; b) C. Boutin, E. Léonce, T. Brotin, A. Jerschow and P. Berthault, *J. Phys. Chem. Lett.* **2013**, *4*, 4172-4176.

[178] a) A. Y. Louie, M. M. Hüber, E. T. Ahrens, U. Rothbächer, R. Moats, R. E. Jacobs, S. E. Fraser and T. J. Meade, *Nat. Biotechnol.* **2000**, *18*, 321-325; b) R. Weissleder, A. Moore, U. Mahmood, R. Bhorade, H. Benveniste, E. A. Chiocca and J. P. Basilion, *Nat. Med.* **2000**, *6*, 351-354; c) B. B. Bartelle, C. A. Berríos-Otero, J. J. Rodriguez, A. E. Friedland, O. Aristizábal and D. H. Turnbull, *Circul. Res.* **2012**, *110*, 938-947; d) P. S. Patrick, J. Hammersley, L. Loizou, M. I. Kettunen, T. B. Rodrigues, D.-E. Hu, S.-S. Tee, R. Hesketh, S. K. Lyons and D. Soloviev, *Proc. Natl. Acad. Sci. USA* **2014**, *111*, 415-420; e) Gil G. Westmeyer, Y. Emer, J. Lintelmann and A. Jasanoff, *Chem. Biol.* **2014**, *21*, 422-429.

[179] a) G. Genove, U. DeMarco, H. Xu, W. F. Goins and E. T. Ahrens, *Nat. Med.* **2005**, *11*, 450-454; b) B. Cohen, H. Dafni, G. Meir, A. Harmelin and M. Neeman, *Neoplasia* **2005**, *7*, 109-117.

[180] O. Zurkiya, A. W. S. Chan and X. Hu, *Magn. Reson. Med.* **2008**, *59*, 1225-1231.

[181] B. B. Bartelle, M. D. Mana, G. A. Suero‐Abreu, J. J. Rodriguez and D. H. Turnbull, *Magn. Reson. Med.* **2015**, *74*, 1750-1757.

[182] R. Weissleder, M. Simonova, A. Bogdanova, S. Bredow, W. S. Enochs and J. A Bogdanov, *Radiology* **1997**, *204*, 425-429.

[183] M. Shapiro, G. Westmeyer, P. Romero, J. Szablowski, B. Kuster, A. Shah, C. Otey, R. Langer, F. Arnold and A. Jasanoff, *Nat. Biotechnol.* **2010**, *28*, 264-U120.

[184] A. A. Gilad, M. T. McMahon, P. Walczak, P. T. Winnard, V. Raman, H. W. van Laarhoven, C. M. Skoglund, J. W. Bulte and P. C. van Zijl, *Nat. Biotechnol.* **2007**, *25*, 217-219.

[185] A. Bar-Shir, G. Liu, K. W. Chan, N. Oskolkov, X. Song, N. N. Yadav, P. Walczak, M. T. McMahon, P. C. van Zijl and J. W. Bulte, *ACS Chem. Biol.* **2013**, *9*, 134-138.

[186] A. Mukherjee, D. Wu, H. C. Davis and M. G. Shapiro, *bioRxiv* **2016**, 037515.

[187] a) V. D. Kodibagkar, J. Yu, L. Liu, H. P. Hetherington and R. P. Mason, *Magn. Reson. Imaging* **2006**, *24*, 959-962; b) L. Liu, V. D. Kodibagkar, J.-X. Yu and R. P. Mason, *The FASEB Journal* **2007**, *21*, 2014-2019; c) Y. Jamin, C. Gabellieri, L. Smyth, S. Reynolds, S. P. Robinson, C. J. Springer, M. O. Leach, G. S. Payne and T. R. Eykyn, *Magn. Reson. Med.* **2009**, *62*, 1300-1304.

[188] a) A. P. Chen, R. E. Hurd, Y.-p. Gu, D. M. Wilson and C. H. Cunningham, *NMR Biomed.* **2011**, *24*, 514-520; b) P. S. Patrick, M. I. Kettunen, S.-S. Tee, T. B. Rodrigues, E. Serrao, K. N. Timm, S. McGuire and K. M. Brindle, *Magn. Reson. Med.* **2015**, *73*, 1401-1406.

[189] a) A. P. Koretsky and B. A. Traxler, *FEBS Lett.* **1989**, *243*, 8-12; b) A. P. Koretsky, M. J. Brosnan, L. H. Chen, J. D. Chen and T. Van Dyke, *Proc. Natl. Acad. Sci. USA* **1990**, *87*, 3112-3116; c) G. Walter, E. R. Barton and H. L. Sweeney, *Proc. Natl. Acad. Sci.* **2000**, *97*, 5151-5155.

[190] a) A. K. Srivastava, D. K. Kadayakkara, A. Bar-Shir, A. A. Gilad, M. T. McMahon and J. W. Bulte, *Dis. Model. Mech.* **2015**, *8*, 323-336; b) A. A. Gilad, K. Ziv, M. T. McMahon, P. C. Van Zijl, M. Neeman and J. W. Bulte, *J. Nucl. Med.* **2008**, *49*, 1905-1908; c) A. Jasanoff, *Curr. Opin. Neurobiol.* **2007**, *17*, 593-600.

[191] T. Prange, M. Schiltz, L. Pernot, N. Colloc'h, S. Longhi, W. Bourguet and R. Fourme, *Proteins: Struct., Funct., Bioinf.* **1998**, *30*, 61-73.
[192] a) E. Locci, Y. Dehouck, M. Casu, G. Saba, A. Lai, M. Luhmer, J. Reisse and K. Bartik, *J. Magn. Reson.* **2001**, *150*, 167-174; b) A. Cherubini and A. Bifone, *Prog. Nucl. Magn. Reson. Spectrosc.* **2003**, *42*, 1-30.
[193] R. Tilton Jr and I. Kuntz Jr, *Biochemistry* **1982**, *21*, 6850-6857.
[194] a) F. Pfeifer, *Nat. Rev. Microbiol.* **2012**, *10*, 705-715; b) A. Walsby, *Microbiol. Rev.* **1994**, *58*, 94-144.
[195] a) E. Harel, L. Schröder and S. Xu, *Annu. Rev. Anal. Chem.* **2008**, *1*, 133-163; b) P. van Zijl and N. N. Yadav, *Magn. Reson. Med.* **2011**, *65*, 927-948.
[196] M. G. Shapiro, P. W. Goodwill, A. Neogy, M. Yin, F. S. Foster, D. V. Schaffer and S. M. Conolly, *Nat Nano* **2014**, *9*, 311-316.
[197] G. J. Lu, A. Farhadi, J. O. Szablowski, S. R. Barnes, A. Lakshmanan, R. W. Bourdeau and M. G. Shapiro, *in preparation*.
[198] Y. Wang, B. W. Roose, E. J. Palovcak, V. Carnevale and I. J. Dmochowski, *Angew. Chem. Int. Ed.* **2016**, DOI 10.1002/anie.201604055.
[199] A. Farkas, *Ortho-hydrogen, para-Hydrogen, and Heavy Hydrogen*, Cambridge University Press, Cambridge, UK, **1935**, p.
[200] a) L. Buljubasich, M. B. Franzoni and K. Munnemann, *Top Curr Chem* **2013**, *338*, 33-74; b) R. Green, R. Adams, S. Duckett, R. Mewis, D. Williamson and G. Green, *Prog. Nucl. Magn. Reson. Spectrosc.* **2012**, *67*, 1-48.
[201] a) B. Feng, A. Coffey, R. Colon, E. Chekmenev and K. Waddell, *J. Magn. Reson.* **2012**, *214*, 258-262; b) J. B. Hövener, S. Bar, J. Leupold, K. Jenne, D. Leibfritz, J. Hennig, S. B. Duckett and D. von Elverfeldt, *NMR Biomed.* **2013**, *26*, 124-131; c) S. Kadlecek, V. Vahdat, T. Nakayama, D. Ng, K. Emami and R. Rizi, *NMR Biomed.* **2011**, *24*, 933-942.
[202] a) P. F. Seidler, H. E. Bryndza, J. E. Frommer, L. S. Stuhl and R. G. Bergman, *Organometallics* **1983**, *2*, 1701-1705; b) S. I. Hommeltoft, D. H. Berry and R. Eisenberg, *J. Am. Chem. Soc.* **1986**, *108*, 5345-5347.
[203] M. G. Pravica and D. P. Weitekamp, *Chem. Phys. Lett.* **1988**, *145*, 255-258.
[204] C. R. Bowers, *eMagRes* **2007**, DOI: 10.1002/9780470034590.emrstm9780470030489.
[205] M. Levitt, *Spin Dynamics: Basics of Nuclear Magnetic Resonance*, John Wiley & Sons, **2001**, p.
[206] J. Kubas Gregory, *Acc. Chem. Res.* **1988**, *21*, 120-128.
[207] F. Reineri, S. Aime, R. Gobetto and C. Nervi, *J. Chem. Phys.* **2014**, *140*, 094307.
[208] I. Horiuti and M. Polanyi, *T. Faraday Soc.* **1934**, *30*, 1164-1172.
[209] A. Eichhorn, A. Koch and J. Bargon, *J. Mol. Catal. A* **2001**, *174*, 293-295.
[210] D. M. Lilburn, G. E. Pavlovskaya and T. Meersmann, *J. Magn. Reson.* **2013**, *229*, 173-186.
[211] a) R. Zhou, E. Zhao, W. Cheng, L. Neal, H. Zheng, R. Quinones, H. Hagelin-Weaver and C. Bowers, *J. Am. Chem. Soc.* **2015**, *137*, 1938-1946; b) A. M. Balu, S. B. Duckett and R. Luque, *Dalton Trans.* **2009**, 5074-5076.
[212] K. Kovtunov, V. Zhivonitko, I. Skovpin, D. Barskiy, O. Salnikov and I. Koptyug, *J. Phys. Chem. C* **2013**, *117*, 22887-22893.
[213] K. Kovtunov, D. Barskiy, R. Shchepin, A. Coffey, K. Waddell, I. Koptyug and E. Chekmenev, *Anal. Chem.* **2014**, *86*, 6192-6196.
[214] V. V. Zhivonitko, K. V. Kovtunov, I. V. Skovpin, D. A. Barskiy, O. G. Salnikov and I. V. Koptyug, *Understanding Organometallic Reaction Mechanisms and Catalysis* **2014**, 145-186.
[215] a) K. Kovtunov, D. Barskiy, A. Coffey, M. Truong, O. Salnikov, A. Khudorozhkov, E. Inozemtseva, I. Prosvirin, V. Bukhtiyarov, K. Waddell, E. Chekmenev and I. Koptyug, *Chem. Eur. J.* **2014**, *20*, 11636-11639; b) E. Zhao, H. Zheng, K. Ludden, Y. Xin, H. Hagelin-Weaver and C. Bowers, *ACS Catal.* **2016**, *6*, 974-978; c) K. Kovtunov, D. Barskiy, O. Salnikov, D. Burueva, A. Khudorozhkov, A. Bukhtiyarov, I. Prosvirin, E. Gerasimov, V. Bukhtiyarov and I. Koptyug, *ChemCatChem* **2015**, *7*, 2581-2584.
[216] D. Barskiy, O. Salnikov, K. Kovtunov and I. Koptyug, *J. Phys. Chem. A* **2015**, *119*, 996-1006.
[217] A. Corma, O. Salnikov, D. Barskiy, K. Kovtunov and I. Koptyug, *Chem. Eur. J.* **2015**, *21*, 7012-7015.
[218] A. Haase, J. Frahm, D. Matthaei, W. Hanicke and K.-D. Merboldt, *J. Magn. Reson.* **1986**, *67*, 258-266.
[219] M. D. Robson, P. D. Gatehouse, M. Bydder and G. M. Bydder, *J. Comput. Assist. Tomogr.* **2003**, *27*, 825-846.
[220] K. V. Kovtunov, A. S. Romanov, O. G. Salnikov, D. A. Barskiy, E. Y. Chekmenev and I. V. Koptyug, *Tomography* **2016**, *2*, 49–55.
[221] K. Kovtunov, M. Truong, D. Barskiy, O. Salnikov, V. Bukhtiyarov, A. Coffey, K. Waddell, I. Koptyug and E. Chekmenev, *J. Phys. Chem. C* **2014**, *118*, 28234-28243.
[222] E. Harel, *Lab Chip* **2009**, *9*, 17-23.
[223] A. J. Moulé, M. M. Spence, S.-I. Han, J. A. Seeley, K. L. Pierce, S. Saxena and A. Pines, *Proc. Natl. Acad. Sci. USA* **2003**, *100*, 9122-9127.
[224] a) J. A. Seeley, S. I. Han and A. Pines, *J. Magn. Reson.* **2004**, *167*, 282-290; b) X. Zhou, D. Graziani and A. Pines, *Proc. Natl. Acad. Sci. USA* **2009**, *106*, 16903-16906.
[225] C. Hilty, E. E. McDonnell, J. Granwehr, K. L. Pierce, S.-I. Han and A. Pines, *Proc. Natl. Acad. Sci. USA* **2005**, *102*, 14960-14963.
[226] J. Granwehr, E. Harel, S. Han, S. Garcia, A. Pines, P. N. Sen and Y.-Q. Song, *Phys. Rev. Lett.* **2005**, *95*, 075503.
[227] E. Harel, J. Granwehr, J. A. Seeley and A. Pines, *Nat. Mater.* **2006**, *5*, 321-327.
[228] V. Telkki, J. Saunavaara and J. Jokisaari, *J. Magn. Reson.* **2010**, *202*, 78-84.
[229] V. Telkki, C. Hilty, S. Garcia, E. Harel and A. Pines, *J. Phys. Chem. B* **2007**, *111*, 13929-13936.
[230] a) V. Telkki, V. Zhivonitko, S. Ahola, K. Kovtunov, J. Jokisaari and I. Koptyug, *Angew. Chem. Int. Ed.* **2010**, *49*, 8363-8366; b) V. Telkki and V. Zhivonitko, *J. Magn. Reson.* **2011**, *210*, 238-245; c) V. Zhivonitko, V. Telkki and I. Koptyug, *Angew. Chem. Int. Ed.* **2012**, *51*, 8054-8058.
[231] a) V. Zhivonitko, V. Telkki, J. Leppaniemi, G. Scotti, S. Franssila and I. Koptyug, *Lab Chip* **2013**, *13*, 1554-1561; b) V. Telkki, V. Zhivonitko, A. Selent, G. Scotti, J. Leppaniemi, S. Franssila and I. Koptyug, *Angew. Chem. Int. Ed.* **2014**, *53*, 11289-11293.
[232] M. Levitt, *Annu. Rev. Phys. Chem.* **2012**, *63*, 89-105.
[233] V. Zhivonitko, K. Kovtunov, P. Chapovsky and I. Koptyug, *Angew. Chem. Int. Ed.* **2013**, *52*, 13251-13255.
[234] A. Tal and L. Frydman, *Prog. Nucl. Magn. Reson. Spectrosc.* **2010**, *57*, 241-292.
[235] S. Ahola, V. Zhivonitko, O. Mankinen, G. Zhang, A. Kantola, H. Chen, C. Hilty, I. Koptyug and V. Telkki, *Nat. Commun.* **2015**, *6*, 8363.
[236] a) S. Ahola and V. Telkki, *ChemPhysChem* **2014**, *15*, 1687-1692; b) J. King, V. Lee, S. Ahola, V. Telkki and T. Meldrum, *Angew. Chem. Int. Ed.* **2016**, *55*, 5040-5043.

[237] a) N. N. Kuzma, P. Hakansson, M. Pourfathi, R. K. Ghosh, H. Kara, S. J. Kadlecek, G. Pileio, M. H. Levitt and R. R. Rizi, *J. Magn. Reson.* **2013**, *234*, 90-94; b) R. K. Ghosh, N. N. Kuzma, S. J. Kadlecek and R. R. Rizi, *Magn. Reson. Med.* **2016**, *75*, 1822-1830.

[238] M. S. Freeman, K. Emami and B. Driehuys, *Phys. Rev. A* **2014**, *90*, 023406.

10.1002/chem.201603884

WILEY-VCH

Entry for the Table of Contents

Layout 1:

MINIREVIEW

This mini-review covers the fundamentals of preparation of hyperpolarized gases and focuses on selected applications of hyperpolarized gases that provide illustrative examples of their utility in biomedicine and materials sciences: remote detection, pulmonary imaging, gas-phase imaging, time-of-flight imaging, brown-fat imaging, and other imaging and spectroscopic applications.

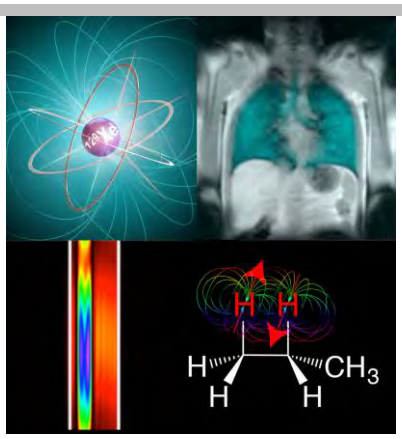

*Danila A. Barskiy, Aaron M. Coffey, Panayiotis Nikolaou, Dmitry M. Mikhaylov, Boyd M. Goodson, Rosa T. Branca, George J. Lu, Mikhail G. Shapiro, Ville-Veikko Telkki, Vladimir V. Zhivonitko, Igor V. Koptyug, Oleg G. Salnikov, Kirill V. Kovtunov, Valerii I. Bukhtiyarov, Matthew S. Rosen, Michael J. Barlow, Shahideh Safavi, Ian P. Hall, Leif Schröder and Eduard Y. Chekmenev**

Page No. – Page No.

NMR Hyperpolarization Techniques of Gases

THE JOURNAL OF PHYSICAL CHEMISTRY C

Article

pubs.acs.org/JPCC

Aqueous NMR Signal Enhancement by Reversible Exchange in a Single Step Using Water-Soluble Catalysts

Fan Shi,[†,∇,¶] Ping He,[†,○,¶] Quinn A. Best,[†,◆] Kirsten Groome,[†] Milton L. Truong,[§] Aaron M. Coffey,[§] Greg Zimay,[†] Roman V. Shchepin,[§] Kevin W. Waddell,[§] Eduard Y. Chekmenev,[§,∥,⊥,#] and Boyd M. Goodson*[,†,‡]

[†]Department of Chemistry and Biochemistry, and [‡]Materials Technology Center, Southern Illinois University, Carbondale, Illinois 62901, United States

[§]Department of Radiology, Vanderbilt University Institute of Imaging Science, Nashville, Tennessee 37232, United States

[∥]Department of Biomedical Engineering, Vanderbilt University, Nashville, Tennessee 37235, United States

[⊥]Vanderbilt-Ingram Cancer Center, Nashville, Tennessee 37232, United States

[#]Russian Academy of Sciences, Leninskiy Prospekt 14, Moscow, 119991, Russia

Supporting Information

ABSTRACT: Two synthetic strategies are investigated for the preparation of water-soluble iridium-based catalysts for NMR signal amplification by reversible exchange (SABRE). In one approach, PEGylation of a variant *N*-heterocyclic carbene provided a novel catalyst with excellent water solubility. However, while SABRE-active in ethanol solutions, the catalyst lost activity in >50% water. In a second approach, synthesis of a novel di-iridium complex precursor where the cyclooctadiene (COD) rings have been replaced by CODDA (1,2-dihydroxy-3,7-cyclooctadiene) leads to the creation of a catalyst [IrCl(CODDA)IMes] that can be dissolved and activated in water—enabling aqueous SABRE in a single step, without need for either an organic cosolvent or solvent removal followed by aqueous reconstitution. The potential utility of the CODDA catalyst for aqueous SABRE is demonstrated with the ∼(−)32-fold enhancement of ^{1}H signals of pyridine in water with only 1 atm of parahydrogen.

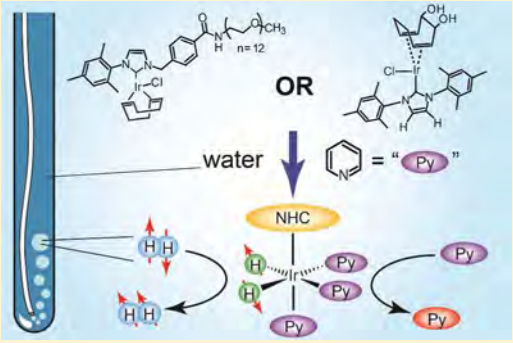

INTRODUCTION

Because of their inherent advantages (including high spatiotemporal resolution, lack of ionizing radiation, and the ability to spectrally distinguish multiple signal sources), magnetic resonance imaging (MRI)-based molecular imaging[1,2] techniques promise to revolutionize clinical imaging—from the screening and diagnosis of disease, to the assessment of treatment response. However, the inherently low detection sensitivity of conventional magnetic resonance techniques makes it challenging to detect and track low-concentration species in vivo, such as gas species in lung spaces or metabolic biomarkers in blood or other tissues. Hyperpolarization[3] techniques like dissolution dynamic nuclear polarization (d-DNP),[4,5] spin-exchange optical pumping (SEOP),[6,7] and parahydrogen induced polarization (PHIP)[8,9] offer the possibility of overcoming the problem of low agent concentration by increasing the nuclear spin polarization—and hence MR signal—by several orders of magnitude.

Signal amplification by reversible exchange (SABRE)[10] is a relatively new hyperpolarization technique pioneered by Duckett, Green, and co-workers in 2009.[11,12] In SABRE, an organometallic catalyst is used to colocate a molecular substrate to be hyperpolarized and parahydrogen (pH_2)—a source of pure nuclear spin order. Like traditional PHIP,[8,9,13−19] SABRE is of interest because it is cost-effective, potentially continuous, scalable, and rapid (achieving polarization enhancement in seconds).[10−12,20−40] However, unlike traditional PHIP, SABRE does not require permanent alteration of the substrate to hyperpolarize it.[11] Since its inception, considerable effort has been put forth to broaden the applicability of SABRE by investigating alternative catalyst structures,[21,28,41−45] improving the nuclear spin polarization achieved for protons[34,46] and various heteronuclei[30,32,47−50] (including through the application of variable applied DC and AC fields), demonstrating high-resolution imaging[25,50] (including at low magnetic field[51]), widening the range of amenable substrate types,[36] achieving enhancement in the limits of both low-[29,52] and high-concentration[49] agents (including in complex mixtures[20]), and demonstrating SABRE with (and separation/reuse of) heterogeneous microscale/nanoscale catalysts.[53,54]

Other efforts have concerned the extension of SABRE to aqueous environments. Because of the poor aqueous solubility

Received: May 4, 2016
Revised: May 11, 2016
Published: May 11, 2016

ACS Publications © 2016 American Chemical Society

DOI: 10.1021/acs.jpcc.6b04484
J. Phys. Chem. C 2016, 120, 12149−12156

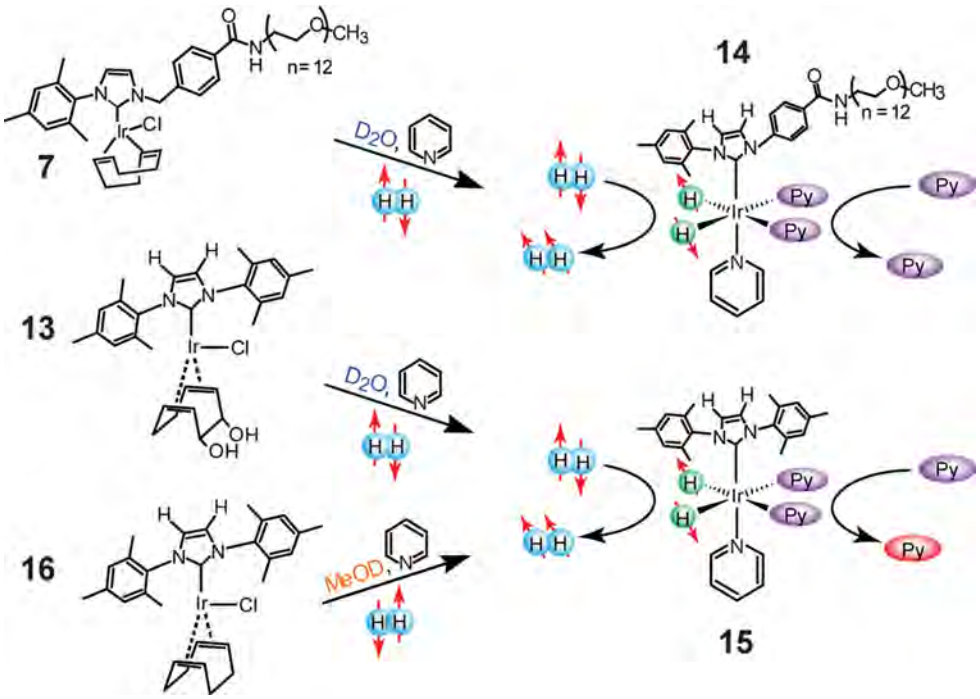

Figure 1. Relevant structures for studying SABRE in aqueous environments in the present work, pre (**7**, **13**, and **16**) and post (**14** and **15**) activation in the presence of H_2 gas and pyridine (py) substrate. **16** is the "traditional" Ir/IMes SABRE catalyst in its preactivated form, whereas **7** and **13** are the water-soluble PEGylated and cyclooctadiene-diol ("CODDA") variants, respectively (the numbering of the above structures is explained in the Supporting Information Figures S1 and S2, which, respectively, summarize the synthesis of structures **7** and **13**).

of the "standard" SABRE catalyst ([IrCl(COD) (IMes)],[46,55,56] where "COD" = cyclooctadiene and "IMes" = 1,3-bis(2,4,6-trimethylphenyl)imidazol-2-ylidene), recent promising efforts have relied on organic cosolvents to achieve SABRE in aqueous/organic mixtures[34,45,50,57] However, in other previous work we recently found that the chemical changes that accompany this catalyst's activation also endow it with water solubility;[57] following activation, the organic solvent may be completely removed and the activated catalyst can be subsequently reconstituted in deuterated water to achieve SABRE enhancement.

Here we report our efforts to develop novel homogeneous catalysts that may lead to improved SABRE in aqueous environments, without the need for separate catalyst activation, organic solvent removal, or subsequent aqueous reconstitution.[58,59] Two different strategies were utilized to alter the structure—and hence aqueous solubility—of the original standard catalyst by targeting either the *N*-heterocyclic carbene moiety or the COD group, respectively (Figure 1). For the former, PEGylation[60] of a variant of the aromatic carbene moiety provided much greater aqueous solubility for the catalyst ("**7**"); however, while that catalyst is SABRE-active in ethanol solutions, it lost activity in >50% water. For the latter, synthesis of a di-iridium complex precursor where the COD rings have been replaced by CODDA (1,2-dihydroxy-3,7-cyclooctadiene) permits creation of a catalyst [IrCl(CODDA)-IMes] ("**13**") that can be dissolved and activated in water, enabling aqueous SABRE in a single step without need for any organic cosolvent. The potential utility of the CODDA catalyst for aqueous SABRE is demonstrated with the ∼(−)32-fold enhancement of ^{1}H signals of pyridine in water with only 1 atm of pH_2. Taken together, these results aid the evaluation of different synthetic approaches for aqueous SABRE that, when improved and combined with other approaches, should help enable a wide range of biological, biomedical, and in vivo spectroscopic and imaging experiments.

■ RESULTS AND DISCUSSION

Exploring SABRE with the PEGylated Catalyst. The PEGylated catalyst **7** was examined to determine its efficacy for SABRE in organic and aqueous environments. SABRE experiments were performed by bubbling pH_2 thoroughly into the NMR tube while located outside of the magnet ("low-field"), followed by immediate transfer of the sample into the 9.4 T NMR magnet for "high-field" detection of enhanced ^{1}H NMR spectra. The catalyst was activated via pH_2 bubbling in the presence of excess substrate prior to use in SABRE experiments, and the low mixing field was somewhat variable (∼11 ± 5 mT) and was not systematically optimized. Enhancements were recorded for the test substrate pyridine (py); results for all of the experiments described in this work are summarized in Table 1.

In an early set of experiments (not shown), bubbling pH_2 at atmospheric pressure gave up to ∼16-fold enhancements for the ^{1}H NMR signals of py in 100% d_6-ethanol. The addition of D_2O to d_4-methanol solutions had lower enhancements than d_6-ethanol, with ∼20% D_2O/∼80% d_4-methanol yielding only ∼6-fold ^{1}H signal enhancements. Higher volume fractions (e.g., 50/50) of D_2O in d_4-methanol resulted in no observable SABRE enhancements under these conditions.

The lower SABRE enhancements in solutions with increasing water fractions were originally rationalized by the ∼15-fold lower solubility of H_2 gas in water compared to that in alcohol-based solvents.[61] To mitigate the H_2 solubility limitation of aqueous solutions, the apparatus was altered to allow pH_2 pressures of up to ∼60 psi positive pressure (∼5.1 atm total H_2 pressure). Bubbling pH_2 at 60 psi into a sample containing 100% d_6-ethanol, ∼3.5 mM of the catalyst **7**, and 35 mM py

DOI: 10.1021/acs.jpcc.6b04484
J. Phys. Chem. C 2016, 120, 12149−12156

Table 1. Polarization Enhancement (ε) Values for Three Aromatic Proton Sites of Pyridine Observed with Different Catalysts in Aqueous and Nonaqueous Environments[a]

catalyst	solvent	ε (H_o)	ε (H_p)	ε (H_m)
7	100% d_6-ethanol	−42	−57	−11
7	100% d_6-ethanol	−45	−61	−11
7	13% D_2O/87% d_6-ethanol	−37	−27	−12
7	13% D_2O/87% d_6-ethanol	−38	−31	−14
7	43% D_2O/57% d_6-ethanol	−9.5	−5.7	−1.3
7	43% D_2O/57% d_6-ethanol	−7.3	−4.9	−0.4
7	63% D_2O/37% d_6-ethanol	∼0	∼0	∼0
13	100% D_2O	−25	−19	−11
13	100% D_2O	−32	−25	−16
16	100% D_2O	∼0	∼0	∼0

[a]Reported ε values are calculated from spectral integrals and are approximate, with estimated uncertainties of ∼10%. Results from the top two acquisitions for each condition are reported.

gave rise to ∼40−60-fold enhancement of the ^{1}H NMR signal from the substrate (e.g., Figure 2b) compared to the signal acquired at thermal equilibrium (Figure 2a; the conventional SABRE catalyst **16** is also effective in 100% d_6-ethanol[57]). Little dependence on temperature was observed, with similar enhancements attained when the temperature was raised from 301 to 321 K.

Next, no SABRE enhancement was observed when pH_2 was bubbled in at high field (9.39 T; Figure 2, parts c and d), unlike the case with the "standard" NHC-Ir catalyst, **16**.[24,57] Also unlike the case with **16**, no strong, purely absorptive signal at ∼(−)22.8 ppm is observed from magnetically equivalent hyperpolarized hydride spins on the activated catalyst structure. Instead, the hydride region exhibits two relatively weak dispersive doublets at ca. −22.2 and ∼−23.1 ppm. These dispersive signals are reminiscent of the enhanced hydride resonances from organometallic catalysts explored previously with PHIP (e.g., $RhH_2(PPh_3)_3Cl$[13]) and, thus, are tentatively assigned to the two hydride sites on the activated catalyst (**14**) rendered effectively inequivalent by the broken symmetry of the PEGylated *N*-heterocyclic carbene. A pair of additional, much weaker dispersive signals (at ca. −22.6 and −25.9 ppm) likely arise from inequivalent hydride sites on a similar structure to **14** originating from a different chemical pathway. The absence of a high-field SABRE effect is likely a combination of inefficient conversion of spin order from pH_2 at high field and the lack of strong *z*-magnetization of the hydride spins, and is consistent with the current picture for the high-field SABRE

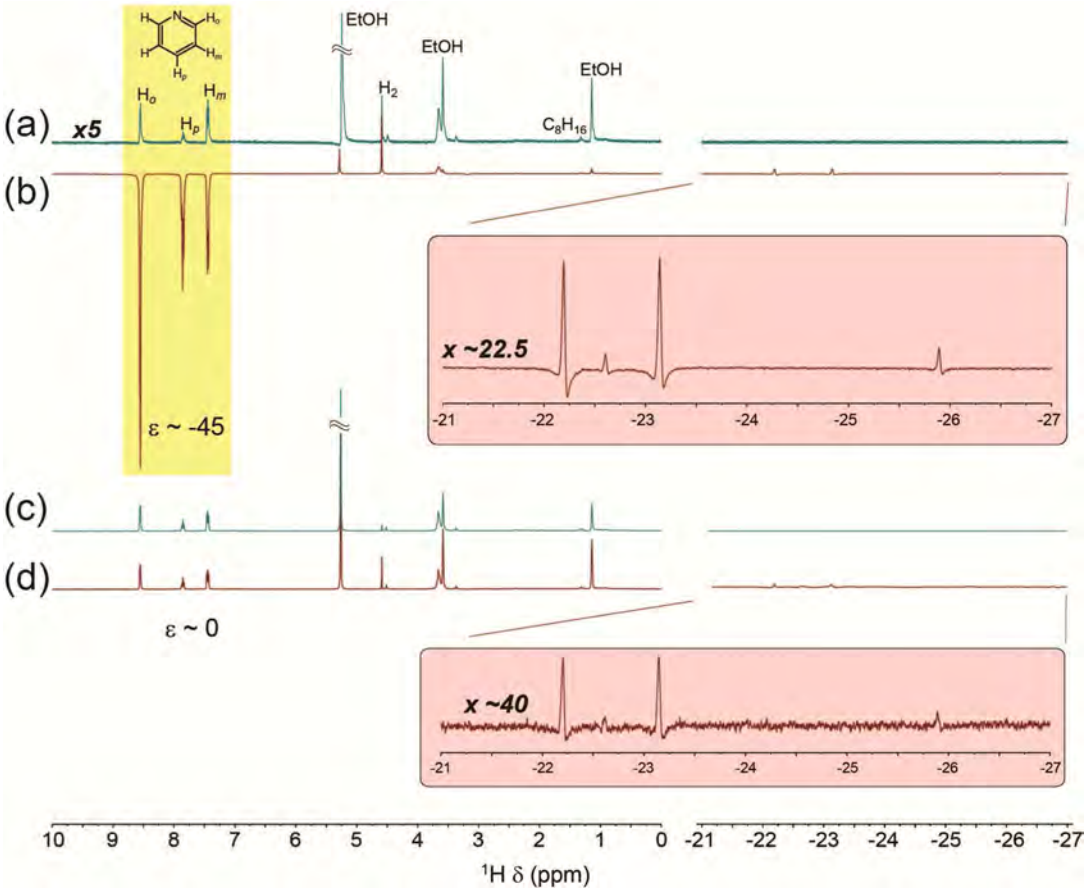

Figure 2. SABRE studies with the PEGylated Ir catalyst (**7**/**14**) in 100% deuterated ethanol. (a) Thermally polarized reference ^{1}H NMR scan from the solution following activation with pH_2 in the presence of excess substrate (py); the spectrum is vertically scaled 5-fold compared to panel b, which shows the successful observation of SABRE enhancement after 1 min of bubbling with ∼5.1 atm of pH_2 at ∼11 mT, then transfer to 9.39 T for high-field acquisition; enhancements up to ∼40−60-fold were observed with 3.5 mM catalyst and the given conditions. Panels c and d show spectra from a separate experiment, where no high-field SABRE effect was observed, i.e., where pH_2 bubbling/SABRE mixing was performed entirely at 9.39 T (d), compared to a corresponding thermally polarized spectrum (c). (Vertical scale for panels c and d is different from that of panels a and b.) Insets show amplified hydride regions from spectra in panels b and d, respectively.

DOI: 10.1021/acs.jpcc.6b04484
J. Phys. Chem. C 2016, 120, 12149−12156

mechanism—cross-relaxation akin to the spin-polarization induced nuclear Overhauser effect.[24,57,62,63]

As shown in Figure 3, parts a and b, modest aqueous fractions (∼13% v/v) had only a minor negative effect on SABRE enhancement (maximum $|\varepsilon| \sim 40$). Here, the concentration of D_2O is already orders of magnitude higher than the concentrations of the catalyst and substrate. Bringing the water fraction to nearly 1:1 dropped the SABRE enhancement by ∼5-fold (Figure 3, parts c and d); this observation is in reasonable agreement with the ∼15-fold lower solubility of H_2 in water versus alcohol-based solvents.[61] However, higher mole fractions of water (e.g., Figure 3d, inset) have not yielded observable enhancements to date. While this second set of experiments represents a marked improvement over the first in terms of both larger enhancements and larger aqueous fractions for the solvent, the origin of the absence of SABRE at higher aqueous fractions remains unclear. One hint may lie in the changes to the hydride region of the spectrum. For example, while the primary dispersive resonances at ca. −22.2 and ∼−23.1 ppm remain in the spectrum from the ∼13% v/v solution (Figure 3b, inset), overall the hydride signal is attenuated, there appears to be a new absorptive resonance at ∼(−)22.5 ppm, and the other weak resonances appear to have bifurcated and shifted several parts per million downfield. With ∼43% D_2O, only a weak dispersive resonance at ca. −22.3 ppm remains, and with higher aqueous fractions, almost no hydride signal can be detected (not shown).

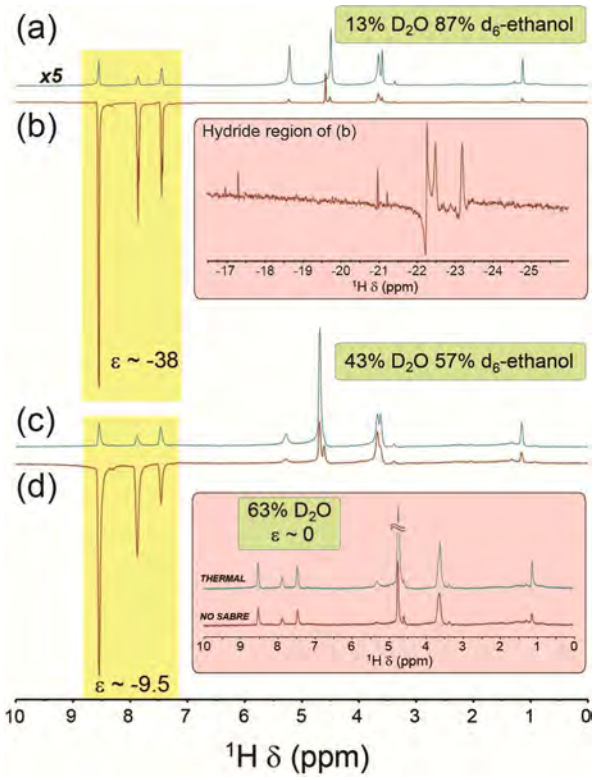

Figure 3. SABRE studies with the PEGylated Ir catalyst (**7**/**14**) in various deuterated ethanol/water mixtures. (a) Thermally polarized reference ^{1}H NMR scan from a D_2O/d_6-ethanol (∼13%/87% v/v) solution following activation; the spectrum is vertically scaled 5-fold compared to panel b, which shows the successful observation of SABRE enhancement of substrate (py) ^{1}H resonances after 1 min of bubbling with 5.1 atm of pH_2 at ∼11 mT, then transfer to 9.39 T for high-field acquisition; enhancements up to ∼40-fold were observed with 3.5 mM catalyst and the given conditions. Changing the D_2O/d_6-ethanol fraction to ∼43%/57% v/v (c and d) and 63%/37% v/v (inset) significantly impacted the magnitude of the SABRE enhancement; the SABRE spectrum in panel d showed less than an ∼10-fold enhancement compared to the corresponding thermal spectrum (c), and no observed SABRE enhancement was observed in the 63%/37% solution.

The observations of reduced (or no) SABRE enhancements in large aqueous fractions are qualitatively similar to those very recently reported by Fekete et al.,[45] who investigated the use of two different synthetic approaches for generating water-soluble iridium-based SABRE catalysts (respectively featuring sulfonated phosphine groups and IMes NHC variants difunctionalized with triazole groups). For those catalysts, significant ^{1}H NMR enhancements could be observed in organic solvents, but little or no SABRE activity was observed when the aqueous fraction was too great. In that work, the absence of SABRE activity was attributed to the much lower solubility of H_2 in water compared to the organic solvents. The observations reported here could be largely explained by the reduced pH_2 concentration; however, other effects may be contributing given the complete lack of SABRE activity with high water fractions, as well as the changes in the hydride spectra. As an aside, the solvent environment during activation (i.e., organic vs aqueous) did not affect the results. Thus, the reduced pH_2 concentration, possibly combined with structural changes of the catalyst that interfere with the formation of effective hydride species, binding of the substrate, and/or subsequent transfer of spin order from pH_2 to substrate spins, likely leads to the loss of SABRE activity with high aqueous fractions—issues that will be the subject of future study.

Exploring SABRE with the CODDA Catalyst. As mentioned above, the standard SABRE catalyst (**16**) is effectively insoluble in water for the present purposes; however, changes accompanying catalyst activation provide a water-soluble structure (e.g., **15**).[57] Thus, in light of the challenges presented by the PEGylated catalyst, an alternative design approach was devised to provide a catalyst structure with improved water solubility (e.g., [IrCl(CODDA)IMes], **13**, Figure 1) that, once activated, should yield the same SABRE-active structure as **15**—with the goal of enabling aqueous SABRE in a single step without need for any organic cosolvent.

Although not as water-soluble as **7** (at least ∼10 mg/mL), according to atomic absorption spectroscopy (AAS) the solubility of the CODDA catalyst (**13**) in water is ∼0.2 mg/mL; thus, a saturated solution of **13** (with ∼0.3 mM dissolved concentration) was prepared in deuterated water with excess py substrate (∼10 mM). Bubbling with pH_2 allowed the activation of the catalyst in an aqueous environment to be monitored in situ via hyperpolarization-enhanced ^{1}H NMR (Figure 4). More specifically, spectra from the hydride region acquired during activation of **13** are shown in Figure 4a, and these results are compared with selected spectra obtained from the standard catalyst (**16**) in deuterated water (Figure 4b) and methanol solvents (Figure 4c), respectively. At first (30 s), the signals from the hydride region for **13** are dramatically different from what is observed during activation of **16**. Reflecting the different intermediate structures present, alternating absorptive/emissive (or dispersive) signals downfield of the activated catalyst's characteristic shift (−22.8 ppm) are virtually absent, and instead the early spectra are dominated by a number of purely absorptive peaks that are mostly further upfield (i.e., with a more negative chemical shift), including a strong peak at

DOI: 10.1021/acs.jpcc.6b04484
J. Phys. Chem. C 2016, 120, 12149−12156

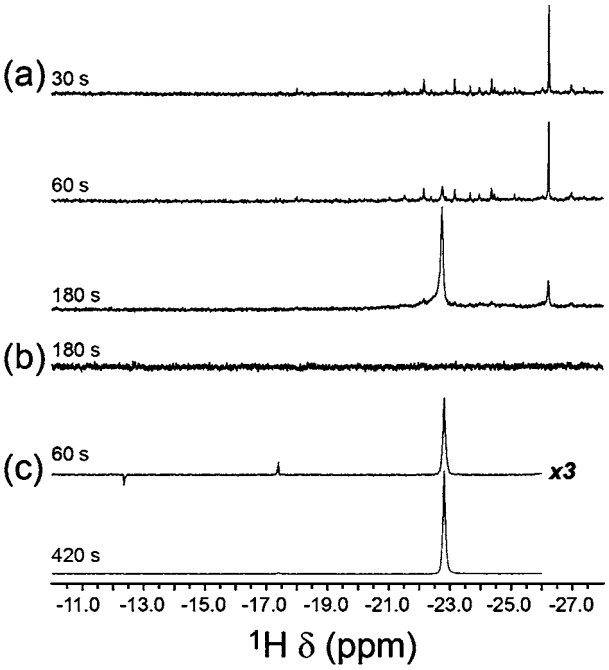

Figure 4. Comparison of the hydride regions of ^{1}H NMR spectra acquired during activation of the water-soluble CODDA/Ir SABRE catalyst **13** (a) and the conventional Ir/IMes SABRE catalyst **16** (b and c). (a) Upfield ^{1}H NMR region showing changes to the hydride resonances during activation of **13** in D_2O observed at 30, 60, and 180 s after pH_2 bubbling began (1 atm). A corresponding attempt to observe activation of the (poorly water-soluble) conventional SABRE catalyst in D_2O (**16**) exhibited no hydride signal (b). Selected spectra obtained separately during activation of **16** in deuterated methanol are shown in panel c, respectively, 60 and 420 s following the onset of pH_2 bubbling. As expected, activation of both **13** and **16** trend toward the same final hydride signal (i.e., a strong singlet at ~22.8 ppm). Spectra in panels a−c possess different vertical scales.

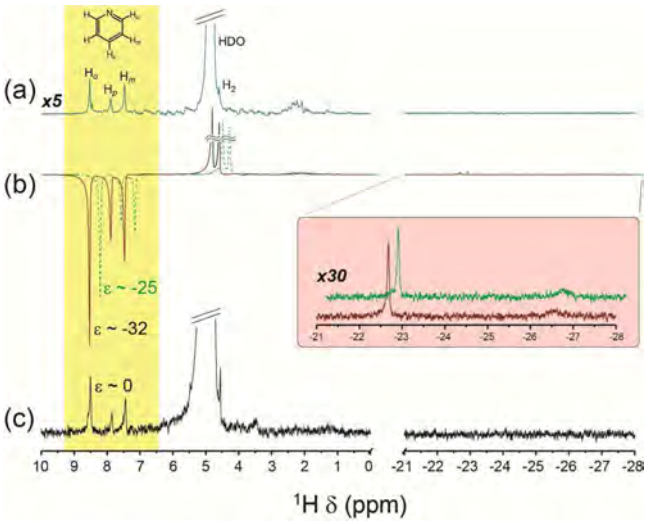

Figure 5. SABRE studies with the water-soluble CODDA/Ir SABRE catalyst (**13**/**15**) in 100% D_2O. (a) Thermally polarized reference ^{1}H NMR scan from the solution following activation with pH_2 in the presence of excess substrate (py); the spectrum is vertically scaled 5-fold compared to panel b, which shows two spectra exhibiting successful observation of SABRE enhancement after bubbling with 1 atm of pH_2 at ~10 mT [total bubbling times of 210 s (30 s immediately prior to acquisition, green dashed curve) and 240 s (30 s immediately prior to acquisition, red solid curve) for the spectra, respectively], then transfer to 9.39 T for high-field acquisition (note that the green curve is shown horizontally offset by a fraction of a ppm to show the enhancement compared to the red curve). Corresponding peak enhancements were ~25-fold and ~32-fold for py in water with only 1 atm of pH_2 bubbling in the two spectra, using a catalyst concentration of 0.3 mM. The inset shows the corresponding hydride region. A separate experiment where SABRE was attempted using the standard Ir/IMes catalyst in deuterated water exhibited no SABRE enhancement (c). (Vertical scale for panel c is different from that of panels a and b.)

−26.2 ppm from a key intermediate structure. Nevertheless, following 180 s of pH_2 bubbling, the expected singlet peak at ca. −22.8 ppm is observed, in excellent agreement with the hydride shift of the activated structure **15** obtained from the standard catalyst in methanol (Figure 4c). However, corresponding efforts to activate **16** directly in D_2O were unsuccessful, yielding a cloudy suspension and no discernible enhanced NMR signals from the hydride region (Figure 4b). In any case, the above results are consistent with successful activation of the novel catalyst **13** in water in just a few minutes to achieve the desired activated structure **15**.

Following successful activation of the CODDA catalyst in deuterated water, the potential of this catalyst for performing SABRE enhancement of ^{1}H NMR in aqueous environments was evaluated using the standard test substrate pyridine (Figure 5). With only 1 atm of pH_2 bubbling (~90% pH_2 fraction) and catalyst and substrate concentrations of ~0.3 and ~10 mM, respectively, an initial enhancement of ca. $\varepsilon = -25$ was achieved for the ortho ^{1}H py position after 30 s of bubbling at ~10 mT fringe field and subsequent transfer to 9.4 T (Figure 5b), compared to the signal from a corresponding thermal spectrum (Figure 5a). The inset of Figure 5b shows the corresponding hydride regions obtained from the CODDA catalyst during the SABRE experiments, indicating that the CODDA catalyst is essentially activated by the time the SABRE spectra were recorded (total pH_2 bubbling time of 210 and 240 s, respectively). Repeating the experiment permitted enhancements as large as ca. −32, −25, and −16 for ortho, para, and meta ^{1}H Py positions to be observed, Figure 5b; Table 1. However, the sample from Figure 4b containing an aqueous suspension of the traditional SABRE catalyst (**16**) yields no SABRE enhancement, Figure 5c.

The experiments described above were performed in deuterated water to facilitate spectral interpretation and quantification; however, this practice poses no impediment to broader application of the approach (including for ultimate in vivo experiments) because SABRE hyperpolarization generally works as well (or better) in protonated solution environments, particularly for heteronuclei.[49,64,65] We also note that these results are similar to what has been achieved using the conventional catalyst following dissolution and activation in organic solvents, drying, and reconstitution in D_2O ($\varepsilon \sim 30$), using a weaker substrate (nicotinamide) but higher pH_2 pressure (~5 atm) and greater (~1:10) catalyst/substrate ratio.[57] In any case, these results indicate the successful preparation, activation, and demonstration of a catalyst capable of easily performing SABRE enhancement in aqueous environments in a single step. This approach obviates the need for either the extra steps associated with reconstitution or the exposure of sensitive biological samples to organic solvents, and thus may also help facilitate biomedical (and ultimately in vivo) applications.

DOI: 10.1021/acs.jpcc.6b04484
J. Phys. Chem. C 2016, 120, 12149−12156

CONCLUSION

In summary, two novel approaches were investigated for creating water-soluble catalysts to increase the nuclear spin polarization of substrates via SABRE. PEGylation of an asymmetric aromatic carbene ligand provided a highly water-soluble structure that yielded ∼40−60-fold ^{1}H NMR enhancements in alcohol-based solvents and in lean water/alcohol mixtures, but lost SABRE activity in more highly aqueous solvent mixtures. In the second strategy, diol functionalization of the COD ring provided a catalyst structure with lower water solubility, but sufficient to dissolve and activate in water to enable aqueous SABRE in a single step—without need for either an organic cosolvent or solvent removal followed by aqueous reconstitution—here demonstrated for the first time. The >30-fold ^{1}H enhancement under our conditions (with only 1 atm pH_2—a mere technical limitation of the bubbler apparatus used for those experiments) is in reasonable agreement with our recent observation of nearly 2000-fold enhancements of ^{1}H signals for the same substrate using the standard SABRE catalyst in deuterated methanol with elevated pH_2 pressures,[41] given the expected ∼75-fold difference in pH_2 concentration; correspondingly, much larger enhancements should be expected upon implementing experimental approaches to greatly increase the pH_2 concentration, including higher-pressure reaction vessels. Moreover, the results presented here likely point the way to achieving higher aqueous catalyst concentrations, which should be possible by employing some combination of the above synthetic approaches (e.g., by functionalizing the COD with moieties that endow greater aqueous solubility). Such improvements, combined with other approaches, should help enable biological and spectroscopic applications that will be pursued in due course.

ASSOCIATED CONTENT

Supporting Information

The Supporting Information is available free of charge on the ACS Publications website at DOI: 10.1021/acs.jpcc.6b04484.

Details of the methods used to synthesize and characterize the catalysts, along with the details concerning the SABRE NMR experiments (PDF)

AUTHOR INFORMATION

Corresponding Author

*E-mail: bgoodson@chem.siu.edu. Phone: 618-453-6427.

Present Addresses

[∇]F.S.: Advanced Imaging Research Center, University of Texas Southwestern Medical Center, Dallas, TX 75390.

[○]P.H.: Pennington Biomedical Research Center, Baton Rouge, LA 70808.

[◆]Q.B.: Department of Chemistry, Louisiana State University, Baton Rouge, LA 70803.

Author Contributions

[¶]F.S. and P.H. contributed equally.

Notes

The authors declare no competing financial interest.

ACKNOWLEDGMENTS

B.M.G. and F.S. thank Professor Jay Means (UCSB) for helpful discussions. Work at SIUC and Vanderbilt is supported by the NIH (1R21EB018014 and 1R21EB020323), NSF (CHE-1416432 and CHE-1416268), and DOD (CDMRP BRP W81XWH-12-1-0159/BC112431, and PRMRP awards W81XWH-15-1-0271 and W81XWH-15-1-0272). E.Y.C. also acknowledges support from Exxon Mobil Knowledge Build. A.M.C. also acknowledges support from NIH NIBIB T32 EB001628. F.S. gratefully acknowledges support from a Gower summer research fellowship (SIUC). B.M.G. is a member of SIUC Materials Technology Center.

REFERENCES

(1) Kurhanewicz, J.; Vigneron, D. B.; Brindle, K.; Chekmenev, E. Y.; Comment, A.; Cunningham, C. H.; DeBerardinis, R. J.; Green, G. G.; Leach, M. O.; Rajan, S. S.; et al. Analysis Of Cancer Metabolism By Imaging Hyperpolarized Nuclei: Prospects For Translation To Clinical Research. *Neoplasia* **2011**, *13*, 81−97.

(2) Weissleder, R. Molecular Imaging in Cancer. *Science* **2006**, *312*, 1168−1171.

(3) Nikolaou, P.; Goodson, B. M.; Chekmenev, E. Y. NMR Hyperpolarization Techniques for Biomedicine. *Chem.—Eur. J.* **2015**, *21*, 3156−3166.

(4) Ardenkjær-Larsen, J. H.; Fridlund, B.; Gram, A.; Hansson, G.; Hansson, L.; Lerche, M. H.; Servin, R.; Thaning, M.; Golman, K. Increase In Signal-To-Noise Ratio Of > 10,000 Times In Liquid-State NMR. *Proc. Natl. Acad. Sci. U. S. A.* **2003**, *100*, 10158−10163.

(5) Day, S. E.; Kettunen, M. I.; Gallagher, F. A.; Hu, D. E.; Lerche, M.; Wolber, J.; Golman, K.; Ardenkjaer-Larsen, J. H.; Brindle, K. M. Detecting Tumor Response To Treatment Using Hyperpolarized C-13 Magnetic Resonance Imaging And Spectroscopy. *Nat. Med.* **2007**, *13*, 1382−1387.

(6) Walker, T. G.; Happer, W. Spin-Exchange Optical Pumping Of Noble-Gas Nuclei. *Rev. Mod. Phys.* **1997**, *69*, 629−642.

(7) Goodson, B. M. Nuclear Magnetic Resonance of Laser-Polarized Noble Gases in Molecules, Materials, and Organisms. *J. Magn. Reson.* **2002**, *155*, 157−216.

(8) Bowers, C. R.; Weitekamp, D. P. Transformation Of Symmetrization Order To Nuclear-Spin Magnetization By Chemical-Reaction And Nuclear-Magnetic-Resonance. *Phys. Rev. Lett.* **1986**, *57*, 2645−2648.

(9) Eisenschmid, T. C.; Kirss, R. U.; Deutsch, P. P.; Hommeltoft, S. I.; Eisenberg, R.; Bargon, J.; Lawler, R. G.; Balch, A. L. Para Hydrogen Induced Polarization In Hydrogenation Reactions. *J. Am. Chem. Soc.* **1987**, *109*, 8089−8091.

(10) Mewis, R. E. Developments and Advances Concerning the Hyperpolarization Technique SABRE. *Magn. Reson. Chem.* **2015**, *53*, 789−800.

(11) Adams, R. W.; Aguilar, J. A.; Atkinson, K. D.; Cowley, M. J.; Elliott, P. I. P.; Duckett, S. B.; Green, G. G. R.; Khazal, I. G.; Lopez-Serrano, J.; Williamson, D. C. Reversible Interactions With Para-Hydrogen Enhance NMR Sensitivity By Polarization Transfer. *Science* **2009**, *323*, 1708−1711.

(12) Atkinson, K. D.; Cowley, M. J.; Elliott, P. P.; Duckett, S. B.; Green, G. G. R.; López-Serrano, J.; Whitwood, A. C. Spontaneous Transfer of Parahydrogen Derived Spin Order to Pyridine at Low Magnetic Field. *J. Am. Chem. Soc.* **2009**, *131*, 13362−13368.

(13) Bowers, C. R.; Weitekamp, D. P. Para-Hydrogen And Synthesis Allow Dramatically Enhanced Nuclear Alignment. *J. Am. Chem. Soc.* **1987**, *109*, 5541−5542.

(14) Haake, M.; Natterer, J.; Bargon, J. Efficient NMR Pulse Sequences to Transfer the Parahydrogen-Induced Polarization to Hetero Nuclei. *J. Am. Chem. Soc.* **1996**, *118*, 8688−8691.

(15) Bhattacharya, P.; Harris, K.; Lin, A. P.; Mansson, M.; Norton, V. A.; Perman, W. H.; Weitekamp, D. P.; Ross, B. D. Ultra-Fast Three Dimensional Imaging Of Hyperpolarized ^{13}C In Vivo. *MAGMA* **2005**, *18*, 245−56.

(16) Goldman, M.; Jóhannesson, H. Conversion Of A Proton Pair Para Order Into C-13 Polarization By RF Irradiation, For Use In MRI. *C. R. Phys.* **2005**, *6*, 575−581.

DOI: 10.1021/acs.jpcc.6b04484
J. Phys. Chem. C 2016, 120, 12149−12156

(17) Goldman, M.; Johannesson, H.; Axelsson, O.; Karlsson, M. Hyperpolarization Of C-13 Through Order Transfer From Para-hydrogen: A New Contrast Agent For MRI. *Magn. Reson. Imaging* **2005**, *23*, 153−157.
(18) Chekmenev, E. Y.; Hovener, J.; Norton, V. A.; Harris, K.; Batchelder, L. S.; Bhattacharya, P.; Ross, B. D.; Weitekamp, D. P. PASADENA Hyperpolarization Of Succinic Acid For MRI And NMR Spectroscopy. *J. Am. Chem. Soc.* **2008**, *130*, 4212−4213.
(19) Kovtunov, K. V.; Beck, I. E.; Bukhtiyarov, V. I.; Koptyug, I. V. Observation Of Parahydrogen-Induced Polarization In Heterogeneous Hydrogenation On Supported Metal Catalysts. *Angew. Chem., Int. Ed.* **2008**, *47*, 1492−1495.
(20) Eshuis, N.; van Weerdenburg, B. J. A.; Feiters, M. C.; Rutjes, F. P. J. T.; Wijmenga, S. S.; Tessari, M. Quantitative Trace Analysis of Complex Mixtures Using SABRE Hyperpolarization. *Angew. Chem., Int. Ed.* **2015**, *54*, 1372−1372.
(21) van Weerdenburg, B. J. A.; Glöggler, S.; Eshuis, N.; Engwerda, A. H. J. T.; Smits, J. M. M.; de Gelder, R.; Appelt, S.; Wymenga, S. S.; Tessari, M.; Feiters, M. C.; Blümich, B.; Rutjes, F. P. J. T. Ligand Effects of NHC−Iridium Catalysts for Signal Amplification by Reversible Exchange (SABRE). *Chem. Commun.* **2013**, *49*, 7388−7390.
(22) Ratajczyk, T.; Gutmann, T.; Bernatowicz, P.; Buntkowsky, G.; Frydel, J.; Fedorczyk, B. NMR Signal Enhancement by Effective SABRE Labeling of Oligopeptides. *Chem.—Eur. J.* **2015**, *21*, 12616−12619.
(23) van Weerdenburg, B. J.; Engwerda, A. H.; Eshuis, N.; Longo, A.; Banerjee, D.; Tessari, M.; Guerra, C. F.; Rutjes, F. P.; Bickelhaupt, F. M.; Feiters, M. C. Computational (DFT) and Experimental (EXAFS) Study of the Interaction of [Ir (IMes)$(H)_2(L)_3$] with Substrates and Co-substrates Relevant for SABRE in Dilute Systems. *Chem.—Eur. J.* **2015**, *21*, 10482−10489.
(24) Barskiy, D. A.; Kovtunov, K. V.; Koptyug, I. V.; He, P.; Groome, K. A.; Best, Q. A.; Shi, F.; Goodson, B. M.; Shchepin, R. V.; Coffey, A. M.; et al. The Feasibility of Formation and Kinetics of NMR Signal Amplification by Reversible Exchange (SABRE) at High Magnetic Field (9.4 T). *J. Am. Chem. Soc.* **2014**, *136*, 3322−3325.
(25) Barskiy, D. A.; Kovtunov, K. V.; Koptyug, I. V.; He, P.; Groome, K. A.; Best, Q. A.; Shi, F.; Goodson, B. M.; Shchepin, R. V.; Truong, M. L.; et al. In Situ And Ex Situ Low-Field NMR Spectroscopy And MRI Endowed By SABRE Hyperpolarization. *ChemPhysChem* **2014**, *15*, 4100−4107.
(26) Daniele, V.; Legrand, F. X.; Berthault, P.; Dumez, J.-N.; Huber, G. Single-Scan Multidimensional NMR Analysis of Mixtures at Sub-Millimolar Concentrations by using SABRE Hyperpolarization. *ChemPhysChem* **2015**, *16*, 3413−3517.
(27) Pravdivtsev, A. N.; Yurkovskaya, A. V.; Vieth, H.-M.; Ivanov, K. L.; Kaptein, R. Level Anti-Crossings Are A Key Factor For Understanding Para-Hydrogen-Induced Hyperpolarization In SABRE Experiments. *ChemPhysChem* **2013**, *14*, 3327−3331.
(28) van Weerdenburg, B. J. A.; Eshuis, N.; Tessari, M.; Rutjes, F. P. J. T.; Feiters, M. C. Application of the π-Accepting Ability Parameter of N-heterocyclic Carbene Ligands in Iridium Complexes for Signal Amplification by Reversible Exchange (SABRE). *J. Chem. Soc., Dalton Trans.* **2015**, *44*, 15387−15390.
(29) Eshuis, N.; Hermkens, N.; van Weerdenburg, B. J.; Feiters, M. C.; Rutjes, F. P.; Wijmenga, S. S.; Tessari, M. Toward Nanomolar Detection by NMR Through SABRE Hyperpolarization. *J. Am. Chem. Soc.* **2014**, *136*, 2695−2698.
(30) Theis, T.; Truong, M. L.; Coffey, A. M.; Shchepin, R. V.; Waddell, K. W.; Shi, F.; Goodson, B. M.; Warren, W. S.; Chekmenev, E. Y. Microtesla SABRE Enables 10% Nitrogen-15 Nuclear Spin Polarization. *J. Am. Chem. Soc.* **2015**, *137*, 1404−1407.
(31) Moreno, K. X.; Nasr, K.; Milne, M.; Sherry, A. D.; Goux, W. J. Nuclear Spin Hyperpolarization of the Solvent Using Signal Amplification by Reversible Exchange (SABRE). *J. Magn. Reson.* **2015**, *257*, 15−23.
(32) Theis, T.; Truong, M. L.; Coffey, A. M.; Chekmenev, E. Y.; Warren, W. S. LIGHT-SABRE Enables Efficient In-Magnet Catalytic Hyperpolarization. *J. Magn. Reson.* **2014**, *248*, 23−26.
(33) Zeng, H.; Xu, J.; Gillen, J.; McMahon, M. T.; Artemov, D.; Tyburn, J.-M.; Lohman, J. A. B.; Mewis, R. E.; Atkinson, K. D.; Green, G. G. R.; et al. Optimization of SABRE for Polarization of the Tuberculosis Drugs Pyrazinamide and Isoniazid. *J. Magn. Reson.* **2013**, *237*, 73−78.
(34) Zeng, H.; Xu, J.; McMahon, M. T.; Lohman, J. A. B.; van Zijl, P. C. M. Achieving 1% NMR Polarization in Water in Less than 1 min. Using SABRE. *J. Magn. Reson.* **2014**, *246*, 119−121.
(35) Dücker, E. B.; Kuhn, L. T.; Münnemann, K.; Griesinger, C. Similarity Of SABRE Field Dependence In Chemically Different Substrates. *J. Magn. Reson.* **2012**, *214*, 159−165.
(36) Mewis, R. E.; Green, R. A.; Cockett, M. C.; Cowley, M. J.; Duckett, S. B.; Green, G. G.; John, R. O.; Rayner, P. J.; Williamson, D. C. Strategies for the Hyperpolarization of Acetonitrile and Related Ligands by SABRE. *J. Phys. Chem. B* **2015**, *119*, 1416−1424.
(37) Pravdivtsev, A. N.; Yurkovskaya, A. V.; Vieth, H.-M.; Ivanov, K. L. RF-SABRE: A Way to Continuous Spin Hyperpolarization at High Magnetic Fields. *J. Phys. Chem. B* **2015**, *119*, 13619−13629.
(38) Pravdivtsev, A. N.; Yurkovskaya, A. V.; Vieth, H.-M.; Ivanov, K. L. Spin Mixing at Level Anti-Crossings in the Rotating Frame Makes Hgh-Field SABRE Feasible. *Phys. Chem. Chem. Phys.* **2014**, *16*, 24672−24675.
(39) Pravdivtsev, A. N.; Yurkovskaya, A. V.; Zimmermann, H.; Vieth, H.-M.; Ivanov, K. L. Transfer of SABRE-Derived Hyperpolarization to Spin-1/2 Heteronuclei. *RSC Adv.* **2015**, *5*, 63615−63623.
(40) Glöggler, S.; Müller, R.; Colell, J.; Emondts, M.; Dabrowski, M.; Blümich, B.; Appelt, S. Para-Hydrogen Induced Polarization of Amino Acids, Peptides and Deuterium−Hydrogen Gas. *Phys. Chem. Chem. Phys.* **2011**, *13*, 13759−13764.
(41) Shi, F.; Porter, E.; Truong, M. L.; Coffey, A. M.; Waddell, K. W.; Chekmenev, E. Y.; Goodson, B. M. Interplay of Catalyst Structure and Temperature for NMR Signal Amplification by Reversible Exchange. Presented at the 56th Experimental Nuclear Magnetic Resonance Conference, Pacific Grove, CA, April 19−24, 2015.
(42) Fekete, M.; Bayfield, O.; Duckett, S. B.; Hart, S.; Mewis, R. E.; Pridmore, N.; Rayner, P. J.; Whitwood, A. Iridium(III) Hydrido N-Heterocyclic Carbene−Phosphine Complexes as Catalysts in Magnetization Transfer Reactions. *Inorg. Chem.* **2013**, *52*, 13453−13461.
(43) Appleby, K. M.; Mewis, R. E.; Olaru, A. M.; Green, G. G. R.; Fairlamb, I. J. S.; Duckett, S. B. Investigating Pyridazine and Phthalazine Exchange in a Series of Iridium Complexes in Order to Define Their Role in the Catalytic Transfer of Magnetisation from Para-Hydrogen. *Chem. Sci.* **2015**, *6*, 3981−3993.
(44) Ruddlesden, A. J.; Mewis, R. E.; Green, G. G.; Whitwood, A. C.; Duckett, S. B. Catalytic Transfer of Magnetism Using a Neutral Iridium Phenoxide Complex. *Organometallics* **2015**, *34*, 2997−3006.
(45) Fekete, M.; Gibard, C.; Dear, G. J.; Green, G. G.; Hooper, A. J.; Roberts, A. D.; Cisnetti, F.; Duckett, S. B. Utilisation of Water Soluble Iridium Catalysts for Signal Amplification by Reversible Exchange. *J. Chem. Soc., Dalton Trans.* **2015**, *44*, 7870−7880.
(46) Cowley, M. J.; Adams, R. W.; Atkinson, K. D.; Cockett, M. C.; Duckett, S. B.; Green, G. G.; Lohman, J. A.; Kerssebaum, R.; Kilgour, D.; Mewis, R. E. Iridium N-Heterocyclic Carbene Complexes As Efficient Catalysts For Magnetization Transfer From Para-Hydrogen. *J. Am. Chem. Soc.* **2011**, *133*, 6134−6137.
(47) Zhivonitko, V. V.; Skovpin, I. V.; Koptyug, I. V. Strong 31P Nuclear Spin Hyperpolarization Produced via Reversible Chemical Interaction with Parahydrogen. *Chem. Commun.* **2015**, *51*, 2506−2509.
(48) Truong, M. L.; Theis, T.; Coffey, A. M.; Shchepin, R. V.; Waddell, K. W.; Shi, F.; Goodson, B. M.; Warren, W. S.; Chekmenev, E. Y. ^{15}N Hyperpolarization By Reversible Exchange Using SABRE-SHEATH. *J. Phys. Chem. C* **2015**, *119*, 8786−8797.
(49) Shchepin, R. V.; Truong, M. L.; Theis, T.; Coffey, A. M.; Waddell, K. W.; Shi, F.; Warren, W. S.; Goodson, B. M.; Chekmenev, E. Y. NMR Signal Amplification by Reversible Exchange of Neat Liquids. *J. Phys. Chem. Lett.* **2015**, *6*, 1961−1967.
(50) Hövener, J.-B.; Schwaderlapp, N.; Borowiak, R.; Lickert, T.; Duckett, S. B.; Mewis, R. E.; Adams, R. W.; Burns, M. J.; Highton, L. A.; Green, G. G.; Olaru, A.; Hennig, J.; von Elverfeldt, D. Toward

DOI: 10.1021/acs.jpcc.6b04484
J. Phys. Chem. C 2016, 120, 12149−12156

Biocompatible Nuclear Hyperpolarization Using Signal Amplification By Reversible Exchange: Quantitative In Situ Spectroscopy And High-Field Imaging. *Anal. Chem.* **2014**, *86*, 1767−1774.
(51) Coffey, A. M.; Kovtunov, K. V.; Barskiy, D. A.; Koptyug, I. V.; Shchepin, R. V.; Waddell, K. W.; He, P.; Groome, K. A.; Best, Q. A.; Shi, F.; et al. High-Resolution Low-Field Molecular Magnetic Resonance Imaging Of Hyperpolarized Liquids. *Anal. Chem.* **2014**, *86*, 9042−9049.
(52) Lloyd, L. S.; Adams, R. W.; Bernstein, M.; Coombes, S.; Duckett, S. B.; Green, G. G. R.; Lewis, R. J.; Mewis, R. E.; Sleigh, C. J. Utilization of SABRE-Derived Hyperpolarization To Detect Low-Concentration Analytes via 1D and 2D NMR Methods. *J. Am. Chem. Soc.* **2012**, *134*, 12904−12907.
(53) Shi, F.; Coffey, A. M.; Waddell, K. W.; Chekmenev, E. Y.; Goodson, B. M. Heterogeneous Solution NMR Signal Amplification By Reversible Exchange. *Angew. Chem.* **2014**, *126*, 7625−7628.
(54) Shi, F.; Coffey, A. M.; Waddell, K. W.; Chekmenev, E. Y.; Goodson, B. M. Nanoscale Catalysts for NMR Signal Enhancement by Reversible Exchange. *J. Phys. Chem. C* **2015**, *119*, 7525−7533.
(55) Torres, O.; Martin, M.; Sola, E. Labile N-Heterocyclic Carbene Complexes Of Iridium. *Organometallics* **2009**, *28*, 863−870.
(56) Vazquez-Serrano, L. D.; Owens, B. T.; Buriak, J. M. The Search For New Hydrogenation Catalyst Motifs Based On N-Heterocyclic Carbene Ligands. *Inorg. Chim. Acta* **2006**, *359*, 2786−2797.
(57) Truong, M. L.; Shi, F.; He, P.; Yuan, B.; Plunkett, K. N.; Coffey, A. M.; Shchepin, R. V.; Barskiy, D. A.; Kovtunov, K. V.; Koptyug, I. V.; et al. Irreversible Catalyst Activation Enables Hyperpolarization And Water Solubility For NMR Signal Amplification By Reversible Exchange. *J. Phys. Chem. B* **2014**, *118*, 13882−13889.
(58) He, P.; Best, Q. A.; Groome, K. A.; Coffey, A. M.; Truong, M. L.; Waddell, K. W.; Chekmenev, E. Y.; Goodson, B. M. A Water-Soluble SABRE Catalyst for NMR/MRI Enhancement. Presented at the 55th Experimental Nuclear Magnetic Resonance Conference, Boston, MA, March 23−18, 2014.
(59) Shi, F.; Truong, M. L.; Coffey, A. M.; Shchepin, R.; Chekmenev, E. Y.; Goodson, B. M. Developments in NMR Signal Enhancement by Reversible Exchange (SABRE): Nanoscale Catalysts for HET-SABRE and a Water-Soluble Ir Catalyst for Aqueous SABRE in a Single Step. Presented at the 56th Experimental Nuclear Magnetic Resonance Conference, Pacific Grove, CA, April 19−24, 2015.
(60) Gallivan, J. P.; Jordan, J. P.; Grubbs, R. H. A Neutral, Water-Soluble Olefin Metathesis Catalyst Based on an N-Heterocyclic Carbene Ligand. *Tetrahedron Lett.* **2005**, *46*, 2577−2580.
(61) Purwanto; Deshpande, R. V.; Chaudhari, R. V.; Delmas, H. Solubility of Hydrogen, Carbon Monoxide, and 1-Octene in Various Solvents and Solvent Mixtures. *J. Chem. Eng. Data* **1996**, *41*, 1414−1417.
(62) Navon, G.; Song, Y. Q.; Room, T.; Appelt, S.; Taylor, R. E.; Pines, A. Enhancement of Solution NMR and MRI with Laser-Polarized Xenon. *Science* **1996**, *271*, 1848−1851.
(63) Pravdivtsev, A. N.; Ivanov, K. L.; Yurkovskaya, A. V.; Petrov, P. A.; Limbach, H. H.; Kaptein, R.; Vieth, H.-M. Spin Polarization Transfer Mechanisms of SABRE: A Magnetic Field Dependent Study. *J. Magn. Reson.* **2015**, *261*, 73−82.
(64) Shchepin, R. V.; Barskiy, D. A.; Coffey, A. M.; Theis, T.; Shi, F.; Warren, W. S.; Goodson, B. M.; Chekmenev, E. Y. ^{15}N Hyperpolarization of Imidazole-$^{15}N_2$ for Magnetic Resonance pH Sensing via SABRE-SHEATH. *ACS Sensors* **2016**, DOI: 10.1021/acssensors.6b00231.
(65) Shchepin, R. V.; Barskiy, D. A.; Mikhaylov, D. M.; Chekmenev, E. Y. Efficient Synthesis of Nicotinamide-1−^{15}N for Ultrafast NMR Hyperpolarization Using Parahydrogen. *Bioconjugate Chem.* **2016**, *27*, 878−882.
(66) Spannring, P.; Reile, I.; Emondts, M.; Schleker, P.; Hermkens, N.; van der Zwaluw, N.; van Weerdenburg, B.; Tinnemans, P.; Tessari, M.; Blumich, B.; Rutjes, F.; Feiters, M. Development and Application of a Water Soluble SABRE Catalyst. Presented at the 57th Experimental Nuclear Magnetic Resonance Conference, Pittsburgh, PA, April 10−16, 2016.

■ NOTE ADDED IN PROOF

Readers may also be interested to note the very recent presentation of Philipp Schleker and co-workers, who reported the preparation and application of a different water-soluble Ir-based SABRE catalyst.[66]

DOI: 10.1021/acs.jpcc.6b04484
J. Phys. Chem. C 2016, 120, 12149−12156

ChemPubSoc Europe
DOI: 10.1002/slct.201600761
Chemistry SELECT Communications

Catalysis

NMR Signal Amplification by Reversible Exchange of Sulfur-Heterocyclic Compounds Found In Petroleum

Roman V. Shchepin[#,[a]] Danila A. Barskiy[#,[a]] Aaron M. Coffey,[a] Boyd M. Goodson,[c] and Eduard Y. Chekmenev*[a, b]

NMR hyperpolarization via Signal Amplification by Reversible Exchange (SABRE) was employed to investigate the feasibility of enhancing the NMR detection sensitivity of sulfur-heterocycles (specifically 2-methylthiophene and dibenzothiophenes), a family of compounds typically found in petroleum and refined petroleum products. SABRE hyperpolarization of sulfur-heterocycles (conducted in seconds) offers potential advantages of providing structural information about sulfur-containing contaminants in petroleum, thereby informing petroleum purification and refining to minimize sulfur content in refined products such as gasoline. Moreover, NMR spectroscopy sensitivity gains endowed by hyperpolarization potentially allows for performing structural assays using inexpensive, low-magnetic-field (*ca.* 1 T) high-resolution NMR spectrometers ideally suited for industrial applications in the field.

NMR hyperpolarization can increase nuclear spin polarization from equilibrium Boltzmann values of 10^{-6}-10^{-5} to the order of unity, resulting in concomitant gains in NMR signal and signal-to-noise ratio (SNR).[1] The vast majority of NMR hyperpolarization techniques require sophisticated, expensive, and low-throughput equipment (dubbed *hyperpolarizers*[1c]) for producing atoms or molecules with hyperpolarized (HP) nuclear spins. As a result, the HP substances produced in such fashion are generally expensive and time-consuming to create. Despite these limitations, hyperpolarization techniques promise to revolutionize biomedical research because the benefits of gaining new insights into fundamental biomedical questions and development of personalized imaging medicines (i.e. molecular probes that can answer questions specific to the disease stage, as well as genetic and metabolic underpinning) outweigh the cost/throughput issues.[2] However, the relatively recent development of NMR Signal Amplification By Reversible Exchange (SABRE)[3] enables inexpensive, high-throughput hyperpolarization without the need for complex hyperpolarizer devices. As a result, SABRE has the potential to transform structural analysis well beyond biomedical research. To date, SABRE hyperpolarization of N-heterocycles has been demonstrated successfully by many research groups.[4] Despite being structurally limited to hyperpolarization of N-heterocycles, the SABRE technique has been applied for structural studies[5] of coffee extracts[6] and biofluids,[7] in addition to hyperpolarization of contrast agents for biomedical applications.[4b,8]

In this work we show that SABRE of sulfur-containing heterocycles (S-SABRE) is feasible, which enables hyperpolarization of a new class of compounds–paving the way to new applications. In particular, this approach could be useful for sensing S-heterocyclic compounds in petroleum and refined petroleum products, where structural information (typically obtained via elemental analysis, solid-state NMR, or other methods) guides the refining process and ultimately determines the sulfur-removal efficiency.[9] Sulfur is a highly unwanted pollutant, and the reduction of its content in fuels (and consequent emission into the atmosphere) continues to be a major effort, as it is necessary to reduce levels in fuels to a few parts per million (ppm).[10] For example, it is predicted that the additional refining efforts to reach the desired future standards will lead to additional fuel cost increases at the pump of ~6-9 cents per gallon.[11]

Here, we demonstrate the feasibility of SABRE with S-heterocycles using two representative examples of substituted thiophenes—sulfur-containing compounds found in petroleum: methylthiophene and dibenzothiophene.[12] In particular, the latter compound and its methylated derivatives occur widely in heavier petroleum fractions.[13]

The activated form of the catalyst previously shown to be the most potent for SABRE of N-heterocycles (Ir–IMes hexacoordinate complex[4a]) was employed for chemical exchange with parahydrogen and the to-be-hyperpolarized sulfur-containing substrates (S), Figure 1a. A previously developed high-pressure setup[14] was employed with a magnetic field for polarization transfer (B_T) provided by a small solenoid (Figure 1b). The latter provided a fine control of B_T vs. a relatively in-

[a] *Prof. R. V. Shchepin,[#] Dr. D. A. Barskiy,[#] Dr. A. M. Coffey, Prof. E. Y. Chekmenev*
Department of Radiology
Vanderbilt University Institute of Imaging Science (VUIIS)
Department of Biomedical Engineering
Vanderbilt-Ingram Cancer Center (VICC)
Vanderbilt University
Nashville, TN 37232 USA
E-mail: eduard.chekmenev@vanderbilt.edu
[b] *Prof. E. Y. Chekmenev*
Russian Academy of Sciences
119991 Moscow Russia
[c] *Prof. B. M. Goodson*
Southern Illinois University
Department of Chemistry and Biochemistry
Materials Technology Center
Carbondale, IL 62901 USA
[#] *These authors contributed equally*

Supporting information for this article is available on the WWW under http://dx.doi.org/10.1002/slct.201600761

© 2016 Wiley-VCH Verlag GmbH & Co. KGaA, Weinheim

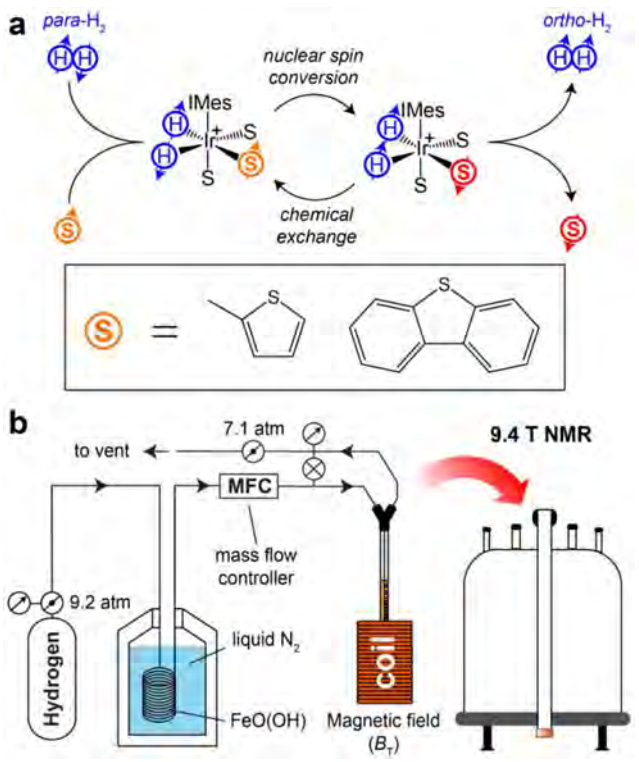

Figure 1. a) Schematic representation of the SABRE hyperpolarization process, which relies on the chemical exchange of the hexacoordinate Ir–IMes catalyst with parahydrogen and a to-be-hyperpolarized sulfur-containing substrate. **b)** A diagram of the experimental setup showing the production of parahydrogen (~50% *para*- state using a liquid N_2 cooling source). Parahydrogen is controlled using mass flow controller (MFC); Ø is a safety valve (~7.1 atm) employed to regulate H_2 pressure in the NMR tube, and ⊗ is a bypass valve to provide rapid cessation of parahydrogen bubbling through the solution in the NMR tube. Following SABRE mixing at B_T the sample tube is rapidly transferred to the 9.4 T to permit high-field NMR acquisition.

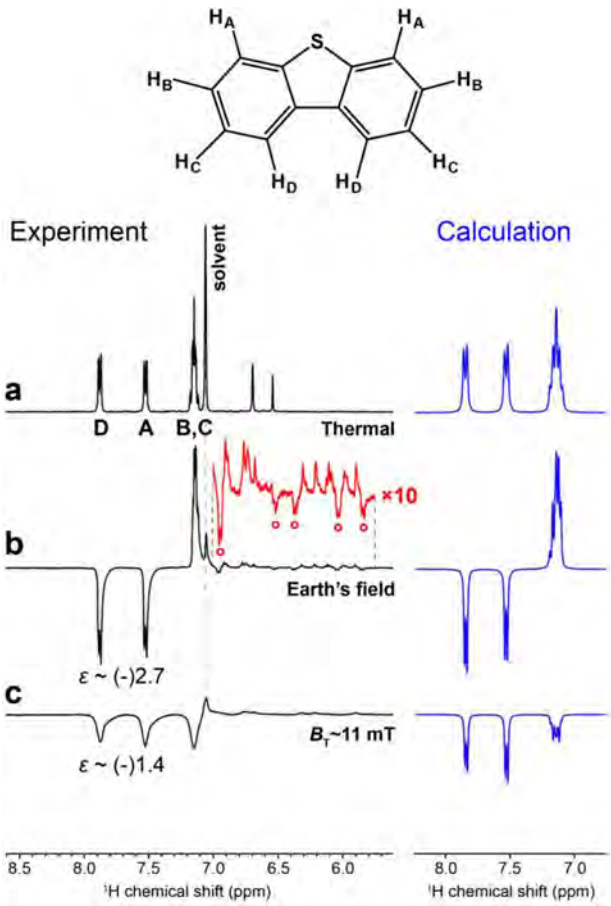

Figure 2. SABRE hyperpolarization of dibenzothiophene. **a)** ^{1}H NMR spectrum of dibenzothiophene at thermal equilibrium of nuclear spin polarization. **b)** ^{1}H NMR spectrum of dibenzothiohene after SABRE hyperpolarization process conducted in the Earth's magnetic field, the process aimed at the pseudo-singlet state overpopulation.[17] Note the NMR resonances labeled with ° correspond to catalyst-bound dibenzothiophene species. **c)** NMR spectrum of dibenzothiohene after performing the SABRE hyperpolarization process at B_T ~ 11 mT.

homogeneous fringe field of the 9.4 T NMR spectrometer used previously.[14] Additional experimental details are provided in the Supporting Information (SI). When B_T is roughly matched to the spin-spin coupling ($J_{H\text{-}H}$) between nascent parahydrogen-derived hydride protons on the metal center,[4b,15] a coherent polarization transfer from hydride protons to the protons of the substrate molecule occurs (Figure 2c)–in accord with conventional SABRE of N-heterocycles.[3,16] Once polarization transfer occurs on the Ir-hexacoordinate complex, the HP substrate molecules and hydride hydrogens exchange with free substrate and parahydrogen in solution, allowing the SABRE hyperpolarization cycle to continue as it reaches the maximum hyperpolarization level at steady state (which typically occurs in seconds).[3,16a] Note the characteristic phase shift of the HP ^{1}H resonances of dibenzothiophene (Figure 2c). When B_T is mismatched, e.g. when the SABRE exchange process is conducted in the Earth's magnetic field of ~50 μT, polarization transfer still occurs[17]—although pseudo-singlet spin-states are being overpopulated, which is manifested by the opposite (absorptive vs. emissive) phases of the $H_{A,D}$ and $H_{B,C}$ ^{1}H NMR resonances (Figure 2b). Importantly, the inverted resonances assigned to catalyst-bound substrate species are detected (Figure 2b inset) indicating the chemical exchange of S-heterocycles on the time scale similar to that seen in SABRE of N-heterocycles.

While the NMR signal enhancements derived from SABRE hyperpolarization processes for sulfur-containing compounds (S-SABRE) were relatively modest (*ca.* (-)5 fold (see SI) – roughly 2–3 orders of magnitude lower than the best ^{1}H polarization enhancements[4a] reported to date for this catalyst), the optimization of the signal enhancement was beyond the scope of this proof-of-principle demonstration: Robust gains in S-SABRE efficiency can likely be obtained by (i) employing near 100% parahydrogen (vs. ~50% para- fraction which reduced the apparent enhancements by approximately a factor of 3), (ii) reducing the concentration of the S-substrate,[18] and (iii) catalyst pre-activation with small molecules (e.g. pyridine) resulting in better Ir center accessibility, because the axial non-exchangeable site (Figure 1a) would be occupied by a less bulky ligand.[19] However, the design of more efficient SABRE catalysts

© 2016 Wiley-VCH Verlag GmbH & Co. KGaA, Weinheim

geared towards hyperpolarization of sulfur- rather than nitrogen-containing heterocycles will likely be required in the future to bring S-SABRE hyperpolarization efficiency on par with conventional SABRE of N-heterocycles, which has been successfully employed for quantitative trace analysis below 1 μM (corresponding to < 0.1 ppm detection capability).[5,19b]

Corresponding ^{1}H SABRE hyperpolarization spectra are provided for methylthiophene in Figure S12. Taken together with dibenzothiophene's SABRE hyperpolarization feasibility (Figure 2), our results support the possibility that the SABRE hyperpolarization technique may be generally applicable to thiophene-based substituted heterocycles, common impurities in crude oil.[12] SABRE-based NMR sensing could therefore potentially provide a convenient means of detecting the presence and structure of sulfur-heterocycles in crude oil samples in the future, because (1) it is an instrumentally non-demanding technique; (2) the HP NMR resonances have an opposite phase with respect to the rest of the protons in the spectrum;[3,20] and (3) the SABRE effect is likely to be at least partially selective for the heterocyclic compounds found in oil.

Although conventional PHIP can be applied for detection of thiophenes[21] and potentially other sulfur-containing compounds with unsaturated chemical bonds, that parahydrogen-based hyperpolarization technique relies on pairwise addition of p-H_2, and therefore leads to chemical modification of the substrate–rendering the NMR spectral interpretation significantly more challenging compared to the SABRE approach. Moreover, only two hyperpolarized protons can be typically visualized with the conventional PHIP approach, whereas the SABRE method demonstrated here allows enhancing multiple proton sites. Furthermore, the conventional hydrogenative PHIP technique is an irreversible process,[1e,22] whereas SABRE allows repeating the hyperpolarization process multiple times,[23] which is useful in the context of multi-dimensional NMR spectroscopy.[5]

In summary, it was shown that substituted (in *ortho*- position) thiophenes are amendable to SABRE hyperpolarization with an already-available catalyst (and an easily-created source of ~50% p-H_2 using liquid N_2 cooling). Moreover, hyperpolarization of relatively distant protons (up to four chemical bonds away from sulfur, Figure 2) is feasible. This result indicates that SABRE can provide rich structural information, because multiple protons of the same sulfur-containing heterocycle can be hyperpolarized and used as spectral signatures for detecting a wide range of compounds simultaneously. This capability is welcome for structural studies of crude oil and other complex mixtures, especially in the context of recently demonstrated 2D SABRE NMR spectroscopy of trace analytes.[5] Furthermore, the extension of SABRE to the new class of heterocycles demonstrated here may be synergistic with the recent development of heterogeneous SABRE catalysis.[24] Finally, because NMR detection of HP compounds can be more sensitive at lower magnetic fields,[25] a number of portable, high-resolution, and low-cost NMR platforms (e.g. SpinSolve, NMReady, etc. at ~1 T field range) can be deployed for low-field NMR SABRE spectroscopy and MRI imaging.[23,26] Finally, the use of low-field NMR spectroscopy for selective detection of S-SABRE hyperpolarized substances in complex mixtures may benefit from the reduced signal background originating from other more abundant but non-hyperpolarized substances.

Supporting Information (SI) is available: experimental details regarding sample preparation and SABRE hyperpolarization, high-resolution NMR spectra, and spin dynamics calculations.

Acknowledgements

This work was supported by NIH 1R21EB018014, 1R21EB020323, T32 EB001628, 1F32EB021840, NSF CHE-1416268 and CHE-1416432, DOD CDMRP W81XWH-12-1-0159/BC112431, W81XWH-15-1-0271 and W81XWH-15-1-0272, and ExxonMobil Research and Engineering Company Knowledge Build. We thank Dr. Fan Shi for assistance with synthesizing the SABRE catalyst, and Dr. Stuart E. Smith and Dr. Mobae Afeworki from ExxonMobil for stimulating discussions.

Keywords: Hyperpolarization · parahydrogen · SABRE · sulfur-heterocycles · petroleum

[1] a) P. Nikolaou, B. M. Goodson, E. Y. Chekmenev, *Chem. Eur. J.* **2015**, *21*, 3156–3166; b) A. Abragam, M. Goldman, *Rep. Prog. Phys.* **1978**, *41*, 395–467; c) J. H. Ardenkjaer-Larsen, B. Fridlund, A. Gram, G. Hansson, L. Hansson, M. H. Lerche, R. Servin, M. Thaning, K. Golman, *Proc. Natl. Acad. Sci. U. S. A.* **2003**, *100*, 10158–10163; d) B. M. Goodson, *J. Magn. Reson.* **2002**, *155*, 157–216; e) C. R. Bowers, D. P. Weitekamp, *Phys. Rev. Lett.* **1986**, *57*, 2645–2648.

[2] a) K. M. Brindle, *J. Am. Chem. Soc.* **2015**, *137*, 6418–6427; b) J. Kurhanewicz, D. B. Vigneron, K. Brindle, E. Y. Chekmenev, A. Comment, C. H. Cunningham, R. J. DeBerardinis, G. G. Green, M. O. Leach, S. S. Rajan, R. R. Rizi, B. D. Ross, W. S. Warren, C. R. Malloy, *Neoplasia* **2011**, *13*, 81–97; c) A. Comment, M. E. Merritt, *Biochemistry* **2014**, *53*, 7333–7357; d) S. J. Nelson, J. Kurhanewicz, D. B. Vigneron, P. E. Z. Larson, A. L. Harzstark, M. Ferrone, M. van Criekinge, J. W. Chang, R. Bok, I. Park, G. Reed, L. Carvajal, E. J. Small, P. Munster, V. K. Weinberg, J. H. Ardenkjaer-Larsen, A. P. Chen, R. E. Hurd, L. I. Odegardstuen, F. J. Robb, J. Tropp, J. A. Murray, *Sci. Transl. Med.* **2013**, *5*, 198ra108.

[3] R. W. Adams, J. A. Aguilar, K. D. Atkinson, M. J. Cowley, P. I. P. Elliott, S. B. Duckett, G. G. R. Green, I. G. Khazal, J. Lopez-Serrano, D. C. Williamson, *Science* **2009**, *323*, 1708–1711.

[4] a) M. J. Cowley, R. W. Adams, K. D. Atkinson, M. C. R. Cockett, S. B. Duckett, G. G. R. Green, J. A. B. Lohman, R. Kerssebaum, D. Kilgour, R. E. Mewis, *J. Am. Chem. Soc.* **2011**, *133*, 6134–6137; b) T. Theis, M. L. Truong, A. M. Coffey, R. V. Shchepin, K. W. Waddell, F. Shi, B. M. Goodson, W. S. Warren, E. Y. Chekmenev, *J. Am. Chem. Soc.* **2015**, *137*, 1404–1407; c) V. V. Zhivonitko, I. V. Skovpin, I. V. Koptyug, *Chem. Comm.* **2015**, *51*, 2506–2509.

[5] N. Eshuis, B. J. A. van Weerdenburg, M. C. Feiters, F. P. J. T. Rutjes, S. S. Wijmenga, M. Tessari, *Angew. Chem. Int. Ed.* **2015**, *54*, 1481–1484.

[6] N. K. J. Hermkens, N. Eshuis, B. J. A. van Weerdenburg, M. C. Feiters, F. P. J. T. Rutjes, S. S. Wijmenga, M. Tessari, *Anal. Chem.* **2016**, *88*, 3406–3412.

[7] I. Reile, N. Eshuis, N. Hermkens, B. J. A. van Weerdenburg, M. C. Feiters, F. P. J. T. Rutjes, M. Tessari, *Analyst* **2016**, *141*, 4001–4005.

[8] a) R. V. Shchepin, D. A. Barskiy, A. M. Coffey, T. Theis, F. Shi, W. S. Warren, B. M. Goodson, E. Y. Chekmenev, *ACS Sensors* **2016**, *1*, 640–644; b) D. A. Barskiy, R. V. Shchepin, A. M. Coffey, T. Theis, W. S. Warren, B. M. Goodson, E. Y. Chekmenev, *J. Am. Chem. Soc.* **2016**, DOI: 10.1021/jacs.1026b04784; c) R. V. Shchepin, M. L. Truong, T. Theis, A. M. Coffey, F. Shi, K. W. Waddell, W. S. Warren, B. M. Goodson, E. Y. Chekmenev, *J. Phys. Chem. Lett.* **2015**, *6*, 1961–1967.

[9] a) S. R. Kelemen, M. Afeworki, M. L. Gorbaty, M. Sansone, P. J. Kwiatek, C. C. Walters, H. Freund, M. Siskin, A. E. Bence, D. J. Curry, M. Solum, R. J.

© 2016 Wiley-VCH Verlag GmbH & Co. KGaA, Weinheim

Pugmire, M. Vandenbroucke, M. Leblond, F. Behar, *Energy & Fuels* **2007**, *21*, 1548–1561; b) S. R. Kelemen, M. Afeworki, M. L. Gorbaty, P. J. Kwiatek, M. Sansone, C. C. Walters, A. D. Cohen, *Energy & Fuels* **2006**, *20*, 635–652.
[10] United States Envirnonment Protection Agency, Office of Transportation and Air Quality, EPA-420-F-14-007, **2014**.
[11] J. Coomes, in *Bloomberg BNA, Daily Environment Report*, Bloomberg, http://www.bna.com/epa-tier-rule-n17179882576/, **2014**.
[12] K. G. Kropp, P. M. Fedorak, *Can. J. Microbiol.* **1998**, *44*, 605–622.
[13] T. C. Ho, *Catal. Today* **2004**, *98*, 3–18.
[14] M. L. Truong, F. Shi, P. He, B. Yuan, K. N. Plunkett, A. M. Coffey, R. V. Shchepin, D. A. Barskiy, K. V. Kovtunov, I. V. Koptyug, K. W. Waddell, B. M. Goodson, E. Y. Chekmenev, *J. Phys. Chem. B* **2014**, *18* 13882–13889.
[15] N. Eshuis, R. L. E. G. Aspers, B. J. A. van Weerdenburg, M. C. Feiters, F. P. J. T. Rutjes, S. S. Wijmenga, M. Tessari, *J. Magn. Reson.* **2016**, *265*, 59–66.
[16] a) R. W. Adams, S. B. Duckett, R. A. Green, D. C. Williamson, G. G. R. Green, *J. Chem. Phys.* **2009**, *131*, 194505; b) A. N. Pravdivtsev, A. V. Yurkovskaya, H.-M. Vieth, K. L. Ivanov, R. Kaptein, *ChemPhysChem* **2013**, *14*, 3327–3331.
[17] T. Theis, G. X. Ortiz, A. W. J. Logan, K. E. Claytor, Y. Feng, W. P. Huhn, V. Blum, S. J. Malcolmson, E. Y. Chekmenev, Q. Wang, W. S. Warren, *Sci. Adv.* **2016**, *2*, e1501438.
[18] D. A. Barskiy, A. N. Pravdivtsev, K. L. Ivanov, K. V. Kovtunov, I. V. Koptyug, *Phys. Chem. Chem. Phys.* **2016**, *18*, 89–93.
[19] a) R. V. Shchepin, D. A. Barskiy, D. M. Mikhaylov, E. Y. Chekmenev, *Bioconjugate Chem.* **2016**, *27*, 878–882; b) N. Eshuis, N. Hermkens, B. J. A. van Weerdenburg, M. C. Feiters, F. P. J. T. Rutjes, S. S. Wijmenga, M. Tessari, *J. Am. Chem. Soc.* **2014**, *136*, 2695–2698.
[20] D. A. Barskiy, K. V. Kovtunov, I. V. Koptyug, P. He, K. A. Groome, Q. A. Best, F. Shi, B. M. Goodson, R. V. Shchepin, A. M. Coffey, K. W. Waddell, E. Y. Chekmenev, *J. Am. Chem. Soc.* **2014**, *136*, 3322–3325.
[21] O. G. Salnikov, D. B. Burueva, D. A. Barskiy, G. A. Bukhtiyarova, K. V. Kovtunov, I. V. Koptyug, *ChemCatChem* **2015**, *7*, 3508–3512.
[22] C. R. Bowers, D. P. Weitekamp, *J. Am. Chem. Soc.* **1987**, *109*, 5541–5542.
[23] J. B. Hovener, N. Schwaderlapp, T. Lickert, S. B. Duckett, R. E. Mewis, L. A. R. Highton, S. M. Kenny, G. G. R. Green, D. Leibfritz, J. G. Korvink, J. Hennig, D. von Elverfeldt, *Nat. Commun.* **2013**, *4*, 5.
[24] a) F. Shi, A. M. Coffey, K. W. Waddell, E. Y. Chekmenev, B. M. Goodson, *Angew. Chem. Int. Ed.* **2014**, *53*, 7495–7498; b) F. Shi, A. M. Coffey, K. W. Waddell, E. Y. Chekmenev, B. M. Goodson, *J. Phys. Chem. C* **2015**, *119*, 7525–7533.
[25] a) M. Suefke, A. Liebisch, B. Blumich, S. Appelt, *Nat. Phys.* **2015**, 767–771; b) A. M. Coffey, M. L. Truong, E. Y. Chekmenev, *J. Magn. Reson.* **2013**, *237*, 169–174.
[26] a) A. M. Coffey, K. V. Kovtunov, D. Barskiy, I. V. Koptyug, R. V. Shchepin, K. W. Waddell, P. He, K. A. Groome, Q. A. Best, F. Shi, B. M. Goodson, E. Y. Chekmenev, *Anal. Chem.* **2014**, *86*, 9042–9049; b) S. Gloggler, R. Muller, J. Colell, M. Emondts, M. Dabrowski, B. Blumich, S. Appelt, *Phys. Chem. Chem. Phys.* **2011**, *13*, 13759–13764.

Submitted: June 17, 2016
Accepted: June 21, 2016

© 2016 Wiley-VCH Verlag GmbH & Co. KGaA, Weinheim

ACS SENSORS

Letter

pubs.acs.org/acssensors

^{15}N Hyperpolarization of Imidazole-$^{15}N_2$ for Magnetic Resonance pH Sensing via SABRE-SHEATH

Roman V. Shchepin,[†] Danila A. Barskiy,[†] Aaron M. Coffey,[†] Thomas Theis,[∥] Fan Shi,[⊥] Warren S. Warren,[∥] Boyd M. Goodson,[⊥,#] and Eduard Y. Chekmenev*[,†,‡,§,¶]

[†]Vanderbilt University Institute of Imaging Science (VUIIS), Department of Radiology, [‡]Department of Biomedical Engineering, and [§]Vanderbilt-Ingram Cancer Center (VICC), Vanderbilt University, Nashville, Tennessee 37232-2310, United States

[∥]Department of Chemistry, Duke University, Durham, North Carolina 27708, United States

[⊥]Department of Chemistry and Biochemistry and [#]Materials Technology Center, Southern Illinois University, Carbondale, Illinois 62901, United States

[¶]Russian Academy of Sciences, Moscow, Leninskiy Prospekt 14, 119991, Russia

Supporting Information

ABSTRACT: ^{15}N nuclear spins of imidazole-$^{15}N_2$ were hyperpolarized using NMR signal amplification by reversible exchange in shield enables alignment transfer to heteronuclei (SABRE-SHEATH). A ^{15}N NMR signal enhancement of ~2000-fold at 9.4 T is reported using parahydrogen gas (~50% para-) and ~0.1 M imidazole-$^{15}N_2$ in methanol:aqueous buffer (~1:1). Proton binding to a ^{15}N site of imidazole occurs at physiological pH (pK_a ~ 7.0), and the binding event changes the ^{15}N isotropic chemical shift by ~30 ppm. These properties are ideal for in vivo pH sensing. Additionally, imidazoles have low toxicity and are readily incorporated into a wide range of biomolecules. ^{15}N-Imidazole SABRE-SHEATH hyperpolarization potentially enables pH sensing on scales ranging from peptide and protein molecules to living organisms.

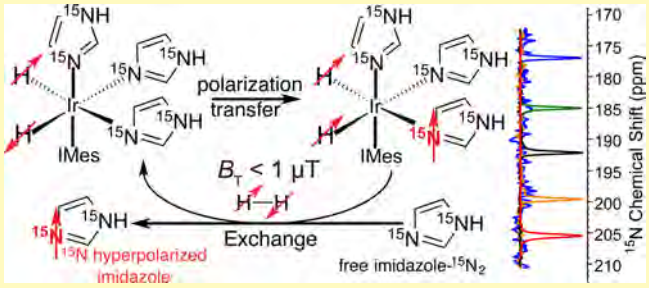

KEYWORDS: *NMR, hyperpolarization, parahydrogen, imidazole, pH sensing, ^{15}N, chemical shift*

Spectral sensing or imaging of local pH variances in vivo has been of long-standing interest for characterizing a host of pathological conditions, including various cancers.[1−6] For example, a variety of MR-based approaches using both exogenous and endogenous agents (e.g., refs 6−17) have been investigated as less invasive alternatives to using microelectrode probes.[6] However, sensitivity presents a significant challenge to otherwise powerful MR-based methods due to the typically low concentrations of probe molecules compared to water in vivo.

One way to combat such MR sensitivity limitations is hyperpolarization. NMR hyperpolarization techniques significantly enhance nuclear spin polarization (P), resulting in large gains in NMR signal.[18−20] One such approach is signal amplification by reversible exchange (SABRE), a technique that relies on exchange of parahydrogen (*para*-H_2) and to-be-hyperpolarized substrate molecules on a catalyst[21−23]—in solutions or in "neat" liquids.[24] Polarization of target nuclear spins (e.g., ^{1}H,[21] ^{15}N,[25,26] or ^{31}P[27]) occurs spontaneously when the applied static magnetic field B_T is "matched" to the corresponding spin−spin couplings between the nascent *para*-H_2 hydride pair and the target nuclei (Figure 1a). Homonuclear (i.e., ^{1}H) SABRE was demonstrated first[21] using B_T in the mT range; the approach was later extended to heteronuclei (e.g., ^{15}N, ^{31}P, etc.) via SABRE in shield enabling alignment transfer to heteronuclei (SABRE-SHEATH[25]) utilizing B_T static fields in the μT range. Alternatives to spontaneous SABRE or SABRE-SHEATH include radiofrequency irradiation targeting level anti-crossings (LAC)[28] and low-irradiation generation of high tesla-SABRE (LIGHT-SABRE).[29] These RF-based approaches are attractive because they yield hyperpolarization directly in the magnet where detection takes place. However, the spontaneous/static-field approaches currently yield larger polarization levels, up to 10% P_{15N} (corresponding to >30 000-fold signal enhancement at 9.4 T). A key advantage of all SABRE hyperpolarization methods is their fast polarization buildup—achieving high P levels in only a few seconds. Moreover, spontaneous SABRE and SABRE-SHEATH are not instrumentally demanding and only require access to readily produced *para*-H_2 and a weak static magnetic field. Furthermore, SABRE-SHEATH addresses a critical challenge faced by all hyperpolarization techniques: Upon injection of hyperpolarized (HP) material into a system of interest, signals usually decay rapidly, with decay constants on the order of

Received: April 6, 2016
Accepted: April 14, 2016

 © XXXX American Chemical Society

DOI: 10.1021/acssensors.6b00231
ACS Sens. XXXX, XXX, XXX−XXX

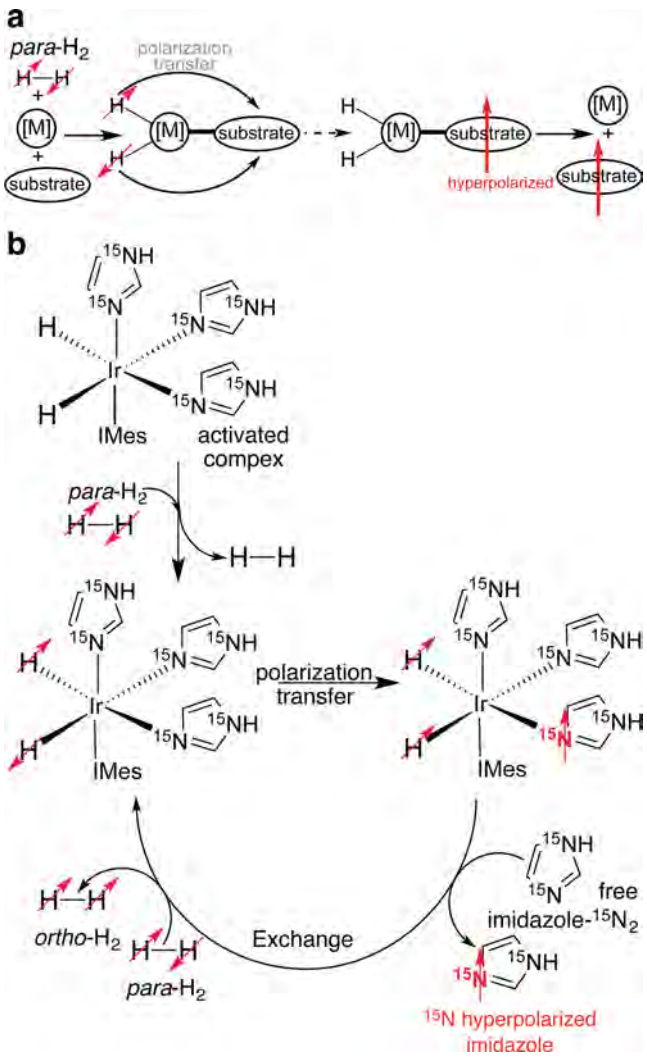

Figure 1. (a) Generalized scheme of SABRE and SABRE-SHEATH hyperpolarization processes. (b) Chemical structure of the activated Ir-IMes hexacoordinate complex after activation with H_2. The complex undergoes fast exchange with *para*-H_2 and free imidazole-$^{15}N_2$, which enables spontaneous polarization transfer from *para*-H_2 (in the form of Ir-hydrides) to ^{15}N nuclei of imidazole-$^{15}N_2$ in μT magnetic fields.[25,26]

seconds up to a minute. However, with SABRE-SHEATH, long-lived ^{15}N sites can be HP with relaxation time constants ranging from 1 min[26] to 10 min.[30] Furthermore, compared to ^{13}C enrichment of leading ^{13}C HP contrast agents (e.g., pyruvate-1-^{13}C[31,32]), spin labeling with ^{15}N uses relatively straightforward chemistry replacing N-sites in N-heterocycles with ^{15}N.[26,33]

The development of all hyperpolarization techniques has largely been driven by their use in biomedicine to image organ function and probe metabolic processes in vivo.[20,31,34,35] While several translational challenges of conventional SABRE have been addressed recently, i.e., demonstration of SABRE in aqueous media,[36−38] and implementation of heterogeneous SABRE catalysts,[39,40] most SABRE-hyperpolarized compounds studied to date have limited biological relevance (although nicotinamide,[21] pyrazinamide, and isoniazid[41] have been demonstrated). Recently, ^{15}N heterocycles have been shown to be potent for pH imaging.[42] In this case, hyperpolarization was performed with the well-established yet expensive dissolution-DNP (dynamic nuclear polarization)[43] modality and pH sensing was achieved by detecting changes in ^{15}N isotropic chemical shifts, which are >90 ppm for the protonated and deprotonated states of the ^{15}N-heterocycles.[42] As a result, ^{15}N isotropic chemical shifts of ^{15}N-hyperpolarized probes may be ideal reporters of in vivo pH. This approach has two key advantages compared to the current HP ^{13}C-bicarbonate pH sensing approach.[15] First, in vivo ^{15}N T_1 is significantly longer than that for ^{13}C (e.g., ∼10 s for ^{13}C bicarbonate[15]). Second, pH sensing using bicarbonate requires measurement and detection of both ^{13}C bicarbonate and its exchanging partner $^{13}CO_2$ via spectroscopic imaging (MRSI)—a demanding approach with respect to SNR, because the relative signal ratio of ^{13}C bicarbonate and $^{13}CO_2$ peaks must be measured with good precision, whereas this approach only requires accurate measurement of ^{15}N frequency, which can be performed with relatively low SNR.

A key challenge for in vivo pH sensing is a relatively narrow pH range for the extracellular compartments for most conditions of interest, requiring that a given pH probe provide a wide dynamic range of signal response over a relatively narrow range of pH values (i.e., ∼1.5 pH units). As a result, the pH sensor must have a pK_a close to physiological pH of ∼7. Initial studies of six-membered N-heterocycles (see Supporting Information Figure S1 and ref 42) identified only one somewhat suitable candidate: 2,6-lutidine,[42] with pK_a ∼ 6.6. However, 2,6-lutidine is not readily amenable to SABRE-SHEATH hyperpolarization.[24] The pK_a of imidazole is ∼7.0—a property that has already been exploited for in vivo tumor pH imaging via proton detection without hyperpolarization.[6,44] Therefore, imidazole nitrogen-15 sites are excellent candidates for ^{15}N HP pH sensing. Indeed, proton binding induces easily measured ^{15}N chemical shifts of ∼30 ppm (Figure 2).[45−47] Note that both ^{15}N sites have the same chemical shift in the deprotonated form because of fast proton hopping between these two sites in aqueous media.[45−47] In the protonated form, both ^{15}N sites are equivalent and have the same chemical shift. As a result, imidazole-$^{15}N_2$ is an excellent delivery vehicle, because its two ^{15}N sites carry twice the hyperpolarization payload of (single-site) pyridine derivatives.

Here, ^{15}N-SABRE-SHEATH hyperpolarization of imidazole-$^{15}N_2$ is demonstrated. Figure 2b shows the exchange process of imidazole-$^{15}N_2$ and *para*-H_2 gas on the activated Ir-IMes hexacoordinate complex of the most potent SABRE hyperpolarization catalyst to date.[23] As shown in Figure 2, ^{15}N signal enhancement ε_{15N} of ∼2000-fold is detected on each of the two ^{15}N sites in a methanol:aqueous (pH ∼ 12) buffer (∼1:1) solution of ∼0.1 M substrate utilizing only 50% *para*-H_2 gas and the hyperpolarization setup described previously.[26] Note the broad appearance of the HP NMR line in pure methanol-d_4 (Figure S3) owing to intermediate proton chemical exchange between the two ^{15}N sites described above; the ^{15}N NMR line is no longer broadened in aqueous solution (Figure 2d). The additional ^{15}N HP resonances (seen as narrow lines) are due to the presence of catalyst-bound ^{15}N imidazoles (Figure 2d inset and Figure S3a)—which have different pK_a values, protonation states, and proton exchange rates. If 100% *para*-H_2 would have been utilized (vs ∼50% *para*-H_2 utilized here), the enhancement would be effectively tripled to ε_{15N} ∼ 6000-fold, corresponding to P_{15N} ∼ 2%. Temperature and B_T[48] of the SABRE-SHEATH procedure were optimized to achieve the largest enhancements under our conditions. We note that unusually (for SABRE) high temperature (>340 K, Figure 2g)

DOI: 10.1021/acssensors.6b00231
ACS Sens. XXXX, XXX, XXX−XXX

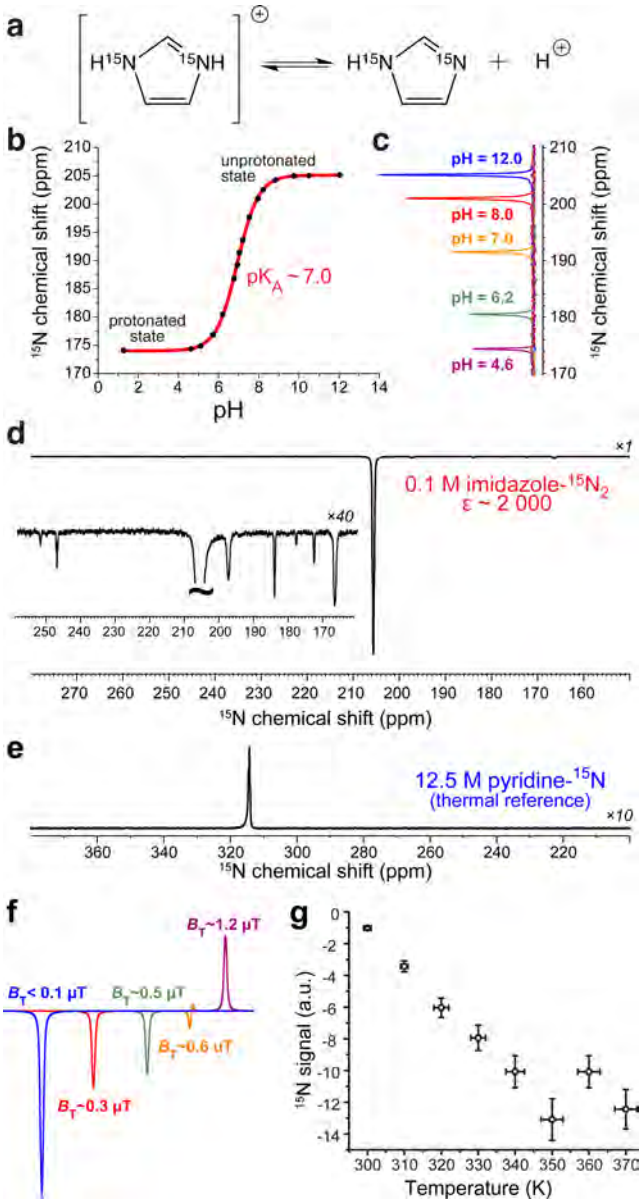

Figure 2. (a) Molecular diagram of imidazole-$^{15}N_2$ protonation; note that the effective molecular symmetry in unprotonated (due to fast proton hopping between two ^{15}N sites) and protonated states results in the same ^{15}N chemical shift of both sites. (b) Determination of imidazole-$^{15}N_2$ pK_a using isotropic ^{15}N chemical shift in aqueous solutions. (c) Selected (thermally-polarized) ^{15}N spectra of imidazole in water used for pK_a determination. (d) ^{15}N NMR spectrum of HP imidazole-$^{15}N_2$ (~0.1 M) in methanol:water (~1:1) produced via SABRE-SHEATH (B_T < 0.1 μT, [catalyst] ~ 4 mM); note the inset spectrum showing the other HP enlarged resonances: the large changes (i.e., ≥10 ppm) of a ^{15}N chemical shift of these species are caused by the imidazole position in the hexacoordinate complex (e.g., equatorial vs axial position, Figure 1b), binding state (e.g., free vs catalyst-bound states, Figure 1b),[25,26] and protonation states.[42] (e) ^{15}N spectrum of a ^{15}N signal reference. (f,g) SABRE-SHEATH optimization of magnetic transfer field B_T and temperature, respectively. All NMR spectra are recorded using a 400 MHz Bruker NMR spectrometer.

was found optimal for 15N SABRE-SHEATH in the aqueous medium (Figure 2f,g).

These results represent the highest payload (defined as the product of ^{15}N concentration and polarization) for any SABRE-hyperpolarized compounds with the exception of ^{15}N-nicotinamide (50 mM and P_{15N} ~ 11% at ~100% *para*-H_2 limit), which was achieved in pure methanol-d_4 using preactivation with pyridine,[33] whereas here, ^{15}N SABRE-SHEATH was performed in an aqueous medium, which is known to provide lower enhancements due to lower *para*-H_2 solubility.[37] A potential solution is a further significant increase of *para*-H_2 pressure (compared to ~6.5 atm used here), which could potentially enable significantly larger polarization levels,[24,26] e.g., P_{15N} ~ 10% or more. ^{15}N T_1 of imidazole-$^{15}N_2$ in methanol:aqueous (pH ~ 12) buffer (~1:1) solution in the presence of SABRE catalyst was 24 ± 1 s at 9.4 T, whereas further reduction of methanol fraction (to an estimated value of <10% by volume) resulted in a T_1 increase to 86 ± 2 s (Figure S2) indicating that the in vivo T_1 (with the absence of both alcohol and exchangeable catalyst) could potentially exceed 1 min.[49] The ^{15}N hyperpolarization lifetime could also be further enhanced via long-lived spin states and the use of lower magnetic fields.[30]

Motivated by potential biomedical translation, SABRE-SHEATH hyperpolarization of imidazole-$^{15}N_2$ in aqueous media was performed at several different pH values (below and above the pK_a, Figure 3) demonstrating that (i) ^{15}N chemical shift of the HP probe indeed changes by ~30 ppm, and (ii) the ^{15}N NMR resonances are sufficiently narrow to discriminate minute changes in pH in the physiologically relevant range. Therefore, this HP molecular probe can potentially enable in vivo pH sensing with an estimated ~15 ppm range covering pH range 6.5 to 7.5, and it should provide resolution of 0.1 unit of pH per 1.5 ppm of ^{15}N shift.

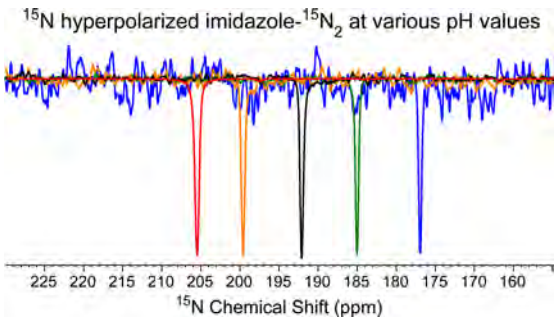

Figure 3. ^{15}N NMR spectra of imidazole-$^{15}N_2$ hyperpolarized via SABRE-SHEATH at various pH values (below and above pK_a) in aqueous solutions containing <50% methanol. Note a minor shift of ~2 ppm between resonances shown in Figure 2c (not color matched) and here due to temperature difference of ~40 °C.

Conventional ^1H-SABRE of methanol-d_4 solution yielded ε_H ~ 50−100-fold (Figure S3e), i.e., values lower than the corresponding ^{15}N enhancements (Figure S3a)—in agreement with previous ^{15}N SABRE-SHEATH studies of ^{15}N-pyridine.[26] Moreover, Figure S3d also shows in situ (or "high-field") SABRE ^1H NMR spectroscopy of imidazole-$^{15}N_2$ recorded inside a 9.4 T spectrometer (the spectrum was recorded approximately 2 s after *para*-H_2 bubbling (conducted at 9.4 T) was stopped—note (i) the partial SABRE signal enhancement of one of the imidazole protons, manifested as the signal with negative (emissive) phase—consistent with the previously described "high-field" SABRE effect;[50] and (ii) upfield ^1H signals from intermediate hydride species formed transiently during the catalyst activation process.[37] Taken together, the ^{15}N SABRE-SHEATH and ^1H SABRE results indicate that

DOI: 10.1021/acssensors.6b00231
ACS Sens. XXXX, XXX, XXX−XXX

imidazole-$^{15}N_2$ reversible exchange (and SABRE in general) have the same key features as the most-studied SABRE substrate, pyridine.

While d-DNP could in principle be employed for hyperpolarization of imidazole-$^{15}N_2$, it is an instrumentationally demanding and expensive hyperpolarization technique, and DNP hyperpolarization processes for this class of compound typically require ∼2 h of polarization build-up.[42] ^{15}N SABRE-SHEATH allows preparation of HP imidazole-$^{15}N_2$ (and potentially other imidazole-based biomolecules) in less than a minute using a very simple experimental setup, paving the way to pH sensing (imaging and localized spectroscopy) in vivo. Furthermore, in combination with recent demonstrations of SABRE in aqueous media[36−38] and in "neat" liquids,[24] the presented work potentially enables the hyperpolarization of ^{15}N-imidazole moieties for structural and functional studies of peptides and proteins.[51,52]

■ ASSOCIATED CONTENT

Supporting Information

The Supporting Information is available free of charge on the ACS Publications website at DOI: 10.1021/acssensors.6b00231.

Table summarizing pK_a values; additional figures providing quantitative measurements of pK_a using ^{15}N NMR spectroscopy; additional experimental details and other supporting figures (PDF)

■ AUTHOR INFORMATION

Corresponding Author

*E-mail: eduard.chekmenev@vanderbilt.edu.

Notes

The authors declare no competing financial interest.

■ ACKNOWLEDGMENTS

This work was supported by NSF under grants CHE-1058727, CHE-1363008, CHE-1416268, and CHE-1416432, NIH (1R21EB018014, 1R21EB020323, and 2R15EB007074-02), DOD CDMRP BRP W81XWH-12-1-0159/BC112431, DOD PRMRP awards W81XWH-15-1-0271 and W81XWH-15-1-0272, T32 EB001628, and Exxon Mobil Knowledge Build.

■ REFERENCES

(1) Vaupel, P.; Kallinowski, F.; Okunieff, P. Blood Flow, Oxygen and Nutrient Supply, and Metabolic Microenvironment of Human Tumors: A Review. *Cancer Res.* **1989**, *49*, 6449−6465.

(2) Tannock, I. F.; Rotin, D. Acid pH in Tumors and Its Potential for Therapeutic Exploitation. *Cancer Res.* **1989**, *49*, 4373−4384.

(3) Martin, G. R.; Jain, R. K. Noninvasive Measurement of Interstitial pH Profiles in Normal and Neoplastic Tissue Using Fluorescence Ratio Imaging Microscopy. *Cancer Res.* **1994**, *54*, 5670−5674.

(4) Gerweck, L. E.; Seetharaman, K. Cellular pH Gradient in Tumor Versus Normal Tissue: Potential Exploitation for the Treatment of Cancer. *Cancer Res.* **1996**, *56*, 1194−1198.

(5) Carmeliet, P.; Jain, R. K. Angiogenesis in Cancer and Other Diseases. *Nature* **2000**, *407*, 249−257.

(6) Gillies, R. J.; Raghunand, N.; Garcia-Martin, M. L.; Gatenby, R. A. pH Imaging. *IEEE Eng. Med. Biol. Mag.* **2004**, *23*, 57−64.

(7) Saha, I.; Chaffee, K. E.; Duanmu, C.; Woods, B. M.; Stokes, A. M.; Buck, L. E.; Walkup, L. L.; Sattenapally, N.; Huggenvik, J.; Gao, Y.; et al. pH-Sensitive MR Responses Induced by Dendron-Functionalized SPIONs. *J. Phys. Chem. C* **2013**, *117*, 1893−1903.

(8) Vermathen, P.; Capizzano, A. A.; Maudsley, A. A. Administration and ^{1}H MRS Detection of Histidine in Human Brain: Application to in Vivo pH Measurement. *Magn. Reson. Med.* **2000**, *43*, 665−675.

(9) Zhou, J.; Payen, J.-F.; Wilson, D. A.; Traystman, R. J.; van Zijl, P. C. M. Using the Amide Proton Signals of Intracellular Proteins and Peptides to Detect pH Effects in MRI. *Nat. Med.* **2003**, *9*, 1085−1090.

(10) Stubbs, M.; Bhujwalla, Z. M.; Tozer, G. M.; Rodrigues, L. M.; Maxwell, R. J.; Morgan, R.; Howe, F. A.; Griffiths, J. R. An Assessment of ^{31}P MRS as a Method of Measuring pH in Rat Tumours. *NMR Biomed.* **1992**, *5*, 351−359.

(11) Gillies, R. J.; Liu, Z.; Bhujwalla, Z. P-31-MRS Measurements of Extracellular pH of Tumors Using 3-Aminopropylphosphonate. *Am. J. Physiol.* **1994**, *267*, C195−C203.

(12) Ackerman, J. J. H.; Soto, G. E.; Spees, W. M.; Zhu, Z.; Evelhoch, J. L. The NMR Chemical Shift pH Measurement Revisited: Analysis of Error and Modeling of a pH Dependent Reference. *Magn. Reson. Med.* **1996**, *36*, 674−683.

(13) Zhang, S.; Winter, P.; Wu, K.; Sherry, A. D. A Novel Europium(III)-Based MRI Contrast Agent. *J. Am. Chem. Soc.* **2001**, *123*, 1517−1518.

(14) Lowe, M. P.; Parker, D.; Reany, O.; Aime, S.; Botta, M.; Castellano, G.; Gianolio, E.; Pagliarin, R. pH-Dependent Modulation of Relaxivity and Luminescence in Macrocyclic Gadolinium and Europium Complexes Based on Reversible Intramolecular Sulfonamide Ligation. *J. Am. Chem. Soc.* **2001**, *123*, 7601−7609.

(15) Gallagher, F. A.; Kettunen, M. I.; Day, S. E.; Hu, D. E.; Ardenkjaer-Larsen, J. H.; in't Zandt, R.; Jensen, P. R.; Karlsson, M.; Golman, K.; Lerche, M. H.; et al. Magnetic Resonance Imaging of pH in Vivo Using Hyperpolarized C-13-Labelled Bicarbonate. *Nature* **2008**, *453*, 940−943.

(16) Raghunand, N.; Howison, C.; Sherry, A. D.; Zhang, S.; Gillies, R. J. Renal and Systemic pH Imaging by Contrast-Enhanced MRI. *Magn. Reson. Med.* **2003**, *49*, 249−257.

(17) Gianolio, E.; Maciocco, L.; Imperio, D.; Giovenzana, G. B.; Simonelli, F.; Abbas, K.; Bisi, G.; Aime, S. Dual MRI-SPECT Agent for pH-Mapping. *Chem. Commun.* **2011**, *47*, 1539−1541.

(18) Abragam, A.; Goldman, M. Principles of Dynamic Nuclear Polarization. *Rep. Prog. Phys.* **1978**, *41*, 395−467.

(19) Carver, T. R.; Slichter, C. P. Polarization of Nuclear Spins in Metals. *Phys. Rev.* **1953**, *92*, 212−213.

(20) Nikolaou, P.; Goodson, B. M.; Chekmenev, E. Y. NMR Hyperpolarization Techniques for Biomedicine. *Chem. - Eur. J.* **2015**, *21*, 3156−3166.

(21) Adams, R. W.; Aguilar, J. A.; Atkinson, K. D.; Cowley, M. J.; Elliott, P. I. P.; Duckett, S. B.; Green, G. G. R.; Khazal, I. G.; Lopez-Serrano, J.; Williamson, D. C. Reversible Interactions with Para-Hydrogen Enhance NMR Sensitivity by Polarization Transfer. *Science* **2009**, *323*, 1708−1711.

(22) Adams, R. W.; Duckett, S. B.; Green, R. A.; Williamson, D. C.; Green, G. G. R. A Theoretical Basis for Spontaneous Polarization Transfer in Non-Hydrogenative Parahydrogen-Induced Polarization. *J. Chem. Phys.* **2009**, *131*, 194505.

(23) Cowley, M. J.; Adams, R. W.; Atkinson, K. D.; Cockett, M. C. R.; Duckett, S. B.; Green, G. G. R.; Lohman, J. A. B.; Kerssebaum, R.; Kilgour, D.; Mewis, R. E. Iridium N-Heterocyclic Carbene Complexes as Efficient Catalysts for Magnetization Transfer from Para-Hydrogen. *J. Am. Chem. Soc.* **2011**, *133*, 6134−6137.

(24) Shchepin, R. V.; Truong, M. L.; Theis, T.; Coffey, A. M.; Shi, F.; Waddell, K. W.; Warren, W. S.; Goodson, B. M.; Chekmenev, E. Y. Hyperpolarization of "Neat" Liquids by NMR Signal Amplification by Reversible Exchange. *J. Phys. Chem. Lett.* **2015**, *6*, 1961−1967.

(25) Theis, T.; Truong, M. L.; Coffey, A. M.; Shchepin, R. V.; Waddell, K. W.; Shi, F.; Goodson, B. M.; Warren, W. S.; Chekmenev, E. Y. Microtesla SABRE Enables 10% Nitrogen-15 Nuclear Spin Polarization. *J. Am. Chem. Soc.* **2015**, *137*, 1404−1407.

(26) Truong, M. L.; Theis, T.; Coffey, A. M.; Shchepin, R. V.; Waddell, K. W.; Shi, F.; Goodson, B. M.; Warren, W. S.; Chekmenev, E. Y. ^{15}N Hyperpolarization by Reversible Exchange Using SABRE-SHEATH. *J. Phys. Chem. C* **2015**, *119*, 8786−8797.

DOI: 10.1021/acssensors.6b00231
ACS Sens. XXXX, XXX, XXX−XXX

(27) Zhivonitko, V. V.; Skovpin, I. V.; Koptyug, I. V. Strong ^{31}P Nuclear Spin Hyperpolarization Produced Via Reversible Chemical Interaction with Parahydrogen. *Chem. Commun.* **2015**, *51*, 2506−2509.
(28) Pravdivtsev, A. N.; Yurkovskaya, A. V.; Vieth, H.-M.; Ivanov, K. L. Spin Mixing at Level Anti-Crossings in the Rotating Frame Makes High-Field SABRE Feasible. *Phys. Chem. Chem. Phys.* **2014**, *16*, 24672−24675.
(29) Theis, T.; Truong, M.; Coffey, A. M.; Chekmenev, E. Y.; Warren, W. S. LIGHT-SABRE Enables Efficient in-Magnet Catalytic Hyperpolarization. *J. Magn. Reson.* **2014**, *248*, 23−26.
(30) Theis, T.; Ortiz, G. X.; Logan, A. W. J.; Claytor, K. E.; Feng, Y.; Huhn, W. P.; Blum, V.; Malcolmson, S. J.; Chekmenev, E. Y.; Wang, Q.; et al. Direct and Cost-Efficient Hyperpolarization of Long-Lived Nuclear Spin States on Universal $^{15}N_2$-Diazirine Molecular Tags. *Sci. Adv.* **2016**, *2*, e1501438.
(31) Kurhanewicz, J.; Vigneron, D. B.; Brindle, K.; Chekmenev, E. Y.; Comment, A.; Cunningham, C. H.; DeBerardinis, R. J.; Green, G. G.; Leach, M. O.; Rajan, S. S.; et al. Analysis of Cancer Metabolism by Imaging Hyperpolarized Nuclei: Prospects for Translation to Clinical Research. *Neoplasia* **2011**, *13*, 81−97.
(32) Nelson, S. J.; Kurhanewicz, J.; Vigneron, D. B.; Larson, P. E. Z.; Harzstark, A. L.; Ferrone, M.; van Criekinge, M.; Chang, J. W.; Bok, R.; Park, I.; et al. Metabolic Imaging of Patients with Prostate Cancer Using Hyperpolarized 1-C-13 Pyruvate. *Sci. Transl. Med.* **2013**, *5*, 198ra108.
(33) Shchepin, R. V.; Barskiy, D. A.; Mikhaylov, D. M.; Chekmenev, E. Y. Efficient Synthesis of Nicotinamide-1-^{15}N for Ultrafast NMR Hyperpolarization Using Parahydrogen. *Bioconjugate Chem.* **2016**, DOI: 10.1021/acs.bioconjchem.6b00148.
(34) Brindle, K. M. Imaging Metabolism with Hyperpolarized ^{13}C-Labeled Cell Substrates. *J. Am. Chem. Soc.* **2015**, *137*, 6418−6427.
(35) Comment, A.; Merritt, M. E. Hyperpolarized Magnetic Resonance as a Sensitive Detector of Metabolic Function. *Biochemistry* **2014**, *53*, 7333−7357.
(36) Zeng, H.; Xu, J.; McMahon, M. T.; Lohman, J. A. B.; van Zijl, P. C. M. Achieving 1% NMR Polarization in Water in Less Than 1 min Using SABRE. *J. Magn. Reson.* **2014**, *246*, 119−121.
(37) Truong, M. L.; Shi, F.; He, P.; Yuan, B.; Plunkett, K. N.; Coffey, A. M.; Shchepin, R. V.; Barskiy, D. A.; Kovtunov, K. V.; Koptyug, I. V.; et al. Irreversible Catalyst Activation Enables Hyperpolarization and Water Solubility for NMR Signal Amplification by Reversible Exchange. *J. Phys. Chem. B* **2014**, *118*, 13882−13889.
(38) Hövener, J.-B.; Schwaderlapp, N.; Borowiak, R.; Lickert, T.; Duckett, S. B.; Mewis, R. E.; Adams, R. W.; Burns, M. J.; Highton, L. A. R.; Green, G. G. R.; et al. Toward Biocompatible Nuclear Hyperpolarization Using Signal Amplification by Reversible Exchange: Quantitative in Situ Spectroscopy and High-Field Imaging. *Anal. Chem.* **2014**, *86*, 1767−1774.
(39) Shi, F.; Coffey, A. M.; Waddell, K. W.; Chekmenev, E. Y.; Goodson, B. M. Heterogeneous Solution NMR Signal Amplification by Reversible Exchange. *Angew. Chem., Int. Ed.* **2014**, *53*, 7495−7498.
(40) Shi, F.; Coffey, A. M.; Waddell, K. W.; Chekmenev, E. Y.; Goodson, B. M. Nanoscale Catalysts for NMR Signal Enhancement by Reversible Exchange. *J. Phys. Chem. C* **2015**, *119*, 7525−7533.
(41) Zeng, H.; Xu, J.; Gillen, J.; McMahon, M. T.; Artemov, D.; Tyburn, J.-M.; Lohman, J. A. B.; Mewis, R. E.; Atkinson, K. D.; Green, G. G. R.; et al. Optimization of SABRE for Polarization of the Tuberculosis Drugs Pyrazinamide and Isoniazid. *J. Magn. Reson.* **2013**, *237*, 73−78.
(42) Jiang, W.; Lumata, L.; Chen, W.; Zhang, S.; Kovacs, Z.; Sherry, A. D.; Khemtong, C. Hyperpolarized ^{15}N-Pyridine Derivatives as pH-Sensitive MRI Agents. *Sci. Rep.* **2015**, *5*, 9104.
(43) Ardenkjaer-Larsen, J. H.; Fridlund, B.; Gram, A.; Hansson, G.; Hansson, L.; Lerche, M. H.; Servin, R.; Thaning, M.; Golman, K. Increase in Signal-to-Noise Ratio of > 10,000 Times in Liquid-State NMR. *Proc. Natl. Acad. Sci. U. S. A.* **2003**, *100*, 10158−10163.
(44) Hashim, A. I.; Zhang, X.; Wojtkowiak, J. W.; Gillies, R. J.; Martinez, G. V. Imaging pH and Metastasis. *NMR Biomed.* **2011**, *24*, 582−591.
(45) Alei, M.; Morgan, L. O.; Wageman, W. E. Nitrogen-15 Magnetic Resonance of Aqueous Imidazole and Zinc(II)-Imidazole Complexes. Evidence for Hexacoordination. *Inorg. Chem.* **1978**, *17*, 2288−2293.
(46) Alei, M.; Wageman, W. E.; Morgan, L. O. Nitrogen-15 Chemical Shifts for Imidazole in Aqueous Cadmium(2+) Solutions. *Inorg. Chem.* **1978**, *17*, 3314−3315.
(47) Alei, M.; Morgan, L. O.; Wageman, W. E.; Whaley, T. W. Ph-Dependence of N-15 NMR Shifts and Coupling Constants in Aqueous Imidazole and 1-Methylimidazole - Comments on Estimation of Tautomeric Equilibrium Constants for Aqueous Histidine. *J. Am. Chem. Soc.* **1980**, *102*, 2881−2887.
(48) Lloyd, L. S.; Asghar, A.; Burns, M. J.; Charlton, A.; Coombes, S.; Cowley, M. J.; Dear, G. J.; Duckett, S. B.; Genov, G. R.; Green, G. G. R.; et al. Hyperpolarisation through Reversible Interactions with Parahydrogen. *Catal. Sci. Technol.* **2014**, *4*, 3544−3554.
(49) Cudalbu, C.; Comment, A.; Kurdzesau, F.; van Heeswijk, R. B.; Uffmann, K.; Jannin, S.; Denisov, V.; Kirik, D.; Gruetter, R. Feasibility of in Vivo N-15 MRS Detection of Hyperpolarized N-15 Labeled Choline in Rats. *Phys. Chem. Chem. Phys.* **2010**, *12*, 5818−5823.
(50) Barskiy, D. A.; Kovtunov, K. V.; Koptyug, I. V.; He, P.; Groome, K. A.; Best, Q. A.; Shi, F.; Goodson, B. M.; Shchepin, R. V.; Coffey, A. M.; et al. The Feasibility of Formation and Kinetics of NMR Signal Amplification by Reversible Exchange (SABRE) at High Magnetic Field (9.4 T). *J. Am. Chem. Soc.* **2014**, *136*, 3322−3325.
(51) Miao, Y.; Cross, T. A.; Fu, R. Differentiation of Histidine Tautomeric States Using ^{15}N Selectively Filtered ^{13}C Solid-State NMR Spectroscopy. *J. Magn. Reson.* **2014**, *245*, 105−109.
(52) Hu, F.; Luo, W.; Hong, M. Mechanisms of Proton Conduction and Gating in Influenza M2 Proton Channels from Solid-State NMR. *Science* **2010**, *330*, 505−508.

DOI: 10.1021/acssensors.6b00231
ACS Sens. XXXX, XXX, XXX−XXX

RSC Advances

COMMUNICATION

View Article Online
View Journal | View Issue

Published on 15 July 2016. Downloaded by Vanderbilt University Library on 22/08/2016 23:41:46.

Cite this: *RSC Adv.*, 2016, **6**, 69728

Received 17th June 2016
Accepted 14th July 2016

DOI: 10.1039/c6ra15808k

www.rsc.org/advances

Toward production of pure ^{13}C hyperpolarized metabolites using heterogeneous parahydrogen-induced polarization of ethyl[1-^{13}C]acetate†

K. V. Kovtunov,*[ab] D. A. Barskiy,[c] O. G. Salnikov,[ab] R. V. Shchepin,[c] A. M. Coffey,[c] L. M. Kovtunova,[bd] V. I. Bukhtiyarov,[bd] I. V. Koptyug[ab] and E. Y. Chekmenev*[ce]

Here, we report the production of ^{13}C-hyperpolarized ethyl acetate *via* heterogeneously catalyzed pairwise addition of parahydrogen to vinyl acetate over TiO_2-supported rhodium nanoparticles, followed by magnetic field cycling. Importantly, the hyperpolarization is demonstrated even at the natural abundance of ^{13}C isotope (*ca.* 1.1%) along with the easiest separation of the catalyst from the hyperpolarized liquid.

Nuclear Magnetic Resonance (NMR) hyperpolarization is a rapidly expanding area of research, because it provides an opportunity to overcome the low sensitivity problem of conventional NMR spectroscopy and imaging *in vitro* and *in vivo*.[1–4] One of these approaches is the dynamic nuclear polarization (DNP) method based on polarization transfer from electrons to nuclei *via* microwave irradiation of a sample containing free radicals.[5,6] DNP enables hyperpolarization of ^{13}C-labeled substrates such as lactate and pyruvate[7,8] for metabolic MRI to provide unique information about different pathologies in cancer, heart disease and others.[9,10] Despite the wide range of molecular targets that can be hyperpolarized by DNP, it is a very expensive hyperpolarization technique, and it requires a relatively long time (~1 h) for production of polarization, which significantly limits the broad application of this technique. An alternative approach to achieve the hyperpolarized (HP) state in biomolecules is parahydrogen-induced polarization (PHIP),[11,12] which relies on hydrogenation of some unsaturated precursors with parahydrogen. In PHIP, pairwise hydrogen addition leads to formation of compounds in which the two nascent H atoms from the parahydrogen molecule are no longer magnetically equivalent, which is manifested as near unity nuclear spin polarization (P).[13,14] While fluids hyperpolarized by PHIP can be employed as contrast agents for imaging applications,[15,16] they typically have relatively short T_1 values, *i.e.* depolarize within seconds.[17] To increase short lifetime of HP fluids, more sophisticated agents with ^{13}C labeled sites were developed, where these ^{13}C sites are hyperpolarized *via* polarization transfer from nascent parahydrogen atoms using spin–spin couplings. While this polarization transfer can be accomplished by radio frequency pulse sequences, a less instrumentation demanding alternative is a magnetic field cycling (MFC) approach.[15,18–20] Angiographic ^{13}C HP agent 2-hydroxyethyl propionate (HEP) produced by PHIP was demonstrated at the very dawn of hyperpolarization era.[15] A few other ^{13}C-labeled PHIP hyperpolarized compounds were developed later for potential biomedical applications: succinate,[2,21,22] tetrafluoropropionate,[23] phospholactate,[24–26] and others, despite the chemistry-related challenge of unsaturated precursor design with sophisticated isotope labelling patterns. However, PHIP using side-arm hydrogenation (SAH) that was pioneered by Reineri and co-workers recently,[27,28] may significantly expand the scope of the PHIP method with regard to the potentially amenable biomolecules. Hyperpolarization of pyruvate and acetate were reported to date,[27,28] with many more biomolecules likely to follow soon. Furthermore, novel ^{13}C enrichment chemistry to enable simple and low cost incorporation of ^{13}C tags was recently developed for PHIP-SAH method, which can potentially yield hyperpolarized contrast agents with % $P_{^{13}C}$ of 20–50%.[29]

However, until recently the PHIP technique primarily relied on homogeneous pairwise hydrogenations with transition metal complexes as catalysts for production of HP contrast agents.[30,31] The main disadvantage of this approach is the presence of the dissolved homogeneous catalyst, which is expensive and is challenging to separate from the hyperpolarized compounds.[32,33] Recently, however, PHIP was

[a]*Laboratory of Magnetic Resonance Microimaging, International Tomography Center SB RAS, Institutskaya St. 3A, 630090 Novosibirsk, Russia. E-mail: kovtunov@tomo.nsc.ru*

[b]*Novosibirsk State University, Pirogova St. 2, 630090 Novosibirsk, Russia*

[c]*Vanderbilt University, Institute of Imaging Science (VUIIS), Department of Radiology, Department of Biomedical Engineering, Vanderbilt-Ingram Cancer Center (VICC), Nashville, Tennessee, 37232-2310, USA. E-mail: eduard.chekmenev@vanderbilt.edu*

[d]*Boreskov Institute of Catalysis, SB RAS 5 Acad. Lavrentiev Pr., Novosibirsk, 630090 Russia*

[e]*Russian Academy of Sciences, Leninskiy Prospect 14, 119991 Moscow, Russia*

† Electronic supplementary information (ESI) available: Catalysts preparation procedure, additional NMR spectra. See DOI: 10.1039/c6ra15808k

This journal is © The Royal Society of Chemistry 2016

Published on 15 July 2016. Downloaded by Vanderbilt University Library on 22/08/2016 23:41:46.

observed in the heterogeneous reactions in the gas[34] and in the liquid phases[35,36] over immobilized complexes,[37] supported metals[34,38] and ligand-capped nanoparticles.[39,40] Observation of ^{13}C HP resonance and therefore, production of ^{13}C-hyperpolarized molecules *via* heterogeneous hydrogenation with parahydrogen was so far shown only for ^{13}C HEP during hydrogenation of 2-hydroxyethyl acrylate over platinum nanoparticles capped with glutathione.[40] However, the conversion level was extremely low (see Fig. S3 in the ESI† of ref. 40) and may be estimated as *ca.* 0.03% over 15 seconds of reaction time. Moreover, along with low degree of substrate conversion the filtration procedure to separate 2 nm nanoparticles is also a translational challenge, which cannot be mitigated by a straightforward decantation of HP fluids from the solid catalyst during the time frame comparable to ^{13}C T_1 (typically on the order of tens of seconds). Furthermore, HEP has no direct metabolic relevance, and its potential use is limited to angiography.[15]

Herein, we report ^{13}C NMR hyperpolarization of a biomolecule *via* heterogeneous liquid phase hydrogenation of vinyl acetate over solid Rh/TiO$_2$ catalysts. The ^{13}C nuclear spin polarizations achieved in these experiments are the first reported to date involving heterogeneous reactions over supported metal catalysts.

Titania-supported rhodium catalysts are the best supported metal catalysts for HET-PHIP in both liquid[36,41] and gas phases.[17] Therefore, two variants of Rh/TiO$_2$ catalysts corresponding to two different loadings of the metal (1 wt% and 23.2 wt%) were prepared (see ESI for details†).

In the first set of experiments, both catalysts were tested in the gas phase hydrogenation of propene to propane with parahydrogen to check their efficiencies in terms of both the percentage of pairwise hydrogen addition level and the overall hydrogenation activity/yield. Both catalysts were active and yielded HP propane (Fig. S1 in the ESI†), which is in good agreement with the previous observations.[17] It should be noted that Rh/TiO$_2$ catalyst with 23.2 wt% rhodium loading resulted in the NMR spectrum with lower intensities of HP lines in comparison to that with 1 wt% rhodium loading despite a higher (*ca.* 100% *vs.* 75%) chemical yield of the reaction product. Next, both catalysts were used in the liquid phase heterogeneous hydrogenation of vinyl acetate in three organic solvents: benzene-d$_6$, dimethyl sulfoxide (DMSO)-d$_6$ and methanol-d$_4$. A high-pressure setup allowing to carry out hydrogenation reaction at *ca.* 7 atm of gas pressure *in situ* was employed[42] which allowed us to monitor the reaction inside a 5 mm NMR tube filled with vinyl acetate solution. The schematic presentation of the experimental setup with field cycling procedure is shown in Fig. 1. Utilization of DMSO-d$_6$ as the solvent was ineffective because no ethyl acetate formation was detected in the case of both catalysts. In contrast, when benzene-d$_6$ was used as a solvent (Fig. S2 in the SI†) and hydrogenation of vinyl acetate with parahydrogen was performed *in situ* in the 9.4 T NMR magnet (corresponding to PASADENA[11] conditions), very intense and clearly recognized HP peaks of ethyl acetate were detected at *ca.* 7 atm of hydrogen pressure. A relatively high pressure of H$_2$ gas along with its high solubility in benzene allowed us to observe weak PHIP effects even several minutes after interrupting hydrogen bubbling (Fig. S2 in the ESI†), indicating that hydrogenation of vinyl acetate is relatively slow. The highly polarized ALTADENA-shaped[12] signatures of HP NMR lines for ethyl acetate were also observed when hydrogenation experiments were conducted in the Earth's magnetic field (Fig. 2) or at ~0.1 μT inside the magnetic shield with the subsequent fast transfer to the high field of the 9.4 T NMR spectrometer (Fig. S3 in the ESI†). Importantly, utilization of Rh/TiO$_2$ catalyst with 23.2 wt% rhodium loading for vinyl acetate hydrogenation in benzene-d$_6$ solution results in the loss of parahydrogen-derived hyperpolarization of ethyl acetate despite greater chemical reaction yield compared to Rh/TiO$_2$ with 1 wt% Rh loading. The use of high parahydrogen pressure is very important, and it is clear that higher concentration of dissolved H$_2$ increases the reaction yields. For example, the intensities of HP lines were approximately four-fold greater when ~7 atm parahydrogen total pressure was used *vs.* ~1 atm under otherwise the same heterogeneous hydrogenation conditions in methanol-d$_4$ solvent (Fig. S4 in the ESI†). This situation is common, and utilization of relatively high parahydrogen pressures along with the use of efficient rhodium catalyst (23.2 wt% Rh loading) in methanol-d$_4$ solvent allowed us to observe HP lines in the ALTADENA experiments (Fig. 2b) with *ca.* 9-fold enhancement ε_H corresponding to % $P_H \sim 0.03\%$.

The possibility to produce HET-PHIP in the liquid phase opens up new horizons not only for the liquid phase ^{1}H contrast agents production but also for polarization transfer from HP protons to heteronuclei *via* MFC.[15,27–29,43]

By utilization of the MFC approach and heterogeneous hydrogenation over supported metals we demonstrate hyperpolarization of 1-^{13}C resonance of ethyl[1-^{13}C]acetate ($\varepsilon_{^{13}C} \sim 44$, % $P_{^{13}C} \sim 0.035\%$) at 98% ^{13}C enrichment (Fig. 3). ^{13}C HP signal is also readily detectable at natural abundance (~1.1%) of the ^{13}C isotope (Fig. S5 in the ESI†). Hydrogenation reaction was carried out in the Earth's magnetic field *via* parahydrogen bubbling through 80 mM solution of vinyl acetate-1-^{13}C in methanol-d$_4$ for approximately 25 s. Then the bubbling was terminated and the NMR tube with the reaction mixture and the solid catalyst was transferred inside a magnetic shield with a weak (~0.1 μT) magnetic field for a short period of time (~2 s) and then to the 9.4 T NMR spectrometer for ^{13}C NMR spectra acquisition (Fig. 3b). This MFC procedure was found to be over

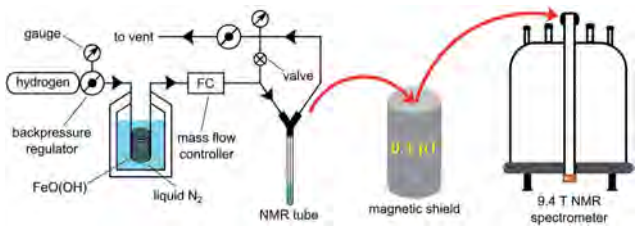

Fig. 1 Schematics of the experimental setup for liquid phase heterogeneous hydrogenation over supported metal catalysts with magnetic field cycling (MFC) for effective polarization transfer from ^{1}H to ^{13}C using PHIP-MFC.

Published on 15 July 2016. Downloaded by Vanderbilt University Library on 22/08/2016 23:41:46.

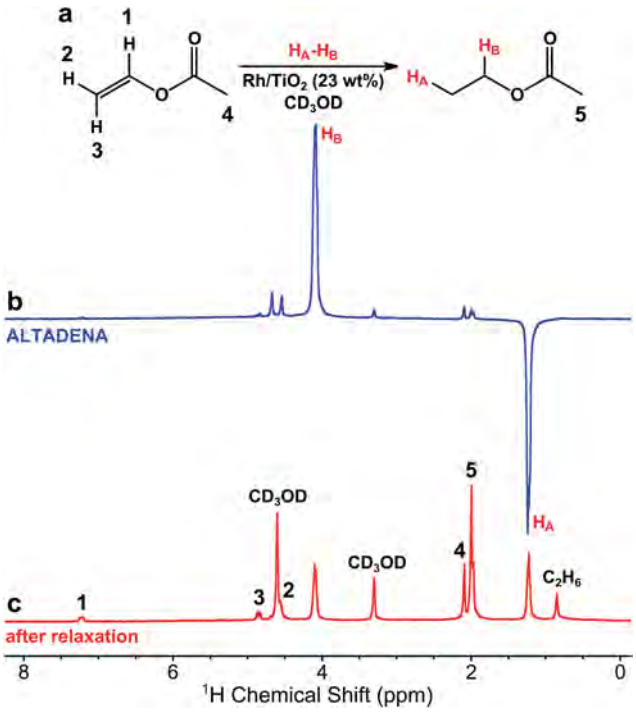

Fig. 2 (a) Reaction scheme of vinyl acetate hydrogenation with parahydrogen to yield HP ethyl acetate. (b) ^{1}H NMR spectrum of the solution after heterogeneous hydrogenation of vinyl acetate to ethyl acetate with parahydrogen over 23.2 wt% Rh/TiO_2 catalyst in methanol-d_4 (ALTADENA-type experiment). (c) Corresponding ^{1}H NMR spectrum of fully relaxed reaction mixture obtained after PHIP hydrogenation experiment shown in (b).

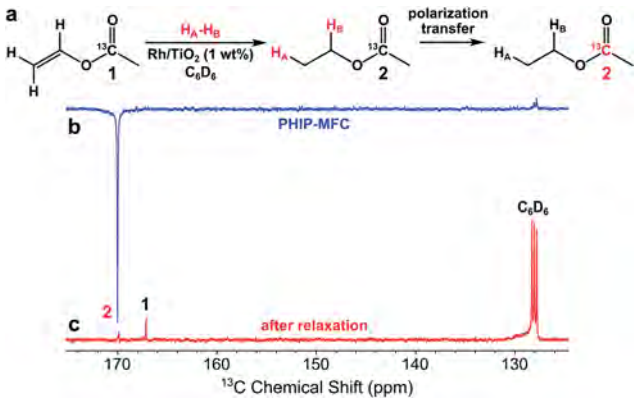

Fig. 3 (a) Reaction scheme of vinyl acetate-1-^{13}C heterogeneous hydrogenation by parahydrogen over 1 wt% Rh/TiO_2 catalyst in benzene-d_6 solution with subsequent polarization transfer from protons to ^{13}C (*via* MFC), (b) ^{13}C NMR spectrum of HP ethyl[1-^{13}C] acetate, and (c) corresponding ^{13}C spectrum of thermally polarized reaction mixture after hyperpolarization experiments shown in (b).

three times more efficient (Fig. S6 in the ESI†) than carrying out the hydrogenation reaction inside the magnetic shield.[29] A plausible explanation is a more efficient proton relaxation at ~0.1 μT *vs.* that at the Earth's magnetic field. In addition to achieving $\varepsilon_{^{13}C} \sim 44$ for ethyl[1-^{13}C]acetate *via* HET-PHIP, the chemical conversion was relatively high (*ca.* 25% conversion of 80 mM vinyl acetate-1-^{13}C reagent in benzene-d_6). ^{13}C enhancement of ~44 is approximately 50 times lower than that ($\varepsilon_{^{13}C} \sim 2200$) obtained using similar MFC procedure when homogeneous Rh-based hydrogenation catalyst in methanol-d_4 was utilized.[29] This significant difference can be primarily explained by two factors: (i) longer hydrogenation time (~25 s *vs.* ~10 s (ref. 29)) resulting in T_1 depolarization of proton hyperpolarization pool at the Earth's magnetic field, and (ii) lower percentage of pairwise parahydrogen addition on supported metal catalysts[44] *vs.* that for homogeneous catalysts. Further optimization of HET catalysts for production of solutions of HP contrast agents is required to improve % $P_{^{13}C}$ and the reaction yields. Moreover, the use of near 100% parahydrogen produced with a parahydrogen generator rather than ~50% parahydrogen used here would effectively triple % $P_{^{13}C}$ to ~0.1%. Furthermore, 100% conversion of vinyl acetate to ethyl acetate may provide a four-fold increase in the amount of polarized product, thereby improving the production of the payload (defined as the product of concentration and % P) of HP contrast agent.

To further emphasize that HET-PHIP catalyst should be optimized and matched for a specific task/PHIP precursor system, we utilized the 23.2 wt% Rh/TiO_2 catalyst in PHIP-MFC experiments. It was shown that hydrogenation of 80 mM vinyl [1-^{13}C]acetate *via* parahydrogen bubbling at *ca.* 7 atm in methanol-d_4 solution yielded ^{13}C PHIP polarized resonance of ethyl [1-^{13}C]acetate (Fig. S7 in the ESI†) with the intensity similar to that observed with the 1 wt% Rh/TiO_2 catalyst in benzene-d_6 (Fig. 3). Moreover, these relatively high ^{13}C hyperpolarization levels (along with high chemical conversion) of ethyl[1-^{13}C] acetate allow one to detect ^{13}C PHIP-MFC hyperpolarized resonance even at the natural abundance of ^{13}C nuclei (Fig. S5 in the ESI†). This ^{13}C PHIP polarization produced by using HET hydrogenation with parahydrogen is reported for the first time for an unlabeled compound. The relative simplicity of the presented setup (coupled with convenient production of ~50% parahydrogen using liquid N_2) will enable screening of wide range of molecular PHIP-SAH precursors for their utility to serve as HP contrast agents. In particular, screening of SAH in esters of pyruvate, lactate, amino acids, *etc.* may enable HET-PHIP of molecules with biological relevance to answer questions about metabolism and function *in vivo*.

In conclusion, we have prepared and successfully used two Rh/TiO_2 HET catalysts for effective pairwise hydrogen addition to produce HP biomolecule in two organic solvents. Optimization of the experimental setup and the use of elevated pressure of hydrogen for heterogeneous hydrogenation experiments allowed us to produce ^{1}H PHIP hyperpolarized patterns for ethyl acetate, which can be potentially a useful molecular probe for cancer and brain metabolism.[29] Magnetic field cycling (MFC) allowed us to observe hyperpolarized ^{13}C resonance of ethyl [1-^{13}C]acetate *via* polarization transfer from protons to slower relaxing 1-^{13}C site. Because a wide range of biomolecules can be potentially hyperpolarized using PHIP-SAH and MFC, the approach presented here would be useful for preparing pure (*i.e.*, catalyst free) HP contrast agents. The reported results are the first to date demonstration of HP ^{13}C resonance in ^{13}C

 This journal is © The Royal Society of Chemistry 2016

Published on 15 July 2016. Downloaded by Vanderbilt University Library on 22/08/2016 23:41:46.

isotopically labeled and unlabeled (natural abundance of ^{13}C) biomolecule produced over supported metal catalysts in the liquid phase. And presented technique can yield 0.1% ^{13}C polarization.

Acknowledgements

ITC team acknowledge the grant from the Russian Science Foundation (14-13-00445) for the support of heterogeneous hydrogenation experiments, and FASO Russia project # 0333-2014-0001 for basic funding. VIB and LMK thank RSF grant (# 14-23-00146) for the support of catalysts preparation. The US team thank NIH 1F32EB021840, 1R21EB018014 and 1R21EB020323, NSF CHE-1416268, DOD CDMRP W81XWH-12-1-0159/BC112431, and W81XWH-15-1-0271, and ExxonMobil Research and Engineering Company Knowledge Build for MFC experiments and setup building.

Notes and references

1 R. E. Hurd, Y. Yen, D. Mayer, A. Chen, D. Wilson, S. Kohler, R. Bok, D. Vigneron, J. Kurhanewicz, J. Tropp, D. Spielman and A. Pfefferbaum, *Magn. Reson. Med.*, 2011, **63**, 1137–1143.
2 N. M. Zacharias, H. R. Chan, N. Sailasuta, B. D. Ross and P. Bhattacharya, *J. Am. Chem. Soc.*, 2012, **134**, 934–943.
3 A. Comment and M. E. Merritt, *Biochemistry*, 2014, **53**, 7333–7357.
4 P. Nikolaou, B. M. Goodson and E. Y. Chekmenev, *Chem.–Eur. J.*, 2015, **21**, 3156–3166.
5 J. H. Ardenkjaer-Larsen, B. Fridlund, A. Gram, G. Hansson, L. Hansson, M. H. Lerche, R. Servin, M. Thaning and K. Golman, *Proc. Natl. Acad. Sci. U. S. A.*, 2003, **100**, 10158–10163.
6 T. Maly, G. T. Debelouchina, V. S. Bajaj, K.-N. Hu, C.-G. Joo, M. L. Mak-Jurkauskas, J. R. Sirigiri, P. C. A. van der Wel, J. Herzfeld, R. J. Temkin and R. G. Griffin, *J. Chem. Phys.*, 2008, **128**, 052211.
7 C. Harrison, C. Yang, A. Jindal, R. J. DeBerardinis, M. A. Hooshyar, M. Merritt, A. Dean Sherry and C. R. Malloy, *NMR Biomed.*, 2012, **25**, 1286–1294.
8 T. H. Witney, M. I. Kettunen and K. M. Brindle, *J. Biol. Chem.*, 2011, **286**, 24572–24580.
9 K. Brindle, *Nat. Rev. Cancer*, 2008, **8**, 94–107.
10 K. M. Brindle, S. E. Bohndiek, F. A. Gallagher and M. I. Kettunen, *Magn. Reson. Med.*, 2011, **66**, 505–519.
11 C. R. Bowers and D. P. Weitekamp, *J. Am. Chem. Soc.*, 1987, **109**, 5541–5542.
12 M. G. Pravica and D. P. Weitekamp, *Chem. Phys. Lett.*, 1988, **145**, 255–258.
13 C. R. Bowers and D. P. Weitekamp, *Phys. Rev. Lett.*, 1986, **57**, 2645–2648.
14 T. C. Eisenschmid, R. U. Kirss, P. P. Deutsch, S. I. Hommeltoft, R. Eisenberg, J. Bargon, R. G. Lawler and A. L. Balch, *J. Am. Chem. Soc.*, 1987, **109**, 8089–8091.
15 K. Golman, O. Axelsson, H. Jóhannesson, S. Månsson, C. Olofsson and J. S. Petersson, *Magn. Reson. Med.*, 2001, **46**, 1–5.
16 P. Bhattacharya, K. Harris, A. P. Lin, M. Mansson, V. A. Norton, W. H. Perman, D. P. Weitekamp and B. D. Ross, *Magn. Reson. Mater. Phys., Biol. Med.*, 2005, **18**, 245–256.
17 K. V. Kovtunov, D. A. Barskiy, A. M. Coffey, M. L. Truong, O. G. Salnikov, A. K. Khudorozhkov, E. A. Inozemtseva, I. P. Prosvirin, V. I. Bukhtiyarov, K. W. Waddell, E. Y. Chekmenev and I. V Koptyug, *Chem.–Eur. J.*, 2014, **20**, 11636–11639.
18 M. Goldman, H. Jóhannesson, O. Axelsson and M. Karlsson, *C. R. Chim.*, 2006, **9**, 357–363.
19 L. T. Kuhn and J. Bargon, *Top. Curr. Chem.*, 2007, **276**, 25–68.
20 C. Cai, A. M. Coffey, R. V. Shchepin, E. Y. Chekmenev and K. W. Waddell, *J. Phys. Chem. B*, 2013, **117**, 1219–1224.
21 P. Bhattacharya, E. Y. Chekmenev, W. H. Perman, K. C. Harris, A. P. Lin, V. A. Norton, C. T. Tan, B. D. Ross and D. P. Weitekamp, *J. Magn. Reson.*, 2007, **186**, 150–155.
22 E. Y. Chekmenev, J. Hövener, V. A. Norton, K. Harris, L. S. Batchelder, P. Bhattacharya, B. D. Ross and D. P. Weitekamp, *J. Am. Chem. Soc.*, 2008, **130**, 4212–4213.
23 P. Bhattacharya, E. Y. Chekmenev, W. F. Reynolds, S. Wagner, N. Zacharias, H. R. Chan, R. Bunger and B. D. Ross, *NMR Biomed.*, 2011, **24**, 1023–1028.
24 R. V. Shchepin, A. M. Coffey, K. W. Waddell and E. Y. Chekmenev, *J. Am. Chem. Soc.*, 2012, **134**, 3957–3960.
25 R. V. Shchepin, A. M. Coffey, K. W. Waddell and E. Y. Chekmenev, *Anal. Chem.*, 2014, **86**, 5601–5605.
26 R. V. Shchepin, W. Pham and E. Y. Chekmenev, *J. Labelled Compd. Radiopharm.*, 2014, **57**, 517–524.
27 F. Reineri, T. Boi and S. Aime, *Nat. Commun.*, 2015, **6**, 5858.
28 E. Cavallari, C. Carrera, T. Boi, S. Aime and F. Reineri, *J. Phys. Chem. B*, 2015, **119**, 10035–10041.
29 R. V. Shchepin, D. A. Barskiy, A. M. Coffey, I. V. Manzanera Esteve and E. Y. Chekmenev, *Angew. Chem., Int. Ed.*, 2016, **55**, 6071–6074.
30 S. B. Duckett and N. J. Wood, *Coord. Chem. Rev.*, 2008, **252**, 2278–2291.
31 R. A. Green, R. W. Adams, S. B. Duckett, R. E. Mewis, D. C. Williamson and G. G. R. Green, *Prog. Nucl. Magn. Reson. Spectrosc.*, 2012, **67**, 1–48.
32 F. Reineri, A. Viale, S. Ellena, T. Boi, V. Daniele, R. Gobetto and S. Aime, *Angew. Chem., Int. Ed.*, 2011, **50**, 7350–7353.
33 J.-B. Hövener, E. Y. Chekmenev, K. C. Harris, W. H. Perman, T. T. Tran, B. D. Ross and P. Bhattacharya, *Magn. Reson. Mater. Phys., Biol. Med.*, 2009, **22**, 123–134.
34 K. V. Kovtunov, V. V. Zhivonitko, I. V. Skovpin, D. A. Barskiy and I. V. Koptyug, *Top. Curr. Chem.*, 2013, **338**, 123–180.
35 A. M. Balu, S. B. Duckett and R. Luque, *Dalton Trans.*, 2009, 5074–5076.
36 I. V. Koptyug, V. V. Zhivonitko and K. V. Kovtunov, *ChemPhysChem*, 2010, **11**, 3086–3088.
37 V. V. Zhivonitko, K. V. Kovtunov, I. V. Skovpin, D. A. Barskiy, O. G. Salnikov and I. V. Koptyug, in *Understanding Organometallic Reaction Mechanisms and Catalysis: Computational and Experimental Tools*, ed. V. P. Ananikov, Wiley-VCH Verlag GmbG & Co. KGaA, Weinheim, 2014, vol. 7, pp. 145–185.

Published on 15 July 2016. Downloaded by Vanderbilt University Library on 22/08/2016 23:41:46.

38 R. Zhou, E. W. Zhao, W. Cheng, L. M. Neal, H. Zheng, R. E. Quiñones, H. E. Hagelin-Weaver and C. R. Bowers, *J. Am. Chem. Soc.*, 2015, **137**, 1938–1946.
39 M. Irfan, N. Eshuis, P. Spannring, M. Tessari, M. C. Feiters and F. P. J. T. Rutjes, *J. Phys. Chem. C*, 2014, **118**, 13313–13319.
40 S. Glöggler, A. M. Grunfeld, Y. N. Ertas, J. McCormick, S. Wagner, P. P. M. Schleker and L.-S. Bouchard, *Angew. Chem., Int. Ed.*, 2015, **54**, 2452–2456.
41 O. G. Salnikov, K. V. Kovtunov and I. V. Koptyug, *Sci. Rep.*, 2015, **5**, 13930.
42 M. L. Truong, F. Shi, P. He, B. Yuan, K. N. Plunkett, A. M. Coffey, R. V. Shchepin, D. A. Barskiy, K. V. Kovtunov, I. V. Koptyug, K. W. Waddell, B. M. Goodson and E. Y. Chekmenev, *J. Phys. Chem. B*, 2014, **118**, 13882–13889.
43 V. V. Zhivonitko, I. V. Skovpin and I. V. Koptyug, *Chem. Commun.*, 2015, **51**, 2506–2509.
44 D. A. Barskiy, O. G. Salnikov, K. V. Kovtunov and I. V. Koptyug, *J. Phys. Chem. A*, 2015, **119**, 996–1006.

 This journal is © The Royal Society of Chemistry 2016

analytical chemistry

Article

pubs.acs.org/ac

Open-Source Automated Parahydrogen Hyperpolarizer for Molecular Imaging Using ^{13}C Metabolic Contrast Agents

Aaron M. Coffey,[†,‡] Roman V. Shchepin,[†,‡] Milton L. Truong,[†,‡] Ken Wilkens,[†] Wellington Pham,[†,‡,§,∥] and Eduard Y. Chekmenev*[,†,‡,§,∥,⊥]

[†]Vanderbilt University Institute of Imaging Science (VUIIS), [‡]Department of Radiology, [§]Department of Biomedical Engineering, [∥]Vanderbilt-Ingram Cancer Center (VICC), Vanderbilt University, Nashville, Tennessee 37232-2310, United States

[⊥]Russian Academy of Sciences, Leninskiy Prospekt 14, Moscow, 119991, Russia

Supporting Information

ABSTRACT: An open-source hyperpolarizer producing ^{13}C hyperpolarized contrast agents using parahydrogen induced polarization (PHIP) for biomedical and other applications is presented. This PHIP hyperpolarizer utilizes an Arduino microcontroller in conjunction with a readily modified graphical user interface written in the open-source processing software environment to completely control the PHIP hyperpolarization process including remotely triggering an NMR spectrometer for efficient production of payloads of hyperpolarized contrast agent and *in situ* quality assurance of the produced hyperpolarization. Key advantages of this hyperpolarizer include: (i) use of open-source software and hardware seamlessly allowing for replication and further improvement as well as readily customizable integration with other NMR spectrometers or MRI scanners (i.e., this is a multiplatform design), (ii) relatively low cost and robustness, and (iii) *in situ* detection capability and complete automation. The device performance is demonstrated by production of a dose (∼2−3 mL) of hyperpolarized ^{13}C-succinate with $\%P_{13C} \sim 28\%$ and 30 mM concentration and ^{13}C-phospholactate at $\%P_{13C} \sim 15\%$ and 25 mM concentration in aqueous medium. These contrast agents are used for ultrafast molecular imaging and spectroscopy at 4.7 and 0.0475 T. In particular, the conversion of hyperpolarized ^{13}C-phospholactate to ^{13}C-lactate *in vivo* is used here to demonstrate the feasibility of ultrafast multislice ^{13}C MRI after tail vein injection of hyperpolarized ^{13}C-phospholactate in mice.

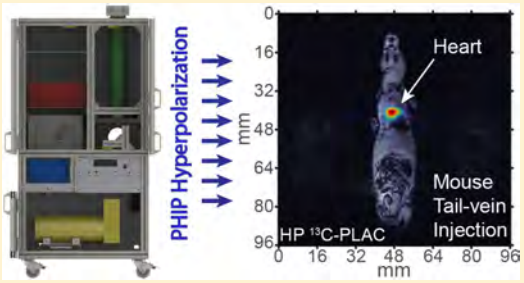

Nuclear spin polarization (P) can be increased by orders of magnitude compared to the equilibrium thermal polarization level induced by a magnetic field through a process denoted as hyperpolarization.[1,2] While the hyperpolarized (HP) state is temporary in nature with exponential decay time constants on the order of seconds to tens of minutes,[3,4] HP biomolecules have been successfully used as metabolic contrast agents.[5,6] Once injected in living organisms at sufficient quantity and high polarization, these HP contrast agents (HCA) can serve as quantitative imaging biomarkers reporting on abnormal metabolism in cancer, heart diseases, and other diseases.[7−10]

Several hyperpolarization techniques exist, but only dissolution dynamic nuclear polarization (d-DNP)[11] and parahydrogen induced polarization (PHIP)[12−14] methods have been shown to be useful to date for producing liquid-state HCAs which have shown promise *in vivo*.[7,15] D-DNP is the most widely used hyperpolarization technique, where a source of unpaired electrons is introduced to a biomolecule such as pyruvic acid (commonly by mixing with a free radical), and the HP state of nuclei is created by high-power microwave irradiation of electrons at low temperature and high magnetic field; i.e., high Boltzmann polarization of unpaired electrons is transferred to $^{13}C_1$ carbon of pyruvic acid under microwave irradiation.[11] This process is highly efficient, and up to 70% ^{13}C polarization levels can be achieved in as little as 20 min.[16] The d-DNP technique has been applied to a broad range of molecules.[7,8,17] The widespread accessibility of d-DNP beyond custom-built research platforms was significantly enhanced by the introduction of commercial hyperpolarization equipment suitable for preclinical trials of this technology in small rodents[6,18−21] and, later, the introduction of a sterile-path d-DNP hyperpolarizer intended for clinical use.[22] These technical developments for d-DNP ultimately enabled the first clinical trial in 2013,[23] a remarkable achievement only 10 years after the first proof-of-principle study.[11,24]

Despite these advances, however, d-DNP technology has yet to address two major challenges: (i) the high cost of the device producing hyperpolarized nuclear spin states (also denoted the "*hyperpolarizer*") and, more importantly, (ii) the relatively slow speed of the hyperpolarization process, varying from 0.3 to 2 h dependent on the HCA choice.[16,25]

PHIP provides an alternative to d-DNP hyperpolarization, and it is free from the above limitations. This technique relies

Received: May 31, 2016
Accepted: July 20, 2016
Published: August 1, 2016

ACS Publications © 2016 American Chemical Society

DOI: 10.1021/acs.analchem.6b02130
Anal. Chem. 2016, 88, 8279−8288

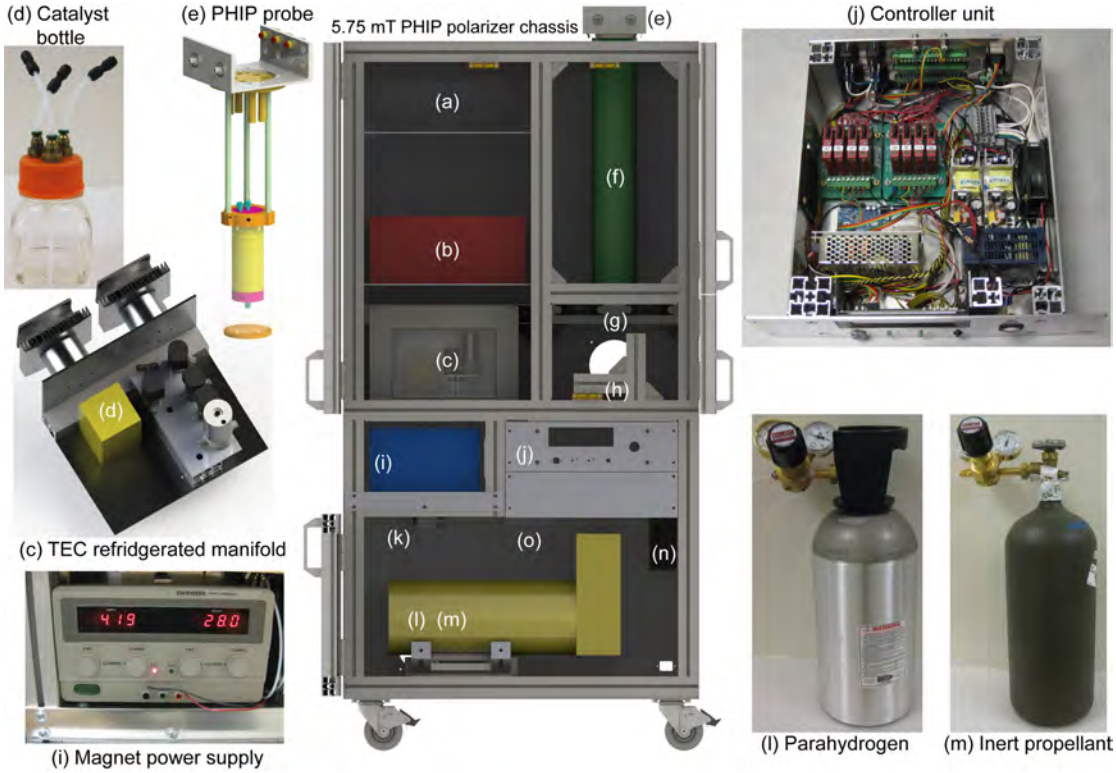

Figure 1. Schematic of the PHIP hyperpolarizer. The system consists of the following key elements: (a) a device frame, (b) NMR spectrometer and RF amplifier(s), (c) thermoelectric cooled (TEC) manifold, (d) catalyst/precursor containing bottle, (e) PHIP probe, (f) B_0 magnet, (g) B_0 magnet/RF probe cooling fans, (h) interface to HyperBridge, (i) B_0 magnet power supply unit (PSU), (j) controller unit, (k) solenoid valves, (l) *para*-H_2 tank, (m) propellant inert gas tank, (n) power distribution unit, and (o) step-down pressure regulator. The overall hyperpolarizer dimensions are ~68 in. (height) by ~21 in. (depth) by 33 in. (width). See additional details in the text and Supporting Information.

on the high-speed, pairwise addition of parahydrogen (*para*-H_2) by a catalyst across an unsaturated carbon−carbon bond (C═C or C≡C)[12−14] followed by polarization transfer from nascent protons to longer-lived (i.e., with greater T_1 time constant) ^{13}C nucleus via the *J*-couplings.[5,26−29] As a result of this rapid catalysis, HCA can be produced in seconds.[26−29] The requirement of a ^{13}C labeled site being adjacent to an unsaturated carbon−carbon bond with a sufficiently strong *J*-coupling is the main drawback of the PHIP hyperpolarization method, which has significantly slowed down the progress of implementing this hyperpolarization technique for metabolic imaging after its initial demonstration for ^{13}C hyperpolarization of 2-hydroxyethyl propionate (HEP), useful for angiographic applications,[27,28,30] although at least three other HP ^{13}C biomolecules have been recently developed for PHIP hyperpolarization with sufficient payloads of net magnetization suitable for biomedical applications: succinate[31] for cancer imaging,[32] tetrafluoropropyl propionate[33,34] for atheroma imaging,[35] and phospholactate[36−38] for lactate imaging probing elevated glycolysis in cancer similarly to HP pyruvate by DNP. As a result, commercial PHIP hyperpolarizers (beyond prototype devices[30] produced by Amersham Biosciences, Healthcare company) have never emerged, which in turn further inhibited the adoption of PHIP for biomedical purposes.

However, a recent (ca. 2015) introduction of PHIP using side arm hydrogenation (PHIP-SAH)[29,39] significantly expanded the reach of amenable biologically relevant molecules for PHIP. Importantly, hyperpolarization of acetate and pyruvate is now feasible with PHIP-SAH, and therefore, PHIP can potentially complement d-DNP. Moreover, we have recently demonstrated an efficient and robust synthesis of biomolecular precursors for PHIP-SAH hyperpolarization of ^{13}C-acetate and beyond.[40] Although the demonstrated P_{13C} of ~2% was relatively low by PHIP-SAH, Reineri and co-workers noted that further %P_{13C} improvement to ~25% would require an efficient PHIP hyperpolarizer device capable of fast *para*-H_2 pairwise addition and efficient polarization transfer from protons to ^{13}C nuclei.[39]

A few examples of PHIP hyperpolarizers and platforms have been demonstrated over the years with mixed success. Early reports described the first partially automated PHIP hyperpolarizer, based on a LabView platform, but its performance was susceptible to external magnetic field fluctuations, and it lacked *in situ* detection capability.[41,42] The *in situ* detection capability was later demonstrated in an automated 0.0475 T PHIP hyperpolarizer, where control codes and timing delays embedded into the NMR spectrometer pulse sequence provided a convenient means of controlling and sequencing the radio frequency (RF) polarization transfer pulse sequence with gas manifold events related to handling of liquids and gases: producing an aliquot of precursor molecule, injecting it with *para*-H_2 into a chemical reactor during ^{1}H RF decoupling, applying the RF pulse sequence, liquid ejection, etc.[43,44] Other recently reported designs of automated PHIP hyperpolarizers were also based on custom LabView platforms and lacked the *in situ* detection capability.[45,46] This capability is essential for quality assurance (QA) of the HCA prior to injection *in vivo* as well as for optimization of the hyperpolarizer performance. For example, %P_{13C} of only 1% was achieved by a design (lacking *in*

DOI: 10.1021/acs.analchem.6b02130
Anal. Chem. 2016, 88, 8279−8288

situ detection capability) presented by Wagner and co-workers.[45] It should also be noted that LabView-based PHIP hyperpolarizers utilize custom (and typically proprietary) software, which is very difficult for sharing among those wanting to replicate or build more advanced variants of PHIP hyperpolarizers.

While *in situ* detection capability certainly advanced the field of PHIP hyperpolarizers, the original demonstration was based on a relatively expensive Halbach array permanent magnet,[43] and more importantly, the software controlling auxiliary components (e.g., solenoid valves) were tied into the software of the NMR spectrometer (i.e., preventing seamless multiplatform sharing and adaptation). Furthermore, the spectrometer-based design has a limited potential for integration of more complex sensors for process control including pressure, temperature, etc. Such capability has proven essential for feedback controls improving hyperpolarizer performance and safety interlocks as demonstrated in automated ^{129}Xe hyperpolarizers.[47,48]

Building on experience constructing clinical-scale ^{129}Xe spin-exchange optical pumping (SEOP) hyperpolarizers,[47−51] here we present an open-source automated PHIP hyperpolarizer design with significant advantages compared to previous PHIP hyperpolarizers. The "brain" of the hyperpolarizer is an open-source Arduino microcontroller (~$30 USD), which provides complete control of the device and permits integration with any NMR spectrometer capable of applying a PHIP RF polarization transfer sequence. All details of the design are provided in the main text and the Supporting Information, including all drawings and part sources sufficient to replicate and customize this design. The provided open-source PHIP hyperpolarizer software (Arduino microcontroller code and a graphical user interface based on free and open-source Processing software) readily enables future extension of the capabilities of the presented polarizer design: e.g., integration of sensors, safety interlocks, etc.[47,48] The device has a relatively low cost and produces payloads of HCA sufficient for preclinical studies in rodents. Having utilized this PHIP hyperpolarizer in conjunction with a HyperBridge (a magnetized HP tracer transfer pathway) previously used to show the potential for high-resolution molecular imaging studies,[52] here we demonstrate the efficacy of the presented hyperpolarizer with an example of *in vivo* ^{13}C spectroscopy of HP 1-^{13}C-succinate and pioneering *in vivo* imaging and spectroscopy of a previously reported HCA/1-^{13}C-phospholactate.[36,38]

■ EXPERIMENTAL METHODS

Overall Design of PHIP Hyperpolarizer. The design of the PHIP hyperpolarizer is shown, and a listing of all the major components is provided in Figure 1; the graphical user interface (GUI) software windows are shown in Figure 2. Figure S1 and Tables S1 and S2 provide a detailed system diagram and list the part numbers and source information for all commercially available components and technical drawings of the custom-made components of the PHIP hyperpolarizer, and further, the Supporting Information zip file also includes the GUI and PHIP microcontroller programming code.

Device Frame. The device frame was designed using CAD software (see Supporting Information for further details in addition to Figure 1), and the frame is made available as a part number from MiniTec, Victor, NY (P/N MT101315-1). The PHIP controller unit (i.e., for the electronics) enclosure should be ordered separately as P/N MT101315-2. The frame (~50 × 82 × 163 cm) incorporates all components excluding the RF amplifiers situated on top of or adjacent to the main frame.

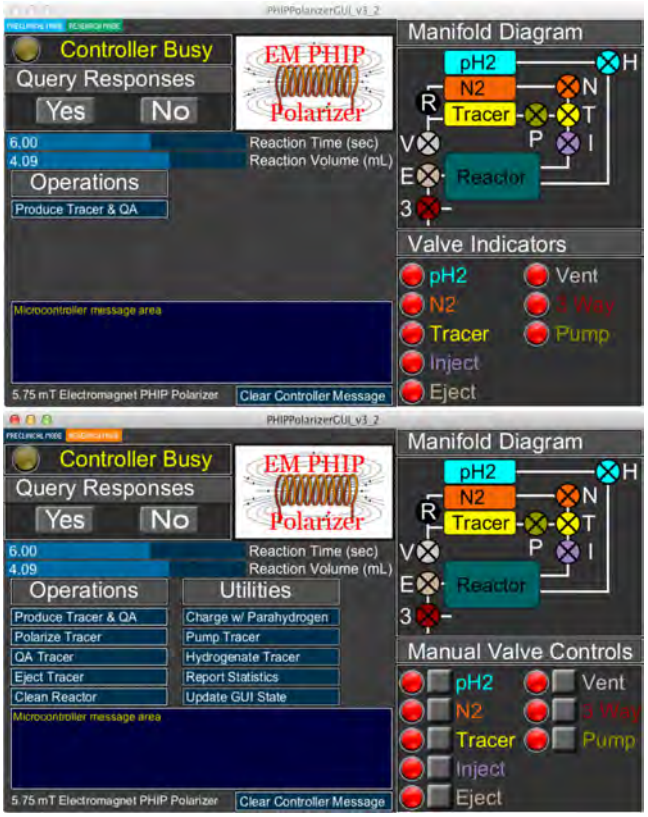

Figure 2. Screenshots of the Graphical User Interface (GUI) software showing two different modes of PHIP hyperpolarizer operation: (top) a preclinical mode where device operation is simplified to "single-button" operation; (bottom) research mode gaining access to a series of automated protocols and manual control of manifold components.

Magnet and RF Coils. The magnet coil (Figure 1) utilizes a solenoid design (Figure S2) and generates a B_0 field of ~5.75 mT using ~120 W of power, which allows for convenient heating of the reactor and the sample injection loop. The temperature (40−75 °C range) is controlled by the main fans of the chassis. Two tuned (and matched to 50 Ohm) RF Helmholtz saddle coils (Supporting Information) with their alternating B_1 fields geometrically orthogonal to each other and also orthogonal to the static B_0 field of the solenoid magnet surround the reactor. These RF coils provide very short RF pulses (≤0.5 ms) at low power (≤2.5 W) and good B_1 homogeneity (Figure S3).

High-Pressure Reactor. The high-pressure reactor of the PHIP hyperpolarizer (shown in detail in Figure 3c) is housed inside the RF coils, which cover its ~56 mL volume completely. The reactor (Supporting Information) is made of thick-wall polysulfone material and allows operation at up to 90 °C and up to ~21 atm pressure.

NMR Spectrometer and RF Amplifier and RF Probe. A dual channel Kea-2 NMR spectrometer (Magritek, Wellington, New Zealand) and custom-built Tomco RF amplifier (P/N BT00250-AlphaS-Dual, Tomco Technologies, Stepney, Australia) were utilized.

Preparation of Solutions Containing Catalyst and PHIP Precursors. *HP 1-^{13}C-Succinate-d_2 (SUX).* Stock solution (30 mM, pH = 10.3 measured by a pH meter) of 1-^{13}C-fumaric acid-d_2 acid (Cambridge Isotopes, CDLM-6062-

DOI: 10.1021/acs.analchem.6b02130
Anal. Chem. 2016, 88, 8279−8288

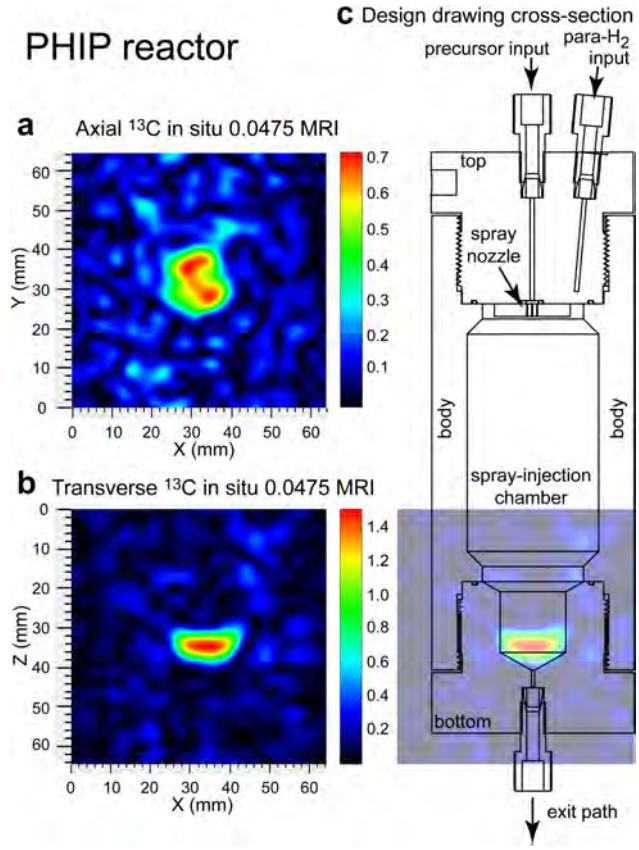

Figure 3. *In operando* 2D ^{13}C MRI postproduction in the PHIP reactor. Hyperpolarized ^{13}C 2D MRI (projection imaging of HP HEP) of the PHIP reactor was conducted at 0.0475 T[43,44] in (a) an axial projection (top-to-bottom view) and in (b) a transverse projection (side view) and (c) a cross-sectional overlay of the PHIP reactor onto the ^{13}C hyperpolarized image shown in (b). Further reactor design details are given in the main text and the Supporting Information. The presented MRI images were acquired with 2 × 2 mm^2 spatial resolution and a 64 × 64 mm^2 field of view and were bilinearly interpolated to higher resolution in order to enhance the appearance.

PK, 1-^{13}C 99%, 2,3-D_2 98%, 3.00 mmol, 0.357 g) and trisodium phosphate 12-hydrate, $Na_3PO_4 \times 12\ H_2O$ (3.00 mmol, 1.14 g) were dissolved in deuterium oxide, D_2O (Sigma, 99.8% D, 756822, 100 mL), and pH was adjusted by a diluted sodium deuteroxide (NaOD) solution made of commercially available NaOD (Sigma, 164488, 30 wt % in D_2O, 99 atom % D). The resulting solution was placed in a Buchi evaporation flask (1 L) and was degassed using a rotational evaporator (model R-215 equipped with V-710 pump, Buchi, New Castle, DE) fitted with an argon gas (high purity Argon) input by repeating twice the following sequence: (a) the pressure was slowly (to avoid boiling over) decreased from 70 to 15 mbar over approximately 5 min; (b) the pressure was adjusted back to ambient level by filling the content of the 1 L flask with Argon gas (1 bar). The phosphorus ligand, disodium salt of 1,4-bis[(phenyl-3-propanesulfonate)phosphine]butane (717347, Sigma-Aldrich-Isotec, 0.360 g, 0.64 mmol) was added, and the procedure followed with an additional degassing described above. Finally, rhodium(I) catalyst, bis(norbornadiene) rhodium(I) tetrafluoroborate (0.200 g, 0.54 mmol, 45-0230, CAS 36620-11-8, Strem Chemicals, MA) was dissolved in ∼5 mL of acetone and was added dropwise to the phosphine ligand solution to limit undesirable rhodium precipitation. The described above degassing procedure was repeated one more time to eliminate acetone.

HP 1-^{13}C-Phospholactate-d_2 (PLAC). The unsaturated precursor, monopotassium salt of 1-^{13}C-phosphoenol-pyruvate-d_2 (1-^{13}C-PEP-d_2 or PEP), was produced by the protocol described in ref 38. The batch used in this study contained ∼15 mol % of its reduced form 1-^{13}C-phospholactate-d_2 (PLAC). While the presence of PLAC in the starting material does not influence the ultimate chemical outcome of hyperpolarization, its presence was accounted for in polarization level calculations. Therefore, potassium salt of 1-^{13}C-phosphoenol-pyruvate-d_2, 1-^{13}C-PEP-d_2 (85% with 15% of PLAC, 2.50 mmol, 0.628 g), and trisodium phosphate 12-hydrate, $Na_3PO_4 \times 12\ H_2O$ (3.00 mmol, 1.14 g), were dissolved in deuterium oxide, D_2O (Sigma, 99.8% D, 756822, 100 mL), and pH was adjusted to ∼10.3 (monitored by a pH meter) by diluted sodium deuteroxide (NaOD) solution made from commercially available NaOD (Sigma, 164488, 30 wt % in D_2O, 99 atom % D). The resulting solution was filtered and placed in a Buchi evaporation flask (1 L), and it was degassed using the rotational evaporator fitted with an argon gas (high purity Argon) input by repeating twice the following sequence: (a) the pressure was slowly (to avoid boiling over) decreased from 70 to 15 mbar over approximately 5 min; (b) pressure was adjusted back to the ambient level by opening the Argon valve. The phosphorus ligand, disodium salt of 1,4-bis[(phenyl-3-propanesulfonate)phosphine]butane (717347, Sigma-Aldrich-Isotec, 0.720 g, 1.28 mmol) was added, and it was followed with an additional degassing step as described above. Finally, rhodium(I) catalyst, bis-(norbornadiene) rhodium(I) tetrafluoroborate (0.400 g, 1.04 mmol, 45-0230, CAS 36620-11-8, Strem Chemicals, MA) dissolved in ∼5 mL of acetone, was added dropwise to the phosphine ligand solution to limit undesirable rhodium precipitation. The above described degassing procedure was repeated one more time to eliminate acetone.

The hydrogenation reactions inside the PHIP hyperpolarizer were deemed to reach ∼100% yield as tested by high-resolution NMR assays of reaction mixtures.[38] Please note that for the case of preparations of aqueous solutions, deuterium oxide was replaced by HPLC grade water (Fisher Scientific) and sodium deuteroxide was replaced by regular sodium hydroxide.

PHIP Hyperpolarizer Operation. The PHIP hyperpolarizer is operated via Graphical User Interface (GUI), Figure 2. The primary automated HCA production routine performs the following steps: (i) charging the heated reactor chamber with ∼6 atm *para*-H_2 gas (∼12 s), (ii) loading the solution containing catalyst and PHIP precursor into the heated injection loop (∼2 s), (iii) triggering the NMR spectrometer (<0.1 s), (iv) injecting the warmed solution from the injection loop and spraying it into atmosphere of hot *para*-H_2 gas using the back-pressure (∼17 atm) of propellant gas (e.g., ultrahigh purity N_2 or Argon) under conditions of ^{1}H decoupling provided by the RF pulse sequence of the triggered NMR spectrometer (3−12 s), (v) polarization transfer using a RF pulse sequence developed by Goldman and Johannesson[26] (∼0.3 s), and (vi) *in situ* ^{13}C polarimetry of the produced HCA to determine its $\%P_{13C}$ using a small-angle RF pulse (∼0.5 s). The entire fully automated polarization procedure requires less than 1 min.

The produced HCA is located at the bottom of the chemical reactor by the end of the injection step (as seen in the *in situ* 2D ^{13}C MRI images (Figure 3) recorded using the same reactor in combination with a previously demonstrated PHIP setup at

DOI: 10.1021/acs.analchem.6b02130
Anal. Chem. 2016, 88, 8279−8288

47.5 mT[44]) and then is conveniently ejected by opening the eject valve, and aqueous HCA can be transferred to a container (e.g., syringe) for its further use. While HP HEP is relatively immune to exposure to ambient low magnetic fields, HP SUX and PLAC (Figure 4) can depolarize rapidly, and therefore, the

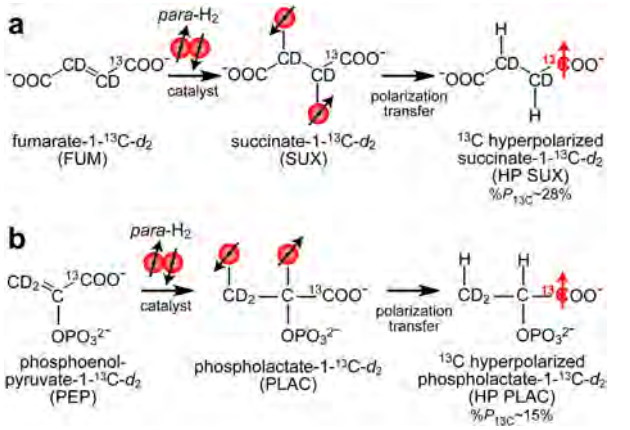

Figure 4. Hyperpolarization of 1-^{13}C-succinate-d_2 (SUX) (a) and 1-^{13}C-phospholactate-d_2 (PLAC) (b) using parahydrogen induced polarization (PHIP).[12,13] 1-^{13}C-fumarate-d_2 (FUM) and 1-^{13}C-phosphoenolpyruvate-d_2 (PEP) molecular precursors undergo catalytic pairwise addition of *para*-H_2 in aqueous medium during continuous-wave (CW) ^{1}H decoupling to yield, respectively, ^{1}H HP products corresponding to the PASADENA regime.[14] The ^{1}H polarization of these PASADENA-enhanced protons is then transferred to ^{13}C nucleus using the 3-spin Goldman polarization transfer sequence[26] using previously described schemes[31,38,55] and known spin−spin couplings.[36,55]

transfer path for these molecules was protected by a polarization-preserving magnetized path[53] denoted a Hyper-Bridge.[52] Additional routines (HCA ejection and hyperpolarizer cleaning) require less than 2 min resulting in a PHIP cycle of less than 3 min.

These additional automated routines were developed for hyperpolarizer cleaning using purging with propellant gas or for performing other basic operations in an automated fashion (Figure 2). Typically, more than 90% *para*-H_2 was used for the experiments described with initially produced ∼98% *para*-state purity using a previously described *para*-H_2 generator (we note that *para*-H_2 fraction decayed from 98% during storage in a pressurized aluminum cylinder after the initial production step).[54]

■ RESULTS AND DISCUSSION

^{13}C PHIP of SUX and PLAC. Relatively high levels of ^{13}C polarization were achieved for both HP SUX and HP PLAC: 28% ± 5% and 15% ± 3%,[38] respectively (Figure 5). The HP SUX level is approximately a factor of 1.6 greater than the highest polarization level previously reported using a PHIP hyperpolarizer,[55] despite an approximately 8 times greater concentration (30 mM vs 3.5 mM).[55] This apparent gain in %P_{13C} can be largely attributed to the *in situ* polarimetry (i.e., detection inside the hyperpolarizer immediately after production) compared to the previous hyperpolarizer design, where ^{13}C polarimetry was carried out after transfer of the material (a process taking ∼10−20 s) from the hyperpolarizer to a high-field NMR detector.[41,55] We note that additional optimization of operating parameters (catalyst/PHIP precursor solution

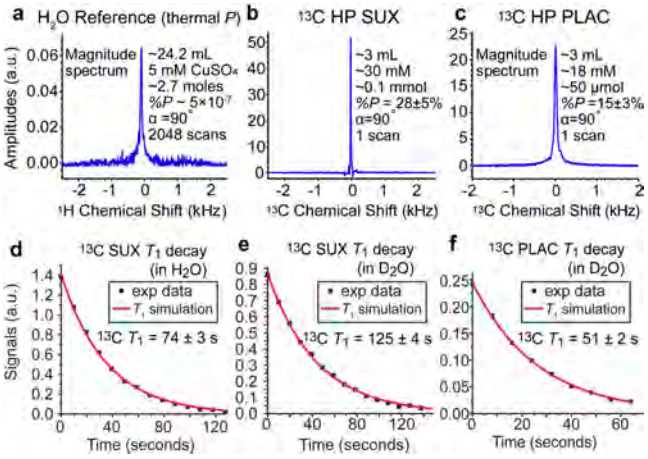

Figure 5. ^{13}C and ^{1}H NMR spectroscopy *in situ* of PHIP hyperpolarizer at 62 kHz resonant frequency. (a) ^{1}H signal reference spectrum recorded using a sample of thermally polarized $CuSO_4$ (∼5 mM) doped water, (b) ^{13}C spectrum of HP SUX, (c) ^{13}C spectrum of HP PLAC, (d) ^{13}C T_1 decay of HP SUX in H_2O measured using 30° excitation radio frequency (RF) pulses, (e) ^{13}C T_1 decay of HP SUX in D_2O measured using 30° excitation radio frequency (RF) pulses, and (f) ^{13}C T_1 decay of HP PLAC in D_2O measured using 30° excitation radio frequency (RF) pulses.

preheating delay and reaction time) was required to achieve the best hyperpolarization yields, Figure S7.

HP PLAC polarization was ∼1.9 times lower than that of HP SUX, which can likely be explained by the effective presence of a four-spin system: two nascent *para*-H_2 protons with ^{13}C and ^{31}P coupled to them in PLAC vs the three-spin system in SUX (two nascent *para*-H_2 protons with coupled ^{13}C). This is supported by two other observations. First, while performance of the hyper-SHIELDED RF pulse sequence (data not shown) was nearly identical to the performance of the Goldman pulse sequence for HP SUX,[26] the hyper-SHIELDED sequence[56] results yielded an order of magnitude lower %P_{13C} than the Goldman sequence[26] (data not shown) for HP PLAC. This is not surprising because the hyper-SHIELDED sequence is specifically geared for robust performance in three-spin systems.[56] Second, a theoretical study by Hövener and co-workers[57] provided 2D plots of %P_{13C} dependence on the timings of the Goldman polarization transfer sequence (using a three spin formalism),[57] which we successfully experimentally reproduced here (Figure S3) for HP SUX. It should be noted that these 2D plots exhibit well-defined local and global maxima and minima of %P_{13C}. The corresponding 2D HP PLAC plots (Figure S3) yielded a pattern without such characteristics indicating that a three-spin formalism is indeed too simplistic. Therefore, %P_{13C} in PLAC can be potentially remedied by more advanced RF pulse sequences potentially including ^{31}P irradiation.

PHIP Hyperpolarizer Compatibility and Potential Improvements. The presented hyperpolarizer is compatible with other HCAs[58] produced using RF-based polarization approaches including those already utilized *in vivo*: diethyl-succinate-^{13}C,[32] tetrafluoropropyl propionate,[33,34] and HEP.[30,43] Other single- or dual-channel RF pulse sequences could be utilized readily including those described earlier.[26,27,56,59−61] Moreover, this hyperpolarizer can be tailored to accommodate PHIP using field-cycling-based polarization transfer,[5,29] thereby enabling PHIP of other compounds[62−64]

DOI: 10.1021/acs.analchem.6b02130
Anal. Chem. 2016, 88, 8279−8288

most notably including acetate-^{13}C[29,40] and pyruvate-^{13}C[29,39] as well as the production of compounds with long-lived spin states (LLSS[65]) prepared by pairwise addition of *para*-H_2.[66−68]

While the hyperpolarizer demonstrated excellent performance from the perspective of automation and robust performance, certain improvements of the current design can be envisioned. In particular, B_0 homogeneity can be improved by further magnetic field shimming using additional compensating turns at the ends of the solenoid magnet.[69] Moreover, significantly less powerful, smaller, and less expensive RF amplifiers (e.g., ∼5 W[70]) and NMR spectrometers (e.g., ref 71) can be employed, because the presented hyperpolarizer design requires ≤2.5 W of RF power per channel. Additional gains in efficiency of RF coils' performance can be potentially made by increasing the bore size of the magnet (to reduce RF coil coupling to the magnet) and maximize the use of the wire conductor.[72]

We also note that, while the relatively low magnetic field of the PHIP polarizer (∼5.75 mT) does not offer sufficient chemical shift resolution to differentiate HP metabolites and contrast agents (due to diminished ^{13}C chemical shift dispersion), this is not necessarily a drawback, because high-field NMR detection can be employed by the PHIP hyperpolarizer contrast agents to delineate between metabolite signatures and injected HP contrast agent *in vivo*, e.g., HP ethyl succinate and its metabolites reported earlier by Bhattacharya and co-workers.[32]

^{13}C Spectroscopy and Imaging in Small Rodents. The efficient production of HP SUX and HP PLAC using the presented hyperpolarizer enables one to probe *in vivo* mechanisms and pathways using molecular imaging and spectroscopy. The feasibility of *in vivo* ^{13}C detection was tested for HP SUX at a low magnetic field of 0.0475 T. Figure 6a shows ^{13}C T_1 decay of an approximately ∼2 mL bolus of HP SUX (∼30 mM concentration in D_2O in a plastic syringe) monitored by 15° excitation pulses using a volume RF probe designed for small animal imaging.[72]

In a separate experiment, an anesthetized young rat (∼200 g) placed inside a volume RF coil[44] was injected with ∼1 mL of HP SUX solution (∼30 mM in H_2O) into the tail vein. The effective imaging region of the magnet (∼8 cm long) covered the torso of the rat. ^{13}C spectra were recorded every 2 s using a ∼ 15° excitation RF pulse. The nonlocalized ^{13}C *in vivo* spectroscopy detected an initial rise of the ^{13}C HP signal followed by its decay due to T_1 decay, signal depletion by RF pulses, and metabolic processes. These results demonstrated the feasibility of *in vivo* ^{13}C HP detection using ultra low-field magnetic resonance.

Additional *in vivo* experiments employed HP PLAC in a nude mouse animal model using a 4.7 T MRI scanner. In the first set of experiments, nonlocalized ^{13}C NMR spectroscopy was performed after injection of ∼0.2 mL of HP PLAC (∼25 mM) via the tail vein (see the Supporting Information for details). The volume RF coil covered the entire mouse body. ^{13}C NMR spectra were acquired every 3 s using ∼15° excitation RF pulses. ^{13}C signal initially increased, because more HP PLAC reached the body of the animal during injection, and it was followed by the decay of HP signal due to T_1 decay, signal depletion by RF pulses, and metabolic processes (Figure 6d).

Only one NMR resonance was detected in Figure 6d. Note the *in vivo* line width at half height (LWHH) of ∼120 Hz or ∼2.5 ppm (Figure 6d, inset), which makes PLAC and lactate (LAC) spectroscopically indistinguishable, because of their

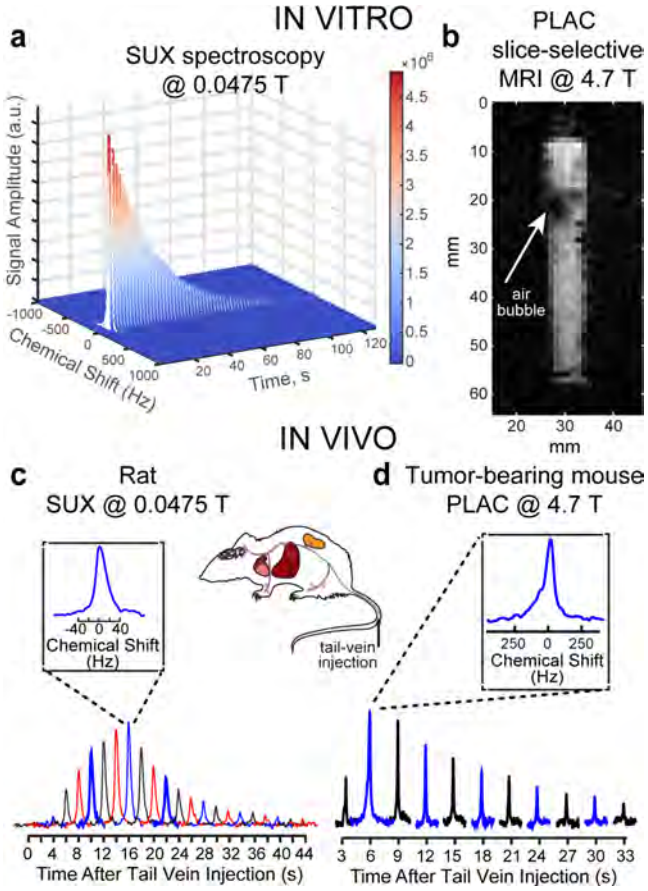

Figure 6. NMR and MRI detection of HP PLAC and SUX *in vivo* and *in vitro*. (a) ^{13}C T_1 decay of HP SUX (30 mM, D_2O, T_1 ∼ 125 s) monitored by small-angle RF pulses (α = 15°) at 0.0475 T, (b) selected 2D slice of ^{13}C gradient echo (GRE) image acquired at 4.7 T (raw 2D data shown, image of a 5 mL syringe partially filled with ∼1.5 mL of HP PLAC in D_2O was acquired using field of view (FOV) of 64 × 64 mm^2, 1 × 1 mm^2 pixel size (spatial resolution) and 3 mm slice thickness (note the air bubbles creating dark spots in otherwise uniform approximately expected cylindrical shape)), (c) nonlocalized *in vivo* ^{13}C spectroscopy of a rat conducted after tail-vein injection of HP SUX at 0.0475 T (α = 15°), and (d) nonlocalized *in vivo* ^{13}C spectroscopy of a mouse conducted after tail-vein injection of HP PLAC at 4.7 T (α = 15°).

small chemical shift difference of ∼0.3 ppm.[73] It should be additionally noted that ^{13}C *in vivo* LWHH is ∼2.5 times smaller (∼40 Hz) than at 4.7 T, clearly demonstrating that low-field MR is far less vulnerable to susceptibility-induced magnetic field gradients (this effect is even more pronounced in the ^{13}C *in vitro* MRI image of a syringe filled with foamy solution of HP PLAC, where air bubbles create large field gradients resulting in the appearance of low-SNR black spots in the image).

Because direct spectroscopic *in vivo* differentiation between HP LAC and PLAC was challenging due to LWHH being significantly greater than the chemical shift difference between PLAC and LAC and because only one resonance was seen in Figure 6d, the final *in vivo* experiments proceeded with performing ^{13}C slice-selective gradient echo (GRE) imaging after PLAC injection in the tail vein of a nude mouse, Figure 7 (see the Supporting Information for details). A series of 6 mm-thick 2D slices was recorded every 4 s with 3 × 3 mm^2 in-plane resolution and FOV of 96 × 96 mm^2 to probe spatial biodistribution of HP PLAC. ^{13}C HP images were later

DOI: 10.1021/acs.analchem.6b02130
Anal. Chem. 2016, 88, 8279−8288

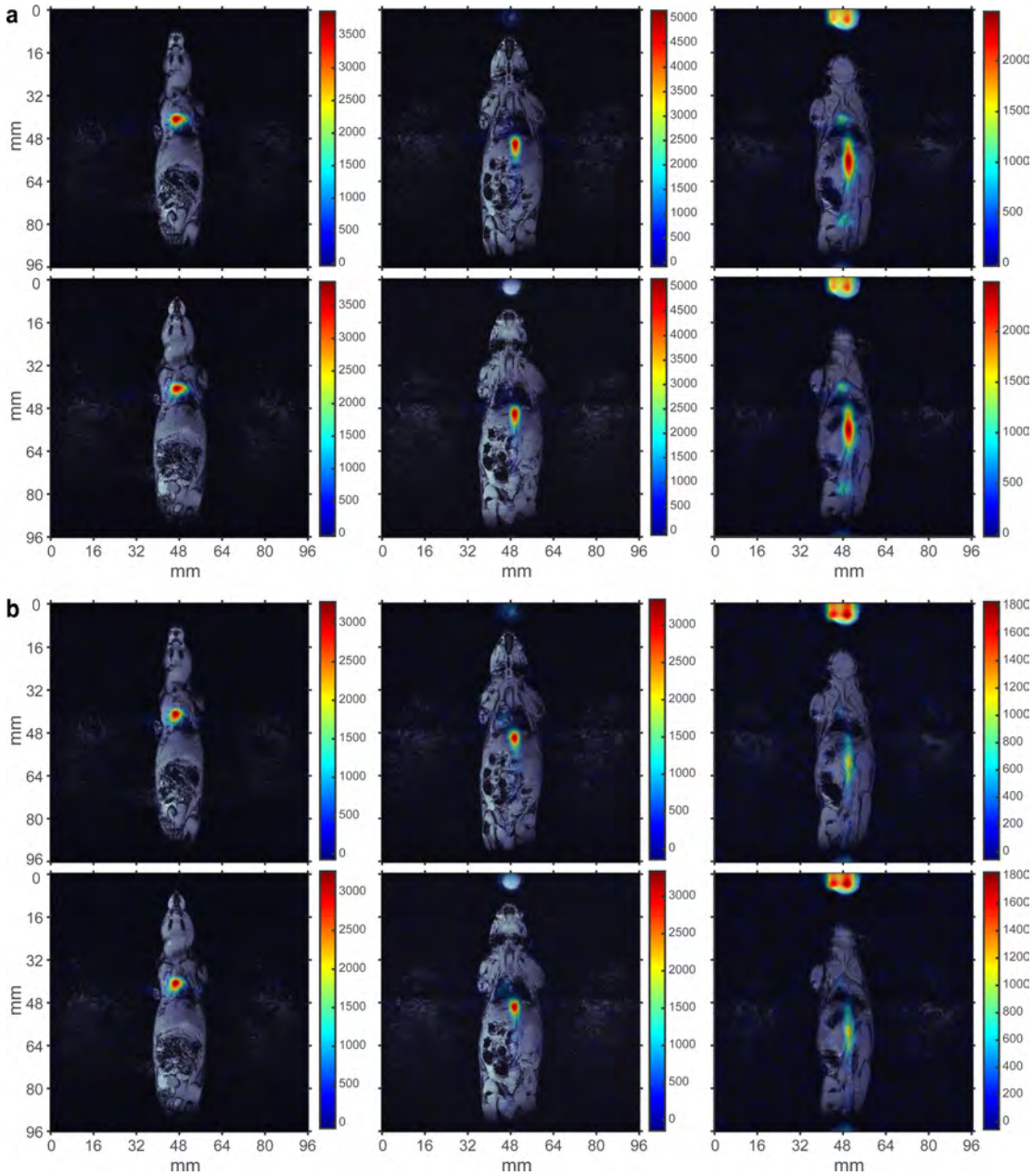

Figure 7. *In vivo* molecular imaging using HP PLAC contrast agent at 4.7 T. ^{13}C gradient echo (GRE) images (in color) are overlaid over representative anatomical ^{1}H proton images. Six coronal ^{13}C images (3 × 3 mm^2 in-plane resolution, 6 mm slice thickness, FOV = 96 × 96 mm^2) were acquired approximately 5−10 s after injection of HP PLAC via tail vein (∼0.2 mL, ∼30 mM dose) in a nude mouse (prior tumor implantation). Two representative sets of ^{13}C images (a) and (b) separated by ∼4 s are shown and overlaid over the same set of anatomical ^{1}H images.

coregistered with anatomical proton images, Figure 7. Two representative sets of images are shown in Figure 7a,b, respectively. The presence of HCA is seen in the vasculature of the animal, and additional uptake is detected in the heart and in the bladder. This result is consistent with the previous high-resolution NMR biodistribution study of non-HP PLAC,[73] which identified that PLAC undergoes dephosphorylation in blood followed by LAC uptake by the heart and other organs with no PLAC signatures found in the heart and other organs. However, the previous study[73] lacked the temporal resolution available by HP molecular imaging (Figure 7). On the basis of the *in vivo* ^{13}C images (Figure 7), we conclude that HP PLAC follows the same metabolic fate: (i) it undergoes dephosphorylation in the blood, followed by (ii) exchange with endogenous lactate[74] present in tissues and organs. Therefore, injection of HP PLAC results in HP LAC imaging, because HP LAC is produced immediately after HP PLAC injection. As a result, we note the produced HP LAC via PHIP offers a good alternative (to d-DNP HP ^{13}C pyruvate (PYR)) for metabolic imaging, which has already been proven for cardiac applications by comparing the performance of HP LAC and HP PYR metabolism *in vivo*.[75]

Serial acquisition of slice-selective ^{13}C HP PLAC images can also be used for HCA washout kinetics analysis. An example of such analysis is shown in Figure S6 based on the pixel-by-pixel analysis of the raw ^{13}C images (Figure S5) in the heart region. It demonstrates that the useful MRI data acquisition time window was ∼12 s using our HCA administration protocol. On

DOI: 10.1021/acs.analchem.6b02130
Anal. Chem. 2016, 88, 8279−8288

the basis of the preliminary feasibility results, future *in vivo* studies of cancer imaging using HP PLAC injections are certainly warranted given the upregulation of endogenous lactate in many cancers.[19,20,23,76]

CONCLUSION

A fully automated open-source low-cost PHIP hyperpolarizer is reported. Sufficient hardware details and operating software are provided for convenient device replication and potential further improvements in the context of PHIP hyperpolarization, as well as potential extensions for other hyperpolarization techniques utilizing *para*-H_2, e.g., conventional NMR signal amplification by reversible exchange (SABRE),[77,78] because the main B_0 field (~5.75 mT) of this hyperpolarizer matches the optimal static magnetic field required for coherent polarization transfer by conventional ^{1}H SABRE.[79] It should also be noted that this hyperpolarizer design can be potentially tailored for ^{15}N hyperpolarization via recently developed SABRE-SHEATH (SABRE in in SHield Enables Alignment Transfer to Heteronuclei)[80−82] in the micro-Tesla magnetic field regime, although the required equipment modifications would likely include the integration of a mu-metal zero field chamber around the main magnet, operation in micro-Tesla versus milli-Tesla regime, and hyperpolarization detection using zero-field NMR.[83] ^{15}N SABRE-SHEATH provides robust hyperpolarization levels of up to 30%[84,85] and can be used to hyperpolarize pH sensors,[86] hypoxia sensors,[84] and Schiff bases[87] potentially useful for molecular imaging applications *in vivo*. The presented PHIP hyperpolarizer enables record levels of polarization for SUX ($\%P_{13C}$ = 28% ± 5%) metabolic HCA and enabled efficient ($\%P_{13C}$ = 15 ± 3%) hyperpolarization of HP PLAC. The hyperpolarizer can produce a dose of HCA (~2−3 mL in aqueous medium) as fast as every 3 min. The use of HP SUX was demonstrated for low-field *in vivo* MR paving the way for future low-field MRI of ^{13}C HCAs. Moreover, the production of HP PLAC enabled the preliminary feasibility study of *in vivo* spectroscopy and metabolic imaging, demonstrating that HP PLAC likely results in HP LAC after the *in vivo* dephosphorylation step. The produced HP LAC undergoes *in vivo* uptake by the heart and bladder clearance consistent with previous studies. We hope the reported PHIP design can be embraced by other laboratories working at the frontiers of molecular *in vivo* imaging.

ASSOCIATED CONTENT

Supporting Information

The Supporting Information is available free of charge on the ACS Publications website at DOI: 10.1021/acs.analchem.6b02130.

CAD schematics; additional figures; detailed drawing; the lists of materials (PDF)

GUI and programming codes for the PHIP hyperpolarizer (ZIP)

AUTHOR INFORMATION

Corresponding Author

*Phone: 615-322-1329. Fax: 615-322-0734. E-mail: eduard.chekmenev@vanderbilt.edu.

Notes

The authors declare no competing financial interest.

ACKNOWLEDGMENTS

We thank Dr. Andrew Coy and Dr. John Trail (Magritek, Wellington, New Zealand) for their technical advice and guidance with low-field NMR and MRI hardware, Prof. Kevin W. Waddell for access to the *para*-H_2 generator, and Prof. John C. Gore for institutional support.[54] This work was supported by NIH 1R21EB018014, 1R21EB020323, 1F32EB021840, T32 EB001628, and R01 CA160700 (W.P.) and NSF CHE-1416268, DOD CDMRP W81XWH-12-1-0159/BC112431, and W81XWH-15-1-0271.

REFERENCES

(1) Abragam, A.; Goldman, M. *Rep. Prog. Phys.* **1978**, *41*, 395−467.
(2) Carver, T. R.; Slichter, C. P. *Phys. Rev.* **1953**, *92*, 212−213.
(3) Theis, T.; Ortiz, G. X.; Logan, A. W. J.; Claytor, K. E.; Feng, Y.; Huhn, W. P.; Blum, V.; Malcolmson, S. J.; Chekmenev, E. Y.; Wang, Q.; Warren, W. S. *Sci. Adv.* **2016**, *2*, e1501438.
(4) Nonaka, H.; Hata, R.; Doura, T.; Nishihara, T.; Kumagai, K.; Akakabe, M.; Tsuda, M.; Ichikawa, K.; Sando, S. *Nat. Commun.* **2013**, *4*, 2411.
(5) Golman, K.; Axelsson, O.; Johannesson, H.; Mansson, S.; Olofsson, C.; Petersson, J. S. *Magn. Reson. Med.* **2001**, *46*, 1−5.
(6) Golman, K.; in't Zandt, R.; Thaning, M. *Proc. Natl. Acad. Sci. U. S. A.* **2006**, *103*, 11270−11275.
(7) Kurhanewicz, J.; Vigneron, D. B.; Brindle, K.; Chekmenev, E. Y.; Comment, A.; Cunningham, C. H.; DeBerardinis, R. J.; Green, G. G.; Leach, M. O.; Rajan, S. S.; Rizi, R. R.; Ross, B. D.; Warren, W. S.; Malloy, C. R. *Neoplasia* **2011**, *13*, 81−97.
(8) Comment, A.; Merritt, M. E. *Biochemistry* **2014**, *53*, 7333−7357.
(9) Brindle, K. M. *J. Am. Chem. Soc.* **2015**, *137*, 6418−6427.
(10) Witte, C.; Schroder, L. *NMR Biomed.* **2013**, *26*, 788−802.
(11) Ardenkjaer-Larsen, J. H.; Fridlund, B.; Gram, A.; Hansson, G.; Hansson, L.; Lerche, M. H.; Servin, R.; Thaning, M.; Golman, K. *Proc. Natl. Acad. Sci. U. S. A.* **2003**, *100*, 10158−10163.
(12) Eisenschmid, T. C.; Kirss, R. U.; Deutsch, P. P.; Hommeltoft, S. I.; Eisenberg, R.; Bargon, J.; Lawler, R. G.; Balch, A. L. *J. Am. Chem. Soc.* **1987**, *109*, 8089−8091.
(13) Bowers, C. R.; Weitekamp, D. P. *Phys. Rev. Lett.* **1986**, *57*, 2645−2648.
(14) Bowers, C. R.; Weitekamp, D. P. *J. Am. Chem. Soc.* **1987**, *109*, 5541−5542.
(15) Nikolaou, P.; Goodson, B. M.; Chekmenev, E. Y. *Chem. - Eur. J.* **2015**, *21*, 3156−3166.
(16) Jannin, S.; Bornet, A.; Melzi, R.; Bodenhausen, G. *Chem. Phys. Lett.* **2012**, *549*, 99−102.
(17) Comment, A. *J. Magn. Reson.* **2016**, *264*, 39−48.
(18) Kurhanewicz, J.; Bok, R.; Nelson, S. J.; Vigneron, D. B. *J. Nucl. Med.* **2008**, *49*, 341−344.
(19) Albers, M. J.; Bok, R.; Chen, A. P.; Cunningham, C. H.; Zierhut, M. L.; Zhang, V. Y.; Kohler, S. J.; Tropp, J.; Hurd, R. E.; Yen, Y.-F.; Nelson, S. J.; Vigneron, D. B.; Kurhanewicz, J. *Cancer Res.* **2008**, *68*, 8607−8615.
(20) Day, S. E.; Kettunen, M. I.; Gallagher, F. A.; Hu, D. E.; Lerche, M.; Wolber, J.; Golman, K.; Ardenkjaer-Larsen, J. H.; Brindle, K. M. *Nat. Med.* **2007**, *13*, 1382−1387.
(21) Gallagher, F. A.; Kettunen, M. I.; Day, S. E.; Hu, D. E.; Ardenkjaer-Larsen, J. H.; in't Zandt, R.; Jensen, P. R.; Karlsson, M.; Golman, K.; Lerche, M. H.; Brindle, K. M. *Nature* **2008**, *453*, 940−U973.
(22) Ardenkjaer-Larsen, J. H.; Leach, A. M.; Clarke, N.; Urbahn, J.; Anderson, D.; Skloss, T. W. *NMR Biomed.* **2011**, *24*, 927−932.
(23) Nelson, S. J.; Kurhanewicz, J.; Vigneron, D. B.; Larson, P. E. Z.; Harzstark, A. L.; Ferrone, M.; van Criekinge, M.; Chang, J. W.; Bok, R.; Park, I.; Reed, G.; Carvajal, L.; Small, E. J.; Munster, P.; Weinberg, V. K.; Ardenkjaer-Larsen, J. H.; Chen, A. P.; Hurd, R. E.; Odegardstuen, L. I.; Robb, F. J.; Tropp, J.; Murray, J. A. *Sci. Transl. Med.* **2013**, *5*, 198ra108.

DOI: 10.1021/acs.analchem.6b02130
Anal. Chem. 2016, 88, 8279−8288

(24) Ardenkjaer-Larsen, J. H. *J. Magn. Reson.* **2016**, *264*, 3−12.
(25) Kumagai, K.; Kawashima, K.; Akakabe, M.; Tsuda, M.; Abe, T.; Tsuda, M. *Tetrahedron* **2013**, *69*, 3896−3900.
(26) Goldman, M.; Johannesson, H. *C. R. Phys.* **2005**, *6*, 575−581.
(27) Goldman, M.; Johannesson, H.; Axelsson, O.; Karlsson, M. *Magn. Reson. Imaging* **2005**, *23*, 153−157.
(28) Goldman, M.; Johannesson, H.; Axelsson, O.; Karlsson, M. *C. R. Chim.* **2006**, *9*, 357−363.
(29) Reineri, F.; Boi, T.; Aime, S. *Nat. Commun.* **2015**, *6*, 5858.
(30) Bhattacharya, P.; Harris, K.; Lin, A. P.; Mansson, M.; Norton, V. A.; Perman, W. H.; Weitekamp, D. P.; Ross, B. D. *MAGMA* **2005**, *18*, 245−256.
(31) Bhattacharya, P.; Chekmenev, E. Y.; Perman, W. H.; Harris, K. C.; Lin, A. P.; Norton, V. A.; Tan, C. T.; Ross, B. D.; Weitekamp, D. P. *J. Magn. Reson.* **2007**, *186*, 150−155.
(32) Zacharias, N. M.; Chan, H. R.; Sailasuta, N.; Ross, B. D.; Bhattacharya, P. *J. Am. Chem. Soc.* **2012**, *134*, 934−943.
(33) Chekmenev, E. Y.; Chow, S. K.; Tofan, D.; Weitekamp, D. P.; Ross, B. D.; Bhattacharya, P. *J. Phys. Chem. B* **2008**, *112*, 6285−6287.
(34) Chekmenev, E. Y.; Norton, V. A.; Weitekamp, D. P.; Bhattacharya, P. *J. Am. Chem. Soc.* **2009**, *131*, 3164−3165.
(35) Bhattacharya, P.; Chekmenev, E. Y.; Reynolds, W. F.; Wagner, S.; Zacharias, N.; Chan, H. R.; Bünger, R.; Ross, B. D. *NMR Biomed.* **2011**, *24*, 1023−1028.
(36) Shchepin, R. V.; Coffey, A. M.; Waddell, K. W.; Chekmenev, E. Y. *J. Am. Chem. Soc.* **2012**, *134*, 3957−3960.
(37) Shchepin, R. V.; Chekmenev, E. Y. *J. Labelled Compd. Radiopharm.* **2013**, *56*, 655−662.
(38) Shchepin, R. V.; Coffey, A. M.; Waddell, K. W.; Chekmenev, E. Y. *Anal. Chem.* **2014**, *86*, 5601−5605.
(39) Cavallari, E.; Carrera, C.; Boi, T.; Aime, S.; Reineri, F. *J. Phys. Chem. B* **2015**, *119*, 10035−10041.
(40) Shchepin, R. V.; Barskiy, D. A.; Coffey, A. M.; Manzanera Esteve, I. V.; Chekmenev, E. Y. *Angew. Chem., Int. Ed.* **2016**, *55*, 6071−6074.
(41) Hövener, J.-B.; Chekmenev, E. Y.; Harris, K. C.; Perman, W.; Tran, T.; Ross, B. D.; Bhattacharya, P. *MAGMA* **2009**, *22*, 123−134.
(42) Hövener, J.-B.; Chekmenev, E. Y.; Harris, K. C.; Perman, W.; Robertson, L.; Ross, B. D.; Bhattacharya, P. *MAGMA* **2009**, *22*, 111−121.
(43) Waddell, K. W.; Coffey, A. M.; Chekmenev, E. Y. *J. Am. Chem. Soc.* **2011**, *133*, 97−101.
(44) Coffey, A. M.; Shchepin, R. V.; Wilkens, K.; Waddell, K. W.; Chekmenev, E. Y. *J. Magn. Reson.* **2012**, *220*, 94−101.
(45) Agraz, J.; Grunfeld, A.; Li, D.; Cunningham, K.; Willey, C.; Pozos, R.; Wagner, S. *Rev. Sci. Instrum.* **2014**, *85*, 044705.
(46) Kadlecek, S.; Vahdat, V.; Nakayama, T.; Ng, D.; Emami, K.; Rizi, R. *NMR Biomed.* **2011**, *24*, 933−942.
(47) Nikolaou, P.; Coffey, A. M.; Walkup, L. L.; Gust, B. M.; Whiting, N.; Newton, H.; Barcus, S.; Muradyan, I.; Dabaghyan, M.; Moroz, G. D.; Rosen, M.; Patz, S.; Barlow, M. J.; Chekmenev, E. Y.; Goodson, B. M. *Proc. Natl. Acad. Sci. U. S. A.* **2013**, *110*, 14150−14155.
(48) Nikolaou, P.; Coffey, A. M.; Walkup, L. L.; Gust, B. M.; Whiting, N. R.; Newton, H.; Muradyan, I.; Dabaghyan, M.; Ranta, K.; Moroz, G.; Patz, S.; Rosen, M. S.; Barlow, M. J.; Chekmenev, E. Y.; Goodson, B. M. *Magn. Reson. Imaging* **2014**, *32*, 541−550.
(49) Nikolaou, P.; Coffey, A. M.; Barlow, M. J.; Rosen, M.; Goodson, B. M.; Chekmenev, E. Y. *Anal. Chem.* **2014**, *86*, 8206−8212.
(50) Nikolaou, P.; Coffey, A. M.; Ranta, K.; Walkup, L. L.; Gust, B.; Barlow, M. J.; Rosen, M. S.; Goodson, B. M.; Chekmenev, E. Y. *J. Phys. Chem. B* **2014**, *118*, 4809−4816.
(51) Nikolaou, P.; Coffey, A. M.; Walkup, L. L.; Gust, B.; LaPierre, C.; Koehnemann, E.; Barlow, M. J.; Rosen, M. S.; Goodson, B. M.; Chekmenev, E. Y. *J. Am. Chem. Soc.* **2014**, *136*, 1636−1642.
(52) Coffey, A. M.; Kovtunov, K. V.; Barskiy, D.; Koptyug, I. V.; Shchepin, R. V.; Waddell, K. W.; He, P.; Groome, K. A.; Best, Q. A.; Shi, F.; Goodson, B. M.; Chekmenev, E. Y. *Anal. Chem.* **2014**, *86*, 9042−9049.
(53) Vuichoud, B.; Milani, J.; Bornet, A.; Melzi, R.; Jannin, S.; Bodenhausen, G. *J. Phys. Chem. B* **2014**, *118*, 1411−1415.
(54) Feng, B.; Coffey, A. M.; Colon, R. D.; Chekmenev, E. Y.; Waddell, K. W. *J. Magn. Reson.* **2012**, *214*, 258−262.
(55) Chekmenev, E. Y.; Hovener, J.; Norton, V. A.; Harris, K.; Batchelder, L. S.; Bhattacharya, P.; Ross, B. D.; Weitekamp, D. P. *J. Am. Chem. Soc.* **2008**, *130*, 4212−4213.
(56) Cai, C.; Coffey, A. M.; Shchepin, R. V.; Chekmenev, E. Y.; Waddell, K. W. *J. Phys. Chem. B* **2013**, *117*, 1219−1224.
(57) Bär, S.; Lange, T.; Leibfritz, D.; Hennig, J.; Elverfeldt, D. v.; Hövener, J.-B. *J. Magn. Reson.* **2012**, *225*, 25−35.
(58) Roth, M.; Koch, A.; Kindervater, P.; Bargon, J.; Spiess, H. W.; Muennemann, K. *J. Magn. Reson.* **2010**, *204*, 50−55.
(59) Haake, M.; Natterer, J.; Bargon, J. *J. Am. Chem. Soc.* **1996**, *118*, 8688−8691.
(60) Kadlecek, S.; Emami, K.; Ishii, M.; Rizi, R. *J. Magn. Reson.* **2010**, *205*, 9−13.
(61) Pravdivtsev, A. N.; Yurkovskaya, A. V.; Lukzen, N. N.; Vieth, H.-M.; Ivanov, K. L. *Phys. Chem. Chem. Phys.* **2014**, *16*, 18707−18719.
(62) Reineri, F.; Viale, A.; Giovenzana, G.; Santelia, D.; Dastru, W.; Gobetto, R.; Aime, S. *J. Am. Chem. Soc.* **2008**, *130*, 15047−15053.
(63) Reineri, F.; Viale, A.; Ellena, S.; Alberti, D.; Boi, T.; Giovenzana, G. B.; Gobetto, R.; Premkumar, S. S. D.; Aime, S. *J. Am. Chem. Soc.* **2012**, *134*, 11146−11152.
(64) Trantzschel, T.; Bernarding, J.; Plaumann, M.; Lego, D.; Gutmann, T.; Ratajczyk, T.; Dillenberger, S.; Buntkowsky, G.; Bargon, J.; Bommerich, U. *Phys. Chem. Chem. Phys.* **2012**, *14*, 5601−5604.
(65) Carravetta, M.; Levitt, M. H. *J. Am. Chem. Soc.* **2004**, *126*, 6228−6229.
(66) Kovtunov, K. V.; Truong, M. L.; Barskiy, D. A.; Koptyug, I. V.; Coffey, A. M.; Waddell, K. W.; Chekmenev, E. Y. *Chem. - Eur. J.* **2014**, *20*, 14629−14632.
(67) Canet, D.; Bouguet-Bonnet, S.; Aroulanda, C.; Reineri, F. *J. Am. Chem. Soc.* **2007**, *129*, 1445−1449.
(68) Zhang, Y. N.; Soon, P. C.; Jerschow, A.; Canary, J. W. *Angew. Chem., Int. Ed.* **2014**, *53*, 3396−3399.
(69) Borowiak, R.; Schwaderlapp, N.; Huethe, F.; Lickert, T.; Fischer, E.; Bär, S.; Hennig, J.; Elverfeldt, D.; Hövener, J.-B. *MAGMA* **2013**, *26*, 491−499.
(70) Begus, S.; Jazbinsek, V.; Pirnat, J.; Trontelj, Z. *J. Magn. Reson.* **2014**, *247*, 22−30.
(71) Michal, C. A. *Meas. Sci. Technol.* **2010**, *21*, 105902.
(72) Coffey, A. M.; Truong, M. L.; Chekmenev, E. Y. *J. Magn. Reson.* **2013**, *237*, 169−174.
(73) Shchepin, R. V.; Pham, W.; Chekmenev, E. Y. *J. Labelled Compd. Radiopharm.* **2014**, *57*, 517−524.
(74) Kennedy, B. W. C.; Kettunen, M. I.; Hu, D.-E.; Brindle, K. M. *J. Am. Chem. Soc.* **2012**, *134*, 4969−4977.
(75) Mayer, D.; Yen, Y. F.; Josan, S.; Park, J. M.; Pfefferbaum, A.; Hurd, R. E.; Spielman, D. M. *NMR Biomed.* **2012**, *25*, 1119−1124.
(76) Gatenby, R. A.; Gillies, R. J. *Nat. Rev. Cancer* **2004**, *4*, 891−899.
(77) Adams, R. W.; Duckett, S. B.; Green, R. A.; Williamson, D. C.; Green, G. G. R. *J. Chem. Phys.* **2009**, *131*, 194505.
(78) Cowley, M. J.; Adams, R. W.; Atkinson, K. D.; Cockett, M. C. R.; Duckett, S. B.; Green, G. G. R.; Lohman, J. A. B.; Kerssebaum, R.; Kilgour, D.; Mewis, R. E. *J. Am. Chem. Soc.* **2011**, *133*, 6134−6137.
(79) Barskiy, D. A.; Kovtunov, K. V.; Koptyug, I. V.; He, P.; Groome, K. A.; Best, Q. A.; Shi, F.; Goodson, B. M.; Shchepin, R. V.; Truong, M. L.; Coffey, A. M.; Waddell, K. W.; Chekmenev, E. Y. *ChemPhysChem* **2014**, *15*, 4100−4107.
(80) Theis, T.; Truong, M. L.; Coffey, A. M.; Shchepin, R. V.; Waddell, K. W.; Shi, F.; Goodson, B. M.; Warren, W. S.; Chekmenev, E. Y. *J. Am. Chem. Soc.* **2015**, *137*, 1404−1407.
(81) Truong, M. L.; Theis, T.; Coffey, A. M.; Shchepin, R. V.; Waddell, K. W.; Shi, F.; Goodson, B. M.; Warren, W. S.; Chekmenev, E. Y. *J. Phys. Chem. C* **2015**, *119*, 8786−8797.
(82) Shchepin, R. V.; Truong, M. L.; Theis, T.; Coffey, A. M.; Shi, F.; Waddell, K. W.; Warren, W. S.; Goodson, B. M.; Chekmenev, E. Y. *J. Phys. Chem. Lett.* **2015**, *6*, 1961−1967.

DOI: 10.1021/acs.analchem.6b02130
Anal. Chem. 2016, 88, 8279−8288

(83) Theis, T.; Ledbetter, M. P.; Kervern, G.; Blanchard, J. W.; Ganssle, P. J.; Butler, M. C.; Shin, H. D.; Budker, D.; Pines, A. *J. Am. Chem. Soc.* **2012**, *134*, 3987−3990.
(84) Barskiy, D. A.; Shchepin, R. V.; Coffey, A. M.; Theis, T.; Warren, W. S.; Goodson, B. M.; Chekmenev, E. Y. *J. Am. Chem. Soc.* **2016**, *138*, 8080−8083.
(85) Shchepin, R. V.; Barskiy, D. A.; Mikhaylov, D. M.; Chekmenev, E. Y. *Bioconjugate Chem.* **2016**, *27*, 878−882.
(86) Shchepin, R. V.; Barskiy, D. A.; Coffey, A. M.; Theis, T.; Shi, F.; Warren, W. S.; Goodson, B. M.; Chekmenev, E. Y. *ACS Sensors* **2016**, *1*, 640−644.
(87) Logan, A. W. J.; Theis, T.; Colell, J. F. P.; Warren, W. S.; Malcolmson, S. J. *Chem. - Eur. J.* **2016**, *22*, 10777−10781.

DOI: 10.1021/acs.analchem.6b02130
Anal. Chem. 2016, 88, 8279−8288

JACS
JOURNAL OF THE AMERICAN CHEMICAL SOCIETY
Communication
pubs.acs.org/JACS

Over 20% ^{15}N Hyperpolarization in Under One Minute for Metronidazole, an Antibiotic and Hypoxia Probe

Danila A. Barskiy,[†,#] Roman V. Shchepin,[†,#] Aaron M. Coffey,[†] Thomas Theis,[‡] Warren S. Warren,[‡] Boyd M. Goodson,[§] and Eduard Y. Chekmenev*[,†,∥,⊥]

[†]Department of Radiology, Vanderbilt University Institute of Imaging Science, Vanderbilt University Medical Center, Nashville, Tennessee 37232, United States

[‡]Department of Chemistry, Duke University, Durham, North Carolina 27708, United States

[§]Department of Chemistry and Biochemistry and Materials Technology Center, Southern Illinois University, Carbondale, Illinois 62901, United States

[∥]Department of Biomedical Engineering, Vanderbilt-Ingram Cancer Center, Vanderbilt University, Nashville, Tennessee 37232, United States

[⊥]Russian Academy of Sciences, Leninskiy Prospekt 14, Moscow 119991, Russia

Supporting Information

ABSTRACT: Direct NMR hyperpolarization of naturally abundant ^{15}N sites in metronidazole is demonstrated using SABRE-SHEATH (Signal Amplification by Reversible Exchange in SHield Enables Alignment Transfer to Heteronuclei). In only a few tens of seconds, nuclear spin polarization $P_{^{15}N}$ of up to ∼24% is achieved using parahydrogen with 80% *para* fraction corresponding to $P_{^{15}N} \approx 32\%$ if ∼100% parahydrogen were employed (which would translate to a signal enhancement of ∼0.1-million-fold at 9.4 T). In addition to this demonstration on the directly binding ^{15}N site (using $J^2_{H\text{-}^{15}N}$), we also hyperpolarized more distant ^{15}N sites in metronidazole using longer-range spin−spin couplings ($J^4_{H\text{-}^{15}N}$ and $J^5_{H\text{-}^{15}N}$). Taken together, these results significantly expand the range of molecular structures and sites amenable to hyperpolarization via low-cost parahydrogen-based methods. In particular, hyperpolarized nitroimidazole and its derivatives have powerful potential applications such as direct *in vivo* imaging of mechanisms of action or hypoxia sensing.

NMR hyperpolarization techniques increase nuclear spin polarization from thermal equilibrium levels of 10^{-6}–10^{-5} by orders of magnitude—in some cases approaching 100%.[1−4] Adequately chosen nuclear spin sites can retain their hyperpolarized (HP) state for many minutes, decaying exponentially back to thermal equilibrium; when this decay is slow enough, HP substances can be used as exogenous contrast agents to probe metabolism and function *in vivo*.[2,5,6] ^{15}N sites are particularly interesting because of their greater (e.g., compared to ^{13}C) decay constants of up to 20 min.[7−10] Moreover, ^{15}N isotopic enrichment is frequently performed using relatively straightforward and efficient chemistries and therefore could be significantly more cost-effective than production of ^{13}C-enriched compounds such as 1-^{13}C-pyruvate.[11,12] Currently, the rapidly growing field of HP ^{13}C molecular contrast agents is dominated by dissolution Dynamic Nuclear Polarization (d-DNP), which typically achieves ^{13}C polarization levels well above 10%.[13] However, for hyperpolarization of ^{15}N sites, the efficiency of d-DNP has been limited to a few percent and currently requires hours of polarization time. To date, ^{15}N-choline ($P_{^{15}N} \approx 3\%$ in 2.5 h),[14] pH sensors ($P_{^{15}N} \leq 3\%$ in 2 h),[15] and a calcium sensor ($P_{^{15}N} < 2\%$)[16] have been polarized by d-DNP for potential use as injectable HP contrast agents.

Direct hyperpolarization of heteronuclei with NMR Signal Amplification By Reversible Exchange (SABRE[17]) is possible via SABRE-SHEATH (SABRE in SHield Enables Alignment Transfer to Heteronuclei).[18,19] Unlike d-DNP, SABRE-SHEATH[18,19] is scalable, provides efficient hyperpolarization in seconds, and uses very simple and inexpensive hardware.[7,20] ^{15}N SABRE-SHEATH of several biomolecules has been demonstrated (including nicotinamide,[11,18] imidazole,[21] and diazirines[7]), producing $P_{^{15}N}$ of up to 10% in ≤1 min. It is our goal to expand the range of biomedically useful compounds amenable to SABRE-SHEATH, which may enable unprecedented molecular imaging and spectroscopy experiments that would provide direct visualization of biochemical processes.

Despite the success of ^{15}N SABRE-SHEATH, so far this new approach has been limited to hyperpolarization of ^{15}N sites directly binding to the polarization-transfer catalyst. This pathway exploits short-range two-bond spin−spin couplings ($J^2_{H\text{-}^{15}N}$) for polarization transfer from parahydrogen to ^{15}N sites (Figure 1a) in a μT magnetic field (B_T).[18,19] Furthermore, sterically hindering groups (e.g., methyl groups) in the ortho-positions of six-membered N-heterocycles significantly reduce the efficiency of polarization transfer.[22] These shortcomings limit the use of ^{15}N-SABRE-SHEATH.

Here we overcome these limitations and demonstrate ^{15}N SABRE-SHEATH on metronidazole, a member of an important group of antibiotics—the nitroimidazoles. Nitroimidazoles were discovered in the 1950s as a class of antibiotics acting on a wide range of anaerobic bacterial infections.[23]

Received: May 9, 2016
Published: June 20, 2016

ACS Publications © 2016 American Chemical Society

DOI: 10.1021/jacs.6b04784
J. Am. Chem. Soc. 2016, 138, 8080−8083

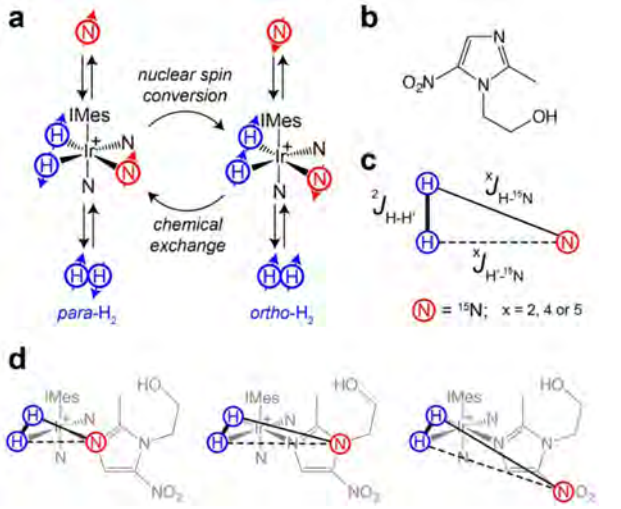

Figure 1. (a) Schematic diagram of the SABRE process: coherent polarization transfer from parahydrogen-derived hydrides to ^{15}N heteronuclei. (b) Molecular structure of metronidazole. (c) Schematic representation of the AA′B spin system in the polarization transfer complex. Red circles represent naturally abundant ^{15}N nuclei. (d) Most-probable metronidazole-bound structures of the complex with relevant AA′B spin systems.

Anaerobic conditions protect the organism's employment of pyruvate synthase, which consequently acts irreversibly on the nitroimidazole moiety—leading to selective drug uptake by anaerobic bacterial cells in the host.[23] The sensitivity of nitroimidazole moieties to anaerobic conditions was later exploited for hypoxia sensing in cancer. Despite a different mechanism of action[23] in mammalian anaerobic cancer cells, the end result is the same: the chemical reaction of the nitro moiety leads to irreversible binding in hypoxic cells.[24,25] A number of nitroimidazole compounds were employed as molecular contrast agents to probe hypoxia and upregulation of hypoxia inducible factor (HIF-1α) using Positron Emission Tomography (PET),[26] and Magnetic Resonance (MR) imaging and spectroscopy.[27] Hypoxia is a hallmark of some aggressive forms of cancer,[28,29] and its imaging can be used as a biomarker for cancer screening and monitoring response to treatment.[26,30] The investigational use of fluoromisonidazole (FMISO),[26] SR4554,[27] and numerous other related nitroimidazole-based agents for hypoxia imaging has advanced well into clinical trials. Furthermore, the intravenous injection of up to 1.4 g/m^2 of nitroimidazole derivatives is well tolerated in patients,[27] which would certainly be sufficient for HP imaging.[31]

In the present SABRE-SHEATH hyperpolarization studies, we employed the most efficient IrIMes polarization-transfer catalyst (using the established Ir catalyst precursor [IrCl(COD)(IMes)]; IMes = 1,3-bis(2,4,6-trimethylphenyl)-imidazol-2-ylidene; COD = cyclooctadiene)[32,33] and metronidazole with ^{15}N at natural abundance (~0.364%). As this abundance is low, the statistically most-abundant polarization-transfer species contains only one ^{15}N site. Therefore, the relevant spin system for polarization transfer contains only three spins: two magnetically inequivalent protons and one ^{15}N site (Figure 1c).[22,34] Because metronidazole contains three nitrogen sites, it can form three types of AA′B spin systems, respectively involving two-bond, four-bond, or five-bond spin–spin couplings (Figure 1d). The ^{15}N NMR signal from nitrogens only two bonds away from the nascent parahydrogen pair was enhanced by ~72 000-fold at 9.4 T (corresponding to $P_{^{15}\mathrm{N}} \approx 24\%$; see Supporting Information (SI) for additional experimental and analysis details) in 50 mM solution of metronidazole in methanol-d_4 using ~80% parahydrogen (Figure 2b); these results may be extrapolated to expect $P_{^{15}\mathrm{N}}$

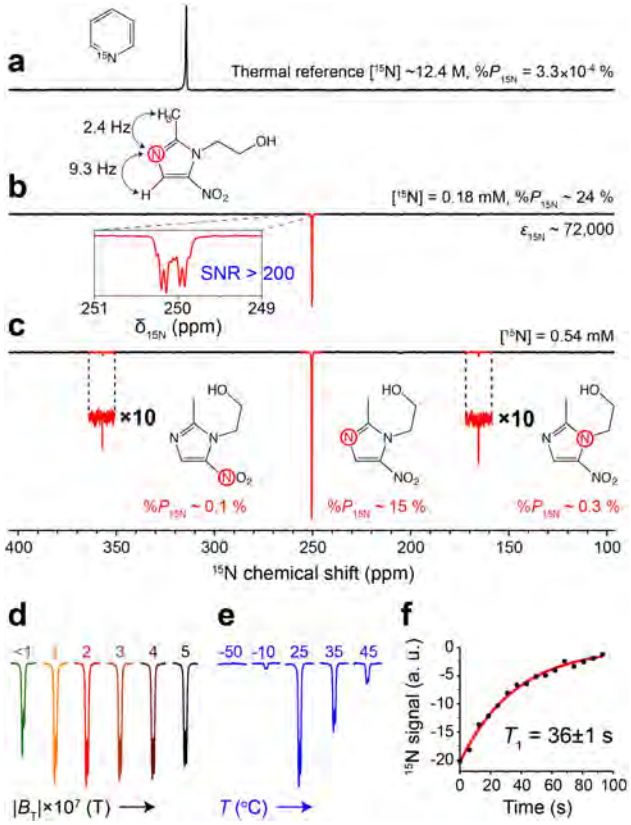

Figure 2. (a) ^{15}N NMR spectrum of thermally polarized signal reference, neat pyridine-^{15}N (~12.4 M). (b) ^{15}N spectrum of HP natural abundance 50 mM metronidazole at ~298 K. Note the appearance of NMR resonances as a doublet of quartets due to spin–spin coupling of ^{15}N with aromatic and methyl protons (inset). (c) ^{15}N spectrum of HP natural abundance 150 mM metronidazole at ~298 K. (d) Optimization of HP metronidazole ^{15}N NMR signal by varying the magnetic field in the shield (B_T). (e) Optimization of HP metronidazole ^{15}N NMR signal by varying the temperature (estimated values) of the sample. (f) ^{15}N T_1 signal decay of HP metronidazole in methanol-d_4 at 9.4 T. All HP ^{15}N spectra shown were obtained using 80% parahydrogen gas.

≈ 32% if ~100% parahydrogen were employed. Note that the ^{15}N polarization was sampled ~8 s after cessation of parahydrogen bubbling, and the measurement does not take into account polarization decay losses that have occurred during the sample transfer from the hyperpolarization setup into the bore of the 9.4 T NMR spectrometer. The $P_{^{15}\mathrm{N}}$ value of ~24% is the highest ^{15}N hyperpolarization level achieved by any technique to date by at least several-fold, and it is demonstrated despite the presence of one or two ortho substituents, which have previously prevented the observation of SABRE-SHEATH enhancement of six-membered N-heterocycles.[22] This high level of $P_{^{15}\mathrm{N}}$ is not far away from the practical limit of 50% theoretically predicted in recent literature.[34−36] Furthermore, investigations using more concentrated solutions (~150 mM, Figure 2c, and ~100 mM, Figure S5) additionally enabled detection of relatively efficient SABRE-SHEATH

DOI: 10.1021/jacs.6b04784
J. Am. Chem. Soc. 2016, 138, 8080−8083

hyperpolarization of the other two ^{15}N sites (more weakly coupled, via $J^4_{H\text{-}^{15}N}$ and $J^5_{H\text{-}^{15}N}$ couplings). Although these other two sites exhibited significantly more modest $P_{^{15}N}$ values of 0.1−0.3% (i.e., "only" ∼1000-fold enhancements), it should be noted that neither the μT field nor the exchange rates governing the SABRE-SHEATH process were optimized for hyperpolarization of these two remote ^{15}N sites. The feasibility of ^{15}N SABRE-SHEATH processes via long-range (up to $J^5_{H\text{-}^{15}N}$) spin−spin couplings (in a manner similar to homonuclear SABRE[17,32,37]) enables ^{15}N hyperpolarization of a wider range of biomolecules via SABRE-SHEATH, because more ^{15}N and potentially other heteronculear sites become amenable to SABRE-SHEATH.

It should also be emphasized that ^{15}N NMR spectra with high signal-to-noise ratios (SNRs >200 and >100) were recorded despite the low natural abundance of ^{15}N and despite using only 80% parahydrogen (Figure 2) and 50% parahydrogen (see SI spectra), respectively. Moreover, this SNR level is more than sufficient for optimization of experimental conditions, i.e., the μT magnetic field for polarization transfer B_T, temperature, and measurements of relaxation parameters (see Figure 2d−f). Furthermore, the reported ^{15}N T_1 (36 ± 1 s) relaxation is dominated by ^{15}N Chemical Shift Anisotropy (CSA) at high magnetic field (e.g., 9.4 T used here), and T_1 is significantly extended (by several-fold) at the clinically relevant fields of 1.5 T and below.[7] An expected *in vivo* ^{15}N T_1 of 1−2 min[14] may be sufficient for hypoxia sensing, because nitroimidazole-based compounds reach the hypoxic region within the first minute after intravenous injection.[38,39] Moreover, while other tissues may also absorb the injected hypoxia sensor,[27,38,39] the ^{15}N chemical shifts of the reduced form of the nitroimidazole moiety may be sufficiently different to provide a good mechanism of contrast of hypoxic regions versus surrounding tissues—mitigating the requirement for clearance of the background signal (the subject of future work).

In conclusion, record-level ^{15}N hyperpolarization was achieved via SABRE-SHEATH in seconds for a representative compound from the nitroimidazole class of antibiotics/contrast agents. Substituted five-membered N-heterocycles can be efficiently hyperpolarized via SABRE-SHEATH even in the presence of ortho substituents. ^{15}N SABRE-SHEATH of distant nitrogen sites via long-range spin−spin couplings is demonstrated. Moreover, high levels of $P_{^{15}N}$ enable detection of HP ^{15}N compounds even at natural abundance and 50% parahydrogen (see SI for additional ^{15}N spectra), which can be conveniently utilized for screening of large libraries of compounds. Finally, the advances presented here will likely be synergistically compatible with recent developments of heterogeneous SABRE[40,41] and SABRE in aqueous media,[20,42−45] key elements for future biomedical translation of this work into animal models and ultimately clinical trials.

■ ASSOCIATED CONTENT

Supporting Information

The Supporting Information is available free of charge on the ACS Publications website at DOI: 10.1021/jacs.6b04784.

Additional experimental details, table of calculated values, and NMR spectra in Figures S1−S5 (PDF)

■ AUTHOR INFORMATION

Corresponding Author

*eduard.chekmenev@vanderbilt.edu

Author Contributions

#D.A.B. and R.V.S. contributed equally.

Notes

The authors declare no competing financial interest.

■ ACKNOWLEDGMENTS

This work was supported by NSF under grants CHE-1058727, CHE-1363008, CHE-1416268, and CHE-1416432; NIH under T32EB001628, 1R21EB018014, and 1R21EB020323; DOD CDMRP BRP W81XWH-12-1-0159/BC112431; DOD PRMRP awards W81XWH-15-1-0271 and W81XWH-15-1-0272; and ExxonMobil Research and Engineering Company Knowledge Build. We thank Dr. Fan Shi for assistance with the SABRE catalyst.

■ REFERENCES

(1) Nikolaou, P.; Goodson, B. M.; Chekmenev, E. Y. *Chem. - Eur. J.* **2015**, *21*, 3156.
(2) Kurhanewicz, J.; Vigneron, D. B.; Brindle, K.; Chekmenev, E. Y.; Comment, A.; Cunningham, C. H.; DeBerardinis, R. J.; Green, G. G.; Leach, M. O.; Rajan, S. S.; Rizi, R. R.; Ross, B. D.; Warren, W. S.; Malloy, C. R. *Neoplasia* **2011**, *13*, 81.
(3) Bowers, C. R.; Weitekamp, D. P. *Phys. Rev. Lett.* **1986**, *57*, 2645.
(4) Mewis, R. E. *Magn. Reson. Chem.* **2015**, *53*, 789.
(5) Brindle, K. M. *J. Am. Chem. Soc.* **2015**, *137*, 6418.
(6) Golman, K.; in't Zandt, R.; Thaning, M. *Proc. Natl. Acad. Sci. U. S. A.* **2006**, *103*, 11270.
(7) Theis, T.; Ortiz, G. X.; Logan, A. W. J.; Claytor, K. E.; Feng, Y.; Huhn, W. P.; Blum, V.; Malcolmson, S. J.; Chekmenev, E. Y.; Wang, Q.; Warren, W. S. *Sci. Adv.* **2016**, *2*, e1501438.
(8) Nonaka, H.; Hata, R.; Doura, T.; Nishihara, T.; Kumagai, K.; Akakabe, M.; Tsuda, M.; Ichikawa, K.; Sando, S. *Nat. Commun.* **2013**, *4*, 2411.
(9) Gabellieri, C.; Reynolds, S.; Lavie, A.; Payne, G. S.; Leach, M. O.; Eykyn, T. R. *J. Am. Chem. Soc.* **2008**, *130*, 4598.
(10) Pileio, G.; Carravetta, M.; Hughes, E.; Levitt, M. H. *J. Am. Chem. Soc.* **2008**, *130*, 12582.
(11) Shchepin, R. V.; Barskiy, D. A.; Mikhaylov, D. M.; Chekmenev, E. Y. *Bioconjugate Chem.* **2016**, *27*, 878.
(12) Oppenheimer, N. J.; Matsunaga, T. O.; Kam, B. L. *J. Labelled Compd. Radiopharm.* **1978**, *15*, 191.
(13) Ardenkjaer-Larsen, J. H.; Fridlund, B.; Gram, A.; Hansson, G.; Hansson, L.; Lerche, M. H.; Servin, R.; Thaning, M.; Golman, K. *Proc. Natl. Acad. Sci. U. S. A.* **2003**, *100*, 10158.
(14) Cudalbu, C.; Comment, A.; Kurdzesau, F.; van Heeswijk, R. B.; Uffmann, K.; Jannin, S.; Denisov, V.; Kirik, D.; Gruetter, R. *Phys. Chem. Chem. Phys.* **2010**, *12*, 5818.
(15) Jiang, W.; Lumata, L.; Chen, W.; Zhang, S.; Kovacs, Z.; Sherry, A. D.; Khemtong, C. *Sci. Rep.* **2015**, *5*, 9104.
(16) Hata, R.; Nonaka, H.; Takakusagi, Y.; Ichikawa, K.; Sando, S. *Chem. Commun.* **2015**, *51*, 12290.
(17) Adams, R. W.; Aguilar, J. A.; Atkinson, K. D.; Cowley, M. J.; Elliott, P. I. P.; Duckett, S. B.; Green, G. G. R.; Khazal, I. G.; Lopez-Serrano, J.; Williamson, D. C. *Science* **2009**, *323*, 1708.
(18) Theis, T.; Truong, M. L.; Coffey, A. M.; Shchepin, R. V.; Waddell, K. W.; Shi, F.; Goodson, B. M.; Warren, W. S.; Chekmenev, E. Y. *J. Am. Chem. Soc.* **2015**, *137*, 1404.
(19) Truong, M. L.; Theis, T.; Coffey, A. M.; Shchepin, R. V.; Waddell, K. W.; Shi, F.; Goodson, B. M.; Warren, W. S.; Chekmenev, E. Y. *J. Phys. Chem. C* **2015**, *119*, 8786.
(20) Truong, M. L.; Shi, F.; He, P.; Yuan, B.; Plunkett, K. N.; Coffey, A. M.; Shchepin, R. V.; Barskiy, D. A.; Kovtunov, K. V.; Koptyug, I. V.; Waddell, K. W.; Goodson, B. M.; Chekmenev, E. Y. *J. Phys. Chem. B* **2014**, *118*, 13882.
(21) Shchepin, R. V.; Barskiy, D. A.; Coffey, A. M.; Theis, T.; Shi, F.; Warren, W. S.; Goodson, B. M.; Chekmenev, E. Y. *ACS Sensors* **2016**, DOI: 10.1021/acssensors.6b00231.

DOI: 10.1021/jacs.6b04784
J. Am. Chem. Soc. 2016, 138, 8080−8083

(22) Shchepin, R. V.; Truong, M. L.; Theis, T.; Coffey, A. M.; Shi, F.; Waddell, K. W.; Warren, W. S.; Goodson, B. M.; Chekmenev, E. Y. *J. Phys. Chem. Lett.* **2015**, *6*, 1961.
(23) Upcroft, P.; Upcroft, J. A. *Clin. Microbiol. Rev.* **2001**, *14*, 150.
(24) Kizaka-Kondoh, S.; Konse-Nagasawa, H. *Cancer Sci.* **2009**, *100*, 1366.
(25) Masaki, Y.; Shimizu, Y.; Yoshioka, T.; Tanaka, Y.; Nishijima, K.-i.; Zhao, S.; Higashino, K.; Sakamoto, S.; Numata, Y.; Yamaguchi, Y.; Tamaki, N.; Kuge, Y. *Sci. Rep.* **2015**, *5*, 16802.
(26) Hendrickson, K.; Phillips, M.; Smith, W.; Peterson, L.; Krohn, K.; Rajendran, J. *Radiother. Oncol.* **2011**, *101*, 369.
(27) Lee, C. P.; Payne, G. S.; Oregioni, A.; Ruddle, R.; Tan, S.; Raynaud, F. I.; Eaton, D.; Campbell, M. J.; Cross, K.; Halbert, G.; Tracy, M.; McNamara, J.; Seddon, B.; Leach, M. O.; Workman, P.; Judson, I. *Br. J. Cancer* **2009**, *101*, 1860.
(28) Hanahan, D.; Weinberg, R. A. *Cell* **2011**, *144*, 646.
(29) Gillies, R. J.; Verduzco, D.; Gatenby, R. A. *Nat. Rev. Cancer* **2012**, *12*, 487.
(30) Evans, S. M.; Jenkins, W. T.; Joiner, B.; Lord, E. M.; Koch, C. J. *Cancer Res.* **1996**, *56*, 405.
(31) Nelson, S. J.; Kurhanewicz, J.; Vigneron, D. B.; Larson, P. E. Z.; Harzstark, A. L.; Ferrone, M.; van Criekinge, M.; Chang, J. W.; Bok, R.; Park, I.; Reed, G.; Carvajal, L.; Small, E. J.; Munster, P.; Weinberg, V. K.; Ardenkjaer-Larsen, J. H.; Chen, A. P.; Hurd, R. E.; Odegardstuen, L. I.; Robb, F. J.; Tropp, J.; Murray, J. A. *Sci. Transl. Med.* **2013**, *5*, 198ra108.
(32) Cowley, M. J.; Adams, R. W.; Atkinson, K. D.; Cockett, M. C. R.; Duckett, S. B.; Green, G. G. R.; Lohman, J. A. B.; Kerssebaum, R.; Kilgour, D.; Mewis, R. E. *J. Am. Chem. Soc.* **2011**, *133*, 6134.
(33) Appleby, K. M.; Mewis, R. E.; Olaru, A. M.; Green, G. G. R.; Fairlamb, I. J. S.; Duckett, S. B. *Chem. Sci.* **2015**, *6*, 3981.
(34) Barskiy, D. A.; Pravdivtsev, A. N.; Ivanov, K. L.; Kovtunov, K. V.; Koptyug, I. V. *Phys. Chem. Chem. Phys.* **2016**, *18*, 89.
(35) Levitt, M. H. *J. Magn. Reson.* **2016**, *262*, 91.
(36) Knecht, S.; Pravdivtsev, A. N.; Hovener, J.-B.; Yurkovskaya, A. V.; Ivanov, K. L. *RSC Adv.* **2016**, *6*, 24470.
(37) Eshuis, N.; Aspers, R. L. E. G.; van Weerdenburg, B. J. A.; Feiters, M. C.; Rutjes, F. P. J. T.; Wijmenga, S. S.; Tessari, M. *J. Magn. Reson.* **2016**, *265*, 59.
(38) Komar, G.; Seppänen, M.; Eskola, O.; Lindholm, P.; Grönroos, T. J.; Forsback, S.; Sipilä, H.; Evans, S. M.; Solin, O.; Minn, H. *J. Nucl. Med.* **2008**, *49*, 1944.
(39) Shi, K.; Souvatzoglou, M.; Astner, S. T.; Vaupel, P.; Nüsslin, F.; Wilkens, J. J.; Ziegler, S. I. *J. Nucl. Med.* **2010**, *51*, 1386.
(40) Shi, F.; Coffey, A. M.; Waddell, K. W.; Chekmenev, E. Y.; Goodson, B. M. *Angew. Chem., Int. Ed.* **2014**, *53*, 7495.
(41) Shi, F.; Coffey, A. M.; Waddell, K. W.; Chekmenev, E. Y.; Goodson, B. M. *J. Phys. Chem. C* **2015**, *119*, 7525.
(42) Hövener, J.-B.; Schwaderlapp, N.; Borowiak, R.; Lickert, T.; Duckett, S. B.; Mewis, R. E.; Adams, R. W.; Burns, M. J.; Highton, L. A. R.; Green, G. G. R.; Olaru, A.; Hennig, J.; von Elverfeldt, D. *Anal. Chem.* **2014**, *86*, 1767.
(43) Zeng, H.; Xu, J.; McMahon, M. T.; Lohman, J. A. B.; van Zijl, P. C. M. *J. Magn. Reson.* **2014**, *246*, 119.
(44) Shi, F.; He, P.; Best, Q. A.; Groome, K.; Truong, M. L.; Coffey, A. M.; Zimay, G.; Shchepin, R. V.; Waddell, K. W.; Chekmenev, E. Y.; Goodson, B. M. *J. Phys. Chem. C* **2016**, *120*, 12149.
(45) Spannring, P.; Reile, I.; Emondts, M.; Schleker, P. P. M.; Hermkens, N. K. J.; van der Zwaluw, N. G. J.; van Weerdenburg, B. J. A.; Tinnemans, P.; Tessari, M.; Blümich, B.; Rutjes, F. P. J. T.; Feiters, M. C. *Chem. - Eur. J.* **2016**, DOI: 10.1002/chem.201601211.

DOI: 10.1021/jacs.6b04784
J. Am. Chem. Soc. 2016, 138, 8080−8083

THE JOURNAL OF PHYSICAL CHEMISTRY C

Subscriber access provided by Vanderbilt Libraries

Article

NMR SLIC Sensing of Hydrogenation Reactions Using Parahydrogen in Low Magnetic Fields

Danila A Barskiy, Oleg G. Salnikov, Roman V Shchepin, Matthew Feldman, Aaron M Coffey, Kirill V. Kovtunov, Igor V. Koptyug, and Eduard Y Chekmenev

J. Phys. Chem. C, **Just Accepted Manuscript** • DOI: 10.1021/acs.jpcc.6b07555 • Publication Date (Web): 26 Oct 2016

Downloaded from http://pubs.acs.org on October 26, 2016

Just Accepted

"Just Accepted" manuscripts have been peer-reviewed and accepted for publication. They are posted online prior to technical editing, formatting for publication and author proofing. The American Chemical Society provides "Just Accepted" as a free service to the research community to expedite the dissemination of scientific material as soon as possible after acceptance. "Just Accepted" manuscripts appear in full in PDF format accompanied by an HTML abstract. "Just Accepted" manuscripts have been fully peer reviewed, but should not be considered the official version of record. They are accessible to all readers and citable by the Digital Object Identifier (DOI®). "Just Accepted" is an optional service offered to authors. Therefore, the "Just Accepted" Web site may not include all articles that will be published in the journal. After a manuscript is technically edited and formatted, it will be removed from the "Just Accepted" Web site and published as an ASAP article. Note that technical editing may introduce minor changes to the manuscript text and/or graphics which could affect content, and all legal disclaimers and ethical guidelines that apply to the journal pertain. ACS cannot be held responsible for errors or consequences arising from the use of information contained in these "Just Accepted" manuscripts.

ACS Publications

The Journal of Physical Chemistry C is published by the American Chemical Society. 1155 Sixteenth Street N.W., Washington, DC 20036

Published by American Chemical Society. Copyright © American Chemical Society. However, no copyright claim is made to original U.S. Government works, or works produced by employees of any Commonwealth realm Crown government in the course of their duties.

NMR SLIC Sensing of Hydrogenation Reactions Using Parahydrogen in Low Magnetic Fields**

D. A. Barskiy,[a,] O. G. Salnikov,[b,c] R. V. Shchepin,[a] M. A. Feldman,[a] A. M. Coffey,[a] K. V. Kovtunov,[b,c] I. V. Koptyug,[b,c] and E. Y. Chekmenev[a,d,]**

a Vanderbilt University Institute of Imaging Sciences, Nashville, TN 37232 (USA)

b International Tomography Center, Novosibirsk 630090 (Russia)

c Novosibirsk State University, Novosibirsk 630090 (Russia)

d Russian Academy of Sciences, Moscow 119991 (Russia)

[**] SLIC = spin-lock induced crossing

*Corresponding Authors:

danila.barskiy@vanderbilt.edu (Dr. Danila A. Barskiy)

eduard.chekmenev@vanderbilt.edu (Dr. Eduard Y. Chekmenev)

Phone: (615) 322-1329

Fax: (615) 322-0734

Vanderbilt University Institute of Imaging Science

1161 21st Avenue South, Nashville, TN 37232

Abstract

Parahydrogen-induced polarization (PHIP) is an NMR hyperpolarization technique that increases nuclear spin polarization by orders of magnitude, and it is particularly well suited to study hydrogenation reactions. However, the use of high-field NMR spectroscopy is not always possible, especially in the context of potential industrial-scale reactor applications. On the other hand, the direct low-field NMR detection of reaction products with enhanced nuclear spin polarization is challenging due to near complete signal cancellation from nascent parahydrogen protons. We show that hydrogenation products prepared by PHIP can be irradiated with weak (on the order of spin-spin couplings of a few Hz) alternating magnetic fields and consequently efficiently detected at low magnetic field (*e.g.* 0.05 T used here) using examples of several types of organic molecules containing vynil moiety. The detected hyperpolarized signals from several reaction products at tens of milli-molar concentrations were enhanced by 10000-fold, producing NMR signals an order of magnitude greater than the background signal from protonated solvents.

Introduction

Nuclear magnetic resonance (NMR) spectroscopy is a powerful analytical tool used for a broad range of applications.[1-3] One of the main limitations of NMR is low detection sensitivity dictated by the weak interaction energy of nuclear spins with the static magnetic field B_0.[4-6] Hence, methods for increasing the sensitivity of NMR detection are welcome, because they decrease the detection limit and acquisition time. Nuclear spin hyperpolarization techniques such as dissolution dynamic nuclear polarization (d-DNP),[6] spin exchange optical pumping (SEOP) of noble gases,[7-8] and parahydrogen-induced polarization (PHIP)[5, 9-11] can temporarily increase nuclear spin polarization (P) by several orders of magnitude (>10000 at high magnetic fields[6] and hundreds of millions at low fields[12]) and thus, have become very popular in the last decade.[13-14] Motivated by biomedical applications, d-DNP and SEOP have been introduced into the clinical research realm to probe metabolism, function, response to treatment, *etc*.[13, 15-17]

Recent PHIP innovations have demonstrated relatively inexpensive chemistries for production of contrast agents,[18,19] use of aqueous media[20] and heterogeneous catalysts[10, 21] making PHIP a promising means for generating new classes of hyperpolarized (HP) molecular contrast agents for *in vivo* applications.[22] PHIP offers a number of advantages compared to d-DNP and SEOP, *i.e.* (i) very fast (<1 min) hyperpolarization production speed, (ii) low cost, and (iii) straightforward scalability.[8] In addition, PHIP naturally employs hydrogenation reactions and therefore can find promising applications beyond biomedicine. For example, it could be a useful modality for *in situ* detection and imaging of industrial-scale hydrogenation and hydrogen-involving reactions,[23,24] which represent a significant fraction of all industrial chemical processes.[25]

While the PHIP hyperpolarization technique is inexpensive and high-throughput in principle, high-resolution NMR spectroscopic detection is most often conducted at high fields using expensive superconducting magnets, which additionally have significant limitations regarding small sample size. Therefore, despite the low-cost nature of the PHIP hyperpolarization process, the high-field detection renders the entire analysis process generally expensive and limited to small samples – counter to the

goals of industrial-scale applications.[26] Alternatively, cheap low-field magnets can be efficiently used for PHIP signal detection,[27-31] because detection sensitivity for HP states has a very weak ($B_0^{1/4}$) magnetic field dependence.[27, 32] Moreover, low-field detection offers other advantages: (i) reduced B_0 susceptibility gradients, and (ii) the possibility of construction of relatively low-cost large homogeneous magnets that in principle can encompass large chemical reactors.[24, 31-34]

However, the direct NMR detection of PHIP hyperpolarization in low magnetic fields is fundamentally challenging. Indeed, even if the magnetic equivalence of the parahydrogen (p-H_2) singlet state is broken during the hydrogenation reaction, two p-H_2-nascent spins will still reside in the non-observable pseudo-singlet state[35-36] at low magnetic field, **Figure 1a**. In practice, this results in the collapse of the NMR lines, because the difference in the chemical shift of the two nascent protons is too small with respect to the spin-spin coupling (J_{HH}), and also with respect to the magnetic field homogeneity. As a result, the direct detection of PHIP products suffers from massive (more than two orders of magnitude) signal cancellation.[37-39]

Here we show that application of spin-lock induced crossing (SLIC)[40] allows for direct proton readout of HP products at low magnetic field (*e.g.*, 47.5 mT used here). The SLIC sequence is a simple low-power radio-frequency (RF) pulse with B_1 strength on the order of J_{HH}. Specifically, more than 10000-fold NMR signal enhancement enabled direct ^{1}H low-field detection of 80 milli-molar solutions of 2-hydroxyethyl propionate, ethyl acetate, 2-ethylpyridine, and (ethyl)trimethylammonium chloride hyperpolarized via PHIP (**Fig. 1**). The presented methodology of PHIP-enhanced milli-Tesla NMR with SLIC sensing (vs. conventional NMR where a hard RF pulse is applied for signal detection) can be used for fast screening of potential HP contrast agents by PHIP and potentially without expensive high-field NMR instruments and isotopic labeling. Moreover, the presented methodology may be potentially conveniently applied to the visualization of industrial-scale processes *in situ*.

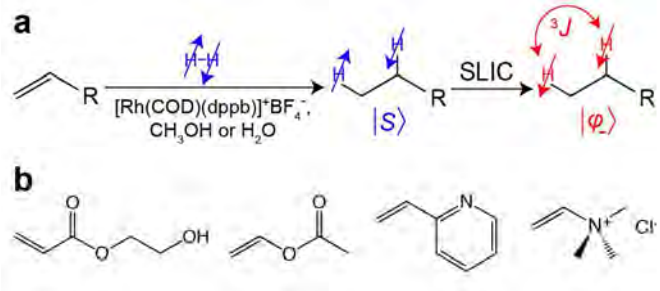

Figure 1. a) Molecular diagram of unsaturated precursors hydrogenation by p-H_2 leading to the hydrogenated product with p-H_2-nascent protons residing in the pseudo-singlet state;[35] then, pseudo-singlet state is converted to observable magnetization by using SLIC RF excitation. b) Chemical structures of investigated organic molecules containing vinyl moiety: 2-hydroxyethyl acrylate (**HEA**), vinyl acetate (**VA**), 2-vinylpyridine (**VPy**), (vinyl)trimethylammonium chloride (**VTMA**).

Methods

Preparation of catalyst/precursor solutions. Methanol (80 mL) was placed in 4 square bottles (431430, Corning Life Sciences, NY, USA) and degassed by the repetitive (3 times) sequence: argon flushing, closing the cap, and vortexing the solution. Rhodium catalyst [(bicyclo[2.2.1]hepta-2,5-diene)[1,4-bis-(diphenylphosphino)-butane]-rhodium(I) tetrafluoroborate, 0.40 mmol, 0.150 g, 5.00 mM final concentration] was placed in each bottle. Vinyl acetate (6.40 mmol, 0.551 g, 80.0 mM final concentration), 2-hydroxyethyl acrylate (6.40 mmol, 0.742 g, 80.0 mM final concentration), trimethyl(vinyl)ammonium chloride (6.40 mmol, 1.06 g, 80.0 mM final concentration), 2-vinylpyridine (6.40 mmol, 0.672 g, 80.0 mM final concentration) were added to individual bottles. Water-soluble rhodium catalyst was prepared as described earlier.[20] Vinyl acetate (8.00 mmol, 0.688 g, 80.0 mM final concentration) and 2-hydroxyethyl acrylate (8.00 mmol, 0.928 g, 80.0 mM final concentration) were dissolved in the aqueous solution of rhodium catalyst (100 mL, 2.60 mM) each. Trimethyl(vinyl)ammonium chloride (4.00 mmol, 0.664 g, 80.0 mM final concentration), 2-vinylpyridine (4.00 mmol, 0.420 g, 80.0 mM final concentration) were dissolved in aqueous rhodium catalyst solution (50 mL, 5.30 mM). Each bottle containing the catalyst/precursor solutions was connected to an automated PHIP polarizer[41] for further experiments.

Preparation of parahydrogen gas. For parahydrogen (p-H_2) preparation, normal hydrogen was passed through a spiral copper tube packed with FeO(OH) (Sigma-Aldrich, P/N 371254, 30–50 mesh) and immersed into a liquid N_2 Dewar. This procedure produces a stream of hydrogen enriched with *ca*. 50% *para*-isomer.[10]

PHIP polarizer and hydrogenation reaction. A fully automated parahydrogen-based polarizer was employed for hydrogenation.[42] The prepared stock solutions containing catalyst and precursor molecule were connected to the heated injection loop of the polarizer. Hydrogenation of the unsaturated compounds (**Fig. 1b**) was conducted in a chemical reactor (~56 mL volume) of the polarizer at an ~7.8 atm p-H_2 pressure by injecting the warmed solution from the injection loop and spraying it into atmosphere of hot p-H_2 gas using the back-pressure (~17 atm) of N_2 gas (**Fig. 2a**). Reactor temperature was held within the range of 55-60 ^{o}C. After a variable reaction time, t_R (**Fig. 2b**), 2-2.5 mL of the solution was ejected from the polarizer into an ~50 mL detection chamber located inside the RF probe within a 47.5 mT magnet. The magnet was located ~0.5 m away from the polarizer allowing very short (<1 s) ejection time of the reacted solution from the reactor to the detection chamber (Corning 50mL PP Centrifuge Tube). TTL microcontroller of the PHIP polarizer was used to switch solenoid valves that control gas and chemical delivery to the high-pressure reactor and ejection to the detection chamber. The detection chamber was cleaned after each NMR signal acquisition before a new portion of the solution from polarizer was ejected.

Low-field (2 MHz) NMR detection. A commercially available MR Kea2 spectrometer (Magritek, Wellington, New Zealand) was used for NMR detection as described by Waddell et al.[43] The magnet (2 MHz Magritek Core Analyzer, Halbach array, radial field direction) had a homogeneity of 20 ppm over 4 cm diameter of spherical volume (DSV). The detection chamber was placed in the home-built ^{1}H RF coil[44] located in the magnet (**Fig. S1**). Radio frequency calibration using a 5 mM aqueous solution of $CuSO_4$ in a 2.8 mL spherical phantom yielded a 90° ^{1}H excitation pulse width of 177 μs at 0.22 W.

SLIC RF pulse sequence. Spin order of the p-H_2 singlet state was converted to observable magnetization using the spin-lock induced crossing (SLIC) sequence developed by DeVience et al.[40] In

order to generate low power (~1 μW) SLIC pulses, additional attenuators (Bird Technologies, 10 Watt, A Series, Male/Female N Connector, 30 dB and 20 dB) were inserted between the output of the Tomco RF amplifier (P/N BT00250-AlphaS-Dual, Tomco Technologies, Stepney, Australia) and TR switch of the spectrometer (**Fig. S1**). The SLIC pulse amplitude was calibrated by measuring the TR switch voltage output on an oscilloscope (Tektronix, TDS 3034C) and comparing it to the measurements for the π/2 RF pulse calibrated by nutation experiment. Acquisition of ^{1}H NMR signal started immediately after injection of the reactor content to the detection chamber followed by a SLIC pulse (**Fig. 2b**). Optimization of SLIC parameters (B_1 amplitude and duration, τ_{SLIC}) was performed for the 2-hydroxyethyl propionate (the product of 2-hydroxyethyl acrylate hydrogenation) and then parameters found were used for the detection of all other substrates under the study.

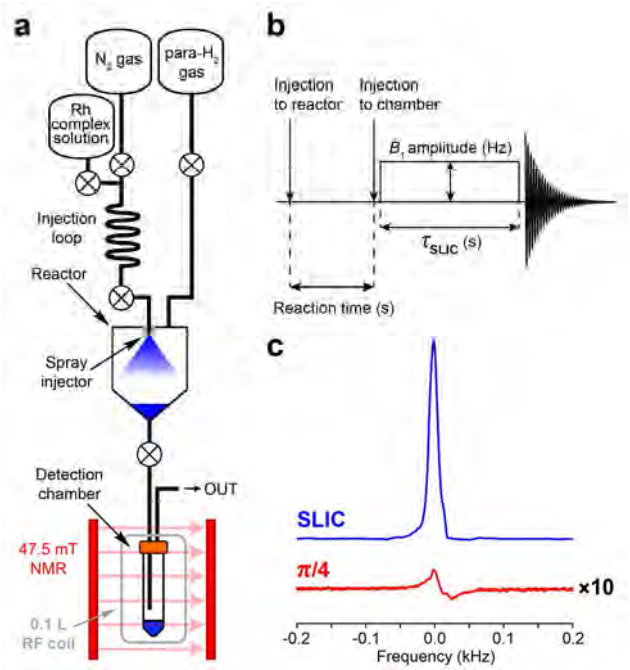

Figure 2. a) Schematic diagram of experimental setup. The reactor was kept at 50-60 °C. b) Sequence of events: injection of Rh complex solution (in CH_3OH or in H_2O) into reactor filled with ~7.8 atm of *p*-H_2, variable reaction time, injection into the detection chamber located inside a 47.5 mT magnet, subsequent application of SLIC pulse and signal acquisition. c) ^{1}H NMR signal of HEP in methanol obtained after application of SLIC pulse (blue) and NMR signal obtained after application of a hard π/4 RF pulse (red), note the scaling by a factor of 10.

Results

We carried out hydrogenation of several molecules containing vinyl moiety (**Fig. 1**): 2-hydroxyethyl acrylate (**HEA**), vinyl acetate (**VA**), 2-vinylpyridine (**VPy**), (vinyl)trimethylammonium chloride (**VTMA**), with *p*-H_2, using home-built automated PHIP polarizer (**Fig. 2a**). The compounds were chosen based on their importance in the context of potential PHIP applications. For example, ethyl acetate can be potentially employed to trace the metabolism of a brain damage and cancer; 2-ethylpyridine has shown the potential for ^{15}N pH mapping/imaging;[45] (ethyl)trimethylammonium is structurally similar to choline, which is a key metabolic signature in many cancers;[46-48] 2-hydroxyethyl propionate can be used for *in vivo* angiography and it is also a typical test-molecule for PHIP studies.[49-50] Hydrogenation of the vinyl motif (-CH=CH_2) by *p*-H_2 for the molecules studied leads to ethyl group (-CH_2-CH_3) formation, where two hydrogens come from the same *p*-H_2 molecule, and these nascent parahydrogen nuclei are incorporated into two chemically inequivalent positions. Due to the identical structure of the intentionally chosen hydrogenated motif for all substrates investigated (**Fig. 1b**), their NMR parameters and *J*-coupling patterns are relatively similar (**Table S1**).

Use of the automated home-built low-field PHIP-polarizer made possible fast conversion of 80 mM unsaturated substrates into hydrogenation reaction products. Reactions were carried out by fast (<4 s) injection of 3-5 mL of the catalyst/precursor solution into an atmosphere of *p*-H_2. Then reaction solutions were quickly (<1 s) pushed to the detection chamber located in the bore of a 47.5 mT magnet; the SLIC RF pulse was applied immediately, and it was followed by ^{1}H NMR signal acquisition (**Fig. 2a,b**). The intensity of the NMR signal obtained after SLIC was at least two orders of magnitude greater than the signal intensity obtained after application of a hard $\pi/4$ pulse as typically employed in high-field PHIP experiments,[11] **Fig. 2c**.

We note that the hydrogenation reactions were carried out in non-deuterated solvents, such as methanol and water. NMR signal resulting from ~80 mM of hydrogenated material after SLIC was 10-30 times greater than the NMR signal originating from the solvent (**Fig. 3a,b**). Besides providing a direct comparison with HP signal, utilization of non-deuterated solvents here advantageously allowed

calibration of experimental parameters (*e.g.*, RF pulses, B_1 frequency offset and adjustments to account for minor magnetic field drift typical for low-field scanners based on permanent magnets and in the absence of deuterium spin-lock apparatus). The signal enhancement of HP resonances was evaluated by computing the ratio of HP signal to the signal originating from the thermally polarized solvent (since the amount of material injected to the detection chamber each time may vary). Maximal apparent polarization percentage (P^{APP}) of ~0.23% was found for 2-hydroxyethyl propionate (**HEP**) when hydrogenation reaction of **HEA** was performed in methanol. Lower values were found for ethyl acetate and when water was used as a solvent. Hydrogenation of **VPy** and **VTMA** was also detected by SLIC, but their NMR signals were significantly lower (see Discussion).

Varying the reaction time allowed detecting the build-up and decay of the hyperpolarized signal (**Fig. 3c,d**). We found that the signal decayed with the time constant T_S ranged between 5-15 seconds depending on the studied molecule and the solvent. The T_S values obtained correlate well with prior results in the literature. For example, T_S of 6.4±1.2 s was measured for **EA** at Earth's magnetic field in ALTADENA conditions,[18] while the present study yielded T_S of **EA** to be 7.2±0.5 s in methanol (see **Table 1** for the T_S values for all studied substrates in methanol and in water). One may also estimate the effective hydrogenation reaction kinetic constant k_r by fitting the experimental data with suitable analytical expression (eq. S1) describing the build-up and decay of hyperpolarized signal (Fig. 3c,d and SI).

Table 1. Kinetic and relaxation parameters extracted from fitting of the build-up and decay curves for studied molecules: 2-hydroxyethyl propionate (**HEP**), ethyl acetate (**EA**), (ethyl)trimethylammonium chloride (**ETMA**), 2-ethylpyridine (**EPy**). Catalyst concentration was 5 mM.

Methanol	**HEP**	**EA**	**ETMA**	**EPy**
k_r (s^{-1})	11.8±1.8	11.5±2.3	14.1±2.5	2.8±0.5
T_S (s)	5.5±0.2	7.2±0.5	17.1±1.2	---
Water	**HEP**	**EA**	**ETMA**	**EPy**
k_r (s^{-1})	12.8±3.9	14.4±5.9	21.9±4.2	---
T_S (s)	8.3±0.8	4.3±0.5	13.2±1.4	---

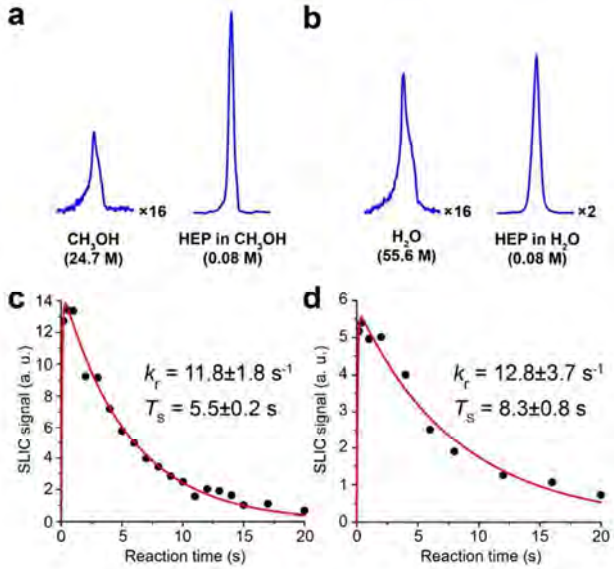

Figure 3. ^{1}H NMR spectroscopy of HEP at 47.5 mT. a) Left – ^{1}H NMR signal of reaction mixture injected into the detection chamber at equilibrium nuclear spin polarization; the NMR signal originates primarily from methanol solvent; right – ^{1}H HP NMR signal obtained after SLIC pulse applied to the reaction mixture (~0.08 M of 2-hydroxyetyl propionate (**HEP**) in methanol). b) Left – ^{1}H NMR signal of reaction mixture injected into the detection chamber at equilibrium nuclear spin polarization; the NMR signal originates primarily from water solvent; right – ^{1}H HP NMR signal obtained after SLIC pulse applied to the reaction mixture (~0.08 M of HEP in water). c) Dependence of the SLIC signal (normalized to the thermal signal of the solvent) on the reaction time for HEP in methanol. d) Dependence of the SLIC signal (normalized to the thermal signal of the solvent) on the reaction time for **HEP** in water.

In principle, usage of an automated PHIP polarizer with a high-pressure injection reactor is not mandatory, *i.e.* high-pressure NMR tubes with *p*-H_2 bubbling can be employed (similar to the recent studies of ^{13}C-VA hydrogenation and hyperpolarization with Signal Amplification by Reversible Exchange).[18, 51] Nevertheless, the use of automated PHIP polarizer benefited the present study, because a series of experiments could be performed routinely and identically, which allowed us to quickly find

optimal conditions for performing a singlet-to-magnetization transformation, *i.e.* optimal RF pulse amplitude, frequency offset and duration of the SLIC pulse (Fig. 4).

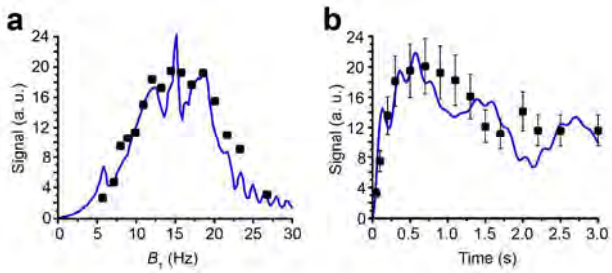

Figure 4. a) Dependence of the SLIC signal of HEP in methanol (normalized to the thermal signal of the solvent) vs. B_1 amplitude at the SLIC duration (τ_{SLIC}) of 0.6 s; black squares correspond to experimental results*, blue line corresponds to simulation assuming ±5 Hz RF pulse offset (*i.e.* simulating B_0 inhomogeneity). b) Dependence of the SLIC signal vs. SLIC duration (time) at B_1 amplitude of 15 Hz*; black squares correspond to experimental results, and blue line corresponds to simulation.

Discussion

The true singlet state of two spins *i.e.* the state with total spin 0, is not NMR detectable, because the singlet state has no magnetic moment.[52] The best example is the nuclear spin singlet state of p-H_2 that produces no NMR signal. Another way to explain the absence of the observable NMR signal is the realization that the transitions between exchange anti-symmetric singlet state and exchange-symmetric triplet states are forbidden. However, once the magnetic equivalence of the two H atoms is broken, (*e.g.*, by introducing two hydrogen atoms from the same p-H_2 molecule into a non-symmetric molecular environment), the spin order of the singlet state can be manifested as a nearly 100% nuclear spin polarization.[53] Hydrogenation reactions can be employed in a way that both hydrogen atoms from the same p-H_2 molecule are transferred to the product as a pair (pairwise addition) resulting in canonical PHIP effect.[11, 53-54] However, the singlet state is considered to be truly broken (*i.e.*, resulting in two well-resolved resonances in the NMR spectrum) only if the chemical shift difference between p-H_2-nascent protons (δ_{HA} and δ_{HB}) is greater than the spin-spin coupling constant $J_{HA\text{-}HB}$ between them (corresponding to the condition of a weak coupling regime).[55] Otherwise—in a strong coupling regime (sometimes referred to as inverse weak coupling regime[56]), *i.e.* $(\delta_{HA} - \delta_{HB}) < J_{HA\text{-}HB}$—the two nascent protons reside in a pseudo-singlet state even after the act of pairwise addition of p-H_2.[35] For example, for the case where $(\delta_{HA} - \delta_{HB})$ is 3 ppm and J-coupling is 7 Hz, the strong coupling regime occurs for magnetic fields below 0.055 T. Ethyl moiety ($-CH_2-CH_3$) is a chemical motif found in a wide range of organic molecules which has a typical J-coupling constant of ~7 Hz between methylene and methyl groups and the corresponding chemical shift difference $(\delta_{METHYLENE} - \delta_{METHYL})$ ranging from 0.5 to 3 ppm (**Table S1**). Since hydrogenation of a vinyl group produces an ethyl group, all four molecules studied form strongly coupled spin systems if hydrogenation by p-H_2 is carried out in the fields below 0.055 T.

Although the pseudo-singlet state is not directly detectable by NMR in the strong coupling regime,[38, 56-58] the spin order from the pseudo-singlet spin state can be transformed into the observable

magnetization using the SLIC sequence introduced by DeVience and co-workers.[40, 59] They demonstrated that low-power continuous wave (CW) decoupling (with alternating magnetic field B_1 amplitude on the order of $J_{\text{HA-HB}}$ and with frequency set at $(\delta_{\text{HA}}+\delta_{\text{HB}})/2$) enables coherent transfer of population between the singlet state $|\boldsymbol{S}\rangle = (|\boldsymbol{\alpha\beta}\rangle - |\boldsymbol{\beta\alpha}\rangle)/\sqrt{\mathbf{2}}$ and the state $|\boldsymbol{\varphi}_{-}\rangle = (|\boldsymbol{\alpha\alpha}\rangle - |\boldsymbol{\alpha\beta}\rangle - |\boldsymbol{\beta\alpha}\rangle + |\boldsymbol{\beta\beta}\rangle)/\mathbf{2}$. The latter term corresponds to magnetization aligned along the $-x$ axis in a rotating frame, and it is readily observable by NMR.[52] The optimum duration of SLIC RF irradiation depends on the combination of NMR resonance frequency, $J_{\text{HA-HB}}$, and $(\delta_{\text{HA}}-\delta_{\text{HB}})$. Advantageously, this transformation does not require any other RF pulses making it relatively straightforward to implement from the hardware perspective.

However, we found that while the analytical model presented by DeVience et al. works well for the simple case of a two-spin system, it cannot properly describe the observed patterns obtained in the experiment with the 5-spin systems of ethyl groups studied here. For example, our results show that instead of a relatively narrow maximum at $B_1 = J_{\text{HA-HB}}$ as predicted by the simple theory, there is a broad maximum at $B_1 \sim 2 \cdot J_{\text{HA-HB}}$ and the optimal SLIC pulse duration is about $\sqrt{\mathbf{2}}/\Delta\boldsymbol{\upsilon}$ (where $\Delta\boldsymbol{\upsilon}$ is the chemical shift difference ($\delta_{\text{METHYLENE}} - \delta_{\text{METHYL}}$) expressed in Hz), *i.e.* two times longer than that predicted for the two-spin model[40] (**Fig. 4**). Here, detailed spin dynamics simulations were carried out (see ESI) resulting in the graphs (**Fig. 5**) where SLIC signal is plotted vs. SLIC B_1 amplitude, SLIC B_1 offset and SLIC duration, where NMR signal maxima form concentric waves with radii of approximately $3 \cdot J_{\text{HA-HB}}/2$, $2 \cdot J_{\text{HA-HB}}$, and $5 \cdot J_{\text{HA-HB}}/2$. The pattern of the map also changes with SLIC duration, although there is a clear indication of an optimal pulse duration (τ_{SLIC}) yielding the global maximum of the produced signal. We note that the spin dynamics is much more complex for 5-spin systems than that for 2-spin systems, but yet relatively easily predictable using density matrix formalism.

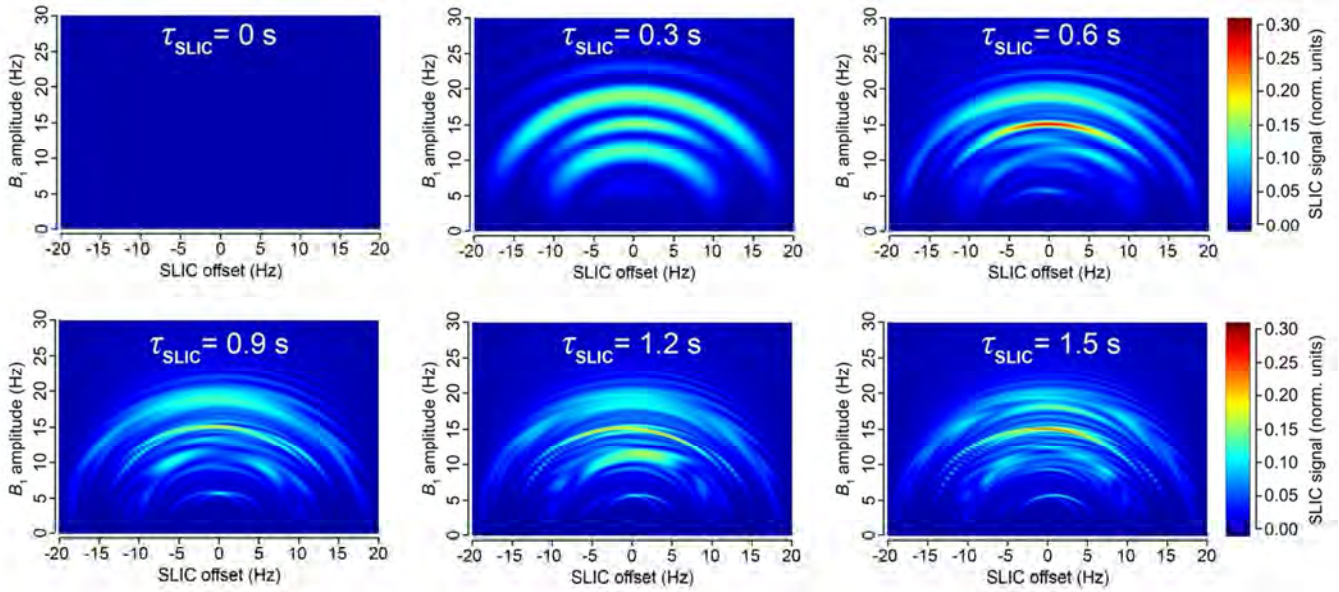

Figure 5. Simulation of ^{1}H NMR signal dependence in -CH_2CH_3 system on SLIC parameters: B_1 amplitude (Hz), pulse offset (Hz) (position of zero offset corresponds to the center frequency between CH_3 and CH_2 resonances) and SLIC pulse duration (τ_{SLIC}). Relaxation effects were not included in the simulation. See Electronic supporting Information (ESI) for animated gif files and the corresponding signal dependences for two-spin system.

Although low-field PHIP hyperpolarizers have been used previously to prepare HP molecules via pairwise *p*-H_2 addition,[43, 49] prior attempts to perform direct ^{1}H NMR signal detection of nascent HP protons resulted in a very weak anti-phase NMR signal.[60] Without SLIC or other singlet-to-magnetization pulse sequences,[61] direct proton detection at low fields is unlikely to yield high SNR to study reaction conversion and pairwise selectivity. Building on our previous experience with SLIC detection of HP propane gas prepared via heterogeneous PHIP,[38] SLIC proton detection of HP liquid was employed in a low magnetic field of 47.5 mT, and the ^{1}H NMR signal obtained was approximately 2 orders of magnitude greater than ^{1}H NMR signal obtained using conventional hard (*i.e.*, short duration and high-amplitude) RF pulses (**Fig. 2c**). To the best of our knowledge, the fact that the action of hard RF pulses on a spin system leads to significantly lower NMR signal than that obtained by low-frequency irradiation is somewhat unique in the field of NMR spectroscopy. Moreover, one can entertain an analogy with a safe, which is hard to open using brute force (*e.g.*, a hammer), but a tiny key with

appropriate symmetry can easily crack the lock. It should also be emphasized that unlike the vast majority of hyperpolarization techniques, where the preparation of singlet states requires additional preparation steps, direct creation of pseudo-singlet states is an inherent and unique feature of the PHIP technique.

By varying the "reaction" time (*i.e.*, the time period that the reaction solution remains in the reactor following the injection), we measured singlet state lifetime (T_S) (Fig. 3c,d). It was found that the NMR signal decays with a time constant of about 5-15 seconds depending on the solvent nature (*i.e*. methanol vs. water) (**Table 1**, ESI). These values indicate that despite the spin systems being in pseudo-singlet states, their lifetimes were not significantly longer compared to T_1-s, *i.e*. they were not several fold greater. This is, however, not surprising, because the existence of long-lived spin states (LLSS) requires specific symmetry properties, which may not be present in the systems studied here.[62-64] One should note, however, that such examples can occur in principle, *e.g*. previously reported long-lived HP propane states.[38, 65] Future studies are certainly warranted to identify other examples of long-lived HP spin states that could find use in biomedical and material science applications.[66]

The efficiency of a singlet-to-magnetization conversion by SLIC may be analysed using the boundary transformation methodology presented by Levitt.[67] In the case of the two-spin system it is possible to "extract" nearly 100% of singlet spin order and transform it into observable magnetization (~91% when using the SLIC pulse sequence). At the same time for a 5-spin system, such as $–CH_2-CH_3$, it is fundamentally possible to transform up to only 55% of spin order (ESI). Our calculations for SLIC show ~27% transformation efficiency (**Fig. 5**), indicating that there could be a more efficient RF pulse-sequence alternative to the SLIC implementation employed here.[68-69] This inefficiency partially explains the relatively low apparent polarization level of ~0.23% obtained for HEP and even lower values for other studied molecules. Other factors that likely had a significant negative impact on the efficiency of SLIC spin transformation include spin relaxation processes and B_0 magnetic field inhomogeneity. Indeed, our calculations show that the efficiency of spin order transfer depends dramatically on the B_1 RF frequency offset (**Fig. 5**). Static B_0 magnetic field drifts and imperfections across the sample can

therefore cause significant shifts away from the optimal transfer conditions, thus, leaving a potentially large fraction of the population hidden in the "dark" unobservable nuclear pseudo-singlet state. The use of more homogeneous B_0 and B_1 fields can likely significantly improve SLIC efficiency and consequently P^{APP} in the future. Strong dependence of singlet-to-magnetization transformation on the magnetic field inhomogeneity is a substantial limitation of the presented SLIC-based low-field detection method.

Simple analysis also determines the limits of the B_0 magnetic field strength, which should be optimal for parahydrogen-based SLIC sensing presented here. First of all, the magnetic field should not be too high (the weakly coupled regime); otherwise, the singlet spin state is no longer an eigenstate of the nuclear spin Hamiltonian. The strong coupling condition can provide a quick estimate of the upper limit of the low magnetic field range, $B_0 < 2\pi J_{\mathrm{HA-HB}}/\gamma\Delta\boldsymbol{\upsilon}$, where γ is the proton gyromagnetic ratio. At the same time, very low magnetic fields can result in prohibitively long SLIC pulse duration (since, generally, $\tau_{\mathrm{SLIC}}\sim 1/\Delta\boldsymbol{\upsilon}$) resulting in significant relaxation losses and/or decoherences during an excessively long SLIC pulse. Thus, the magnetic field of 0.0475 T employed here lies in the "SLIC-safe range" for the studied spin systems, however, the optimal field should be calculated for a particular spin system under study.

We used ^{1}H and ^{13}C high-field (400 MHz) NMR spectroscopy to determine reaction conversion levels by taking aliquots of stock solutions before and after the reaction. One can see that measured conversion values were relatively high for all studied molecules (**Fig. 6**). Lower levels for conversion of **VPy** and **VTMA** (25-40%) compared to nearly 100% conversion for **HEA** and **VA** can be explained by the presence of nitrogen in the former molecules. In case of **VPy**, the electron-donating N-site can potentially compete with the double bond for a binding event to the Rh center, thereby lowering the probability of forming the active catalytic species and, consequently, decreasing reaction yields. For **VTMA**, the nitrogen atom possesses positive charge, which can lead to repulsion of the molecule from the positively charged cationic Rh center due to electrostatic interactions of charged ions. The determined conversion can be compared with the intensity of SLIC signal for the same experiments

(**Fig. 6**). The SLIC signal from reaction products does not linearly correlate with the conversion and decreases in the following order of substrates used in hydrogenation: **HEA** > **VA** > **VTMA** > **VPy**.

One should not find surprising that the different substrates show different SLIC signal. This is a result of different chemical dynamics and pairwise addition behavior in hydrogenation reactions. It is known that the interplay between the substrate and the catalyst is very important and variations of the substrate or catalyst structure that seem insignificant at the first glance, may have drastic consequences on a pairwise addition performance.[70] A good recent example supporting this statement is the homogeneous batch-mode hydrogenation of propylene in methanol using two Rh-based catalysts: $[Rh(COD)(dppb)]BF_4$ and $[Rh(NBD)(dppb)]BF_4$ (where COD = 1,5-cyclooctadiene, NBD = norbornadiene, dppb – 1,4-bis-(diphenylphosphino)-butane).[71] Despite the fact that their structure is very similar and differ only in the structure of the ligand, PHIP effects observed for propane are 3-8 times higher when the latter catalyst is used. While non-correspondence between the conversion and the SLIC signal can be treated as a disadvantage for a general applicability of the presented method for low-field monitoring of hydrogenation reactions, this observation is advantageous for probing the pairwise nature of p-H_2 addition (*i.e.*, reaction selectivity) for HP NMR and MRI. This means that large libraries of compounds can be screened to identify promising candidates for PHIP HP contrast agents and for optimization of PHIP processes and hyperpolarization equipment. Moreover, since such selectivity probing does not require chemical shift dispersion (which is generally lacking at low magnetic fields), the low-field NMR modality presented here can be used to monitor the production of HP products in larger, more complex reactors operating with high pressures and temperatures; for example, the reactor used here already operated at >17 atm of gas pressure, and >55 °C. We foresee that low-field NMR (and MRI) of large-scale industrial hydrogenation processes—hydrogenation of vegetable oils, hydrodesulfurization of petroleum and other large-scale applications of hydrogenation in the industry—can become a useful spectroscopic and imaging tool.

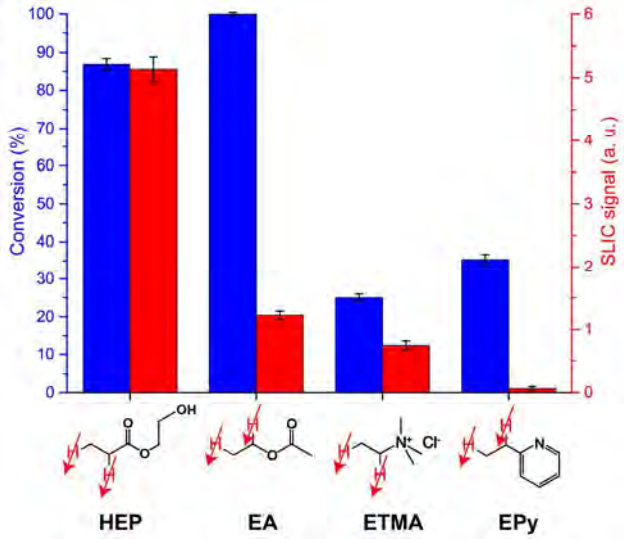

Figure 6. Hydrogenation reaction conversion and SLIC signal (normalized to the signal of the solvent) for substrates in water. Conversion was measured using high-resolution high-field ^{1}H 400MHz NMR of aliquots before and after the reaction.

Conclusions

In conclusion, we have shown that low-field NMR and low amplitude RF irradiation termed spin-lock induced crossing (SLIC) can be used to detect the signal originating from HP molecules produced via hydrogenation reactions with *p*-H_2. Signal enhancement of more than 10000 allowed detecting the build-up and decay of HP reaction products upon hydrogenation of several organic molecules (2-hydroxyethyl acrylate, vinyl acetate, 2-vinylpyridine, (vinyl)trimethylammonium chloride). Moreover, since the signal from ≤ 80 mM HP reaction products was significantly greater than the signal of thermally polarized solvents, direct proton detection was demonstrated in protonated solvents such as methanol and water, which can provide a significant potential application for molecular sensing of industrial scale processes in the presence of large concentrations of background species. While it was shown that chemical conversion and SLIC signal are not directly correlated, this finding can be very useful for quick analysis of selectivity of hydrogen addition in catalysis, and for production of HP contrast agents by PHIP technique: *i.e.* despite the efficient overall hydrogenation, some compounds may exhibit lower degree of *p*-H_2 pairwise addition. Moreover, the presented method allows for a quality assurance of the HP state of the molecules before performing experiments with more expensive isotopically enriched (*e.g.*, ^{13}C) compounds[29, 72] using polarization transfer schemes. Lastly, we showed that spin dynamics during the SLIC pulse for five-spin systems (*e.g.*, molecules such as presented here, containing CH_3-CH_2- moiety) is much more complex than SLIC for 2-spin systems. However, it is possible to adequately predict optimal detection parameters, such as B_1 amplitude, offset and SLIC time. Low-field NMR signals are generally far less sensitive to susceptibility-induced magnetic field gradients (because these gradients scale linearly with B_0 strength), which is a useful property for studies of heterogeneous reactions (*e.g.* liquid/gas, liquid/solid, gas/solid) frequently practiced in industrial hydrogenation processes. Combined with greater penetration depth, which also scales inversely with B_0, low-field SLIC sensing may potentially provide a complementary analytical technology for analysis of hydrogenation reactions on a large scale.

Supporting Information

Supporting Information Available. It includes additional experimental details and theoretical calculations for singlet-to-magnetization conversion efficiency.

Acknowledgments.

This work was supported by NIH 1R21EB018014, 1R21EB020323 and 1F32EB021840, NSF CHE-1416268 and CHE-1416432, DOD CDMRP W81XWH-12-1-0159/BC112431 and W81XWH-15-1-0271, ExxonMobil Research and Engineering Company. The Russian team thank the Russian Science Foundation (grant 14–35–00020) for support of the hydrogenation experiments.

References

1. Ernst, R. Nuclear Magnetic Resonance Fourier Transform Spectroscopy (Nobel Lecture). *Angew. Chem. Int. Ed.* **1992,** *31*, 805-823.

2. Zalesskiy, S.; Danieli, E.; Bluemich, B.; Ananikov, V. Miniaturization of NMR Systems: Desktop Spectrometers, Microcoil Spectroscopy, and "NMR on a Chip" for Chemistry, Biochemistry, and Industry. *Chem. Rev.* **2014,** *114*, 5641-5694.

3. Gladden, L. Magnetic Resonance in Reaction Engineering: Beyond Spectroscopy. *Curr. Opin. Chem. Eng.* **2013,** *2*, 331-337.

4. Ardenkjaer-Larsen, J.; Boebinger, G.; Comment, A.; Duckett, S.; Edison, A.; Engelke, F.; Griesinger, C.; Griffin, R.; Hilty, C.; Maeda, H., et al. Facing and Overcoming Sensitivity Challenges in Biomolecular NMR Spectroscopy. *Angew. Chem. Int. Ed.* **2015,** *54*, 9162-9185.

5. Green, R.; Adams, R.; Duckett, S.; Mewis, R.; Williamson, D.; Green, G. The Theory and Practice of Hyperpolarization in Magnetic Resonance Using Parahydrogen. *Prog. Nucl. Magn. Reson. Spectrosc.* **2012,** *67*, 1-48.

6. Ardenkjaer-Larsen, J.; Fridlund, B.; Gram, A.; Hansson, G.; Hansson, L.; Lerche, M.; Servin, R.; Thaning, M.; Golman, K. Increase in Signal-to-noise Ratio of > 10,000 Times in Liquid-state NMR. *Proc. Natl. Acad. Sci. USA* **2003,** *100*, 10158-10163.

7. Goodson, B. Nuclear Magnetic Resonance of Laser-polarized Noble Gases in Molecules, Materials, and Organisms. *J. Magn. Reson.* **2002,** *155*, 157-216.

8. Nikolaou, P.; Goodson, B.; Chekmenev, E. NMR Hyperpolarization Techniques for Biomedicine. *Chem. Eur. J.* **2015,** *21*, 3156-3166.

9. Natterer, J.; Bargon, J. Parahydrogen Induced Polarization. *Prog. Nucl. Magn. Reson. Spectrosc.* **1997,** *31*, 293-315.

10. Kovtunov, K.; Zhivonitko, V.; Skovpin, I.; Barskiy, D.; Koptyug, I. Parahydrogen-Induced Polarization in Heterogeneous Catalytic Processes. *Top. Curr. Chem.* **2013,** *338*, 123-180.

11. Bowers, C.; Weitekamp, D. Parahydrogen and Synthesis Allow Drammatically Enhanced Nuclear Alignment. *J. Am. Chem. Soc.* **1987,** *109*, 5541-5542.

12. Nikolaou, P.; Coffey, A.; Barlow, M.; Rosen, M.; Goodson, B.; Chekmenev, E. Temperature-Ramped Xe-129 Spin-Exchange Optical Pumping. *Anal. Chem.* **2014,** *86*, 8206-8212.

13. Kurhanewicz, J.; Vigneron, D.; Brindle, K.; Chekmenev, E.; Comment, A.; Cunningham, C.; DeBerardinis, R.; Green, G.; Leach, M.; Rajan, S., et al. Analysis of Cancer Metabolism by Imaging Hyperpolarized Nuclei: Prospects for Translation to Clinical Research. *Neoplasia* **2011,** *13*, 81-97.

14. Ardenkjaer-Larsen, J. On the Present and Future of Dissolution-DNP. *J. Magn. Reson.* **2016,** *264*, 3-12.

15. Harzstark, A.; Weinberg, V.; Grycz, K.; Hurd, R.; Ardenkjaer-Larsen, J.; Murray, J.; Chen, A.; Ferrone, M.; Park, I.; Reed, G., et al. A First-in-human Phase I Imaging Study Using Hyperpolarized (1)C-13 Pyruvate (H-Py) in Patients (Pts) With Localized Prostate Cancer (I-PCa). *J. Clin. Oncol.* **2012,** *30*.

16. Nelson, S.; Kurhanewicz, J.; Vigneron, D.; Larson, P.; Harzstark, A.; Ferrone, M.; van Criekinge, M.; Chang, J.; Bok, R.; Park, I., et al. Metabolic Imaging of Patients with Prostate Cancer Using Hyperpolarized [1-C-13]Pyruvate. *Sci. Transl. Med.* **2013,** *5*, 198ra108.

17. Mugler, J.; Altes, T. Hyperpolarized 129Xe MRI of the Human Lung. *J. Magn. Reson. Imaging* **2013,** *37*, 313-331.

18. Shchepin, R.; Barskiy, D.; Coffey, A.; Manzanera Esteve, I.; Chekmenev, E. Efficient Synthesis of Molecular Precursors for Para-Hydrogen-Induced Polarization of Ethyl Acetate-1-13C and Beyond. *Angew. Chem. Int. Ed.* **2016,** *55*, 6071-6074.

19. Reineri, F.; Boi, T.; Aime, S. Parahydrogen-Induced Polarization of C-13 Carboxylate Resonance in Acetate and Pyruvate. *Nat. Commun.* **2015,** *6*, 5858.

20. Shchepin, R.; Coffey, A.; Waddell, K.; Chekmenev, E. Parahydrogen Induced Polarization of 1-C-13-Phospholactate-d(2) for Biomedical Imaging with > 30,000,000-fold NMR Signal Enhancement in Water. *Anal. Chem.* **2014,** *86*, 5601-5605.

21. Glöggler, S.; Grunfeld, A. M.; Ertas, Y. N.; McCormick, J.; Wagner, S.; Schleker, P. P. M.; Bouchard, L. S. A Nanoparticle Catalyst for Heterogeneous Phase Para-Hydrogen-Induced Polarization in Water. *Angew. Chem. Int. Ed.* **2015,** *54*, 2452-2456.

22. Bhattacharya, P.; Harris, K.; Lin, A.; Mansson, M.; Norton, V. A.; Perman, W.; Weitekamp, D. P.; Ross, B. D. Ultra-fast Three Dimensional Imaging of Hyperpolarized 13C In Vivo. *Magn. Reson. Mater. Phy.* **2005,** *18*, 245-256.

23. Lysova, A.; Koptyug, I. Magnetic Resonance Imaging Methods for In Situ Studies in Heterogeneous Catalysis. *Chem. Soc. Rev.* **2010,** *39*, 4585-4601.

24. Barskiy, D.; Kovtunov, K.; Koptyug, I.; He, P.; Groome, K.; Best, Q.; Shi, F.; Goodson, B.; Shchepin, R.; Truong, M., et al. In Situ and Ex Situ Low-Field NMR Spectroscopy and MRI Endowed by SABRE Hyperpolarization. *ChemPhysChem* **2014,** *15*, 4100-4107.

25. Ramachandran, R.; Menon, R. K. An Overview of Industrial Uses of Hydrogen. *Int. J. Hydrogen Energy* **1998,** *23*, 593-598.

26. Blumich, B.; Casanova, F.; Appelt, S. NMR at Low Magnetic Fields. *Chem. Phys. Lett.* **2009,** *477*, 231-240.

27. Gong, Q.; Gordji-Nejad, A.; Blumich, B.; Appelt, S. Trace Analysis by Low-Field NMR: Breaking the Sensitivity Limit. *Anal. Chem.* **2010,** *82*, 7078-7082.

28. Gloggler, S.; Blumich, B.; Appelt, S.; Heise, H.; Matthews, S. NMR Spectroscopy for Chemical Analysis at Low Magnetic Fields. *Top. Curr. Chem.* **2013,** *335*, 1-22.

29. Bhattacharya, P.; Chekmenev, E.; Reynolds, W.; Wagner, S.; Zacharias, N.; Chan, H.; Bunger, R.; Ross, B. Parahydrogen-Induced Polarization (PHIP) Hyperpolarized MR Receptor Imaging In Vivo: a Pilot Study of C-13 Imaging of Atheroma in Mice. *NMR Biomed.* **2011,** *24*, 1023-1028.

30. Hovener, J.; Schwaderlapp, N.; Lickert, T.; Duckett, S.; Mewis, R.; Highton, L.; Kenny, S.; Green, G.; Leibfritz, D.; Korvink, J., et al. A Hyperpolarized Equilibrium for Magnetic Resonance. *Nat. Commun.* **2013,** *4*.

31. Suefke, M.; Liebisch, A.; Blumich, B.; Appelt, S. External High-quality-factor Resonator Tunes Up Nuclear Magnetic Resonance. *Nat. Phys.* **2015,** *11*, 767-771.

32. Coffey, A.; Truong, M.; Chekmenev, E. Low-field MRI Can Be More Sensitive Than High-field MRI. *J. Magn. Reson.* **2013,** *237*, 169-174.

33. Hovener, J.; Schwaderlapp, N.; Borowiak, R.; Lickert, T.; Duckett, S.; Mewis, R.; Adams, R.; Burns, M.; Highton, L.; Green, G., et al. Toward Biocompatible Nuclear Hyperpolarization Using Signal Amplification by Reversible Exchange: Quantitative In Situ Spectroscopy and High-Field Imaging. *Anal. Chem.* **2014,** *86*, 1767-1774.

34. Ruset, I.; Tsai, L.; Mair, R.; Patz, S.; Hrovat, M.; Rosen, M.; Muradian, I.; Ng, J.; Topulos, G.; Butler, J. A System for Open-access 3He Human Lung Imaging at Very Low Field. *Concepts Magn. Reson. B* **2006,** *29*, 210-221.

35. Singlet and triplet spin states are eigenstates of the nuclear spin Hamiltonian for a two-spin system in the condition of strong coupling regime (sometimes referred to as inverse weak coupling regime). However, for multi-spin systems (e.g., a five-spin systems studied here) versus two-spin systems, this "singlet-triplet" terminology is applicable only in qualitative terms, but it is still quite illustrative: indeed, at the magnetic field of 0.0475 T, the methyl and methylene proton spins of the studied molecular systems are strongly coupled and essentially represent a system of five almost magnetically equivalent spins. This is why we use the term "pseudo-singlet state" to describe the nuclear state of the of the $–CH_2CH_3$ system populated after molecular addition of p-H_2 to the unsaturated precursor.

36. Olaru, A. M.; Roy, S. S.; Lloyd, L. S.; Coombes, S.; Green, G. G. R.; Duckett, S. B. Creating a Hyperpolarised Pseudo Singlet State Through Polarisation Transfer From Parahydrogen Under SABRE. *Chem. Commun.* **2016,** *52*, 7842-7845.

37. Ratajczyk, T.; Gutmann, T.; Dillenberger, S.; Abdulhussaein, S.; Frydel, J.; Breitzke, H.; Bommerich, U.; Trantzschel, T.; Bernarding, J.; Magusin, P. C., et al. Time Domain Parahydrogen Induced Polarization. *Solid State Nucl. Magn. Reson.* **2012,** *43*, 14-21.

38. Kovtunov, K.; Truong, M.; Barskiy, D.; Koptyug, I.; Coffey, A.; Waddell, K.; Chekmenev, E. Long-Lived Spin States for Low-field Hyperpolarized Gas MRI. *Chem. Eur. J.* **2014,** *20*, 14629-32.

39. Prina, I.; Buljubasich, L.; Acosta, R. Parahydrogen Discriminated PHIP at Low Magnetic Fields. *J. Magn. Reson.* **2015,** *251*, 1-7.

40. DeVience, S.; Walsworth, R.; Rosen, M. Preparation of Nuclear Spin Singlet States Using Spin-Lock Induced Crossing. *Phys. Rev. Lett.* **2013,** *111*, 173002.

41. Coffey, A.; Kovtunov, K.; Barskiy, D.; Koptyug, I.; Shchepin, R.; Waddell, K.; He, P.; Groome, K.; Best, Q.; Shi, F., et al. High-Resolution Low-Field Molecular Magnetic Resonance Imaging of Hyperpolarized Liquids. *Anal. Chem.* **2014,** *86*, 9042-9049.

42. Coffey, A.; Shchepin, R.; Truong, M.; Wilkens, K.; Pham, W.; Chekmenev, E. An Open-Source Automated Parahydrogen Hyperpolarizer for Molecular Imaging Using 13C Metabolic Contrast Agents. *Anal. Chem.* **2016,** *88*, 8279–8288.

43. Waddell, K.; Coffey, A.; Chekmenev, E. In Situ Detection of PHIP at 48 mT: Demonstration Using a Centrally Controlled Polarizer. *J. Am. Chem. Soc.* **2011,** *133*, 97-101.

44. Coffey, A.; Shchepin, R.; Wilkens, K.; Waddell, K.; Chekmenev, E. A Large Volume Double Channel H-1-X RF Probe for Hyperpolarized Magnetic Resonance at 0.0475 T. *J. Magn. Reson.* **2012,** *220*, 94-101.

45. Jiang, W.; Lumata, L.; Chen, W.; Zhang, S.; Kovacs, Z.; Sherry, A. D.; Khemtong, C. Hyperpolarized 15N-pyridine Derivatives as pH-sensitive MRI Agents. *Sci. Rep.* **2014,** *5*, 9104-9104.

46. Kurhanewicz, J.; Vigneron, D. B.; Hricak, H.; Narayan, P.; Carroll, P.; Nelson, S. J. Three-dimensional H-1 MR Spectroscopic Imaging of the In Situ Human Prostate With High (0.24-0.7-cm3) Spatial Resolution. *Radiology* **1996,** *198*, 795-805.

47. Gillies, R. J.; Morse, D. L. In vivo magnetic resonance spectroscopy in cancer. *Annu. Rev. Biomed. Eng.* **2005,** *7*, 287-326.

48. Eliyahu, G.; Kreizman, T.; Degani, H. Phosphocholine as a Biomarker of Breast Cancer: Molecular and Biochemical Studies. *Int. J. Cancer* **2007,** *120*, 1721-1730.

49. Goldman, M.; Johannesson, H.; Axelsson, O.; Karlsson, M. Design and Implementation of C-13 Hyperpolarization from Parahydrogen, for New MRI Contrast Agents. *C. R. Chim.* **2006,** *9*, 357-363.

50. Golman, K.; Axelsson, O.; Johannesson, H.; Mansson, S.; Olofsson, C.; Petersson, J. Parahydrogen-Induced Polarization in Imaging: Subsecond C-13 Angiography. *Magn. Reson. Med.* **2001,** *46*, 1-5.

51. Truong, M.; Shi, F.; He, P.; Yuan, B.; Plunkett, K.; Coffey, A.; Shchepin, R.; Barskiy, D.; Kovtunov, K.; Koptyug, I., et al. Irreversible Catalyst Activation Enables Hyperpolarization and Water Solubility for NMR Signal Amplification by Reversible Exchange. *J. Phys. Chem. B* **2014,** *118*, 13882-13889.

52. Levitt, M. *Spin Dynamics: Basics of Nuclear Magnetic Resonance*. John Wiley & Sons: 2001.

53. Bowers, C.; Weitekamp, D. Transformation of Symmetrization Order to Nuclear Spin Magnetization by Chemical Reaction and Nuclear Magnetic Resonance. *Phys. Rev. Lett.* **1986,** *57*, 2645-2648.

54. Eisenschmid, T.; Kirss, R.; Deutsch, P.; Hommeltoft, S.; Eisenberg, R.; Bargon, J.; Lawler, R.; Balch, A. Parahydrogen Induced Polarization in Hydrogenation Reactions. *J. Am. Chem. Soc.* **1987,** *109*, 8089-8091.

55. Appelt, S.; Hasing, F.; Sieling, U.; Gordji-Nejad, A.; Gloggler, S.; Blumich, B. Paths from Weak to Strong Coupling in NMR. *Phys. Rev. A* **2010,** *81*, 023420.

56. Colell, J.; Turschmann, P.; Gloggler, S.; Schleker, P.; Theis, T.; Ledbetter, M.; Budker, D.; Pines, A.; Blumich, B.; Appelt, S. Fundamental Aspects of Parahydrogen Enhanced Low-Field Nuclear Magnetic Resonance. *Phys. Rev. Lett.* **2013,** *110*.

57. Turschmann, P.; Colell, J.; Theis, T.; Blumich, B.; Appelt, S. Analysis of Parahydrogen Polarized Spin System in Low Magnetic Fields. *Phys. Chem. Chem. Phys.* **2014,** *16*, 15411-15421.

58. Bernarding, J.; Buntkowsky, G.; Macholl, S.; Hartwig, S.; Burghoff, M.; Trahms, L. J-coupling Nuclear Magnetic Resonance Spectroscopy of Liquids in nT Fields. *J. Am. Chem. Soc.* **2006,** *128*, 714-715.

59. DeVience, S.; Walsworth, R.; Rosen, M. Probing Scalar Coupling Differences via Long-Lived Singlet States. *J. Magn. Reson.* **2016,** *262*, 42-49.

60. Kovtunov, K.; Barskiy, D.; Shchepin, R.; Coffey, A.; Waddell, K.; Koptyug, I.; Chekmenev, E. Demonstration of Heterogeneous Parahydrogen Induced Polarization Using Hyperpolarized Agent Migration from Dissolved Rh(I) Complex to Gas Phase. *Anal. Chem.* **2014,** *86*, 6192-6.

61. Tayler, M.; Levitt, M. Singlet Nuclear Magnetic Resonance of Nearly-Equivalent Spins. *Phys. Chem. Chem. Phys.* **2011,** *13*, 5556-60.

62. Levitt, M. Singlet Nuclear Magnetic Resonance. *Annu. Rev. Phys. Chem.* **2012,** *63*, 89-105.

63. Vinogradov, E.; Grant, A. K. Long-Lived States in Solution NMR: Selection Rules for Intramolecular Dipolar Relaxation in Low Magnetic Fields. *J. Magn. Reson.* **2007,** *188*, 176-182.

64. Stevanato, G.; Roy, S. S.; Hill-Cousins, J.; Kuprov, I.; Brown, L. J.; Brown, R. C.; Pileio, G.; Levitt, M. H. Long-Lived Nuclear Spin States Far from Magnetic Equivalence. *Phys. Chem. Chem. Phys.* **2015,** *17*, 5913-5922.

65. Kovtunov, K.; Truong, M.; Barskiy, D.; Salnikov, O.; Bukhtiyarov, V.; Coffey, A.; Waddell, K.; Koptyug, I.; Chekmenev, E. Propane-d(6) Heterogeneously Hyperpolarized by Parahydrogen. *J. Phys. Chem. C* **2014,** *118*, 28234-28243.

66. Zhang, Y.; Duan, X.; Soon, P. C.; Sychrovský, V.; Canary, J. W.; Jerschow, A. Limits in Proton Nuclear Singlet-State Lifetimes Measured with Para-Hydrogen-Induced Polarization. *ChemPhysChem* **2016**.

67. Levitt, M. Symmetry Constraints on Spin Dynamics: Application to Hyperpolarized NMR. *J. Magn. Reson.* **2016,** *262*, 91-99.

68. Theis, T.; Feng, Y.; Wu, T.-l.; Warren, W. S. Composite and Shaped Pulses for Efficient and Robust Pumping of Disconnected Eigenstates in Magnetic Resonance. *J. Chem. Phys.* **2014,** *140*, 014201.

69. Pravdivtsev, A. N.; Kiryutin, A. S.; Yurkovskaya, A. V.; Vieth, H.-M.; Ivanov, K. L. Robust Conversion of Singlet Spin Order in Coupled Spin-1/2 Pairs by Adiabatically Switched RF-fields. *arXiv:1607.00539* **2016**.

70. Reineri, F.; Aime, S.; Gobetto, R.; Nervi, C. Role of the Reaction Intermediates in Determining PHIP (Parahydrogen Induced Polarization) Effect in the Hydrogenation of Acetylene Dicarboxylic Acid With the Complex [Rh(dppb)](+) (dppb: 1,4-bis(diphenylphosphino)butane). *J. Chem. Phys.* **2014,** *140*, 094307.

71. Salnikov, O. G.; Barskiy, D. A.; Coffey, A. M.; Kovtunov, K. V.; Koptyug, I. V.; Chekmenev, E. Y. Efficient Batch-Mode Parahydrogen-Induced Polarization of Propane. *ChemPhysChem* **2016**, DOI: 10.1002/cphc.201600564.

72. Bhattacharya, P.; Chekmenev, E.; Perman, W.; Harris, K.; Lin, A.; Norton, V.; Tan, C.; Ross, B.; Weitekamp, D. Towards Hyperpolarized C-13-succinate Imaging of Brain Cancer. *J. Magn. Reson.* **2007,** *186*, 150-155.

TOC Graphics

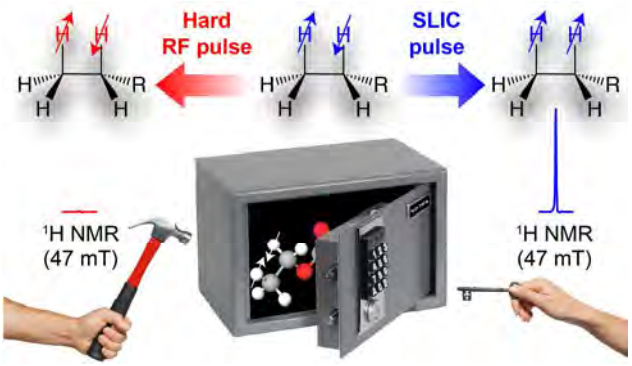

a

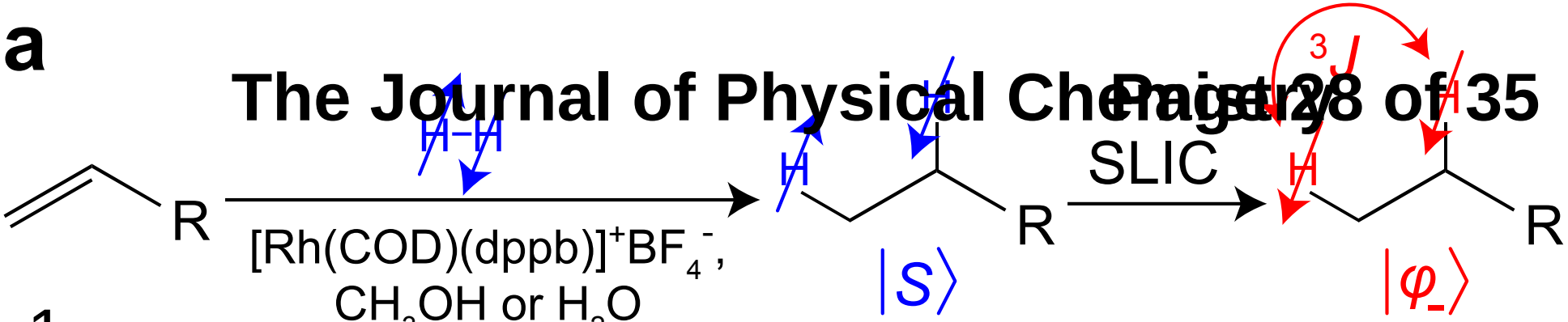

b

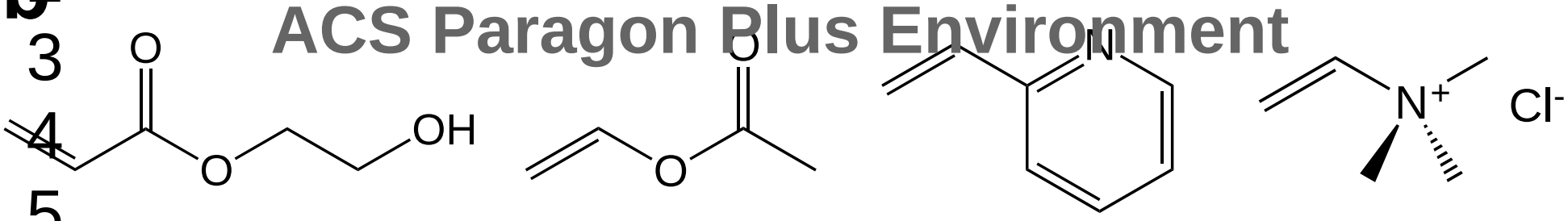

ACS Paragon Plus Environment

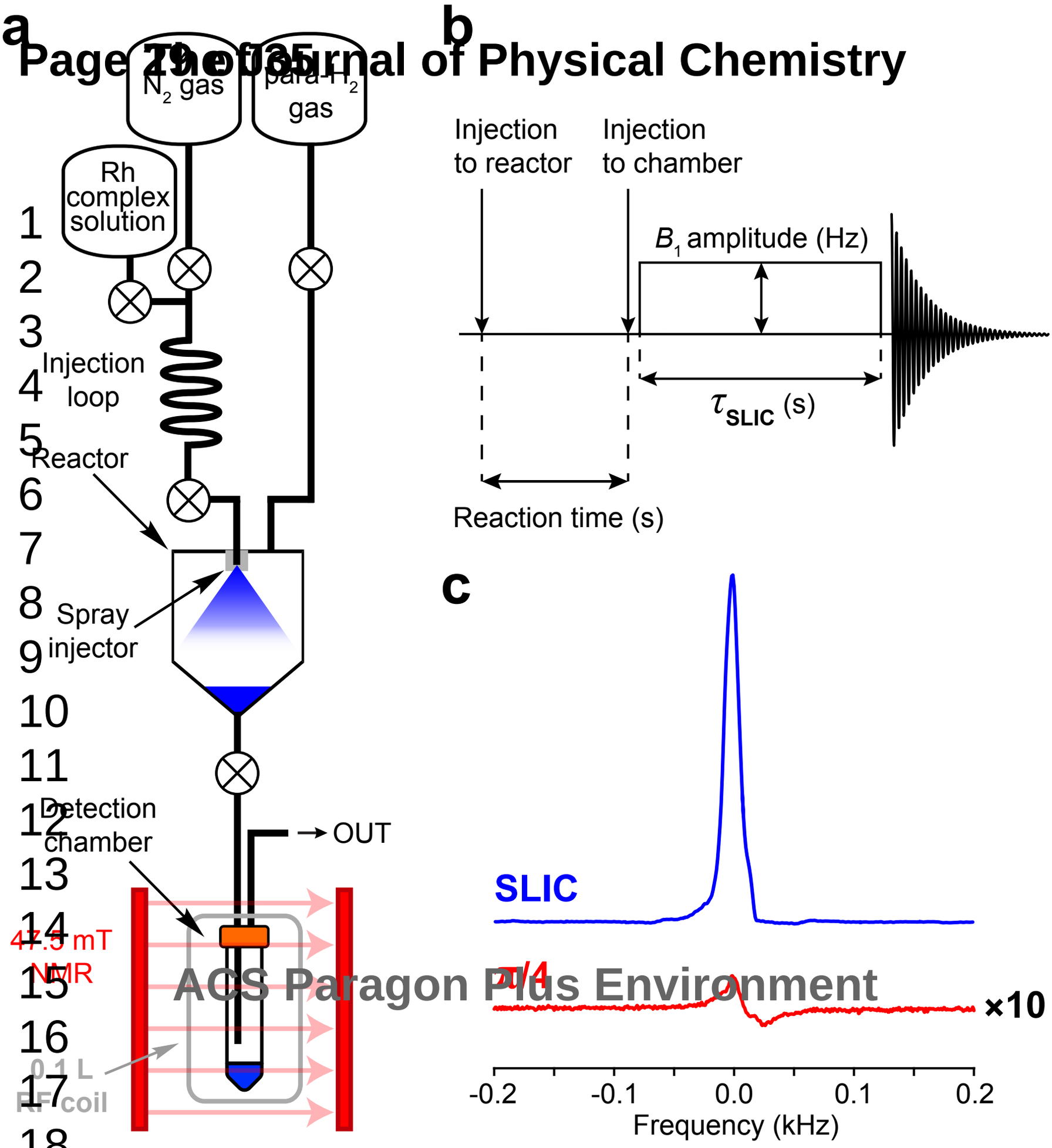

ACS Paragon Plus Environment

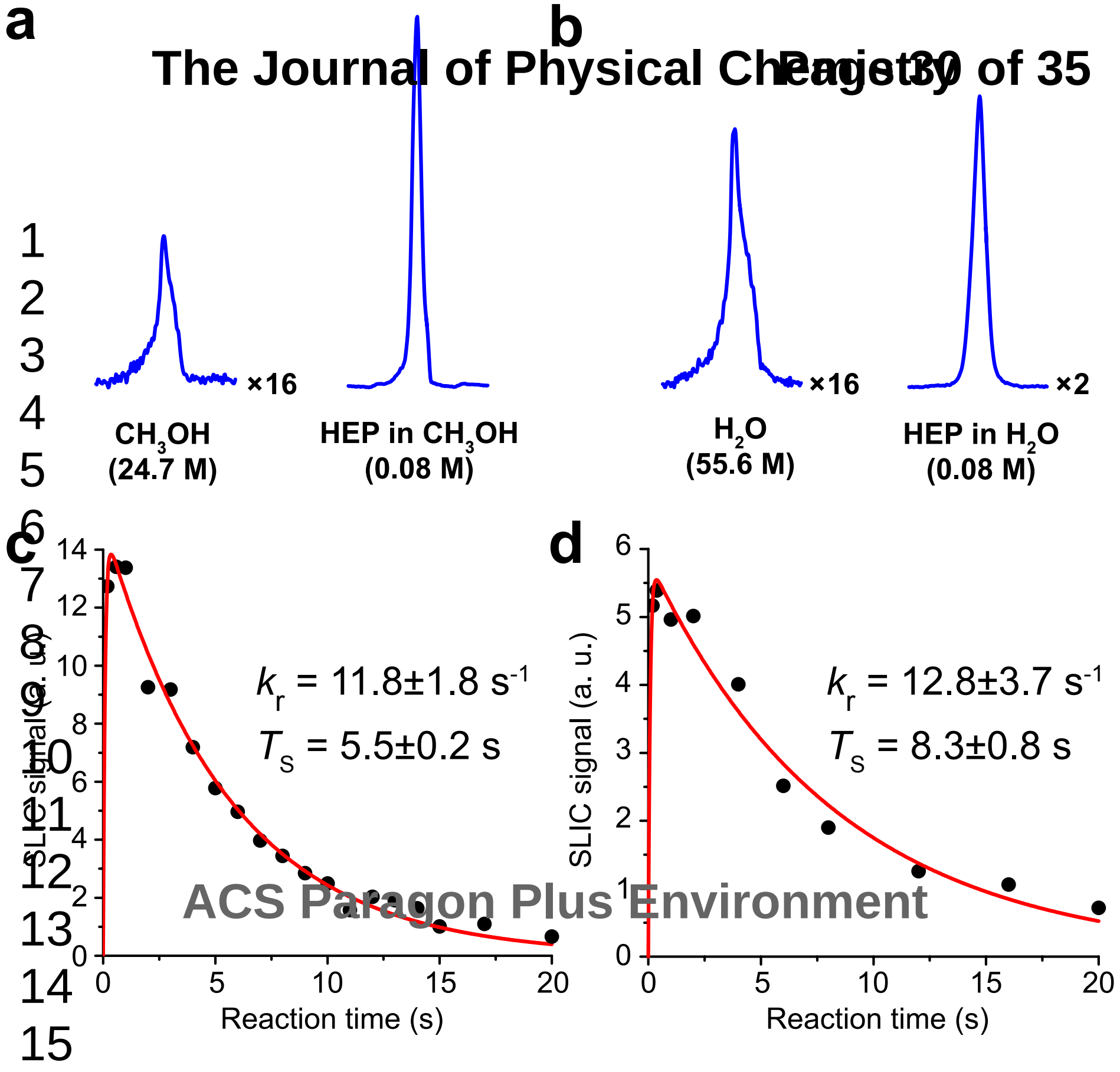

ACS Paragon Plus Environment

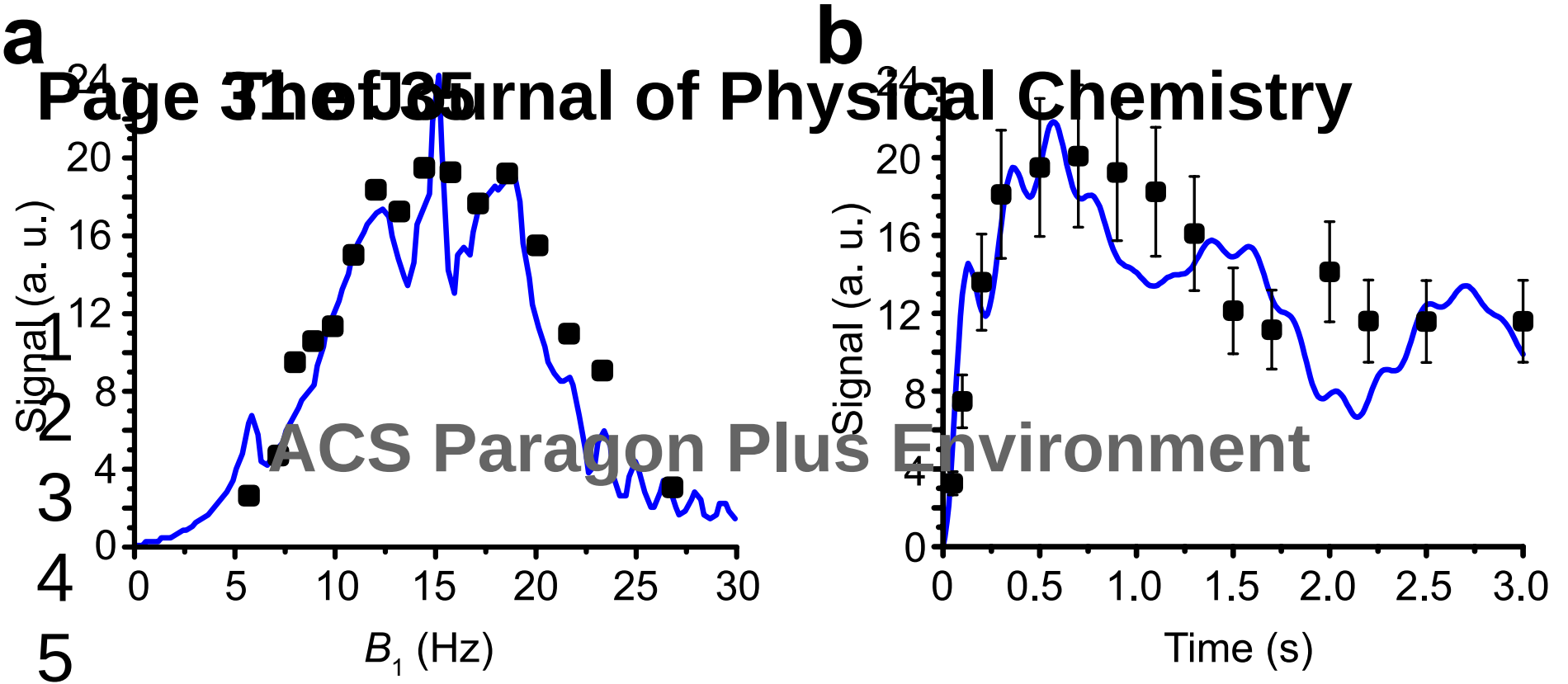

ACS Paragon Plus Environment

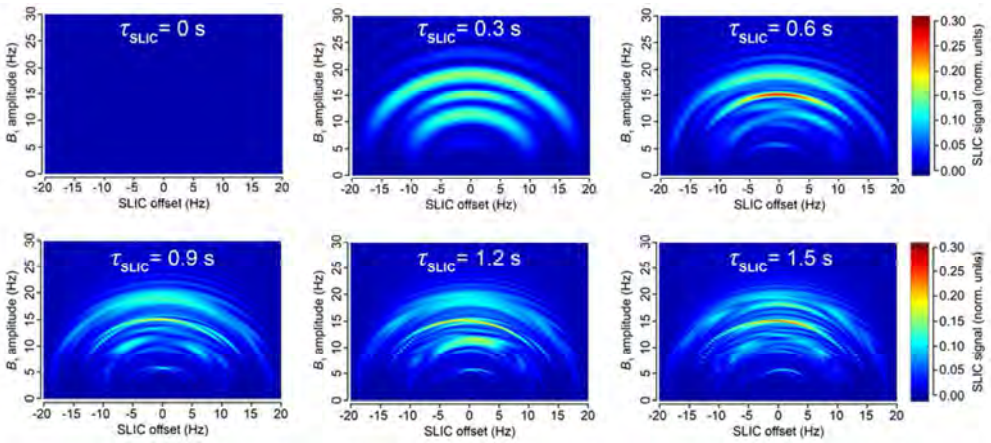

78x34mm (300 x 300 DPI)

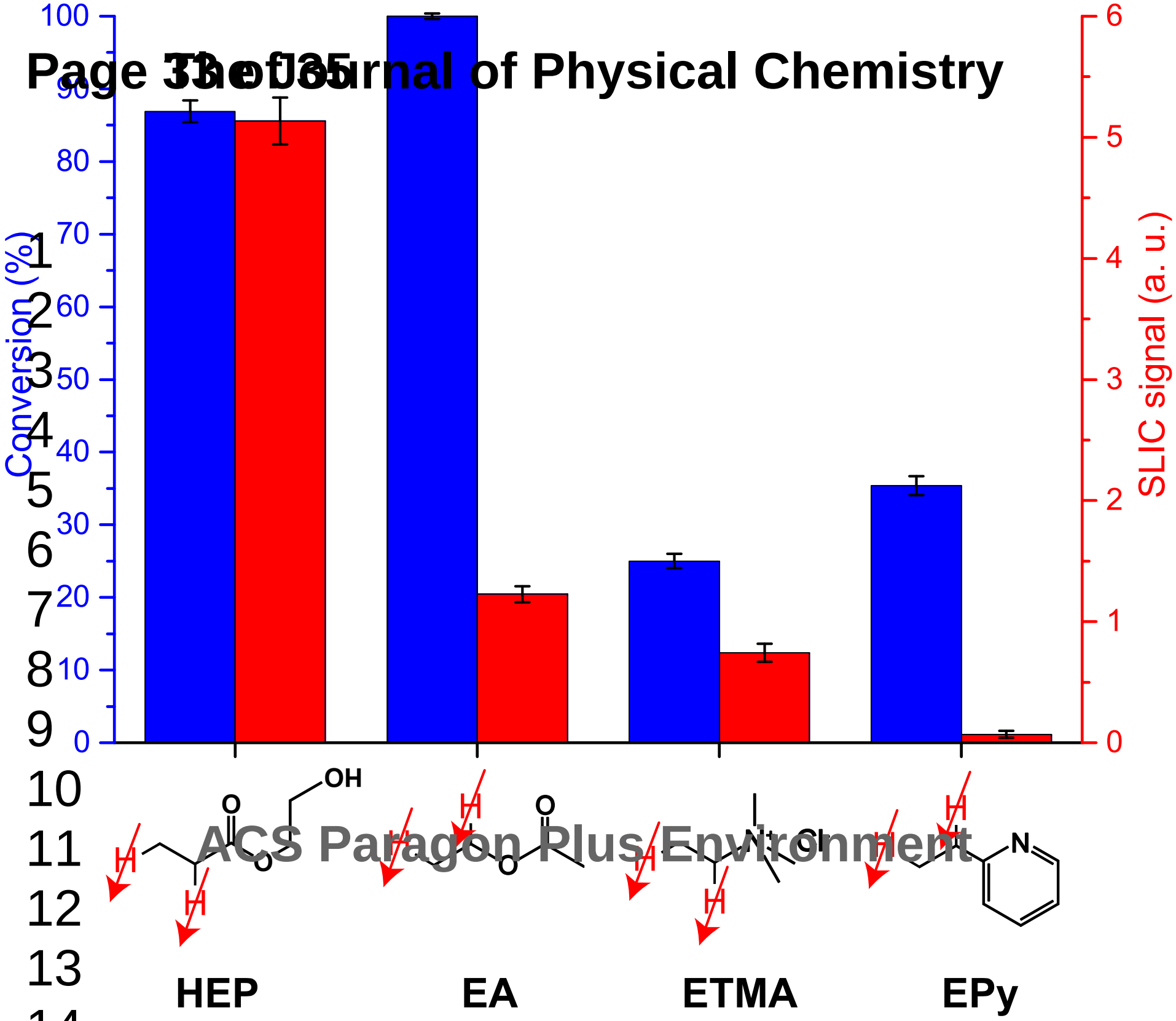

ACS Paragon Plus Environment

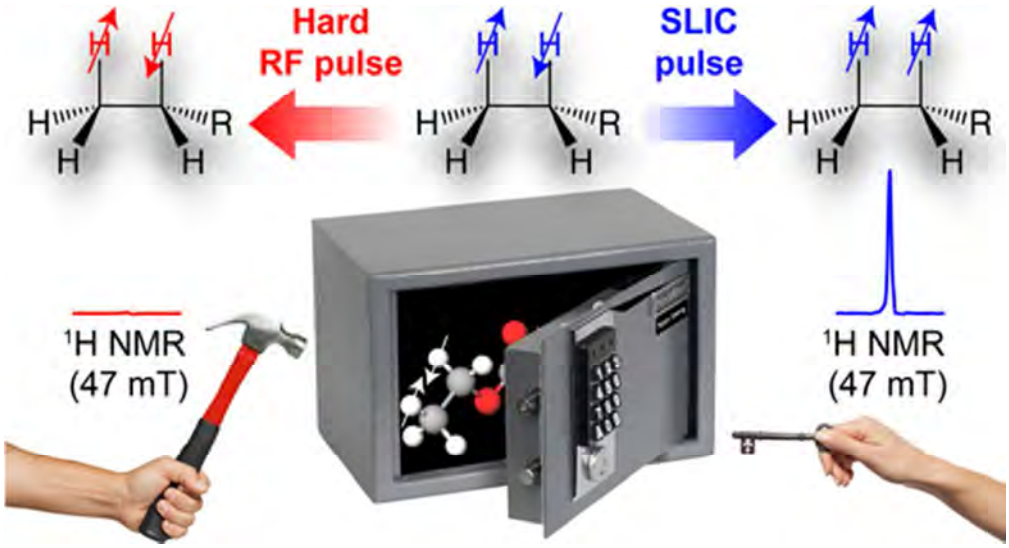

Table of Content graphic

44x23mm (300 x 300 DPI)

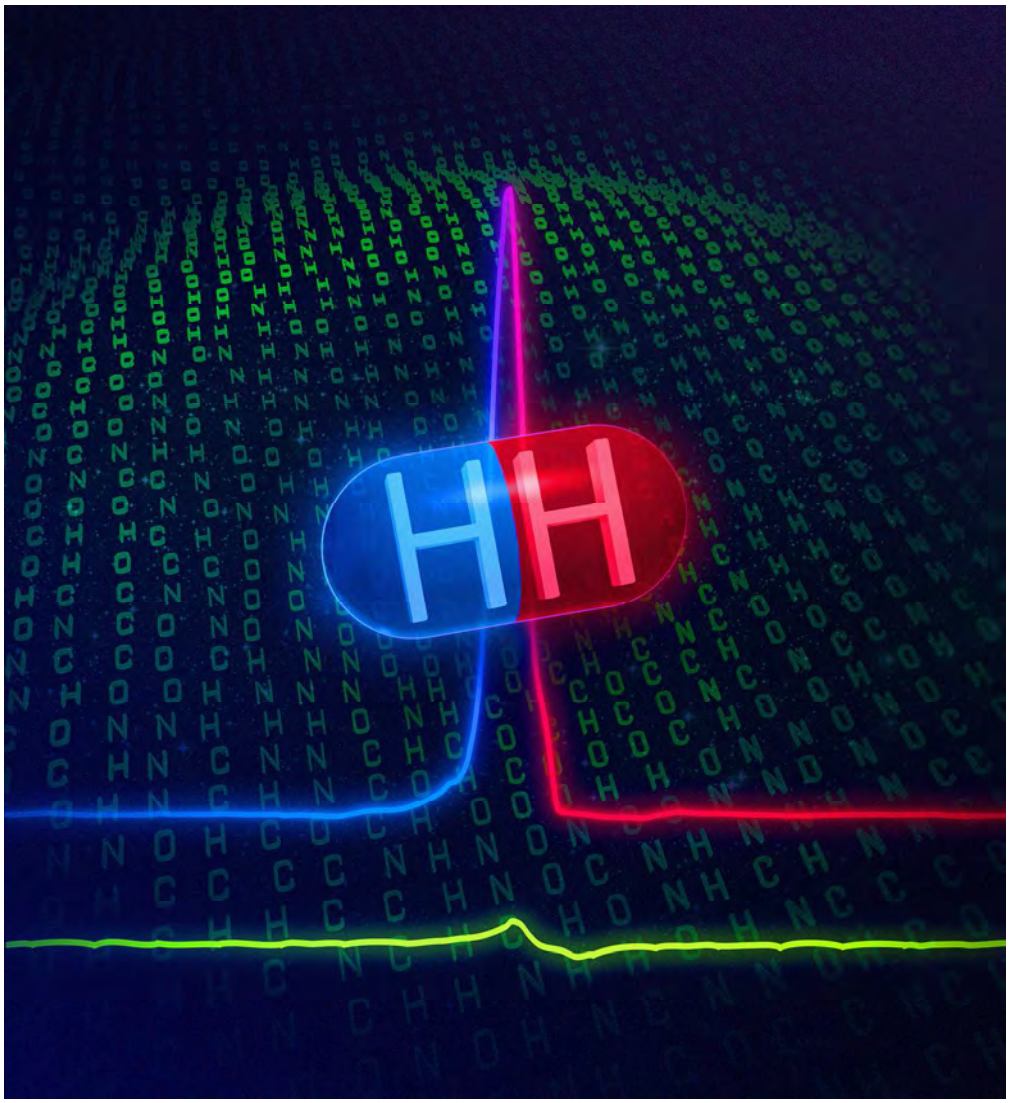

Journal Cover artwork

169x184mm (300 x 300 DPI)

Understanding the interplay between the chemical kinetics and the nuclear spin dynamics for the efficient hyperpolarization by PHIP and SABRE techniques

Danila A. Barskiy[1], Andrey N. Pravdivtsev[2,3], Konstantin L. Ivanov[2,3], Oleg G. Salnikov[2,3], Kirill V. Kovtunov[2,3], Igor V. Koptyug[2,3], Roman V. Shchepin[1], Aaron M. Coffey[1], Eduard Y. Chekmenev[1]

[1]Vanderbilt University Institute of Imaging Science (VUIIS), 1161 21st Avenue South, Medical Center North, AA-1105, Nashville, TN 37232-2310, USA

[2]International Tomography Center, 3A Institutskaya st., Novosibirsk 630090, Russia
[3]Novosibirsk State University, 2 Pirogova st., Novosibirsk 630090, Russia

Parahydrogen-induced polarization (PHIP) and signal amplification by reversible exchange (SABRE) are powerful nuclear spin hyperpolarization techniques which are able to increase NMR signal intensity by several orders of magnitude compared to thermally polarized samples [1-3]. PHIP and SABRE are fast and inexpensive means to boost the sensitivity of heteronuclear detection (e.g. ^{13}C, ^{15}N, ^{31}P) when using various polarization transfer schemes from parahydrogen. While the major theoretical aspects of PHIP and SABRE are well understood (more often relying on the magnetic field dependence of polarization transfer efficiency), the polarization dependence on the chemical system parameters (such as concentrations, reaction rate constants etc.) still remains unclear.

Here we show that relatively simple approach which relies on the introduction of so called "hyperpolarized species" may be used for a combined analysis of chemical kinetics and evolution of the hyperpolarized nuclear spin system. By using this analysis, we have demonstrated the analytical formula for the description of the signal enhancement (ε) in the SABRE process:

$$|\varepsilon| = \eta\left(\frac{4x_p-1}{3}\right)\frac{[\mathrm{C}][\mathrm{H}_2]}{[\mathrm{S}]^2}\frac{\lambda k_{\mathrm{S}}^{\mathrm{d}} k_{\mathrm{H}_2}}{R_{\mathrm{S}}(\lambda k_{\mathrm{S}}^{\mathrm{d}}+R_{\mathrm{C}})+R_{\mathrm{C}}\lambda k_{\mathrm{S}}^{\mathrm{d}}[\mathrm{C}]/[\mathrm{S}]} \quad (1),$$

where η is the maximal theoretically attainable enhancement factor, x_p is the fraction of parahydrogen; $[\mathrm{C}]$, $[\mathrm{H}_2]$ and $[\mathrm{S}]$ are concentrations of catalyst, hydrogen and substrate, respectively; $k_{\mathrm{S}}^{\mathrm{d}}$ and k_{H_2} are substrate and hydrogen dissociation rate constants; R_{S} and R_{C} are relaxation rates for the substrate and the complex and λ is polarization transfer efficiency factor [4]. Although the presented theoretical approach is relatively straightforward, it is in a good agreement with the data published to date by us and others (Fig. 1). Moreover, the derived expression for a signal enhancement provides rationale for deciding which system parameters (i.e. *J*-couplings, relaxation rate and reaction rate constants) have to be optimized foremost in order to improve the overall efficiency of SABRE hyperpolarization process. The concept of "hyperpolarized species" can also be exploited for examining factors lowering the maximum attainable polarization in PHIP. For example, using similar approach in the description of heterogeneous hydrogenation of propylene with parahydrogen, we found that the maximum attainable ^{1}H polarization (%P_{H}) in propane is ~6% while the maximum observable %P_{H} is only ~1% [5]. We anticipate that the presented analysis will be useful for optimization of experimental conditions in PHIP and SABRE for the development of new and optimization of already identified NMR and MRI applications. In particular, finding the optimum conditions for production of highly polarized contrast agents by using PHIP and SABRE will also be beneficial for *in vivo* investigations of structure, metabolism and function.

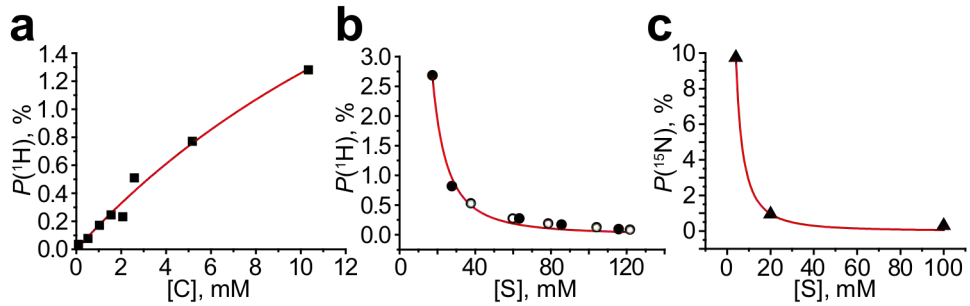

Figure 1. Experimental demonstration of theoretical validation of (1) in the context of SABRE. (**a**) ^{1}H polarization dependence on the catalyst concentration (pyridine concentration is the same for all data points, [S] = 103 mM), data from ref. 1; (**b**) ^{1}H polarization dependence on the substrate concentration, filled circles show data for pyridazine, empty circles show data for phthalazine (catalyst concentration was the same but was not specified by the authors), data from ref. 2; (**c**) ^{15}N polarization dependence on the substrate concentration (catalyst concentration [C] = 0.2 mM was the same for all data points); data from ref. 3. The data sets shown were chosen because they provide polarization dependence on [C] or [S] concentration, with other parameters kept constant.

ACKNOWLEDGEMENTS: NSF CHE-1416268, NIH 1R21EB018014 and 1R21EB020323, DOD CDMRP BRP W81XWH-12-1-0159 BC112431, DOD PRMRP award W81XWH-15-1-0271, and Exxon Mobile Knowledge Build.

REFERENCES:

1. M. J. Cowley, et al. *JACS*, **2011**, 133, 6134–6137.
2. K. M. Appleby, et al. *Chem. Sci.*, **2015**, 6, 3981–3993.
3. M. L. Truong, et al., *J. Phys. Chem. C*, **2015,** 119, 8786–8797.
4. D. A. Barskiy, et al. *PCCP*, **2016**, 18, 89.
5. D. A. Barskiy, et al. *J. Phys. Chem. A,* **2015**, 119, 996–1006.

Exploring Rapid Bulk Heteronuclear Hyperpolarization "On the Cheap" Using PHIP/SABRE-Based Methods

Max Gemeinhardt[1], Banan Alsuhaibani[1], Drake Anthony[1,2], Brian Heine[1,2], Liana Bales[1,2], Jonathan Gesiorski[1,2], Alissa Totheroh[1,2], Fan Shi[1,3], Aaron M. Coffey[4], Roman V. Shchepin[4], Danila Barskiy[4], Eduard Y. Chekmenev[4,5,6,7] and Boyd M. Goodson[1,8]

[1]Department of Chemistry and Biochemistry, Southern Illinois University, Carbondale, IL 62901; [2]Undergraduate Researcher; [3]Advanced Imaging Research Center, University of Texas Southwestern Medical Center, Dallas TX, 75390; [4]Department of Radiology, Vanderbilt University, Nashville, TN, 37232; [5]Department of Biomedical Engineering, Vanderbilt University, Nashville, TN, 37235; [6]Vanderbilt-Ingram Cancer Center, Vanderbilt University, Nashville, TN, 37205; [7]Russian Academy of Sciences, Moscow, Russia; [8]Materials Technology Center, SIUC.

Hyperpolarization[1] refers to any process that can dramatically enhance the nuclear spin polarization of a system to some high, non-equilibrium value—thereby greatly increasing the NMR/MRI sensitivity. PHIP (parahydrogen-induced polarization) refers to the family of approaches where the pure spin order from parahydrogen (pH_2) is transferred to a molecular substrate. Although typically limited by the types of molecules that can be hyperpolarized, PHIP-based approaches are attractive because of their (very) low cost, low instrumentation demands, potential for scalability and continuous production, and their ability to produce hyperpolarized agents very rapidly (i.e., in seconds, compared to 10s of minutes or hours for other hyperpolarization techniques). While "traditional" PHIP[2] involves hydrogenation of unsaturated bonds with pH_2 to create the hyperpolarized agent, a relatively new approach called SABRE[3,4] (signal amplification by reversible exchange, pioneered by Duckett, Green, and co-workers) allows spin order to be transferred from pH_2 without requiring permanent chemical change to the substrate. Instead, SABRE uses iridium-based catalysts to transiently bind both pH_2 and the target substrate within the central Ir atom's ligand sphere; thus, spin order may be spontaneously transferred via scalar couplings during the lifetime of the complex, provided that the external field is sufficiently low to allow the difference in frequencies between the source (hydride) and target (substrate) spins to be roughly matched by the differences in the scalar coupling values in the spin network.[5]

For heteronuclear spins like ^{15}N, the field must be ≤1 μT.[5] In collaboration with the Warren & Theis at Duke, it was recently shown that utilization of a simple magnetic shield during pH_2 delivery to a sample can yield very large nuclear spin polarizations in ^{15}N spins (up to 7-10% so far) of dilute species[5], a technique dubbed "SABRE-SHEATH" (for SABRE in SHield Enables Alignment Transfer to Heteronuclei); very recently we showed this approach can be used to polarize bulk liquids as well.[6] We continue our explorations of this approach as a quick and extremely inexpensive way to generate bulk hyperpolarization in heteronuclei, in part by translating the effort to another lab (at SIUC) and integration with cheap and simple home-built setups (with commercially available components) for pH_2 generation and sample administration—in a setting populated with undergraduate researchers. For example, a simple pH_2 generator (Fig. 1A) was constructed from ~5 ft of coiled 1/4" copper pipe loaded with iron oxide hydroxide catalyst crushed but filtered to ensure containment by 200-mesh (74 micron pore) copper screens capping the two ends (an approach which can generate ~50% enrichment of pH_2 when cooled with liquid N_2; Fig. 1A). The "shield" (Fig. 1B) is a commercial mu-metal shield[6] (for which we used a high-current, low-voltage 60 Hz AC field along an inserted coil of wire was run for a few minutes to de-Gauss the device, confirmed with a Gaussmeter). Combination with a simple pH_2 "bubbler" (similar to that in Ref. [7]) allowed a bulk enhancement of the ^{15}N signal from "neat" pyridine of roughly two orders of magnitude on the first attempt, enabling single-shot observation (Fig. 1B). Involved catalysts include the "standard" Ir SABRE catalyst[4] (Fig. 1C) and heterogeneous analogs (e.g. Fig. 1D). Ongoing efforts include optimization of the approach (to yield higher heteronuclear polarizations), and extending SABRE-SHEATH to aqueous and/or heterogeneous conditions. These efforts support the conclusion that SABRE-SHEATH is by far the "easiest gateway" to creating bulk hyperpolarization in heteronuclear spins and as such, is also highly amenable to experiments involving undergraduate students beginning their research careers.

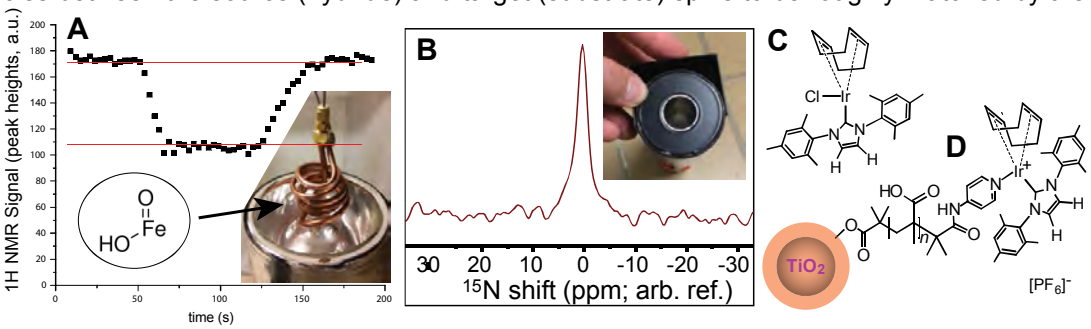

Fig. 1A ^1H NMR from flowing H_2 gas showing characteristic pH_2 formation (50%) when the coil is cooled with ℓ N_2. *Inset* shows scaled-up coil. B Enhanced ^{15}N signal from "neat" pyridine (naturally abundant, ~0.4% ^{15}N); 2 orders of magnitude enhancement estimated by comparison with ^{15}N-labeled sample (not shown); *Inset*: mu-metal shield. C the "standard" iridium SABRE catalyst; D nanoscale heterogeneous analog.[9]

Funding: We thank NSF (CHE-1416432, CHE-1416268, & REU DMR-1461255) NIH (1R21EB018014 & 1R21EB020323), DoD (CDMRP BRP W81XWH-12-1-0159/BC112431, & PRMRP W81XWH-15-1-0271 & W81XWH-15-1-0272). EYC, AMC, & BMG respectively acknowledge the Exxon Mobile Knowledge Build, NIH NIBIB T32 EB1628-12, & SIUC MTC.

References: [1]Nikolaou *et al., CEJ* **2015** *21*, 3156; [2]Bowers & Weitekamp, *JACS*, **1987** *109*, 5541; [3]Adams *et al*., *Science* **2009** *323*, 1708; [4]Cowley *et al*. *JACS*, **2011** *133*, 6134; [5]Theis *et al*. *JACS*, **2015** *137*, 1404; [6]Shchepin *et al*., *JPCL* **2015** 6, 1961; [7]Truong et al., *JPCB* **2014** *118*, 13882; [8]Shi *et al*. *Angew. Chem.* **2014** *126*, 7625; [9]Shi *et al*. *JPCC.* **2015** *119,* 7525.

Clinical-Scale, Stopped-flow 129Xe Hyperpolarizer Development

Aaron M. Coffey[1], Panayiotis Nikolaou[1], Kaili Ranta[2], Iga Muradyan[3], Matthew S. Rosen[4], Samuel Patz[3], Michael J. Barlow[5], Boyd M. Goodson[2], and Eduard Y. Chekmenev[1]

[1]Radiology, Vanderbilt University Institute of Imaging Science, Nashville, TN, United States, [2]Southern Illinois University, Carbondale, IL, United States, [3]Brigham & Women's Hospital, Boston, MA, United States, [4]Harvard University, Cambridge, MA, United States, [5]University of Nottingham, Nottingham, United Kingdom

Synopsis

We report on the development of a first and second generation ^{129}Xe hyperpolarizers, capable of producing high (~25-90%) ^{129}Xe hyperpolarization at high Xe densities (up to 2000 Torr partial pressure), suitable for clinical and materials MRS/MRI applications.

Overview

Owing to the detection sensitivity provided by their high, non-equilibrium nuclear spin polarizations, hyperpolarized (HP) noble gases (e.g. ^{129}Xe and ^{3}He) are utilized in a growing number of MRS/MRI applications—ranging from biomedical imaging and spectroscopy to probing molecular and materials surfaces. Lung imaging with HP ^{129}Xe is of particular interest. Although ^{3}He has a nearly 3-fold greater gyromagnetic ratio, ^{129}Xe has 26% natural abundance and higher solubility in blood and tissues. Moreover, ^{129}Xe's proclivity for interacting with substances and its wide chemical shift range make it a more sensitive MR probe of biological environments.

HP ^{129}Xe is usually created by spin-exchange optical pumping (SEOP). It is traditionally expected that high ^{129}Xe polarizations (P_{Xe}) can only be obtained with low in-cell Xe densities because (i) higher Xe densities increase the destruction of the alkali metal polarization from non-spin-conserving collisions and (ii) higher total pressures tend to quench the more efficient van der Waals contribution to Rb-Xe spin exchange. Indeed, many polarizer designs tend to go to great lengths to produce large amounts of HP ^{129}Xe while still satisfying this condition within the cell. Such polarizers also tend to be complex, expensive, and strictly regulated by their controlling entities—factors that hinder large-scale HP ^{129}Xe generation for many unaffiliated laboratories.

Building upon our previous work exploring batch-mode or "stopped-flow" Rb/Xe SEOP under conditions of high resonant laser flux, we constructed a first-generation large-scale (>1 L/hr) "open-source" xenon polarizer for clinical, pre-clinical, and materials NMR/MRI applications comprised mostly of off-the-shelf components (including a 200 W VHG-narrowed LDA laser) [1–2]. This hyperpolarizer was cleared for preclinical work and approved by the FDA (IND #116,662) for operation at Brigham & Women's Hospital. Unlike most clinical-scale ^{129}Xe polarizers, this first-generation device runs with Xe-rich gas mixtures in single-batch mode. In-cell P_{Xe} values during SEOP of up to ~90%, ~57%, ~50%, and ~28% have been measured for Xe partial pressures of ~300, ~500, ~760, and ~1570 Torr, respectively [1–2].

Experience gained in building this first-generation ^{129}Xe polarizer lead to construction of our second-generation ^{129}Xe polarizer (dubbed "XeUS") [3–5]. The new design encompasses a variety of improvements and new technologies. For example, the water-cooled 200 W VHG-narrowed LDA laser possesses a novel integrated air-cooled optical train assembly. Implementation of a thermoelectric cooler (TEC) and incorporation of a quiet air compressor eliminates the need for external gas or liquid-N_2 supplies for heating/cooling of the OP cell oven or for pneumatic valve operation. The polycarbonate oven for the OP cell is manufactured via 3D printing and houses the TEC module. Further integration of the requisite instrumentation and optics into this 3D-printed oven in conjunction with the laser telescope greatly simplified system construction and laser alignment with the

optical pumping cell. A high-pressure gas manifold using premixed gases also greatly simplifies the first-generation gas manifold design. Taken together, these various improvements have lead to the second-generation hyperpolarizer achieving higher performance, with P_{Xe} of ~74% at 1,000 Torr [3] and P_{Xe} of ~90% at 500 Torr [5] as well as the improvements in the production rate [3-5].

Acknowledgements

Laura Walkup, Brogan Gust, Hayley Newton, and Scott Barcus contributed to this work. Work at SIUC and Vanderbilt is supported by a DoD CDMRP Era of Hope Award W81XWH-12-1-0159/BC112431, W81XWH-15-1-0271 and W81XWH-15-1-0272. M.J.B is supported by the School of Medical & Surgical Sciences, U. of Nottingham.

References

[1] Nikolaou, et al., *PNAS* **110**, 14150-14155 (2013). [2] Nikolaou, et al., *Magn. Reson. Imaging* **32**, 541-550 (2014). [3] Nikolaou, et al., *JACS* **136**, 1636-1642 (2014). [4] Nikolaou, et al., *J Phys Chem B* **118**, 4809-4816 (2014). [5] Nikolaou, et al. *Anal. Chem.*, **86**, 8206-8212 (2014).

Figures

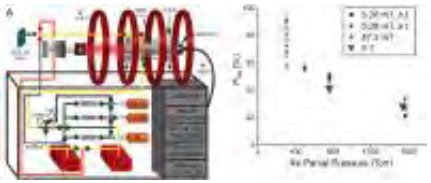

Figure 1. First-generation ^{129}Xe hyperpolarizer schematic (left) and quality assurance NMR spectroscopy measurements (right).

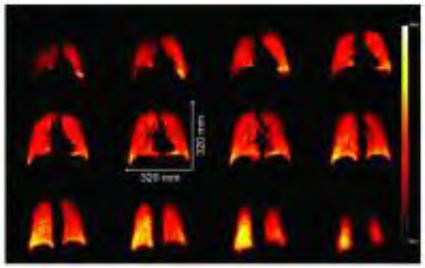

Figure 2. False-color 2D slices from a 3D ^{129}Xe gradient echo chest image from a healthy subject following inhalation of HP ^{129}Xe prepared using the XeNA polarizer (anterior to posterior, reading left to right, top to bottom).

Figure 3. a) Design of XeUS polarizer; b) ^{1}H in situ reference NMR signal from water (100,000 scans), b) ^{129}Xe *in situ* NMR signal from natural abundance ^{129}Xe P_{Xe} = 74% (1 scan) at 1000 Torr Xe pressure, d) IR spectroscopy reporting on P_{Rb} *in situ*.

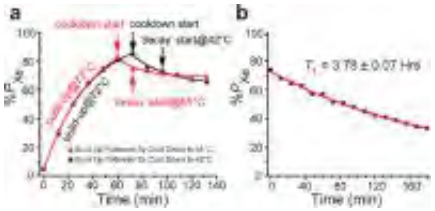

Figure 4. Temperature-ramped SEOP. (a) Exponential fit buildup (72 °C) and decay curves of OP cell cool down to 42 and 55 °C, respectively, of 500 Torr ^{129}Xe. (b) T_1 decay of hyperpolarized ^{129}Xe (500 Torr partial pressure) at room temperature with laser off.

Proc. Intl. Soc. Mag. Reson. Med. 24 (2016)
2185

In Situ NMR Investigation of Clinical-Scale Co-Production of Hyperpolarized ^{131}Xe and ^{129}Xe via Stopped-Flow Spin-Exchange Optical Pumping

Kaili Ranta[1], Megan Murphy[1], Justin Porter[1], Drake Anthony[1*], Shawn Stephenson[1], Matthew S. Rosen[2] and Boyd M. Goodson[1]

[1]Department of Chemistry and Biochemistry, Southern Illinois University, Carbondale, IL 62901; [2]Athinoula A. Martinos Center for Biomedical Imaging, Boston, MA, 02129, USA

Spin exchange optical pumping (SEOP) has become a popular method of preparing hyperpolarized noble gases for use in biochemical and materials research, biomedical imaging[1], and fundamental physics experiments.[2] In SEOP, electron spins of an alkali metal (AM) vapor (e.g. Rb) are polarized via depopulation pumping with a laser, and nuclear spins of the noble gas are subsequently polarized during spin-exchange collisions with those AM atoms. ^{129}Xe is a typical target for polarization, and consequently massive NMR/MRI signal enhancements have been achieved—with nuclear spin polarization now reaching values near unity.[3] However, although much more difficult to hyperpolarize, xenon's other NMR-active isotope—^{131}Xe—has found application in surface studies[4] and has additionally been identified as a potential target of interest for polarized neutron-transmission experiments to study potential violations of fundamental symmetries (e.g. time-reversal invariance[5]).

Fig. 1. SEOP setup using a 125 W narrowed laser (QPC), collimating-polarizing optics (black), 3D-printed forced-air oven[7] (white) with interior NMR detection coil, 2" diam. OP cell in red Helmholtz pair magnet, and low-frequency NMR spectrometer (Magritek Aurora, not shown).

Unlike ^{129}Xe (I=1/2), ^{131}Xe (I=3/2) has a strong quadrupole moment—thereby giving rise to many more contributions to relaxation, and thus greatly limiting both the value and storage potential for any hyperpolarization that might be achieved. Self-relaxation (from collisions with other xenon atoms) typically dominates; for example, the binary collision relaxation pathway has been measured[6] to be 3.95×10^{-2} amg$^{-1}\cdot$s^{-1}, so that time constants for polarization build-up (and decay during storage/experiment) would be optimized at Xe densities significantly lower than what we typically utilize for ^{129}Xe. Persistent Xe dimers add to the short relaxation rates,[4] as do wall collisions: correspondingly, the use of hydrophobic glass coatings often employed to preserve ^{129}Xe polarization must be reconsidered as well.[4]

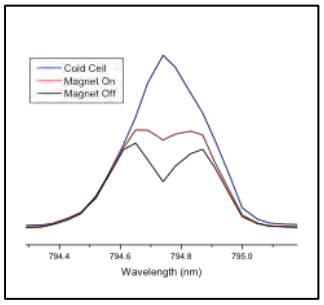

Fig. 2. Transmitted laser spectra used to estimate P_{Rb} with no absorption (cold cell), polarized absorption (Magnet on), and unpolarized absorption (Magnet off); here P_{Rb}~40%.

In the present work, co-production of hyperpolarized ^{131}Xe and ^{129}Xe is investigated under conditions of clinical-scale stopped-flow HP Xe production, high xenon density, and high resonant photon flux (Fig. 1). Comparison with both thermally polarized ^{1}H NMR from water at low field (~15-60 G) and near-IR spectroscopic measurements of transmitted laser profiles (e.g. Fig. 2) allows polarization of ^{131}Xe, ^{129}Xe, and alkali metal electron spins to be estimated and mapped under various conditions (e.g. Fig. 3)—including incident laser powers, cell temperatures, and gas mixtures. Nitrogen is included to quench depolarizing radiative emission/re-absorption processes in the Rb vapor, and helium is investigated to see if its high thermal conductivity can help transfer the resulting heat to the cell walls (thus stabilizing conditions for higher cell temperatures that may permit faster ^{131}Xe SEOP and higher polarizations). For example, successful low-field detection of the ^{131}Xe resonance at 58 G allowed an initial estimate of P_{131Xe} of ~0.1% with a Xe density of 0.4 amg; higher polarizations are anticipated with higher temperatures, higher laser powers, different gas mixtures (e.g. less Xe and more He), and/or different cell designs.

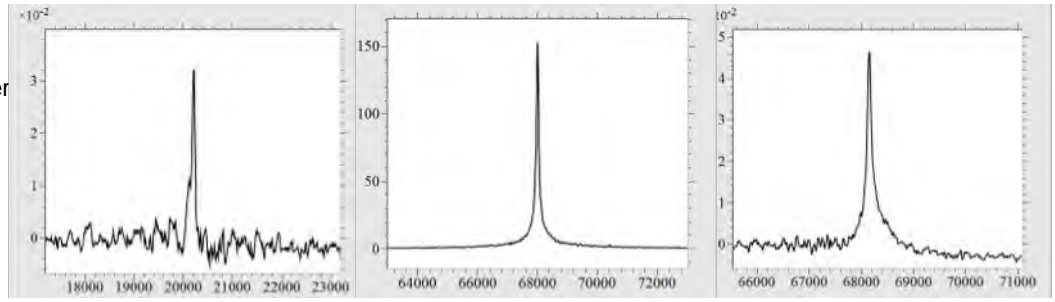

Fig. 3a. ^{131}Xe spectrum acquired at 20.2 kHz after 300 scans (estimated P_{131Xe}~0.1%) with ~60 W incident laser power, ~80 ºC, 6 psi Xe (nat. abund.) and 18.7 psi N_2. **3b.** ^{129}Xe spectrum acquired (1 scan) at 68.2 kHz (estimated P_{129Xe}~80%) **3c.** ^{1}H water signal acquired at 68.2 kHz after 100k scans with Boltzmann polarization of ~5.6×10^{-7}%.

***Acknowledgements**:* This work was funded in part by DoD (W81XWH-15-1-0272) and NSF (REU DMR-1461255); we thank Michael Barlow (Nottingham) for loaning the 125 W laser.

***References**:* [1]B. M. Goodson, *JMR*, **155**, 157, 2002; [2]T. E. Chupp, *et al.*, *Phys. Rev. A*, **38**, 3998, 1988; [3]Nikolaou *et al., PNAS*, **110**, 14150, 2013; [4]K. F. Stupic, *et al.*, *J. Magn. Reson.,* **208**, 58, 2011; [5]J. D. Bowman, V. Gudkov, Phys. Rev. C, **90**, 065503, 2014; [6]D. Brinkmann, *et al.*, *Helv. Phys. Acta*, **35**, 431, 1962; [7]Nikolaou *et al.*, *JACS*, **2014**, 136, 1636.

PTO/AIA/14 (07-14)
Approved for use through 04/30/2017. OMB 0651-0032
U.S. Patent and Trademark Office; U.S. DEPARTMENT OF COMMERCE
Under the Paperwork Reduction Act of 1995, no persons are required to respond to a collection of information unless it contains a valid OMB control number.

Application Data Sheet 37 CFR 1.76	Attorney Docket Number	10644-007PV1
	Application Number	

Title of Invention	METHODS OF DETECTING SULFUR-CONTAINING COMPOUNDS

The application data sheet is part of the provisional or nonprovisional application for which it is being submitted. The following form contains the bibliographic data arranged in a format specified by the United States Patent and Trademark Office as outlined in 37 CFR 1.76.
This document may be completed electronically and submitted to the Office in electronic format using the Electronic Filing System (EFS) or the document may be printed and included in a paper filed application.

Secrecy Order 37 CFR 5.2

☐ Portions or all of the application associated with this Application Data Sheet may fall under a Secrecy Order pursuant to 37 CFR 5.2 (Paper filers only. Applications that fall under Secrecy Order may not be filed electronically.)

Inventor Information:

Inventor 1 Remove

Legal Name

Prefix	Given Name	Middle Name	Family Name	Suffix
	Eduard	Y.	Chekmenev	

Residence Information (Select One) ◉ US Residency ◯ Non US Residency ◯ Active US Military Service

City		State/Province			

Mailing Address of Inventor:

Address 1			
Address 2			
City		**State/Province**	
Postal Code		**Country** i	

Inventor 2 Remove

Legal Name

Prefix	Given Name	Middle Name	Family Name	Suffix
	Roman	V.	Shchepin	

Residence Information (Select One) ◉ US Residency ◯ Non US Residency ◯ Active US Military Service

City		State/Province		Country of Residence i	

Mailing Address of Inventor:

Address 1			
Address 2			
City		**State/Province**	
Postal Code		**Country** i	

All Inventors Must Be Listed - Additional Inventor Information blocks may be generated within this form by selecting the **Add** button. Add

Correspondence Information:

Enter either Customer Number or complete the Correspondence Information section below.
For further information see 37 CFR 1.33(a).

PTO/AIA/14 (07-14)
Approved for use through 04/30/2017. OMB 0651-0032
U.S. Patent and Trademark Office; U.S. DEPARTMENT OF COMMERCE
Under the Paperwork Reduction Act of 1995, no persons are required to respond to a collection of information unless it contains a valid OMB control number.

Application Data Sheet 37 CFR 1.76	Attorney Docket Number	10644-007PV1
	Application Number	
Title of Invention	METHODS OF DETECTING SULFUR-CONTAINING COMPOUNDS	

☐ **An Address is being provided for the correspondence Information of this application.**

Customer Number	96039		
Email Address	docketing@mcciplaw.com	Add Email	Remove Email

Application Information:

Title of the Invention	METHODS OF DETECTING SULFUR-CONTAINING COMPOUNDS		
Attorney Docket Number	10644-007PV1	**Small Entity Status Claimed**	☒
Application Type	Provisional		
Subject Matter	Utility		
Total Number of Drawing Sheets (if any)	4	**Suggested Figure for Publication (if any)**	

Filing By Reference :

Only complete this section when filing an application by reference under 35 U.S.C. 111(c) and 37 CFR 1.57(a). Do not complete this section if application papers including a specification and any drawings are being filed. Any domestic benefit or foreign priority information must be provided in the appropriate section(s) below (i.e., "Domestic Benefit/National Stage Information" and "Foreign Priority Information").

For the purposes of a filing date under 37 CFR 1.53(b), the description and any drawings of the present application are replaced by this reference to the previously filed application, subject to conditions and requirements of 37 CFR 1.57(a).

Application number of the previously filed application	Filing date (YYYY-MM-DD)	Intellectual Property Authority or Country

Publication Information:

☐ Request Early Publication (Fee required at time of Request 37 CFR 1.219)

☐ **Request Not to Publish.** I hereby request that the attached application not be published under 35 U.S.C. 122(b) and certify that the invention disclosed in the attached application **has not and will not** be the subject of an application filed in another country, or under a multilateral international agreement, that requires publication at eighteen months after filing.

Representative Information:

Representative information should be provided for all practitioners having a power of attorney in the application. Providing this information in the Application Data Sheet does not constitute a power of attorney in the application (see 37 CFR 1.32).
Either enter Customer Number or complete the Representative Name section below. If both sections are completed the customer Number will be used for the Representative Information during processing.

Please Select One:	◉ Customer Number	◯ US Patent Practitioner	◯ Limited Recognition (37 CFR 11.9)
Customer Number	96039		

Under the Paperwork Reduction Act of 1995, no persons are required to respond to a collection of information unless it contains a valid OMB control number.

Application Data Sheet 37 CFR 1.76	Attorney Docket Number	10644-007PV1
	Application Number	
Title of Invention	METHODS OF DETECTING SULFUR-CONTAINING COMPOUNDS	

Domestic Benefit/National Stage Information:

This section allows for the applicant to either claim benefit under 35 U.S.C. 119(e), 120, 121, 365(c), or 386(c) or indicate National Stage entry from a PCT application. Providing this information in the application data sheet constitutes the specific reference required by 35 U.S.C. 119(e) or 120, and 37 CFR 1.78.
When referring to the current application, please leave the application number blank.

Prior Application Status			Remove
Application Number	Continuity Type	Prior Application Number	Filing Date (YYYY-MM-DD)

Additional Domestic Benefit/National Stage Data may be generated within this form by selecting the **Add** button.

Foreign Priority Information:

This section allows for the applicant to claim priority to a foreign application. Providing this information in the application data sheet constitutes the claim for priority as required by 35 U.S.C. 119(b) and 37 CFR 1.55. When priority is claimed to a foreign application that is eligible for retrieval under the priority document exchange program (PDX)[i] the information will be used by the Office to automatically attempt retrieval pursuant to 37 CFR 1.55(i)(1) and (2). Under the PDX program, applicant bears the ultimate responsibility for ensuring that a copy of the foreign application is received by the Office from the participating foreign intellectual property office, or a certified copy of the foreign priority application is filed, within the time period specified in 37 CFR 1.55(g)(1).

			Remove
Application Number	Country[i]	Filing Date (YYYY-MM-DD)	Access Code[i] (if applicable)

Additional Foreign Priority Data may be generated within this form by selecting the **Add** button.

Statement under 37 CFR 1.55 or 1.78 for AIA (First Inventor to File) Transition Applications

☐ This application (1) claims priority to or the benefit of an application filed before March 16, 2013 and (2) also contains, or contained at any time, a claim to a claimed invention that has an effective filing date on or after March 16, 2013.
NOTE: By providing this statement under 37 CFR 1.55 or 1.78, this application, with a filing date on or after March 16, 2013, will be examined under the first inventor to file provisions of the AIA.

PTO/AIA/14 (07-14)
Approved for use through 04/30/2017. OMB 0651-0032
U.S. Patent and Trademark Office; U.S. DEPARTMENT OF COMMERCE
Under the Paperwork Reduction Act of 1995, no persons are required to respond to a collection of information unless it contains a valid OMB control number.

Application Data Sheet 37 CFR 1.76	Attorney Docket Number	10644-007PV1
	Application Number	
Title of Invention	METHODS OF DETECTING SULFUR-CONTAINING COMPOUNDS	

Authorization to Permit Access:

☒ Authorization to Permit Access to the Instant Application by the Participating Offices

If checked, the undersigned hereby grants the USPTO authority to provide the European Patent Office (EPO), the Japan Patent Office (JPO), the Korean Intellectual Property Office (KIPO), the World Intellectual Property Office (WIPO), and any other intellectual property offices in which a foreign application claiming priority to the instant patent application is filed access to the instant patent application. See 37 CFR 1.14(c) and (h). This box should not be checked if the applicant does not wish the EPO, JPO, KIPO, WIPO, or other intellectual property office in which a foreign application claiming priority to the instant patent application is filed to have access to the instant patent application.

In accordance with 37 CFR 1.14(h)(3), access will be provided to a copy of the instant patent application with respect to: 1) the instant patent application-as-filed; 2) any foreign application to which the instant patent application claims priority under 35 U.S.C. 119(a)-(d) if a copy of the foreign application that satisfies the certified copy requirement of 37 CFR 1.55 has been filed in the instant patent application; and 3) any U.S. application-as-filed from which benefit is sought in the instant patent application.

In accordance with 37 CFR 1.14(c), access may be provided to information concerning the date o f filing this Authorization.

Applicant Information:

Providing assignment information in this section does not substitute for compliance with any requirement of part 3 of Title 37 of CFR to have an assignment recorded by the Office.

Applicant 1

If the applicant is the inventor (or the remaining joint inventor or inventors under 37 CFR 1.45), this section should not be completed. The information to be provided in this section is the name and address of the legal representative who is the applicant under 37 CFR 1.43; or the name and address of the assignee, person to whom the inventor is under an obligation to assign the invention, or person who otherwise shows sufficient proprietary interest in the matter who is the applicant under 37 CFR 1.46. If the applicant is an applicant under 37 CFR 1.46 (assignee, person to whom the inventor is obligated to assign, or person who otherwise shows sufficient proprietary interest) together with one or more joint inventors, then the joint inventor or inventors who are also the applicant should be identified in this section.

Clear

◉ Assignee	◯ Legal Representative under 35 U.S.C. 117	◯ Joint Inventor
◯ Person to whom the inventor is obligated to assign.	◯ Person who shows sufficient proprietary interest	

If applicant is the legal representative, indicate the authority to file the patent application, the inventor is:

Name of the Deceased or Legally Incapacitated Inventor :

If the Applicant is an Organization check here. ☒

Organization Name	Vanderbilt University

Under the Paperwork Reduction Act of 1995, no persons are required to respond to a collection of information unless it contains a valid OMB control number.

Application Data Sheet 37 CFR 1.76	Attorney Docket Number	10644-007PV1
	Application Number	
Title of Invention	METHODS OF DETECTING SULFUR-CONTAINING COMPOUNDS	

Mailing Address Information For Applicant:			
Address 1	305 Kirkland Hall		
Address 2	2201 West End Avenue		
City	Nashville	**State/Province**	TN
Country i	US	Postal Code	37240
Phone Number		Fax Number	
Email Address			

Additional Applicant Data may be generated within this form by selecting the Add button.

Assignee Information including Non-Applicant Assignee Information:

Providing assignment information in this section does not subsitute for compliance with any requirement of part 3 of Title 37 of CFR to have an assignment recorded by the Office.

Assignee 1

Complete this section if assignee information, including non-applicant assignee information, is desired to be included on the patent application publication . An assignee-applicant identified in the "Applicant Information" section will appear on the patent application publication as an applicant. For an assignee-applicant, complete this section only if identification as an assignee is also desired on the patent application publication.

If the Assignee or Non-Applicant Assignee is an Organization check here. ☐

Prefix	**Given Name**	Middle Name	**Family Name**	Suffix

Mailing Address Information For Assignee including Non-Applicant Assignee:			
Address 1			
Address 2			
City		**State/Province**	
Country i		Postal Code	
Phone Number		Fax Number	
Email Address			

Additional Assignee or Non-Applicant Assignee Data may be generated within this form by selecting the Add button.

Under the Paperwork Reduction Act of 1995, no persons are required to respond to a collection of information unless it contains a valid OMB control number.

Application Data Sheet 37 CFR 1.76	Attorney Docket Number	10644-007PV1
	Application Number	
Title of Invention	METHODS OF DETECTING SULFUR-CONTAINING COMPOUNDS	

Signature:

NOTE: This form must be signed in accordance with 37 CFR 1.33. See 37 CFR 1.4 for signature requirements and certifications.

Signature	/Andrew T. Meunier/			Date (YYYY-MM-DD)	2015-11-30
First Name	Andrew T.	Last Name	Meunier	Registration Number	40726

Additional Signature may be generated within this form by selecting the Add button.

This collection of information is required by 37 CFR 1.76. The information is required to obtain or retain a benefit by the public which is to file (and by the USPTO to process) an application. Confidentiality is governed by 35 U.S.C. 122 and 37 CFR 1.14. This collection is estimated to take 23 minutes to complete, including gathering, preparing, and submitting the completed application data sheet form to the USPTO. Time will vary depending upon the individual case. Any comments on the amount of time you require to complete this form and/or suggestions for reducing this burden, should be sent to the Chief Information Officer, U.S. Patent and Trademark Office, U.S. Department of Commerce, P.O. Box 1450, Alexandria, VA 22313-1450. DO NOT SEND FEES OR COMPLETED FORMS TO THIS ADDRESS. **SEND TO: Commissioner for Patents, P.O. Box 1450, Alexandria, VA 22313-1450.**

Privacy Act Statement

The Privacy Act of 1974 (P.L. 93-579) requires that you be given certain information in connection with your submission of the attached form related to a patent application or patent. Accordingly, pursuant to the requirements of the Act, please be advised that: (1) the general authority for the collection of this information is 35 U.S.C. 2(b)(2); (2) furnishing of the information solicited is voluntary; and (3) the principal purpose for which the information is used by the U.S. Patent and Trademark Office is to process and/or examine your submission related to a patent application or patent. If you do not furnish the requested information, the U.S. Patent and Trademark Office may not be able to process and/or examine your submission, which may result in termination of proceedings or abandonment of the application or expiration of the patent.

The information provided by you in this form will be subject to the following routine uses:

1. The information on this form will be treated confidentially to the extent allowed under the Freedom of Information Act (5 U.S.C. 552) and the Privacy Act (5 U.S.C. 552a). Records from this system of records may be disclosed to the Department of Justice to determine whether the Freedom of Information Act requires disclosure of these records.

2. A record from this system of records may be disclosed, as a routine use, in the course of presenting evidence to a court, magistrate, or administrative tribunal, including disclosures to opposing counsel in the course of settlement negotiations.

3. A record in this system of records may be disclosed, as a routine use, to a Member of Congress submitting a request involving an individual, to whom the record pertains, when the individual has requested assistance from the Member with respect to the subject matter of the record.

4. A record in this system of records may be disclosed, as a routine use, to a contractor of the Agency having need for the information in order to perform a contract. Recipients of information shall be required to comply with the requirements of the Privacy Act of 1974, as amended, pursuant to 5 U.S.C. 552a(m).

5. A record related to an International Application filed under the Patent Cooperation Treaty in this system of records may be disclosed, as a routine use, to the International Bureau of the World Intellectual Property Organization, pursuant to the Patent C o o p eration Treaty.

6. A record in this system of records may be disclosed, as a routine use, to another federal agency for purposes of National Security review (35 U.S.C. 181) and for review pursuant to the Atomic Energy Act (42 U.S.C. 218(c)).

7. A record from this system of records may be disclosed, as a routine use, to the Administrator, General Services, or his/her designee, during an inspection of records conducted by GSA as part of that agency's responsibility to recommend improvements in records management practices and programs, under authority of 44 U.S.C. 2904 and 2906. Such disclosure shall be made in accordance with the GSA regulations governing inspection of records for this purpose, and any other relevant (i.e., GSA or Commerce) directive. Such disclosure shall not be used to make determinations about individuals.

8. A record from this system of records may be disclosed, as a routine use, to the public after either publication of the application pursuant to 35 U.S.C. 122(b) or issuance of a patent pursuant to 35 U.S.C. 151. Further, a record may be disclosed, subject to the limitations of 37 CFR 1.14, as a routine use, to the public if the record was filed in an application which became abandoned or in which the proceedings were terminated and which application is referenced by either a published application, an application open to public inspections or an issued patent.

9. A record from this system of records may be disclosed, as a routine use, to a Federal, State, or local law enforcement agency, if the USPTO becomes aware of a violation or potential violation of law or regulation.

47.5mT Permanent Magnet and Gradient Coil

Acceptance Testing

October 15, 2015

Above is a photo of the magnet and gradient coil under factory test. This is the rear of magnet. Note the gradient din rail connector in the lower right in the photo. The din rail connector accepts 6 to 1/0 AWG wire.

See Drawing: JX475-926C-MG-00_Rev_B.PDF

MAGNET TEST DATA

The magnet was measured with a MetroLab Precision NMR Teslameter (PT2025) and an XYZ stage with 500mm travel (Accuracy 125 µm, Repeatability < 2.5 µm).

Magnetic Field 0.0487 T at 70 deg F.

Homogeneity over 400mm FOV is 18.7 ppm, Peak to peak. The following is a 24 angle x 25 plane, high resolution field map:

Raw field file D:\shimming\MagnetShimSystems\Vanderbilt\ShimJobs\ActonShim\SIGWA_MetroLab_500_24x25_mag1_gradandprotOptLin_Ellipse_FractionalFOVz=400mm_FractionalFOVxy=400mm.plo, peak to peak ppm = 18.6966, VRMS = 2.4278, FWHM = 2.9106

	-199	-195	-189	-179	-167	-152	-135	-116	-94.6	-72.2	-48.8	-24.6	0	24.6	48.8	72.2	94.6	116	135	152	167	179	189	195	199
0	1.9	-0.1	0.2	3.0	5.2	5.5	-0.8	-2.0	1.0	4.4	5.9	9.0	-2.5	-0.8	2.4	1.8	-3.2	-7.9	-7.9	-4.4	-2.8	-5.0	-7.4	-6.4	-3.4
15	1.3	1.0	-0.1	3.3	5.6	3.7	-0.4	-0.1	3.5	7.0	6.6	2.8	-0.1	1.8	4.9	4.0	-1.4	-6.7	-7.4	-4.4	-2.6	-4.6	-7.4	-7.4	-4.3
30	0.1	-1.7	-0.5	3.5	5.9	4.3	1.3	1.1	4.9	8.7	8.3	4.5	-2.0	3.9	7.2	6.5	1.8	-4.7	-6.0	-3.6	-2.1	-4.2	-7.5	-8.1	-5.0
45	0.1	-2.3	-0.2	3.5	5.9	4.3	1.3	1.1	4.9	8.5	8.2	4.7	-2.9	5.6	9.3	8.9	3.3	-2.7	-4.5	-2.7	-1.6	-3.8	-7.5	-8.6	-5.6
60	-0.4	-2.7	0.0	3.3	5.5	5.6	3.6	0.9	4.8	8.4	8.1	4.7	3.1	5.9	9.9	9.7	4.7	0.9	-2.8	-1.8	-0.8	-2.9	-7.1	-8.8	-6.0
75	-0.8	-3.2	1.2	2.8	4.5	7.2	-0.8	-0.4	5.7	7.3	6.9	5.6	-2.1	4.8	8.8	8.7	4.0	1.1	-2.4	-0.5	-0.7	-1.7	-6.3	-8.6	-6.1
90	-1.1	-3.8	-2.1	3.5	2.8	0.2	-2.9	-2.4	1.2	5.4	4.9	1.6	-0.1	3.0	7.1	7.4	-2.9	-2.1	-4.1	-0.5	-1.2	-0.8	-5.4	-8.2	-6.0
105	1.2	-4.5	-3.5	-0.1	-0.8	2.0	-5.2	-4.7	-0.4	3.6	3.4	0.1	1.0	1.7	5.6	5.9	1.7	-2.9	-3.5	-0.7	-1.8	0.2	-4.6	-7.6	-5.7
120	-1.5	-5.1	-5.1	-2.5	-1.5	-3.9	-7.1	-6.8	-2.4	2.0	2.5	-0.0	-1.1	1.6	5.1	4.8	-0.8	-3.8	-3.9	-0.6	1.3	0.2	-4.0	-6.8	-5.2
135	-1.1	-5.6	-6.5	-4.4	-3.2	-5.2	-8.3	-8.3	-4.2	0.5	1.2	0.1	-0.1	2.5	5.8	5.1	0.3	-4.0	-3.8	-0.1	2.3	0.6	-3.5	-5.9	-4.5
150	0.8	-5.6	-7.2	-5.4	-4.0	-5.5	-8.5	-8.9	-4.9	-0.2	-1.2	-0.5	-0.3	2.5	5.9	5.1	0.3	-2.9	-3.3	-0.4	-2.5	0.0	-2.9	-4.9	-3.7
165	-0.2	-5.1	-7.2	-5.6	-3.7	-4.9	-7.8	-8.1	-4.1	0.4	-1.0	-0.2	-0.5	2.4	5.8	5.1	0.8	-3.2	-2.4	-1.8	-3.5	-1.4	-2.3	-3.8	-2.7
180	0.4	-4.1	-6.6	-5.0	-2.8	-3.7	-6.7	-7.3	-3.6	1.2	2.8	1.1	0.8	3.9	7.4	6.8	2.3	-1.2	-0.1	3.5	4.7	1.8	-1.7	-2.6	-1.7
195	1.1	-2.9	-5.6	-4.2	-1.7	-2.4	-5.7	-6.8	-3.2	1.6	3.3	1.8	1.6	4.9	8.5	7.7	3.4	0.7	2.6	6.0	5.8	1.9	-1.4	-1.4	-0.8
210	2.1	-1.5	-4.6	-3.5	-0.5	0.0	-3.9	-5.5	-2.0	3.0	4.6	2.8	2.3	5.7	9.1	8.1	3.7	1.2	4.4	7.6	6.0	1.2	-1.4	-0.4	0.3
225	2.9	-0.2	-3.5	-2.7	0.9	1.3	-1.3	-3.1	-0.1	4.7	5.9	3.6	2.7	6.1	9.9	9.0	4.3	2.1	4.9	7.8	5.5	0.2	-1.5	0.8	0.9
240	3.5	1.1	-2.5	-1.8	2.4	4.1	1.4	-0.9	1.5	5.8	6.6	3.5	1.9	5.0	9.0	8.1	3.6	1.6	4.8	7.8	4.9	0.3	-1.5	1.3	1.4
255	4.0	2.0	1.4	-0.7	3.8	5.8	3.0	0.4	2.5	6.6	7.0	3.4	1.1	4.4	8.3	7.6	3.1	1.1	4.3	7.4	4.5	-0.9	-1.7	1.4	1.6
270	4.3	2.6	-0.7	0.1	4.2	5.8	3.4	-0.6	1.2	5.0	5.2	1.8	-0.1	3.2	7.3	6.9	2.5	0.4	3.4	6.4	3.6	-1.8	-2.4	1.1	1.3
285	4.4	2.3	-0.5	0.0	3.8	4.7	0.3	-2.7	1.1	2.5	2.3	1.5	-3.5	0.1	4.6	4.7	0.8	-1.3	-2.0	5.0	2.1	-3.3	-3.8	0.1	1.1
300	4.2	2.3	0.7	0.0	3.4	3.6	1.0	-5.1	-3.7	0.3	-0.8	-5.0	-7.0	-3.4	1.7	2.1	-2.0	-4.0	-0.8	2.8	0.4	-4.9	-5.4	-1.3	0.8
315	3.8	1.7	0.8	0.3	3.4	3.0	-2.2	-6.3	-5.3	-2.1	-2.5	-6.7	-8.8	-5.7	1.1	-0.1	-4.4	-6.6	-3.2	0.1	-0.9	-5.8	-6.6	-2.8	0.4
330	3.2	1.3	-0.8	1.2	4.0	2.8	-2.5	-6.1	-4.6	-1.5	-2.1	-6.2	-8.6	-6.0	1.8	1.4	-5.0	-7.3	-4.7	-0.8	1.6	-5.8	-7.2	-4.2	1.1
345	2.6	0.4	-0.4	2.2	4.7	3.0	-1.9	-4.5	-2.0	1.4	0.8	-3.4	-6.0	-3.8	0.1	-0.1	-4.1	-7.5	-6.3	-2.8	-2.3	-5.4	-7.4	-5.4	-2.4

GRADIENT TEST DATA

The gradients were measured with 12 angle x 13 plane plot while running about 2 amps into the gradient. The field measurements were done with the same Metrolab PT2025 and the same XYZ stage. The results are as follows:

Gradient Field performance

	X Gradient	Y Gradient	Z Gradient
Linearity 400mm FOV	+6.03%, -6.35%	+6.09%, -6.01%	+2.32%, -2.06%
Linearity 300mm FOV	+2.89%, -3.03%	+2.60%, -2.96%	+1.08%, -0.89%
Linearity 200mm FOV	+1.23%, -1.27%	+1.09%, -1.22%	+0.49%, -0.41%
Gradient Strength (mT/m/100A)	7.42	7.45	9.30
Amperage for 20mT/m	269 amps	268 amps	215 amps

Gradient Electrical Characteristics

	Inductance (uH)	Resistance Ohms (20℃)	Resistance Ohms (40℃)
X/Y	1472	0.1170	0.1263
Z	1364	0.0721	0.07784

Each gradient plate was Hypot tested at 4000V for 60 seconds and passed.

Gradient interconnect wiring is 600V rated 6 AWG. Gradient DIN rail connection are rated at 600V.

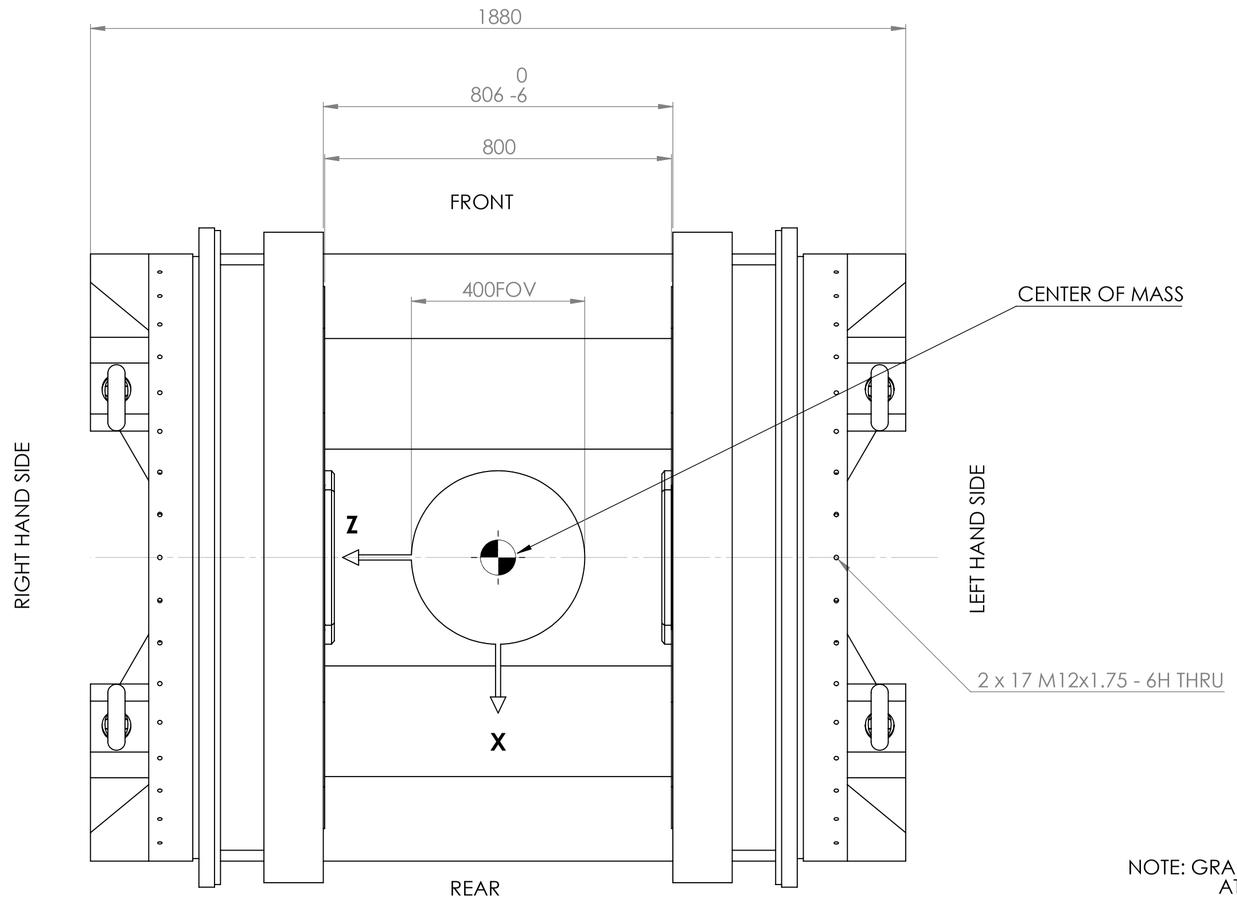

SCALE 1 : 10

NOTE: GRADIENT CONNECTOR DIN RAIL AT REAR OF MAGNET

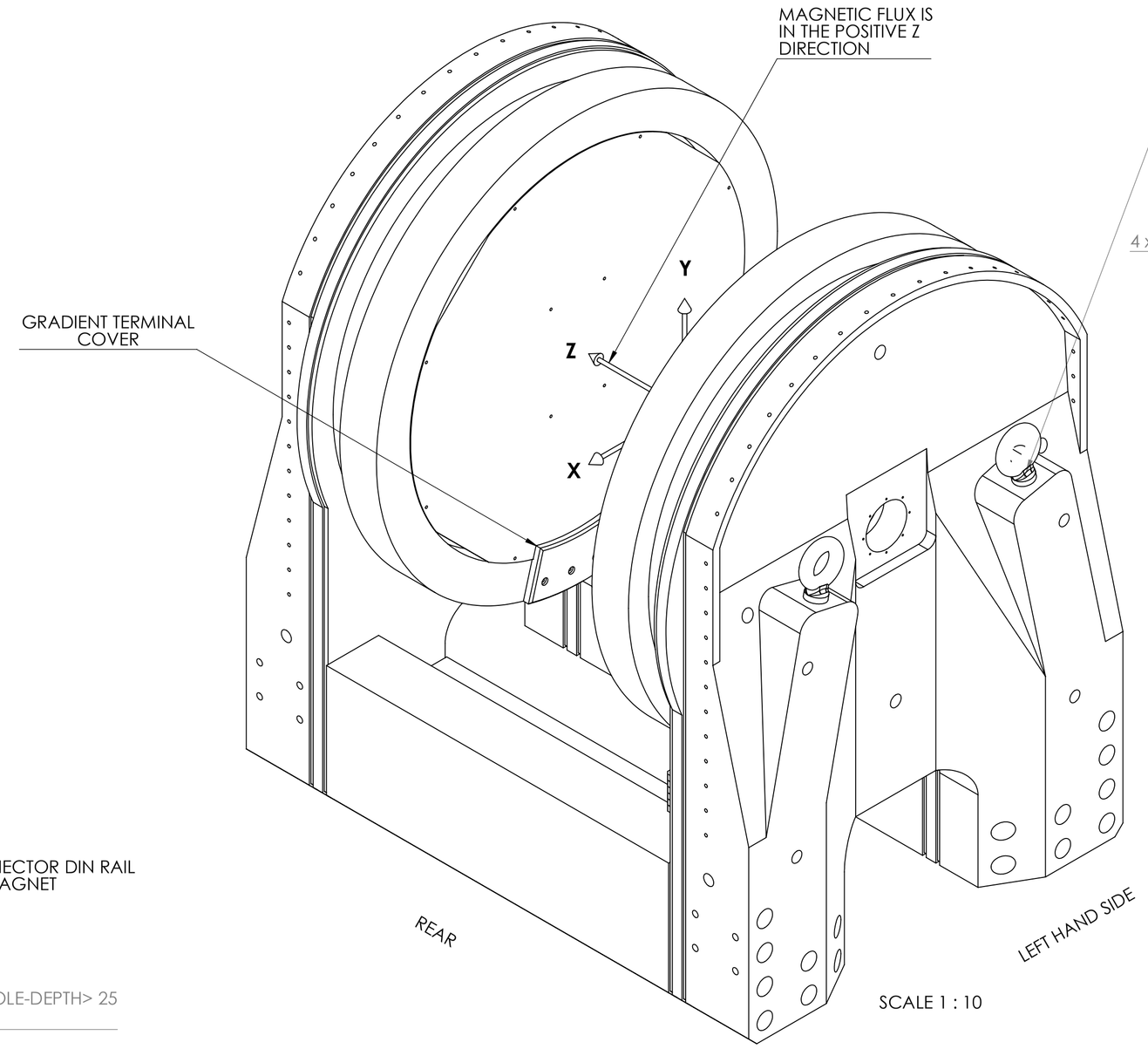

SCALE 1 : 10

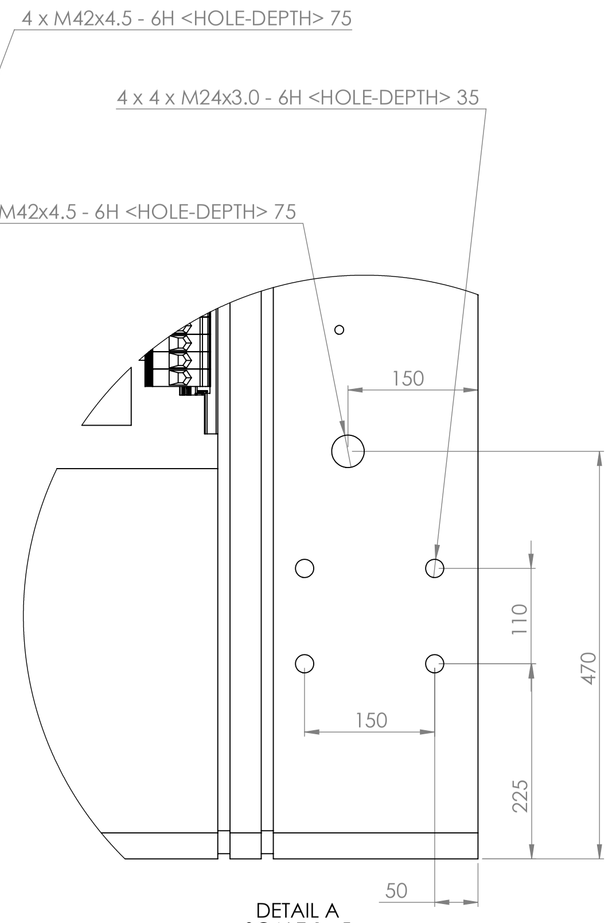

DETAIL A
SCALE 1 : 5

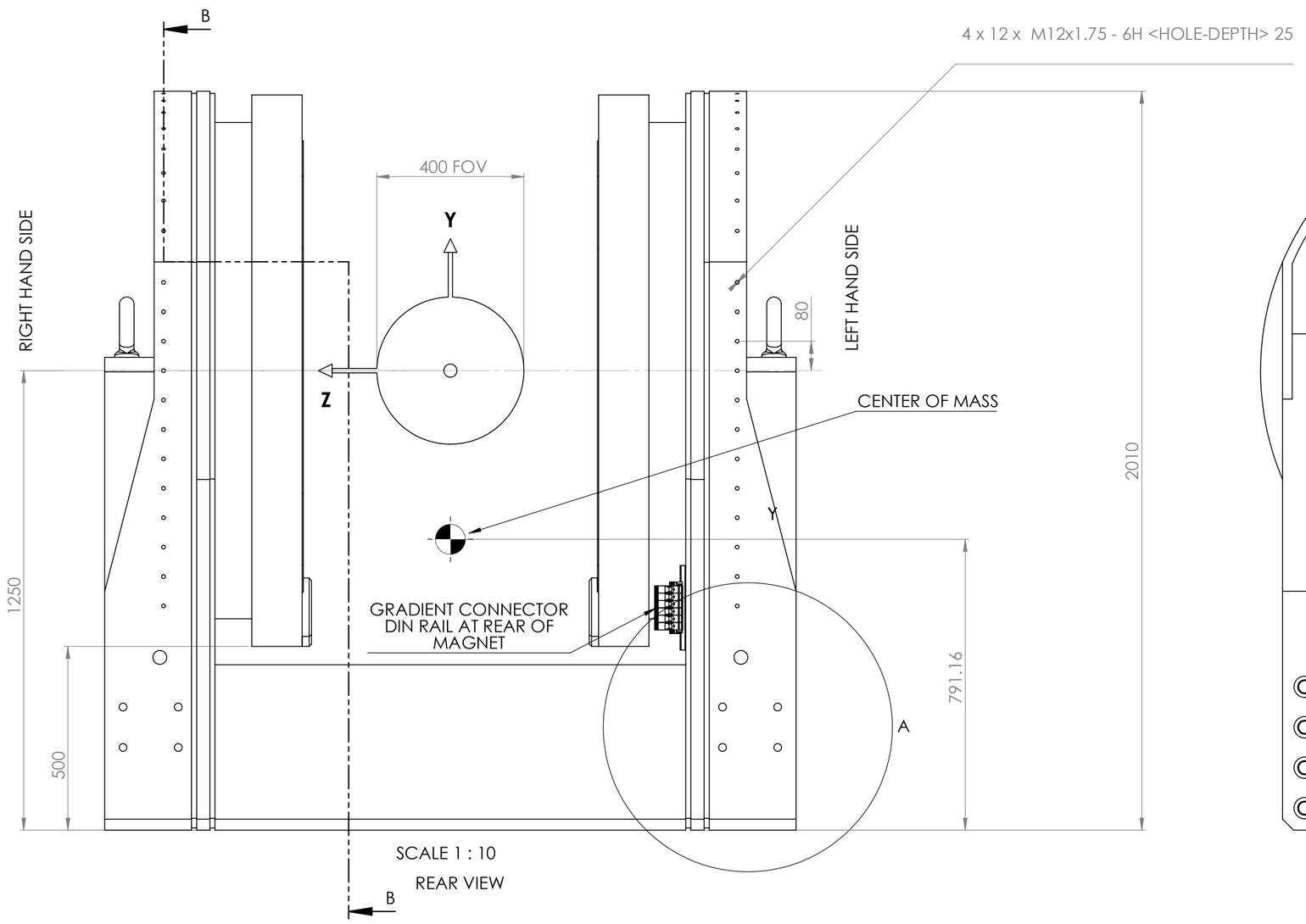

SCALE 1 : 10

REAR VIEW

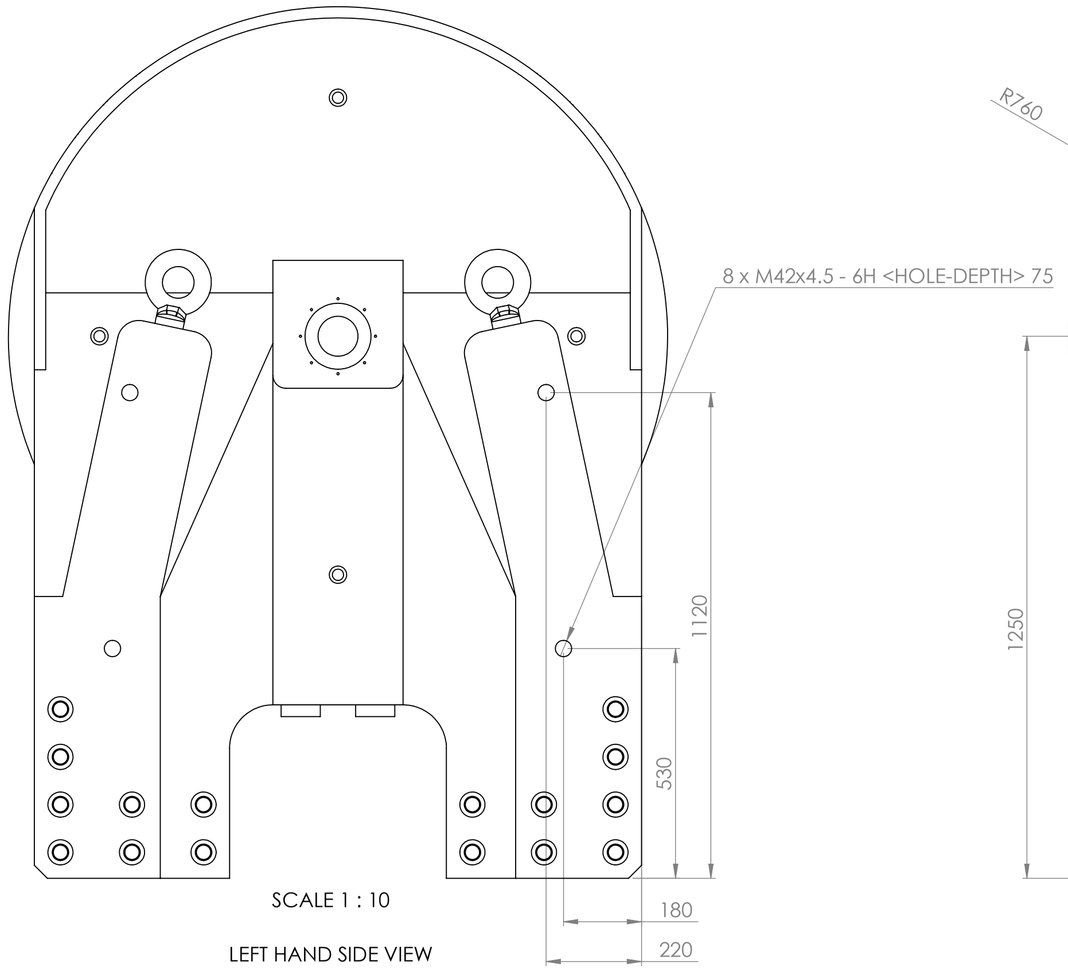

SCALE 1 : 10

LEFT HAND SIDE VIEW

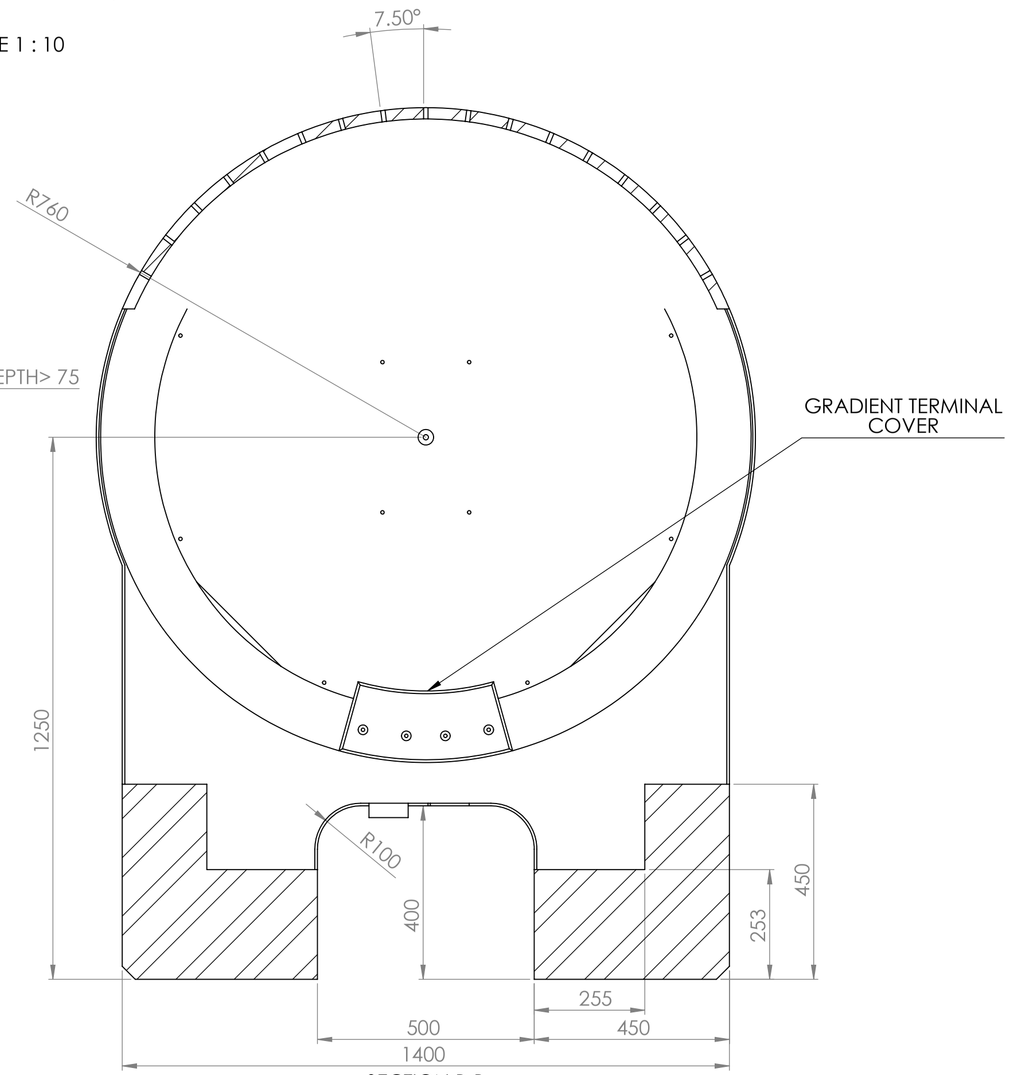

SECTION B-B
SCALE 1 : 10

SAFETY INFORMATION:
1) THIS IS A VERY HEAVY ASSEMBLY. RIGGING SHOULD BE CHECKED BY A LICENSED ENGINEER. THE USE OF SPREADER BARS IS REQUIRED FOR OVERHEAD LIFTING.
2) THE 5 GAUSS ZONE EXTENDS TO 2500 MM FROM THE MAGNET ISOCENTER. USE STANDARD MRI SAFETY PRACTICES WITHIN THE 5 GAUSS ZONE.
3) THIS IS A LIVE MAGNET. THE MAGNET CANNOT BE TURNED OFF. FERROUS OBJECTS WILL EXPERIENCE EXTREME FORCE CLOSE TO THE MAGNET, AND CAN BECOME PROJECTILES OR STUCK TOTHE MAGNET. USE STANDARD MRI SAFETY PRACTICES WITHIN THE 5 GAUSS ZONE.

UNLESS OTHERWISE SPECIFIED: DIMENSIONS ARE IN MILLIMETERS SURFACE FINISH: TOLERANCES: LINEAR: ANGULAR:	FINISH:				DEBUR AND BREAK SHARP EDGES	DO NOT SCALE DRAWING	REVISION B
	NAME	SIGNATURE	DATE			TITLE: SIGWA 0.0475T MAGNET AND GRADIENT COIL
DRAWN	MATHEW HASS	MATHEW HASS	10/15/2015			
CHK'D	MATHEW HASS	MATHEW HASS	10/15/2015			
APPV'D	MATHEW HASS	MATHEW HASS	10/15/2015			
MFG						
Q.A				MATERIAL:		DWG NO. JX475-926C-MG-00 A1
				WEIGHT: 13379.64 KG		SCALE:1:20 SHEET 1 OF 1

- **Are you a patient?** Visit VanderbiltHealth.com (http://www.vanderbilthealth.com)

VANDERBILT UNIVERSITY MEDICAL CENTER

Monroe Carell Jr. Children's Hospital at Vanderbilt (http://www.childrenshospital.vanderbilt.org/)
Vanderbilt University School of Medicine (http://medschool.vanderbilt.edu/)
Vanderbilt University School of Nursing (http://www.nursing.vanderbilt.edu/)
Vanderbilt University (http://www.vanderbilt.edu/)
Research at Vanderbilt (http://research.vanderbilt.edu/)
For Patients and Visitors (http://www.vanderbilthealth.com)
Resources for Researchers, Employees and Students (http://www.mc.vanderbilt.edu)

VUMC's Chekmenev elected to Russian Academy of Sciences

by Bill Snyder (http://news.vanderbilt.edu/author/billsnyder/) | Thursday, Mar. 3, 2016, 9:25 AM

Vanderbilt researcher Eduard Chekmenev, Ph.D., has been elected to the Russian Academy of Sciences (RAS) for his efforts to develop imaging markers for cancer and lung disease using hyperpolarized magnetic resonance imaging (MRI).

(http://news.vanderbilt.edu/2016/03/chekmenev-elected-to-russian-academy-of-sciences/checkmenev_eduard/)

Eduard Chekmenev, Ph.D.

Chekmenev, who holds dual citizenship in Russia and the United States, said that, to his knowledge, he is the first American scientist to receive the honorary title of Professor of the RAS. The official award ceremony will be held in Moscow on March 21.

A native of Perm, Russia, Chekmenev earned his Ph.D. in Physical Chemistry at the University of Louisville and joined the Vanderbilt faculty in 2009. He currently is associate professor of Radiology and Radiological Sciences and Biomedical Engineering.

He and his team are developing hyperpolarized MRI probes that can produce significantly enhanced signals in high-throughput and low-cost molecular imaging. One day the probes may be used for population screening and to monitor the response of tumors to drug treatment, for example.

Chekmenev said the academy's honor comes with great responsibility.

As an RAS Professor, he joins a new generation of young scientists who provide expertise of the highest caliber to the Russian National Academy and other government agencies. He also will promote science to the general public.

Media Inquiries:
Bill Snyder, (615) 322-4747
william.snyder@Vanderbilt.Edu (mailto:william.snyder@Vanderbilt.Edu)

Recent Stories from VUMC News and Communications Publications

- Hope
  Care for Life (http://www.childrenshospital.vanderbilt.org/hope/?p=2232)
- Vanderbilt Medicine
  Off Limits: Doctors are working to research and treat the increasing number of Americans with severe food allergies (http://www.mc.vanderbilt.edu/vanderbiltmedicine/off-limits/)
- Vanderbilt Medicine 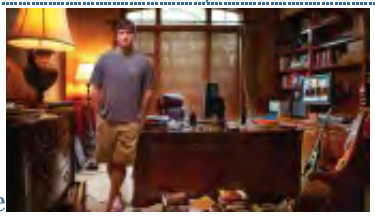
  These Doctors Mean Business: Med school graduates contributing in non-clinical roles (http://www.mc.vanderbilt.edu/vanderbiltmedicine/these-doctors-mean-business/)
- Momentum 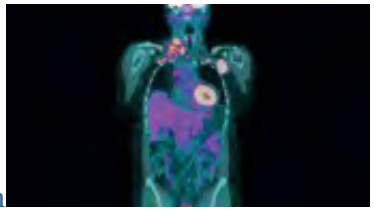
  Bringing Cancer to Light: Radiology's invisible energies play lead role in cancer care (http://www.vanderbilt.edu/magazines/momentum/2014/05/bringing-cancer-to-light/)
- Vanderbilt Nurse

Serving the never-served (http://www.vanderbilt.edu/vanderbiltnurse/2014/05/serving-the-never-served/)

more (http://news.vanderbilt.edu/section/vumc-publications/)

Find Us On:

(http://www.youtube.com/user/vanderbilthealth) (http://twitter.com/vumchealth) (http://www.facebook.com/VanderbiltHealth)

Like 177,071 people like this. Be the first of your friends.

Health Topics (http://www.vanderbilthealth.com/main/healthtopics) Doctors (http://www.vanderbilthealth.com/main/findadoc) Locations (http://www.vanderbilthealth.com/main/maps) Guide to VUMC (http://www.vanderbilthealth.com/newsite/information.php) My Health at Vanderbilt (https://www.myhealthatvanderbilt.com/myhealth-portal/app)
For Referring Physicians (http://staging.vanderbilthealth.com/main/24065) Giving (http://www.vanderbilthealth.com/main/27710) Volunteer (http://www.vanderbilthealth.com/volunteeratvanderbilt/) Media (http://www.mc.vanderbilt.edu/root/vumc.php?site=npa&doc=207) Quality Answers (http://www.vanderbilthealth.com/main/11159)
Careers (http://www.mc.vanderbilt.edu/careers/) Pay Your Bill (https://vanderbilt.patientcompass.com/hc/sp/vanderbilt/blindPayment) About VUMC (http://www.vanderbilthealth.com/main/guide) Feedback (http://www.vanderbilthealth.com/feedback.html?site=main&doc=11160&TB_iframe=true&height=460&width=400) Privacy Policy (http://www.vanderbilthealth.com/main/23526)
Popular Links A-Z Directory (http://www.vanderbilthealth.com/main/AtoZDirectory) Medical Record Information (http://www.vanderbilthealth.com/main/guide) Key Telephone Numbers (http://www.vanderbilthealth.com/main/guide)
Make an Appointment (http://www.vanderbilthealth.com/main/guide)
Vanderbilt University Medical Center
1211 Medical Center Drive
Nashville, TN 37232
(http://www.vanderbilthealth.com/main/maps)

(615) 322-5000

VANDERBILT UNIVERSITY MEDICAL CENTER (http://www.vanderbilthealth.com)

Vanderbilt University is committed to principles of equal opportunity and affirmative action. © (http://news.vanderbilt.edu/manage/wp-admin/) 2016 Vanderbilt University Medical Center.
Site Development: University Web Communications (http://web.vanderbilt.edu/)